

A - OPERATION AND ECONOMICS

- THE NORTHERN SEA ROUTE AS A NEW ROUTE FOR MARITIME TRANSPORT BETWEEN THE FAR EAST AND EUROPE** **A74**
A. Dávid, A. Galieriková, J. Tengler, V. Stupalo
- THE VISCOSITY EFFECT ON VELOCITY OF A MACROSCOPIC VEHICULAR TRAFFIC MODEL** **A80**
E. J. Lopez-Sanchez, N. Y. Sanchez-Torres, P. E. Olivera Martinez
- THE MODEL OF CONTAINER FEEDER LINE ORGANIZATION FOCUSED ON THE NATURE AND PARAMETERS OF EXTERNAL CONTAINER FLOWS** **A94**
O. Drozhzhyn, Y. Koskina
- COVID-19 GROUNDED AIRCRAFT - PARKING AND STORING** **A103**
F. Serrano, A. Kazda
- UNDERSTANDING HOUSEHOLD'S TRAVEL COSTS BUDGET FRONTIER IN BANDA ACEH, INDONESIA** **A116**
S. Sugiarto, Lulusi, M. Isya, F. Apriandy, F. Ramadhan

B - MECHANICAL ENGINEERING

- CORROSION BEHAVIOUR OF PRESERVED PEO COATING ON AZ31 MAGNESIUM ALLOY** **B76**
F. Pastorek, M. Štrbák, D. Kajánek, M. Jacková, J. Pastorková, Z. Florková
- OPTIMIZATION OF INGREDIENTS UPON DEVELOPMENT OF THE PROTECTIVE POLYMERIC COMPOSITE COATINGS FOR THE RIVER AND SEA TRANSPORT** **B89**
A. Buketov, S. Yakushchenko, A. Menou, O. Bezbakh, R. Vrublevskiy, Y. Kalba, T. Cherniavska, D. Zhytnyk, O. Danylyuk
- GENERAL CHARACTERISTICS FOR LOADING THE WORKING ELEMENTS OF DRILLING AND MILLING MACHINES WHEN MOVING IN THE CLAY SOLUTION** **B97**
A. Kadyrov, Z. Zhunusbekova, A. Ganyukov, I. Kadyrova, A. Kukesheva
- POSSIBILITIES OF ENERGY HARVESTING FROM THE SUSPENSION SYSTEM OF THE INTERNAL COMBUSTION ENGINE IN A VEHICLE** **B106**
J. Caban, G. Litak, B. Ambrozkiewicz, L. Gardyński, P. Stączek, P. Wolszczak
- FUZZY LOGIC METHOD FOR THE SPEED ESTIMATION IN ALL-WHEEL DRIVE ELECTRIC RACING VEHICLES** **B117**
A. Bonfitto, S. Feraco, M. Rossini, F. Carlomagno
- ASSESSMENT OF TECHNICAL CONDITION OF AN ACCUMULATOR COMMON RAIL INJECTOR BY TEMPERATURE OF ITS UNITS** **B130**
I. Gabitov, A. Negovora, A. Valiev, V. Ilin, D. Plotnikov, M. Razyapov
- INTERPRETING THE MAIN POWER CHARACTERISTICS CHOICE OF THE WHEEL VEHICLES GUIDED CUSHIONING SYSTEM** **B139**
B. Sokil, O. Lyashuk, M. Sokil, Y. Vovk, V. Dzyura, V. Aulin, R. Khoroshun

FORMING COMFORTABLE MICROCLIMATE IN THE BUS COMPARTMENT VIA DETERMINING THE HEAT LOSS	B150
O. Kravchenko, I. Hrabar, J. Gerlici, S. Chuiko, K. Kravchenko	

DYNAMICS AND CONTROL OF THE GYROSCOPIC HEAD USED FOR THE LASER ILLUMINATION OF A GROUND TARGET FROM THE QUADCOPTER DECK	B158
Z. Koruba, I. Krzysztofik	

C - ELECTRICAL ENGINEERING

A FRAMEWORK COUPLING VISSIM AND OMNET++ TO SIMULATE FUTURE INTELLIGENT TRANSPORTATION SYSTEMS	C23
T. Petrov, I. Finkelberg, N. Zarkhin, P. Počta, L. Buzna, A. Gal-Tzur, T. Kováčiková, T. Toledo, M. Dado	

MODELS OF THE COMPUTER INTELLECTUALIZATION OPTIMAL STRATEGY OF THE POWER SUPPLY FAST-FLOWING TECHNOLOGICAL PROCESSES OF THE RAILWAYS TRACTION SUBSTATIONS	C30
A. Stasiuk, V. Kuznetsov, L. Goncharova, P. Hubsnyi	

ENERGY CHARACTERISTICS OF THE DC DISTRIBUTED POWER SUPPLY SYSTEMS	C37
V. Sychenko, V. Kuznetsov, A. Rojek, P. Hubsnyi, Y. Kosariev	

CLASSIFICATION ACCURACY ENHANCEMENT BASED MACHINE LEARNING MODELS AND TRANSFORM ANALYSIS	C44
H. A. R. Akkar, W. A. H. Hadi, I. H. Al-Dosari, S. M. Saadi , A. I. Ali	

MATHEMATICAL MODELLING OF OSCILLATORY PROCESSES IN TRANSMISSION OF MOVEMENT OF AN ELECTRIC DRIVE WITH NON-LINEAR LONG ELASTIC ELEMENTS	C54
A. Chaban, T. Perzynski	

IMITATION MODELING OF AN INTER-TURN SHORT CIRCUIT OF AN ASYNCHRONOUS MOTOR STATOR WINDING FOR DIAGNOSTICS OF AUXILIARY ELECTRIC DRIVES OF TRANSPORT INFRASTRUCTURE	C65
S. Goolak, J. Gerlici, O. Gubarevych, T. Lack, M. Pustovetov	

D - CIVIL ENGINEERING IN TRANSPORT

MEASUREMENT AND ANALYSIS OF THE NOISE LEVEL IN SELECTED ZONES OF BUS STOPS IN THE CITY OF RADOM	D26
T. Perzyński	

E - MANAGEMENT SCIENCE AND INFORMATICS

THE GPS / EGNOS POSITIONING QUALITY IN APV-1 AND LPV-200 FLIGHT PROCEDURES	E23
G. Grunwald, A. Ciećko, K. Krasuski, R. Kaźmierczak	

F - SAFETY AND SECURITY ENGINEERING

SELECTED ASPECTS OF THE ROAD TRAFFIC SAFETY MANAGEMENT SYSTEM	F33
M. Stoma, J. Caban, A. Dudziak, A. Kuranc	

**A CASE STUDY INTO THE SAFETY COMPLIANCE WITHIN THE ROAD FREIGHT
TRANSPORT SECTOR WITH REGARDS TO SECURING CARGO**

J. Ližbetin, M. Stopková

F43

G - TRAVEL AND TOURISM STUDIES IN TRANSPORT DEVELOPMENT

**USING DATA ON BIKE-SHARING SYSTEM USER STOPOVERS IN SMART TOURISM:
A CASE STUDY**

K. Banet

G1

THE NORTHERN SEA ROUTE AS A NEW ROUTE FOR MARITIME TRANSPORT BETWEEN THE FAR EAST AND EUROPE

Andrej Dávid^{1,*}, Andrea Galieriková¹, Jiří Tengler¹, Vlatka Stupalo²

¹University of Zilina, Zilina, Slovakia

²University of Zagreb, Zagreb, Croatia

*E-mail of corresponding author: andrej.david@fpedas.uniza.sk

Resume

Asian countries such as China, Malaysia, India or Bangladesh belong to the largest producers of consumer goods in the world that is mainly transported by container vessels to other parts of the world. One of the busiest maritime trade route is the route between Europe and Asia. It leads through the North Pacific, Indian and the North Atlantic Oceans and their seas. There is also an alternative trade route that runs along the coast of the Russian Federation across the Arctic Ocean. On one hand the ice in this area is gradually declining due to global warming, on the other hand the duration of navigation times is being extended for several months of the year. One of the advantages of this route is the reduction of sailing times between Asian and European maritime ports. The basic goals of the paper are to focus on the current transport situation on this trade route and a new trade route that leads along the coast of Russia.

Article info

Received 11 May 2020

Accepted 27 May 2020

Online 17 December 2020

Keywords:

maritime transport,
piracy,
maritime trade routes,
Northern Sea Route

Available online: <https://doi.org/10.26552/com.C.2021.2.A74-A79>

ISSN 1335-4205 (print version)

ISSN 2585-7878 (online version)

1 Introduction

Maritime transport has got the biggest share in the cargo transport by seagoing vessels in the world. Asian countries such as China, India, Bangladesh or Vietnam have become the leaders in the production of consumer goods since the end of the 20th century. Brand mark companies that have got their headquarters in the developed countries situated in North America or Europe have moved their subsidiaries into developing countries located in Asia. These countries provide not only cheap labour force but also produce the goods that are accessible for most consumers from the point of view of price.

Transport of these goods takes a few weeks and seagoing vessels have to sail thousands of nautical miles. Most of these goods are transported into containers due to faster handling operation in the maritime ports and the protection of goods against stealing, loss or damage. In the last twenty years the volume of containers between Asia and Europe has increased more than four times. The old maritime trade route runs through the North Pacific Ocean, the South China Sea, the Strait of Malacca, the Indian Ocean, the Bab-el-Mandeb Strait, the Suez Canal, the Mediterranean Sea and the North Atlantic. There are some risk areas as the result of piracy.

There is also an alternative trade route (Northern Sea Route), which runs along the coast of the Russian Federation across the Arctic Ocean. On one hand global warming has led to a gradual ice decline in the region, on

the other hand the voyage period has been extended to several months. This route is shorter than the old maritime trade route, but it still has some disadvantages such as the duration of navigation period or the dependence on the weather conditions. The basic goal is to focus on this route from the point of various criteria and to bring a new view on transport of cargo by maritime transport.

In the last few years the authors of the paper have performed their research that have been focused on transport of cargo by maritime transport between the Far East and Europe including the environmental changes in the Arctic zone as the result of the global warming, their impact on traffic and transport of cargo including the legislation that regulates maritime transport and transport of cargo in this part of the world. The part of this research is also presented in this paper with emphasis on an alternative trade route between the Far East and Europe along the coast of the Russian Federation.

2 Changing conditions in the Arctic

The Arctic is an area close to the North Pole. Its boundaries can be determined in various ways. It is either defined as the area in the north from the Arctic Circle, or as the area where the average temperature does not reach more than 10 °C even in the summer months. The Arctic Ocean is spread over most of the Arctic and it is completely covered with ice or partially thawed with floating hatchets



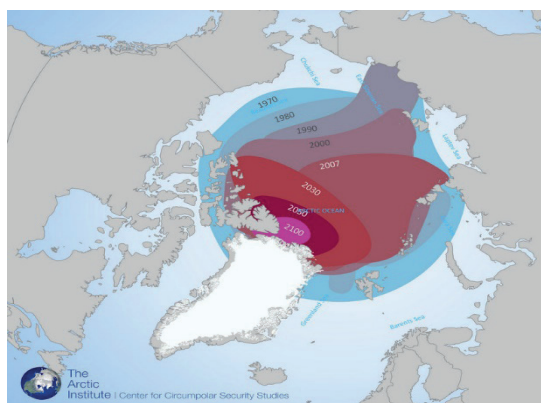


Figure 1 Development of Arctic glaciation for the period 1970 - 2100 [2]

for most of the year. The rest of the territory is made up of the northern parts of Asia, Europe and Greenland. The Arctic covers 8% of the earth's surface and due to climate change, the global warming is most pronounced here. The melting rate of glaciers is twice as originally expected. Since 1979, the frozen area has decreased by up to 40%. In 2012, there was the largest decrease in these areas. The frozen area was 14.5 million km² in the area around the North Pole. It was approximately 1.1 million km² less than the long-term average for the period 1981-2010. There is usually the most sea ice in February. The lowest measured value in this month was in 2015. Arctic ice will decrease by an average of 3.8% over a period of ten years. If this trend continues, in the second half of this century there will be no more ice in the Arctic during the summer. The following figure shows the level of glaciation since 1970. It can be seen that the ice surface is receding rapidly. In addition, it captures possible future developments until 2100, when the icy area in the Arctic is expected to be minimal and to reach only the northern part of Canada (Figure 1) [1].

International law states that no state owns the North Pole or the ocean in its immediate vicinity. However, there are the so-called "Arctic states", which include the USA, Russia, Canada, Norway and Greenland. Each of these states can claim an exclusive economic zone representing a marine area within a distance of 370 km from the coast. However, there are several contradictions as to whether other parts of the sea fall within areas belonging to national or international waters. The Arctic states also include Sweden, Finland and Iceland, despite extending into the area north of the Arctic Circle only in part of their territory. These states have been the core of the so-called Arctic Council, which is currently probably the most important international forum of the states of the Arctic region. Russia is considered the strongest player because it is investing tens of billions of US dollars (USD) to build infrastructure in the area. These are mainly investments in the mining industry. It is estimated that up to 95% of the Russian Federation's natural gas reserves and 60% of oil reserves are hidden in the Arctic. The Arctic region should hold as much as 25% of the world's oil and gas reserves. The local waters are also rich in other sources of mineral wealth such as phosphates, iron ore, nickel, cobalt, copper, uranium and

gold. Due to climate change, the extraction of raw materials in this area is becoming more and more achievable. In addition to Russia, China is also interested in local mining opportunities, as it is one of the world's major importers of the raw materials. There are two benefits to extending the period of ice melting in the Arctic. The first is availability of minerals for mining companies, the second is the possibility of these companies to use one of the offered sea routes for transport of the raw materials [3].

As the results of the changes mentioned above, the authors suggest updating the present legislation that regulates maritime transport in the Arctic zone. On one hand these changes may stimulate maritime transport and transport of cargo in this part of the world. On the other hand, they may influence development of environment negatively such as an accelerated process of melting of icebergs or harmful impact on the animals living in in this part of the world. A lot of animals that live there are on the edge of extinction.

3 The main trans - Arctic routes

A global warming in the area around the North Pole offers new opportunities from the point of maritime transport. The parts of the Arctic may become more reliable for navigation during the summer months of the year. The term "major trans-Arctic routes" includes the Northwest Passage (NWP) and the Northeast Passage (NEP).

While on the NWP is one of the possible routes connecting the Pacific and Atlantic Oceans along the Canadian coast, NEP is any sea route connecting Europe and Asia bordering the northern coasts of Norway and Russia (Figure 2).

The Northwest Passage is not as easily accessible as the Northeast Passage. This is mainly due to the wider ice cover of the Canadian islands in the Arctic. Another reason is the almost non-existent infrastructure and commercial transport. Only 10% of this area is sufficiently mapped, so any activity in this area is more for research purposes. In 2011, only 26 vessels used this route, but none of them carried cargo [5]. An alternative route for the Northwest Passage is a route through the Panama Canal. The Northeast



Figure 2 The main trans-Arctic routes (comparison) [4], adapted by authors

Passage could compete with the shipping route leading through the Suez Canal. At on the first glance, a significant difference in distances is visible. In both cases, the route through the Arctic is significantly shorter than the present shipping routes. The NWP is 7,000 km shorter than the Panama Canal route, the length of NEP is two-thirds that of the traditional Suez Canal route. Shorter distances mean shorter transport times, fuel consumption and costs.

The Northern Sea Route is a shipping route that runs along the Russian Arctic coast from the Kara Sea, along Siberia, to the Bering Strait. While on the NEP includes all the East Arctic seas and connects the Atlantic and Pacific oceans, the Northern Sea Route does not include the Barents Sea and it therefore does not reach the Atlantic.

4 The Northern Sea Route

The Northern Sea Road runs along the Siberian coast. The routes leading through this area connect Russian ports, Far Eastern ports and the mouths of Siberian navigable rivers into one transport system. The North Sea Route begins in the Barents Sea and ends in Providence Bay.

Recently, the situation around this route has begun to change rapidly. Due to the effects of global warming, the navigation period of vessels has increased significantly. Whereas in the past the navigation period lasted from July to September, it currently lasts from June to November. In addition, several factors need to be taken into account that may attract the attention of foreign companies in this direction in the coming years:

1. The average delivery time through the Suez Canal is 48 days and the route across the Arctic seas is 35 days, i.e. consequently, delivery times, fuel and transport costs are significantly reduced and saved.
2. There are no delays and fees for the passage of vessels (unlike the Suez Canal). The only charge is use of an icebreaker, which navigates this route.
3. Absence of illegal actions (pirate raids).
4. No restrictions on vessels related to their size and tonnage [6].

4.1 The arising risks during the cargo ship voyages

A big problem in implementation of voyages on these routes is the equipment of ships. Most of today's vessels are not capable of navigating in the Arctic conditions. Even in the periods when the route is navigable, the terrain remains unpredictable and very dangerous. Only special vessels that are able to withstand local conditions are adapted to navigate in the difficult conditions. Navigation in the Arctic is not just about making the route through the frozen or semi-frozen ocean. It also involves very demanding planning. To avoid the high pressure on the hull, it is necessary to choose a route that avoids the hidden ice stream. An experienced captain should be present during the voyage to avoid an adverse situation due to the human factor. Most ships passing through the Arctic cannot be accompanied by icebreakers throughout the journey. Russia and Canada use icebreakers only in the most frozen parts of the Arctic sea routes, due to their high costs. Therefore, passing ships are at great risk (hidden glaciers). In the event of a collision, there is a high chance for a disaster, due to the fact that there are currently not enough rescue services in the Arctic [7-8].

Development of the maritime transport in the Arctic is hampered by a number of factors, such as short voyage time during the year, unpredictability of ice, high costs of sailing with icebreakers and costs of permitting navigation along the Russian coast, absence of a sufficient number of ships capable of sailing in frozen areas and the high costs of risk insurance. This is especially true for the container transport, for which regular crossing of the North Sea Road is still in sight. For development of the container transport in this area, it is necessary to increase shipping traffic so that consignments can be consolidated. Due to implementation of a lower number of cruises in this area, this is not possible. Therefore, the costs remain higher.

The weaknesses in the current maritime route from China to Europe are beginning to manifest with the growth of international trade. On one hand there are pirate attacks on this route. On the other hand, the Suez Canal is often congested and vessels wait several hours. Development of

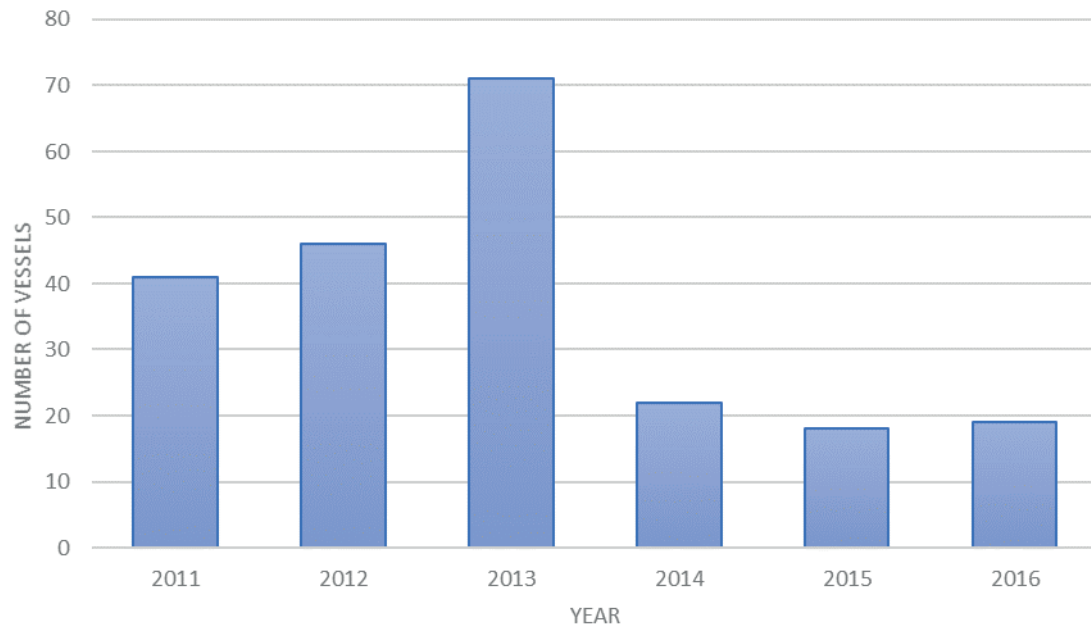


Figure 3 The number of vessels that passed through the Northern Sea Route between 2011 and 2016 [2]

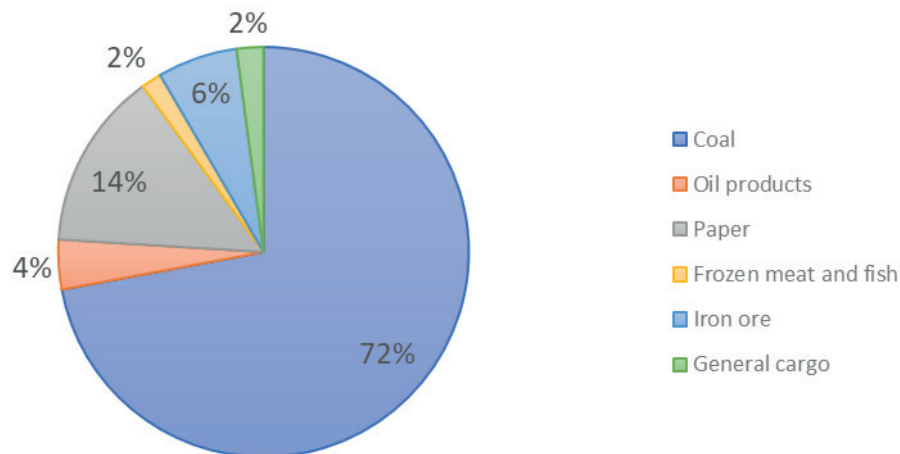


Figure 4 Type of cargo transported on the North Sea Road in 2016 [2]

the North Sea Route is a multilateral project, which will also contribute to the socio-economic recovery of the northern regions of Russia. As a result, Russia could increase its share of international commodity markets in this area. The Northern Sea Route is the only link in the Arctic region between Russia's subarctic and Arctic regions. It has a great influence on development of the north of Russia [7].

Analysts estimate that the route along the Russian coast has a throughput of about 50 million tons per year [8]. This route is becoming more popular every year. The reason is the growing activity of oil and gas companies in the Arctic. Private investors also play a major role. Until 2000, Russia paid little attention to Arctic infrastructure. However, the government has recently taken active steps in this direction. Russia aims to regain its former dominance in the Arctic. In 2008, Russia adopted the "Strategy for Development of the Arctic Region of the Russian Federation until 2020",

in which the Arctic acts as a key strategic territory of the country. The main objectives of this strategy are:

- creation of a common transport area,
- more involvement in the global transport chain while making maximum use of its own transport routes,
- provision of affordable and quality transport services,
- reducing the negative environmental impacts in the Arctic.

Development of the transport infrastructure and transportation in this area can have a positive impact on the Russian economy. The interest in the development of the North Sea Route in Russia is also due to the fact that it owns by far the largest fleet of icebreakers in the world. It can get big money for renting them. Japan is also interested in participating in the development of this route. Due to the location of this country, its use is more important than for other states. For Japan, this is the fastest way to deliver

goods to Europe. The Japanese estimate that up to 40% of their goods imported into Europe should be exported through this route. In addition to Japan, China is also interested in the area, which has its own ground program called the “Silk Road” [9].

4.2 Transport of cargo

Arctic maritime routes allow more efficient, shorter and several times faster transport between the Far East and Europe. There are big differences in transport statistics (Figure 3). While in 2010, the fewest vessels passed through this area (only four vessels), in 2013, 71 vessels passed through the Arctic. In 2014, there was a significant decrease, only 25 ships crossed the Russian coast. In 2016, 19 ships crossed the route. These vessels carried approximately 214,500 tons of cargo. This route had the greatest expansion in 2017, when up to 9.7 million tons of cargo were transported. The stagnant development of maritime transport in the Arctic is mainly attributed to difficult natural conditions and shipping companies, which perceive it as unprofitable.

In 2016, the most coal was transported on this route (154,522 tons), which represented up to 72% of the total transported cargo (Figure 4). The second most important item was paper (30,042 tonnes), about 14% of the total. Other commodities were also transported here, the volumes of which were not as extensive as in the previous cases. These were mainly iron ore, petroleum products, piece cargo, frozen meat and fish.

5 Discussion

As the result of the carbon burning the human-being has been producing harmful gases (carbon dioxide or methane) that influence the gradual raising of the atmosphere temperature, consequent iceberg melting and sea level rise. If the human-being does not reduce the pace of production of these gases, in a near future we will face gradual flooding of some parts of the world, population migration or extinction of some animal species.

In spite of the changes that have happened in the construction of new engines that use fuels with lower level of sulphur, nitrogen and carbon, the maritime transport, especially the sea going vessels, also belong to the biggest producers of these harmful gases. Maritime transport has had the biggest share in transport of all the types of cargo between the continents in comparison to other modes of transport. The ship-owners have optimized the cargo ship voyages due to faster cargo delivery, reducing of transport costs and profit maximization. They have also tried to find new alternative ways how to transport cargo.

The Northern Sea Route that leads along the coast of the Russian Federation could become a new trade and transport route between the countries of the Far East and the European Union. The former Soviet Union used it for

transport of raw materials extracted in the Arctic zone. The navigation time has been prolonged in this part of the world as a result of the global warming. In the near future, ship-owners could use it due to faster cargo transport between Europe and Asia. On the other hand, these voyages could have negative impact on the environment in the Arctic zone in the form of faster iceberg melting and extinction of some animal species. The humans should consider what is more advantageous for them.

6 Conclusions

It will take about another two decades for the North Sea Road to be integrated into the main maritime trade routes. In spite of the fact this route is a shorter route than the present trade route that leads the Far East and Asia, one of the biggest disadvantages of this route is the fact that there is no possibility of rescue in the case of a dangerous situation. The Russian Federation is trying to build nine rescue centres that could help in the accident events. Each of these centres will be equipped with helicopters, fire and rescue services. The plan also includes the construction of thirty automated observation stations and weather monitoring equipment [10].

The Russian government's forecasts are very positive. They expect the volume of cargo transported in this area to increase by 20% over the next 15 years. This would mean an increase of more than 80 million tons of cargo. However, after many analyses, this development seems slightly exaggerated. Especially for the container transport, such estimates are unrealistic. Some experts believe that this route will be mainly the international transport of hydrocarbons in the future.

Using this route eliminates the problem of piracy, which occurs mainly in the Straits of Malacca, the island of Sumatra or the Gulf of Aden. There are also no narrowed places or canals up to the Bering Strait. The biggest shortcoming of the North Sea Road is the lack of infrastructure for regular voyages. Development of transport in the Arctic could also be prevented by various groups of animal welfare workers. If regular transports took place in the Arctic, it could have a negative impact on the local ecosystems and the melting of glaciers. Therefore, some environmental organizations are very critical of the use of this route.

Based on the latest estimates, it is estimated that in 15 to 20 years, the North Sea Road would be used throughout the year. At present, the interest of carriers for its use is rather declining. It may take several more decades for a regular liner shipping route to operate here. The container transport is already technically possible, but not so economically advantageous.

The main advantage of this route is that the transport time and distance is shorter, but the fees associated with implementation of transport are higher. In addition to the Russian Federation, China also plans to transport 5 to 15% of its cargo via the container route over the next ten years [11-12]. However, despite the major shortcomings,

the North Sea Road has its advantages. If the price of oil increases, the usability of the northern sea route may increase sharply [13-14]. The following facts need to be resolved for the successful development of this route:

- the authorization process for the passage of vessels through this area - the decision should be clear and comprehensible to the carrier,
- the need to introduce uniform rates for transport along the entire North Sea route,
- it is necessary to attract the world's major shipping companies so that they can take part in the planning of vessels operating on Arctic routes,

- establishing coordination of work of all the ports through which the North Sea Road passes.

Acknowledgements

The paper is supported by the VEGA Agency by the Project 1/0798/21 "The Research on the Measures to Introduce Carbon Neutrality in the Rail and Water Transport" that is solved at Faculty of Operation and Economics of Transport and Communications, University of Zilina.

References

- [1] JANSKY, B. Impact of Climate Changes on the Arctic / Vliv klimatických zmen na Arktickou oblast (in Czech). *Geografické rozhledy* [online] [accessed 2020-05-10]. 2011, 5(10-11), p. 22-25. ISSN 1210-3004. Available from: <https://www.geograficke-rozhledy.cz/archiv/clanek/506/pdf>
- [2] Russian PM orders to increase Northern Sea Route capacity by 20 times [online] [accessed 2019-05-10]. Available from: <https://www.rt.com/business/265756-northern-sea-route-medvedev/>
- [3] The emerging artic - Council on foreign relations [online] [accessed 2019-03-18]. 2014. Available from: http://www.cfr.org/polar-regions/emerging-arctic/p32620#/?cid=otr_marketing_use-arctic_Infoguide#
- [4] World map [online] [accessed 2019-03-11]. Available from: https://en.wikipedia.org/wiki/File:World_Map_WSF.svg.png
- [5] Short and sharp - The economist [online] [accessed 2019-01-28]. 2012. Available from: <http://www.economist.com/node/21556803>
- [6] The Northern Sea Route [online] [accessed 2019-02-18]. 2017. Available from: <https://xsreality.org/sk/severnyj-morskoj-put-severnyj-morskoj-put-ego-osvoenie-i-razvitie-vyzyvaet-bolshoj-interes-uchenyh-issledovatelej-nashej-strany-i-zarubezhnyh-spetsialistov-ego-istoriya-eto-interesnejshie-ekspeditsi/>
- [7] GEORGESCU, C. Northern Sea Route. Knowledge Horizons - Economics [online] [accessed 2019-03-19]. 2014. Available from: http://www.orizonturi.ucdc.ro/arhiva/2014_khe_6_pdf4/georgescu_1.pdf
- [8] BAMBULYAK, A., EHLERS, S. Oil spill damage: a collision scenario and financial liability estimations for the Northern Sea Route area. *Ship Technology Research* [online]. 2020, 67(3), p. 148-164. ISSN 0937-7255, eISSN 2056-7111. Available from: <https://doi.org/10.1080/09377255.2020.1786932>
- [9] WANG, D., DING, R., GONG, Y., WANG, R., WANG, J., HUANG, X. Feasibility of the Northern Sea Route for oil shipping from the economic and environmental perspective and its influence on China's oil imports. *Marine Policy* [online]. 2020, 118, 104006. ISSN 0308-597X. Available from: <https://doi.org/10.1016/j.marpol.2020.104006>
- [10] The Northern Sea Route Facts - Arctic-lio [online] [accessed 2019-03-18]. 2016. Available from: http://www.arctic-lio.com/nsr_transits
- [11] The Most Ambitious Chinese Megaproject Mapped – a New Silky Road - Financial market [online] [accessed 2018-01-18]. 2018. Available from: <https://www.financnytrh.com/najambicioznejši-cínsky-megaprojekt-zmapovaný-nova-hodvábna-cesta/>
- [12] BENNETT, M. The Northwest Passage versus the Northern Sea Route [online] [accessed 2019-01-19]. 2011. Available from <https://cryopolitics.com/2011/08/19/the-northwest-passage-versus-northern-sea-route/>
- [13] Arctic shipping. Position paper - ICS [online] [accessed 2019-03-07]. 2014. Available from <http://www.icsshshipping.org/docs/default-source/resources/policy-tools/ics-position-paper-on-arctic-shipping.pdf?sfvrsn=20>
- [14] JURKOVIC, M., KALINA, T., SOSEDOVA, J., TVRDA, E. Globalisation of the LNG trade in Caspian region. In: 16th International Scientific Conference Globalization and its socio-economic consequences: proceedings. University of Zilina. 2016. ISBN 978-80-8154-191-9, ISSN 2454-0943, p. 793-799.

THE VISCOSITY EFFECT ON VELOCITY OF A MACROSCOPIC VEHICULAR TRAFFIC MODEL

Erick Javier Lopez-Sanchez^{1,*}, Norma Yanet Sanchez-Torres², Patricia Eugenia Olivera Martinez³

¹Faculty of Philosophy and Letters, National Autonomous University of Mexico, Coyoacan, Mexico

²Faculty of Sciences, National Autonomous University of Mexico, Coyoacan, Mexico

³Critical Urban Studies Seminar, Geography Department, Faculty of Philosophy and Letters, National Autonomous University of Mexico, Coyoacan, Mexico

*E-mail of corresponding author: lsej@ciencias.unam.mx

Resume

Traffic in Mexico City poses a serious problem of vehicle saturation that causes a decrease in speed and increased transport time in the streets that suffer mobility collapses. A macroscopic model of vehicular traffic is used to show the effect of viscosity on the vehicular variables (speed and vehicle density), applied to two avenues in Mexico City, is studied. The input parameters were calculated following the Greenberg model. As the original model presents numerical divergences, the two assumptions corresponding to conservation of the vehicle's mass and the viscous term are modified. The results suggest that the viscosity depends on time and that it can be adapted to recommend modifications in urban mobility parameters, or even to implement the public planning policies in construction of infrastructure for urban transport, to make vehicle flow more efficient.

Article info

Received 15 May 2020

Accepted 11 August 2020

Online 18 December 2020

Keywords:

Greenberg traffic model, viscosity, vehicular density, vehicular velocity, numerical simulations

Available online: <https://doi.org/10.26552/com.C.2021.2.A80-A93>

ISSN 1335-4205 (print version)

ISSN 2585-7878 (online version)

1 Introduction

Transport is a part of the urbanization process produced within a host of intentions, such as real estate, residential developments, productive location and points of commerce in its various formats. The transport is implicit to any of them and together they continually reorganize the urban spaces, forming and destroying networks of exchange of these activities. The transport role is very significant for organization of urban spatiality since transport systems in large metropolises are essential for labor and student mobility, circulation of goods, delivery of services, and many other reasons in the productive and social spheres. According to the differential intensities of local, intrametropolitan, and even regional scales, the transport saturation derived from vehicular flows and vehicular densities generates frequent problems of mobility.

Time plays a critical role, jointly mobility is associated with transport efficiency. The traffic volume also responds to a group of elements, such as increases in population density, structure of the hierarchical road map, routes of means of transport and their connectivity, mass of circulating vehicles and the transport hubs that are configured in the metropolis by the origin-destination concentrations. Vehicular traffic is studied over the world because of increase of the mobility generalized problems. Most of the studies are centered in the vehicular flow, in

which they relate the vehicular speed and the density of the traffic.

Vehicular traffic models have been developed since 1935. From measured data of speed, vehicular flow and vehicular density using a 16mm simplex movie camera to take pictures and an electric motor driven by an automobile storage battery operated the camera with a constant time interval between exposures, Greenshields [1] deduced one of the first traffic models. Later, Lighthill and Whitman [2] and Richards [3] built their model based on the advection equation. Macroscopic traffic models were made based on the Navier-Stokes and continuity equations, for example, the Greenberg model [4], Newell model [5], Paveri-Fontana model [6], Helbing model [7], among others [8-16]. A genealogy of traffic models has been described by van Wageningen-Kessels et al. [17].

Most of these models are validated in segments of streets or avenues in which they do not have intermediate entries or exits of vehicles, i. e. the number of cars that enter from one side of the road, is the same as the one that leaves from the other side. In that sense, there is a conservation of mass. However, most vehicular roads do not have that property. Some streets end in avenues, while there are streets that interconnect with other ones. In this aspect, there is no necessarily a mass conservation. For instance, the Greenberg model is based on the fundamental equations of fluid mechanics, assuming that the vehicle



flow is compressible. Greenberg's data match with his model because they referred to the extreme sides of the Lincoln tunnel under the Hudson River, which divides New Jersey from New York. In this place, there is no possibility of an intersecting street. Greenberg proposes that speed is a function of vehicle density, which simplifies the equations for the analytical solution.

On the other hand, vehicular traffic in Mexico City entails serious challenges due to saturation, conflicting nodes, intermittent connectivity, because the transport demand is greater than the transport offer and the growing vehicle park, all of them causing the drop-in velocity. Because of the traffic saturation, travel time increases gradually. According to travel costs, collective public transport does not raise tariffs, but private transport expenditures augment, as well for transport companies.

In the Metropolitan Area of Mexico City (ZMCM) in 2017, there were 34,558,217 trips per day, within the urban area of 214,791 hectares [18]. In 1994 there were 20,573,700 trips per day [19], that is, these increased by more than 608,000 trips per year. In Mexico City, the average travel distance is 20.9 km. The mean speed of all the kinds of transport has fallen from 38.5 km h⁻¹ in 1990 to 13.8 km h⁻¹ in 2017 [20]. The average speed of a bus is 8.8 km h⁻¹, the mean velocity in the metro is 21.1 km h⁻¹, in express transport (Metrobus) is 13.9 km h⁻¹. The average travel time is 90.6 minutes and it continues to increase [21]. The vehicular speed between the origin and destination points are decreasing slowly [22].

The problems that aggravate the road congestion in the ZMCM are associated with the growing private fleet. In 2017 it reached more than 6 million vehicles [18], the private only mobilize 30% of total trips, and the concessional has a low capacity of transportation [21]. The urban layout and the continuity of the primary roads are interrupted because of the conurbation of more than 145 native towns. With immigrants from the whole country, these old towns grew rapidly conserving a very narrow road network.

In this paper, a modified Greenberg model is used, which considers the loss or gain of vehicular mass in the selected road segment with intermediate inputs and outputs [23-25], and the viscosity term to the motion equation, to simulate the traffic variables in two cases. The viscosity is interpreted as the high-grade driver anticipation [26].

The model is solved completely using a numerical method. The initial and boundary conditions (Dirichlet conditions [27-29]) of the traffic model are measured data about speed, vehicular density and vehicular flow that has been taken at peak hours, registered for 3 hours in a working day in two roads of Mexico City.

The objective of this work was to study the effect of viscosity on the traffic variables by simulating with a modified Greenberg model, using measured data of the traffic variables as the initial and boundary conditions. Simulations are carried out to observe behavior of the traffic variables in the entire domain when the viscosity varies. The viscosity is important because it can relate to urban mobility parameters.

The work is organized as follows. The data collection methodology is shown in section 3. The modified traffic model is presented in a general way in section 2. The places of observation and data collection in Mexico City, as well as the data analysis, are shown in section 4. Section 3.2 contains the numerical method used to solve the system of partial differential equations of the traffic model and the numerical results are presented in section 5. Finally, a summary is presented in section 6.

2 Theoretical framework

2.1 The Greenberg model

Greenberg built his model from the one-dimensional motion of a fluid equation [30]:

$$\frac{Du}{Dt} = -\frac{c^2}{k} \frac{\partial k}{\partial x}, \quad (1)$$

where u : traffic velocity, km per hour, k : density of traffic, vehicles per km; x : distance along the road, t : time, c : a parameter that is determined from the state of the fluid and $D/Dt = \partial/\partial t + u\partial/\partial x$ is the material derivative.

The continuity equation is written as:

$$\frac{\partial k}{\partial t} + \frac{\partial q}{\partial x} = 0. \quad (2)$$

Here $q = u k$ is the traffic flow [vehicles per hour], it represents the flow rate in fluids. All of them are functions of the position x and the time t :

$$q(x, t) = u(x, t)k(x, t). \quad (3)$$

The Greenberg's model [4] has a significant assumption, which is demonstrated that it was not always satisfied. That supposition is the velocity depends on the density $u = u(k)$, and then the system Equations (1) and (2) becomes the following equation¹:

$$\frac{du}{dk} = -\frac{c}{k}. \quad (4)$$

The solution of Equation (4) is

$$u(k) = c \ln\left(\frac{k_{jam}}{k}\right), \quad (5)$$

where k_{jam} is the density for the traffic jam ($u = 0$). That means the density as a function of the velocity has the form:

$$k(u) = k_0 e^{-u/c}. \quad (6)$$

2.2 Viscosity in the traffic

Equation (1) contains terms that are interpreted as actions concerning drivers: the nonlinear term ($u\partial u/\partial x$) is the convection and it represents changes of the average

¹ see [4] for details.

speed in a very small cell due to vehicles entering with different speeds; the pressure term ($c^2 k^{-1} \partial k / \partial x$) is the anticipation, that is, changes in speed due to anticipation of drivers in traffic conditions later on [26]. In this case, the pressure is directly proportional to the density ($P = c^2 k$), since the vehicular flow is assumed to be an ideal gas [24]. In this work, the viscous term is added as a pressure for which the speed changes with respect to the position:

$$P = c^2 k - \eta \frac{\partial u}{\partial x}. \quad (7)$$

The viscosity term in the acceleration equation is represented by the diffusive term in the traffic system. The speed diffusion is useful to improve the numerical properties of a model. Besides that, it helps to investigate the effects of numerical diffusion, which are unavoidable when numerically integrating macroscopic models [31]. The modified Greenberg model is:

$$\frac{\partial u}{\partial t} + u \frac{\partial u}{\partial x} = -\frac{c^2}{k} \frac{\partial k}{\partial x} + \frac{\eta}{k} \frac{\partial^2 u}{\partial x^2}, \quad (8)$$

$$\frac{\partial k}{\partial t} + \frac{\partial q}{\partial x} = f(t), \quad (9)$$

where η is the viscosity [km h^{-1}] and $f(t)$ must be proposed, estimated, or measured from the observational data.

The viscosity term can represent the driver's anticipation against any event [26]. If δ_v is the visibility distance (the distance at which the driver detects the eventuality: a person crossing the street, a bottleneck, a car slowing down, etc.) and τ_a the anticipation time, *i.e.* the time that the driver takes to prevent a crash, then one can define the viscosity as:

$$\eta = \frac{\delta_v}{\tau_a}. \quad (10)$$

3 Methodology

3.1 Data collection

Once the observation points are chosen, the traffic variables involved in the model are measured, namely, speed u , density k and capacity q . The speed is measured by fixing the two points on the road and observing the time that the vehicles spend to travel the distance between them. Subsequently, the distance between these two points is measured. With this, the average speed is calculated.

To measure the flow rate, vehicles passing through a fixed point in the road for one minute were counted. The number of vehicles per hour is estimated by multiplying the quantity measured by 60.

The density was measured by counting the number of vehicles in the segment between the points that were set to measure the speed. Thus, the number of vehicles per unit of distance was obtained. With a simple proportional relationship, the number of vehicles per km is determined.

These measurements were made every 10 min for approximately 3 h. To obtain an estimate of the intermediate

points among the measured data (where no measurements were taken), a cubic spline interpolation was carried out with each variable. The interpolated data were entered as input values in the model. Thus, the known values of the variables at the borders (Dirichlet conditions [27-29]) were obtained.

The model is solved by the finite difference method in combination with an iterative method [32-33]. The details are shown in section 3.2.

3.2 Numerical method

The system of the Equations (8)-(9) was solved numerically using the second-order finite differences method, backward for time and centered for position. The method convergence was evaluated increasing the number of mesh points. The mesh refinement finished when the solution was practically the same between the two consecutive refinements. The initial and boundary conditions were taken from the measured data. There was no assumption that velocity depends on density, as Greenberg did it (see section 2), the system of Equations (8)-(9) was solved as a whole. The solutions convergence was verified through the Courant number, defined as [24, 34]:

$$Co = |u| \frac{\Delta t}{\Delta x}. \quad (11)$$

If this non-dimensional number is lower than 1, then the solution converges.

The functions $k(0, t)$, $k(l, t)$, $u(0, t)$ and $u(l, t)$ (where l is the end of the line) were measured in discrete values, and $f(t)$ was calculated with those discrete values (see section 5). Then, all these functions have discrete domains. The cubic spline method was used to calculate the intermediate points and matching with the numerical meshes.

The numerical code was written in Matlab-script.

4 Observational traffic data

The observational data were obtained at two places in Mexico City, in a major avenue: Insurgentes at South of the city and Mexico-Toluca freeway at the western city entrance. These ways were chosen because they had a few lateral inners and exits, so that the function f should be very close to zero, but this was not quite possible.

4.1 Insurgentes Sur Ave

Figure 1 shows the first road section of the collected traffic data. This record was made on November 21, 2018. The variables $u(x, t)$, $k(x, t)$ and $q(x, t)$ were taken for three and a half hours at two points. An observer was collocated in a pedestrian bridge at South (point 1), and the other one was placed on a pedestrian bridge at the North (point 2).

The measured flow's direction is South-North, so the input is at 1 and the output is at 2. The measurements were

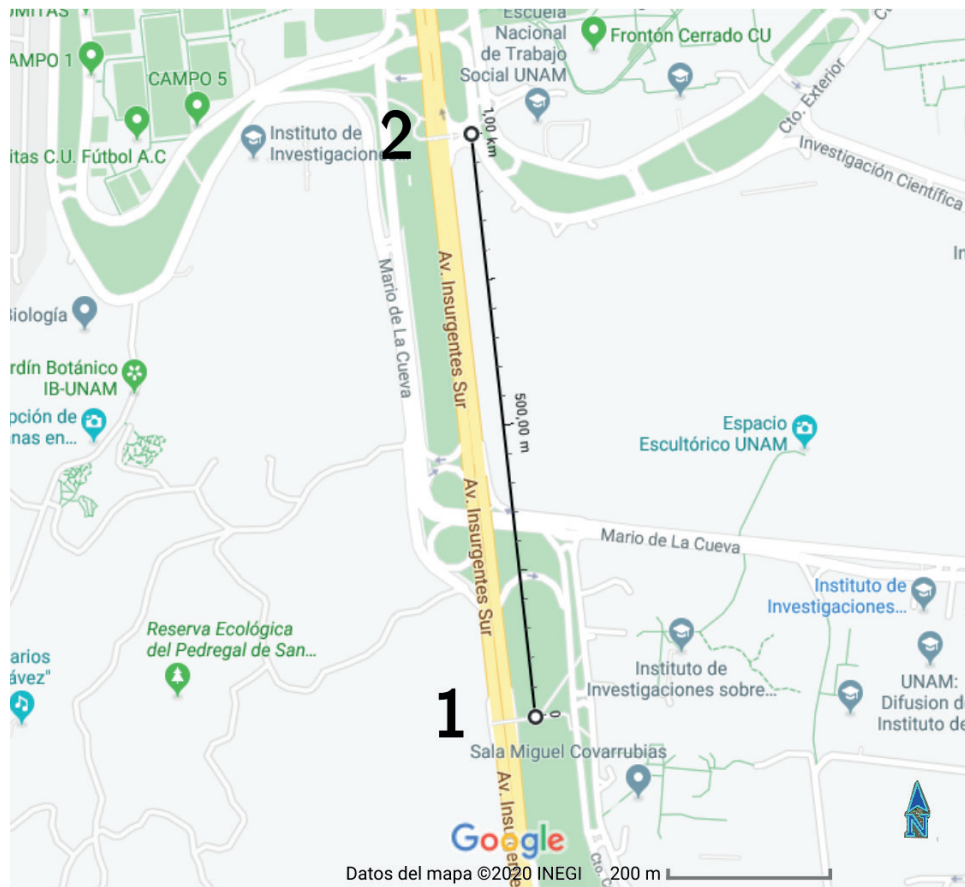


Figure 1 Insurgentes Sur, Mexico City, taken from Google Earth Pro 2018

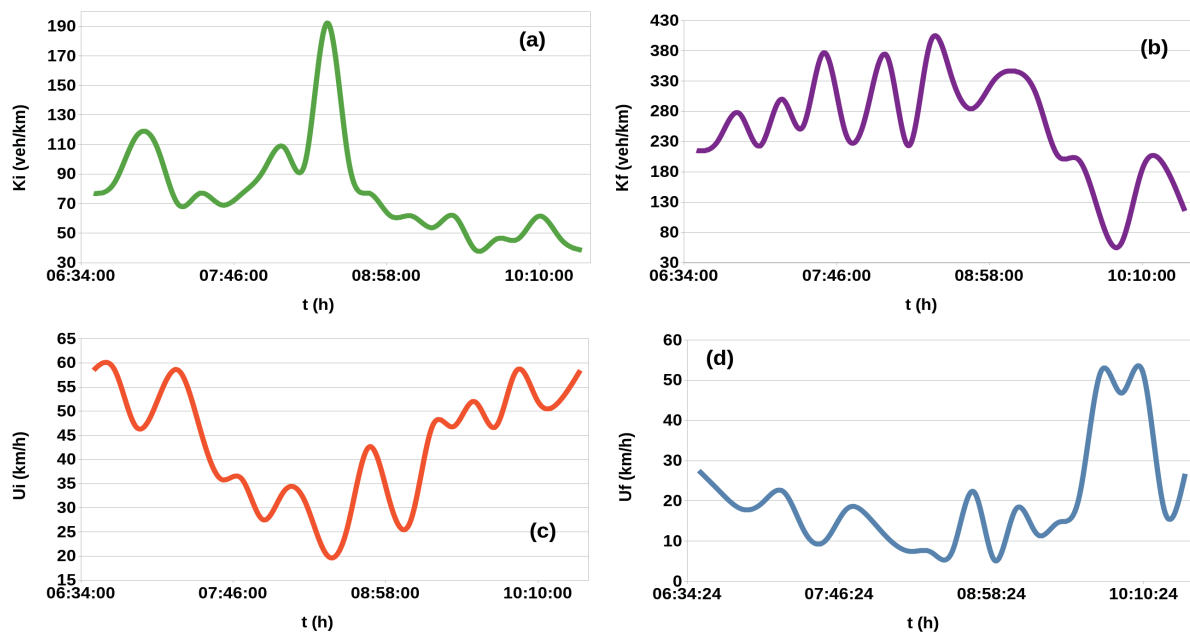


Figure 2 (a) Density of traffic at point 1, (b) Density of traffic at point 2, (c) Velocity of traffic at point 1, (d) Velocity of traffic at point 2, see Figure 1

made from 6:40 hrs to 10:20 h. One can see that there is a big vehicle exit-entrance at 350m from 1 and another small vehicle's entry at 200m from 1. In this case, $\Delta x \approx 1$ km and $\Delta t = 10$ min, i. e. $\Delta t = 1/6$ h.

One can see in Figure 2 that the density and velocity of traffic have a qualitatively opposite behavior, as

Greenberg's prediction says. One also can compare the measured traffic flow $\bar{Q}_{measured}$ and the calculated traffic flow $\bar{Q}_{calculated} = \bar{k}_{measured} \times \bar{u}_{measured}$, where the bar means "the average of." Even though the slope of the straight line is close to 1, the linear regression shows a weak correlation between $\bar{Q}_{measured}$ and $\bar{Q}_{calculated}$ ($R^2 = 0.28$ Figure 3).

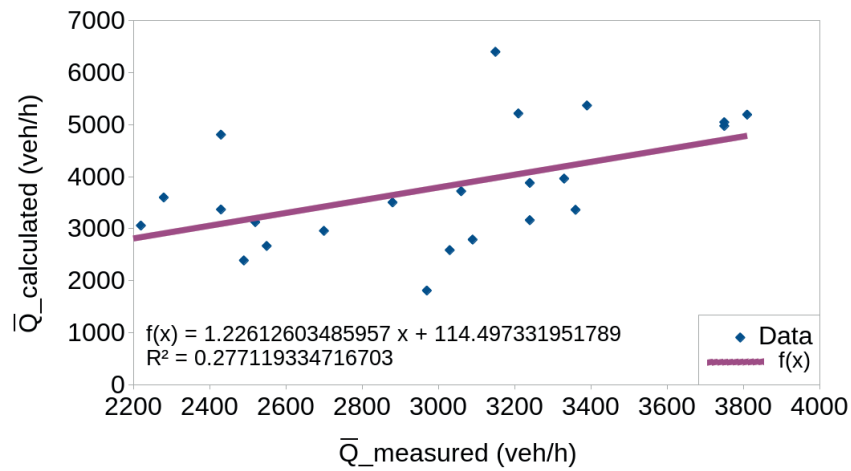


Figure 3 Relation between the calculated traffic flow and the measured traffic flow for the Insurgentes Sur case

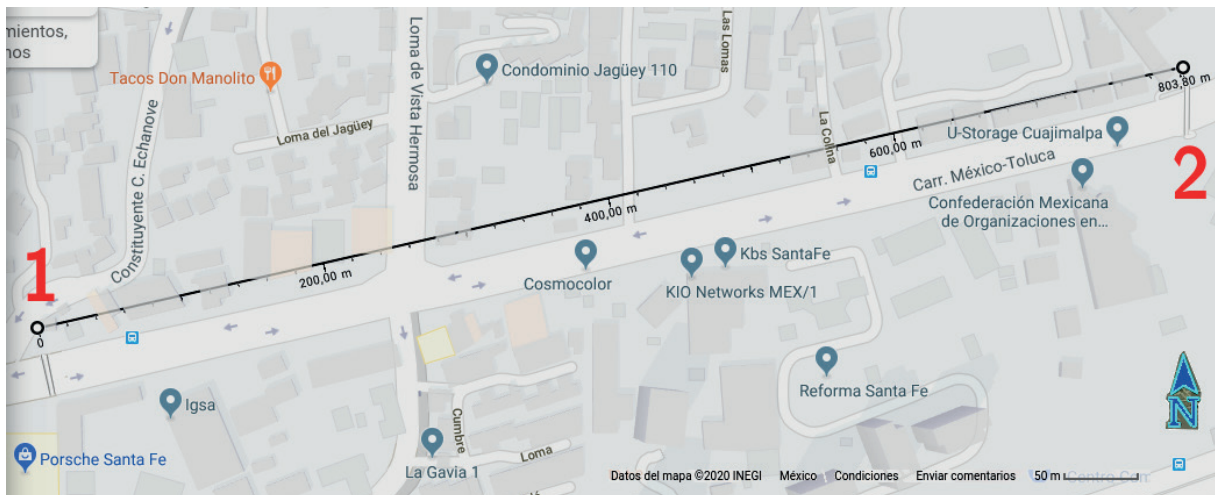


Figure 4 Mexico-Toluca Federal road, Mexico City, taken from Google Earth Pro 2018

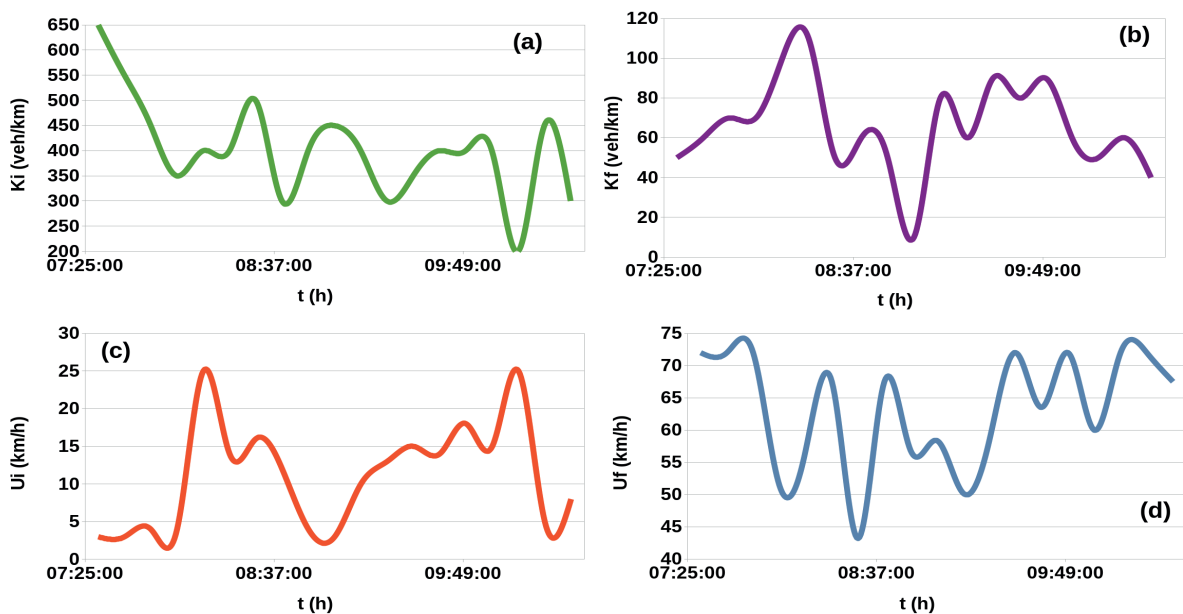
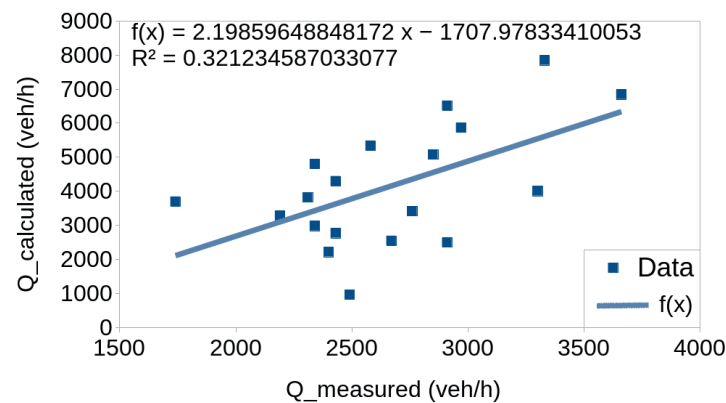
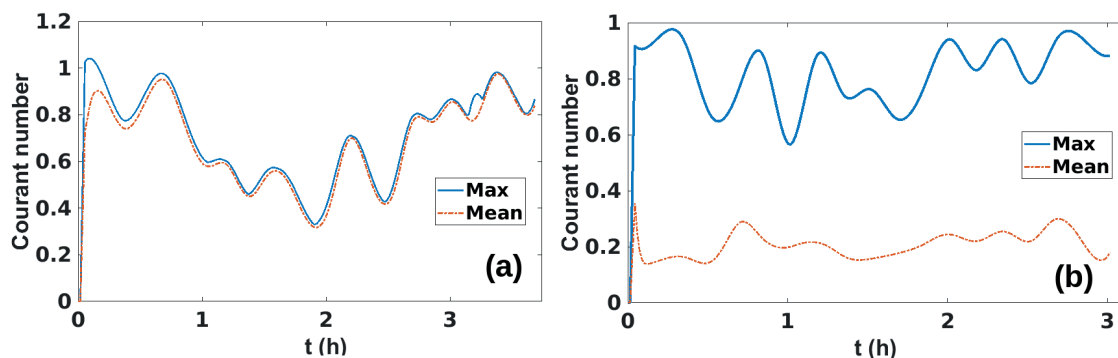


Figure 5 (a) Density of traffic at point 1, (b) Density of traffic at point 2, (c) Velocity of traffic at point 1, (d) Velocity of traffic at point 2

Table 1 Some combinations of anticipation distance, time and viscosity (Equation (10))

δ_v (m)	τ_a (s)	η (km h ⁻¹)
250	1.5	600
500	4	450
290	2.75	380
210	3.4	220
100	3.6	100
50	9	20

**Figure 6** Relation between the calculated traffic flow and the measured traffic flow for the Mexico-Toluca case**Figure 7** Courant number, $\eta = 600 \text{ km h}^{-1}$, (a) for the Insurgentes Sur case, (b) for the Mexico-Toluca case

4.2 Mexico-Toluca free road

Figure 4 shows the second road section of the traffic data collection. This record was made on November 13, 2018. The variables $u(x, t)$, $k(x, t)$ and $q(x, t)$ were taken for three hours at two points. An observer was placed on a pedestrian bridge at West (point 1) and the other was put in a pedestrian bridge at East (point 2).

The measured flow's direction is West-East, so the input is 1 and the output is 2. The measures were taken from 7:30 h to 10:30 h. One can observe that there is an important vehicle exit at 250 m from 1. In this case, $\Delta x \approx 0.8 \text{ km}$ and $\Delta t = 1/6 \text{ h}$.

In Figure 5, one can see a contrary behavior of density and velocity too, but it is not as evident as in Figure 2. In the same way as in the Insurgentes Sur case, one can compare the measured traffic flow $\bar{Q}_{measured}$ and the calculated traffic

flow $\bar{Q}_{calculated}$ (see Figure 6). In this case, the slope of the straight line is greater than 2, besides the linear regression shows a weak correlation between $\bar{Q}_{measured}$ and $\bar{Q}_{calculated}$ ($R^2 = 0.32$).

5 Numerical results

Numerical results are presented as the three-dimensional graphs of variables $u(x, t)$ and $k(x, t)$. In addition, a time series of those variables are shown in two-dimensional graphs, which are presented at different values of fixed positions. Finally, the space-phase (known as "fundamental diagram" [17, 31, 35-36]) is presented for combinations of the three variables: u , k and q . The calculations were carried out varying the parameter η , which took the values:

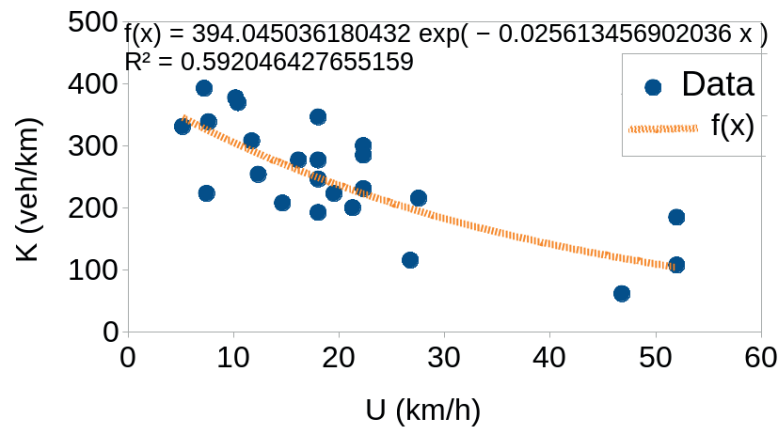


Figure 8 Phase portrait of the density and the velocity for the Insurgentes Sur case

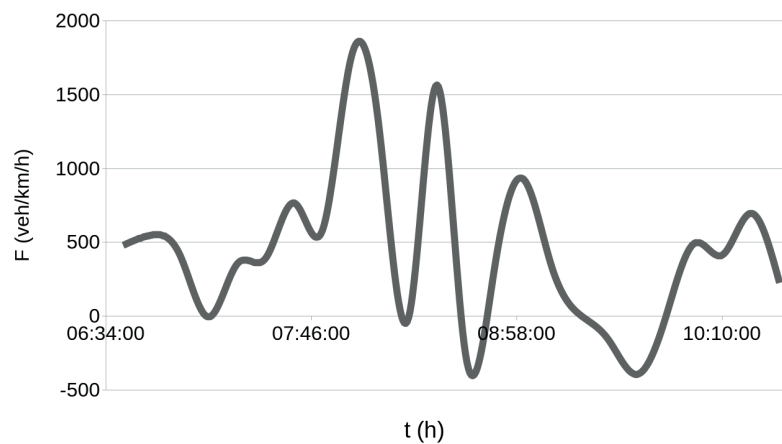


Figure 9 Function of the continuity equation for the Insurgentes Sur Ave

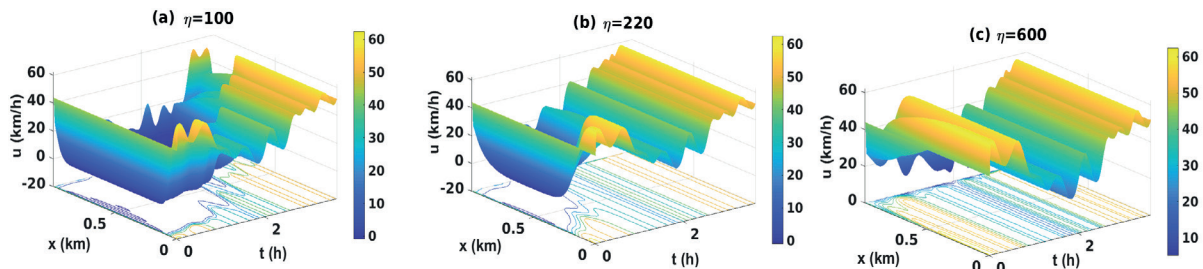


Figure 10 Velocity as a function of x and t for the Insurgentes Sur case, (a) $\eta = 100 \text{ km h}^{-1}$, (b) $\eta = 220 \text{ km h}^{-1}$, (c) $\eta = 600 \text{ km h}^{-1}$

$\eta \in \{0, 1, 5, 10, 20, 50, 100, 220, 380, 450, 600\} \text{ km h}^{-1}$.

These values were defined based on the Kerner-Konhauser fundamental diagram [37-38], who have reported the value of $\eta = 600 \text{ km h}^{-1}$.

Table 1 shows several combinations of the visibility distance and the anticipation time to get various values of the viscosity.

To see the convergence of the solutions, the behavior of the Courant number in terms of time is shown in Figure 7. In Figure 7(a), the Courant number is greater than 1 only at the beginning, but its values become lower than 1 for the rest of the time. In the Mexico Toluca case (see Figure 7(a)), the Courant number is always lower than 1 all the time, therefore the numerical method is stable in both cases.

Function f of the non-homogeneous continuity equation (Equation (9)) was calculated as follow:

$$f(t) \approx \frac{\Delta k}{\Delta t} + \frac{\Delta q}{\Delta x}, \quad (12)$$

with $\Delta k = k_2(t) - k_1(t)$ and $\Delta q = q_2(t) - q_1(t)$ (see Figures 1 and 4).

5.1 Numerical results for Insurgentes Sur Avenue

Insurgentes Sur is a 2-lane road for private vehicles and one lane confined to public transport service. If one estimates the number of vehicles in the case of traffic jams,

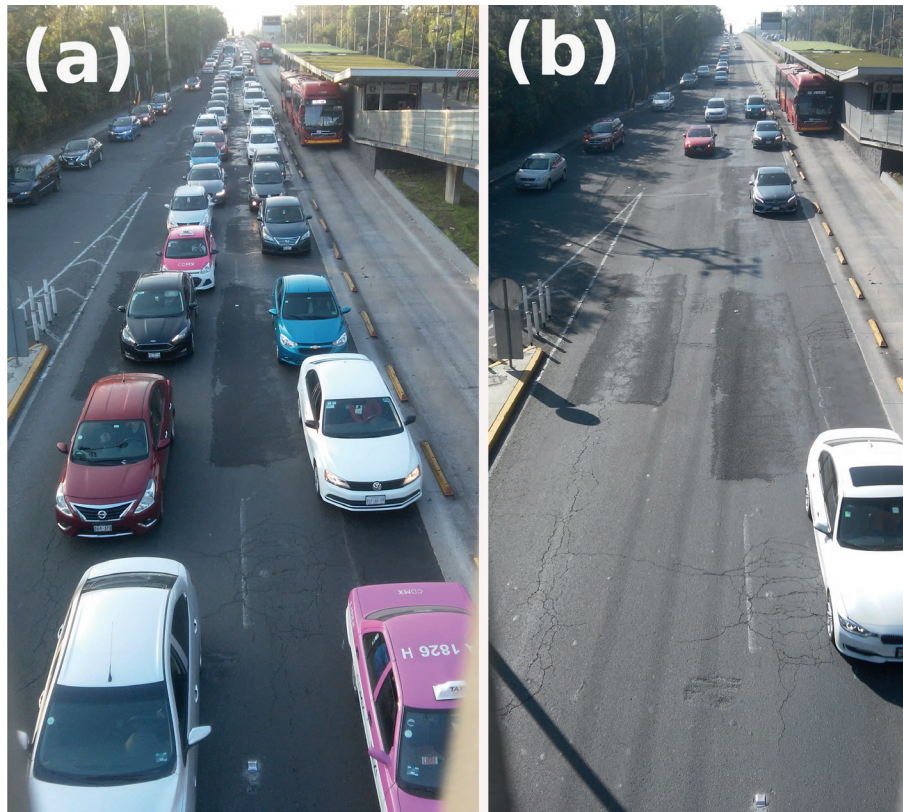


Figure 11 Insurgentes Sur, picture taken at point 2 of Figure 1, (a) at 7:26 am, (b) at 9:41 am.

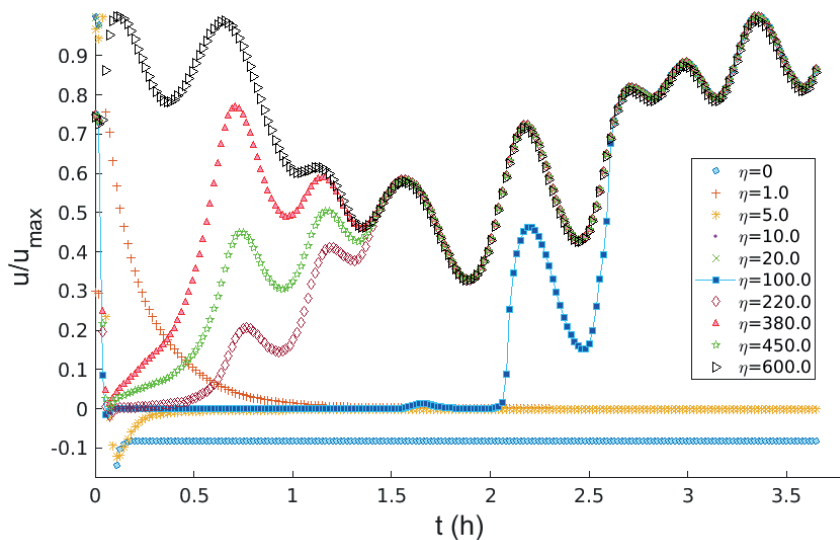


Figure 12 Normalized velocity time series for several values of the η at the fixed point $x = 500$ m, Insurgentes Sur case

there is a maximum of 750 veh km^{-1} (taking into account vehicles of 4m in length and without a space between them).

The phase-space (k, u) for the Insurgentes Sur case is shown in Figure 8. The least square regression (LSR) was used to calculate the coefficient of determination (R^2) to determine how strong is the negative exponential relation (see Equation (6)) between k and u . The relation found was the following:

$$k(u) = 394 e^{-u/39.04}, \quad (13)$$

with $R^2 = 0.59$. It means that $c = 39.04$. This value was utilized in the numerical simulation.

The function of the non-homogeneous continuity equation for the Insurgentes Sur case is shown in Figure 9. Except in the points where the sign changes, one can observe that this function is different from zero almost all the time. This function has more positive than negative

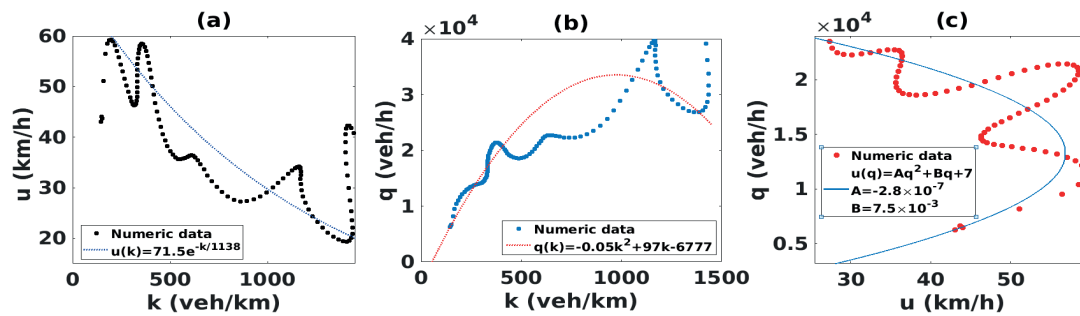


Figure 13 Fundamental diagrams for the Insurgentes Sur case, (a) u vs. k with a negative exponential trend line, (b) q vs. k with a parabolic trend line, (c) q vs. u with a parabolic trend line

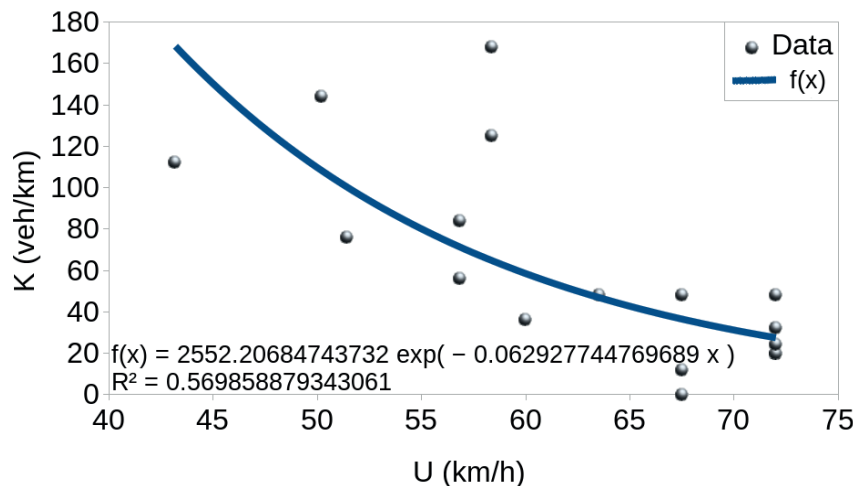


Figure 14 Phase portrait of the density and the velocity for the Mexico-Toluca case

values, which means that more vehicles came out than those that entered. So, there was a vehicle entry at an intermediate point on the avenue segment studied.

Velocity's 3D-graphs are shown in Figure 10 for three different values of η . If the viscosity is $\eta = 100$ km h⁻¹, there are times and positions when the speed vanishes (see Figures 10(a) and 12); but if the viscosity is increasing towards $\eta = 600$ km h⁻¹ the speed is always positive (see Figures 10(b) and 10(c)). Velocity increases (until the limit value) as the viscosity increases. In the Insurgentes Sur case, $u \in (0.65)$ km h⁻¹ for $\eta > 10$ km h⁻¹.

It is worth mentioning that the velocity diverges when the viscosity is small (or zero). Big negative and positive values of the velocity appear (more than 200 km/h and close to -800 km h⁻¹). This case is numerically unstable. If the viscosity increases, the method becomes stable and the negative values disappear.

Figure 11 shows two moments at point 2 of Figure 1, (a) at 7:26 am and (b) at 9:41 am. An estimated viscosity value can be made observing each photograph. For example, a large number of vehicles are seen in Figure 11(a), the speed is low, so it can be related to Figure 10(a), the viscosity at that time would have a value $\eta = 100$ km h⁻¹. Figure 11(b) shows fewer vehicles than in Figure 11(a); it means that the speed has increased along the road segment. Qualitatively, it can be related to Figure 10(c). In this case,

it would be $\eta = 600$ km h⁻¹. These facts are better observed in Figure 12. Time series of normalized velocity for different values of η at a fixed point $x = 500$ m show the behavior of the velocity for the η values.

For this position, the velocity is negative if $\eta = 0$; it decreases to zero if $1 \leq \eta \leq 100$ km h⁻¹. When $t = 2$, $u \neq 0$ for $\eta = 100$ km h⁻¹. From the value $t = 1.5$ h⁻¹, the speed is the same for $\eta > 200$ km h⁻¹. The fundamental diagrams are shown in Figure 13. In all the cases, curves superimposed on the numerical data show a trend of said data. For the space phase $u - k$ (Figure 13a), a negative exponential was assigned. Parabolic curves, whose equations are shown in the Figure 13, were superimposed on spaces $q - k$ and $q - u$ (Figures 13(b) and 13(c) respectively).

5.2 Numerical results for Mexico-Toluca free road

Mexico-Toluca freeway is a 2-lane road for all the kinds of transport vehicles. The phase-space (k, u) is shown in Figure 14. The LSR shows that the determination coefficient for this case is $R^2 = 0.57$, which is very similar to the previous case. The negative exponential relation (Equation (6)) between k and u is:

$$k(u) = 2552 e^{-u/15.89}. \quad (14)$$

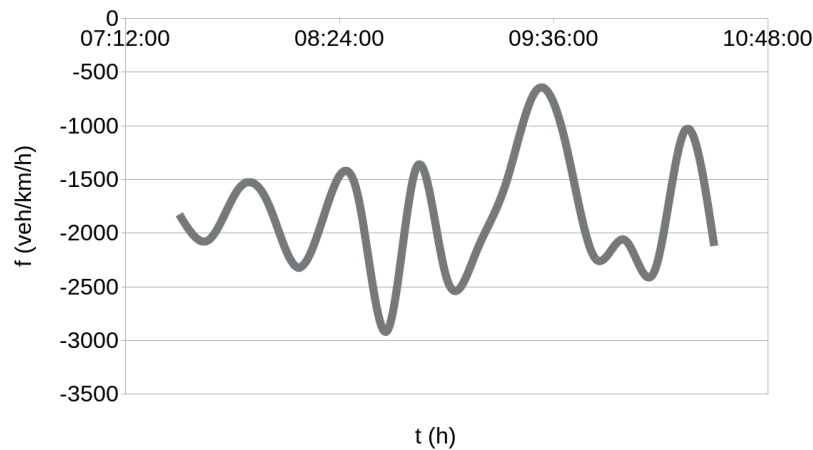


Figure 15 Function of the continuity equation for the Mexico-Toluca road

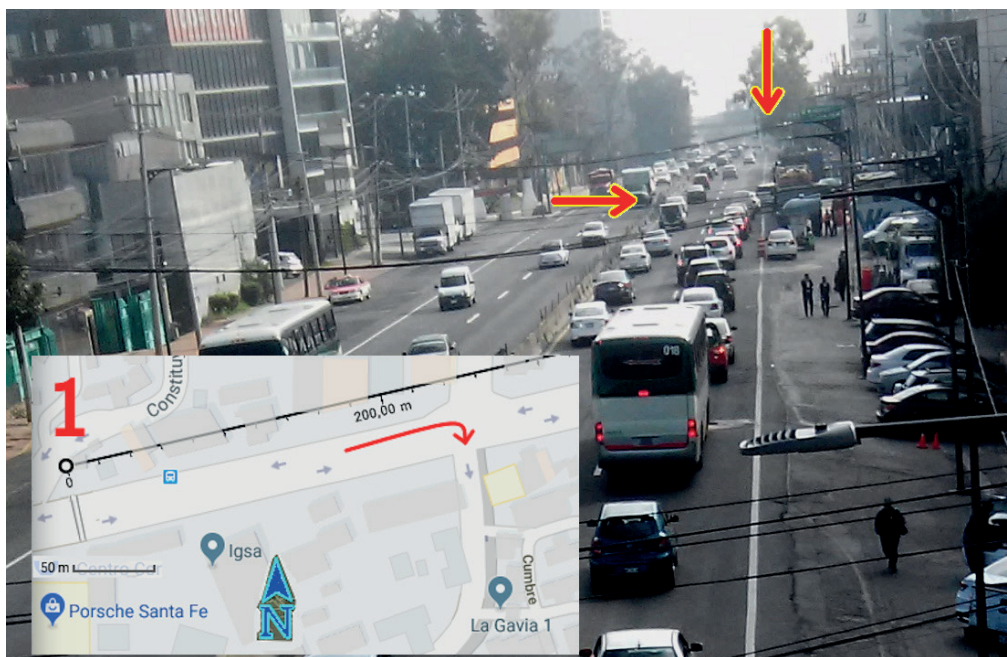


Figure 16 Cars are going out of the road to study at an intermediate point, a close-up of Figure 4 is added to the lower-left corner of the picture to locate the vehicle exit from a map.

It means that $c = 15.89$. This value was utilized in the numerical simulation.

Function of the non-homogeneous continuity equation for the Mexico-Toluca case is shown in Figure 15. One can observe this function is different from zero all time. In fact, f takes negative values. One can interpret this result like more vehicles to come in the road than those that leave the road. This interpretation is accurate, to many vehicles go out for the street ahead of point 1 (see Figure 16).

Figure 17 shows velocity 3D-graphs for three different values of η . Notably, if the viscosity is small, the velocity has non-realistic values. Negative velocities can appear in the model results. Physically, it implies a back movement, but a car does not move to 1000 km h^{-1} in reverse. This case is numerically unstable. However, if the viscosity increases, the velocity takes values ranging from zero to 75 km h^{-1} .

When the viscosity value is 20 km h^{-1} , the velocity drops to zero in practically the entire domain of the function (except at

borders, see Figure 17(a)). When the viscosity increases again, the velocity increases too, but it does not exceed the limits of values at the boundaries (Figures 17(b) and 17(c)).

Figure 18 shows photographs taken at point 1 of Figure 4 at three different times. Many cars can be seen on the street in Figure 18 (a). This situation can be related to Figure 17 (b), that is, the viscosity value can be $\eta = 20 \text{ km h}^{-1}$. Figure 18 (b) show fewer cars than Figure 18 (a). Depending on the particular characteristics of the researchers' study, in this case, this picture can be associated with Figure 18 (b), i. e. the viscosity can take the value $\eta = 100 \text{ km h}^{-1}$. There are no cars in Figure 18 (c) in the studied lane, so, vehicles can move at any speed. In this case, the vehicle velocity can approach the velocity shown in Figure 17 (c).

The normalized velocity (see Figure 19) shows that several values for viscosity (not necessarily the maximum values) cause the velocity to drop to zero (for example, $\eta = 50 \text{ km h}^{-1}$).

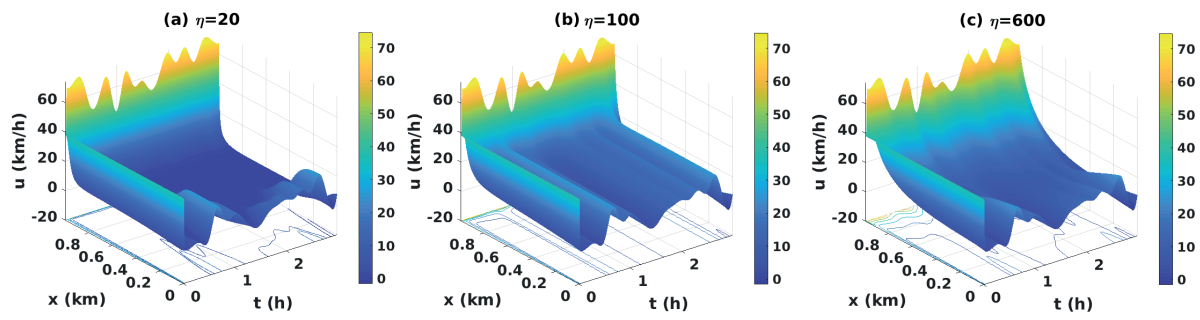


Figure 17 Velocity as a function of x and t for the Mexico-Toluca case, (a) $\eta = 20 \text{ km h}^{-1}$, (b) $\eta = 100 \text{ km h}^{-1}$, (c) $\eta = 600 \text{ km h}^{-1}$



Figure 18 Mexico-Toluca, picture taken at point 1 of Figure 4, (a) at 8:32 am, (b) at 9:17 am, (c) at 10:32 am, pictures: Authors

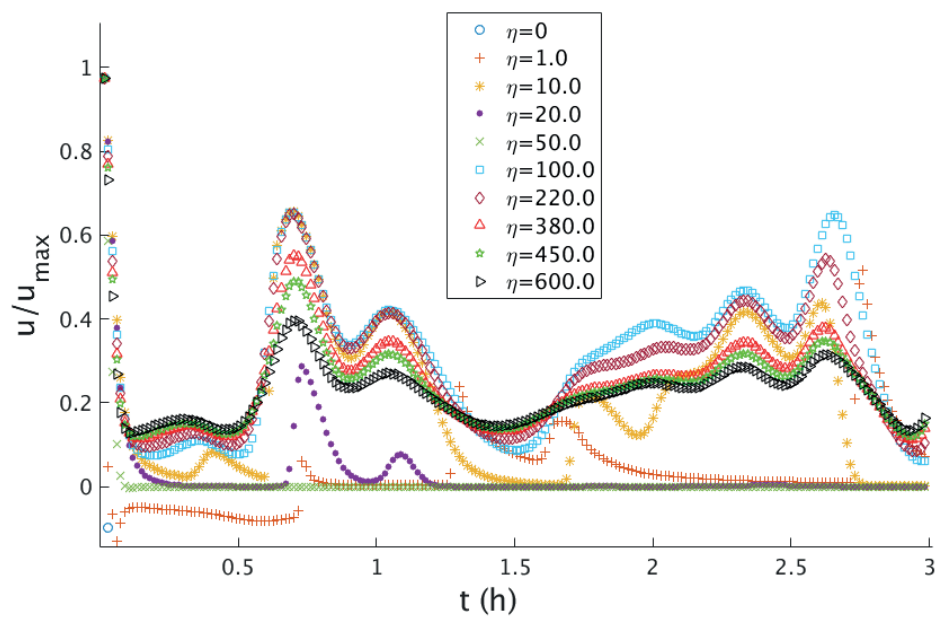


Figure 19 Normalized velocity time series for several values of the η , Mexico-Toluca case

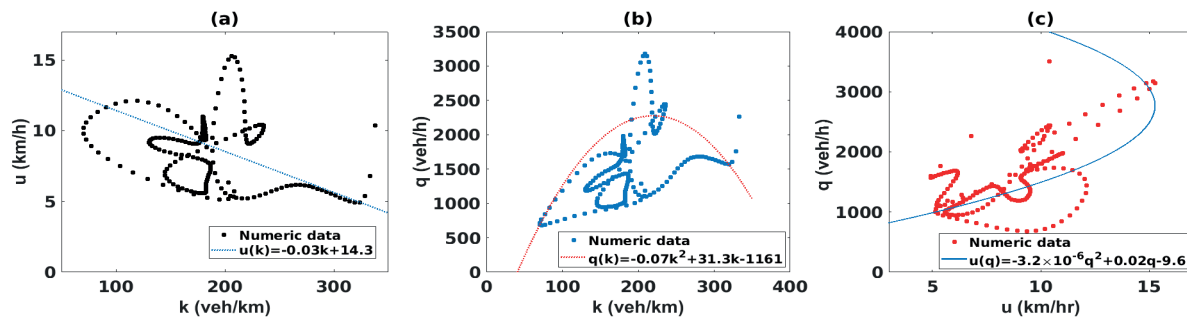


Figure 20 Fundamental diagrams for the Mexico-Toluca case, (a) u vs. k with a negative slope straight line trend, (b) q vs. k with a parabolic trend line, (c) q vs. u with a parabolic trend line

Expected trends in the fundamental diagrams in the case of the Mexico-Toluca freeway (Figure 20) are less clear than in the case of the Insurgentes Sur Ave. (Figure 12).

In this case, at the $u - k$ phase-space a line was inserted with a negative slope as a tendency of the inverse relationship of u and k , Figure 20(a), instead of the negative exponential function that was used for the previous case.

A parabolic shape was imposed on the other two-phase spaces, as one can see in Figures 20(b) and 20(c).

6 Summary

A traffic study in two points of Mexico City is developed. Velocity, vehicular density, and vehicular flow were measured for approximately 3 h in sections of around 1 km long of two crowded streets. The aim of making these measurements was to get information on the initial and boundary conditions to perform the numerical simulation.

To estimate the parameter c , which was used as an input data in the numerical model, an analysis of the observed data was carried out following the Greenberg methodology. A qualitatively inverse relationship of u and k can be observed (Figure 2), as in literature [4, 39]. Nonetheless, this inverse relation is weakly correlated logarithmically.

Using the usual continuity equation (homogeneous equation), the model gave a constant value for the speed, at all the times and for practically the entire spatial domain, except in the vicinity of the border. Other numerical tests were made using the Neumann conditions [27-29]. The velocity was constant (these results are not shown in this paper), even on the borders.

The solutions of the inviscid model (or with small values of the viscosity) are numerically unstable. Non-realistic values for vehicular density and speed are obtained. The solution gets expected values if the viscosity increases. The diffusion term (i. e. the viscosity term) added to the motion equation makes the model to become stable [31], that is, the solutions take realistic or expected values.

Although the correlation between $k_{measured}$ and $u_{measured}$ is weak, the numerical results show expected values for k and u . The phase-space or fundamental diagrams have expected trends.

The Courant number (see Figure 7) is less than 1 over all the solution integration's time. Thus, there is a convergence of the solution.

In the cases studied here, the viscosity value depends on the traffic time. The viscous term can be useful to define changes in the road parameters such as speed limits, reversible lanes, etc. to improve urban mobility.

One still needs to consider the effect of traffic lights, bottlenecks and block outs. In the future work, authors will consider the solution behavior of a fractional Greenberg model, which also has the effect of slowing down and with this, impairing in mobility.

Acknowledgments

To Dr. Gerardo Ruiz and MSc. Sergio Hernandez for the technical support and use of the Taller de Fluidos' computer servers in the Faculty of Sciences, UNAM. The authors thank SNI for support. E. J. Lopez-Sanchez thanks DGAPA-UNAM for the postdoctoral fellowship.

References

- [1] GREENSHIELDS, D. B., BIDDINS, R. J., CHANNING, S. W., MILLER, H. H. A study in highway capacity. In: 14th Annual Meeting of the Highway Research Board: proceedings. Vol. 14. Highway Research Board, 1935. ISSN 0096-102, p. 448-477.
- [2] LIGHTHILL, M. J., WHITMAN, G. B. On kinematic waves. II. A theory of traffic flow on long crowded roads. In: Royal Society of London: proceedings [online]. Vol. 229 A. 1955. ISSN 0080-4630, p. 317-345 Available from: <https://royalsocietypublishing.org/doi/pdf/10.1098/rspa.1955.0089>
- [3] RICHARDS, P. I. Shock waves on the highway. *Operations Research* [online]. 1956, 4(1), p. 1-137. ISSN 0030-364X. Available from: <https://doi.org/10.1287/opre.4.1.42>

- [4] GREENBERG, H. An analysis of traffic flow. *Operations Research* [online]. 1959, **7**(1), p. 79-85. ISSN 0030-364X. Available from: <http://dx.doi.org/10.1287/opre.7.1.79>
- [5] NEWELL, G. F. Nonlinear effects in the dynamics of car following. *Operations Research* [online]. 1961, **9**(2), p. 209-229. ISSN 0030-364X. Available from: <https://doi.org/10.1287/opre.9.2.209>
- [6] PAVERI-FONTANA, S. L. On Boltzmann-like treatments for traffic flow: a critical review of the basic model and an alternative proposal for dilute traffic analysis. *Transportation Research* [online]. 1975, **9**, p. 225-235. Available from: [https://doi.org/10.1016/0041-1647\(75\)90063-5](https://doi.org/10.1016/0041-1647(75)90063-5)
- [7] HELBING, D. Gas-kinetic derivation of Navier-Stokes-like traffic equations. *Physical Review E* [online]. 1996, **53**(3), p. 2366-2381. ISSN 2470-0045. Available from: <https://doi.org/10.1103/PhysRevE.53.2366>
- [8] PIPES, L. A. An operational analysis of traffic dynamics. *Journal of Applied Physics* [online]. 1953, **24**, p. 274-281. ISSN 0021-8979. Available from: <https://doi.org/10.1063/1.1721265>
- [9] PRIGOGINE, I., ANDREWS, F. C. A Boltzmann-like approach for traffic flow. *Operations Research* [online]. 1960, **8**(6), p. 789-797. ISSN 0030-364X. Available from: <https://doi.org/10.1287/opre.8.6.789>
- [10] DRAKE, J. S., SCHOFER, J. L., MAY, A. D. A statistical analysis of speed-density hypotheses. In: 45th Annual Meeting of the Highway Research Board: proceedings [online]. Vol. 154. Highway Research Board, 1967. ISSN 0096-102, p. 53-87. Available from: <http://onlinepubs.trb.org/Onlinepubs/hrr/1967/154/154-004.pdf>
- [11] PAYNE, H. J. Models of freeway traffic and control. In: *Mathematical Models of Public Systems*. Vol. 1. La Jolla, USA: Simulation Councils, INC., 1971. p. 51-61.
- [12] SMULDERS, S. Control of freeway traffic flow by variable speed signs. *Transportation Research Part B: Methodological* [online]. 1990, **24**(2), p. 111-132. ISSN 0191-2615. Available from: [https://doi.org/10.1016/0191-2615\(90\)90023-R](https://doi.org/10.1016/0191-2615(90)90023-R)
- [13] DAGANZO, C. F. The cell transmission model: a dynamic representation of highway traffic consistent with the hydrodynamic theory. *Transportation Research Part B: Methodological* [online]. 1994, **28**(4), p. 269-287. ISSN 0191-2615. Available from: [https://doi.org/10.1016/0191-2615\(94\)90002-7](https://doi.org/10.1016/0191-2615(94)90002-7)
- [14] NELSON, P. Synchronized traffic flow from a modified Lighthill-Whitman model. *Physical Review E* [online]. 2000, **61**(6), R6052. ISSN 2470-0045. Available from: <https://doi.org/10.1103/PhysRevE.61.R6052>
- [15] ZHANG, H. M. A non-equilibrium traffic model devoid of gas-like behavior. *Transportation Research Part B: Methodological* [online]. 2002, **36**(3), p. 275-290. ISSN 0191-2615. Available from: [https://doi.org/10.1016/S0191-2615\(00\)00050-3](https://doi.org/10.1016/S0191-2615(00)00050-3)
- [16] VELASCO, R. M., MARQUEZ, W. Navier-stokes-like equations for traffic flow. *Physical Review E* [online]. 2005, **72**, 046102. ISSN 2470-0045. Available from: <https://doi.org/10.1103/PhysRevE.72.046102>
- [17] VAN WAGENINGEN-KESSELS, F., VAN LINT, H., VUIK, K., HOOGENDOORN, S. Genealogy of traffic flow models. *EURO Journal on Transportation and Logistics* [online]. 2015, **4**, p. 445-473. ISSN 2192-4376, eISSN 2192-4384. Available from: <https://doi.org/10.1007/s13676-014-0045-5>
- [18] Origin destination survey of households in the Metropolitan Area of the Valley of Mexico / Encuesta origen destino en hogares de la Zona Metropolitana Valle de Mexico (in Spanish) - Inegi and Cdmx-Gov [online] [accessed 2019-10-02]. Available from: https://www.inegi.org.mx/contenidos/programas/eod/2017/doc/resultados_eod_2017.pdf
- [19] ASUAD, N. E. The main challenges of the Mexico City conurbation and metropolitan transportation / Principales retos de la conurbacion de la Ciudad de Mexico y el transporte metropolitano (in Spanish) [online] [accessed 2019-04-10]. Available from: <http://www.economia.unam.mx/cedrus/descargas/Retos%20transporte%20ZMCM.pdf>
- [20] MUNOZ, J. C., BATARCE, M., TORRES, I.). Comparison of the level of public transport service in six Latin American cities / Comparacion del nivel de servicio del transporte publico en seis ciudades latinoamericanas (in Spanish). In: XVI Congreso Chileno de Ingenieria de Transporte: proceedings [online]. Vol. 18. 2013. p. 10-16. Available from: <https://auroradechile.uchile.cl/index.php/CIT/article/view/28452/30173>
- [21] Inegi [online] [accessed 2019-11-25] Available from: <https://www.inegi.org.mx>
- [22] MIRALLES-GUASH, C., CEBOLLADA, A. *Mobility and transportation. Political options for the city / Movilidad y transporte. Opciones politicas para la ciudad* (in Spanish) [online]. Madrid: Laboratorio de Alternativas, 2003. ISBN 84-96204-28-6. Available from: https://www.fundacionalternativas.org/public/storage/laboratorio_documentos_archivos/xmlimport-GVOoD4.pdf
- [23] HELBING, D., HENNECKE, A., TREIBER, M., SHVETSOV, V. Master: macroscopic traffic simulation based on a gas-kinetic, non-local traffic model. *Transportation Research Part B: Methodological* [online]. 2001, **35**, p. 183-211. ISSN 0191-2615. Available from: [https://doi.org/10.1016/S0191-2615\(99\)00047-8](https://doi.org/10.1016/S0191-2615(99)00047-8)
- [24] DELGADO, J., SAAVEDRA, P., VELASCO, R. M. *Modeling of traffic flow problems / Modelacion de problemas de flujo vehicular* (in Spanish) [online]. Iztapalapa, Mexico: CBI UAM, 2012. Available from: https://www.academia.edu/27515488/Modelaci%C3%B3n_de_problemas_de_flujo_vehicular
- [25] FANG, J., YE, H., EASA, S. M. Modified traffic flow model with connected vehicle microscopic data for proactive variable speed limit control. *Journal of Advanced Transportation* [online]. 2019, 8151582, p. 1-11. ISSN 0197-6729. Available from: <https://doi.org/10.1155/2019/8151582>
- [26] GOMEZ-HERNANDEZ, E. *Development of a vehicle simulation model to improve traffic light synchronization/ Desarrollo de un modelo de simulacion vehicular para la mejora en la sincronizacion de semaforos* (in

- Spanish). PhD thesis. Puebla, Mexico: INAOE, 2009. Available from: <https://inaoe.repositorioinstitucional.mx/jspui/bitstream/1009/379/1/GomezHE.pdf>
- [27] ASMAR, N. H. *Partial differential equations with Fourier series and boundary value problems*. 2. Ed. USA: Pearson: Prentice-Hall, 2005. ISBN 0-13-148096-0.
- [28] WEBER, H. J., ARFKEN, G. B. *Essential mathematical methods for physicists*. USA: Academic Press, 2003. ISBN 0-12-059877-9.
- [29] BOAS, M. L. *Mathematical methods in the physical sciences*. 3. ed. USA: John Wiley & Sons., 2005. ISBN 978-0-471-19826-0.
- [30] GUYON, E., HULIN, J.-P., PETIT, L. *Hidrodynamique physique*. Paris: EDP Sciences, CNRS Ed., 2001. ISBN 2-86883-502-3.
- [31] TREIBER, M, A. KESTING, A. *Traffic flow dynamics. data, models and simulation*. Berlin Heidelberg: Springer-Verlag, 2013. ISBN 978-3-642-32460-4.
- [32] BURDEN, R. L., FAIRES, J. D. *Numerical analysis*. 9. ed. USA: Cengage Learning, 2011. ISBN-13: 978-0-538-73351-9.
- [33] MATTHEWS, J. H., FINK, K. D. *Numerical methods: using Matlab*. 3. edition. USA: Prentice-Hall, 1999. ISBN-13: 978-0132700429.
- [34] ESI-OpenCFD. OpenFOAM. The open-source CFD toolbox. Programmer's guide. Version 3.0.1. [online] [accessed 2019-12-14]. Available from: <http://foam.sourceforge.net/docs/Guides-a4/ProgrammersGuide.pdf>
- [35] KESSELS, F. *Traffic flow modelling. Introduction to traffic flow theory through a genealogy of models*. Cham, Switzerland: Springer, 2019. ISBN 978-3-319-78695-7.
- [36] SMALL, K. A., VERHOEF, E. T. *The economics of urban transportation*. 2. ed. New York, USA: Taylor & Francis and Routledge, 2007. ISBN-13: 978-0415285155.
- [37] KERNER, B. S., KONHAUSER, P. Structure and parameters of clusters in traffic flow. *Physical Review E*. 1994, **50**(1), p. 54-83. ISSN 2470-0045.
- [38] DELGADO, J. SAAVEDRA, P. Global bifurcation diagram for the Kerner and Konhauser traffic flow model. *International Journal of Bifurcation and Chaos* [online]. 2015, **25**(5), 1550064. ISSN 0218-1274. Available from: <https://doi.org/10.1142/S0218127415500649>
- [39] HABERMAN, R. *Mathematical models*. Philadelphia, USA: Society for Industrial and Applied Mathematics, 1998. ISBN 0-89871408-7.

THE MODEL OF CONTAINER FEEDER LINE ORGANIZATION FOCUSED ON THE NATURE AND PARAMETERS OF EXTERNAL CONTAINER FLOWS

Oleksii Drozhzhyn*, Yuliia Koskina

Odesa National Maritime University, Odesa, Ukraine

*E-mail of corresponding author: alexey.drozhzhyn@ukr.net

Resume

This article considers the trunk lines, connected with the feeder region as the external environment for the system - feeder lines (its subsystems are container flows, ports and container ships). Hub ports are considered to be the boundary of the system and the external environment. Thus, mathematical models were simulated for the two levels. At the first level, container flows are determined (based on statistical data), which enter and exit the hub. At the second level, the mathematical model allows to find for the feeder line: volumes of container flows, the total capacity of the ships which serves the cargo, and parts of the distribution of this capacity between feeder ports.

Article info

Received 16 July 2020

Accepted 24 August 2020

Online 2 February 2021

Keywords:

feeder line,
container transportation,
liner shipping,
transport technologies,
transport systems

Available online: <https://doi.org/10.26552/com.C.2021.2.A94-A102>

ISSN 1335-4205 (print version)

ISSN 2585-7878 (online version)

1 Introduction

There are many scientific papers regarding hub and spoke systems in maritime container shipping. The topic of the presented paper covers three large sections simultaneously: geography of transport systems [1], organization of ship's operation [2] and container network technologies optimization [3].

The new generation research-studies, dedicated to container shipping, often use the models, proposed by highly cited authors [4-5].

Trunk and feeder network design problems were suggested to be solved by methods like: variable neighborhood search [6], genetic algorithm-based heuristic [7], liner programming, particularly, using simplex algorithm [8], mixed integer liner programming [9-10].

2 The model of relationship between the feeder system parameters for the container traffic and external environment

Feeder container lines are not a separate system; they are in close interaction with the environment - a system of trunk container lines. Their interaction is an integral part of the world container shipping system - the trunk-feeder communication and their interrelation occurs at the level of vessels, ports and container flows. Making the decisions

about organizing a feeder line, the ship-owner (or operator) must determine the region and, accordingly, the basic ports of call of the created line, which cannot be done without the information about how the trunk container lines in the region are working. That is, container flows that arise or fade in the routes of trunk container lines and their distribution between ports are the main input information for substantiating the structure of the feeder line.

The above-mentioned system and the external environment are hierarchical: the system of feeder lines is "subordinated" to the system of trunk container lines. Thus, these systems function (probably must function) as agreed ones to ensure delivery of cargoes in containers during the trunk-feeder service in acceptable time for cargo owners, that is impossible without the coordination of the basic parameters of these systems. To such parameters, in this case, are referred the fleet container capacity, the volume of container flows between ports and the transport links "hub port - feeder port". The latter, in turn, form areas of feeder lines.

Figure 1 presents the model of interrelation of ports, vessels and container flows which are the parts of the systems of trunk and feeder lines. The following is a brief description.

First of all, it is necessary to determine the relationship between these systems at the port level. In the system of trunk container lines, hubs are to be allocated, between which the goods in containers are carried as a part of the



This is an open access article distributed under the terms of the Creative Commons Attribution 4.0 International License (CC BY 4.0), which permits use, distribution, and reproduction in any medium, provided the original publication is properly cited. No use, distribution or reproduction is permitted which does not comply with these terms.

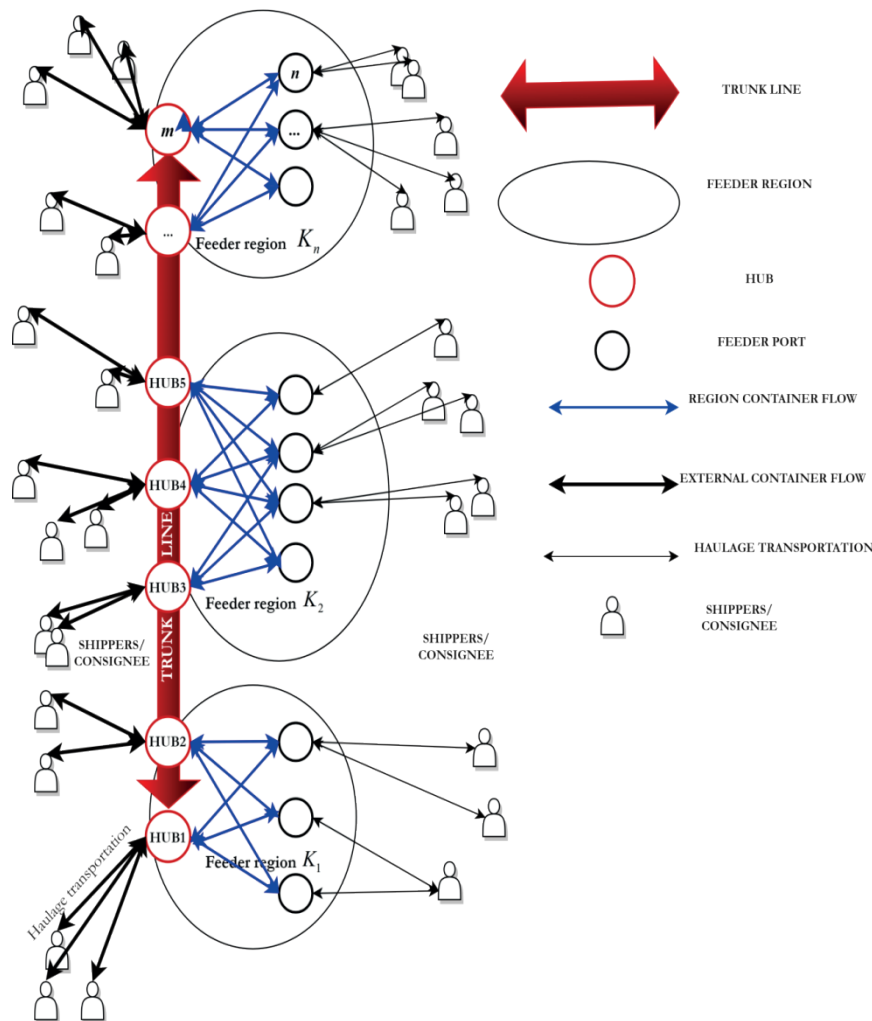


Figure 1 The model of the interrelation of ports, vessels and container flows

global commodity flows of world trade. This means that the volumes of container flows in the system of trunk lines are formed according to the structure and volume of the world trade.

There are m hubs and $i = \overline{1, m}$ are the indexes of these ports. All the hub ports can be geographically divided into groups. As such, a region is established within which rational consideration of feeder directions is considered. That is, n feeder regions are separated. The aggregate of the feeder regions forms the geographical characteristics of the feeder line system. In fact, the feeder regions are superimposed on the main trunk routes, providing full coverage of all the hub ports and feeder ports. Thus, one more index $j = \overline{1, n}$ is introduced for the hub ports, which determines that the hub port belongs to the feeder region. That is, hubs are considered as the points of intersection of the feeder system and the external environment (trunk lines), which is formally taken into account in the double indexation of ports - from the point of view of trunk lines ($i = \overline{1, m}$) and from the point of view of belonging to the feeder regions ($j = \overline{1, n}$). In each feeder region feeder ports K_j are selected, $j = \overline{1, n}$ and $k_j = \overline{1, K_j}$, $j = \overline{1, n}$ - the index of feeder ports of the feeder region j .

In the system of feeder container lines, hubs are

connected with the feeder ports by corresponding services. Note that the given feeder ports are considered as potential ports to be included in feeder services and, consequently, the set of considered feeder ports may not be fully involved in the feeder service at a given time. Thus, depending on volumes of the container traffic in the feeder region and their distribution among the ports of the region in this time period, this or that port may be included or excluded from the feeder services. For each hub port, the volume of incoming (or outbound) container flow $Q_{ij}^{exp}, Q_{ij}^{imp}$ respectively can be determined. It is obvious that the information completeness and reliability (quantitative and qualitative parameters), regarding the container flows, play a key role for this problem solving.

For consideration, only general cargoes typical for containerization should be accepted. Although the bulk cargoes are also involved in the practice, contested proposed problem, they cannot be included in the analysis. Most often, the container transportation of such bulk cargoes is profitable for the carrier only when it is necessary to utilize the free space (on unbalanced routes). Such cases revenue is additional.

The container flows information sources are provided by analytical companies that offer marketing research at

PARAMETERS			
quantitative		qualitative	
direction	▼ in (import); ▼ out (export).	economic	▼ Incoterms basis; ▼ commodity price; ▼ shipment size.
volume	▼ stable; ▼ unstable; ▼ seasonal; ▼ episodal.	transport	▼ general; ▼ individual.

Figure 2 Data groups for container flows evaluation

the request of the carrier (Figure 2).

These values are formed as a result of integration of incoming (or output) container flow from/to other hub ports. A data set of container flows links the system of hubs within the trunk lines.

Geographically, in each feeder region $j = \overline{1, n}$ there are hub ports (one and more) and a set of feeder ports.

The feeder ports are an intermediate (in most cases) link in the intermodal container delivery system (it means that some cargo in containers is delivered to the region where the feeder port is located), as the rest of the cargo goes to the regions of the country (or several countries). At the same time, the situation may arise that the same dispatch (destinations) points may be attracted to different feeder ports, that may result in use of several feeder ports simultaneously.

Therefore, when creating a feeder container line and solving the issue of inclusion of this or that feeder (potential) port in the line should be taken into account the geography of regions of the cargo flow origin. Thus, for each feeder port of a given region, quantities $Q_{ikj}^{in}, Q_{ikj}^{out}$ can be determined that characterize the potential volumes of input and output containers for the feeder ports in a certain direction, taking into account the geography of foreign trade links.

Considering the above-mentioned substantiation that the same container ports can be attracted to various feeder ports, the following is true:

$$\sum_{k_j=1}^{K_j} Q_{ikj}^{in} \geq Q_{ij}^{imp}, (i = \overline{1, n}, i \in G_j), \quad (1)$$

$$\sum_{k_j=1}^{K_j} Q_{ikj}^{out} \geq Q_{ij}^{exp}, (i = \overline{1, n}, i \in G_j), \quad (2)$$

where G_j is a set of the hub ports in the region.

In accordance with these inequalities, the volume of input/output container flows in/from feeder ports may exceed the volume of input/output container ports of hubs precisely because the values $Q_{ikj}^{in}, Q_{ikj}^{out}$ are potential, while $Q_{ij}^{exp}, Q_{ij}^{imp}$ are already established. Note that the feeder service is more flexible than trunk, therefore, from the point of view of the tasks solved in this study, $Q_{ikj}^{in}, Q_{ikj}^{out}$ are considered as the potential ones.

Some regional container traffics are served by feeder

vessels of companies operating in a particular region. Based on the analysis of existing feeder services in each region, it is possible to establish the average volume of containers that are already served (meaning that the transportation of this number of containers is provided by already functioning feeder services). These volumes can be estimated as:

$$\sum_{i \in G_j} \sum_{l_j=1}^{L_j} D_{ikj}^{l_j} \cdot s_{ikj}^{l_j} \cdot p_{ikj}^{l_j}, (k_j = \overline{1, K_j}, j = \overline{1, n}), \quad (3)$$

where l_j - current feeder service in region j ; L_j - number of feeder services in region j ; $D_{ikj}^{l_j}$ - container capacity of the vessels of l_j feeder service in region j that connects the feeder port with hub port i ; $p_{ikj}^{l_j}$ - coefficient of variation, which allows moving from the container capacity of the vessel to the carrying capacity (in TEU); $0 < s_{ikj}^{l_j} \leq 1$ - coefficient that corrects the carrying capacity of vessels considering their actual loading capacity. Here, the following should be noted. Depending on the port and the time period considered, the vessels operating between the feeder ports can use container capacity fully or just partly. The coefficient $s_{ikj}^{l_j}$ allows to consider this fact when assessing the potentially possible volume of carrying work on the new feeder line. It can also be used in estimating the competitiveness of the existing feeder service, namely: if this service is characterized by the low competitiveness (for instance, due to inappropriate pricing policy, timetable, etc.), then the new service has a chance to “take away” part of cargo flows. Thus, the coefficient $s_{ikj}^{l_j}$ performs two functions, it takes into account the real terms of the operation of feeder vessels both at the level of their operating and at the level of competition.

Considering the “covered” container flows on the ports, it is possible to determine the value of Q_{ikj}^{fp} , which defines the potential volume of carriage for each feeder port in the region:

$$Q_{ikj}^{fp} = (Q_{ikj}^{in} + Q_{ikj}^{out}) - \sum_{i \in G_j} \sum_{l_j=1}^{L_j} D_{ikj}^{l_j} \cdot s_{ikj}^{l_j} \cdot p_{ikj}^{l_j}, \quad (4)$$

$$(k_j = \overline{1, K_j}, j = \overline{1, n}),$$

Thus, the interrelation of the environment containing a set of trunk lines and the feeder system of container lines at the port and container traffic levels is considered.

The next step is to establish a relationship between the data system and the environment at the vessel level. It should be noted here that the vessel itself is not an element of the system and the environment and their relationship is manifested indirectly through the container traffic. In essence, the feeder and trunk vessels provide the interrelation of the system and the environment through the container flows, realizing the physical distribution and their mating.

The segmentation of vessels to the trunk and feeder is inherent in commercial practice, that is, there are no architectural and constructive types of “feeder” or “trunk” vessels, as while the basis of segmentation is a container capacity, which also determines the vessel draft, and hence the physical possibility of the vessel call at one or another feeder port.

In the world container fleet sets of the trunk and feeder vessels are distinguished. The trunk vessels belong to the system of trunk lines; feeder ones, respectively, belong to the system of feeder lines. The container capacity is used to characterize the fleet of both systems.

The world container fleet capacity serving the trunk lines D^t , TEU (Twenty-foot Equivalent Unit) is determined on the forecasts of volumes of vessel demolition D^d and ordering the new vessels D^b :

$$D^t = D^{t'} + D^b + D^d, \quad (5)$$

where $D^{t'}$ - container capacity (TEU) of the trunk vessels at the current moment. This container capacity D^t is distributed between trunk lines that cover port hubs.

In the system of trunk-feeder lines, it is necessary to allocate subsystems connected with specific regions. These subsystems include relevant elements of the trunk-level system (port-hub of the region) and feeder ports of the region. Each region is separate, which is determined by the specificity of cargo flows caused by the world trade. Interrelation of regions is determined solely in the form of a single connecting link - the main and feeder fleet, which is distributed by region, considering the demand.

Container capacity of the fleet serving feeder lines is D^f (TEU). This value is also established based on forecasting the amount of demolition of tonnage D^{fd} (TEU) and supplies of new vessels D^{fb} (TEU). So:

$$D^f = D^{f'} + D^{fb} + D^{fd}, \quad (6)$$

where $D^{f'}$ - container capacity (TEU) of feeder vessels at the current time.

The feeder fleet is distributed among feeder regions. So, the following is true:

$$D^f = \sum_{j=1}^n \sum_{i \in G_j} \sum_{k_j=1}^{K_i} \sum_{l_j=1}^{L_j} D_{ikj}^{l_j}. \quad (7)$$

Thus, at the conceptual and formalized levels, interrelations between the two hierarchical levels, which are parts of the world system of container lines, are

established. As a result, the container capacity of the fleet, the volume of container flows and their distribution between ports are formalized.

3 Substantiation of ports, vessels and the prospective volume of carriage for feeder lines considering the interrelations with the external environment

The presented above model harmonizes container flows and ports on the two levels of the international sea container carriage system - trunk and feeder.

Based on information on perspective container cargo flows and changes in the structure of the fleet at both levels, the ship-owner willing to organize the feeder service should substantiate promising feeder ports and volumes of transportation, as well as determine whether there is enough fleet available to ensure the functioning of both existing and new lines and to solve the task of distributing this fleet considering commercial interests. The presented above conceptual model can just help in solving these tasks.

The next stage is modeling on that base the next one model which will consider the specificity of the hierarchy, as well as its other properties of the levels, in accordance with parameters that were defined above. So, this can be stipulated as follows: for a given shipping company, it is necessary to find the optimal transport links “feeder port/hub port” (for organization of the feeder lines in the future) and distribute the fleet available to the company in such a way that the efficiency of feeder services to be maximal. As the efficiency of feeder services, one means here the annual profit from the operation of the container vessels on the feeder lines, which would satisfy the specified profitability. Thus, it is necessary to maximize profit, provided it is limited to a given value of profitability. This approach fully corresponds to the practice of modern shipping business.

Since the searching interrelation is hierarchically two-level, its description is mathematically expressed in the form of models of two levels: trunk and feeder. Theoretically, the trunk model covers all the trunk lines and corresponding ports. The feeder-level model covers all the regions and feeder ports (already involved in feeder services and potential). However, in practice, companies that organize feeder lines do not even potentially consider their presence in all the regional markets, so it is advisable to specify the limits for the task and the corresponding models, that is, the establishment of the set of regions that are considered by the company as potential ones.

Assume that $j = \overline{1, n'}$ - this is an ordered subset of the set of all the regions allocated in the system of the sea container transport. As it was mentioned previously the regions can be identified as a subsystem of the hierarchical unity of the “trunk-feeder lines”.

Therefore, there is one trunk-level model that covers hubs of selected regions $j = \overline{1, n'}$ and n' feeder-level models, corresponding to the regional subsystems of the

feeder system. Each model is optimization, since the desire to maximize the efficiency of transport services is natural for the modern transport services market at any level of its searching.

Special situations that arise for some participants in the market of transport services (or their associations), in relatively small periods of time due to competition, when the efficiency provides secondary to other objectives of competition, in the context of the searched problem may be omitted without violating the specificity in accordance with a situation that is modeled.

Mathematically, this structure is a set of $n' + 1$ interconnected optimization models, which in terms of further solution is well understood in modern scientific literature.

The trunk-level model should provide an optimal distribution of the container traffic between regions and hubs, considering the information on the output of hub ports. As a criterion of optimality, it is proposed to use the generalized profit of ship-owners and companies operating in the system of trunk lines. At the core of the profit origin is the averaged information on costs and revenues of carriers. This model has to provide, as outgoing information, the "landmark" for the distribution of container traffic between regions and hub ports, considering interests of ship-owners and attraction of container traffic to hubs and regions in general. In turn, the information received on volumes of traffic (container traffic) at the trunk level is the input (exogenous) information for the feeder system (as previously noted, the linkage of the models of the trunk and feeder levels are container flows). Therefore, in the model of the trunk level of the container traffics are variables and their optimal values will provide efficiency for the fleet of companies (in general), considering the above limiting conditions.

Assume that the container capacity of the fleet, serving the trunk lines D^v , is enough to make a service of trunk lines, so it is not to be used in optimizing.

The data for modeling are the following:

$P_j (j = \overline{1, n})$ - total capacity of container terminals in region j ; $K_{jk} (j, k = \overline{1, n})$ - potential cargo flows (volumes and structure) of the region for the transportation of containerized cargo from region j to region k for container flows considering the possibility of their attraction to different ports and regions (this means the inland part of transportation). Volumes K_{jk} are established based on the maritime world trade geography analysis;

$f_{jk} (j, k = \overline{1, n})$ - averaged profit rate (for TEU) for transportation between regions j, k ;

$r_{jk} (j, k = \overline{1, n})$ - averaged cost standard (for TEU) for transportation between regions j, k .

The parameters are $Y_{jk} \geq 0$ the volumes of transportations between regions $j, k = \overline{1, n}, j \neq k$.

The objective function reflects the generalized revenue from the operating of vessels in traffic between regions:

$$\sum_{j=1}^{n\Sigma} \sum_{k=1}^{n\Sigma} Y_{jk} \cdot (f_{jk} - r_{jk}) \rightarrow \max \quad (8)$$

In this case, the constraints on the capacity of container terminals of regions should be ensured:

$$\sum_{k=1}^n Y_{jk} \sum_{k \neq j}^n Y_{kj} \leq P_j, (j = \overline{1, n}), \quad (9)$$

where $\sum_{k=1}^n Y_{jk}$ - volumes of container flows from region j ;

$\sum_{k=1}^n Y_{kj}$ - volumes of container flows to region j .

In addition, the constraint on potential cargo flows must be fulfilled:

$$Y_{jk} \leq K_{jk}, (j, k = \overline{1, n}). \quad (10)$$

The optimal values of Y_{jk}^* allow to estimate $Q_{ij}^{\text{exp}}, Q_{ij}^{\text{imp}}$, ($i = \overline{1, m}, j = \overline{1, n}$) - the distribution of container flows between hub ports as follows:

$$Q_{ij}^{\text{exp}} = v_{ij} \cdot \sum_{k=1}^n Y_{ik}^*, (j = \overline{1, n}, i \in G), \quad (11)$$

$$Q_{ij}^{\text{imp}} = v_{ij} \cdot \sum_{k=1}^n Y_{kj}^*, (j = \overline{1, n}, i \in G), \quad (12)$$

where v_{ij} - the coefficients of the distribution of container flows that occurs in the region on the hub port providing the inequality: $\sum_{i \in G_j} v_{ij} = 1, (j = \overline{1, n})$. Wherein the values of v_{ij} can be set based on the existing statistics of distribution of container flows in ports of the region.

Transport links "feeder port/hub port" are displayed as a container traffic that connects these two categories of ports.

Feeder services that are considered L_j in region j , $L_j = 1$ is existing or hypothetical (that is, considered as a potential) service of the company for which the network of the feeder lines is substantiated. Thus, other $L_j - 1$ services in each region j are in varying degrees competing. The degree of competition depends, first of all, on the intersection of ports of the feeder services and is further determined by the tariff policy of companies and other factors.

If $X_{ikj}^{\text{in}}, X_{ikj}^{\text{out}}, (j = \overline{1, n}, i \in G_j, k_j = \overline{1, K})$ are volumes of container flows to/from the port k_j from/to the hub port i of region j , they are potential cargoes for the network of the feeder lines to be organized. These values are variables in feeder-level models and are determined in the process of optimization. These potential cargo flows can match the capabilities of this company's fleet, and may not meet (for example, the shipping capacity of the company's fleet may not be enough to provide the entire volume of containers that will be claimed for transportation in the future).

According to the indicated above that $L_j = 1, (j = \overline{1, n})$ corresponds to the strategy of the company on the organization of the feeder lines network, the fleet of feeder vessels of this company is characterized by $D^* = \sum_{j=1}^{n'} \sum_{k_j=1}^{K_j} D_{ikj}^{L_j}, (L_j = 1)$ as the container capacity and D^* includes all the feeder vessels of a company operating on all the services. Naturally, the individual components of this value are $D_{ikj}^{L_j} = 0, (L_j = 1)$ for some i, j, k_j .

Since the task in question is regarding the distribution of the fleet of the company between the planned possible feeder lines, the control parameters $z_{ikj} \geq 0$, ($j = \overline{1, n}, i \in G_j, k_j = \overline{1, K_j}$) are introduced being the container capacity of the vessels for servicing in region j of the feeder line destined to hub port i and feeder port k_j .

For these control parameters the following is true:

$$\sum_{j=1}^{n'} \sum_{i \in G_j} \sum_{k_j=1}^{K_j} z_{ikj} = D^*. \quad (13)$$

It should be noted that the optimal variant of distribution of the total container capacity of the company's fleet will correspond to values of individual z_{ikj} ones that are inappropriate in terms of logic: for instance, $z_{ikj} = 34$ or $z_{ikj} = 5$ or the others alike, for individual i, j, k_j , since there are no ships of this container type physically, therefore these values are not valid in the given terms and for the given task. Therefore, the following ways to correct the situation are proposed: firstly, it is necessary to specify A - the lower limit of z_{ikj} considering the actual container capacity of company's vessels. Secondly, the result of optimization on the model is a basis for the decision-making and subject to manual adjustment in the light of common sense.

Thus, the constraint on container capacity of vessels is following:

$$z_{ikj} \geq A, (j = \overline{1, n}, i \in G_j, k_j = \overline{1, K_j}). \quad (14)$$

Besides, it is necessary to take into account the port limits of allowable draft of vessels, so there should be constraints on the container capacity of vessels A_{ikj} regarding ports of call:

$$z_{ikj} \geq A_{ikj}, (j = \overline{1, n}, i \in G_j, k_j = \overline{1, K_j}). \quad (15)$$

Distribution of the fleet should correspond to cargo flows. Therefore, it is necessary to introduce the term of conformity of the vessels' capacity to volumes of potential container flows. To do this, the process of forming the cargo flows is analyzed and formalized.

Data on volumes of transportation (container flows) in the trunk container system $Q_{ikj}^{in}, Q_{ikj}^{out}$, ($j = \overline{1, n}, i \in G_j, k_j = \overline{1, K_j}$) is the input (exogenous) information for the feeder system. In particular, based on this information, based on belonging of hub ports for a specific region, aggregate information is generated on volume of the container flows in the region:

$$\sum_{i \in G_j} Q_{ij}^{imp}, (j = \overline{1, n}), \quad (16)$$

$$\sum_{i \in G_j} Q_{ij}^{exp}, (j = \overline{1, n}), \quad (17)$$

where G_j is a set of hub ports in the region.

Not all the container trunk lines are assimilated by the feeder ports, since some cargoes in containers follow the inland transport, that is, in the maritime transportation for such cargoes, the port-hub is the final (or initial) destination

(departure).

Each hub port has coefficients $0 \leq \lambda_{ij}^{imp} \leq 1$ and $0 \leq \lambda_{ij}^{exp} \leq 1$ that represent the proportion of containerized cargo delivered by the trunk-and-feeder system:

$$\lambda_{ij}^{imp} = \frac{Q_{ij}^{imp} - Q_{ij}^{imp,fin}}{Q_{ij}^{imp}}, \quad (18)$$

$$\lambda_{ij}^{exp} = \frac{Q_{ij}^{exp} - Q_{ij}^{exp,st}}{Q_{ij}^{exp}}, \quad (19)$$

where $Q_{ij}^{imp,fin}$ - volumes of the input container flows to hub port i of region j for which this hub port is the final point of destination;

$Q_{ij}^{exp,st}$ - volumes of the output container flows from hub port i of region j for which this hub port is the starting point of sea carriage.

Thus, for the feeder ports (which are involved in feeder services or those potentially considered for new services) from the trunk container traffic the following volume is allocated:

$$\lambda_{ij}^{imp} \sum_{i \in G_j} Q_{ij}^{imp}, (j = \overline{1, n}), \quad (20)$$

$$\lambda_{ij}^{exp} \sum_{i \in G_j} Q_{ij}^{exp}, (j = \overline{1, n}). \quad (21)$$

Obviously, all the container lines of existing feeder lines (with their specified particulars) and those lines that are organized (new ones) should be appropriate to the input/output container hub ports in the region:

$$\lambda_{ij}^{imp} \cdot Q_{ij}^{imp} = \sum_{k_j=1}^{K_j} X_{ikj}^{out} + \sum_{k_j=1}^{K_j} \sum_{l_j=2}^{L_j} v_{ikj}^{out} \cdot D_{ikj}^{l_j} \cdot s_{ikj}^{l_j} \cdot p_{ikj}^{l_j}, (j = \overline{1, n}, i \in G_j), \quad (22)$$

$$\lambda_{ij}^{exp} \cdot Q_{ij}^{exp} = \sum_{k_j=1}^{K_j} X_{ikj}^{in} + \sum_{k_j=1}^{K_j} \sum_{l_j=2}^{L_j} v_{ikj}^{in} \cdot D_{ikj}^{l_j} \cdot s_{ikj}^{l_j} \cdot p_{ikj}^{l_j}, (j = \overline{1, n}, i \in G_j), \quad (23)$$

where $v_{ikj}^{in}, v_{ikj}^{out}$ - coefficients that take into account the imbalance of export/import between the feeder ports and port hubs of the given region. The introduction of these coefficients allows the fleet's carrying capacity not to be evenly distributed (50%:50%) between the two directions of transportation (in hub ports, from the hub ports), but to consider the uneven use of the fleet, as well. The following formulas can be used to calculate the coefficients:

$$v_{ikj}^{out} = \frac{Q_{ikj}^{out}}{Q_{ikj}^{in} + Q_{ikj}^{out}}, (j = \overline{1, n}, i \in G_j, k_j = \overline{1, K_j}), \quad (24)$$

$$v_{ikj}^{in} = \frac{Q_{ikj}^{in}}{Q_{ikj}^{in} + Q_{ikj}^{out}}, (j = \overline{1, n}, i \in G_j, k_j = \overline{1, K_j}). \quad (25)$$

In Equations (22-23) $Q_{ikj}^{in}, Q_{ikj}^{out}$ are estimate potential volumes of input/output containers for feeder ports k_j in the direction to/from hub port i .

Thus, Equations (24-25) reflect the balance of the container flows in the feeder system and the environment on each hub port of each region in each direction (import

/ export). In the left parts of the equations are container flows of trunk lines, considering the share of feeder ports.

At the same time, in the right part of these constraints, the feeder services $l_j = \overline{2, L_j}, (j = \overline{1, n})$ are considered, that is, in the regional services of all the companies other than those for which research is conducted. In this case, even the existing services of the company are excluded from consideration, and the distribution of the fleet is carried out again, not but as a change of existing. This is expedient, since by adding or correcting a structure that has ceased to be optimal under the new terms, it is quite difficult to achieve an optimum approximation. While approaching the distribution of ships in the new environment, without considering the existing service structure, it is possible to get better distribution in terms of efficiency.

If companies are required to maintain any kind of feeder services in their current form, for certain circumstances (for example, a competitive strategy for a particular region), then this can be taken into account by exception of such $D_{ikj}^{l_j} (l_j = 1)$ determining D^* . Another way that can be used is to put Z_{ikj} as constants when forming $\sum_{j=1}^{n'} \sum_{i \in G_j} \sum_{k_j=1}^{K_j} Z_{ikj} = D^*$.

Note that unlike the feeder ports, the container traffic redistribution between hub ports is much less frequent, as the inertia increases, depending on the size of the object, in this case, such an object is the container hub port. However, such a task as the redistribution of container traffic is the subject of special research and is not considered in this paper.

Next, it is necessary to "link" the distribution of vessels with container traffic.

Previously, it was determined that considering the "covered" container traffic by ports, it is possible to determine the prospects (traffic volumes) for each feeder port in the region.

Considering the withdrawal of services of the carrier company, one can obtain:

$$Q_{ikj}^{fp} = (Q_{ikj}^{in} + Q_{ikj}^{out}) - \sum_{i \in G_i} \sum_{l_j=2}^{L_j} D_{ikj}^{l_j} \cdot s_{ikj}^{l_j} \cdot p_{ikj}^{l_j}, (k_j = \overline{1, K_j}, j = \overline{1, n}), \quad (26)$$

and then the following reflects the potential demand for transport services:

$$X_{ikj}^{in} + X_{ikj}^{out} \leq Q_{ikj}^{fp}, (j = \overline{1, n}, i \in G_j, k_j = \overline{1, K_j}). \quad (27)$$

The condition of "linking" the fleet of the company and the total potential demand:

$$\sum_{j=1}^{n'} \sum_{i \in G_i} \sum_{k_j=1}^{K_j} (X_{ikj}^{in} + X_{ikj}^{out}) - \sum_{j=1}^{n'} \sum_{i \in G_i} \sum_{k_j=1}^{K_j} (Z_{ikj} + Z_{ikj}^{add}) \cdot s_{ikj} \cdot p_{ikj} = 0, \quad (28)$$

where $\sum_{j=1}^{n'} \sum_{i \in G_i} \sum_{k_j=1}^{K_j} (X_{ikj}^{in} + X_{ikj}^{out})$ is the total

potential carriage for the company in the region (in both directions of transportation - from hub and to hub);

$\sum_{j=1}^{n'} \sum_{i \in G_i} \sum_{k_j=1}^{K_j} Z_{ikj} \cdot s_{ikj} \cdot p_{ikj}$ is the annual capacity (in TEU) of vessels of a company which is adjusted considering the actual loading of the vessel $0 < s_{ikj}^{l_j} \leq 1$ in capacity;

$\sum_{j=1}^{n'} \sum_{i \in G_i} \sum_{k_j=1}^{K_j} Z_{ikj}^{add} \cdot s_{ikj} \cdot p_{ikj}$ - annual carrying capacity of vessels, which is needed to be additionally involved in serving feeder services in the region;

Z_{ikj}^{add} - is a control parameter that displays the required additional container capacity of the vessels operating in the region in the direction of the hub port-feeder port. The necessity of this parameter is explained by the fact that the container capacity of the fleet of the company may not correspond to the prospective volume of traffic. For the correctness of the further solution and compliance with requirement of inevitability of the variables, and, in particular, $Z_{ikj}^{add} \geq 0$ there is requirement:

$$\sum_{j=1}^{n'} \sum_{i \in G_i} \sum_{k_j=1}^{K_j} (X_{ikj}^{in} + X_{ikj}^{out}) \geq \sum_{j=1}^{n'} \sum_{i \in G_i} \sum_{k_j=1}^{K_j} Z_{ikj} \cdot s_{ikj} \cdot p_{ikj}. \quad (29)$$

After a detailed description of the control parameters and constraints of the model, it is necessary to formulate an objective function, that is an optimization criterion that corresponds to the natural condition - the ship owner's request for maximizing efficiency. It was determined above that, under the effectiveness of feeder services the annual profit from the operating of container vessels on the feeder network is understood, which would satisfy the specified necessary level of profitability.

Efficiency of the vessels is formed from two components, such as costs (variable and fixed) and revenues from carriages of goods in containers. For this level, the freight rate per 1 TEU and the costs per unit container capacity can only be determined in aggregated way (for example, without considering the structure of container traffic, etc.).

Variable r_{ikj} means the averaged level of operating costs for use of the container vessels (in this case, use of the container capacity of the vessels) in the direction hub port i - feeder port k (and it is assumed that this level includes both variable and fixed costs of vessels, considering the specificity of the feeder vessels and searched ports) and if f_{ikj} is the average profit rate from use of the container vessels (using container capacity of vessels) in the direction hub port i - feeder port k , then the profit from operating of the company's vessels on the feeder lines will be:

$$\sum_{j=1}^{n'} \sum_{i \in G_i} \sum_{k_j=1}^{K_j} (f_{ikj} - r_{ikj}) (Z_{ikj} + Z_{ikj}^{add}) s_{ikj} \cdot p_{ikj} - r^{add} \sum_{j=1}^{n'} \sum_{i \in G_i} \sum_{k_j=1}^{K_j} Z_{ikj}^{add} \rightarrow \max, \quad (30)$$

where $r^{add} \cdot Z_{ikj}^{add}$ is the cost of engaging the additional tonnage by time chartering (for example, available tonnage in the market from other regions), respectively, r^{add} is the average time charter rate per a container unit.

It was noted above that the profit should not be simply maximized, but should correspond to profitability $I_R \geq 0$ of the fleet operating, so the model should introduce an appropriate constraint:

$$\frac{\sum_{j=1}^{n'} \sum_{i \in G_j} \sum_{k=1}^{K_j} f_{ikj} \cdot (Z_{ikj} + Z_{ikj}^{add}) \cdot s_{ikj} \cdot p_{ikj}}{\sum_{j=1}^{n'} \sum_{i \in G_j} \sum_{k=1}^{K_j} r_{ikj} \cdot (Z_{ikj} + Z_{ikj}^{add}) \cdot s_{ikj} \cdot p_{ikj} + r^{add} \sum_{j=1}^{n'} \sum_{i \in G_j} \sum_{k=1}^{K_j} Z_{ikj}^{add}} \geq I_R. \quad (31)$$

In Equation (31) describes the revenue component of the operation of the vessel in feeder services; and $\sum_{j=1}^{n'} \sum_{i \in G_j} \sum_{k=1}^{K_j} r_{ikj} \cdot (Z_{ikj} + Z_{ikj}^{add}) \cdot s_{ikj} \cdot p_{ikj} + r^{add} \sum_{j=1}^{n'} \sum_{i \in G_j} \sum_{k=1}^{K_j} Z_{ikj}^{add}$ are all the costs for the fleet operating and for the time-chartering of the additional tonnage.

Note that for many models on fleet distribution, it is typical to take into account just the final efficiency of the fleet, which is actual in solving the problem of container cargo servicing and subject to the secondary economic indicators. Therefore, for the actual situation on the container transport market, when every feeder service and operation of the vessel on it are commercially substantiated, it is necessary to introduce an additional constraint on the generalized efficiency of each service (here it means that the structure of the feeder service is determined at the next stage of the organization of feeder lines, therefore, at this stage, the feeder service is formed in general, in the form of a set of "hub ports - feeder ports").

$$\frac{\sum_{j=1}^{n'} \sum_{i \in G_j} \sum_{k=1}^{K_j} f_{ikj} \cdot (Z_{ikj} + Z_{ikj}^{add}) \cdot s_{ikj} \cdot p_{ikj}}{\sum_{k=1}^{K_j} r_{ikj} \cdot (Z_{ikj} + Z_{ikj}^{add}) \cdot s_{ikj} \cdot p_{ikj} - r^{add} \sum_{k=1}^{K_j} Z_{ikj}^{add}} \geq I_R. \quad (32)$$

Note that these constraints can take into account "regional" profitability coefficients $I_R \geq 0, (j = \overline{1, n})$, which are related, for example, to the lower performance requirements for certain regions, for example, through a particular marketing strategy.

Thus, the model of perspective directions of operation of vessels "hub port - feeder ports" and the distribution of the company's fleet in these areas is established. Combining separate components of the model presented above, in the final version are obtained:

The objective function:

$$\sum_{j=1}^{n'} \sum_{i \in G_j} \sum_{k=1}^{K_j} (f_{ikj} - r_{ikj}) (Z_{ikj} + Z_{ikj}^{add}) s_{ikj} \cdot p_{ikj} - r^{add} \sum_{j=1}^{n'} \sum_{i \in G_j} \sum_{k=1}^{K_j} Z_{ikj}^{add} \rightarrow \max. \quad (33)$$

The constraint on the fleet general effectiveness:

$$\frac{\sum_{j=1}^{n'} \sum_{i \in G_j} \sum_{k=1}^{K_j} f_{ikj} \cdot (Z_{ikj} + Z_{ikj}^{add}) \cdot s_{ikj} \cdot p_{ikj}}{\sum_{j=1}^{n'} \sum_{i \in G_j} \sum_{k=1}^{K_j} r_{ikj} \cdot (Z_{ikj} + Z_{ikj}^{add}) \cdot s_{ikj} \cdot p_{ikj} + r^{add} \sum_{j=1}^{n'} \sum_{i \in G_j} \sum_{k=1}^{K_j} Z_{ikj}^{add}} \geq I_R. \quad (34)$$

The constraint on effectiveness of the feeder services for each hub port:

$$\frac{\sum_{j=1}^{n'} \sum_{i \in G_j} \sum_{k=1}^{K_j} f_{ikj} \cdot (Z_{ikj} + Z_{ikj}^{add}) \cdot s_{ikj} \cdot p_{ikj}}{\sum_{k=1}^{K_j} r_{ikj} \cdot (Z_{ikj} + Z_{ikj}^{add}) \cdot s_{ikj} \cdot p_{ikj} - r^{add} \sum_{k=1}^{K_j} Z_{ikj}^{add}} \geq I_R. \quad (35)$$

The general compliance of the fleet distribution by volume of carriages:

$$\sum_{j=1}^{n'} \sum_{i \in G_i} \sum_{k=1}^{K_j} (X_{ikj}^{in} + X_{ikj}^{out}) - \sum_{j=1}^{n'} \sum_{i \in G_i} \sum_{k=1}^{K_j} (Z_{ikj} + Z_{ikj}^{add}) \cdot s_{ikj} \cdot p_{ikj} = 0, \quad (36)$$

The compliance of incoming container flows to the hub port with the volume of carriage in the direction from the given hub port to the feeder ports of the region:

$$\lambda_{ij}^{imp} \cdot Q_{ij}^{imp} = \sum_{k=1}^{K_j} X_{ikj}^{out} + \sum_{k=1}^{K_j} \sum_{l_j=2}^{L_j} v_{ikj}^{out} \cdot D_{ikj}^{l_j} s_{ikj}^{l_j} p_{ikj}^{l_j}, \quad (j = \overline{1, n}, i \in G_j). \quad (37)$$

The compliance of outgoing container flows from the port hub with the volume of carriage towards this hub port from the feeder ports of the region:

$$\lambda_{ij}^{exp} \cdot Q_{ij}^{exp} = \sum_{k=1}^{K_j} X_{ikj}^{in} + \sum_{k=1}^{K_j} \sum_{l_j=2}^{L_j} v_{ikj}^{in} \cdot D_{ikj}^{l_j} s_{ikj}^{l_j} p_{ikj}^{l_j}, \quad (j = \overline{1, n}, i \in G_j). \quad (38)$$

The constraint on volumes of carriages, considering the attraction of cargo base to feeder ports:

$$X_{ikj}^{in} + X_{ikj}^{out} \leq Q_{ikj}^{fp} (j = \overline{1, n}, i \in G_j, k_j = \overline{1, K_j}). \quad (39)$$

The constraint on the container capacity of the company's fleet:

$$\sum_{j=1}^{n'} \sum_{i \in G_j} \sum_{k=1}^{K_j} Z_{ikj} = D^*. \quad (40)$$

The constraint on the minimum acceptable container capacity of the feeder vessel:

$$Z_{ikj} \geq A, (j = \overline{1, n}, i \in G_j, k_j = \overline{1, K_j}). \quad (41)$$

The constraint on the acceptable size of the vessel according to characteristics of the feeder ports of the network:

$$Z_{ikj} \geq A_{ikj}, (j = \overline{1, n}, i \in G_j, k_j = \overline{1, K_j}). \quad (42)$$

The constraint of integrity of the control parameters:

$$Z_{ikj} \geq 0, (j = \overline{1, n}, i \in G_j, k_j = \overline{1, K_j}), \quad (43)$$

$$Z_{ikj}^{add} \geq 0, (j = \overline{1, n}, i \in G_j, k_j = \overline{1, K_j}), \quad (44)$$

$$X_{ikj}^{in} \leq 0, (j = \overline{1, n}, i \in G_j, k_j = \overline{1, K_j}), \quad (45)$$

$$X_{ikj}^{out} \leq 0, (j = \overline{1, n}, i \in G_j, k_j = \overline{1, K_j}). \quad (46)$$

Equations (33)-(46) is a nonlinear programming model due to the nonlinearity of the constraint on the profitability of the fleet as a whole and vessels in particular feeder directions.

The transformation of these constraints gives:

$$\begin{aligned} & \sum_{j=1}^{n'} \sum_{i \in G_j} \sum_{k_j=1}^{K_j} f_{ikj} (Z_{ikj} + Z_{ikj}^{add}) \cdot s_{ikj} \cdot p_{ikj} \geq \\ & \geq I_R \left(\sum_{j=1}^{n'} \sum_{i \in G_j} \sum_{k_j=1}^{K_j} r_{ikj} (Z_{ikj} + Z_{ikj}^{add}) \cdot \right. \\ & \cdot s_{ikj} \cdot p_{ikj} - r^{add} \cdot \sum_{j=1}^{n'} \sum_{i \in G_j} \sum_{k_j=1}^{K_j} Z_{ikj}^{add} \cdot \end{aligned} \quad (47)$$

$$\begin{aligned} & \sum_{k_j=1}^{K_j} f_{ikj} (Z_{ikj} + Z_{ikj}^{add}) \cdot s_{ikj} \cdot p_{ikj} \geq \\ & \geq I_{Rj} \left(\sum_{k_j=1}^{K_j} r_{ikj} (Z_{ikj} + Z_{ikj}^{add}) \cdot s_{ikj} \cdot p_{ikj} \right), \end{aligned} \quad (48)$$

and allows one to bring the model to the class of linear programming.

4 Conclusions

The presented model allows the liner carrier to make the right decision not only to organize a container feeder line in a specific feeder region, but to evaluate the main container flows, to choose the most profitable region as possible, as well. The adopted restrictions on the level of profitability are set depending on the strategy and level of investment of the feeder operator. The model takes into account the level of competition in the region in the form of the total container capacity of the fleet, which already operates in the region. The bottleneck is the difficulty of obtaining complete and reliable information on volume and nature of the container flows (already operating and forecasting).

References

- [1] RODRIGUE, J.-P., NOTTEBOOM, T. The geography of containerization: half a century of revolution, adaptation and diffusion. *GeoJournal* [online]. 2008, **74**(1), p.1-5 [accessed 2020-01-03]. ISSN 1572-9893. Available from: <https://doi.org/10.1007/s10708-008-9210-4>
- [2] NOTTEBOOM, T., VERNIMMEN, B. The effect of high fuel costs on liner service configuration in container shipping. *Journal of Transport Geography* [online]. 2009, **17**(5), p.325-337 [accessed 2020-02-03]. ISSN 0966-6923. Available from: <https://doi.org/10.1016/j.jtrangeo.2008.05.003>
- [3] CHEN, G., YANG, Z. Optimizing time windows for managing export container arrivals at Chinese container terminals. *Maritime Economics and Logistics*. 2010, **12**(1), p. 111-126. ISSN 1479-2931.
- [4] CHANG, Y.-T., LEE, S.-Y., TONGZON, J. Port selection factors by shipping lines: different perspectives between trunk liners and feeder service providers. *Marine Policy* [online]. 2008, **32**(6), p. 877-885. ISSN 0308-597X. Available from: <https://doi.org/10.1016/j.marpol.2008.01.003>
- [5] TAKANO, K., ARAI, M. A genetic algorithm for the hub-and-spoke problem applied to containerized cargo transport. *Journal of Marine Science and Technology* [online]. 2008, **14**, p. 256-274 [accessed 2020-06-05]. eISSN 1437-8213. Available from: <https://doi.org/10.1007/s00773-008-0035-0>
- [6] POLAT, O., GUNTHER, H.-O., KULAK, O. The containership feeder network design problem: the new Izmir port as hub in the black sea. In: 2nd International Conference on Logistics and Maritime Systems: proceedings. 2012. p. 347-356.
- [7] SHINTANI, K., IMAI, A., NISHIMURA, E., PAPADIMITRIOU, S. The container shipping network design problem with empty container repositioning. *Transportation Research Part E: Logistics and Transportation Review*. 2007, **43**(1), p. 39-59. ISSN 1366-5545.
- [8] KOS, S., ZENZEROVIC, Z. Model of optimal cargo transport structure by full container ship on predefined sailing route. *Promet-Traffic and Transportation* [online]. 2004, **16**(1), p. 15-20. ISSN 0353-5320. Available from: <https://traffic.fpz.hr/index.php/PROMTT/article/view/568>
- [9] JI, M., SHEN, L., SHI, B., XUE, Y., WANG, F. Routing optimization for multi-type containerships in a hub-and-spoke network. *Journal of Traffic and Transportation Engineering* [online]. 2015, **2**(5), p. 362-372. ISSN 2095-7564. Available from: <https://doi.org/10.1016/j.jtte.2015.08.008>
- [10] MARAS, V., KONINGS, R., RADMILOVIC, Z., DAVIDOVIC, T. Towards the optimal solution of feeder container ships routing with empty container repositioning. *Journal of Maritime Research*. 2012, **9**(3), p. 11-20. ISSN 1697-4840.

COVID-19 GROUNDED AIRCRAFT - PARKING AND STORING

Francisco Serrano^{1,2}, Antonín Kazda^{1,*}

¹University of Zilina, Zilina, Slovakia

²Hamad International Airport, Doha, Qatar

*E-mail of corresponding author: antonin.kazda@fpedas.uniza.sk

Resume

Air transport industry is one the many sectors significantly impacted by the COVID-19 pandemic. Travel restrictions and bans resulted in reduction in aircraft operation. Airlines have no option than to limit their services by grounding their fleet: as of April 2020, out of 22,000 passenger aircraft around the world, almost 14,400 were grounded [1]. Airport operators are trying to accommodate most of the grounded aircraft by utilizing their main operational space as aprons, taxiways and runways. The limited space at airports often means that aircraft have to be parked in non-standard positions, which may affect the airport daily operations. While planning aircraft parking, safety is the top priority. The effect of long-term load was not considered in the pavement design and could result in increased pavement maintenance requirements. Airport operators must also reflect aircraft maintenance needs in terms of engines, hydraulics, braking system, cabin interior and others.

Article info

Received 9 July 2020

Accepted 6 October 2020

Online 23 February 2021

Keywords:

aircraft grounding,
parking positions,
storing aircraft,
pavement strength,
aircraft maintenance

Available online: <https://doi.org/10.26552/com.C.2021.2.A103-A115>

ISSN 1335-4205 (print version)

ISSN 2585-7878 (online version)

1 Introduction

Specifications for the aprons and aircraft stands are globally defined by the International Civil Aviation Organization (ICAO), Annex 14, Volume I, Aerodrome Design and Operations [2]; in the EU by the Regulation (EU) No 139/2014 [3]; or in the USA by the Federal Aviation Administration (FAA) Airport Design and Engineering Standards AC, 150/5300-13, Apron, (Appendix 5) [4]. More details about apron and stand characteristics can be found in the ICAO Aerodrome Design Manual, Part 2, Taxiways, Aprons and Holding Bays [5]. To build an apron and stand a standard documentation for building permit is usually required, which depending on a particular state, could be very time consuming. The unexpected epidemic of COVID-19 created an emergency and urgent situation in terms of aircraft parking requirements. Besides the planning and design requirements, there are operational issues, which significantly differ from the normal airport and airline operation.

The non-standard parking positions for the aircraft at an airport becomes an urgent problem for an airport and airlines during this COVID-19 pandemic. There were airports that had to close their critical facilities to accommodate aircraft due to reduced number of services. On 20 March 2020, the FAA issued National Part 139 CertAlert No. 20-02 [6] to provide recommendation for airport operators while handling the Temporary Parking of Overflow Aircraft. This CertAlert also provides a list of considerations for an

airport operator when making decision for overflow aircraft parking.

Another FAA document, The Safety Alert for Operators (SAFO) 20005 [7] provides information for pilots and flight operators on the potential effects of parking overflow aircraft in excess of airport capacity. While the FAA CertAlert has also been used by non-US airports (e.g. in Australia), other countries have issued their own guidance, for example France with a 'Flash Info' on the Storage of Aeroplanes. The upcoming Airport Cooperative Research Program (ACRP), a 'toolbox' on enhancing the management of adverse conditions is being developed by the company WSP USA, will feature reference sheet on the temporary parking of overflow aircraft. Finally, the Infrastructure Workgroup of the French-Speaking Airports (UAF&FA) will be preparing an extensive guidebook on the same matter later this year.

The COVID-19 pandemic led to drastic and unparalleled collapse in air traffic which grounded significant part of the global airline fleet. As mentioned by Le Bris [8], with reference to Airports Council International (ACI) World report, more than 75% of commercial airports around the world have already plans in place to accommodate overflow parking. It means that airports will turn into active aircraft storage and such active storage at an airport will need to be arranged, coordinated and synchronized between stakeholders to ensure aircraft protection and encourage easy recovery.

This paper provides a summary of comprehensive



research in the field of non-standard aircraft parking, analyzes the impacts on airport operations and compares the best of the recommendations and guidance related to non-standard overflow parking positions for aircraft at airports during the COVID-19 pandemic.

2 Research methodology

In this research, the focus was on the issue of the COVID-19 pandemic impact on civil aviation, specifically on the area of aircraft grounded and the need for aircraft parking, storing and maintenance. The scale of the problem and especially the speed as it arose is not comparable to any other crisis in the civil aviation. When grounding the Boeing 737 Max 8 it was necessary to provide parking for less than 800 aircraft (387 delivered to customers as of March 2019 [9] and approximately 400 produced and stored as of December 2019 [10]) in case of aircraft parking during the COVID-19 pandemic almost 14,400 aircraft had to be parked [1].

The conducted research is a type of an explanatory research. Referring to [11] 'it explains and confirms the behavior or dependencies in the system and tries to explain the patterns in the behavior of the system, its processes and structure; explanation is an attempt to understand the causes of the phenomena, factors and mechanisms that cause them'. The inductive explanation strategy was used in this research. Behaviour of the system was tried to be explained using some of the 'known' principles, setting general rules and recommendations based on specific cases [12]. The problem of induction could be that '...mind often draws conclusions from relatively limited experiences that appear correct but which are actually far from certain' [13]. When using induction, there is often a problem with the results verification. In this case, the results were verified and confirmed by comparing solutions and findings from different cases [12]. Although the history of COVID-19 is relatively short, the historical method was primarily used in our research. Historical method allows to examine particular events or processes that occurred over short spans of time [14]. In this research a large range of available materials, reports, guidelines, standards and recommended practices published by international organizations, state authorities, airlines and airports, were studied. The historical method comprises the techniques and guidelines by which one uses the primary sources and other evidence to research. The historical research can also mean gathering data from situations that have already occurred and performing statistical analysis on this data just as it would be done in a traditional experiment [15].

We also used a monographic method concentrated in our research on one particular case - problem of overflow aircraft parking. This method understands the researched problem as a whole in contrast to typological method that selects just one aspect [15].

3 Temporary aircraft parking requirements

As during this pandemic airports became aircraft storage, parking space is currently very limited and additional parking aprons are a critical need. With apron space at maximum capacity the airport must resort to less desirable options such as parking in non-pavement areas and using space designated for temporary parking. In terms of airport operations and traffic requirements, it could be recommended to use all the space at gates and aprons first, before considering taxiways and runways as parking area options. Concrete pavements should be favored for the long term parking, rather than flexible asphalt pavements.

The options include contact and remote gates, remote overnight parking and aircraft de-icing pads, and active taxiways that could be closed to traffic. A parking situation lasting several months should be reviewed regularly. Existing gates should be utilized first. Once all the stands at the gates are occupied, other options might be considered e.g. the densification of parking on ramps and aprons and then taxiways.

At taxiways selected for aircraft storage different sections that will be closed sequentially can be defined. Taxiway lighting should be turned off on the closed sections and the portion of taxiways leading to these sections (e.g. exits from active taxiway). The parking areas should be closed with barricades with red lights installed as at the airfield construction zone. If a taxiway is closed for aircraft parking, US Department of Transportation also mentioned that the deactivation of the taxiway lighting circuits is a good practice to follow [16]. If deactivation is not feasible as other taxiways on the same circuit must remain open it is advised not to remove the lamp-bulb from energized fixtures because an excessive number of isolation transformers with open end can damage the constant current regulators and/or increase the current flow above its normal value. In this case the solution could be to cover the light fitting so that light leakage can be avoided. It is necessary to secure, identify and place any above ground temporary wiring in conduit to prevent electrocution and fire ignition sources.

In order to use any taxiway for aircraft parking, it must be temporarily closed. The US Department of Transportation has published advisory circular [16] for the airport operators to apply specific markings on the ground to maintain safe operations, such as:

- Place cordons outside the safety area of crossing taxiways;
- To place a mark such as X mark at the entrance of closed taxiway so that it visible from the runway (RWY);
- In the case that the airport operator has a plan to close a taxiway for a long term it is a good practice to remove the centreline marking including the one that is leading to the closed section.

Later, in situation that the taxiway will reopen, the airport operator shall repaint the centreline marking. As



Figure 1 Closed RWY 04/22 at Praha/Ruzyně airport with COVID-19 grounded aircraft parking; marked with 'closed runway marking'; author: Vocolka, T.

already mentioned, the airport operator shall use all the stands at gates and the whole apron as much as they can considering operations safety. If an apron is fully occupied, it must not impede aircraft movement between the stands in operation and the terminal area. However, the airport operator could maximize the use of intermediate taxiway(s) for potential parking.

Runways as temporary parking should be avoided as far as practicable due to the potential of increased safety risk of inadvertent landings on a closed runway. According to FAA guidelines runway closing should become the last option for airport operators due to potential high risk [17]. The FAA took a clear position on this matter in its Part 139 CertAlert on temporary aircraft parking. This is justified by data records of aircraft performing final approaches over temporarily closed runways, some of them with massive obstacles or equipment on the runway that should have alerted pilots or even taxiways occupied by aircraft. However, permanently closed and decommissioned runways can be considered (see Figure 1).

The planning and design of aircraft stands is an important part to support the execution of the new aircraft parking operation. It can be checked and optimized by a full airside exercise before the implementation of the plan. It is also important not only to consider the number and size of stands, but also flows of traffic around the parking area. In order to minimize taxi waiting times and push back interference, different aircraft routing scenarios need to be considered. With the current situation, ACI World published a recommendation for airport operator to develop and update a comprehensive temporary aircraft parking plan [18]. The purpose of a temporary aircraft-parking plan is to identify parking options and priorities and clearly indicate where to park different types of aircraft. The plan should

be continuously monitored and updated when required and should identify at least:

- Locations for long, intermediate and short-term parking of aircraft;
- Safety impact of parking options on obstacle limitation surfaces and operations;
- Clearance distances between aircraft;
- Non-standard parking locations that could be used safely for aircraft overflow parking;
- Notification procedures and safety measures when the non-standard parking locations are used (such as runways and taxiways).

Some airports reported using geographic information systems and digital tools to complement the plan and monitor the implementation of changes. Insertion of pictures and diagrams is highly recommended.

For instance, as written by Creedy [19], Brisbane airport expects to have up to 100 aircraft parked ranging from an A380 to QantasLink Dash-08s. The airport has therefore created additional ten dedicated parking zones to accommodate the increased demand. The new additional parking areas include runway, taxiway, logistic apron and various other aprons.

To design or plan the additional parking positions, airport operators should take into account the following considerations:

- The additional position should be created in a way that it can be returned to their original purpose when needed;
- Parking positions of aircraft should allow their regular maintenance;
- The maintenance staff should have an easy and unrestricted access to aircraft in order to perform their duties.

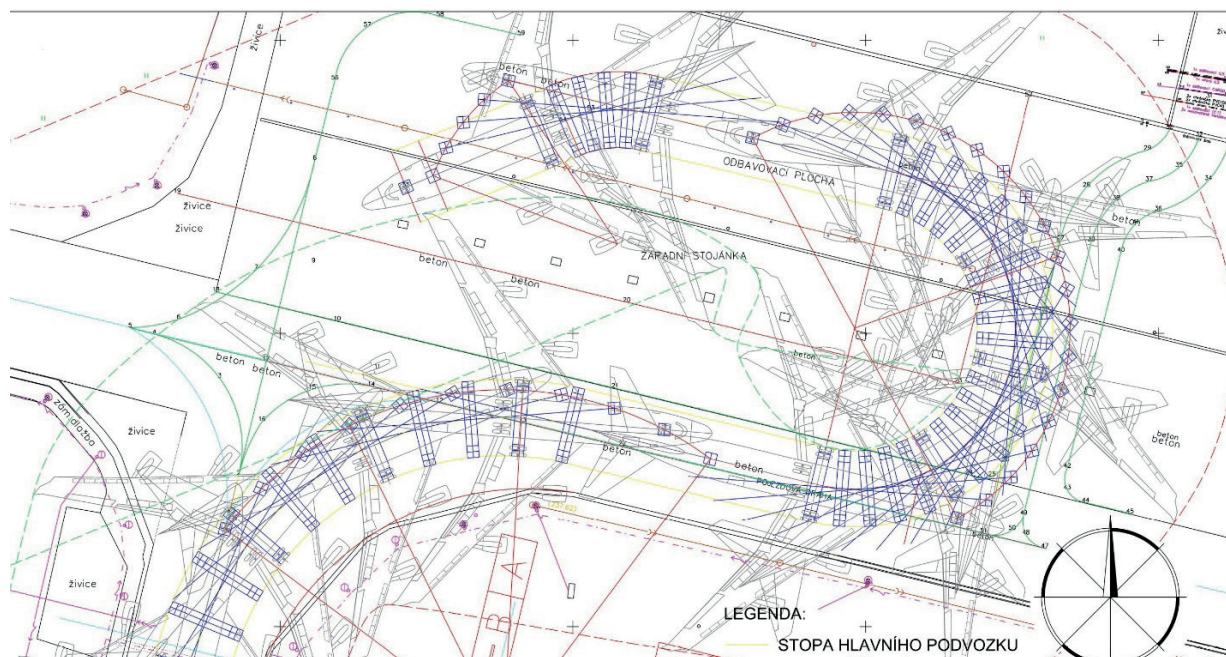


Figure 2 Visualization of B-747-400 maneuvering at Brno-Turany airport; author: Kazda, A.

An overflow parking is happening at most of airports around the world as an impact of COVID-19 pandemic. The FAA released national Part 139 CertAlert as an solution for an airport to handle the parking situation [17]. Le Bris states that it is a good practice to establish a parking plan and a procedure for temporary parking of overflow aircraft [8]. It should be prepared collaboratively by a workgroup or committee made of representatives of stakeholders potentially involved with such situations and should include airport operator, Rescue and Fire Fighting (RFF), Air Traffic Control (ATC), aircraft operators, ground handling service providers, fixed base operators, maintenance, repair and overhaul (MRO), etc. The plan should be scalable i.e. adaptable to different numbers and types of aircraft to pave the way for a timely and adequate response for the next time if the airport faces overflow of aircraft. This effort should consider and balance the needs of stakeholders, explore the short-term and long-term parking options and document the rationales behind the choices made. The plan and procedure should be regularly updated based on lessons learned and evolution of the airport conditions.

The plan should ideally be drawn using CAD applications (see Figure 2). This would facilitate the discussion with stakeholders, enhance the identification of potential geometric, safety issues and provide the teams in the field with an accurate depiction of the parking plan. This plan must feature support to position each aircraft. This can be the location of the nose and main gears. This assistance should be consistent with the means available in the field. For instance, if the GPS receivers or other surveying tools are not available to the crews, visual aids (e.g. number or identification number of concrete pavement slab) are recommended to supplement the geo referencing. Temporary markings can be provided as well.

Below are presented considerations recommended

by the FAA [17] that should be applied when overflow of temporarily parking of aircraft at an airport is happening due to overcapacity during the COVID-19 emergency. This list should be considered as a minimum list of considerations and not as a complete list. Safety to the public and aircraft operations should remain the highest priority:

- Create an aircraft parking plan committee (airport operators are encouraged to work together as a committee with members of airlines and other related stakeholders).
- Document the aircraft parking plan considerations.
- Coordination of the plan (coordinate the plan for temporary parking of overflow aircraft at the airport with all the airport users as appropriate).

4 Temporary aircraft parking risk assessment

The airport operator is responsible for the rules and procedures that safeguard movements of aircraft on stands or apron and for dissemination of information to airline company operators. In line with the ACI airside safety book [20], it is the responsibility of airport operators to conduct a risk assessment to develop an objective of the risk associated with a specific activity. The risk assessments should be conducted for each task to be carried out by staff and can be carried out on a higher level of the operational business for example, prioritize the non-standard parking position. At the end, the risk assessment results could give airport operator an option while activating the non-standard parking positions.

It is critical to assess the safety impact of overflow aircraft parking on infrastructure, obstacle limitation surfaces and operations and take the adequate measures to mitigate the risks, including the collision risks. It is also

recommend by ACI World in their bulletin that the airport operators adjust to the specific conditions depending on their airports by creating safety risk assessment template [18]. The template could show a particular assessment such as hazards, consequences, the risk control rating, mitigation actions and new control for the specific risk events.

It is understood that most of the airport operators are facing the same challenge of finding new appropriate location for the aircraft to handle demand from the airlines as an impact of COVID-19 pandemic. According to ACI on their bulletin [18], this situation may lead to risks to the airport infrastructure and safety including:

- Damage from the use of pavement in a way not originally intended;
- Aircraft damage especially the risk of collision during the parking manoeuvres with minimum clearances;
- Runway or taxiway incursions;
- Issues around aircraft access and availability.

Most importantly, the parking plan and procedure must put safety first. Performing a safety risk assessment is necessary [21]. An airport must be able to continue operations safely. Closing part of the airport for storing aircraft means that a new taxiway layout is being created. This new, temporary layout must be able to accommodate the throughput and address the usual safety concerns including, but not limited to, runway incursions, NAVAIDS integrity and pilot deviations.

In addition, the line of sight from the tower to the active parts of the movement area must not be obstructed. Pilots need to be made aware of the runways and taxiways closed for parking aircraft. Specific Notices to Airmen (NOTAMs) shall be issued for raising situational awareness. In return, pilots shall report any issues such as the deviation or inaccuracy of the Instrument Landing System (ILS) signals or reflections lights which may cause confusion.

Adequate markings and signage should be provided as needed. Even if aircraft are parked on movement area pavements designed for regular use of aircraft, the positioning of the aircraft for the long-term parking may compromise safety. For instance, the tail of an aircraft parked diagonally on a taxiway might infringe runway protection surfaces or disturb the ILS signal while they are perfectly fine when an aircraft is aligned on the centerline.

The various safety areas and surfaces preventing safety issues and that protect flight operations shall be verified before parking aircraft. This is the reason why the FAA requests submittal of an FAA 7460 form if there is any potential impact on these surfaces in order to confirm potential hazard issues. If temporary engine run-up spots are provided, jet blast shall be carefully considered as well.

5 Pavement loading characteristics

During this time airports are bounded with limited parking capacity and considering other areas among them, as well with flexible pavements, to allocate the aircraft. Static loads from aircraft over a prolonged period may

result in pavement deterioration, in particular in the case of flexible - asphalt pavements. Today aircraft operators and airports are facing medium to long-term aircraft storage issues. As aprons and parking areas are not designed for accommodating long term static loads prolonged aircraft storage on those areas can increase the risk of permanent deformations.

For pavement preservation while considering aircraft storage for long time, it is recommended to prefer areas with rigid pavements. Flexible type of pavements (asphalt) are not the best solution for parking areas for stands with high loadings. They are more sensitive than concrete paving to static loads and more sensitive to high temperatures due to bitumen's rheological properties, or more specifically, static loads from aircraft over a prolonged period, especially on flexible pavements, may result in pavement deterioration. In addition, while aircraft are parked, airlines need to conduct aircraft maintenance and any resulting fuel or oil spills could cause deterioration of asphalt pavement.

A pavement analysis should be carried out if the storage area is not designed to store aircraft for a long time considering as an overload on pavement. Parking and aprons, where aircraft operate at low to very low speed, are usually made of cement concrete pavements. The bearing strength of taxiways (moderate speed section) is greater than runways (except in some cases on runway thresholds), but lower than parking/aprons, which are purposely designed for accommodating static aircraft loads considering the movement [22]. The slower the speed, the lower the (complex) modulus of elasticity and the higher the shear strain at the bottom of the bituminous layer. Bituminous materials have a viscoelastic behavior and their modulus of elasticity depends on the temperature and the load frequency/speed (bituminous material rheological properties). Following the above consideration, it is implied that taxiways subjected to static aircraft loads are more sensitive to permanent deformation than those subjected to moderate or high-speed loadings.

In order to support airlines and airports with respect to aircraft storage for a long term, Airbus has produced a document for pavement and asset preservation that is supported by ACI. Furthermore, the document defines the best practices for aircraft storage on taxiways and runways. The main consideration for airlines and airports, while planning the long-term aircraft storage can be found on Airbus Consulting Services - Recommendations for pavement (storage area) preservation document [23].

As stated by the ACI in their advisory bulletin for mitigating the risk created by overflow aircraft parking, it is important to assess pavement strength to accommodate the loads and to check Aircraft Classification Number (ACN) and Pavement Classification Number (PCN) compatibility [18]. Technical analysis should be carried out before overloading pavements by more than 10% relative to reported pavement strength.

In addition, in the case that overloading cannot be avoided by the airport operator due to any reason (aircraft traffic/aircraft parking), according to advisory circular



Figure 3 Intersecting cracks, cement concrete pavement slabs; author: Kazda, A.

published by FAA No:150/5335-5B [24], the airport authority has three options when making a pavement strength rating selection:

1. Let the PCN remains as derived from the technical evaluation method, but assess the pavement load/overload with respect to local specifics, such as planned repairs or reconstructions. Experience with operation of a particular type of aircraft in a specific traffic mix can also have an impact on decision to operate with the ACNs that exceed the published PCN or at a reduced weight not to exceed the PCN.
2. Provide for an increased PCN by either adding an overlay or by reconstructing to accommodate aircraft with the higher ACNs.
Adjust the PCN upward to that of the aircraft with the highest ACN, but recognize the need to expect possible severe maintenance. This will result in earlier than planned reconstruction or overlay due to reduced pavement life.
3. The pavement load also depends on the tire pressure, which affects the size of the contact area between the tire and the pavement [22]. While planning aircraft storage for a long period, aircraft should be made as light as possible by unloading anything that can be appropriately and safely removed without jeopardizing its resistance to the wind. The load may be distributed over a larger contact area by deflating tires, but not less than recommended by the manufacturer.

In addition, as stated by Goodyear Aviation, one of the

aircraft tire manufacturer in their published document, it is important to monitor the tire pressure at the prescribed values during the aircraft parking [25]. Tire pressures should always be checked when tires are cool, with the tire being at ambient temperatures. A tire/wheel assembly can lose as much as five percent of the inflation pressure in a 24-hour period and still be considered normal. This means that tire pressures change on a daily basis.

For instance, Qantas airlines maintenance team has put tire maintenance as one of their maintenance schedule during this massive grounding plan. The maintenance team ensures that aircraft have their wheels rotated-by being towed on tarmac or jacked up into the air to be rolled to ensure to perform tire maintenance as stated by Bloomberg [26].

6 Pavement maintenance

As stated by ACI, in their published bulletin pavement condition should be inspected regularly to monitor potential pavement deterioration [18]. When inspecting the pavement, deterioration that should be documented and include, but are not limited to:

- Depressions on flexible pavements under wheels;
- Ripples and bumps;
- Puncturing in case of inadequate pavement design;
- Damage from fluid leakage (in those areas, protection should be provided by a solvent-resistant surface).

In addition to the above, Federal Aviation

Administration (FAA) published in their advisory circular No 150/5380-6C that the airport authority is advised to conduct Pavement Management Program (PMP), which is an effective maintenance and repair system [27]. In addition, it is a systematic and consistent procedure for scheduling maintenance and rehabilitation based on maximizing benefits and minimizing costs. It is also explained that the primary component of any PMP is the ability to track a pavement's deterioration and determine the cause of the deterioration condition.

Pavements could deteriorate quickly if they are subjected to aircraft loadings that exceed their structural design strength. There are many formations of pavement deterioration according to the type, extent and severity conditions, as cited in filed guide report of Airport Cooperative Research Program (ACRP) [28]. Among them, one is intersecting cracks (see Figure 3) that break a slab into four or more pieces due to overloading, inadequate support, or both. Furthermore, pavement deterioration signs and probable cause are defined in pavement evaluation and rating document as per ICAO [29].

7 Airport - airlines cooperation and coordination

It is recommended that airports establish an aircraft parking committee that will review the temporary aircraft parking plan when necessary. All the relevant stakeholders should be represented in that committee. For proposed temporary parking of aircraft on aprons and taxiways airport operators are encouraged to work collectively as a committee with airline representatives, aircraft owners and fixed base operators, the air navigation services provider, rescue and firefighting corps, airport security team, airport safety team including airside safety and standards and airport schedulers [30].

The range of problems to be discussed within the aircraft parking committee could be wide. As explained by Laubrock [31], there are many other tasks and optimization potentials with respect to aircraft stands and gates. In particular, all the kinds of airports need an-effective IT solution, which could be customized depending on the airport stakeholder requirements [32]. For this, a collaboration is required between an airport operator, aircraft parking committee and IT team in order to plan a realistic operational plan and predictions [33] for proactive stand management, stand and gate capacity analysis, seasonal planning, airside capacity estimation, validation of airside planning, demand-capacity balancing, what-if - scenario testing and operational ad-hoc allocation [34].

8 Aircraft grounding

A remote parking plan should address the needs of different stakeholders. Aircraft operators have several needs and constraints that are specific to their aircraft storage strategy and should be discussed with them.

A parked aircraft is not just a dead weight that can be left for days without attention. It is a living piece of aviation engineering that is subject to strict airworthiness criteria. Systems and engines shall be turned on regularly otherwise a longer process will be required to return the aircraft to commercial operations. Aircraft hardware and software systems need care and attention. Manufacturers should establish extensive procedures in the Aircraft Maintenance Manuals (AMM) to preserve their airworthiness during the short and long-term parking. Procedures exist for servicing and protecting the aircraft parked for different periods. Consequently, maintenance teams should have access to the aircraft as far as practicable without an escort.

Some service roads might be restricted to specific airfield driver's license or might be closed by gates. Some roads might not have the adequate bearing strength for supporting all the vehicles used for aircraft servicing. For the same purpose of providing access an aircraft might be offset instead of centered on the taxiway to leave a side corridor for low-clearance vehicles.

The COVID-19 pandemic has put airlines on the edge of their business. Airlines do not have much choice except to reduce their service and park their aircraft for a long time or store them. As pointed out in [35], Brussels Airlines, for example, had to reduce their scheduled services due to COVID-19 and ground a large part of their fleet.

To provide support in this situation, Airframer, an aircraft manufacturing company, has developed dedicated instructions for storing the aircraft in a safe manner. Airframer states that it is important for the airlines to follow the instruction precisely so that 'they can easily and efficiently bring the aircraft back to normal operations'. At the same time, this will reduce the risk of additional work and costs when the aircraft is put back into service [36].

In the current situation, Brussels Airlines, for example, needs to spend about 400 man-hours to store an Airbus A330. This time is spent mainly to protect the aircraft to keep it clean and protected, such as by taping windows to avoid direct sunlight which could damage the cabin interior, covering the seats to keep them clean also covering the engines and landing gear to avoid any debris while restoring.

In addition to storing an aircraft, airlines say that aircraft cannot be left parked for a long period of time. Within the daily and weekly routine checks the maintenance staff has to slightly turn the aircraft wheels to avoid deformation due to the long-term load of the aircraft.

9 Aircraft maintenance

Another important issue for an airline to consider when grounding an aircraft is the responsibility to maintain the aircraft performance in accordance with the rules and regulation of the aviation authority. In addition to that, for an aircraft that is still on lease it is a mandatory requirement from the lessor to the lessee (airline) to maintain and conduct the maintenance of the aircraft until

the termination of the lease. This requirement has the objective to maintain a valid certificate of airworthiness for aircraft at all time. Moreover, for an airline that is having a leased aircraft it is requested by the lessor to have various insurances to cover any kind of risks such as loss, damage and destruction of an aircraft, which could occur when aircraft is grounded for a long period. Realizing such kind of risks, instead of keeping the aircraft on ground and having difficulty to pay the lease, according to authors of [36], some airlines prefer to return the aircraft to the lessor or, if they own the aircraft, sell it and lease the aircraft back to obtain financial resources.

The procedure to store aircraft is commonly highlighted in aircraft manuals and the maintenance programmes. Additionally, each civil aviation regulatory authority has a set of standards that an airline operator has to follow. Parking an aircraft is usually covered with a section dedicated to parking, storage and return to service. As explained by Pandey [37], there are few procedures that an airline should follow before the aircraft is put into storage such as:

- Fuel and oil-levels are recorded and adjusted as required. The key risk that has to be guarded against is contamination of fuel in the wing tanks and ensuring adequate oil levels to guard against parts drying out. Some companies also add an element to fuel tanks called Biobor to keep microbial growth in the tanks at bay. As far as the airframe is concerned, visual inspections are carried out with all the possible inlets being carefully covered.
- Depending on weather conditions, landing gear and windows may have to be covered.
- Hydraulics, flaps, slats and auxiliary power unit (APU) may have to be periodically tested to ensure that the lubrication is adequate.
- Avionics may also be powered on to ensure these are in working condition.

There is always a risk for an aircraft when it is parked for a long period. Tsai from Boeing [38], clearly mentions that aircraft parking creates a risk that the aircraft may not be properly protected and may not be properly restored when they resume normal operations. As each aircraft has a different system of software and hardware means, the airlines need to pay more and more attention to protect and restore the aircraft after parking.

When the aircraft is parked, airlines need to have a scheduled maintenance in place to avoid more damage to the aircraft. It is also important to pay attention to verify the aircraft airworthiness such as aircraft configuration and operational status of aircraft system. Most of the airline MROs already noticed that any aircraft being restored to normal service after a long period of parking time would need an extra attention [39].

It is necessary to establish clear procedures and restrictions for aircraft access for fueling, cleaning and maintenance, including the engine runs; specify when access is needed day or night and decide who has the access. Measures should also be introduced to maintain

the security of parked aircraft. Necessary equipment such as chocks, cones and tie-downs should be allocated and procedures determined, as well as using a clear identification or reference for each temporary parking position. It is also desirable to provide portable lighting for remote areas that are having limitation for lighting.

Inside the aircraft, certain systems must be deactivated. All windows and doors should be covered (ideally), as well as the landing gear and tires. This is towards protecting them from the elements. All the carts should be emptied out; seats covered with plastic sheets if required and in certain cases some equipment should be removed from the aircraft. The inside cabin should also be aired to ensure minimal moisture and mitigate any impact of heat. All of this is also critical towards ensuring that the aircraft, once ready to fly, can be put back to use in the fastest possible time.

For airlines, as an advice from author of [40], it is a good practice to apply protection to the aircraft exterior and interior before parking, as it will ensure that the paint remains undamaged. In addition, it is a good idea to regularly air out the cabin of the airplane by opening all possible access points including the baggage/cargo compartment as it is better to getting air moving through the cabin as much as possible.

Etihad Airways chose another approach to aircraft maintenance during the COVID-19 pandemic. As mentioned by Guillot [41], the national carrier of the United Arab Emirates (UAE) is reacting in different way by launching the most extensive maintenance program in the history of the airline. They took this initiative as an effect of COVID-19 that forced them to ground most of their fleet at Abu Dhabi International Airport. Etihad takes advantage of the situations to clean, refresh, repair and if required, to improve aircraft cabins before resuming the service. This includes conducting an update to the In-flight Entertainment (IFE). For the cabin interior part the airlines did massive cleaning and laundry such as the leather upholstery that belong to the first and business class seats. The aim of all of these actions is to keep the aircraft ready when the operations resume.

10 Engine maintenance

More than 40% of Direct Operating Cost for a typical wide body aircraft can be directly attributed to engine performance, design and reliability [42]. Engines are the most expensive item and, unfortunately, are the most variable and sensitive to operation standards. The only way how one can predict maintenance actions or to adjust to industry average, it is to properly reflect on all the aspects of operations [43]. In addition to the aircraft storage, engine storage has its own set of requirements. Lessors' permit airlines to enter into engine maintenance costs per flight hour, power by the hour (PBTH), fleet management programs (FMPs) or similar agreements with engine manufacturers or any other engine maintenance



Figure 4 Engine inlets properly sealed and wheels thoroughly covered; author: Melus, M.

facility, provided the terms of such an agreement are fully in compliance with requirements in the lease agreement. This often helps airlines to reduce significantly maintenance costs without compromising on the quality of the work.

Currently, most of airlines MRO department are working continuously for maintaining the fleet of grounded aircraft. In terms of engine maintenance, new processes and procedures had to be set up that includes the running engines, powering up the aircraft, covering the sensors to protect from sand and dust as well as checking flight control instruments. Engineers, duly trained and certified by the relevant authorities among other things, have to ensure that the engine parts and bearings are properly lubricated, all inlets covered and sealed (see Figure 4). Each aircraft comes with a set of engine covers and thus one sees aircraft parked with engines covered. Aircraft engines also need to be run at regular intervals. As an example, when the Boeing 737Max issue surfaced and aircraft were grounded maintenance programs required that engineers power up the engines once a week to vaporize any moisture in the oil and fuel systems. Running up the engines also allows for circulation and fuel change in the system to prevent degradation of seals and rubber parts in the pipes and fuel pumps [44].

Large fleet of parked aircraft therefore requires availability of technical staff. For example, 650 parked aircraft represent 1300 engines with 14 variants across 5 manufacturers, which will have to be powered and run at idle for a specific amount of time, depending on manufacturer recommendations.

Siebenmark mentions that engines require specific treatment such as the use of engine cover [40]. Desiccants mounted in the inlet and outlet of the engine as well as humidity indicators, should be used in the covered engine to ensure that the humidity does not exceed the limits. The other important thing is to conduct regular scheduled inspections while the aircraft remains in long-term storage.

11 Aircraft return to service

Once the go-ahead is given for a return to service, airlines cannot simply take the aircraft and return it to flight operations. Extensive documentation and checks should again be carried out. The primary goal of aviation is safety and ensuring continued airworthiness. This also poses a regulatory challenge since a regulator is simply not staffed to oversee such a large volume of aircraft. How the return to service will be managed remains a matter of much debate within aviation circles.

An advice from one of the aircraft manufacture technical person [38] is that the operational status of an airplane in service is significantly different from an aircraft after returning from maintenance or parking for more than one day. If an operational testing is required after a long period of grounding of an aircraft, then the maintenance measures must be carried out. In addition, recommendations from each person involved in returning the aircraft to service are crucial for the airlines to maintain the safety of the aircraft.

12 Airport returning to normal

Airport operators should consider re-certification of runway and taxiway pavements used to park aircraft during the COVID-19 pandemic before resuming operations. If some pavement distresses have not been identified at the return to normal service of the area, the risk will be transferred to aircraft and in those cases required repairs would affect operations. It is not only the airport operators, many aviation authority and regulator are not able to perform their standard administration of various licenses as their operations have also been impacted by the COVID-19 outbreak.

To handle this, ICAO in their press release [45] established a system called COVID-19 Contingency Related Differences (CCRD) to support all the states to be able to record any kind of differences related to their standard policies. With this action, ICAO will be able to ensure the safe continuity of flights between countries in a good manner and to have this documented once operations back to normal.

13 Conclusion and further research

The COVID-19 adverse impact on the whole aviation industry has forced airlines and airports to significantly reduce their operations according to the depleted travel demand and restrictions imposed by the states. This situation turned challenging for airport operators when the airlines are forced to store their fleet for a long term. In order to facilitate airline requirements for storing aircraft, airport operators had to prepare plans in collaboration with key stakeholders to ensure that all the essential matters are addressed, while maintaining safety of operations.

In order to respond to the situation, both airline and airport operators along with aircraft manufactures, have taken various measures from accommodating grounded aircraft on specific parking slots to create a heavy maintenance schedule to keep aircraft safe and airworthy by adhering to standards and requirements. Furthermore, appropriate precautions need to be considered to ensure

serviceability as aircraft and related equipment are static for a long period. Storing aircraft for a long time could become a massive problem for airlines if they could not manage and maintain it appropriately.

In addition to above, the airline maintenance team has a key role to play in order to maintain grounded aircraft. They need to have a precise schedule including the preparation when aircraft needs to fly again. The engine, cabin interior and exterior, avionics, wheels, are the critical assets that airlines need to pay more attention to. For this, as the best practice the airlines can always refer to Aircraft Maintenance Manual provided by manufacturing company.

Similarly, airport operator needs to draw more attention to ensure pavement condition is safe, secure for aircraft performance and to accommodate airlines line maintenance team to conduct necessary scheduled maintenance activity on grounded aircraft. In addition, the airport operator shall ensure access to current and new parking stands is available and maintained to avoid any delay that can affect aircraft performance.

Ultimately, the airports and airlines are suggested to always ensure safety as a top priority as advice by ICAO, ACI, FAA, EASA and the aircraft manufacturing companies. All the key stakeholders need to ensure and understand the current operational environment as vital for the long-term sustainability of aviation industry.

The problem of aircraft long-term parking is associated with other issues as, for example, airport pavements long-term static loadings, which may be a subject of further research.

Acknowledgment

This research was supported under the project of Operational Programme Integrated Infrastructure: Research and development of contactless methods for obtaining geospatial data for forest monitoring to improve forest management and enhance forest protection, ITMS code 313011V465. The project is co-funding by European Regional Development Fund.

References

- [1] KINGSLEY-JONES, M. Mixed fortunes globally as active fleet drops towards 7,000 aircraft [online] [accessed 2020-04-20]. 2020. Available from: <https://www.flightglobal.com/fleets/mixed-fortunes-globally-as-active-fleet-drops-towards-7000-aircraft/137893.article>
- [2] ICAO. Annex 14, Aerodromes. Vol. I. Aerodrome Design and Operations. 8. ed. Montreal: International Civil Aviation Organisation, 2018.
- [3] EASA. Easy Access Rules for Aerodromes [online] [accessed 2019-05-30]. 2019. Available from: <https://www.easa.europa.eu/newsroom-and-events/news/easy-access-rules-aerodromes-updated>
- [4] FAA. Airport Design and Engineering Standards. AC 150/5300-13A, Apron, (Appendix 5). Washington, 2012.
- [5] ICAO. Aerodrome Design Manual. Part 2. Taxiways, Aprons and Holding Bays. Montreal: International Civil Aviation Organization, 2005.
- [6] FAA. Temporary Parking of Overflow Aircraft [online] [accessed 2020-04-01]. 2020. Available from: https://www.faa.gov/airports/airport_safety/certalerts/media/part-139-cert-alert-20-02-COVID-19-temporary-aircraft-parking.pdf

- [7] FAA. Safety Alert for Operators [online] [Accessed 2020-05-31]. 2020. Available from: https://www.faa.gov/other_visit/aviation_industry/airline_operators/airline_safety/safo/all_safos/media/2020/SAFO20005.pdf
- [8] LE BRIS, G. Best practices on the temporary parking of overflow aircraft [online] [accessed 2020-04-18]. 2020. Available from: <https://www.wsp.com/en-NZ/insights/2020-temporary-parking-of-overflow-aircraft>
- [9] Boeing. Boeing Commercial Airplanes - Orders and Deliveries - 737 Model Summary [online] [accessed 2020-07-07] 2018. Available from: <http://active.boeing.com/commercial/orders/displaystandardreport.cfm?cboCurrentModel=737&optReportType=AllModels&cboAllModel=737&ViewReportF=View+Report>
- [10] HEMMERDINGER, J. Boeing to halt 737 production in January [online] [accessed 2020-07-07]. 2019. Available from: <https://www.flightglobal.com/programmes/boeing-to-halt-737-production-in-january/135807.article>
- [11] MOLNAR, Z., MILDEOVA, S., BRIXI, R., KALINA, J. *Advanced methods of scientific work / Pokročile metody vedeckej práce* (in Czech). Praha: Edition Profess Consulting, s.r.o., 2012. ISBN 978-80-7259-064-3.
- [12] SERRANO, F., KAZDA, A. The future of airport post COVID-19. *Journal of Air Transport Management* [online]. 2020, **89**, 101900. ISSN 0969-6997. Available from: <https://doi.org/10.1016/j.jairtraman.2020.101900>
- [13] Stanford Encyclopedia of Philosophy. The problem of induction [online]. 2018. Available from: <https://plato.stanford.edu/entries/induction-problem>
- [14] ANILKUMAR, P. D. Historical method [online] [accessed 2020-08-24]. 2014. Available from: https://www.academia.edu/22583546/Historical_Method_of_Research
- [15] KAZDA, A. *Business operation, selected parts / Obchodná prevádzková činnosť, vybrané state* (in Slovak) - Business operation, selected parts. Bratislava: Alfa, 1985. Order N°3430/84.
- [16] US.DOT. Advisory Circular-Operational Safety on Airport during Construction [online] [Accessed 2020-05-09]. 2011. Available from: https://www.faa.gov/documentlibrary/media/advisory_circular/150_5370_2f.pdf
- [17] FAA. FAA National Part 139 CertAlert No. 20-02 [online] [accessed 2020-03-28]. 2020. Available from: https://www.faa.gov/airports/airport_safety/certalerts/media/part-139-cert-alert-20-02-COVID-19-temporary-aircraft-parking.pdf
- [18] ACI. ACI Advisory bulletin-mitigating the risk created by overflow aircraft parking [online] [accessed 2020-05-30]. 2020. Available from: https://aci.aero/wp-content/uploads/2020/04/200423-Airfield-Parking-Advisory-Bulletin-FINAL_001.pdf
- [19] CREEDY, S. Parking planes in the time of COVID-19. The Airport Professional [online] [accessed 2020-04-11]. 2020. Available from: <https://airportprofessional.asn.au/major-airports/parking-planes-in-the-time-of-covid-19>
- [20] ACI. Airside Safety Handbook. 4. ed. [online] [accessed 2020-05-21]. 2010. Available from: <https://www.skybrary.aero/bookshelf/books/3171.pdf>
- [21] GALIERIKOVA, A., MATERNA, M., SOSEDOVA, J. Analysis of risks in aviation. In: International Conference Transport Means: proceedings. 2018. Vol. 22. p. 1427-1431.
- [22] KAZDA, A. CAVES, R. E. *Airport design and operation*. 3rd ed. Bingley: Emerald Group Publishing Limited, 2015. ISBN 978-1-78441-870-0.
- [23] Airbus. Airbus Consulting Services: Recommendations for pavement (storage area) preservation [online] [accessed 2020-05-30]. 2020. Available from: <https://services.airbus.com/en/newsroom/stories/2020/04/covid-19-aircraft-long-term-storage-asset-preservation.html>
- [24] US.DOT-FAA. Standardized method of reporting airport pavement strength – PCN [online] [accessed 2020-05-30]. 2011. Available from: https://www.faa.gov/documentLibrary/media/Advisory_Circular/150_5335_5B.pdf
- [25] Goodyear Aviation. Aircraft tire care and maintenance [online] [accessed 2020-05-30]. 2004. Available from: <https://www.spilve.lv/library/procedures/Aircraft%20Tire%20Care%20and%20Maintenance.pdf>
- [26] Bloomberg. Here's what you do with two-thirds of the world's jets when they can't fly [online] [Accessed 2020-04-24]. 2020. Available from: <https://www.bloombergquint.com/business/coronavirus-travel-what-happens-to-planes-grounded-by-covid-19>
- [27] US.DOT – FAA. Guidelines and procedures for maintenance of airport pavements [online] [accessed 2020-05-30]. 2014. Available from: https://www.faa.gov/documentlibrary/media/advisory_circular/150-5380-6c.pdf
- [28] ACRP. Field guide for the airport pavement maintenance recommendation tool for ACRP report 159 [online] [accessed 2020-05-30]. 2020. Available from: http://onlinepubs.trb.org/onlinepubs/acrp/acrp_rpt_159_FieldGuide.pdf
- [29] The Louis Berger Group. Pavement evaluation & rating [online] [accessed 2020-05-31]. 2012. Available from: <https://www.icao.int/SAM/Documents/2012/IX.ALACPA/2-final%2009-08-2012%20Topic%202%20Airfield%20Pavement%20Surface%20Evaluation%20and%20Rating.pdf>
- [30] BADANIK, B. Airlines' point of view as a new approach to measuring quality of service at airports. In: 26th Congress of International Council of the Aeronautical Sciences ICAS 2008: proceedings. 2008.
- [31] LAUBROCK, M. New approach for scenario based stand & gate allocation and planning - airport research center. Airport Research Center [online] [accessed 2020-05-30]. 2020. Available from: <https://arc.de/article-new-approach-for-scenario-based-stand-allocation-and-planning>
- [32] NOVAK SEDLACKOVA, A., NOVAK, A. Simulation at the Bratislava airport after application of directive 2009/12/EC on airport charges. *Transport and Telecommunication*. 2010, **11**(2), p. 50-59. ISSN 1407-6160, eISSN 1407-6179.

- [33] LAZAR, T., NOVAK SEDLACKOVA, A., BREDA, R. Regression in personal air transport of passengers evolution at selected airport time series method. *Nase More* [online]. 2015, **62**(3), p. 228-232. ISSN 0469-6255, eISSN 1848-6320. Available from: <https://doi.org/10.17818/NM/2015/SI26>
- [34] MATAS, M., NOVAK, A. Models of processes as components of air passenger flow model. *Communications - Scientific Letters of the University of Zilina* [online]. 2008, **10**(2), p. 50-54. ISSN 1335-4205, eISSN 2585-7878. Available from: <http://komunikacie.uniza.sk/index.php/communications/article/view/1045>
- [35] PROKOPOVIC, K. How do airlines prepare their fleet for hibernation? [online] [accessed 2020-04-21]. Available from: <https://aviationvoice.com/how-do-airlines-prepare-their-fleet-for-hibernation-202004110139>
- [36] SPRINGTHORPE, R., BATCHELOR, D. COVID-19 and the practical implications for the global aviation industry [online] [accessed 2020-04-01]. 2020. Available from: <https://www.nortonrosefulbright.com/de-de/wissen/publications/895cf5ba/covid-19-and-the-practical-implications-for-the-global-aviation-industry>
- [37] PANDEY, S. Lockdown woes: storage and return to service of grounded aircraft [online] [accessed 2020-04-03]. 2020. Available from: <https://sarinlaw.com/lockdown-woes-storage-and-return-to-service-of-grounded-aircraft>
- [38] TSAI, B. Boeing - airplane return to service after extended downtime [online] [Accessed 2020-05-30]. 2020. Available from: https://www.boeing.com/commercial/aeromagazine/aero_04/textonly/s02txt.html
- [39] PAGE, R. What happens when an airplane is parked for too long [online] [accessed 2020-08-21]. 2020. Available from: <https://www.airspacetechnologies.com/blog/what-happens-when-an-airplane-is-parked-for-too-long>
- [40] SIEBENMARK, J. Parking an airplane? Here's what you need to know [online] [accessed 2020-04-18]. 2020. Available from: <https://www.ainonline.com/aviation-news/business-aviation/2020-04-15/parking-airplane-heres-what-you-need-know>
- [41] GUILLOT, R. The largest maintenance programme in Etihad's history is underway. *Le Journal de L'Aviation* [online] [accessed 2020-05-03]. 2020. Available from: <https://www.journal-aviation.com/en/news/44234-the-largest-maintenance-programme-in-etihad-s-history-is-underway>
- [42] KANG, M., OGAJI, S., PILIDIS, P., KONG, C. An approach to maintenance cost estimation for aircraft engines. In: *ASME Turbo Expo 2008: Power for Land, Sea and Air: proceedings. Aircraft Engine; Ceramics; Coal, Biomass and Alternative Fuels; Manufacturing, Materials and Metallurgy; Microturbines and Small Turbomachinery*. Vol. 1. 2008. ISBN 9780791843116, p. 71-79.
- [43] BUGAJ, M., URMINSKY, T., ROSTAS, J., PECHO, P. Aircraft maintenance reserves - new approach to optimization. *Transportation Research Procedia* [online]. 2019, **43**, p. 31-40. ISSN 2352-1465. Available from: <https://doi.org/10.1016/j.trpro.2019.12.016>
- [44] PECHO, P., BUGAJ, M. Vibration fault detection of fuel pump using recurrence quantification analysis. *Transportation Research Procedia* [online]. 2018, **35**, p. 287-294. ISSN 2352-1465. Available from: <https://doi.org/10.1016/j.trpro.2018.12.009>
- [45] ICAO. COVID-19 contingency related differences (CCRD) [online] [accessed 2020-05-29]. 2020. Available from: <https://www.icao.int/safety/COVID-19OPS/Pages/ccrd.aspx>

List of abbreviations

abbreviation	meaning/phrase
ACN	Aircraft Classification Number
AMM	Aircraft Maintenance Manuals
ACRP	Airport Cooperative Research Program
ACI	Airports Council International
ATC	Air Traffic Control
APU	Auxiliary Power Unit
CCRD	COVID -19 Contingency Related Differences
EASA	European Union Aviation Safety Agency
FAA	Federal Aviation Administration
FMPs	Fleet Management Programs
GPS	Global Positioning System
IFE	In-flight Entertainment
ILS	Instrument Landing System
ICAO	International Civil Aviation Organization
MRO	Maintenance, Repair and Overhaul
NOTAM	Notices to Airmen
RFF	Rescue and Fire Fighting
RWY	Runway
PCN	Pavement Classification Number
PMP	Pavement Management Program
PBTH	Power by the Hour
SAFO	Safety Alert for Operators
UAE	United Arab Emirates

UNDERSTANDING HOUSEHOLD'S TRAVEL COSTS BUDGET FRONTIER IN BANDA ACEH, INDONESIA

Sugianto Sugianto^{1,*}, Lulusi¹, Muhammad Isya¹, Fadhlullah Apriandy¹, Fuadh Ramadhan²

¹Department of Civil Engineering, Universitas Syiah Kuala, Banda Aceh, Indonesia

²Alumni, Department of Civil Engineering, Universitas Syiah Kuala, Banda Aceh, Indonesia

*E-mail of corresponding author: sugianto@unsyiah.ac.id

Resume

This study aims to explore the constraints of the Travel Costs Budget Frontier (TCBF) before a full-charged fare is implemented for the bus system known as the "Trans Koetaradja" in the city of Banda Aceh, Indonesia. A stochastic frontier analysis was used to identify how people allocate their share of income for transportation in line with their mobility and socio-demographic characteristics. The findings showed the TCBF to be influenced by commuting trip activities, private mode usage, owning car and motorcycle and income limits. Barriers were observed to be restricting the low-medium income groups. Owning their own private modes within the low-medium income groups does mean household disbursement and could impose their transport expenditure rather than public modes usage. There is a need to devise policies considering the low-medium incomes to implement impartial full-charge to ensure affordable bus fare.

Article info

Received 13 August 2020

Accepted 21 October 2020

Online 4 March 2021

Keywords:

travel costs,
budget,
frontier,
stochastic frontier,
urban bus,
Indonesia

Available online: <https://doi.org/10.26552/com.C.2021.2.A116-A124>

ISSN 1335-4205 (print version)

ISSN 2585-7878 (online version)

1 Introduction

Rapid motorization, promising economic growth and the aftermath of rapid urbanization have increased the time and money spent by people on daily travels and this has further affected their expenditure significantly. In modern society, other factors with a substantial effect on travel costs expenditure include changes in technology, incomes, attitudes, social demographics, and travel behaviors [1].

The use of personal mobility in Indonesia, including Banda Aceh, causes certain transport-related problems such as increased travel time, fuel consumption and environmental deterioration [2-3]. This has, however, driven government and transport planners to alleviate high dependence on the private mode by encouraging changes in the travel mode. Therefore, public transport such as the bus system is commonly recognized as the valid transport policy to reduce the use of the private mode of transportation. Moreover, a public transport system has recognized as a low-carbon transport strategy and a vital for sustainable urban development. However, introducing such a system in emerging cities could be a challenge as people are usually traveling using private vehicles [4]. To encourage changes in the travel mode previous studies have paid much intention to working on travel behavior adoption and forecast the demand for bus usage by incommuting travel behavior adaptation. For instance, research by [5] has concluded that improving attitudes towards the physical activity can increase bus use and reduce physical

inactivity, partly caused by car dependence. Furthermore, an examination of the potential effect of attitudes towards physical activity on the bus utility in the context of a rural Japan, studied by authors of [6], has shown that the level and opportunity for physical activity are generally low. In terms of the public transport demand forecasting, forecasting the demand for new public transportation is essential for appropriate policymaking. The effects of social interactions on individual choices are attracting considerable attention and these interactions have been evaluated in the relationship between the individual's behavior and the group's behavior [7].

Particularly in Banda Aceh, several earliest studies have investigated the effect of motorcycles usage on commuting patterns [8] and approval of the public for adoption of bus reform proposed by the Government in 2016 [9]. This works concluded that it is necessary to consider the motorcycle commuting patterns due to the significant influence of motorcyclists on commuting trips [10], thereby, leading to implementation of a bus reform known as the "Trans Koetaradja" by the government which is currently being run as a trial, free of charge, within running corridors with the full charge for the services expected to start by 2020 [3, 9]. Furthermore, regarding the free of charge during a trial run, the government has operated the Trans Koetaradja bus in order to mitigate highly private mode dependency. As the initial stage, since the bus reform introduced and implemented by the year 2016, the subsidy for the free fare for all the bus users is applied by the government as the



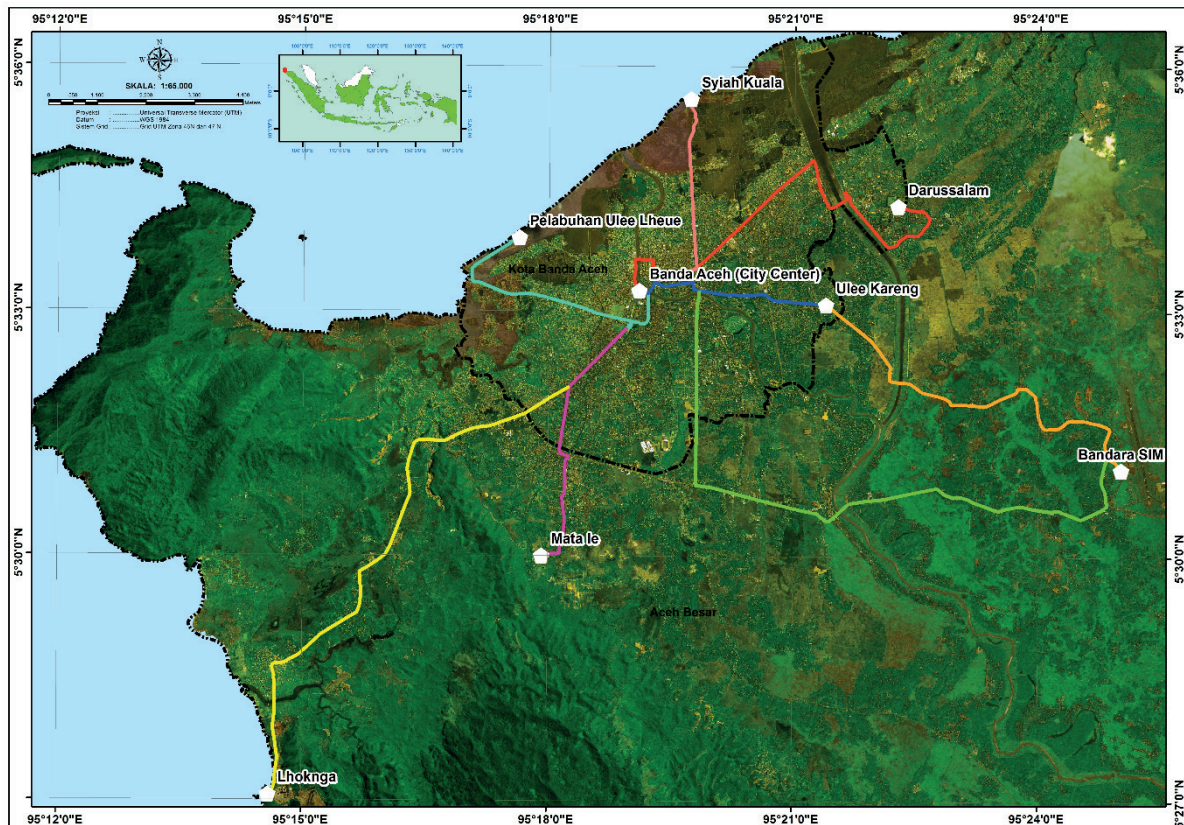


Figure 1 Banda Aceh city and Trans Koetaradja Lines

incentive for private mode users in order to shift from their own car and motorcycle to the bus. By the year 2020, the government has planned and has under consideration to maintain the subsidy only for low-income households and students.

Implementation of the full charge is exceptionally problematic especially for primarily low-income commuters requiring adequate access to public transport as necessary municipal facilities due to the monetary expenditures it is expected to impose on them. It is also presumed that certain income groups save the travel costs expenditure due to income constraints. This means there is a need to understand the money expended on traveling and other factors necessary to determine travelers' behavior before implementing a full fare for the bus system. This study was, therefore, conducted to explore travel costs frontier constraints before the implementation of a full-charged tariff for the urban bus system in the city of Banda Aceh.

Stochastic production frontier was used in this study considering the aggregation of household income groups, including the low-medium and high monthly income groups. According to [1], Travel Costs Budget Frontier (TCBF) is defined as a maximum or unobserved capacity amount of money a specific income group is willing to allocate for travel routines. Therefore, the observed household travel costs in a month was treated as an exogenous variable using the data collected in six districts of Banda Aceh in late 2018, as indicated in Figure 1. The remaining part of this article is categorized into several sections to describe the

survey and data profiles, model formulation and estimation after which the discussion and conclusions are presented at the end.

2 Area of study

Household transport survey (HTS) was conducted on householders in six districts of Banda Aceh including Ulee Kareng, Lueng Bata, Kuta Radja, Meuraxa, Syiah Kuala and Kuta Alam, as illustrated in Figure 2. This was a paper-pencil-based direct interview in late 2018 with a total of 400 valid questionnaires collected and used in the preliminary analysis, with the summary provided in Table 1 consisting of the time of the survey, target area, distribution method, number of valid samples and outline. The focus was to collect information related to travel and social-economic attributes.

3 Method and data distribution

The questionnaires were designed to capture relevant information on travel behavior and socio-demographic attributes from targeted respondents using the paper-pencil-based direct interviews based on Stated Preference choices [3, 9, 11-12] to design questionnaires for 400 samples.

The modeling approach of Stochastic Frontier Analysis (SFA) introduced initially by [13] and widely applied to travel

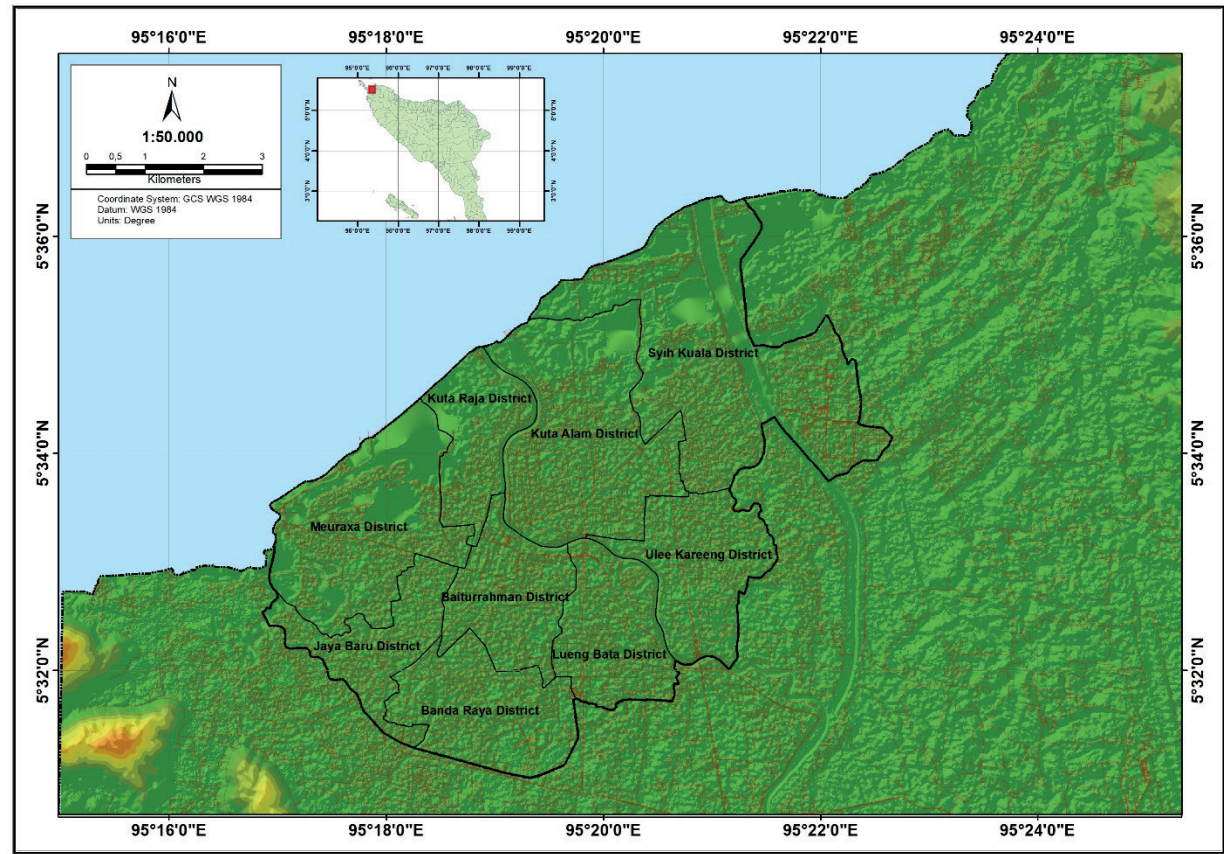


Figure 2 Banda Aceh city and its district areas

Table 1 Summary of SP questionnaire

description	detail
time of survey	November 2018
target location	Banda Aceh, Aceh province
distribution methods	a paper-pencil based direct interviews and collected by the enumerator
number of questionnaires valid	400 samples
questionnaire outline:	mode use, the purpose of traveling, origin zone, destination zone, travel distance,
part 1: travel attributes	travel time, frequency use of representative mode
part 2: social-economic attributes	monthly income, monthly travel expenditure, gender, age, education level, occupancy, housing owned status, household member, number of household work, car ownership, motorcycle ownership

time expenditures was adopted in this study. Moreover, household attributes have been used by [14] to explore the travel time expenditure across the United States, India and Switzerland and found quite different values in the average travel time frontier across the international contexts. Another research by [15] investigated unseen stochastic limit and variations of individual travel time using data set from the UK National Travel Survey.

Further application of the SFA on the travel time expenditure frontier done by [16], they investigated and showed differences in the frontier values and trends in the ratio of travel time expenditure to frontier values differ considerably across socio-demographic groups in the United States. However, the travel costs expenditures were considered a more crucial issue due to their direct

burden on income constraints compared to travel time expenditure. Perhaps, the earliest studies on the travel costs expenditure or transportation expenditure have been conducted by [1, 17]. They utilized the SFA to estimate unobserved travel costs frontier or capacity within the targeted household. They explored how the household spends the money on transportation, as well as how life stages and related household attributes contributed to transportation fee expenditures in the Jakarta Metropolitan Area. The substantial characteristics of household attributes among life stage categories are taken into consideration. They concluded that a larger amount of the travel costs expenditure is found for a single-person and families only with adults and the transportation expenditure in Jakarta is influenced by household attributes and life environments.

Table 2 Distribution of Socio-demographic attributes

item	category	number of samples	share (%)
gender	male	331	83
	female	69	17
age	19 years or less	2	1
	20 - 29 years	58	15
	30 - 39 years	125	31
	40 - 49 years	127	32
	50 - 59 years	79	19
	60 years or more	9	2
education	primary school	219	55
	college	53	13
	university/bachelor	91	23
	university/postgraduate	37	9
monthly income	1.9 million IDR (135.62 USD) or less	71	18
	2 - 4.9 million IDR (142.76-349.77 USD)	197	49
	5 - 6.9 million IDR (356.90-492.53 USD)	90	23
	7 million IDR (499.66) or more	42	11
monthly travel costs	0.19 million IDR (13.56 USD) or less	54	14
	0.2-0.99 million IDR (14.28-64.24 USD)	128	32
	1-1.49 million IDR (71.38-106.36 USD)	164	41
	1.5-1.99 million IDR (107.07-135.62 USD)	38	10
	2 million IDR (142.76 USD) or more	16	4
occupation	working	318	80
	university student	30	8
	housewife	23	6
	part-time worker	29	7
housing own status	owned	363	92
	renting	31	8

Further exploration of the travel costs budget is conducted by authors of [11], which have investigated factors affecting household travel costs budget in Banda Aceh considering household life stages and applying only for bus usages. This investigation is the first stage of the same funding with this work. The differences between this work and work done by [11] are in the targeted respondents and group of households. This work focuses on how people in Banda Aceh spent their monthly transportation expenditure considering income group segmentations, while the previous work [11] is more specific investigating the bus usage, using an onboard survey and has targeted groups based on household life stages. The modeling framework used for both exploring travel time and travel costs frontier is based on the SFA or also known as the Stochastic Frontier Model (SFM).

The SFA is used to estimate unobserved travel costs frontier or capacity within the targeted household and it was found to be always greater than or equal to the observed travel costs expenditure. Therefore, the modeling

of travel costs budget frontier (TCBF) was based on inequality and non-negative term or production function. A log transformation of travel costs budget (TCB) was also used to ensure positive prediction due to the highly skewed nature dataset of TCB distribution [1].

$$\text{Let } T_i = \ln(t_i), \text{ and } T_i = t_i - u_i, \quad (1)$$

where i denotes the observation, t_i is observed transportation expenditure and u_i is a random component with non-negative values. Moreover, τ_i represents an unobserved frontier for T_i and found to be always greater than or equal to T_i and this means that it is possible to write the production function of TCBF as:

$$\tau_i = \beta' X_i + v_i, \quad (2)$$

then,

$$T_i = \beta' X_i + \varepsilon_i = \beta' X_i + v_i - u_i, \quad (3)$$

Table 3 Summary of Respondent's Mobility Attributes

item	category	number of samples	share (%)
travel mode choice	car	125	31
	motorcycle	207	52
	public transport (bus)	68	17
driver's license	has driver's license	342	86
	has no driver's license	58	14
car owned within household	has owned car	135	34
	has no owned car	265	66
motorcycle owned within household	has owned motorcycle	376	94
	has no owned motorcycle	24	6

where β' is a coefficient vector of independent variables, X_i is a vector of explanatory variables, v_i is a random error term such that $-\infty < v_i < \infty$. The random variable of v_i is typically assumed to be normally identical and independent distributed IID as $N(0, \sigma^2)$ while a half normal or truncated-normal distribution is commonly used for the error component of u_i . Moreover, the ratio (R) value was considered to gain more information on how households spend their travel costs capacity or frontier. The amount of R was calculated as:

$$R = \frac{E(t_i)}{E(TCBF_i)} = E[\exp(-u_i)]. \quad (4)$$

The ratio value implies that people are expected to spend R time of (TCBF) of a certain group/household income as monthly expenditure. The R -value indicates the extent to which each household is spending in terms of frontiers and a large value shows they mostly use their frontiers and vice versa.

The respondent's socio-demographic attributes were aggregated, as described in Table 2, before the estimation model and results showed that the male respondents were predominant compared to females with 83%. The respondents were also slightly dominated by people between 30 to 50 years by having a total of 63%, while more than half have education level up to primary school as indicate by 55%. The findings also showed 80% were working while the remaining were university students, housewives and part-time workers. Moreover, approximately 92% have their own house while only 8% lived in a rented apartment and the monthly income attribute indicated 67% are categorized as low-medium with income below 5 million IDR [17]. The information also showed 73% spent 0.2 to 1.5 million IDR (1 USD \approx 14.09 thousand IDR) of their monthly income on travel.

Table 3 describes the aggregation results for respondent's mobility attributes during the distributed questionnaires. The aggregation of the data depicts that people in Banda Aceh have significantly private mode dependency accounting for 31% and 52% for car and motorcycle usage, respectively, while it shows that only a few of them (17%) used public transport. It is quite clear

that respondents prefer to use their own mode compared to public transit. Furthermore, the data reveal that close to 86% of respondents are licensed drivers. This result is quite consistent with the share of private mode choice as much as 83% among respondents has preferred to use their own mode. Moreover, the data reveal that a high percentage of respondents have owned a motorcycle (94%) within a household compared to the owned car (34%) within the household. Surprisingly, only a few of the household has no owned motorcycle (6%) in this city. Therefore, it seems that people rely heavily on their own mode, which offers more convenience in terms of flexibility.

4 Empirical setting and result

The TCBF was calibrated for the two income groups which are the low-medium and high, while the observed travel costs in a month (in million rupiahs (IDR)) were treated as an exogenous variable. The setting and statistical characteristics, including the mean and standard deviation of both exogenous and endogenous variables used in this study, are presented in Table 4. It is important to note that the information in Table 2 shows 268 represented by 67% of the 400 households analyzed have the low-medium income at < 5 million IDR per month while the remaining 132 families have the high income at > 5 million IDR per month. The average income was, however, found to be approximately 3.228 million IDR per month.

Table 5 depicts the effect of calibrated parameters on the travel costs frontier across the household income groups and the sign (-) represents explanatory variables with insignificant t-statistics. The endogenous variables varied among the two groups were distance, travel time, frequency of using the private mode, household income and household members. The findings, however, showed that the household income, private mode ownership including car and motorcycle and individual mode dummy variables have a positive impact on travel costs frontier for low-income groups. This is associated with their limited income, which makes owning and using private modes to have a significant impact on their daily transport expenditure;

Table 4 Variables' setting and statistical characteristics

variable setting	low-medium income group		high-income group	
	mean	std. dev	mean	std. dev
travel costs (million IDR), numerical	0.856	0.356	1.575	0.351
private mode user dummy 1, otherwise 0	0.668	0.472	0.992	0.087
commuter trip dummy 1, otherwise 0	0.806	0.396	0.962	0.191
distance (km)	3.287	2.226	4.821	2.236
travel time (minutes)	9.174	5.359	13.024	5.396
frequency using private mode (number/week)	5.074	1.310	5.636	1.086
household income (million IDR)	2.690	0.552	6.318	0.467
male dummy 1, otherwise 0	0.757	0.429	0.969	0.172
low education dummy 1, otherwise 0	0.242	0.409	0.121	0.327
household member (number)	1.459	0.549	2.295	0.576
car ownership (number)	0.086	0.281	1.068	0.608
motorcycle ownership (number)	1.407	0.661	2.227	0.613
sample size	268		132	

Table 5 The TCF model calibrated parameters across income groups

variable	low-medium income group		high-income group	
	coefficient	sig.	coefficient	sig.
private mode user dummy 1, otherwise 0	0.129	0.002	-	-
commuter trip dummy 1, otherwise 0	0.212	0.002	0.331	0.000
distance (km)	-	-	0.0168	0.012
travel time (minutes)	0.0126	0.001	-	-
frequency using private mode (number/week)	0.020	0.028	-	-
household income (million IDR)	0.129	0.002	-	-
male dummy 1, otherwise 0	-	-	0.163	0.038
low education dummy 1, otherwise 0	-	-	-0.135	0.002
household member (number)	0.198	0.000	-	-
car ownership (number)	0.292	0.000	0.144	0.000
motorcycle ownership (number)	0.173	0.000	0.0982	0.000
intercept (constant)	-1.294	0.000	-0.344	0.005
number of observations (N)	268		132	
log-likelihood function (LL)	-48.609		-59.029	
wald χ^2 (sig.)	221.09 (0.000)		142.82 (0.000)	
variance:				
sigma-squared (v)	0.442		0.178	
sigma-squared (u)	0.144		0.113	
lambda (λ)	3.059		1.573	
r (exp(-u))	0.642		0.837	

rather than use of a public mode. Meanwhile, the monthly income of the high-income group was found not to have any effect on the travel costs expenditure and this is assumed to be based on two reasons, which include having a buffer to their income capacity and spending most of their capacity on expenditures. The commuting trip variable was discovered to have a significant statistical sign across all the groups with both recorded to have the tendency to use their income resources for mandatory activities such as working and dropping/picking-up kids in and from schools.

The male gender was observed to have a significant

positive influence on the travel costs frontier for a high-income household with the male respondents found to spend more on travel than their female counterparts and the same was also discovered with the commuter trips variable. This is possibly due to the fact that there are more males in high-income households as shown in Table 2. Furthermore, Table 5 represents how owning a car and motorcycle within a household could significantly be influencing the corresponding household in allocating transportation expenditure. It is implied that car and motorcycle ownership has a significantly positive

correlation on the transportation expenditure frontier for both the low-income and high-income segmentation. The impact of owning private vehicles on the transport expenditure for the low-income groups seems to have a higher coefficient compared to the high-income one. This means that car and motorcycle ownership does mean household disbursement in our dataset. That is, the private modes may possibly impose their monthly expenditure on transportation rather than bus usage. However, in this study, the exploration among specific income groups by considering the number of owning cars or motorcycles within a household has remained a future direction of this study.

The variance value of the half-normal random component (Sigma-squared (u)) was discovered to be substantially small for both income groups and this indicates that the observed travel costs across income groups is closer to the capacity or frontier. Moreover, the calibrated model parameters in Table 5 were found to be corresponding with income groups as observed with the tendency to be constrained by spending more income on commuting trips, private mode usage, owning private mode of transportation and based on the household members, as well as the limited income, which restricts certain group from spending on transportation. Furthermore, the *R*-value for the low-medium and high-income groups was recorded to be 0.642 and 0.837, respectively and this means that the high-income group actual costs expenditure is closer to their frontier values, while those in a low-medium group mostly use their frontier due to lack of buffer [1, 17].

5 Conclusion

The stochastic frontier analysis implemented in this study showed the frontier costs to be substantially influenced by commuting trip activities, private mode usage, owning car and motorcycle and constraints from monthly income. The finding further reported an average income groups considerably spending more than one-half of their maximum expenditure on transport routine while.

The ratio value indicated high-income group has the higher travel costs frontier compared to the low-medium groups. This difference is prospectively due to the limitation in the money attributable to travel mode, household members and owning car and motorcycle within income groups. Moreover, some barriers were observed to be restricting the low-medium income groups from spending money on transportation. The constraints may include their household's income limitation.

The empirical results further showed that the people in Banda Aceh save money for travel expenditure due to owning a car and motorcycle particularly for the low-medium income groups. Car and motorcycle ownership within the low-medium income groups means household disbursement and may impose their monthly expenditure on transportation rather than public modes usage. This information is expected to provide an insight for policymakers while considering the monetary constraints in deciding the fare to charge for the bus system, as well as in determining the best policies to be implemented based on income groups, especially in relation to factors inhibiting them from commuting trips. Therefore, policies reflecting the needs of certain income groups need to be formulated to ensure impartiality during the implementation of the full-charge in the bus system and make it more affordable. It is also better to understand the travel behavior of residents to achieve successful and more efficient transport planning, particularly dealing with behavioral adopting the commuting trip in emerging cities [18-21].

Acknowledgment

The authors express their gratitude to the Universitas Syiah Kuala for providing financial support for this study under Contract No. 522/UN11/SPK/PNBP/2019. The authors also appreciate the staff and students of Transportation System Laboratory, Civil Engineering Department of Syiah Kuala University for providing substantial help with data collection. The authors also take responsibility for the remaining oversight in this study.

References

- [1] SUGIARTO, S., MIWA, T., SATO, H., MORIKAWA, T. Transportation expenditure frontier models in Jakarta Metropolitan Area. *Procedia-Social and Behavioral Sciences* [online]. 2014, **138**, p. 148-158. ISSN 1877-0428. Available from: <https://doi.org/10.1016/j.sbspro.2014.07.190>
- [2] SUGIARTO, S., MIWA, T., SATO, H., MORIKAWA, T. Congestion charging: influence of public consciousness on acceptability in Jakarta Metropolitan Area. In: 21st World Congress on Intelligent Transport Systems: proceedings. Vol. 12914. 2014.
- [3] SALEH, S. M., SUGIARTO, S., SALMANNUR, A. Attitudinal dataset for mediating the effects of public acceptance on bus reform scheme in a developing country context. *Data in Brief* [online]. 2019, **25**, 104035. ISSN 2352-3409. Available from: <https://doi.org/10.1016/j.dib.2019.104035>
- [4] NGUYEN, T. N., MIWA, T., MORIKAWA, T. Response to the planned public transport system in Ho Chi Minh City: analysis of latent classes. *Clean Technologies and Environmental Policy* [online]. 2019, **21**(10), p. 1925-1935. ISSN 1618-954X, eISSN 1618-9558. Available from: <https://doi.org/10.1007/s10098-018-1638-8>

- [5] TRAN, Y., YAMAMOTO, T., SATO, H., MIWA, T., MORIKAWA, T. Attitude toward physical activity as a determinant of bus use intention: a case study in Asuke, Japan. *IATSS Research* [online]. 2020, article in press. ISSN 0386-1112. Available from: <https://doi.org/10.1016/j.iatssr.2020.03.002>
- [6] TRAN, Y., YAMAMOTO, T., SATO, H., MIWA, T., MORIKAWA, T. The analysis of influences of attitudes on mode choice under highly unbalanced mode share patterns. *Journal of Choice Modelling* [online]. 2020, **36**, 100227. ISSN 1755-5345. Available from: <https://doi.org/10.1016/j.jocm.2020.100227>
- [7] NGUYEN, T. N., MIWA, T., MORIKAWA, T. Demand forecast of public transportation considering positive and negative mass effects. *Transportation Research Part D: Transport and Environment* [online]. 2020, **85**, 02466. ISSN 1361-9209. Available from: <https://doi.org/10.1016/j.trd.2020.102466>
- [8] SALEH, S. M., SUGIARTO, S., HILAL, A., ARIANSYAH, D. A Study on the traffic impact of the road corridors due to flyover construction at Surabaya Intersection, Banda Aceh of Indonesia. *AIP Conference Proceedings* [online]. 2017, **1903**(1), 06005. ISSN 0094-243X, eISSN 1551-7616. Available from: <https://doi.org/10.1063/1.5011559>
- [9] SALEH, S. M., SUGIARTO, S., ANGGRAINI, R. Analysis on public's response toward bus reform policy in Indonesia considering latent variables. *The Open Transportation Journal* [online]. 2019, **13**, p. 17-24. ISSN 1874-4478, eISSN 2667-1212. Available from: <http://dx.doi.org/10.2174/1874447801913010017>
- [10] AGGRAINI, R., SUGIARTO, S., PRAMANDA, H. Factors affecting trip generation of motorcyclist for the purpose of non-mandatory activities. *AIP Conference Proceedings* [online]. 2017, **1903**(1), 060011. ISSN 0094-243X, eISSN 1551-7616. Available from: <https://doi.org/10.1063/1.5011565>
- [11] SUGIARTO, S., LULUSI, L., MUTIAWATI, C., SALEH, S. M., AYUNI Q., ISKANDAR, I. An exploration of factor affecting household's travel cost budget considering household life stages applying to urban bus ridership. *Aceh International Journal of Science and Technology* [online]. 2020, **9**(1), p. 12-21. ISSN 2088-9860, eISSN 2503-2348. Available from: <https://doi.org/10.13170/aijst.9.1.16405>
- [12] SUGIARTO, S., MIWA, T., MORIKAWA, T. Inclusion of latent constructs in utilitarian resource allocation model for analyzing revenue spending options in congestion charging policy. *Transportation Research Part A: Policy and Practice* [online]. 2017, **103**, p. 36-53. ISSN 0965-8564. Available from: <https://doi.org/10.1016/j.tra.2017.05.019>
- [13] AIGNER, D., KNOX LOVELL, C.A., SCHMIDT, P. Formulation and estimation of stochastic frontier production function models. *Journal of Econometrics* [online]. 1997, **6**(1), p. 21-37. ISSN 0304-4076. Available from: [https://doi.org/10.1016/0304-4076\(77\)90052-5](https://doi.org/10.1016/0304-4076(77)90052-5)
- [14] BANARJEE, A., Y. X., PENYALA, M. R. Understanding travel time expenditures around the world: exploring the nation of a travel time frontier. *Transportation* [online]. 2007, **34**, p. 51-65. ISSN 0049-4488, eISSN 1572-9435. Available from: <https://doi.org/10.1007/s11116-006-0004-6>
- [15] SUSILO, O. Y., AVINERI, E. The impacts of household structure on the individual stochastic travel and out of home activity time budgets. *Journal of Advanced Transportation* [online]. 2013, **48**(5) p. 454-470. ISSN 1042-7163, eISSN 1098-1071. Available from: <https://doi.org/10.1002/atr.1234>
- [16] VOLOSIN, E. S., PAUL, S., CHRISTIAN, P. K., KONDURI, C. K., PENDYALA, M. R. Exploring the dynamics in travel time frontiers. *Transportation Research Record: Journal of the Transportation Research Board* [online]. 2013, **2382**, p. 20-27. ISSN 0361-1981, eISSN 2169-4052. Available from: <https://doi.org/10.3141/2382-03>
- [17] SALEH, S. M., SUGIARTO, S. Stochastic production frontier models to explore constraints on household travel expenditures considering household income classes. *Aceh International Journal of Science and Technology* [online]. 2016, **5**(1), p. 9-17. ISSN 2088-9860, eISSN 2503-2348. Available from: <https://doi.org/10.13170/aijst.5.1.3839>
- [18] SUGIARTO, S., MIWA, T., SATO, H., MORIKAWA, T. The tendency of public's attitudes to evaluate urban congestion charging policy in Asian megacity perspective: case a study in Jakarta, Indonesia. *Case Studies on Transport Policy* [online]. 2020, **8**(1), p. 143-152. ISSN 2213-624X. Available from: <https://doi.org/10.1016/j.cstp.2018.09.010>
- [19] SUGIARTO, S., SALEH, S. M. Investigating public perceptions and its implication toward Trans Koetardja policy considering latent motivation. *IOP Conference Series: Materials Science and Engineering* [online]. 2019, **523**, 012036. ISSN 1757-8981, eISSN 1757-899X. Available from: <https://doi.org/10.1088/1757-899X/523/1/012036>
- [20] TOSA, C., SATO, H., MORIKAWA, T., MIWA, T. Commuting behavior in emerging urban areas: findings of a revealed-preferences and stated-intentions survey in Cluj-Napoca, Romania. *Journal of Transport Geography* [online]. 2018, **68**, p. 78-93. ISSN 0966-6923. Available from: <https://doi.org/10.1016/j.jtrangeo.2018.02.011>
- [21] TOSA, C., MITREA, A., SATO, H., MORIKAWA, T., MIWA, T. Economic growth and urban metamorphosis: a quarter century of transformations within the metropolitan area of Bucharest. *Journal of Transport and Land Use* [online]. 2018, **11**(1), p. 273-295. ISSN 1938-7849. Available from: <https://doi.org/10.5198/jtlu.2018.1242>

Abbreviation

abbreviation	meaning/phrase
HTS	Household Transport Survey
IDR	Indonesian Rupiah
IID	Identical and Independent Distributed
LL	Log-Likelihood
SFA	Stochastic Frontier Analysis
SFM	Stochastic Frontier Model
TCB	Travel Costs Budget
TCBF	Travel Costs Budget Frontier



University of Žilina

In its over 65 years of successful existence, the University of Žilina (UNIZA) has become one of the top universities in Slovakia.



Scientific conferences organized by University of Žilina in the second and third quarters of the 2021

Horizons of Railway Transport 2020

Date and venue: 21. – 22.4. 2021, Žilina
Contact: jozef.gasparik@fpedas.uniza.sk
Web: <https://fpedas.uniza.sk/~horizonty/>

Sustainable Energy Forum

Date and venue: May 2021, Liptovský Mikuláš, SK
Contact: pavel.simon@uniza.sk
Web: <https://www.energiaweb.sk/smart-energy-forum-slovakia>

37th International colloquium ADVANCED MANUFACTURING AND REPAIR TECHNOLOGIES IN VEHICLE INDUSTRY

Date and venue: 24.5.2021 – 26.5.2021, University of Žilina, SK
Contact: lenka.kucharikova@fstroj.uniza.sk
Web: <http://kmi2.uniza.sk/>

International Scientific Conference on Sustainable, Modern and Safe Transport TRANSCOM 2021

Date and venue: 26. 5. - 28. 5. 2021, Virtual event
Contact: transcom@uniza.sk
Web: <http://www.transcom-conference.com>

Conference InvEnt 2021

Date and venue: Jun 2021, online
Contact: luboslav.dulina@fstroj.uniza.sk

30. R-S-P Seminar, Theoretical Foundation of Civil Engineering (30RSP) (TFoCE 2021)

Date and venue: September, 2021, Moskva, Russia
Contact: andrea.husarikova@uniza.sk

UNIVERSITY OF ŽILINA

Science & Research Department

Univerzitná 8215/1, 010 26 Žilina, Slovakia
Ing. Janka Macurová
tel.: +421 41 513 5143
e-mail: janka.macurova@uniza.sk



CORROSION BEHAVIOUR OF PRESERVED PEO COATING ON AZ31 MAGNESIUM ALLOY

Filip Pastorek*, Milan Štrbák, Daniel Kajánek, Martina Jacková, Jana Pastorková, Zuzana Florková

University of Zilina, Zilina, Slovak Republic

*E-mail of corresponding author: filip.pastorek@rc.uniza.sk

Resume

A surface treatment process, composed of plasma electrolytic oxidation (PEO) and sealing by temporary oil preservation system containing corrosion inhibitors, was performed on AZ31 magnesium alloy in order to improve its corrosion resistance in environments containing chlorides. Both atmospheric and immersion conditions were evaluated by electrochemical tests in 0.1M NaCl solution together with salt spray test according to STN EN ISO 9227 standard. The obtained results confirmed significant improvement of corrosion resistance reached by the PEO sealing in aggressive environments compared to the pure PEO coating on AZ31 surface. Hence, such a duplex coating is a very perspective alternative for magnesium alloy applications in severe conditions or for temporary protection of magnesium products coated by the PEO during marine transport.

Article info

Received 17 July 2020

Accepted 3 November 2020

Online 16 December 2020

Keywords:

plasma electrolytic oxidation, magnesium alloy, inhibitor, surface treatment, corrosion, electrochemical techniques

Available online: <https://doi.org/10.26552/com.C.2021.2.B76-B88>

ISSN 1335-4205 (print version)

ISSN 2585-7878 (online version)

1 Introduction

Magnesium alloys are the lightest commercially used metal structural material. Their weight saving potential exceeds 50 % for some components, which leads to an increased usage of Mg alloys in the industrial fields in the last few years. Specifically, substituting other materials for Mg alloys in automotive and aircraft industry, leads to reduction in fuel and CO₂ emission, being a very actual topic [1-2]. Apart from extensive use in automotive industry, Mg-based alloys are utilized in production of parts for computers and other portable devices, aircraft, military, recreational and orthopaedic equipment, diving gear and sports goods [3-4]. However, magnesium has many undesirable properties, as well, including low abrasion resistance, low creep resistance, high-chemical reactivity, including flammability and especially very low corrosion resistance [5]. The addition of several alloying elements such as Al, Zn and rare earths can improve the corrosion resistance of Mg alloys. However, the technological requirements for several applications remain still unsatisfied [6-7]. Therefore, magnesium alloys must be treated before they are used in practice by appropriate surface treatment techniques including electrochemical plating, chemical conversion, physical vapour deposition, laser cladding, anodic oxidation, plasma electrolytic oxidation, etc. [8-10].

Among these techniques, the plasma electrolytic oxidation (PEO), provides a thick and adherent ceramic-like coating on metal substrates improving the corrosion

resistance in chloride-containing solution and also providing high wear resistance. Unfortunately, the performance of PEO coatings on magnesium alloys deteriorates drastically under the long-term exposure in aggressive environments [11-12]. This is caused by the presence of defects as pores and cracks in the PEO layer, created naturally during the PEO process, which form the pathways for corrosive species impairing the total protective effect of PEO [3]. Additionally, the PEO process increases surface roughness, which can be harmful if the alloy has to be used in sliding parts [13]. Considerable strategies, regarding optimization of factors influencing the PEO process (electrolyte composition and additives, electrical parameters setting, etc.) have been proposed for improving the corrosion performance of the PEO coatings. However, complete elimination of the micro pores and defects during the PEO treatment is still impracticable due to its discharge assisted growth mechanism [14]. A desirable strategy to overcome this drawback is to seal these defects or to create the second layer that would fill the pores and even improve the overall surface qualities.

Different surface post-treatment approaches for the PEO coatings were investigated, including organic, sol-gel and polymer coatings, in order to avoid the early failure of the PEO coatings on Mg alloys due to their permeability to the environment [6]. It is possible to meet with chemical conversion, electrophoretic deposition, hydrothermal treatment, chemical vapour deposition (CVD) and other standard techniques optimized for this purpose [14]. Very



Table 1 Chemical composition of AZ31 magnesium alloy (wt. %)

component	Al	Zn	Mn	Si	Cu	Ni	Fe	Mg
wt. %	2.96	0.828	0.433	0.004	0.004	<0.001	0.002	rest

hot topic represents application of various impregnators containing corrosion inhibitors [14-15].

However, the above mentioned techniques of post-treatment create a permanent duplex coatings that are not suitable for applications where just temporary corrosion protection of the PEO is required (for example a marine transport of final Mg products treated by PEO) or these techniques are not cost effective. For these reasons, the effective preservation method of applying mineral oil containing corrosion inhibitors meeting the above criteria and its effect on level of corrosion protection of AZ31 magnesium alloy covered by PEO was studied in this paper.

2 Experimental material and methods

The tested material was continually casted AZ31 magnesium alloy homogenized at 420 °C for 16 hours used also in previous studies [16-20]. Its chemical composition is listed in Table 1.

The process of PEO preparation was based on authors' experience from previous studies [21-23]. The plates of AZ31 (5 mm thick) were ground by an emery paper p1000 to provide the same roughness across the treated surface. Subsequently, samples were rinsed by demineralized water, ethanol and air-dried. The PEO process was performed on a laboratory DC power source Keysight N8762A. The sample was connected as an anode in the two-electrode system. The cathode was provided by stainless steel plate. The PEO electrolyte was composed of 12 g/l $\text{Na}_3\text{PO}_4 \cdot 12\text{H}_2\text{O}$ and 1 g/l KOH and its pH was adjusted to 12.3 at 22 ± 1 °C. The electrolyte was cooled with water and constantly stirred during the PEO procedure in order to ensure the better distribution of active species and to keep the temperature below 50 °C. The current density was set to 0.05 A/cm² for 14 minutes. Applied current was maintained at a constant value. The morphology of the prepared PEO coating was observed using the Carl Zeiss Merlin scanning electron microscope (SEM).

The created PEO coating was subsequently sealed by commercially available preservation mineral oil VpCI®-369 containing corrosion inhibitors, applied by brushing while dipping, in order to reach complete uniform coverage within a single applied layer (average thickness ~ 100 µm). After the application, the samples were left for 24 hours in desiccator in order to give the inhibitors enough time to naturally impregnate through the PEO coating and seal the pores.

Two different electrochemical measurement techniques were used to compare and determine the corrosion resistance of AZ31 magnesium alloy after the PEO process and sealing: the potentiodynamic polarization

measurements (PDP) and the electrochemical impedance spectroscopy (EIS) measurements in a solution of 0.1M NaCl (simulating an environment containing aggressive chloride ions). All the electrochemical measurements were performed at 22 ± 2 °C on at least three samples of each type, so that reproducibility of the test results was ensured. The most representative curves are presented in graphs.

A technique with a constant potential change per time unit was used for the PDP measurements. The PDP tests were performed over the potential range from -200 mV to +500 mV vs. an open circuit potential (E_{oc}) value after 1 hour of stabilization in the 0.1M NaCl test environment. The constant change of applied potential during the measurements was 1 mV.s⁻¹. The measured area of samples was 1 cm². The Tafel analysis of the measured curves was performed using the EC-Lab V11.10 software.

The EIS measurements were realized after various exposure times from 1 to 168 hours in order to observe behaviour of the electrochemical system on AZ31 samples with sealed PEO coating. The measurements were performed in the frequency range from 100 kHz to 10 mHz with the frequency 10 times per decade. Amplitude of the applied AC voltage was 15 mV around the open circuit potential value (E_{oc}). The outputs of the EIS measurements were represented by the Nyquist diagrams, which were analysed by the equivalent circuits (Figure 1) with the EC-Lab V11.10 software. The main evaluated element was a polarization resistance (R_p) representing the element, which is inversely proportional to the corrosion rate and is estimated from the Nyquist diagram as

$$R_p = |Z(j\omega)|_{\omega \rightarrow 0} - |Z(j\omega)|_{\omega \rightarrow \infty} \quad (1)$$

$z(j\omega)$ that denotes the impedance as a function of radial frequency ω in an imaginary unit j according to an expression analogous to the Ohm's law. The solution resistance (R_s) was estimated from the impedance at high frequency ($|Z(j\omega)|_{\omega \rightarrow \infty}$), while the sum of R_p and R_s was estimated from the impedance at low frequency ($|Z(j\omega)|_{\omega \rightarrow 0}$). The difference between these two impedance values results in the polarization resistance [24]. In a system with one capacitive loop, R_p is equivalent to pore resistance (R_{po}). In the case of 2 capacitive loops, the R_p value was the sum of the pore resistance (R_{po}) and charge transfer resistance (R_{ct}). The R_{po} is generally interpreted as the pore resistance of the coating resulting from the penetration of the electrolyte and is detected in the high-frequency region. The R_{ct} is resistance to charges transfer, determining the corrosion rate of reaction and is a measure of electric charges transfer

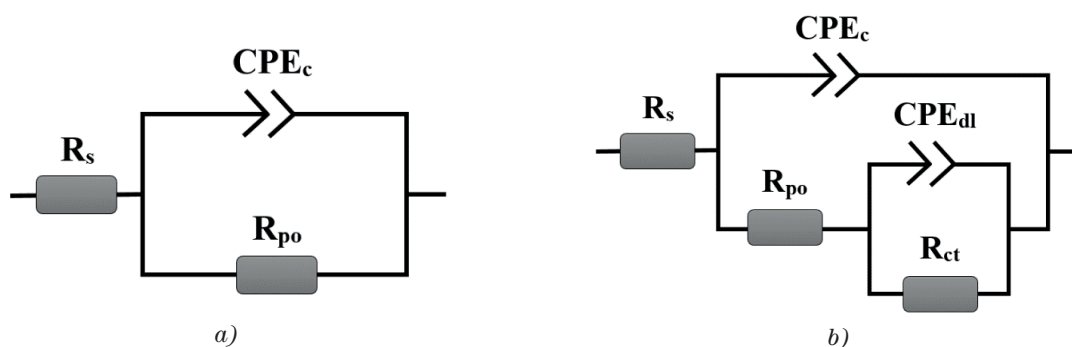


Figure 1 Equivalent circuits for diagrams with one capacitance loop (a) and two capacitance loops (b)

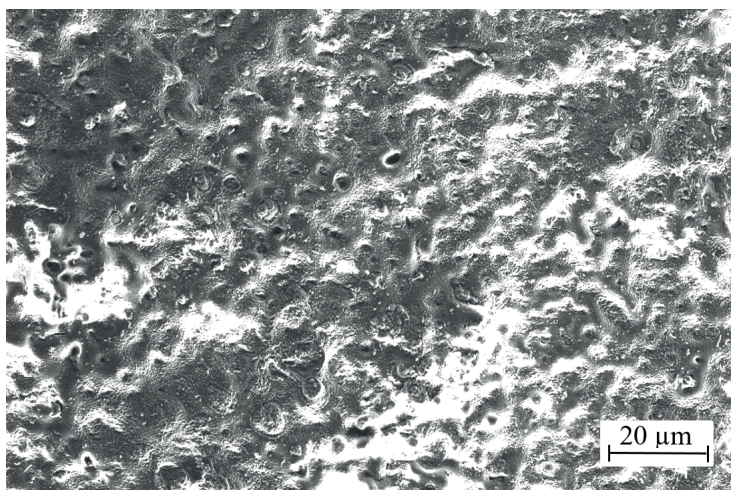


Figure 2 Surface morphology of prepared PEO coating

through the electrode surface [25-27]. In practical, the measured impedance spectra may differ from ideal or theoretical behaviour. The loops (or time constants) do not show a perfect semi-circle shape in the Nyquist representation. This non-ideal behaviour may arise from coating heterogeneities as roughness, inhomogeneous composition, etc. In such a case, the coating cannot be described by a simple capacitor [28]. This one is generally replaced by a constant phase element (CPE) that is defined as [29]:

$$CPE \approx C = [C(j\omega)^n]^{-1}, \quad (2)$$

where n accounts for non-ideal behaviours: when it equals to 1, the CPE is a pure capacitance and when it equals zero, the CPE is a pure resistance. The CPE_c is a suitable parameter to show the amount of penetration of water into the coating, while the CPE_{dl} indicates the capability of the adhesive bond failure and penetration of electrolyte to the interface of coating/metal [30].

The corrosion tests were performed in a simulated neutral salt spray atmosphere according to STN EN ISO 9227 standard in Votsch VSC KWT 1000 corrosion chamber. The test was carried out at a continuous temperature of 35 °C. The sodium chloride solution for the salt spray production was prepared by dissolution of pure sodium chloride of concentration 50 g/l \pm 5 g/l in demineralised water with a conductivity not higher than

20 μS/cm at 25 °C. The pH of the solution was within the required range from 6.5 to 7.2 (measured at 35 \pm 1 °C) during the whole salt spray test. In order to prevent evaporation of water from the sprayed droplets, the air was humidified before entering the atomizer, by passage through a saturation tower containing water with a temperature 45 °C. The absolute pressure of the used compressed air was set to 120 kPa. The tested samples were inserted to the chamber on an inert plastic holder.

3 Results and discussion

The SEM image of the PEO coating prepared on tested AZ31 magnesium alloy in accordance to authors' experience from previous studies [21-23] is presented in Figure 2. The PEO layer exhibits a porous structure typical for the PEO process. Formation of micropores is associated with presence of the molten oxides and gas bubbles produced during the discharges occurred on the surface of samples [22, 31].

Evaluation of the PEO surface treatment effect on the corrosion resistance of magnesium alloy AZ31 in 0.1M NaCl solution, using PDP and EIS tests, was already performed in authors' previous studies [21-23]. Some of these results are used in the following discussion.

The results from the potentiodynamic polarization measurements of the AZ31 samples, covered by the

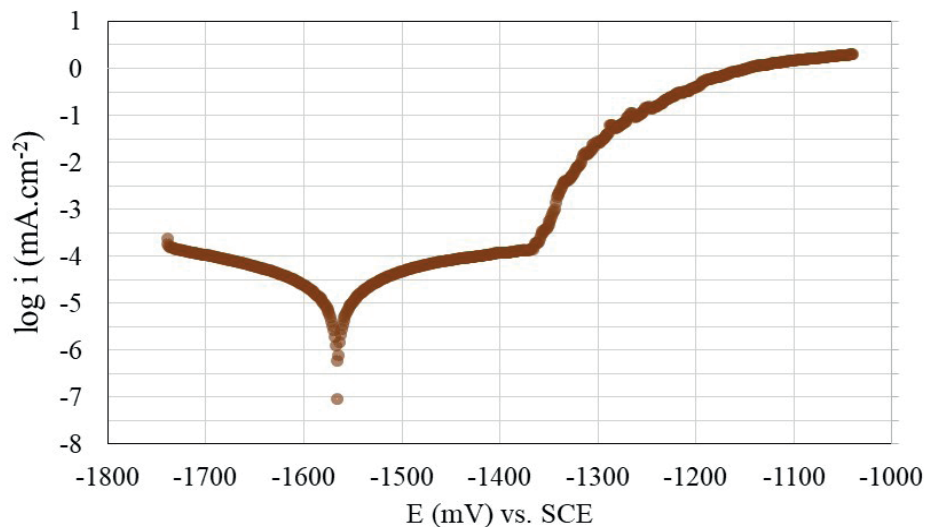


Figure 3 Potentiodynamic curve of the PEO coating sealed by oil based preservation layer containing corrosion inhibitors on AZ31 in 0.1M NaCl solution

Table 2 Electrochemical corrosion characteristics obtained from potentiodynamic curve of the PEO coating sealed by oil based preservation layer containing corrosion inhibitors on AZ31 in 0.1M NaCl solution

E_{corr} (mV)	E_{pit} (mV)	i_{corr} ($\mu\text{A.cm}^{-2}$)	β_a (mV/dec.)	β_c (mV/dec.)	r_{corr} ($\mu\text{m.year}^{-1}$)
-1568 \pm 22	-1367 \pm 30	0.014 \pm 0.007	159 \pm 12	159 \pm 3	0.53 \pm 0.16

sealed PEO coating, are presented in a form of the average potentiodynamic polarization curve shown in Figure 3. The average values of individual electrochemical corrosion characteristics were obtained by Tafel analysis and are presented in Table 2. When comparing to results from the PDP measurements reported in the previous work [21], it can be seen that sealing of the PEO layer with the tested preservative containing corrosion inhibitors caused a slight deterioration of the PEO, what is documented by shifting the average corrosion potential to more negative values by 67 mV compared to the simple PEO layer prepared at the longest processing time. Hence, as a consequence of sealing the PEO coating with the tested preservation system ultimately reached a corrosion potential almost identical to the corrosion potential of the base material (the difference of 11 mV is negligible in terms of measurement deviations). Thus, it can be stated that the tendency of the sealed PEO surface system to corrosion in the tested environment is almost identical compared to the base material from the thermodynamic point of view. On the contrary, there is a theoretical deterioration caused by impregnation compared to the simple PEO coating. However, this degradation of the thermodynamic corrosion properties is negligible from a practical point of view due to still extremely low nobility of the overall surface system. More important is a kinetic aspect. There, impregnation of the PEO coating with a preservative containing corrosion inhibitors effectively reduced the sensibility of the system to polarization in the anodic region, to the level

comparable to cathodic polarization (almost identical values of β_a and β_c). The surface system also exhibited similar behaviour to that observed for some metals able to create passive layers. This is underlined by the presence of a step potential change in the anodic region responding to the pitting potential (E_{pit}) [32-34]. At this point, there is a severe local corrosion damage present on the surface of the sample. The potential region in which the E_{pit} was located was almost identical to the region recorded on the simple PEO coating. Much more radical was the change in kinetic electrochemical corrosion characteristics, which provide information on the rate of corrosion reactions in a corrosion environment. A simple PEO coating can reduce the instantaneous corrosion rate of the AZ31 alloy surface by more than three orders of magnitude to a level of about 2 $\mu\text{m.year}^{-1}$. Sealing this layer with the tested preservative reduced this corrosion rate to just 0.53 $\mu\text{m.year}^{-1}$. Thus, the instantaneous corrosion rate of this duplex coating system on AZ31 alloy, in an aqueous environment containing chlorides, can be considered to be almost zero even after one hour of exposure. Unfortunately, these excellent values are not sustainable in the long run, as the environment constantly interacts with this system during the longer exposure, which is reflected in its degradation and decline in its protective function. However, it is more appropriate to use a non-destructive method such as EIS to monitor this process, which can be used to continuously assess development of individual relevant electrochemical characteristics on the same sample over a longer time horizon.

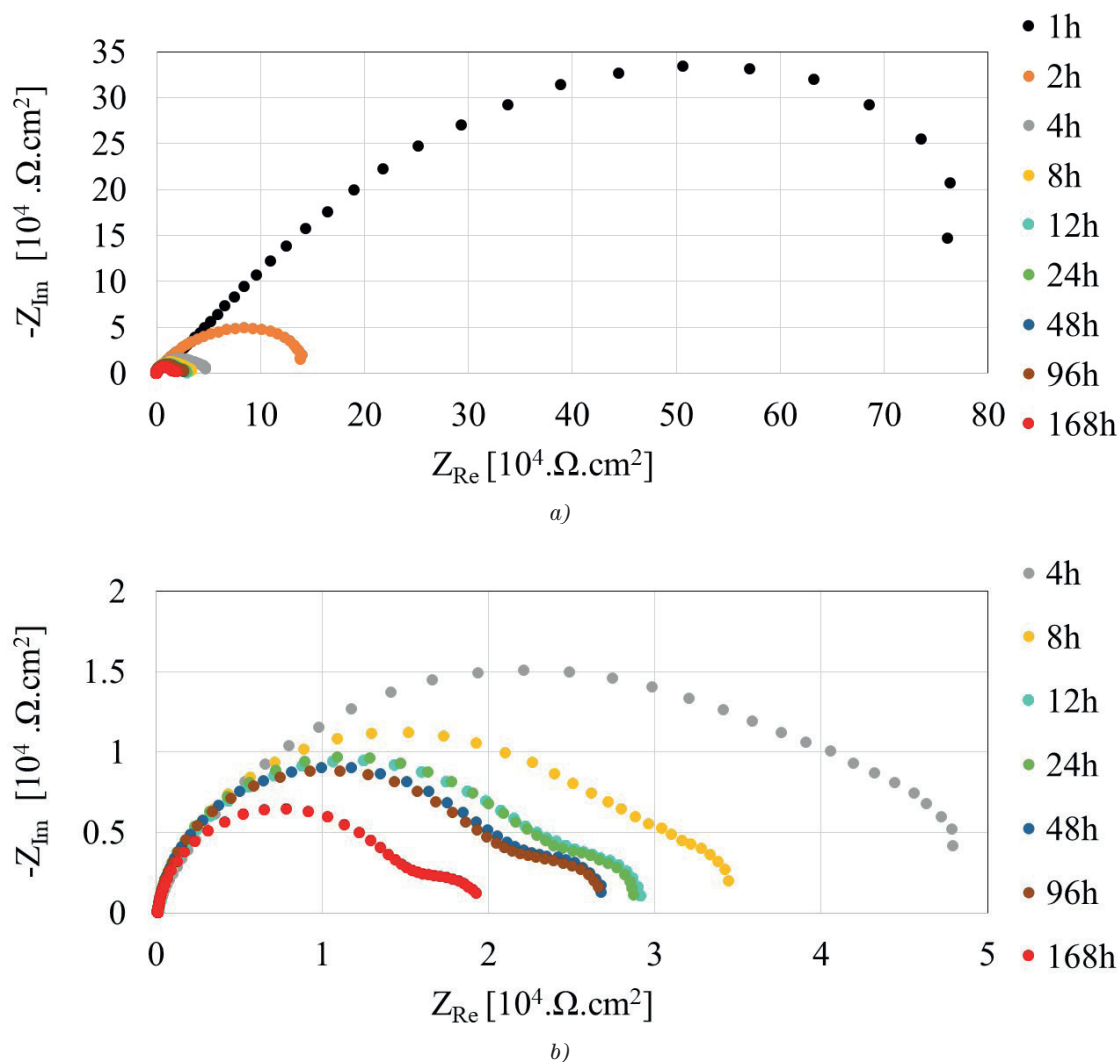


Figure 4 Nyquist diagrams of PEO coating sealed by oil based preservation layer containing corrosion inhibitors on AZ31 in 0.1M NaCl solution after various exposure times: a) overall view; b) detail of higher exposure times

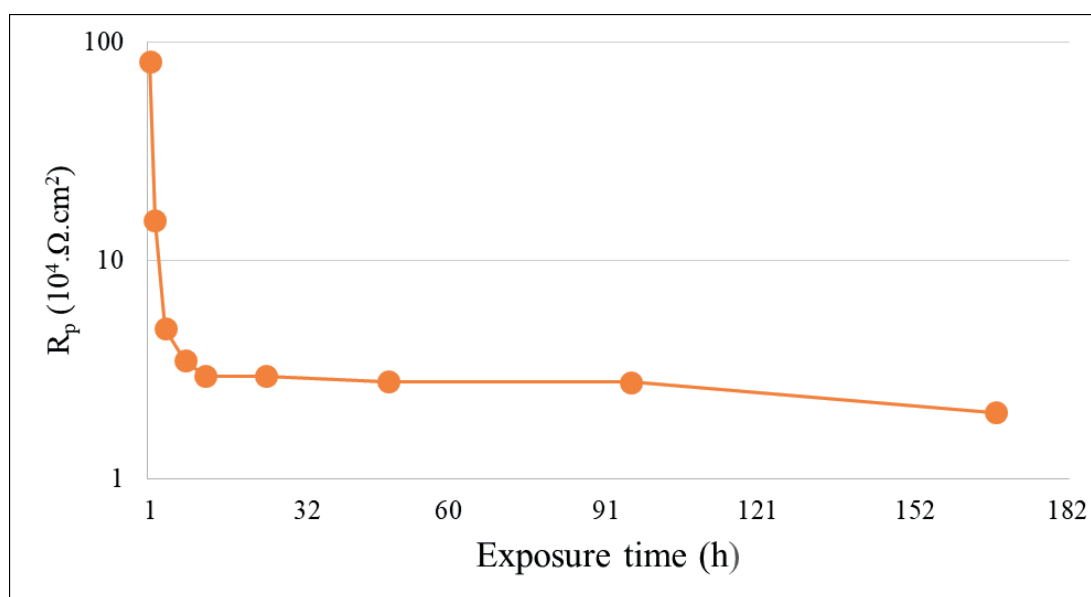
The measured Nyquist diagrams of AZ31 alloy with sealed PEO coating after various exposure times are shown in Figure 4. The electrochemical characteristics obtained by their analysis are shown in Table 3 and the graph of evolution of the R_p values obtained on the sealed PEO coating after individual exposure times in 0.1M NaCl solution is shown in Figure 5. After 1 hour of exposure to the electrolyte, the sealed PEO surface reached more than four times higher R_p value compared to the simple PEO layer [23], which fully corresponds to the results of kinetic corrosion parameters evaluation within the PDP measurements. This improvement is primarily caused by the physical barrier effect of the added preservative in the initial stages of exposure. However, since it is not a permanent, but only a temporary liquid preservative system, the barrier effect gradually lost its effectivity with prolonged exposure and the electrolyte penetrated further through the PEO to the base material. When the penetrating electrolyte reached the base material under the PEO coating, a second capacitive loop was recorded on the Nyquist diagram revealing the detection of a new interface. This was observed after 4 hours of exposure in the considered case. Up to that point,

the entire resistance of the surface to the corrosion process was held by R_{po} . From 4 hours of exposure, R_{et} contributed to the total polarization resistance of the system, as well. As can be seen from Figure 5, the decrease in the total polarization resistance was very sharp in the first stages of exposure up to 12 hours, which was mainly related to weakening of the barrier effect of the preservative and PEO coating, saturation of the surface system with electrolyte and degradation of the soluble MgO (its dissolution process in NaCl solution is described elsewhere [35-36]) representing the substantial part of created PEO coating [37]. Subsequently, the decrease was significantly inhibited to near saturation trend, which was caused by action of the corrosion inhibitors retarding the corrosion processes at the base material / electrolyte interface and also by sealing the critical areas by corrosion products forming a certain barrier to the corrosion processes (an effect similar to that observed on unprotected material during long-term exposure [23].) This theory is supported by values and trends of individual partial electrochemical corrosion characteristics.

The R_{po} provided the largest portion in the total

Table 3 Electrochemical corrosion characteristics obtained from the Nyquist diagrams of the PEO coating sealed by oil based preservation layer containing corrosion inhibitors on AZ31 in 0.1M NaCl solution after various exposure times

Time	R_s ($\Omega \cdot \text{cm}^2$)	R_{po} ($\Omega \cdot \text{cm}^2$)	R_{ct} ($\Omega \cdot \text{cm}^2$)	R_p ($\Omega \cdot \text{cm}^2$)	CPE_c ($\text{F} \cdot \text{s}^{-1} \cdot 10^{-6}$)	CPE_{dl} ($\text{F} \cdot \text{s}^{-1} \cdot 10^{-6}$)	n_1	n_2
1h	120	814065		814065	1.7		0.8	
2h	125	151776		151776	2.5		0.7	
4h	134	23125	25562	48687	2.7	12.8	0.8	0.8
8h	137	23962	10702	34664	3.2	74.2	0.9	0.8
12h	138	20162	9384	29546	3.7	124.8	0.9	0.8
24h	138	19777	9652	29429	4.2	137.1	0.9	0.7
48h	138	18096	9699	27795	4.5	151.2	0.9	0.7
96h	136	17877	9683	27560	4.9	175.6	0.9	0.7
168h	138	13145	6933	20078	5.6	247.4	0.9	0.7

**Figure 5** Evolution of the R_p on AZ31 magnesium alloy coated by the PEO and sealed by oil based preservation layer containing corrosion inhibitors in 0.1M NaCl solution after various exposure times

polarization resistance of the system AZ31+PEO+sealing in all the stages of exposure. Due to the sealing of the pores and the barrier effect of the preservative, a high level of corrosion protection was achieved at the beginning of the exposure comparable to the passive layer on titanium [38]. This type of resistance depends on several factors playing a key role in terms of a longer exposure in electrolytes. It can be determined according to Equation [28]:

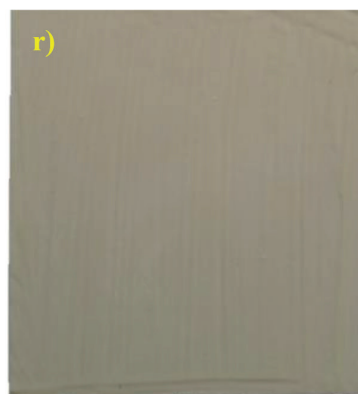
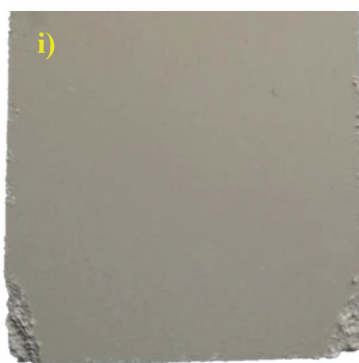
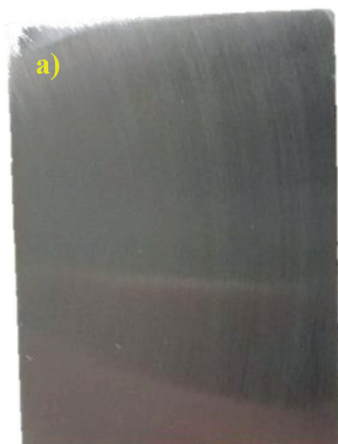
$$R_{po} = \frac{\rho \cdot d}{A_p}, \quad (3)$$

where ρ is the electrolyte resistivity in the pores, d the pore length (~coating thickness) and A_p the total pore surface area.

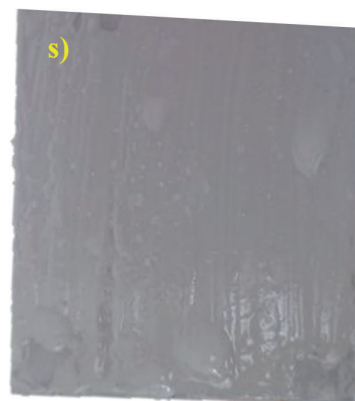
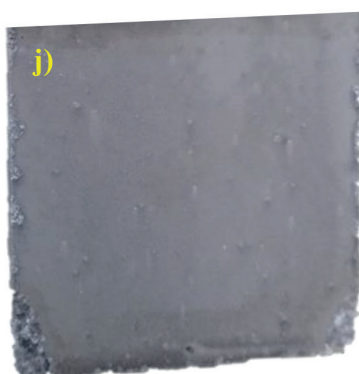
Generally R_{po} decreases as the electrolyte penetrates the coating and fills the pores [28]. In this case, the highly conductive electrolyte containing chloride ions entered the surface pores where diffused through the sealing system and further penetrated through the PEO coating while filling the empty pores and lowering intensively the overall

resistivity. This was one of the main reasons for the massive R_{po} decrease in the first hours of immersion. The decrease of R_{po} with time was also related to increase of A_p , which could be explained by an increase of number of the filled pores or an increase of their area if delamination occurs [28]. When the process of electrolyte penetration through the coating system was finished, the rapid decline in the R_{po} values was significantly decelerated, with the gradual dissolution of the PEO coating and its associated reduction (reduction of parameter d) becoming the main factor responsible for the further R_{po} decrease. However, the dissolution rate of the PEO coating was considerably inhibited by the oil-based preservative, which has a non-polar character and thus did not directly interact with the polar 0.1M NaCl aqueous solution. This deceleration was also supported by the above-mentioned formation of the corrosion products at the base material / PEO coating interface, which filled the formed and emerging pores from the inside.

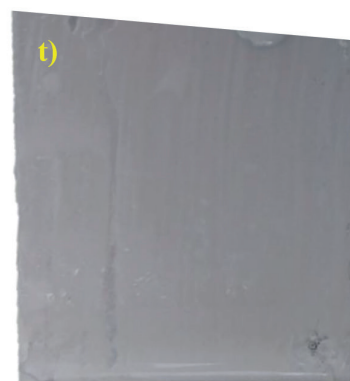
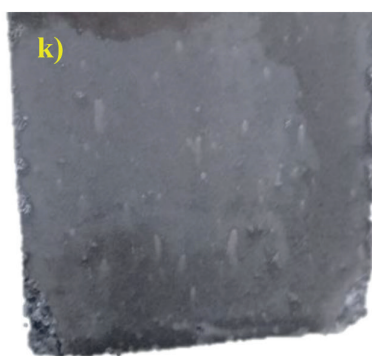
The R_{ct} is the resistance to charges transfer, determining the corrosion rate of reaction and is a measure of electric



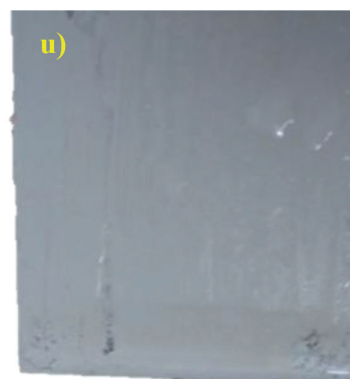
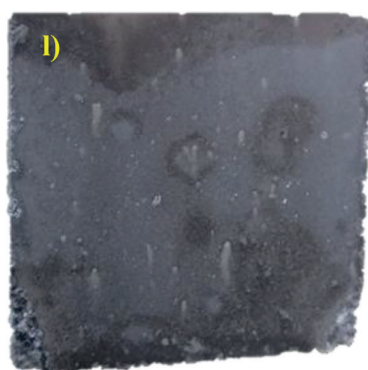
Prior to exposure



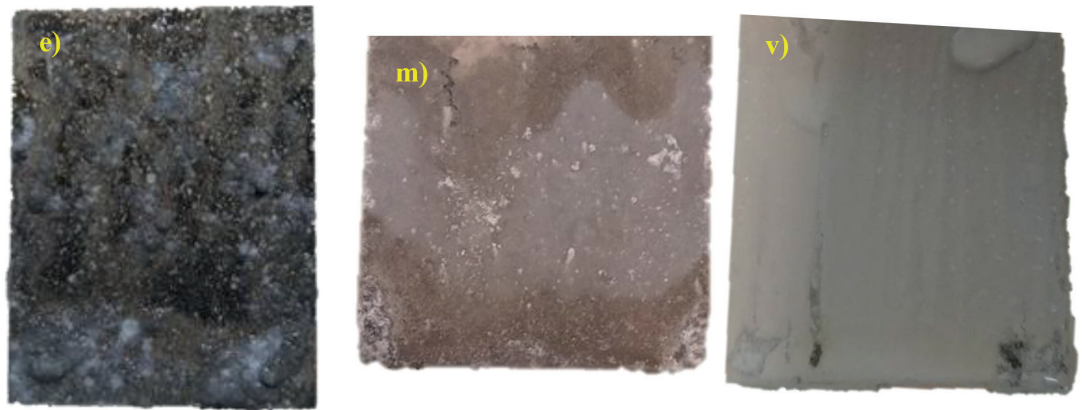
After 1 day of exposure



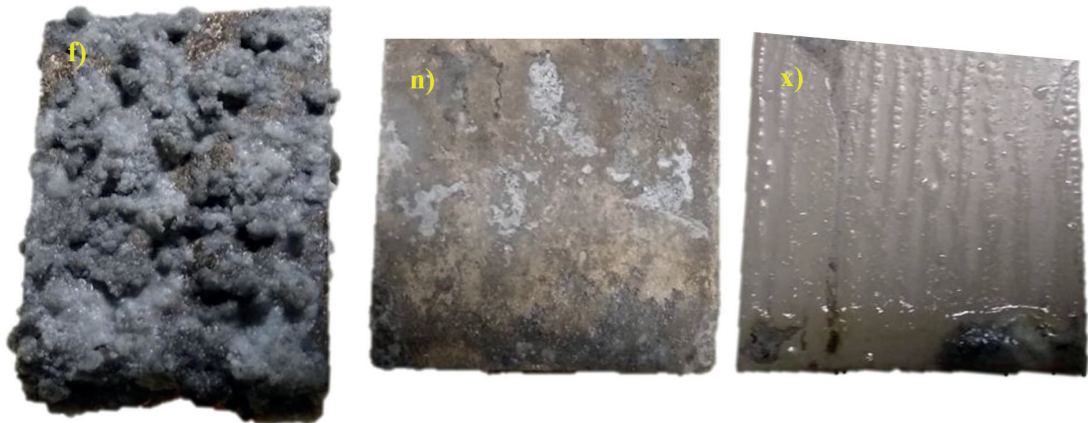
After 2 days of exposure



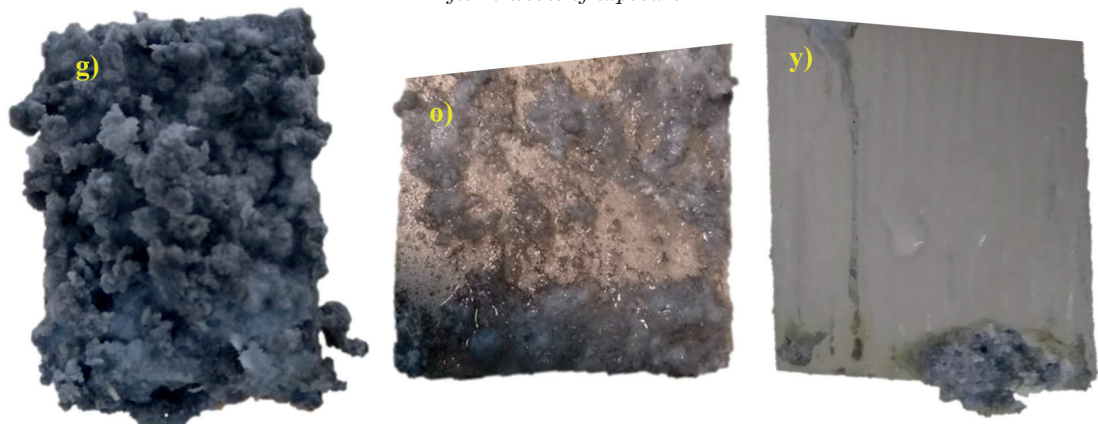
After 3 days of exposure



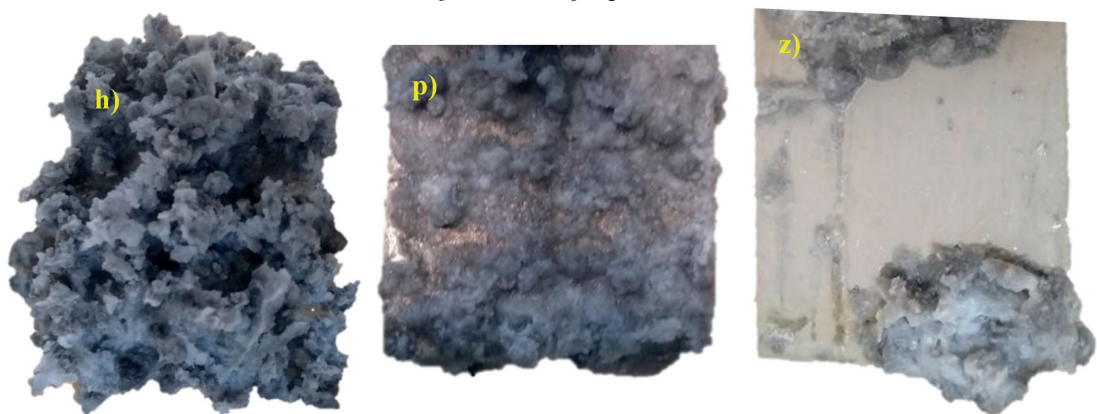
After 1 week of exposure



After 2 weeks of exposure



After 3 weeks of exposure



After 4 weeks of exposure

Figure 6 AZ31 samples after various surface treatment and exposure to the salt spray test according to STN EN ISO 9227: a)-h) ground surface (P1000); i)-p) PEO treatment; r)-z) PEO + sealing

charges transfer through the electrode surface (or metal / electrolyte interface in our case) [26]. It is an appropriate parameter to evaluate the corrosion in the beneath coating and separation of coating from the metal substrate [30]. Generally, high values of the charge transfer resistance and low values of double layer capacitance signify a coating of better performance [39]. In the considered case, the R_{ct} appeared after 4 hours of exposure and decreased for more than one-half in next 4 hours. Subsequently, the decrease significantly decelerated. However, it is unlikely that the process of delamination caused by the gradual penetration of the electrolyte through the PEO and its degradation was finished at that moment. The explanation is indicated by evolution of the CPE_{dl} values. Since the value of the parameter n_2 is almost constant and approaching the value 1 during the whole exposure, one can describe development of the CPE_{dl} by parameters influencing the C_{dl} . The C_{dl} is the double electric layer capacitance resulting from ions and water molecules adsorbed, due to the potential difference between the electrode suffering corrosion and the electrolyte [26]. Hence, the double-layer capacitance is proportional to the active metallic area (area in contact with the electrolyte) [28]. Since the CPE_{dl} values continually increased even after 4 hours of exposure in this case, the process of delamination and enlargement of the active area was still not finished. An explanation of the non-corresponding trend of the R_{ct} development lies in the effect of added corrosion inhibitors, which did not prevent the increase of the active area of the base material and delamination of the PEO layer, but slowed down the electrode processes, namely charge transfer through the interfacial interface leading to moderate decrease of the R_{ct} values.

The synergistic effect of an oil-based preservative and corrosion inhibitors resulted in significantly better corrosion protection of AZ31 alloy coated by the PEO in aqueous media containing aggressive chlorides, when even after 168 hours of exposure the total polarization resistance of the surface system was almost 2-times higher than R_p of the simple unsealed PEO surface after the same exposure time (based on results from [23]).

In addition to electrochemical tests in an aqueous medium containing chlorides, the salt spray tests were performed on the tested samples according to STN EN ISO 9227, as well. Magnesium and its alloys are generally well corrosion resistant to atmospheric conditions as long as relatively low humidity and low content of impurities and contaminants are maintained. However, the salt spray test according to STN EN ISO 9227 represents a very aggressive environment for magnesium alloys combining the high air humidity, increased temperature and increased oxygen content compared to exposure tests in aqueous solution and especially high content of aggressive chloride ions. Moreover, the aggressive atmosphere is continually changed to fresh (opened circuit), thus preventing the depletion of aggressive components or local increase in pH, which could change the nature of corrosion products and thus affect the corrosion protection of the surface treatment system. The corrosion attack on individual test

samples with various level of surface treatment during the exposure in the salt spray is shown in Figure 6. During the PEO process performed for longer times (in order to form a thicker oxide layer), sharp edges on the samples/products can be dissolved. However, even these damaged edges are well covered with a protective layer. This rare phenomenon was also chosen for evaluation in the salt spray test (Figure 6i), in order to see its effect on the corrosion attack of the whole sample. The PEO-coated sample, sealed with the tested preservative, was visually flawless prior to exposure.

The course of the corrosion attack on the ground unprotected AZ31 sample, which served as a reference, was very intense (Figure 6a-h). The local form of the corrosion attack in the first days of exposure can be attributed to the typical microstructure of AZ31 alloy, which contains the intermetallic β -phase $Mg_{17}Al_{12}$ acting as a microcathode, which causes microgalvanic corrosion of the matrix in its vicinity [40]. Generally, the film formed on an Mg surface, after exposure to humid air at higher relative humidity and temperature, is formed by a bilayer structure with an apparently dense outer layer (mainly $Mg(OH)_2$) and a cellular inner layer (mainly MgO). However, the structure and formation mechanism of this surface film are affected by the chemical composition of the Mg alloy, the constituents of the atmosphere, the temperature and humidity [40]. This mechanism was observed on the unprotected sample of AZ31 in the considered case too, where it was possible to observe formation of the black MgO in the initial stages and the growth of the coarse white $Mg(OH)_2$ corrosion products in the later stages. However, the presence of chlorides in the atmosphere significantly increased their solubility and reduced their protective barrier effect. Chlorides also caused the formation of their own reaction products with the magnesium base material in a form of unstable $MgCl_2$, thus further disrupting the integrity of the oxide layers. As a result, the tested sample of unprotected magnesium alloy was almost completely corroded after 4 weeks of exposure (Figure 6h), which completely eliminates its unprotected use in industrial applications in aggressive environments containing chloride ions.

Local corrosion initiation centres can be observed after only 1 day of exposure on a sample with an unsealed PEO layer (Figure 6j). The presence of pores significantly accelerated the progress of chlorides and moisture to the base material and also the intensity of dissolution of the PEO layer, which was visually observed after only 2 days of exposure (formation of areas with different colour shades on the surface). However, the resulting corrosion centres were relatively stabilized up to 1 week of exposure and the sample did not significantly change its volume, so the main degradation mechanism was the dissolution of the PEO layer. However, intense corrosion of the base material through the already weak layer of the PEO was observed after 2 weeks of exposure, which also led to development of the corrosion products of a large volume. This caused a significant change in geometry of the original sample. After 4 weeks of exposure, more than 90 % of the sample was already covered with corrosion products, which means that

the PEO layer has already lost its protective function and the sample would behave as unprotected with continued exposure. An interesting trend of the corrosion attack was observed on the mentioned corroded corners of the sample, which did not represent a significant initiation centre of the corrosion attack during the exposure, as the rate of corrosion attack at these places was almost similar to the rest of the sample. This was an important fact from a practical point of view.

The best results were obtained on AZ31 sample with the sealed PEO coating (Figure 6r-z). Although the first local corrosion initiation centres were observed after only two days of exposure in the salt spray, the overall geometry of the sample remained almost unchanged until 2 weeks of exposure. The barrier effect of the preservative and its non-polar character, significantly inhibiting corrosion processes on the sample, were well manifested in this type of corrosion test. However, the course of the corrosion attack was not widespread as in previous cases, but was very localized. Even after 4 weeks of exposure, a large part of the surface was almost unchanged from a visual point of view. The corrosion attack of the base material spread from the local initiation corrosion centres on the sealed PEO surface by the delamination mechanism, by which the active components of the environment overcame the protective surface barrier even in places with almost perfect coverage. The fact that the whole process of the corrosion attack focused only on the local areas becoming local anodes, caused the corrosion attack at this areas to reach larger dimensions than on a simple unprotected sample with the PEO coating. However, the cause of such a weak critical point could have a different possible origins out of standard considered presence of pores and microcracks in the PEO layer. These problems could appear also due to the base material including presence of impurities, cracks, or other phases protruding to the surface where the PEO layer did not form properly. Another danger was represented by the surface areas with the most intense adsorption of the condensate (bottom of the sample where droplets form from the flowing condensate). In order to achieve the maximum corrosion protection of the AZ31 alloy surface, it is therefore necessary to ensure the cleanest possible microstructure without defects, creation of very homogeneous PEO coating, very precise application of preservative and elimination of increased environmental humidity, which could lead to subsequent crevice or local microgalvanic corrosion.

4 Conclusions

Based on the measured data and analyses we concluded:

1. Application of an oil-based preservative containing

corrosion inhibitors to the PEO coating caused a negligible deterioration of the nobility of the surface system in a 0.1M NaCl solution from a thermodynamic point of view. However, an almost 4-fold reduction in the instantaneous corrosion rate in a given environment was caused by this sealing of PEO coating compared to the unsealed PEO coating.

2. Sealing the PEO coating with a preservative caused a significant increase in the overall polarization resistance of the surface system. Moreover, this beneficial effect was maintained even after 168 hours of exposure in 0.1M NaCl solution.
3. Decrease in the R_p values during the exposure in 0.1M NaCl could be divided into two stages: 1. intense decrease caused by electrolyte penetration through the surface system during the first 12 hours of exposure; 2. a very slight stabilized decrease caused by an action of the corrosion inhibitors at the base material / electrolyte interface in combination with the additive barrier effect of the non-polar preservative.
4. Sealing of the PEO layer using a preservation system ensured a significant extension of the protection period of the AZ31 alloy sample even in an aggressive simulated atmosphere containing chlorides. However, any corrosive attack on a given surface system had a significant local character causing intensive delamination of the surface protective layer.
5. Temporary additional surface treatment of the PEO coated magnesium alloy with an oil-based preservative containing corrosion inhibitors, which can be safely and ecologically removed with a degreaser, represents a simple and ecological solution to increase corrosion protection of AZ31 magnesium alloy for overseas transport or applications, where it may come into contact with aggressive environments containing chloride ions both in aqueous or atmospheric environments.

Acknowledgements

The research is supported by European regional development fund and Slovak state budget by the projects ITMS 26220220121 and ITMS2014+ 313011T426. The research is supported by Science Grant Agency of the Slovak Republic through project No. 1/0045/17. Authors are grateful for the support in experimental works to the University of Zilina by the projects No. 7950 and 8003. This publication was also realized with support of Operational Program Integrated Infrastructure 2014 - 2020 of the project: Innovative Solutions for Propulsion, Power and Safety Components of Transport Vehicles, code ITMS 313011V334, co-financed by the European Regional Development Fund.

References

- [1] BULING, A., ZERRER, J. Increasing the application fields of magnesium by ultracera[®]: corrosion and wear protection by plasma electrolytical oxidation (PEO) of Mg alloys. *Surface and Coatings Technology* [online]. 2019, **369**, p. 142-155 [accessed 2020-07-10]. ISSN 0257-8972. Available from: <https://doi.org/10.1016/j.surfcoat.2019.04.025>
- [2] AGHION, E., BRONFEN, B., ELIEZER, D. The role of the magnesium industry in protecting the environment, *Journal of Materials Processing Technology* [online]. 2001, **117**(3), p. 381-385 [accessed 2020-07-10]. ISSN 0924-0136. Available from: [https://doi.org/10.1016/S0924-0136\(01\)00779-8](https://doi.org/10.1016/S0924-0136(01)00779-8)
- [3] LAMAKA, S. V., KNORNSCHILD, G., SNIHIROVA, D. V., TARYBA, M. G., ZHELUDKEVICH, M. L., FERREIRA, M. G. S. Complex anticorrosion coating for ZK30 magnesium alloy. *Electrochimica Acta* [online]. 2009, **51**(1), p. 131-141 [accessed 2020-07-10]. ISSN 0013-4686. Available from: <https://doi.org/10.1016/j.electacta.2009.08.018>
- [4] GHOLAMI-KERMANSHAHI, M., NEUBERT, V. D., TAVAKOLI, M., PASTOREK, F., SMOLA, B., NEUBERT, V. Effect of ECAP processing on corrosion behavior and mechanical properties of the ZFW MP magnesium alloy as a biodegradable implant material. *Advanced Engineering Materials* [online]. 2018, **20**(10), 1800121 [accessed 2020-07-10]. ISSN 1527-2648. Available from: <https://doi.org/10.1002/adem.201800121>
- [5] GAWEL, L., NIEUZYL, L., NAWRAT, G., DAROWICKI, K., SLEPSKI, P. Impedance monitoring of corrosion degradation of plasma electrolytic oxidation coatings (PEO) on magnesium alloy. *Journal of Alloys and Compounds* [online]. 2017, **722**, p. 406-413 [accessed 2020-07-10]. ISSN 0925-8388. Available from: <https://doi.org/10.1016/j.jallcom.2017.06.120>
- [6] MOHEDANO, M., BLAWERT, C., ZHELUDKEVICH, M. L. Cerium-based sealing of PEO coated AM50 magnesium alloy. *Surface and Coatings Technology* [online]. 2015, **269**, p. 145-154 [accessed 2020-07-10]. ISSN 0257-8972. Available from: <https://doi.org/10.1016/j.surfcoat.2015.01.003>
- [7] GHALI, E., DIETZEL, W., KAINER, K. U. General and localized corrosion of magnesium alloys: a critical review. *Journal of materials engineering and performance* [online]. 2004, **13**(1), p. 7-23 [accessed 2020-07-10]. ISSN 1059-9495. Available from: <https://doi.org/10.1361/10599490417533>
- [8] SONG, G. L., ATRENS, A. Corrosion mechanisms of magnesium alloys. *Advanced engineering materials* [online]. 2000, **1**(1), p. 11-33 [accessed 2020-07-10]. ISSN 1527-2648. Available from: [https://doi.org/10.1002/\(SICI\)1527-2648\(199909\)1:1<11::AID-ADEM11>3.0.CO;2-N](https://doi.org/10.1002/(SICI)1527-2648(199909)1:1<11::AID-ADEM11>3.0.CO;2-N)
- [9] AN, L., MA, Y., LIU, Y., SUN, L., WANG, S., WANG, Z. Effects of additives, voltage and their interactions on PEO coatings formed on magnesium alloys. *Surface and Coatings Technology* [online]. 2018, **354**, p. 226-235 [accessed 2020-07-10]. ISSN 0257-8972. Available from: <https://doi.org/10.1016/j.surfcoat.2018.09.026>
- [10] KAJANEK, D., HADZIMA, B., PASTOREK, F., NESLUSAN JACKOVA, M. Electrochemical impedance spectroscopy characterization of ZW3 magnesium alloy coated by DCPD using LASV deposition technique. *Acta Metallurgica Slovaca* [online]. 2017, **23**(2), p. 147-154 [accessed 2020-07-10]. ISSN 1338-1156. Available from: <https://doi.org/10.12776/ams.v23i2.900>
- [11] ALABBASI, A., MEHJABEEN, A., KANNAN, M. B., YE, Q., BLAWERT, C. Biodegradable polymer for sealing porous PEO layer on pure magnesium: An in vitro degradation study. *Applied Surface Science* [online]. 2014, **301**, p. 463-467 [accessed 2020-07-10]. ISSN 0169-4332. Available from: <https://doi.org/10.1016/j.apsusc.2014.02.100>
- [12] RAPHEAL, G., KUMAR, S., BLAWERT, C., DAHOTRE, N.B. Wear behavior of plasma electrolytic oxidation (PEO) and hybrid coatings of PEO and laser on MRI 230D magnesium alloy. *Wear* [online]. 2011, **271**(9-10), p. 1987-1997 [accessed 2020-07-10]. ISSN 0043-1648. Available from: <https://doi.org/10.1016/j.wear.2010.12.013>
- [13] CASTELLANOS, A., ALTUBE, A., VEGA, J. M., GARCIA-LECINA, E., DIEZ, J. A., GRANDE, H. J. Effect of different post-treatments on the corrosion resistance and tribological properties of AZ91D magnesium alloy coated PEO. *Surface and Coatings Technology* [online]. 2015, **278**, p. 99-107 [accessed 2020-07-10]. ISSN 0257-8972. Available from: <https://doi.org/10.1016/j.surfcoat.2015.07.017>
- [14] YANG, J., BLAWERT, C., LAMAKA, S. V., SNIHIROVA, D., LU, X., DI, S., ZHELUDKEVICH, M. L. Corrosion protection properties of inhibitor containing hybrid PEO-epoxy coating on magnesium. *Corrosion Science* [online]. 2018, **140**, p. 99-110 [accessed 2020-07-10]. ISSN 0010-938X. Available from: <https://doi.org/10.1016/j.corsci.2018.06.014>
- [15] CHEN, Y., LU, X., LAMAKA, S. V., JU, P., BLAWERT, C., ZHANG, T., WANG, F., ZHELUDKEVICH, M. L. Active protection of Mg alloy by composite PEO coating loaded with corrosion inhibitors. *Applied Surface Science* [online]. 2020, **504**, p. 144462 [accessed 2020-07-10]. ISSN 0169-4332. Available from: <https://doi.org/10.1016/j.apsusc.2019.144462>
- [16] PASTOREK, F., HADZIMA, B., OMASTA, M., MHAEDE, M. Effect of electrodeposition temperature on corrosion resistance of calcium phosphate. *Acta Metallurgica Slovaca* [online]. 2014, **20**(2), p. 200-208 [accessed 2020-07-10]. ISSN 1338-1156. Available from: <http://dx.doi.org/10.12776/ams.v20i2.290>
- [17] PASTOREK, F., HADZIMA, B., DOLEZAL, P. Electrochemical characteristics of Mg-3al-1Zn magnesium alloy surface with hydroxyapatite coating. *Communications - Scientific Letters of the University of Zilina* [online]. 2012, **14**(4), p. 26-30 [accessed 2020-07-10]. ISSN 2585-7878. Available from: <http://komunikacie.uniza.sk/index.php/communications/article/view/769>

- [18] KAJANEK, D., HADZIMA, B., PASTOREK, F., NESLUSAN JACKOVA, M. Corrosion performance of AZ31 magnesium alloy treated by ultrasonic impact peening (UIP). *Materials Today: Proceedings* [online]. 2018, **5**(13), p. 26687-26692 [accessed 2020-07-10]. ISSN 2214-7853. Available from: <https://doi.org/10.1016/j.matpr.2018.08.136>
- [19] HADZIMA, B., MHAEDE, M., PASTOREK, F. Electrochemical characteristics of calcium-phosphatized AZ31 magnesium alloy in 0.9 % NaCl solution. *Journal of Materials Science: Materials in Medicine* [online]. 2014, **25**(5), p. 1227-1237 [accessed 2020-07-10]. ISSN 1573-4838. Available from: [10.1007/s10856-014-5161-0](https://doi.org/10.1007/s10856-014-5161-0)
- [20] HADZIMA, B., JANECEK, M., BUKOVINA, M., KRAL, R. Electrochemical properties of fine-grained AZ31 magnesium alloy. *International Journal of Materials Research* [online]. 2009, **100**(9), p. 1213-1216 [accessed 2020-07-10]. ISSN 1862-5282. Available from: <https://doi.org/10.3139/146.110186>
- [21] KAJANEK, D., HADZIMA, B., TKACZ, J., PASTORKOVA, J., JACKOVA, M., WASSERBAUER, J. Corrosion resistance of AZ31 magnesium alloy treated by plasma electrolytic oxidation. *Koroze a Ochrana Materialu* [online]. 2019, **63**(2), p. 65-71 [accessed 2020-07-10]. ISSN 0452-599X. Available from: DOI:10.2478/kom-2019-0008
- [22] KAJANEK, D., HADZIMA, B., BREZINA, M., JACKOVA, M. Effect of applied current density of plasma electrolytic oxidation process on corrosion resistance of AZ31 magnesium alloy. *Communications - Scientific Letters of the University of Zilina* [online]. 2019, **21**(2), p. 32-36 [accessed 2020-07-10]. ISSN 2585-7878. Available from: <https://doi.org/10.26552/com.C.2019.2.32-36>
- [23] KAJANEK, D., HADZIMA, B., BUHAGIAR, J., WASSERBAUER, J., JACKOVA, M. Corrosion degradation of AZ31 magnesium alloy coated by plasma electrolytic oxidation. *Transportation Research Procedia* [online]. 2019, **40**, p. 51-58 [accessed 2020-07-10]. ISSN 2352-1465. Available from: <https://doi.org/10.1016/j.trpro.2019.07.010>
- [24] CAMPOS-SILVA, I. E., RODRIGUEZ-CASTRO, G. A. Boriding to improve the mechanical properties and corrosion resistance of steels. In: *Thermochemical surface engineering of steels*. Woodhead Publishing, 2015, p. 651-702. ISBN 978-0-85709-592-3.
- [25] AMIRUDIN, A., THIENY, D. Application of electrochemical impedance spectroscopy to study the degradation of polymer-coated metals. *Progress in Organic Coatings* [online]. 1995, **26**(1), p. 1-28 [accessed 2020-07-10]. ISSN 0300-9440. Available from: [https://doi.org/10.1016/0300-9440\(95\)00581-1](https://doi.org/10.1016/0300-9440(95)00581-1)
- [26] RIBEIRO, D. V., SOUZA, C. A. C., ABRANTES, J. C. C. Use of electrochemical impedance spectroscopy (EIS) to monitoring the corrosion of reinforced concrete. *Revista IBRACON de Estruturas e Materiais* [online]. 2015, **8**(4), p. 529-546 [accessed 2020-07-10]. ISSN 1983-4195. Available from: <https://doi.org/10.1590/S1983-41952015000400007>
- [27] HADZIMA, B., PASTOREK, F., BORKO, K., FINTOVA, S., KAJANEK, D., BAGHERIFARD, S., GHOLAMI-KERMANS SHAHI, M., TRSKO, L., PASTORKOVA, J., BREZINA, J. Effect of phosphating time on protection properties of hurealite coating: differences between ground and shot peened HSLA steel surface. *Surface and Coatings Technology* [online]. 2019, **375**, p. 608-620 [accessed 2020-07-10]. ISSN 0257-8972. Available from: <https://doi.org/10.1016/j.surfcoat.2019.07.056>
- [28] OLIVIER, M. G., POELMAN, M. Use of electrochemical impedance spectroscopy (EIS) for the evaluation of electrocoatings performances. In: *Recent Researches in Corrosion evaluation and protection*. London: IntechOpen Limited., 2012, p. 1-26. ISBN 978-953-307-920-2.
- [29] CAVALCANTI, E., FERRAZ, O., DI SARLI, A.R. The use of electrochemical impedance measurements to assess the performance of organic coating systems on naval steel. *Progress in Organic Coatings* [online]. 1993, **23**(2), p. 185-200 [accessed 2020-07-10]. ISSN 0300-9440. Available from: [https://doi.org/10.1016/0033-0655\(93\)80010-8](https://doi.org/10.1016/0033-0655(93)80010-8)
- [30] GOLABADI, M., ALIOFKHAZRAEI, M., TOORANI, M., ROUHAGHDAM, A.S. Corrosion and cathodic disbondment resistance of epoxy coating on zinc phosphate conversion coating containing Ni²⁺ and Co²⁺. *Journal of Industrial and Engineering Chemistry* [online]. 2017, **47**, p. 154-168 [accessed 2020-07-10]. ISSN 1226-086X. Available from: <https://doi.org/10.1016/j.jiec.2016.11.027>
- [31] YEROKHIN, A. L., NIE, X., LEYLAND, A., MATTHEWS, A., DOWEY, S. J. Plasma electrolysis for surface engineering. *Surface and Coatings Technology* [online]. 1999, **122**(2-3), p. 73-93 [accessed 2020-07-10]. ISSN 0257-8972. Available from: [https://doi.org/10.1016/S0257-8972\(99\)00441-7](https://doi.org/10.1016/S0257-8972(99)00441-7)
- [32] ZAID, B., MADDACHE, N., SAIDI, D., SOUAMI, N., BACHA, N., AHMED, A. S. Electrochemical evaluation of sodium metabisulfite as environmentally friendly inhibitor for corrosion of aluminum alloy 6061 in a chloride solution. *Journal of Alloys and Compounds* [online]. 2015, **629**, p. 188-196 [accessed 2020-07-10]. ISSN 0925-8388. Available from: <https://doi.org/10.1016/j.jallcom.2015.01.003>
- [33] FINTOVA, S., DRABIKOVA, J., PASTOREK, F., TKACZ, J., KUBENA, I., TRSKO, L., HADZIMA, B., MINDA, J., DOLEZAL, P., WASSERBAUER, J., PTACEK, P. Improvement of electrochemical corrosion characteristics of AZ61 magnesium alloy with unconventional fluoride conversion coatings. *Surface and Coatings technology* [online]. 2019, **357**, p. 638-650 [accessed 2020-07-10]. ISSN 0257-8972. Available from: <https://doi.org/10.1016/j.surfcoat.2018.10.038>
- [34] FINTOVA, S., DRABIKOVA, J., HADZIMA, B., TRSKO, L., BREZINA, M., DOLEZAL, P., WASSERBAUER, J. Degradation of unconventional fluoride conversion coating on AZ61 magnesium alloy in SBF solution. *Surface and Coatings Technology* [online]. 2019, **380**, p. 125012 [accessed 2020-07-10]. ISSN 0257-8972. Available from: <https://doi.org/10.1016/j.surfcoat.2019.125012>

- [35] LIANG, J., SRINIVASAN, P. B., BLAWERT, C., DIETZEL, W. Influence of pH on the deterioration of plasma electrolytic oxidation coated AM50 magnesium alloy in NaCl solutions. *Corrosion Science* [online]. 2010, **52**(2), p. 540-547. [accessed 2020-10-8]. ISSN 0010-938X. Available from: <https://doi.org/10.1016/j.corsci.2009.10.011>
- [36] XIA, S. J., YUE, R., RATEICK JR, R. G., BIRSS, V. I. Electrochemical studies of AC/DC anodized Mg alloy in NaCl solution. *Journal of The Electrochemical Society* [online]. 2004, **151**(3), p. 179-187 [accessed 2020-10-8]. ISSN 0013-4651. Available from: <https://doi.org/10.1149/1.1646139>
- [37] DARBAND, G. B., ALIOFKHAZRAEI, M., HAMGHALAM, P., VALIZADE, N. Plasma electrolytic oxidation of magnesium and its alloys: Mechanism, properties and applications. *Journal of Magnesium and Alloys* [online]. 2017, **5**(1), p. 74-132 [accessed 2020-10-8]. ISSN 2213-9567. Available from: <https://doi.org/10.1016/j.jma.2017.02.004>
- [38] PASTOREK, F., HADZIMA, B., FINTOVA, S., MHAEDE, M. Influence of anodic oxidation on the polarization resistance of Ti6Al4V alloy after shot peening. *Materials Science Forum* [online]. 2015, **811**, p. 59-62 [accessed 2020-07-10]. ISSN 1662-9752. Available from: <https://doi.org/10.4028/www.scientific.net/MSF.811.59>
- [39] SANKARA NARAYANAN, T. S. N. Surface pretreatment by phosphate conversion coatings. *Reviews in Advanced Materials Science* [online]. 2005, **9**, p. 130-177 [accessed 2020-07-10]. ISSN 1338-1156. Available from: http://www.ipme.ru/e-journals/RAMS/no_2905/narayanan.pdf
- [40] LIU, H., CAO, F., SONG, G. L., ZHENG, D., SHI, Z., DARGUSCH, M. S., ATRENS, A. Review of the atmospheric corrosion of magnesium alloys. *Journal of Materials Science and Technology* [online]. 2019, **35**(9), p. 2003-2016 [accessed 2020-07-10]. ISSN 1005-0302. Available from: <https://doi.org/10.1016/j.jmst.2019.05.001>

OPTIMIZATION OF INGREDIENTS UPON DEVELOPMENT OF THE PROTECTIVE POLYMERIC COMPOSITE COATINGS FOR THE RIVER AND SEA TRANSPORT

Andriy Buketov¹, Serhii Yakushchenko¹, Abdellah Menou², Oleh Bezbakh¹, Roman Vrublevskiy¹, Yaroslava Kalba³, Tetyana Cherniavska¹, Danylo Zhytnyk¹, Olha Danylyuk^{3,*}

¹Kherson State Maritime Academy, Kherson, Ukraine

²International Academy of Civil Aviation, Casablanca, Morocco

³Ternopil Volodymyr Hnatiuk National Pedagogical University, Ternopil, Ukraine

*E-mail of corresponding author: laboratory22b@gmail.com

Resume

It is proved that in order to increase the operational characteristics of parts of the river and sea transport, including their physical and mechanical properties, it is advisable to use the protective polymeric composite coatings.

The effect of fillers on the flexural stresses of the developed epoxy composite was analyzed. The critical content of components was determined by the method of mathematical planning of the experiment: the synthesized powder mixture - 0.05 pts.wt., discrete fibers - 0.10 to 0.15 pts.wt. per 100 pts.wt. of epoxy oligomer ED-20. Introduction of such ingredients into the epoxy binder allows to increase the flexural stresses to $\sigma_f=77.4...78.6$ MPa. The obtained results allow to create materials with improved values of physical and mechanical properties.

Article info

Received 5 May 2020

Accepted 10 August 2020

Online 18 December 2020

Keywords:

composite,
epoxy matrix,
method of mathematical planning
of the experiment,
regression equation

Available online: <https://doi.org/10.26552/com.C.2021.2.B89-B96>

ISSN 1335-4205 (print version)

ISSN 2585-7878 (online version)

1 Introduction

Development of the river and sea transport involves creation of new materials to protect equipment parts from corrosion and wear. Use of the polymer composite materials (PCM) and protective coatings based on them is relevant in this context. Polymer composites are characterized by improved performance, which conditions a wide range of applications in the transport industry to increase the service life of machines and mechanisms [1-2]. It should be noted that nowadays the problem of improving cohesive properties of the known materials is current, which is decisive in analysis of reliability of equipment under critical conditions.

The authors [3-9] have shown that it is advisable to introduce fillers at a critical content in order to improve the properties of coatings, which are operated in the conditions of influence of corrosive environments and variable temperatures, in the complex. At the same time, it is important to choose the additives that should be active to the physical and chemical interaction with the polymer during the crosslinking. It was believed that introduction of fillers in the form of powder and discrete fibers can provide a synergistic effect in improving the material properties. In this context, it is advisable to use the method of mathematical planning of the experiment, which will

reduce the number of conducted studies and optimize the content of ingredients to obtain material with the highest parameters of the studied characteristics.

Aim of the investigation - to optimize the content of dispersed and fibrous discrete fillers for the protective coatings of the river and sea transport by the method of mathematical planning of an experiment.

2 Materials and methods

The epoxy diene oligomer ED-20 was selected as the main component for the binding when forming epoxy composite materials (CM), which is distinguished by the high adhesive and cohesive strength. For the cross-linking action of epoxy compositions, polyethylene polyamine hardener was used, which allows materials' curing at room temperatures. The PEPA is a low molecular weight substance consisting of monomer units with the following form: $[-CH_2-CH_2-NH-]_n$. A micro-dispersed filler, the synthesized powder mixture (SPM) of the following composition: Fe (70%) + Ti (10%) + TiC (15%) + Fe_3C (5%) and a mixture of discrete fibers (MDF) in the form of fibrous filler: modal (42%), polyacryl (38%), polyamide (38%), were used for experimental studies.

Epoxy CM's forming technology is following [3-5]:

heating of the resin up to the temperature $T = (353 \pm 2)$ K and exposure at this temperature during $\tau = (20 \pm 0.1)$ min; dosage of the filler and its further loading into the epoxy binder; hydrodynamic blending of the oligomer ED-20 and filler during $\tau = (10 \pm 0.1)$ min; ultrasonic processing of the composition during $\tau = (1.5 \pm 0.1)$ min; cooling of the composition to the ambient temperature during $\tau = (60 \pm 5)$ min; introduction of the curing agent PEPA and mechanical blending of the composition during $\tau = (5 \pm 0.1)$ min. Then the curing of the PCM was conducted according to the mode: formation of the specimens and their curing during $\tau = (12.0 \pm 0.1)$ hours at the temperature $T = (293 \pm 2)$ K; heating with the rate of $v = 3$ K/min to the temperature $T = (393 \pm 2)$ K; holding of the PCM during $\tau = (2.0 \pm 0.05)$ hours, slowly cooling to the temperature $T = (293 \pm 2)$ K. To stabilize the structural processes to occur in the CM they were kept during $\tau = 24$ hours in the open air at the temperature $T = (293 \pm 2)$ K before testing.

The flexural stresses of the PCM were studied in the work according to ASTM D 790 - 03 [10]. To obtain the high performance CMs, after the preliminary experiments, a method of mathematical planning of the experiment was used, which simultaneously allowed to take into account the ratio of components and technological parameters of obtaining composites with a considerable reduction of experimental works [7].

A model of the full factorial experiment 2^2 was used for the design of experiments. The factor levels and variation intervals were selected based on the previous experiments. The root mean square deviation for the coefficients was determined by the formula:

$$S(a_i) = \sqrt{S^2(a_i)} = \frac{S^2(y)}{\sum_l x_{il} l}, \quad (1)$$

$$S^2(y) = \sum_{l=1}^N \sum_{i=1}^n (Y_l - y_{il})^2, \quad (2)$$

$$S^2(Y) = \frac{S^2(y)}{n}, \quad (3)$$

where:

$S^2(y)$ - dispersions of adequacy;

$S^2(Y)$ - average dispersions of adequacy;

N - number of experiments according to the plan;

n - number of parallel experiments;

x_i - coded variable.

Significance of the regression coefficients was determined by the Student's test:

$$t_i = \left| \frac{d_i}{S(a_i)} \right|, \quad (4)$$

where a_i - the coefficient value.

The condition of significance of the equation coefficients has the form $t_i > t_p$, where t_p was determined from the table in reference [11] in 5% significance level. The adequacy of the description of the process of obtaining the CM was tested using the Fisher test:

$$F_i = \frac{S_R^2}{S^2(y)}, \quad (5)$$

$$S_R^2 = \frac{\sum_l Y_l^2 - \sum_l a_i \sum_l x_{il} y_l}{f_1}, \quad (6)$$

where:

S_R^2 - residual dispersion;

f_1 - number of degrees of freedom.

The numbers of degrees of freedom f_1 and f_2 were determined by the formulas:

$$f_1 = N - (k + 1), \quad (7)$$

$$f_2 = N(n - 1), \quad (8)$$

where k - the number of the polynomial coefficients.

The table value F of the criterion F_p , taking into account f_1 and f_2 , was found for the 5% significance level. Given $F_i < F_p$, it was considered that the polynomial adequately describes the process under study [12-16].

In order to reduce the error in the study of properties and search for optimal values, five or six parallel measurements were performed and the arithmetic mean was found:

$$y = \frac{y_1 + \dots + y_n}{n}, \quad (9)$$

where:

$y_1 + \dots + y_n$ - results of individual experiments;

y - arithmetic mean of all parallel experiments;

n - number of parallel experiments.

To eliminate false values, the Student's criterion was used [15]:

$$\frac{y_i - y}{S} \geq t, \quad (10)$$

where:

y_i - the results of a single experiment;

y - the arithmetic mean of all results;

S - quadratic error;

t - the tabular value of the Student test.

The quadratic error was determined by the formula:

$$S = \frac{\sqrt{\sum_l (y_i - y)^2}}{n}. \quad (11)$$

An experiment was considered false if the experimental value of the criterion is greater than the table value: $|t_{\text{exp.}}| \geq t_{\text{table.}}$

3 Results

The flexural stresses, as one of the main properties of composites with different content of micro-dispersed filler and discrete fibers, were investigated in order to optimize the content of ingredients in formation of the

Table 1 Levels of variables on conditional and natural scale

components	factor	average level, q , pts.wt.	variation step, Δq , pts.wt.	values of variables (pts.wt.) that correspond to conditional units		
				-1	0	+1
SPM	x_1	0.10	0.05	0.05	0.10	0.15
MDF	x_2	0.10	0.05	0.05	0.10	0.15

Table 2 Scheme of experiment planning

no. of experiment (u)	x_0	x_1	x_2	$x_3 = x_1^2 - d$	$x_4 = x_1^4 - d$	$x_1 x_2$
1	1	-1	-1	0.33	0.33	+1
2	1	+1	-1	0.33	0.33	-1
3	1	-1	+1	0.33	0.33	-1
4	1	+1	+1	0.33	0.33	+1
5	1	0	0	-0.67	-0.67	0
6	1	+1	0	0.33	-0.67	0
7	1	-1	0	0.33	-0.67	0
8	1	0	+1	-0.67	0.33	0
9	1	0	-1	-0.67	0.33	0
$\sum_{u=1}^N x_{iu}^2$	9	6	6	2	2	4

Table 3 Results of study of the CM flexural stresses

no. of experiment	content of components, q , pts.wt.		flexural stresses during the flexion, σ_f , MPa
	x_1	x_2	y_2
1	0.05	0.05	65.4
2	0.15	0.05	63.9
3	0.05	0.15	77.4
4	0.15	0.15	65.6
5	0.10	0.10	70.5
6	0.15	0.10	74.3
7	0.05	0.10	78.6
8	0.10	0.15	69.0
9	0.10	0.05	72.5

functional layer of the protective coating. It should be noted that as a micro-dispersed filler, the synthesized powder mixture (SPM) of the following composition was used for experimental studies: Fe (70%) + Ti (10%) + TiC (15%) + Fe₃C (5%). A mixture of discrete fibers (MDF) was used in the form of fibrous filler: modal (42%), polyacryl (38%), polyamide (38%). Each component (filler) was coded by units with consideration of the variation step, for standardization and for simplification of calculations (Table 1).

According to the experiment planning scheme nine experiments ($N = 9$) were conducted, each of which was repeated three times ($p = 3$) in order to exclude system errors (Table 2). In order for the planning matrix to be orthogonal [11], the corrected values of x' level were

entered, which were calculated by the formula:

$$x'_i = (x_i)^2 - \frac{\sum_{u=1}^N x_{iu}^2}{N}. \quad (12)$$

The expanded matrix of planning of the complete factor experiment and its results are shown in Table 2. Results of study of the CM flexural stresses are shown in Table 3.

The mathematical model $y = f(x_1, x_2)$ was formed as a regression equation [12]:

$$y = b_0 + b_1 x_1 + b_2 x_2 + b_{11} x_1^2 + b_{22} x_2^2 + b_{12} x_1 x_2. \quad (13)$$

The regression coefficients were determined by the

Table 4 The coefficients of regression equation

b_0	b_1	b_2	b_{11}	b_{22}	b_{12}
74.33	-2.93	1.70	0.20	-5.50	-2.58

Table 5 Values of dispersions of adequacy (S_{ui}^2) and the mean square error ($\sigma^2\{y\}_i$)

no.	the dispersions of adequacy		the mean square error	
	conditional designation	value	conditional designation	value
1	S_{u1}^2	4.020	$\sigma^2\{y\}_1$	2.010
2	S_{u2}^2	5.180	$\sigma^2\{y\}_2$	2.590
3	S_{u3}^2	4.940	$\sigma^2\{y\}_3$	2.470
4	S_{u4}^2	2.240	$\sigma^2\{y\}_4$	1.120
5	S_{u5}^2	1.220	$\sigma^2\{y\}_5$	0.610
6	S_{u6}^2	1.500	$\sigma^2\{y\}_6$	0.750
7	S_{u7}^2	3.860	$\sigma^2\{y\}_7$	1.930
8	S_{u8}^2	1.680	$\sigma^2\{y\}_8$	0.840
9	S_{u9}^2	1.820	$\sigma^2\{y\}_9$	0.910

formula [13]:

$$b_i = \frac{\sum_{u=1}^N x_i y_i}{\sum_{u=1}^N x_{iu}^2}. \quad (14)$$

Received coefficients of the regression equation are given in Table 4.

As a result, in the analysis of flexural stresses, the following regression equation was determined:

$$y = 74.33 - 2.93x_1 + 1.70x_2 + 0.20x_1^2 - 5.50x_2^2 - 2.58x_1x_2 \quad (15)$$

For the statistical processing of experiment results, a test of reproducibility of experiments by the Cochran test, was conducted:

$$G = \frac{S_{u\max}^2}{\sum_{u=1}^N S_u^2} \leq G_{(0.05; f_1; f_2)}, \quad (16)$$

where:

S_{ui}^2 - dispersion of experiment results on combinations of a few factor levels for $m = 3$;

m - number of parallel experiments;

$S_{u\max}^2$ - the highest dispersion in design line.

Dispersion of adequacy were determined by the formula:

$$S_{ui}^2 = \frac{\sum_{i=1}^m (y_i - \bar{y}_i)^2}{m - 1}, \quad (17)$$

where:

y_{im} - value, received from each parallel experiment;

\bar{y}_i - average value y , received in parallel experiments.

The mean square error was determined as:

$$\sigma^2\{y\} = \frac{\sum_{i=1}^{N=9} \sigma^2\{y\}_i}{N(m-1)}, \quad (18)$$

$$\text{where: } \sigma^2\{y\}_i = \sum_{i=1}^{m=3} (y - \bar{y}_i)^2;$$

$$\sigma^2\{y_{av}\} = \frac{\sigma^2\{y\}}{N}, \text{ or } S_{b_0}^2 = \frac{S_0^2}{N}. \quad (19)$$

Dispersion values are shown in Table 5.

Moreover:

$$\sum_{i=1}^N S_{ui}^2 = 13.23, \sigma^2\{y\} = S_0^2 = 1.470.$$

Then, the calculated value of the Cochran test at the 5% level of significance [14]:

$$G_{calc} = \frac{S_{u\max}^2}{\sum_{i=1}^N S_{ui}^2}, \quad (20)$$

$$G_{calc} = \frac{2.59}{13.23} = 0.196.$$

Testing the experiment results by the Cochran test [14-15] for a fixed probability $\alpha = 0.05$ confirmed the reproducibility of the experiments. Dispersion of experiment results on combinations of a few factor levels: $S_{u\max}^2 = 0.196$. Calculated value of the Cochran test is $G_{calc} = 0.196$.

Table value of the Cochran test is $G_{tab} = 0.478$.

That is, Equation (20) is satisfied:

$$G_{calc} = 0.196 \leq G_{tab} = 0.478.$$

Subsequently, the coefficients significance of regression

Table 6 The experimental results of study of flexural stresses of materials

no. of experiment	flexural stresses, σ_f , MPa			average value, σ_f , MPa
	1	2	3	
1	63.8	66.5	65.9	65.4
2	62.1	64.4	65.2	63.9
3	76.0	77.1	79.1	77.4
4	65.2	64.8	66.8	65.6
5	70.0	70.1	71.4	70.5
6	73.8	75.3	73.8	74.3
7	77.9	77.7	80.2	78.6
8	68.0	69.8	69.2	69.0
9	71.4	73.1	73.0	72.5

Table 7 Dispersion of coefficients of regression (S_b^2) and calculated values of the Student's criterion (t_{calc})

no.	dispersion of coefficients of regression		calculated values of the Student's criterion	
	conditional designation	value	conditional designation	value
1	$S_{b_0}^2$	0.163	t_{0p}	179.49
2	$S_{b_1}^2$	0.245	t_{1p}	5.93
3	$S_{b_2}^2$	0.245	t_{2p}	3.43
4	$S_{b_{11}}^2$	0.735	t_{11p}	0.23
5	$S_{b_{22}}^2$	0.735	t_{22p}	6.42
6	$S_{b_{12}}^2$	0.368	t_{12p}	4.2

equation was determined by analyzing the results according to the experimental design (Table 6).

Then, the dispersions of the regression coefficients (Table 7) were determined by:

$$S_{b_i}^2 = \frac{S_0^2}{\sum_{u=1}^N x_{iu}^2}. \quad (21)$$

The significance of the regression coefficients was determined by the Student's test [16]. Here with the table (t_i) and calculated criterion (t_{calc}) of the Student's test (Table 7) were determined.

Depending on freeness: $f = N(n - 1) = 9(3 - 1) = 18$, the Student's test value was calculated, which is $t_i = 2.1$.

Calculated values of the Student's test (t_{calc}) and coefficients significance were determined: $t_{0p}, t_{1p}, t_{2p}, t_{11p}, t_{22p}, t_{12p} > t_i$.

Moreover:

$$t_i = \frac{|b_i|}{S_{b_i}}. \quad (22)$$

Calculated values of the Student's criterion $t_{0p}, t_{1p}, t_{2p}, t_{12p}, t_{22p}$ are larger than t_i , so it was considered that $b_{0p}, b_{1p}, b_{2p}, b_{12p}, b_{22p}$ coefficients of the regression equation are significant. Calculated values t_{11p} is lower than t_i , so it was considered that b_{11p} coefficient of the regression equation is insignificant. As a result of rejection of the insignificant coefficients, the following regression equation

was received:

$$y = 74.33 - 2.93x_1 + 1.70x_2 - 5.50x_2^2 - 2.58x_1x_2. \quad (23)$$

The adequacy of the model was checked by the Fisher test [17]:

$$F_c = \frac{S_{u\max}^2}{S_y^2} \leq F_{(0.05; f_{ad}; f_y)}, \quad (24)$$

where $S_{u\max}^2 = 2.59$ - calculated value of dispersion of adequacy (Table 5),

$$S_y^2 = \frac{\sum_{i=1}^N S_{ui}^2}{N}, \quad (25)$$

$S_y^2 = 1.470$ - mean square error,

So: $F_c = 0.415$,

$F_{(0.05; f_{ad}; f_{u})}$ - table value of the Fisher test in 5% significance level ($f_i = N - (k + 1) = 9 - (5 + 1) = 3$, $f_z = N(n - 1) = 9(3 - 1) = 18$). So: $F_{(i)} = 3.16$ [18].

Calculated value of Fisher test is less than the table one, so Equation (21) is satisfied. It is possible to assume that equation adequately characterizes the composition.

Interpretation process of the obtained mathematical model, as a rule, is not just determination of factors influence. A simple comparison of absolute value of linear coefficients does not determine the relative degree factors

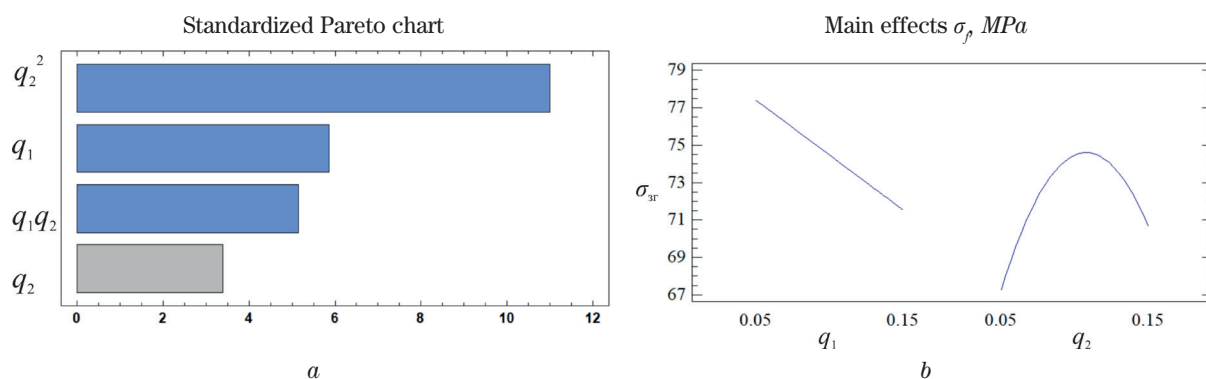


Figure 1 Standardized Pareto chart (a) and main effects (b)

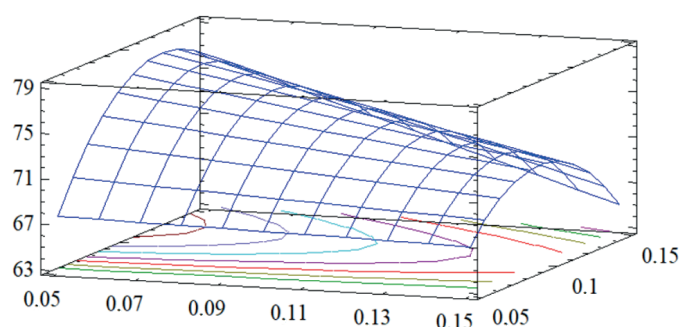


Figure 2 Estimated surface $\sigma_f = f(q_1, q_2)$

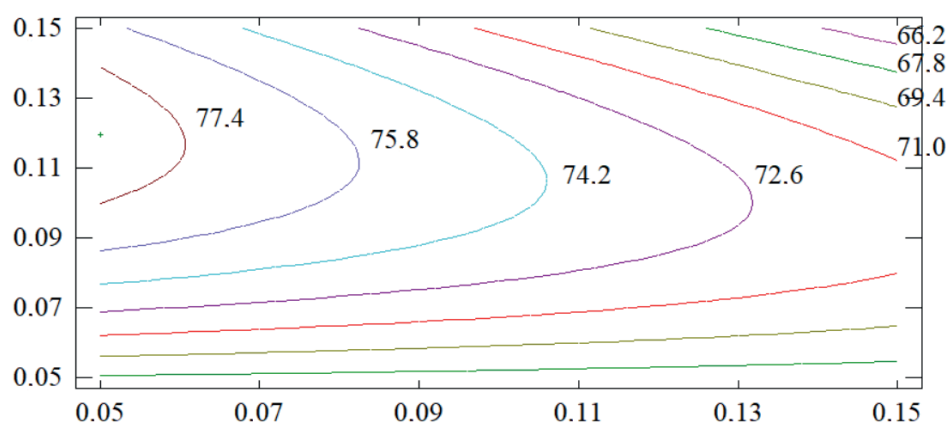


Figure 3 Contours of estimated response surface, which illustrate dependence of the flexural stresses on the content of the two fillers in the complex

influence, since there are also quadratic squared terms and paired interactions. In a detailed analysis of the obtained adequate model, it is necessary to take into account the fact that for a quadratic model the degree of factor influence on the change of output value is not constant.

4 Discussion

Dependencies that connect normalized and natural values of the variables are as follows:

$$x_i = \frac{q_i - q_{i0}}{\Delta q_i}, \quad (26)$$

where:

q_i - value of i experiment factor,

q_{i0} - value of zero level,

Δq_i - variation interval.

Substituting these values in accordance with Equation (26) into the regression equation and transforming it, one obtains the following regression equation with the natural values of the variables:

$$\sigma_f = 44.63 + 44.33q_1 + 577.0q_2 - 1030.0q_1q_2 - 2200.0q_2^2. \quad (27)$$

Given equation in natural values allows only predicting the output value for any point in the middle of the range of factor variations. However, with its help it is possible to construct graphs of dependence of the output value (flexural stresses) from any factor (or two factors). Geometric interpretation of the response surface is shown in Figures 1-3.

Based on the experimental studies, it has been found that both factors are significant. It should be noted that effect of content of the SPM on values of the flexural stresses is higher compared to the MDF (according to the Pareto chart). It was determined that the optimal values of the flexural stresses have a developed epoxy composite with the SPM and the MDF at the following contents: the SPM is 0.05 pts.wt., MDF - 0.10 to 0.15 pts.wt. ($\sigma_f = 77.4$ to 78.6 MPa) by analyzing the calculated response surface.

The obtained results indicate that both factors of the regression equation are significant. It should be noted that the greatest influence on the output parameters of the composite have a quadratic dependence of the first factor and linear dependence of the second factor. In the course of the analysis, it was found that values of the flexural stresses have the maximal values at the optimal content of components. In particular, from Figure 2 it is noticeable that an additional increase in the flexural stresses is possible when the content of the SPD filler is increased.

The developed PCMs will be used for the repair of equipment, mechanisms and systems of a marine vessel [19], such as:

- pipeline systems characterized by the corrosion damage;
- deck mechanisms (cargo devices).

5 Conclusions

The critical content of the dispersive and fiber fillers: the synthesized powder mixture is 0.05 pts.wt., the mixture of discrete fibers - 0.10 to 0.15 pts.wt. per 100 pts.wt. of epoxy oligomer ED-20 was found by the method of mathematical planning of the experiment. Introduction of such ingredients into the epoxy binder allows to increase the flexural stresses of the epoxy composites from $\sigma_f = 48.0$ MPa (for epoxy matrix) to $\sigma_f = 77.4$ to 78.6 MPa.

It was analyzed that with increasing the content of the synthesized powder mixture it is possible to increase values of the flexural stresses. These studies will be presented in the future works. The obtained results allow to create materials with improved physical and mechanical properties in the complex. The obtained materials can be used as the protective coatings to increase the performance and for repairing of the vehicle parts.

References

- [1] FRIEDRICH, K. Polymer composites for tribological applications. *Advanced Industrial and Engineering Polymer Research* [online]. 2018, **1**(1), p. 3-39. ISSN 2542-5048. Available from: <https://doi.org/10.1016/j.aiepr.2018.05.001>
- [2] GUZANOVA, A., BREZINOVA, J., DRAGANOVSKA, D., MARUSCHAK, P. O. Properties of coatings created by HVOF technology using micro-and nano-sized powder. *Koroze a Ochrana Materialu* [online]. 2019, **63**, p. 86-93. eISSN 1804-1213. Available from: <https://doi.org/10.2478/kom-2019-0011>
- [3] BUKETOV, A. V., SAPRONOV, O. O., BRAILO, M. V., MARUSCHAK, P. O., YAKUSHCHENKO, S. V., PANIN, S. V., NIGALATYI, V. D. Dynamics of destruction of epoxy composites filled with ultra-dispersed diamond under impact conditions. *Mechanics of Advanced Materials and Structures* [online]. 2020, **27**(9), p. 725-733. ISSN 1537-649, eISSN 1537-6532. Available from: <https://doi.org/10.1080/15376494.2018.1495788>
- [4] STUKHLYAK, P. D., BUKETOV, A. V., PANIN, S. V., MARUSCHAK, P. O., MOROZ, K. M., POLTARANIN, M. A., VUKHERER, T., KORNIENKO, L. A., LYUKSHIN, B. A. Structural fracture scales in shock-loaded epoxy composites. *Physical Mesomechanics* [online]. 2015, **18**, p. 58-74. ISSN 1029-9599, eISSN 1990-5424. Available from: <https://doi.org/10.1134/S1029959915010075>
- [5] BUKETOV, A. V., BRAILO, M. V., STUKHLYAK, D. P., YAKUSHCHENKO, S. V., SAPRONOV, O. O., CHERNIAVSKYI, V. V., HUSIEV, V. M., DMITRIEV, D. A., YATSYUK, V. M., BEZBAKH, O. M., NEGRUTSA, R. Y. Optimization of components in development of polymeric coatings for restoration of transport vehicles. *Bulletin of the Karaganda University. Mathematics Series* [online]. 2018, **92**(4), p. 119-131. ISSN 2518-7929, eISSN 2663-5011. Available from: <https://doi.org/10.31489/2018M4/119-131>
- [6] ZHANG, L., ZHANG, G., CHANG, L., WETZEL, B., JIM, B., WANG, Q. Distinct tribological mechanisms of silica nanoparticles in epoxy composites reinforced with carbon nanotubes, carbon fibers and glass fibers. *Tribology International* [online]. 2016, **104**, p. 225-236. ISSN 0301-679X. Available from: <https://doi.org/10.1016/j.triboint.2016.09.001>
- [7] BUKETOV, A. V., STUKHLYAK, P. D., KALBA, E. M. *Physicochemical processes in the formation of epoxy composite materials* (in Ukrainian). Ternopil: Zbruch, 2005.
- [8] MARINI, M., RIVALTA, E., MOLENDI, P., DI SILVESTRI, P., BONACINI, C. Mechanical analysis of structural adhesive for marine joints. *Journal of Adhesion Science and Technology* [online]. 2013, **27**, p. 820-824. ISSN 0169-4243, eISSN 1568-5616. Available from: <https://doi.org/10.1080/01694243.2012.727152>
- [9] DAS, G., BISWAS, S. Physical, mechanical and water absorption behaviour of coir fiber reinforced epoxy composites filled with Al_2O_3 particulates. *IOP Conference Series: Materials Science and Engineering* [online]. 2016, **115**, 012012. ISSN 1757-8981, eISSN 1757-899X. Available from: <https://doi.org/10.1088/1757-899X/115/1/012012>

- [10] ASTM D790-03. Standard Test methods for flexural properties of unreinforced and reinforced plastics and electrical insulating materials [online]. Available from: <https://www.astm.org/database.cart/historical/D790-03.htm>.
- [11] BRAILO, M. V., BEZBAKH, O. M., HUSIEV, V. M., YAKUSHCHENKO, S. V. Modified epoxy matrix with improved properties for protection of transport vehicles. *Bulletin of the Karaganda University. Mathematics series*. 2019, **95**(3), p. 88-100. ISSN 2518-7929, eISSN 2663-5011.
- [12] ASGHAR, A., RAMAN, A., AZIZ, A., DAUD, W. M. A. W. A comparison of central composite design and Taguchi method for optimizing Fenton process. *The Scientific World Journal* [online]. 2014, **2014**, 869120. ISSN 2356-6140, eISSN 1537-744X. Available from: <https://doi.org/10.1155/2014/869120>
- [13] RAJMOHAN, T., PALANIKUMAR, K. Application of the central composite design in optimization of machining parameters in drilling hybrid metal matrix composites. *Measurement* [online]. 2013, **46**(4), p. 1470-1481. ISSN 0263-2241. Available from: <https://doi.org/10.1016/j.measurement.2012.11.034>
- [14] WILRICH, P. T. Critical values of Mandel's h and k, the Grubbs and the Cochran test statistic. *AStA Advances in Statistical Analysis* [online]. 2013, **97**(1), p. 1-10. ISSN 1863-8171, eISSN 1863-818X. Available from: <https://doi.org/10.1007/s10182-011-0185-y>
- [15] BAXEVANAKIS, C., JEULIN, D., VALENTIN, D. Fracture statistics of single-fibre composite specimens. *Composites Science and Technology* [online]. 1993, **48**(1-4), p. 47-56. ISSN 0266-3538. Available from: [https://doi.org/10.1016/0266-3538\(93\)90119-2](https://doi.org/10.1016/0266-3538(93)90119-2)
- [16] BALESCU, R. C. *Equilibrium and non-equilibrium statistical mechanics*. John Wiley & Sons, 1975. ISBN 9780471046004.
- [17] KIM, H. Y. Statistical notes for clinical researchers: chi-squared test and Fisher's exact test. *Restorative Dentistry and Endodontics* [online]. 2017, **42**(2), p. 152-155. ISSN 2234-7658, eISSN 2234-7666. Available from: <https://doi.org/10.5395/rde.2017.42.2.152>
- [18] COHEN, J. *Statistical power and analysis for the behavioral sciences*. 2nd ed. Hisdale, NJ: Lawrence Erlbaum Associates;1988, p. 79-8.
- [19] BUKETOV, A., MARUSCHAK, P., SAPRONOV, O., ZINCHENKO, D., YATSYUK, V., PANIN, S. Enhancing performance characteristics of equipment of sea and river transport by using epoxy composites. *Transport* [online]. 2016, **31**(3), p. 333-342. ISSN 1648-4142, eISSN 1648-3480. Available from: <https://doi.org/10.3846/16484142.2016.1212267>

GENERAL CHARACTERISTICS FOR LOADING THE WORKING ELEMENTS OF DRILLING AND MILLING MACHINES WHEN MOVING IN THE CLAY SOLUTION

Adil Kadyrov¹, Zhanara Zhunusbekova^{1,*}, Aleksandr Ganyukov¹, Irina Kadyrova², Aliya Kukeshova¹

¹Karaganda State Technical University, Karaganda, Kazakhstan

²Karaganda State Medical University, Karaganda, Kazakhstan

*E-mail of corresponding author: zhzhzh_84@mail.ru

Resume

The article is devoted to influence of the clay thixotropic solutions on the strength of resistance to movement of the earthmoving machines' working elements.

The forces of resistance to the movement of a flat plate, a smooth cylinder and real working bodies in a clay solution for various modes of solution flow (bingamian, pseudo-laminar and turbulent) are established.

Mathematical models of movement of the earthmoving machines working elements in clay solution are developed and investigated.

Dynamics of the working element of an earthmoving machine movement in a clay solution is studied. Dependence of the feed force, torque and dynamic coefficient on the resistance forces, acting on the working body from the clay solution, is established.

Article info

Received 17 May 2020

Accepted 19 July 2020

Online 19 January 2021

Keywords:

clay solution,
working element,
resistance to movement,
motion mode,
loading,
earthmoving machines

Available online: <https://doi.org/10.26552/com.C.2021.2.B97-B105>

ISSN 1335-4205 (print version)

ISSN 2585-7878 (online version)

1 Introduction

During the construction of buried structures using the diaphragm wall method, the excavation works, as usual, are performed under the clay thixotropic solution. There is a hypothesis that additional loading affects the working element (hereinafter referred to as WE) of a trench digger moving in the clay solution [1-2].

This method has already become quite widespread, both in Kazakhstan and abroad in construction of industrial, civil, hydraulic, transport and agricultural facilities. Effectiveness of the "wall in the ground" method depends on the hydro-geological conditions of the construction site, the costs of equipment for performing the work, characteristics of the structure being built and other factors. This method is more promising for reconstruction of enterprises and construction of underground structures in urban development near the existing buildings. The practice of building production has shown that the subsequent development of construction using the "wall in the ground" method is possible only when using machines of mechanical and hydro-mechanical action [3].

Therefore, the study of the working parts loading of earthmoving machines, operated in the clay thixotropic solution, is an urgent task.

Resistance of solids when moving in fluid (flow with fluid) can be characterized with the friction force (T), the

hydrodynamic head resistance P_{hd} and the buoyancy force P_b and in the general case, the following equation can be written:

$$R_{res} = T - P_{hd} - P_b, \quad (1)$$

where R_{res} is the resistance total force to the WE moving in mud.

2 Material and methods

To define the resistance value to the WE moving in the clay solution, it is theoretically and experimentally necessary to determine the values and patterns of changes in the force variation T and P_{hd} , when the mud in motion is relative to the WE in the Swedish, Bingham and pseudo-laminar conditions. Operation of the excavating machines at speeds causing the turbulent movement of the mud is undesirable since there is a possibility for an increase in the WE dynamics [3-4].

At the first stage of the study, the motion of a smooth plate measuring F and a provided small thickness Δ and a smooth cylinder with the radius R and the length L is considered. Then, it is proceed to defining the loading of the WE of excavating machines, which are complex elements in its configuration.



The motion of a thin plate in the clay thixotropic solution is considered, which may be forward, rotation and compound. If the velocity vector lies in the plate plane, the resistance to motion is determined by the friction force T arising on the side surfaces of the plate and the buoyancy force P_o . The hydrodynamic resistance due to the infinite small thickness of the plate can be neglected.

The value of the total drag force R_c for various flow conditions of the mud will be different, this is due to a change in its rheology depending on the flow velocity. For the Swedish conditions, taking into account the Bingham-Kelvin model, the following is true:

- during the plate vertical motion:

$$R_{res} = F = \frac{\eta_1 E_1 E_2 + \sigma_0 t E_1 E_2}{[E_1 (1 - e^{\frac{t}{t_0}}) + E] \eta_1 + t E_1 E_2} - m_n g, \quad (2)$$

where:

m_n - plate mass;

η - relaxation viscosity;

e - relative strain;

E_1 - initial conditional instantaneous shear modulus;

E_2 - elasticity modulus;

σ_0 - elastic limit, below which the residual deformations cannot be developed;

t - time;

t_0 - relaxation time.

and

- when the plate moves in the horizontal direction and zero buoyancy:

$$R_{res} = F = \frac{\eta_1 E_1 E_2 + \sigma_0 t E_1 E_2}{[E_1 (1 - e^{\frac{t}{t_0}}) + E] \eta_1 + t E_1 E_2}. \quad (3)$$

The friction force with the plate motion, at a speed causing appearance of the Bingham conditions of fluid flow, can be determined by the following dependence:

$$T = F\tau = F\left(\tau_0 \pm \eta \frac{dU}{d\delta_T}\right), \quad (4)$$

where:

τ - shear stress;

τ_0 - yield stress.

The “plus” or “minus” sign is used depending on the velocity gradient sign taking into account the requirement to make positive the specific force direction τ .

In the straight line motion of the plate in the clay solution, its speed is equal to the speed of the flow core, which follows from the added masses theory. Considering the $\Delta\rho = 0$, what corresponds to our case, one obtains:

$$U = -\frac{\tau_0}{\eta}(H_g - \delta_T), \quad (5)$$

where:

U - fluid motion speed;

H_g - maximum distance from the plate;

δ_T - boundary-layer thickness;

η - plastic viscosity.

Then the plate velocity gradient in the following:

$$\frac{dU}{d\delta_T} = \frac{\tau_0}{\eta} \quad (6)$$

and the friction force under the condition $V_n = U_{max}$ can be determined by the following formula:

$$T = F\tau = F\left(\tau_0 + \eta \frac{dV}{dn}\right) = 2F\tau_0. \quad (7)$$

In the pseudo-laminar conditions of motion the rheological properties of the clay solution are adequate to the rheological properties of an ordinary viscous fluid. The velocity-distribution law of viscous the fluid flow has a parabolic nature:

$$U = U_{max} \left(1 - \left(\frac{\delta_T}{H_g}\right)^2\right). \quad (8)$$

The plate velocity gradient:

$$\frac{dU}{dn} = -2U_{max} \frac{\delta_T}{H_g} \quad (9)$$

and the plate friction force in the mud can be determined by the following formula:

$$T = F\tau = \pm 2F\mu_p \frac{dU}{dn} = \pm 2F\mu_p U_{max} \frac{\delta_T}{H_{max}}, \quad (10)$$

where:

μ_p - dynamic viscosity.

The maximum value of the friction force corresponds to equality of values H_g and δ_T , in this case:

$$T_{max} = \pm 2F\mu_p \frac{U}{H_g}. \quad (11)$$

Assuming the motion speed for the mud flow to be equal to the speed of the plate motion, one obtains:

$$T_{max} = \pm 2F\mu_p \frac{V_n}{H_g}. \quad (12)$$

In the stream core of the turbulent flow with the developed turbulence speed the fluid flow changes according to the logarithmic law:

$$U = \frac{U^* \ln \delta_T}{\beta + c}, \quad (13)$$

where:

U^* - dynamic velocity or the fluid cutting speed;

β - constant Prandtl, $\beta = 0.360...0.436$ [5]

C - constant value.

The plate velocity gradient is:

$$\frac{dU}{d\delta_T} = \frac{U^*}{\beta \delta_T}. \quad (14)$$

Then, taking into account the shear function during turbulent motion of the mud [6], one gets:

$$\tau = \mu_f \frac{dU}{d\delta_T} + p_c l^2 \frac{dU^2}{d\delta_T} = U^* \left[\frac{\mu_f}{l} + p_c l (U^*)^2 \right], \quad (15)$$

where:

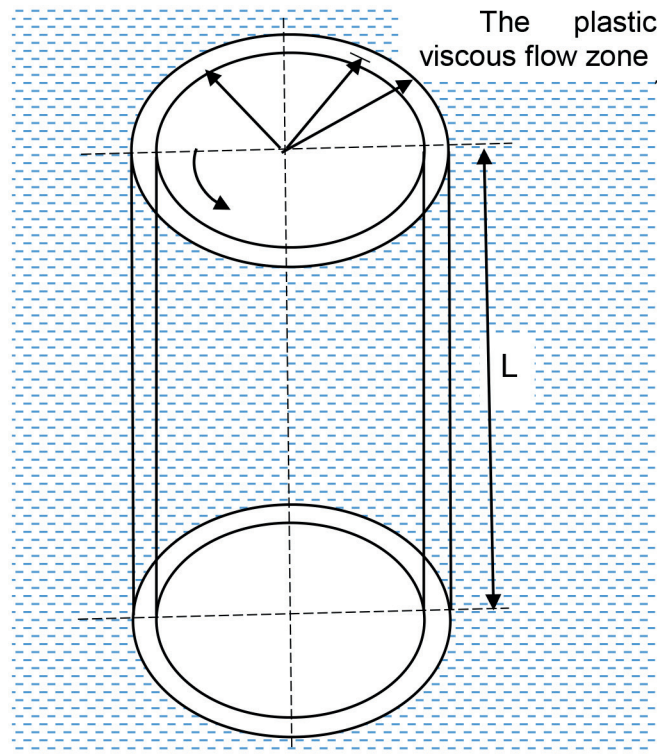


Figure 1 The nature of the flow solution around a rotating smooth cylinder

μ_ϕ - fictitious velocity.

$$T = F\tau = F\frac{U^*}{l}(\mu_f + p_c l U^*). \quad (16)$$

Moreover, as it appears from the theory of the turbulent motion that $l = \beta \delta_T$. When the plate rotates around the horizontal or vertical axis, the moment M_c from the resistance force to motion is determined in the general case by the following dependence:

$$M_{res} = [P_{gd} + T + (P_b - mg)\sin\varphi]R, \quad (17)$$

where:

φ - plate rotation angle about axis of rotation.

In the case of the plate complex motion, when determining its speed, it is necessary to take into account the value of the angle α between the portable ϑ and relative ωR speeds:

$$\alpha = \arctg \frac{V}{\omega R}. \quad (18)$$

For excavating machines (drilling and milling), as a rule, the portable speed is for one or two orders of magnitude less than the relative, and the value of the α angle does not exceed 2 to 3°. The dependences obtained for the plate complex motion are summarized in Table 1. The same expression (17) is presented as concretized for each mode of the mud motion.

Thus, there have been obtained the formulas for determining the friction forces for each possible motion conditions of the clay thixotropic solution. The following conclusions have been made:

1. During the Swedish conditions of the clay solution motion the resistance to the plate motion is provided by occurring of elastic strains.
2. The plate loading under the Bingham conditions of the mud flow is characterized by its ultimate shear stress τ_0 .
3. The resistance to the plate motion during the pseudolaminar motion of the mud depends on the mud viscosity and its speed.
4. In the turbulent conditions of motion, the resistance force to the plate motion depends on the core size of the flow stream, the medium density, and the fictitious viscosity value.

The smooth cylinder motion (rotational and compound) of the radius R and the length L in the clay thixotropic solution is considered. The cylinder is brought into rotation from a state of rest with an angular velocity ω .

When the cylinder moves at a speed that determines the Swedish conditions of the mud flow, the moment from the resistance force is determined taking into account Equation (3): $M_{res} = R_c R$.

The Bingham fluid flow zone extends only to a finite distance from the rotating cylinder (Figure 1). The rest of the mud will be at rest. A very thin laminar layer forms around the cylinder, behind which there is a zone of the plastic viscous flow. The radius of the plastic viscous flow zone and the fluid velocity are related. When the vector radius r is equal to the radius of extent of the plastic viscous flow zone r_p , the mud velocity is zero and if the values $r = R$ are equal, the mud velocity is maximum [7-8].

The gradient of the normal shear velocity:

$$U = \frac{\tau_0}{2\eta} r \left(\left(\frac{r_T}{r} \right)^2 - 1 - \ln \left(\frac{r_T}{r} \right)^2 \right), \quad (19)$$

is:

$$\frac{dU}{dr} = \frac{\tau_0}{2\eta} \left(1 - \left(\frac{r_T}{r} \right)^2 - \ln \left(\frac{r_T}{r} \right)^2 \right). \quad (20)$$

The resistance moment to the cylinder rotation in the clay thixotropic solution with the steady Bingham conditions, taking into account Equation (20) is expressed by the system of equations:

$$M_{res} = 2\pi R^2 L \left(\tau_0 \pm \eta \frac{dU}{dr} \right) = \begin{cases} \pi R^2 L \tau_0 \left[3 - \frac{r_T^2}{r^2} - \ln \left(\frac{r_T}{r} \right)^2 \right], \\ \pi R^2 L \tau_0 \left[1 + \frac{r_T^2}{r^2} - \ln \left(\frac{r_T}{r} \right)^2 \right] \end{cases} \quad (21)$$

$$(22)$$

In the further studies, the maximum value of the moment, corresponding to the sum of the ultimate shear stress and the product of structural viscosity by the velocity gradient is taken, with the fulfillment of the equality $r = R$. Thus one obtains:

$$M_{res} = 2\pi R^2 L \tau_0 \left[3 - \frac{r_T^2}{R^2} - \ln \frac{r_T^2}{R} \right]. \quad (23)$$

Transforming the series of the Maclaurinequation:

$$M_{res} = 3 + Arw + Brw^2, \quad (24)$$

where:

A_r and B_r - coefficients of the Maclaurin's series.

Introduction of A_r and B_r is required only for the further mathematical analysis.

In Equation (23), the cylinder rotation resistance moment under the Bingham conditions of the mud flow depends on the cylinder dimensions, the ultimate shear stress, and the radius of extent of the flow zone. The radius r_T is a function of the mud rheological characteristics and the cylinder angular velocity.

In the pseudo-laminar flow mode, the Bingham fluid with rheological characteristics is adequate to a viscous fluid with a dynamic viscosity coefficient μ_p . Rotation of the viscous fluid differs from rotation of a solid body in the fact that fluid performs a dynamic rotation, that is, particles of a fluid removed at a different distance from the rotation axis move with different angular velocities [9]. Wherein:

$$U_0 r = C = const, \quad (25)$$

where:

U_0 - fluid circumference speed;

C - certain constant value.

Therefore, with moving of the mud particles away from the rotation axis, their circumference speed decreases due to the layered rotation and presence of friction between the layers. In the boundary layer

$$\omega R = \frac{C}{R}, C = \omega R^2. \quad (26)$$

The gradient of mud velocity:

$$\frac{dU}{dr} = -\frac{C}{r^2}. \quad (27)$$

The friction force on the cylinder surface taking into account the equality of the values r and R is determined by the following formula:

$$T = F\tau = \pm 2\pi R^2 L \mu_p \frac{dU}{dr} = \pm 2\pi R L \omega \mu_p. \quad (28)$$

The moment from the resistive force is:

$$M_{res} = \pm 2\pi R^2 L \omega \mu_p. \quad (29)$$

In the turbulent conditions of the mud flow, its resistance moment to rotation is the following:

$$M_{res} = 2\pi R^2 L \omega \mu_p, \quad (30)$$

where:

τ is determined from Equation (16).

Having found the gradient of the mud velocity, one obtains:

$$M_{res} = 2\pi R^2 L \frac{U^*}{l} (\mu_p + \rho_c l U^*). \quad (31)$$

The compound motion of a smooth cylinder is analyzed next. The cylinder rotates with a constant angular velocity ω and moves with a feed speed V . Here $\omega R \geq V$ for the WE of excavating machines. In this regard, the resistance force to friction in rotational motion is significantly higher than the resistance force to friction in the translational motion. Therefore, with a high degree of accuracy, it is possible to use Equations (21) and (25) for calculations. If the values are comparable to values of the feed rate, it is necessary to take into account the angle α between the portable and relative speeds.


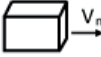

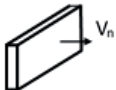
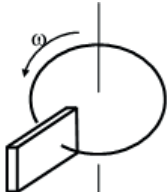
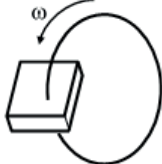
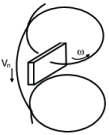
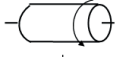
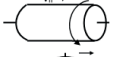
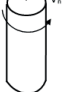
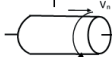
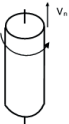
The calculation formulas obtained in this subsection Equations (22), (29), (31) are summarized in the Table1. The same Table shows dependencies for determining the resistance forces during the compound motion of a plate and a cylinder. Analysis of the obtained dependencies has allowed the following conclusions to be drawn:

In the Swedish conditions of the clay solution flow, the resistance to rotation of a cylinder is determined by the elastic properties of gel; in the Bingham conditions, it is determined by the ultimate shear resistance of the medium and the size of the plastic viscous flow zone, and in the case of the pseudo-laminar flow – by the mud dynamic viscosity and its rotation speed.

The cylinder loading during the rotation and the plate during its moving in the mud is generally carried out according to the same physical schemes.

The magnitude and nature of excavating machines loading when moving in the clay thixotropic solution

Table 1 Dependencies for determining the resistance forces during the elementary bodies moving in the clay solution

motion direction	motion mode			
	Swedish	Bingham	pseudo-laminar	bumpy
   	$R_{res} = F \cdot \frac{E_1 E_2 (\eta_1 \varepsilon + \sigma_0 t)}{\eta_1 (E_1 (1 - e^{-\frac{t}{t_0}}) + E_2) + t E_1 E_2}$	$R_{res} = 2F\tau_0 + P_b - mg$ $R_{res} = 2F\tau_0$	$R_{res} = 2F\mu \frac{V}{R_0} + P_b - mg$ $R_{res} = 2F\mu \frac{V_n}{R_0}$	$R_{res} = \frac{FU^*}{l} \cdot (\mu_f + \rho l^2 U^*) + P_b - mg$ $R_{res} = \frac{FU^*}{l} \cdot (\mu_f + \rho l^2 U^*)$
 	$M_{res} = FR^* \cdot \frac{E_1 E_2 (\eta_1 \varepsilon + \sigma_0 t)}{\eta_1 (E_1 (1 - e^{-\frac{t}{t_0}}) + E_2) + t E_1 E_2}$		$M_{res} = P_{gd} R = C_d F \rho \frac{V^2}{2} R$ $M_{res} = \left(C_d F \rho \frac{V^2}{2} + (P_b - mg) \sin \varphi \right) R$	
     	$M_{res} = FR^* \cdot \frac{E_1 E_2 (\eta_1 \varepsilon + \sigma_0 t)}{\eta_1 (E_1 (1 - e^{-\frac{t}{t_0}}) + E_2) + t E_1 E_2}$		$M_{res} = 2\pi R^2 \tau_0 \cdot \left(3 - \frac{\rho}{r^2} + 2 \ln \frac{r}{\rho} \right)$ $M_{res} = 2\pi R^2 L \tau_0 \cdot \left(1 + \frac{1}{2 \cos \alpha} * \left(-\frac{\rho^2}{R^2} + 1 + 2 \ln \frac{R}{\rho} \right) \right)$ $\alpha = \arctg \frac{V_n}{\omega R}$	$M_{res} = 2\pi R^2 L \mu \omega \kappa$ $M_{res} = 2\pi R^2 L \tau_0 \cdot \left(1 + \frac{1}{2 \cos \alpha} * \left(-\frac{\rho^2}{R^2} + 1 + 2 \ln \frac{R}{\rho} \right) \right)$ $\alpha = \arctg \frac{V_n}{\omega R}$ <p>where $V = V_n$, $R_0 = H_\omega, \rho = r_T$</p>

are further determined. To this end, one considers the movement of a hypothetical WE, which is affected by some resistance forces arising both during the cyclic machines operation and positional and continuous machines (milling, drilling bits) [10-11].

It is assumed that the WE is a combination of rotating and translationally moving elements. The rotation is carried

out around the Oz and Oy axes and the rectilinear motion occurs in the zOy plane. The scheme of the adopted loading model of the WE is shown in Figure 2. The Oz and Oy axes are instantaneous and directed along the bar and perpendicular to the WE bar. The decomposition principle allows any WE to lead to a combination of the translationally moving and rotating elements. A compound

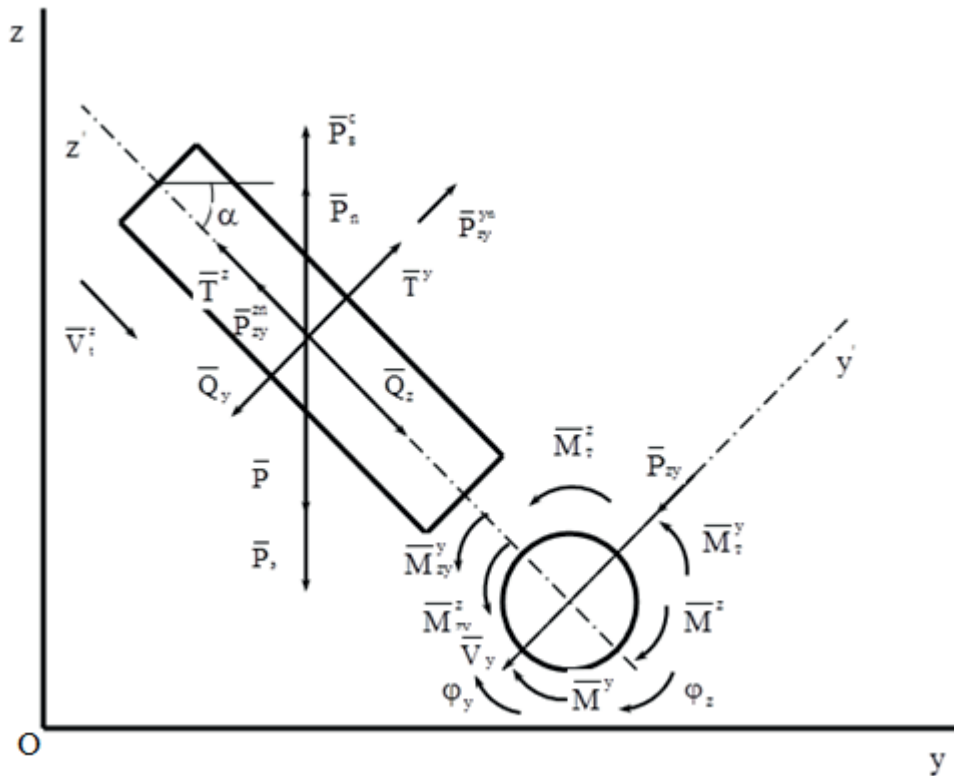


Figure 2 Generalized graphic model for the WE loading of excavating machines in the clay solution

motion of one element can be represented as the moving of the two elements performing translational and rotational movements [12].

The WE experiences a forward force Q (Q^z and Q^y but along the instantaneous axes), a rotational moment M (M^z and M^y when rotating around the instantaneous axes); a buoyancy force P_n^c ; a gravity force P ; frictional resistance of moving forward elements of the WE against the mud T (T^n, T^m); a hydrodynamic drag force P_{gd} , (P_{gd}^z, P_{gd}^m); a reaction force on the conveyor side P_z ; a lifting force arising as a result of the WE rotation P_n ; a moment from the hydrodynamic force on the rotating flat cells M_{gd} , (M_{gd}^z, M_{gd}^y), fractional moment against the mud when rotating a tool M_T , (M_T^z, M_T^y).

The friction and hydrodynamic drag forces are determined from Equations (3), (11), (17), (27), (31) and (32). The buoyancy force is described by formula consisting of a constant part and a term depending on the loading depth:

$$P_n^c = P_b + K_b z = V \rho_c g + g z \rho_c P_m, \quad (32)$$

where:

P_b – buoyancy force affecting a part of the tool of a constant volume;

K_b – the parameter equal to the product of the bar (rod) average section by the clay solution density;

V – WE tool volume;

P_m – rod mid-section area.

For the WE mounted on a rod, the buoyancy force is determined by Equation (32) and for those suspended by

a cable-block system, it is necessary to take into account the second term being equal to zero due to the rod absence [13].

The lifting force and reactive force from the conveyor (for example airlift) are expressed by the following dependencies:

$$P_n = 2\pi\omega R\rho_c V F^{zb}, \quad (33)$$

$$P_c = 4F_c\rho_c(V - V_T)^2, \quad (34)$$

where:

F^{zb} – mid-section of rotating elements when they rotate around the axes;

F_c – conveyor sectional area;

V_T – pulp conveying speed.

The model does not have regard to Bjerknes and Coriolis forces due to their insignificance in magnitude, the WE is taken as a single-mass and completely rigid, there are no oscillations in the system. The WE loading model at the first stage was developed for the steady-state mode provided that the inertia force is equal to zero.

In the Swedish flow conditions, the clay solution is a gel-like body, with no buoyancy and lifting forces. This is due to the presence of structural bonds between the gel molecules [14]. The Swedish flow conditions model of the clay solution characterizes only the initial period of equipment operation after a long absence of exposure to the mud. The model is described by the following set of equations:

Table 2 Values of forces and moments due to the resistance forces when the excavating machines' WEs move in the clay thixotropic solution

conditions	loading parameter value				
	H · m	H · m	H	H	H
Bingham	15.7	275	200	103.6	4400
Pseudo-laminar	13.2	242	175	103.6	4400

$$\begin{cases} Q^z = F^{zn} \sigma \\ Q^y = F^{yn} \sigma \end{cases}, \quad (35)$$

$$\begin{cases} M^z = F^{zb} \sigma R \\ M^y = F^{yb} \sigma R \end{cases}, \quad (36)$$

where:

F^{zn} and F^{yn} - respectively, the midsection areas with the WE motion direction along the Oz and Oy axes,

F^{yb} - midsection of rotating elements when rotating around the Oy axis.

For the Bingham, pseudo-laminar and turbulent conditions, the WE loading model has a formally adequate general form. This is explained by the effect on the RO of the same physical forces, that are only differed by various rheological characteristics of the clay solution. The WE loading model has the following form:

$$\begin{cases} Q^z = T^{zn} + P_{gd}^{zn} + (P_n + P_b + K_b z - P - P_e) \sin \alpha \\ Q^y = T^{yn} + P_{gd}^{yn} + (P_n + P_b + K_b y - P - P_e) \cos \alpha \\ M^z = M_{gd}^z + M_T^z \\ M^y = M_{gd}^y + M_T^y \end{cases}. \quad (37)$$

The first and the second equations of Equations (37) differ only in the form of trigonometric function; the third and the fourth equations are similar. In this regard, further are considered only two equations passing to others, if necessary, by replacing the midsection along to the WE motion direction along the axis Oz to the Oy, and changing $\sin \alpha$ to $\cos \alpha$.

Continuing with determination of the forces' values, included into Equations (36), one can write:

$$\begin{cases} Q^z = 2F^{zn} \tau_0 + 0,5 C_d^n \rho_c (V^{zn})^2 + (2\pi \cdot \\ \cdot \omega R \rho_c V F^{zb} + P_b + P_m \rho_c g z - mg - 4F_c \rho_c \cdot \\ \cdot (V - V_t)^2) \sin \alpha \\ M^z = 0,5 C_d^b F^{zb} \rho_c \omega^2 R^2 + \pi R^2 L \tau_0 \cdot \\ \cdot (3 + A_r \omega + B_r \omega^2) \end{cases}, \quad (38)$$

where:

C_d^n and C_d^b - accordingly hydrodynamic coefficients with the translational and rotational motion of the WE in mud. For the pseudo-laminar conditions of the clay solution moving:

$$\begin{cases} Q^z = 2F^{zn} \mu_b V^z / H_g + 0,5 C_d^n F^{zn} \rho_c (F^z)^2 + \\ + (2\pi \omega R \rho_c V F^{zb} + P_b + P_m \rho_c g z - mg - \\ - 4F_c \rho_c (V - V_t)^2) \sin \alpha \\ M^z = 0,5 C_d^b F^{zb} \rho_c \omega^2 R^3 + 2\pi R^2 L \mu_b \omega \end{cases}. \quad (39)$$

In the turbulent conditions of the clay solution motion, to determine the WE loading in Equations (37), it is necessary to introduce the friction force that is defined by Equation (16). In this case, the general form of Equation (37) remains unchanged.

3 Results

The resulting equation systems allow determining the total resistance force acting on the excavating machines of various designs when moving in the clay solution. To establish the loading magnitude on a particular WE, a part of the forces should be equated to zero. The conditions corpus of the model adequacy to the loading of a particular WE has the following form:

- for the milling and drilling machines with the rigid rod

$$\sin \alpha = 1; \cos \alpha = 1; \quad (40)$$

- for the milling and drilling machines with the flexible suspension [15]

$$\sin \alpha = 1; \cos \alpha = 0; K_b = 0; \quad (41)$$

- for the drag line

$$\begin{aligned} T^{yn} = 0, P_{gd}^{yn} = 0, M_{gd}^{zn} = 0, M_T^{zy} = 0, \\ K_b = 0, P_z = 0, P_n = 0 \end{aligned} \quad (42)$$

- for the dipper shovel with the rigid rod

$$\begin{aligned} P_e = 0, P_n = 0, M_{gd}^{zy} = 0, M_T^{zy} = 0, T^{yn} = 0, \\ P_{gs}^{yn} = 0; \end{aligned} \quad (43)$$

- for the dipper shovel with the flexible suspension

$$P_e = 0, P_n = 0, M_{gd}^{zy} = 0, T^{yn} = 0, P_{gd}^{yn} = 0, K_b = 0; \quad (44)$$

- for the backhoe

$$P_e = 0, P_n = 0, M_{gd}^{zy} = 0, M_T^{zy} = 0. \quad (45)$$

Equations (42) - (45) do not comply with the study purpose. These equations are given to prove the model generalization in Equation (37).

The component forces analysis has shown that at the beginning of the work (at $z=0$), the conveyor reactive force has the greatest weight. As the penetration depth increases over 10 to 15m, the buoyancy force increases sharply, by an order of magnitude greater than the friction force of the rod against the mud. The moment from

the resistance forces to the rotational motion of flat elements is also by an order of magnitude higher than the moment from the friction forces of cylindrical bodies against the mud during the rotational motion. Preliminary calculations based on the obtained dependences (Table 1), showed that when determining the resistance forces to the WE motion, the friction and the moment from the WE friction forces against the mud can be ignored.

As an example, the loading parameters of the milling WE of the UTF-1 (53) are calculated. The calculation was performed for the two conditions of the mud flow: Bingham and pseudo-laminar according to the following Equations (7), (12), (17), (23), (29), (32), (33) and (34), with the following parameters.

$$\begin{aligned} z=y=0, V=1\text{m}^3 F^m=F^n=10\text{ m}^2, \\ F^b=F^v=1\text{ m}^2, V^z=V^y=1\cdot 10^2\text{ M/c}, V_n=1.5\text{ m/s } \omega = 3\text{c}^{-1}, R=0.5\text{m}, \\ \rho_c = 1.1\cdot 10^3\text{ kg/m}^3, \\ F_c=0.25\text{m}^2, \tau_0 = 10\text{ H/m}^2, C_d^u = 0.5, C_d^B = 1, L=1\text{m}, F=0.5\text{ m}^2, \\ V_T=2\text{m/s}. \end{aligned}$$

Calculation of the loading parameters for the pseudo-laminar flow conditions of the drilling mud has shown that

for this case it is approximately 10 to 15% less than those given in the Table 2.

4 Conclusions

Due to the study result the following main conclusions have been made:

The greatest weighting in the total loading of the WE moving in the clay solution has a rotational moment from the resistance forces to the flat cells rotating, reactive force of conveyer and buoyancy force acting on the tool.

The results of experiments, using the SMF-2 testing device, have basically confirmed the dependences obtained analytically in determining the loading when moving the WE in the mud.

The moment due to the resistance forces to the WE moving in the clay solution must be calculated for the Bingham conditions, where the loading is the greatest. It is advisable to calculate the engine rated brake power using the pseudo-laminar conditions, since its parameters are close to the average maximum power parameters of the Bingham conditions.

References

- [1] SAPIN, D. A. Settlement of the adjoining development during construction of trench slurry wall. *Bulletin of Civil Engineers*. 2014, 6(47), p. 133-139. ISSN 1999-5571.
- [2] ANI, O. A., UZOEJINWA, B. B., EZEAMA, A. O., ONWUALU, A. P., UGWU, S. N., OHAGWU, C. J. Overview of soil-machine interaction studies in soil bins. *Soil and Tillage Research* [online]. 2018, 175, p. 13-27. ISSN 0167-1987. Available from: <https://doi.org/10.1016/j.still.2017.08.002>
- [3] KAZAKOV, Y. N., BULANKIN, N. F. Experience of the device of bored piles of the increased bearing capacity. *Foundations and Soil Mechanics*. 2015, 1, p. 15-17. ISSN 0038-0741, eISSN1573-9279.
- [4] GRIGULETSKY, V. G., SAVELYEV, Y. P. Dynamic and thermal fields in turbulent flow of drilling mud in the annular space of pipes. *Oil, Gas and Business*. 2016, 10, p. 3-21. ISSN 2218-4929.
- [5] KOCHETKOVA, R. G. Influence of modern stabilizers on improved properties of clayey soils. *Soil Mechanics and Foundation Engineering*[online]. 2012, 49(1), p. 12-15. ISSN 0038-0741, eISSN 1573-9279. Available from: <https://doi.org/10.1007/s11204-012-9160-1>
- [6] ALIEV, S. B., SULEEV, B. D. Study and calculation of the disk-milling tool. *Ugol- Russian Coal Journal*[online]. 2018, 11, p. 32-34. ISSN 0041-5790, eISSN 2412-8333. Available from: <http://dx.doi.org/10.18796/0041-5790-2018-11-32-34>
- [7] ZHUNUSBEKOVA, Z. Z., KADYROV, A. S. Study of digging machine flat element loading in clay solution. *Scientific Bulletin of National Mining University in Dnipropetrovsk*. 2016, 2(152), p. 30-34. ISSN 2071-2227.
- [8] KADYROV, A. S., AMANGELDIEV, N. E. New specifications of the theory of ground cutting. *Periodico Tchê Química*. 2019, 16(31), p. 922-936. ISSN 1806-0374, eISSN 2179-0302.
- [9] MEDVEDEVSKIKH, Y. G., KHAVUNKO, O. Y., BAZYLYAK, L. I., ZAIKOV, G. E. Viscoelastic properties of the polystyrene in concentrated solutions and melts (Part 1). *Bulletin of Kazan Technological University*. 2012, 1, p. 155-164. ISSN 1998-7072.
- [10] BALOVNEV, V. I., DANILOV, R. G. New methods for calculating resistance of soils innovative cutting working tools. *Mechanization of Construction*. 2016, 77(7), p. 5-13. ISSN 0025-8903, eISSN2409-7594.
- [11] SEMENOV, A. V., VAKHRUSHEV, S. I., TRENOGIN, E. O. Research of mathematical models of certain working operations, which are making up machine working cycle. *Master's journal of Perm National Research Polytechnic University*. 2016, 2, p. 379-390. ISSN 2306-8590, eISSN 2306-8604.
- [12] POLOVOV, B. D., HIMICH, A. A., VALIEV, N. G. Fundamentals of mining: General information and concepts of mining. underground, open and construction geotechnologies. Textbook for Universities. Yekaterinburg: FGBOU VPO "Ural state mining University", 2012.
- [13] PALGUEV, I. P. Drilling rigs AO "Stroydormash" for construction of pile foundations. *Construction and Road Vehicles*. 2017, 6, p. 45-50. ISSN 0039-2391

-
- [14] DULOVA, M. B. Dynamic analysis of working equipment of boring machine in the process of well-drilling. Reshetnev Siberian State Aerospace University. 2016, 12, p. 352-354. ISSN 1816-9724.
- [15] SHEROV, K. T., KHODZHIBERGENOV, D. T., ESIRKEPOV, A. Drilling method and construction of a combined drill-mill bit. Russian Engineering Research. 2019. 39, No 8. p. 665-668. ISSN: 1068-798X

POSSIBILITIES OF ENERGY HARVESTING FROM THE SUSPENSION SYSTEM OF THE INTERNAL COMBUSTION ENGINE IN A VEHICLE

Jacek Caban^{1,*}, Grzegorz Litak¹, Bartłomiej Ambrożkiewicz¹, Leszek Gardyński², Paweł Stączek¹, Piotr Wolszczak¹

¹Department of Automation, Faculty of Mechanical Engineering, Lublin University of Technology, Lublin, Poland

²Department of Materials Engineering, Faculty of Mechanical Engineering, Lublin University of Technology, Lublin, Poland

*E-mail of corresponding author: j.caban@pollub.pl

Resume

The automotive industry faces huge challenge in environmental protection by reducing fossil fuels and energy consumption by developing various practical solutions in energy harvesting. The current analysis is related to the diesel engine power supply system in a passenger off-road vehicle for application of the piezoelectric energy harvesting system. Experimental tests were carried out for the three constant rotational speed values - 800, 1000 and 1500 rpm. The results pertained to operational and simulation tests of available power supply options from the engine suspension system in the vehicle, e.g. to power sensors supervising the engine's operation or other small electrical devices in the vehicle. The simulations of output voltage were conducted by means of a nonlinear model with a resonator coupled to a piezoelectric elastic beam deformed in the magnetic field to improve the band of frequency transducing kinetic mechanic energy into electric energy.

Article info

Received 20 July 2020

Accepted 17 August 2020

Online 26 January 2021

Keywords:

diesel engine,
energy harvesting,
terrain vehicle,
damping oscillator

Available online: <https://doi.org/10.26552/com.C.2021.2.B106-B116>

ISSN 1335-4205 (print version)

ISSN 2585-7878 (online version)

1 Introduction

Pollution of the environment, repletion of natural supplies and growth in the volume of waste disturb the equilibrium of the natural environment [1]. In addition, the constantly increasing demand for energy and continuous technical development lead to the search for new solutions in use and recovery of energy from various technical systems. This pursuit occurs in numerous sectors of the economy and various technical facilities. Transportation, which is one of the most important parts of development, also contributes to environmental issues and energy waste [2]. Currently, we are witnessing a huge transformation in the transport and automotive industry. In the automotive industry, one can see enormous progress in development of the new propulsion systems (electric and hybrid) and in improvement of piston internal combustion engines with both spark ignition [3-5] and compression ignition engines [6-7]. Development of fuels alternative to crude oil has become another area. There is an increasing interest in the fuels of vegetable origin (bio-diesel) [1, 8] gas fuels from biogas plants and other, e.g. LPG, CNG [9-10].

As far as internal combustion engines are concerned, development of the fuel supply systems, exhaust purification systems and diagnostic systems has been particularly important. Recently, vibration signal analyses

have been heavily used for diagnostic purposes of various engine assemblies and systems, as well as other vehicle systems, e.g. suspension or transmission. Many researchers use methods such as Fourier and Wavelet Transforms [11-14] and Hilbert Transform (HT) [15-16], Recurrence Plots [17], Neural Networks [18] in detecting defects and operational parameters in rotating systems. Authors of [8,19] diagnosed the fuel supply systems using vibration signals are noteworthy. Balytskyi et al. [19] investigated degradation of the lock seal ring based upon the loss of combustion engine working gases. In [11, 20-21], authors used a vibration signal to analyze the technical conditions of gears. In [22-25], authors used analysis of the vibration signals to diagnose the vehicle suspension systems.

Reducing vehicle energy losses is necessary in order to improve fuel economy, reduce emissions, and supply other systems' power demand [9, 26-28]. In addition to improving engine and powertrain efficiency, one may also harvest energy wasted in vehicles including the recovery of wasted heat energy [24, 29], regenerative braking energy [30] and vibrational energy of shock absorbers [25, 31]. As demonstrated by Abdelkareem et al. [25], an average power of 350 W can be obtained from a medium-sized sedan (using four energy-harvesting dampers) from vehicle vibration stimulated by road irregularities. For larger vehicles the harvestable power can be greater.



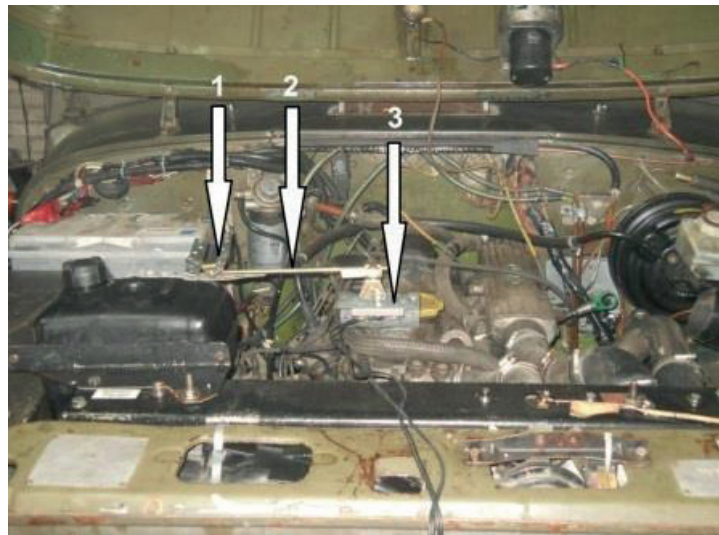


Figure 1 The way of mounting the measurement system in the tested vehicle,
1 - suspension structure of the clamping arm, 2 - potentiometer arm, 3 - linear potentiometer

Energy recovery in the sector of transportation has become an interesting and increasingly undertaken research topic. Obtaining energy from roads as an innovative way to provide green and renewable energy for the needs of sustainable transport is one of the directions [22]. Technologies, which harvest energy from roadways include piezoelectric-based modules [23, 32], asphalt solar collectors [33], thermoelectric systems [34], electromagnetic systems [35] and the solar panels installed in the pavement [36]. Another direction of research is harvesting energy from various components of a vehicle and the internal combustion engine. In this way, previously lost energy can be used to power certain on-board devices or electrical sensors supervising various functions in the vehicle.

The vibration-based energy conversion, termed piezoelectric energy harvesting, has significant advantages when compared to other forms of renewable energy, including the low start-up investment and less complex wiring [37]. The piezoelectric energy harvesting has been identified as a candidate for low-power devices such as portable rechargeable devices [38], wireless electronic devices [39] and sensors [40]. In the considered case, the nonlinear bi-stable resonator with a piezoelectric elastic beam is used. The bi-stable system provides broadband frequency transduction [41-44].

Unlike the small-scale energy-harvesting, such as wireless sensors and electronic devices, systems based on energy harvested from a vehicle's combustion engine suspension have not been sufficiently investigated. However, there is a space to partially recover energy from the suspension system of the internal combustion engine of a vehicle during its operation. This option was tested for aircraft vibrations in multimodal transport [45]. For this purpose, exploratory tests, based on measurements of vibration and displacement of the diesel engine during its operation, were carried out at three different crankshaft rotational speeds (800, 1000 and 1500 rpm).

In this article the focus is on application of the

experimental data as the excitation for the piezoelectric energy harvesting system based on the Duffing oscillator. The remainder of this article is following. In the Section 2, the experimental procedure is described, i.e. the experimental setup, the duty cycle and the measuring circuit. In the Section 3, the information is provided on the bi-stability phenomena, proposed piezoelectric EH system and broadband effect. Next, the output results from simulations, after applying the experimental time series to the mathematical model, are shown. Section 5 summarizes the paper.

2 Materials and Methods

The engine suspension study was conducted on a running diesel engine at selected values of the crankshaft rotational speed (800, 1000 and 1500 rpm) as the most frequently obtained speeds during the standard operation of a vehicle. The subject of the research was the following: a passenger all-terrain vehicle UAZ-31512 (earlier 469B type) with a four-cylinder supercharged diesel engine - 2.5TD with direct injection used in Land Rover Discovery vehicles 200 series.

Despite the green revolution in automotive industry and more and more often application of alternative driving systems, the Diesel engine is still widely used in transportation, industry, agriculture and construction, owing to their high efficiency, reliability and durability [46]. The reason of application of the Diesel engine car in the experiment are relatively high amplitudes of vibrations generated by engine comparing to the gasoline engine [47] and possibility to use the terrain vehicle in off-road having additional natural external source of mechanical vibrations. Nevertheless, the engine operation by different rotational velocities will bring diversified response of energy harvesting system. The tests were carried out for the three rotational speeds on an engine warmed up to

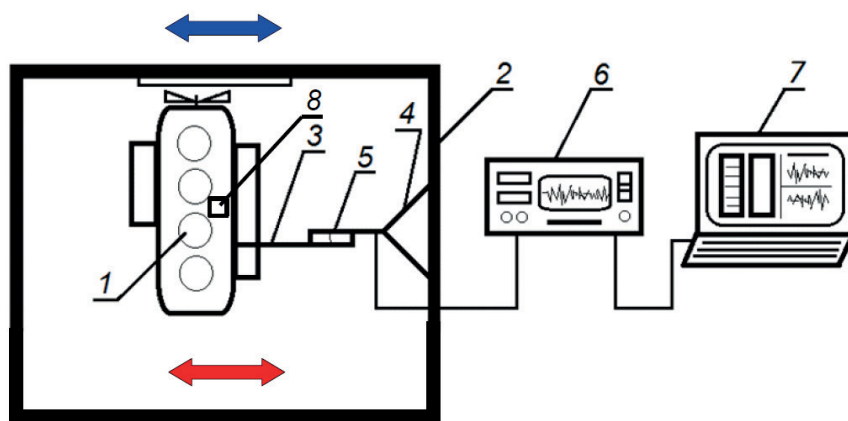


Figure 2 Scheme of the measurement system in a tested vehicle, 1 - diesel engine, 2 - vehicle body, 3 - potentiometer arm, 4 - load-bearing structure, 5 - linear potentiometer, 6 - oscilloscope, 7 - computer, 8 - energy harvesting system, the proposed energy harvester is going to be attached to the engine housing, red arrow denotes horizontal excitation of engine, blue arrow denotes the excitation of a vehicle during the driving

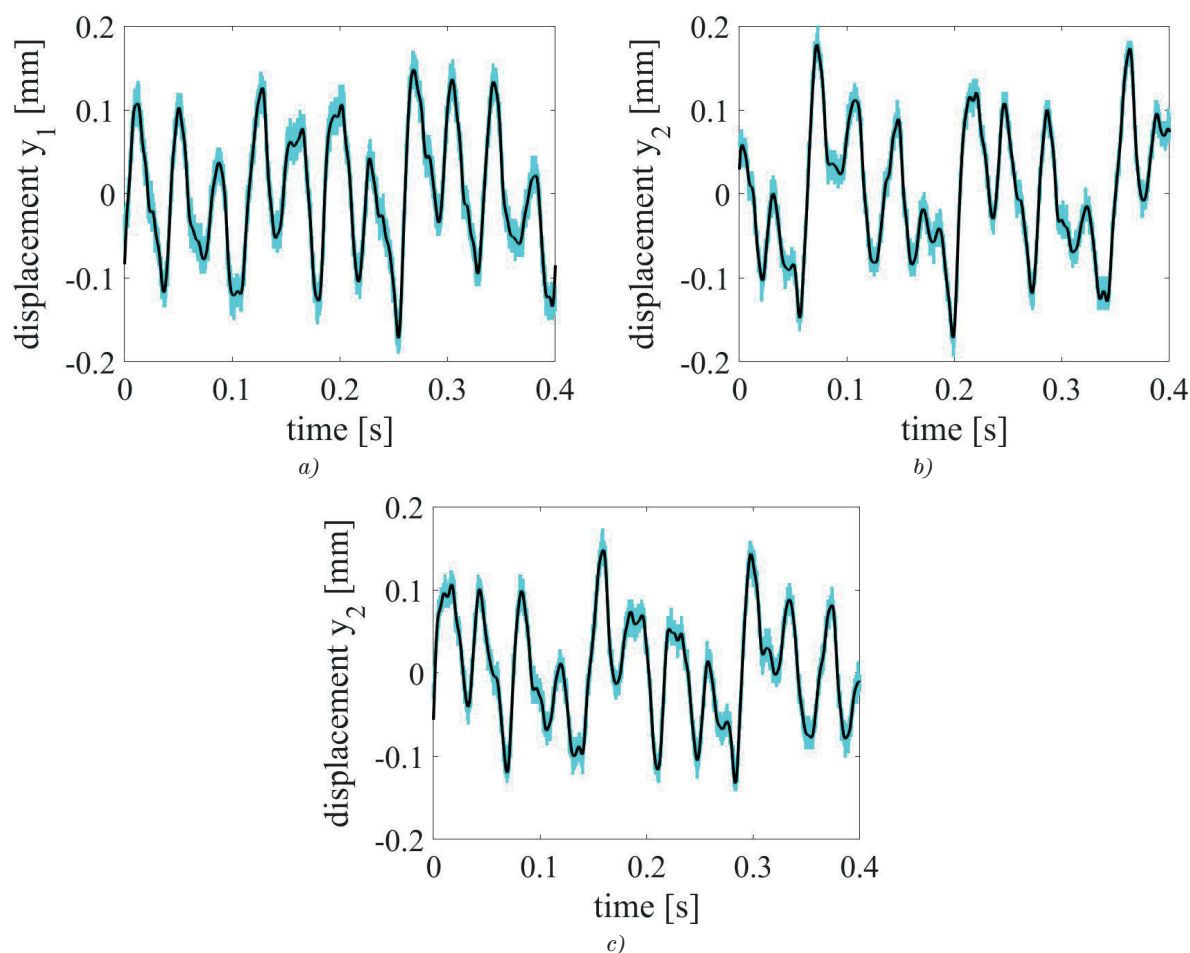


Figure 3 Displacement time series obtained from engine vibrations during driving, three different driving modes $n=\{800; 1000; 1500\}$ [rpm] are considered for (a), (b), and (c) respectively, the acceleration was also measured in voltage, but it is scaled for the accelerometer purpose, note: cyan color denotes the original measurement series and black line the corresponding data after application of the low pass filter with the frequency window below 170 rad.s^{-1}

a normal operating temperature. The way of mounting the measurement system in the engine chamber of the tested vehicle is presented in Figure 1.

The engine's displacement was measured using a specially constructed arm with a potentiometer which

transformed it into voltage and transferred the value to the oscilloscope DSO-2902 256K. The potentiometer transducer was A-linear type with $22 \text{ k}\Omega$ resistance and 0.5% linear tolerance. The diagram of the measurement trajectory of engine-to-body displacement is presented in Figure 2.

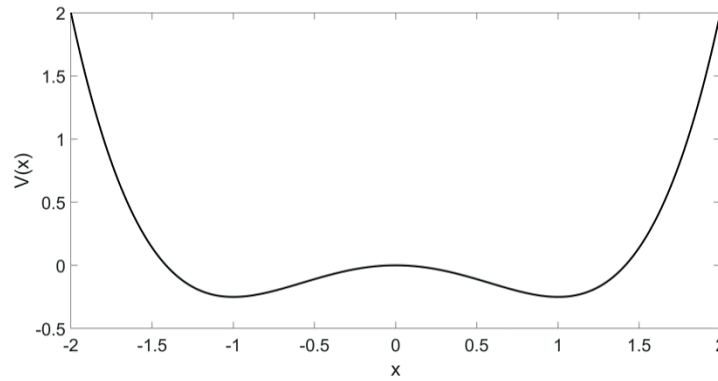


Figure 4 Potential energy $V(x)$ of the system in the Duffing oscillator versus displacement, three equilibrium points creates double-potential well, which is consisting of $x = -1, 1$ for stable and 0 for unstable equilibria (dimensionless model)

The device scale was selected in such a way that the voltage value corresponded to the appropriate displacement value ($1 \text{ V} = 1.6 \text{ mm}$).

Tests measurements of acceleration in the suspension system were performed by means of the experimental setup (Figure 2). The displacement results of the measurements are presented in Figure 3 using the cyan color. In the next sections an energy harvesting system to transform the kinetic inertial excitation energy into electric power is proposed.

Unfortunately, this data is strongly affected by the measurement noise. Therefore, the initial digital signal processing of the experimental signals using the low pass filter is performed (see black curves in Figure 3). These time series are then applied as the source of excitation in the model. The outcomes of the simulation in form of inertial force courses, phase portraits, voltage response are presented in the next sections.

3 The bi-stable energy harvester based on Duffing oscillator

A greater focus is placed on the non-linear behavior in vibratory energy harvesting (VEH) systems and more attention is paid to the bi-stability phenomenon. Such systems are characterized by double-well potential, in which the tested system can get stuck in one of the two equilibrium points with small amplitude oscillations. Alternatively, it can oscillate with a large amplitude going through the potential barrier. One of the main advantages of this type of energy harvesters is the possibility of improving their performance by adjusting the operational frequency to desirable effect in the form of operational frequency or output voltage/power [41]. The design of the proposed system can represent three types of operating modes, i.e. single-well (intra-well) mode, when the system has the tendency to be stuck in one of the wells, chaotic double-well (inter-well) mode or periodic double-well depending on the excitation [46]. However, the strongest effort is placed on the third mode where the system operates in the periodic double-well mode. This constitutes the most desirable behavior.

Stanton et al. [47] found the greatest strain profile nearest the equilibrium point obtaining the highest response. Masana et al. [48] showed the advantage of a bi-stable energy harvesting (EH) system over the mono-stable, superharmonics resonances in that it could activate the inter-well dynamics by even a small amplitude of excitation resulting in higher voltage response. Cottone et al. [49-50] proposed a design of a piezoelectric buckled bridge in which the highest voltage response is in the equilibrium point during the beam compression. In previous works by authors of this paper [51-57], the research focused on a different type of excitations acting on the system with the double-well potential both in mathematical and experimental approaches.

In many studies of vibration energy harvesting mathematical models, the Duffing oscillator, characterized by the double-well potential, is applied. Its equation of motion describes the complex dynamics, but the cubic nonlinearity and properly selected perturbation coefficients bring an advantage in the form of hardening or softening response of the system. This results in wider range of operational frequencies. By combining the piezoelectric coupling with the Duffing oscillator, equation of motion and an addition of the Kirchhoff laws to the circuit with a resistive load, one obtains electromechanical equations describing the system dynamics [41]:

$$\ddot{x} + 2\zeta\dot{x} - \frac{1}{2}x(1 - x^2) - \chi v = F \cos(\omega t), \quad (1)$$

$$\dot{v} + \lambda v + \kappa \dot{x} = 0, \quad (2)$$

where x is the dimensionless displacement of the beam in the transverse direction, ζ is the mechanical damping ratio, χ is the dimensionless piezoelectric coupling term in the mechanical equation, v is the dimensionless voltage across the load resistance, F is the dimensionless excitation force, ω is the dimensionless excitation frequency, λ is the reciprocal of the dimensionless time constant, κ is the dimensionless piezoelectric coupling term in the electrical circuit equation. Solution of Equation (1) gives three equilibrium points, saddle point $(x, \dot{x}) = (0, 0)$ and two sinks $(x, \dot{x}) = (\pm 1, 0)$.

In the next section of this paper, with regard to the

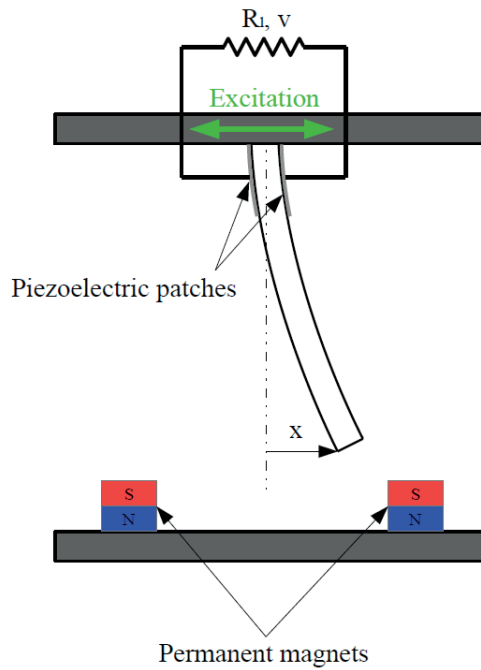


Figure 5 Model of piezoelectric energy harvester. Schematics of a beam with tip mass in form of permanent magnets

excitation of the bi-stable harvester (Figure 4 and Figure 5), application of the signal recorded on the frame of the diesel engine in the SUV vehicle is described. This is an acceleration signal to be considered as the input excitation for the energy harvesting system based on the Duffing oscillator. Energy harvesting systems, based on thermal transformations, have the highest efficiency in automotive. However, small portions of energy obtained from engine vibrations can support sensors placed in the engine such as the crankshaft sensor or oil temperature sensor. The oscillator response, excited with three different random signals, obtained from different road characteristics, is described in the following.

Advantage, coming from the bi-stability phenomena occurring in the system, is a broadband effect resulting in higher mean output power obtained in a wider range of operational frequency. In contrast to the linear system, which has only one specific value of frequency in the resonance region, the nonlinear bi-stable system is characterized by a broad frequency band composed of inclined resonances of one and multiple period responses (Figure 6). In calculations the initial conditions: the displacement was fixed to 1,0 (one of minima in the potential) while velocity was selected random for each frequency, and the initial voltage was nodal. Note that the single well linearized natural frequency is fixed to 1.0 (see Equation (1). These results were obtained using the random initial condition for velocity and 1 for displacement. Similar diagrams were discussed in [43-44, 52]. Note that the sub-harmonic responses with a large voltage output cover a large interval of excitation frequencies. These solutions correspond to the inter-well oscillations of the resonator. On the other hand, the small voltage response is related to the intra-well solutions. Those solutions include non-periodic solutions,

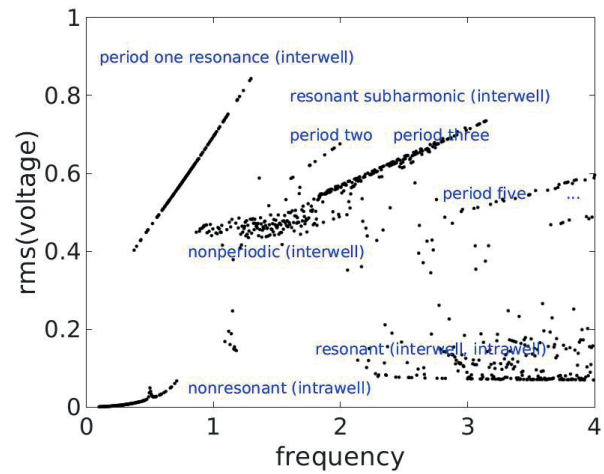


Figure 6 Voltage versus angular frequency showing a frequency (angular) broadband effect calculated from the model (Equations (1)-(2)). with the parameters $\zeta = 0.01$, $\chi = 0.05$, $\lambda = 0.01$, $\kappa = 0.5$, $f = 0.183$ attached to the moving frame. The inertial force is acting on the elastic beam

which are also useful for energy harvesting. In such cases, the system passes through the potential barrier in a non-periodic (chaotic) way.

Disadvantages of the bi-stable VEH proposal are based on appearance of multiple coexisting solutions, including the optimum solution, with questionable robustness in the presence of disturbances such as uncertainties in source and system parameters.

4 System parameters and configuration of the energy harvesting system

In this energy harvester design, attached to the engine suspension (Figure 1), one starts from the original equation

$$m\ddot{z} + 2c\dot{z} - \frac{k}{2}z(1 - z^2) - \chi'V = F'(\tau), \quad (3)$$

where, with respect to the model structure (Figure 5), z is the displacement of the frame / oscillator / harvester, m is an effective mass of the first mode beam motion, c , k are effective damping and nonlinear stiffness coefficient, V is the voltage output and χ' is the coupling parameter, $F'(\tau)$ is the inertial force $F' = -m\ddot{y}$ is the kinematic excitation force governed by the engine relative displacement y . We transform this equation to the dimensionless by adjusting the parameters as follows: $k/m\beta^2 = 1$, where $k/m = \Omega^2$, $c = \zeta/\beta$, where $\beta = \omega/\Omega$, $\Omega\tau = \omega t$, (to transform to dimensionless time into the band ω of [1-4] (see Figure 6)). Finally, the beam tip point z and voltage V will be changed to x and v , with respect to the geometrical, material and electrical properties of the system (to fit Equations (1) and (2)).

The power generator is based on the ferromagnetic beam, two PZT-5A piezo-ceramic layers QP16N are attached

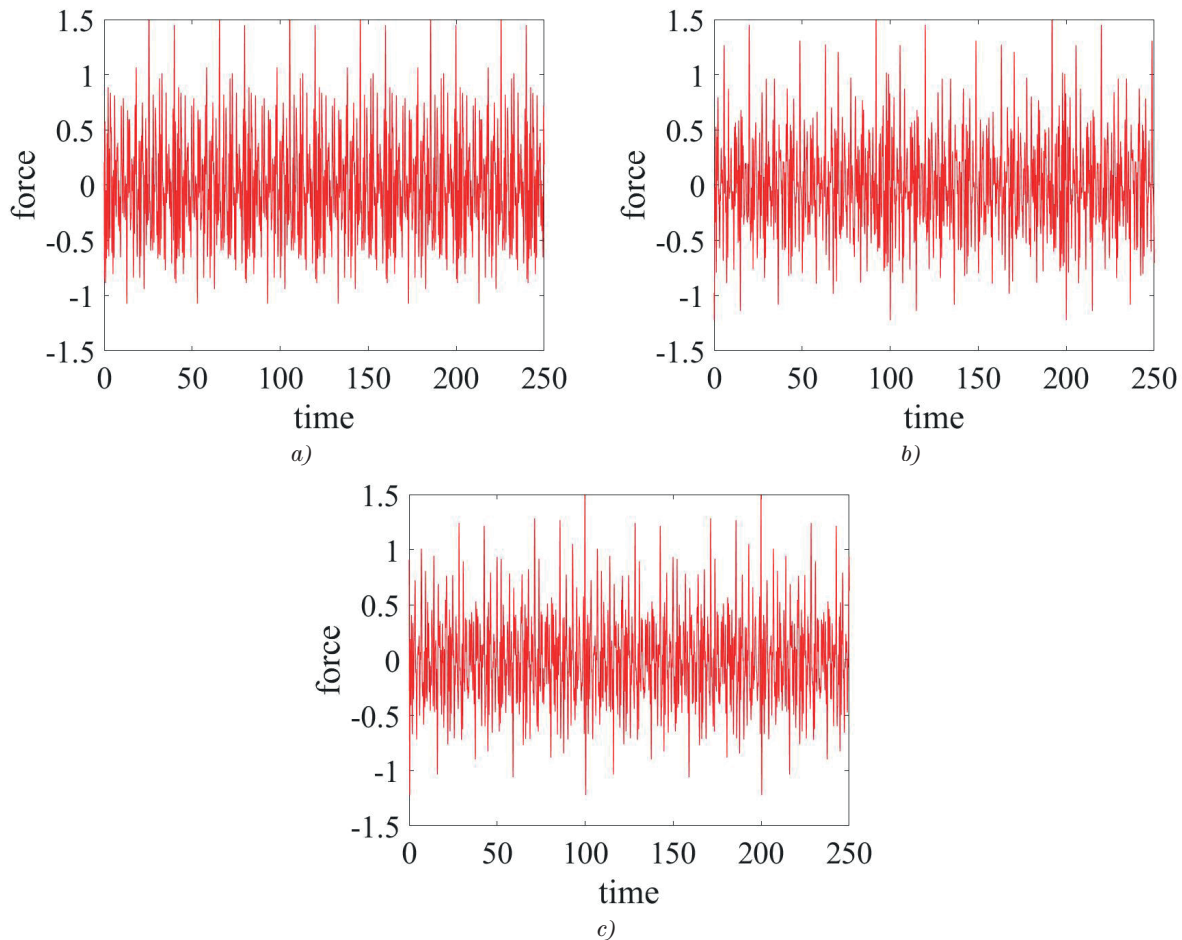


Figure 7 Inertial force time series from the experimental data (dimensionless model Equations (1)-(2)), the cases (a)-(c) have been estimated as the second order time derivatives of displacements in Figures 3 (a)-(c), respectively and expressed in dimensionless units

onto both faces of the beam at the root using a high shear strength epoxy. The modulation of permanent magnets is adjustable in order to obtain bi-stable configuration of the system.

5 Numerical simulations and results

In this section are presented results of the numerical modelling of the proposed EH system excited with the signal coming from vibrations generated by a diesel engine during its operation. For the numerical simulations three rotational velocities of the crankshaft are taken to observe the change of the inertial force of the beam in the additional magnetic field, the output voltage response from the piezoelectric, with phase portraits instead. The behavior of the system is presented below.

The experimental signals were obtained by the three different rotational velocities, i.e. $n = \{800; 1000; 1500\}$ [rpm]. In order to obtain the response in the longer period of time, the signals were multiplied a few times still reflecting the engine operation under one specific rotational velocity. The applied Duffing oscillator works as the filter for the vibration signals. The perturbation parameters in its equation of motion and in the equation

of electromechanical coupling are the following $\zeta = 0.01$, $\chi = 0.05$, $\lambda = 0.01$, $\kappa = 0.5$ (see Equations (1) and (2)). The external force, as presented in Figure 7, is substituted with experimental signals. For all the considered cases the initial conditions are the same at one of the stable equilibrium points ($x(0) = 1$) with the zero initial velocity and voltage.

Regarding the obtained time series of the inertial force-acceleration (Figure 7) it can be stated that the excited beam is getting lumped in the stable equilibrium points. Amplitudes of the inertial force in all the cases are almost the same varying in the frequency. The phase portraits (Figure 8) present the situation when the beam is changing its position from one well to another. As a consequence, the engine's vibrations are able to cause the chaotic movement of the beam by various rotational velocities. It is difficult to interpret the phase portraits at once. However, the output voltage time series of the piezoelectric element in all the cases present strongly non-periodic behavior of the beam. Both the characteristic jumps between the wells and oscillating response are observed in all cases. The highest RMS(V) response (Figure 9) was obtained for $n = 800$ [rpm], but all the outputs were similar, namely, 0.25, 0.18 and 0.20 in cases (a-c) of Figure 9, respectively. Despite the similar values of obtained voltage response, the character of time courses differs for each case. In general, one has the multi-

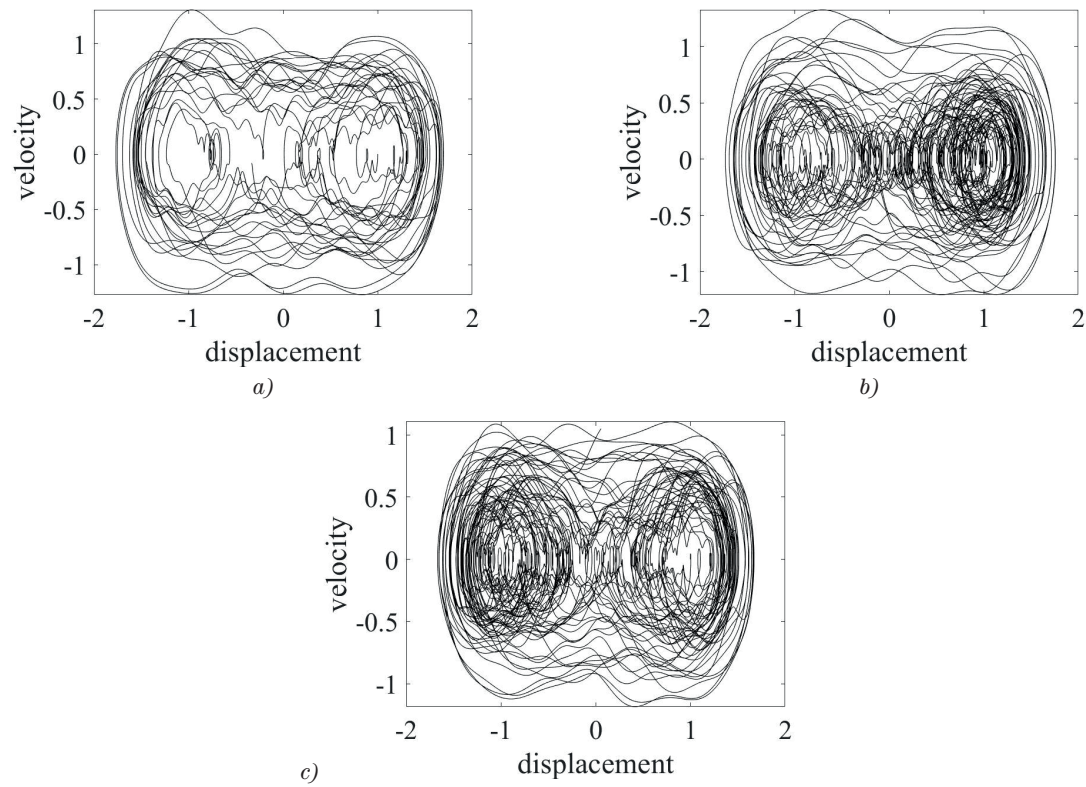


Figure 8 Phase portraits of energy harvesting resonator response excited by the Diesel engine vibrations (dimensionless model)

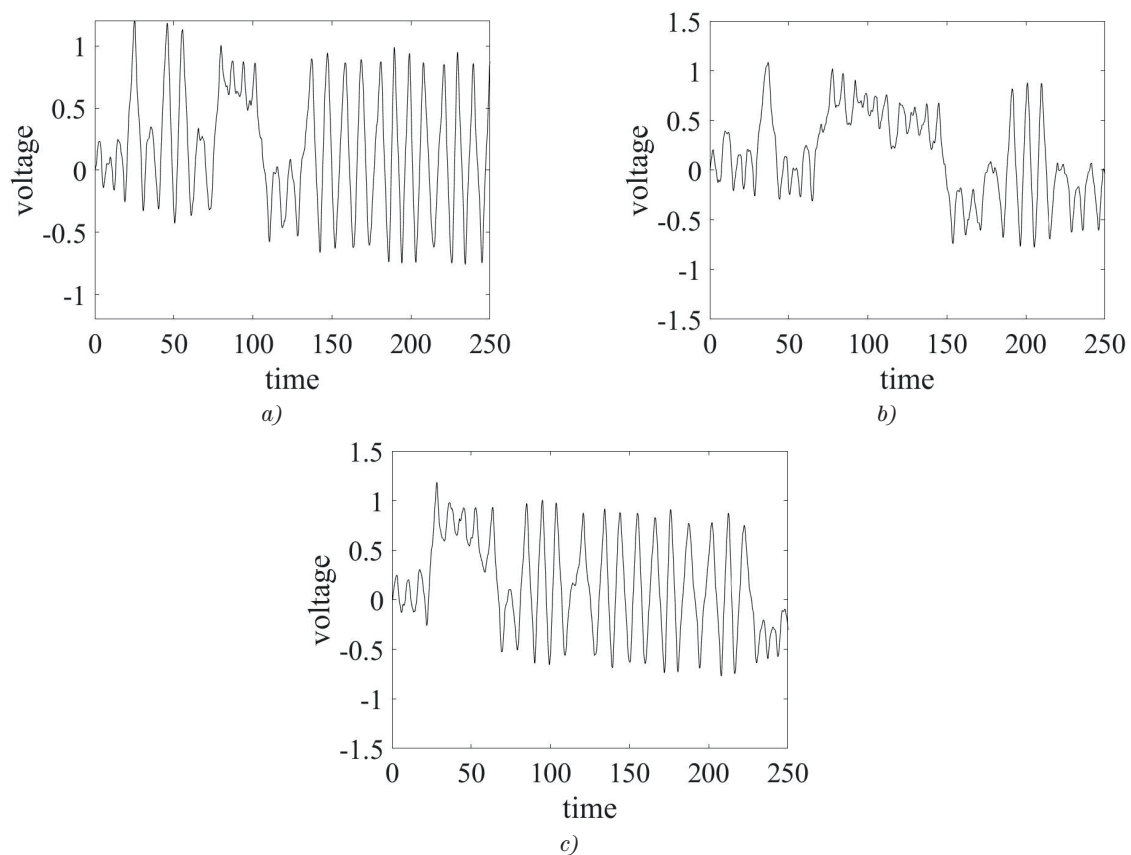


Figure 9 Voltage response of the piezoelectric beam (dimensionless model). The corresponding root mean square of the voltage outputs, $RMS(V)$, were estimated as a) 0.24, b) 0.18 and c) 0.20, respectively

frequency excitation and obtains the periodic response, when the ferromagnetic beam moves between the potential wells and time intervals of beam stuck in wells. The dimensionless model is proposed for the experimental excitation, but the energy system provides possibility to introduce changes in its design within dimensions of the beam and make the system's response adjustable to supply the connected sensor.

6 Conclusions


The main idea in development of the energy harvesting technologies is to apply own concepts in the real environment. In the present paper, application of a piezoelectric EH system, based on the Duffing oscillator in the diesel engine, is proposed. Random vibrations, generated by the engine, caused the movement of the beam with the tip magnet, by different operational velocities of the crankshaft and application of the nonlinear methods (phase portraits and resonance curve) allowed to observe its displacement between the two potential wells. The chaotic character of the beam movement and strong nonlinearity of the system in different duty cycles show the broadband effect in the system. This means that it can be applied in a wider range of operational frequencies than in the linear system. Simulations of the analytical model demonstrated that even the small magnitude of external excitation and proper initial conditions are able to provide the desirable inter-well behavior of the beam. The nonlinear EH system, based on the Duffing oscillator, can adapt to the different source of vibrations generated by the engine still gaining the energy, which can be possibly later used

to power up the low self-powered diagnostics sensors mounted in the engine block. The next step in the research would be to build the prototype of the EH system and test it in the engine block by different duty cycles. Subsequently, the comparable results from the test and the mathematical model would lead to the nonlinear system's optimization in order to reach the maximum output power in the wide range.

Note that the general dimensionless model of the EH is proposed. To design the specific device one should re-examine the properties of the excitation sources (amplitude and frequency of excitation) and scale the size and mass of the resonator accordingly.

In general, not much difference in performance is found in terms of average induced voltage between the applied duty cycles in the experiment; however, this gives the idea to prepare the further research by changing the design of the EH system and perform extended experiment considering not only other rotational velocities but the variable road conditions, as well. The strongly nonlinear behavior of the system also gives another direction of research for applying methods for quantification of nonlinearities in the system. As the energy harvesting technology is still developing, this research presented an opportunity to apply the concept in the real environment.

Acknowledgements

This publication was supported by the program of the Polish Ministry of Science and Higher Education under the project  DIALOG 0019/DLG/2019/10 in the years 2019-2021.

References

- [1] ORYNYCZ, O., SWIC, A. The effects of material's transport on various steps of production system on energetic efficiency of biodiesel production. *Sustainability* [online]. 2018, **10**(8), 2736. eISSN 2071-1050. Available from: <https://doi.org/10.3390/su10082736>
- [2] PARK, Y. S., LIM, S. H., EGILMEZ, G., SZMEREKOVSKY, J. Environmental efficiency assessment of US transport sector: A slack-based data envelopment analysis approach. *Transportation Research Part D Transportation Environment* [online]. 2018, **61**(A), p. 152-164. ISSN 1361-9209. Available from: <https://doi.org/10.1016/j.trd.2016.09.009>
- [3] LONGWIC, A., NIEOCZYM, A., KORDOS, P. Evaluation of the combustion process in a spark-ignition engine based on the unrepeatability of the maximum pressure. *IOP Conference Series, Materials Science and Engineering* [online]. 2018, **421**(4), p. 1-9. ISSN 1757-8981, eISSN 1757-899X. Available from: <https://doi.org/10.1088/1757-899X/421/4/042048>
- [4] TUCKI, K., MRUK, R., ORYNYCZ, O., GOLA, A. The effects of pressure and temperature on the process of auto-ignition and combustion of rape oil and its mixtures. *Sustainability* [online]. 2019, **11**(12), 3451. eISSN 2071-1050. Available from: <https://doi.org/10.3390/su11123451>
- [5] SZPICA, D. Investigating fuel dosage non-repeatability of low-pressure gas-phase injectors. *Flow Measurement and Instrumentation* [online]. 2018, **59**, p. 147-156. ISSN 0955-5986. Available from: <https://doi.org/10.1016/j.flowmeasinst.2017.12.009>
- [6] DANILOV, I., POPOVA, I., MOISEEV, Y. Analysis and validation of the dynamic method for diagnosing diesel engine connecting rod bearings. *Transport Problems* [online]. 2018, **13**(1), p. 123-133. eISSN 2300-861X. Available from: <https://doi.org/10.21307/tp.2018.13.1.11>
- [7] STOECK, T., ABRAMEK, K. F. Application of the polynomial interpolation method for determining performance characteristics of a diesel engine. *Metrology and Measurement Systems* [online]. 2014, **21**(1), p. 157-168. ISSN 0860-8229. Available from: <https://doi.org/10.2478/mms-2014-0015>

- [8] MIKULSKI, M., WIERZBICKI, S., SMIEJA, M., MATLJOSIUS, J. Effect of CNG in a fuel dose on the combustion process of a compression-ignition engine. *Transport* [online]. 2015, **30**(2), p. 162-171. ISSN 1648-4142, eISSN 1648-3480. Available from: <https://doi.org/10.3846/16484142.2015.1045938>
- [9] MAKAREVICIENE, V., MATLJOSIUS, J., PUKALSKAS, S., VEGNERIS, R., KAZANCEVA, I., KAZANCEV, K. The exploitation and environmental characteristics of diesel fuel containing rapeseed butyl esters. *Transport* [online]. 2013, **28**(2), p. 158-165. ISSN 1648-4142, eISSN 1648-3480. Available from: <https://doi.org/10.3846/16484142.2013.801364>
- [10] SETIYO, M., WIDODO, E. M., ROSYIDI, M. I., PURNOMO, T. A., RAHARDJA, B. S., SURYANTORO, S. Economic values and CO₂ Simulation on the application of LPG for public fleets in magelang, indonesia: executive data to support the clean city program. *Periodyca Polytechnica Transportation Engineering* [online]. 2020, **48**(2), p. 159-172. ISSN 0303-7800, eISSN 1587-3811. Available from: <https://doi.org/10.3311/PPtr.12841>
- [11] JEDLINSKI, L., JONAK, J. A disassembly-free method for evaluation of spiral bevel gear assembly. *Mechanical Systems and Signal Processing* [online]. 2017, **88**, p. 399-412. ISSN 0888-3270. Available from: <https://doi.org/10.1016/j.ymssp.2016.11.005>
- [12] SUN, W., YAO, B., ZENG, N., CHEN, B., HE, Y., CAO, X., HE, W. An intelligent gear fault diagnosis methodology using a complex wavelet enhanced convolutional neural network. *Materials* [online]. 2017, **10**(7), 790. eISSN 1996-1944. Available from: <https://doi.org/10.3390/ma10070790>
- [13] SAWALHI, N., RANDALL, R. B. Gear parameter identification in a wind turbine gearbox using vibration signals. *Mechanical Systems and Signal Processing* [online]. 2014, **42**, p. 368-376. ISSN 0888-3270. Available from: <https://doi.org/10.1016/j.ymssp.2013.08.017>
- [14] BOROWIEC, M., LITAK, G., SEN, A. K., HUNICZ, J., KOSZALKA, G., NIEWCZAS, A. Vibrations of a vehicle excited by real road profiles. *Forschung im Ingenieurwesen* [online]. 2010, **74**, p. 99-109. ISSN 0015-7899, eISSN 1434-0860. Available from: <https://doi.org/10.1007/s10010-010-0119-y>
- [15] KARIOJA, K., LAHDELMA, S., LITAK, G., AMBROZKIEWICZ, B. Extracting periodically repeating shocks in a gearbox from simultaneously occurring random vibration. In: 15th International Conference on Condition Monitoring and Machinery Failure Prevention Technologies CM/MFPT 2018: proceedings. 2018. p. 456-464.
- [16] SOUALHI, A., MEDJAHHER, K., ZERHOUNI, N. Bearing health monitoring based on Hilbert-Huang transform, support vector machine and regression. *IEEE Transactions on Instrumentation and Measurement* [online]. 2015, **64**(1), p. 52-62. ISSN 0018-9456, eISSN 1557-9662. Available from: <https://doi.org/10.1109/TIM.2014.2330494>
- [17] LITAK, G., BOROWIEC, M., HUNICZ, J., KOSZALKA, G., NIEWCZAS, A. Vibrations of a delivery car excited by railway track crossing. *Chaos, Solitons and Fractals* [online]. 2009, **42**, p. 270-276. ISSN 0960-0779. Available from: <https://doi.org/10.1016/j.chaos.2008.11.020>
- [18] MARICHAL, G. N., DEL CASTILLO, M. L., LOPEZ, J., PADRON, I., ARTES, M. An artificial intelligence approach for gears diagnostics in AUVs. *Sensors* [online]. 2016, **16**(4), 529. eISSN 1424-8220. Available from: <https://doi.org/10.3390/s16040529>
- [19] BALYTSKYI, A., ABRAMEK, K. F., STOECK, T., OSIPOWICZ, T. Diagnostic of degradation of the lock seal ring by the loss of combustion engine working gases. *Materials Science* [online]. 2014, **50**(1), p. 156-169. ISSN 1068-820X, eISSN 1573-885X. Available from: <https://doi.org/10.1007/s11003-014-9704-9>
- [20] BRUMERCIK, F., LUKAC, M., MAJCHRAK, M., KRZYSIK, Z., KRZYWONOS, L. Teeth geometry and contact pressure calculation of external cycloidal gears. *Scientific Journal of Silesian University of Technology. Series Transport* [online]. 2018, **101**, p. 27-35. ISSN 0209-3324, eISSN 2450-1549. Available from: <https://doi.org/10.20858/sjsutst.2018.101.3>
- [21] FIGLUS, T. A method for diagnosing gearboxes of means of transport using multi-stage filtering and entropy. *Entropy* [online]. 2019, **21**(3), 441. eISSN 1099-4300. Available from: <https://doi.org/10.3390/e21050441>
- [22] GHOLIKHANI, M., TAHAMI, S. A., KHALILI, M., DESSOUKY, S. Electromagnetic energy harvesting technology: key to sustainability in transportation systems. *Sustainability* [online]. 2019, **11**(18), 4906. eISSN 2071-1050. Available from: <https://doi.org/10.3390/su11184906>
- [23] ROSHANI, H., JAGTAP, P., DESSOUKY, S., MONTOYA, A., PAPAGIANNAKIS, A. T. Theoretical and experimental evaluation of two roadway piezoelectric-based energy harvesting prototypes. *Journal of Materials in Civil Engineering* [online]. 2017, **30**, 04017264. ISSN 0899-1561, eISSN 1943-5533. Available from: [https://doi.org/10.1061/\(ASCE\)MT.1943-5533.0002112](https://doi.org/10.1061/(ASCE)MT.1943-5533.0002112)
- [24] ZHANG, Y., GUO, K., WANG, D., CHEN, C., LI, X. Energy conversion mechanism and regenerative potential of vehicle suspensions. *Energy* [online]. 2017, **119**, p. 961-970. ISSN 0360-5442. Available from: <https://doi.org/10.1016/j.energy.2016.11.045>
- [25] ABDELKAREEM, M. A. A., XU, L., ALI, M. K. A., ELAGOUZ, A., MI, J., GUO, S., LIU, Y., ZUO, L. Vibration energy harvesting in automotive suspension system: A detailed review. *Applied Energy* [online]. 2018, **229**, p. 672-699. ISSN 0306-2619. Available from: <https://doi.org/10.1016/j.apenergy.2018.08.030>
- [26] KURANC, A., SLOWIK, T., WASILEWSKI, J., SZYSZLAK-BARGLOWICZ, J., STOMA, M., SARKAN, B. Emission of particulates and chosen gaseous exhausts components during a diesel engine starting process. In: 9th International Scientific Symposium on Farm Machinery and Process Management in Sustainable Agriculture: proceedings [online].

2017. p. 210-215. Available from: <https://doi.org/10.24326/fmpmsa.2017.38>
- [27] LIZBETIN, J., STOPKA, O., KURENKOV, P. V. Declarations regarding the energy consumption and emissions of the greenhouse gases in the road freight transport sector. *The Archives of Automotive Engineering - Archiwum Motoryzacji* [online]. 2019, **83**(1), p. 59-72. eISSN 2084-476X. Available from: <https://doi.org/10.14669/AM.VOL83.ART4>
- [28] SKRUCANY, T., HARANTOVA, V., KENDRA, M., BARTA, D. Reducing energy consumption by passenger car with using of non-electrical hybrid drive technology. *Advances in Science and Technology Research Journal* [online]. 2018, **11**(1), p. 166-172. ISSN 2299-8624. Available from: <https://doi.org/10.12913/22998624/66505>
- [29] ZHAO, D. Waste thermal energy harvesting from a convection-driven thermo-acoustic-piezo system. *Energy Conversion and Management* [online]. 2013, **66**, p. 87-97. ISSN 0196-8904. Available from: <https://doi.org/10.1016/j.enconman.2012.09.025>
- [30] ITANI, K., DE BERNARDINIS, A., KHATIR, Z., JAMMAL, A. Comparative analysis of two hybrid energy storage systems used in a two front wheel driven electric vehicle during extreme start-up and regenerative braking operations. *Energy Conversion and Management* [online]. 2017, **144**, p. 69-87. ISSN 0196-8904. Available from: <https://doi.org/10.1016/j.enconman.2017.04.036>
- [31] WEI, C., JING, X. A comprehensive review on vibration energy harvesting: Modelling and realization. *Renewable and Sustainable Energy Reviews* [online]. 2017, **74**, p. 1-18. ISSN 1364-0321. Available from: <https://doi.org/10.1016/j.rser.2017.01.073>
- [32] WALUBITA, L., SOHOULANDE DJEBOU, D., FARUK, A., LEE, S., DESSOUKY, S., HU, X. Prospective of societal and environmental benefits of piezoelectric technology in road energy harvesting. *Sustainability* [online]. 2018, **10**, 383. eISSN 2071-1050. Available from: <https://doi.org/10.3390/su10020383>
- [33] PASCUAL-MUNOZ, P., CASTRO-FRESNO, D., SERRANO-BRAVO, P., ALONSO-ESTEBANEZ, A. Thermal and hydraulic analysis of multilayered asphalt pavements as active solar collectors. *Applied Energy* [online]. 2013, **111**, p. 324-332. ISSN 0306-2619. Available from: <https://doi.org/10.1016/j.apenergy.2013.05.013>
- [34] DATTA, U., DESSOUKY, S., PAPAGIANNAKIS, A. Harvesting thermoelectric energy from asphalt pavements. *Transportation Research Record Journal of the Transportation Research Board* [online]. 2017, **2628**, p. 12-22. ISSN 0361-1981, eISSN 2169-4052. Available from: <https://doi.org/10.3141/2628-02>
- [35] WANG, L., PARK, J.; ZHOU, W., ZUO, L. A large-scale on-road energy harvester from highway vibration. In: International Design Engineering Technical Conferences and Computers and Information in Engineering Conference ASME 2016: proceedings [online]. New York, NY, USA: American Society of Mechanical Engineers. 2016. ISBN 978-0-7918-5020-6. Available from: <https://doi.org/10.1115/DETC2016-59562>
- [36] EFTHYMIU, C., SANTAMOURIS, M., KOLOKOTSA, D., KORAS, A. Development and testing of photovoltaic pavement for heat island mitigation. *Solar Energy* [online]. 2016, **130**, p. 148-160. ISSN 0038-092X. Available from: <https://doi.org/10.1016/j.solener.2016.01.054>
- [37] JETTANASEN, C., SONGSUKTHAWAN, P., NGAOPITAKKUL, A. Development of micro-mobility based on piezoelectric energy harvesting for smart city applications. *Sustainability* [online]. 2020, **12**(7), 2933. eISSN 2071-1050. Available from: <https://doi.org/10.3390/su12072933>
- [38] SARKER, M. R., JULAI, S., SABRI, M. F., SAID, S. M., ISLAM, M. M., TAHIR, M. Review of piezoelectric energy harvesting system and application of optimization techniques to enhance the performance of the harvesting system. *Sensors and Actuators A: Physical* [online]. 2019, **300**, p. 111634. ISSN 0924-4247. Available from: <https://doi.org/10.1016/j.sna.2019.111634>
- [39] CHALIORIS, C. E., KARAYANNIS, C. G., ANGELL, G. M., PAPADOPOULOS, N. A., FAVVATA, M. J., PROVIDAKIS, C. P. Applications of smart piezoelectric materials in a wireless admittance monitoring system (WiAMS) to Structures - Tests in RC elements. *Case Studies in Construction Materials* [online]. 2016, **5**, p. 1-18. ISSN 2214-5095. Available from: <https://doi.org/10.1016/j.cscm.2016.03.003>
- [40] MICEK, P., GRZYBEK, D. Wireless stress sensor based on piezoelectric energy harvesting for a rotating shaft. *Sensors and Actuators A: Physical* [online]. 2019, **301**, 111744. ISSN 0924-4247. Available from: <https://doi.org/10.1016/j.sna.2019.111744>
- [41] ERTURK, A., HOFFMANN, J., INMAN, D. J. A piezomagnetoelastic structure for broadband vibration energy harvesting. *Applied Physics Letters* [online]. 2009, **94**, 254102. ISSN 0003-6951, eISSN 1077-3118. Available from: <https://doi.org/10.1063/1.3159815>
- [42] VOCCA, H., NERI, I., TRAVASSO, F., GAMMAITONI, L. Kinetic energy harvesting with bistable oscillators. *Applied Energy* [online]. 2012, **97**, p. 771-776. ISSN 0306-2619. Available from: <https://doi.org/10.1016/j.apenergy.2011.12.087>
- [43] HUGUET, T., LALLART, M., BADEL, A. Orbit jump in bistable energy harvesters through buckling level modification. *Mechanical Systems and Signal Processing* [online]. 2019, **128**, p. 202-215. ISSN 0888-3270. Available from: <https://doi.org/10.1016/j.ymssp.2019.03.051>
- [44] HUGUET, T., BADEL, A., LALLART, M. Parametric analysis for optimized piezoelectric bistable vibration energy harvesters. *Smart Materials and Structures* [online]. 2019, **28**, 115009. ISSN 0964-1726, eISSN 1361-665X. Available from: <https://doi.org/10.1088/1361-665X/ab45c6>

- [45] DEL-RIO-RUIZ, R., ECHEVARRIA, J. J., EGUILUZ, X., LOPEZ-GARDE, J.-M., LEGARDA, J. Experimental frequency tuning methodology of a cantilever piezoelectric harvester validated in a multimodal transportation. *Electronics* [online]. 2020, **9**(1), 79. eISSN 2079-9292. Available from: <https://doi.org/10.3390/electronics9010079>
- [46] YANG, T., WANG, T., LI, G., SHI, J., SUN, X. Vibration characteristics of compression ignition engines fueled with blended petro-diesel and Fischer-Tropsch diesel fuel from coal fuels. *Energies* [online]. 2018, **11**(8), 2043. eISSN 1996-1073. Available from: <https://doi.org/10.3390/en11082043>
- [47] TAGHIZADEH-ALISARAEI, A., GHOBADIAN, B., TAVAKOLI-HASHJIN, T., MOHTASEBI, S. S. Vibration analysis of a diesel engine using biodiesel and petrodiesel fuel blends. *Fuel* [online]. 2012, **102**, p. 414-422. ISSN 0016-2361. Available from: <https://doi.org/10.1016/j.fuel.2012.06.109>
- [48] HARNE, R. L., WANG, K. W. On the fundamental and superharmonic effects in bistable energy harvesting. *Journal of Intelligent Material Systems and Structures* [online]. 2013, **25**(8), p. 937-950. ISSN 1045-389X, eISSN 1530-8138. Available from: <https://doi.org/10.1177/1045389X13502856>
- [49] STANTON, S. C., MCGEHEE, C. C., MANN, B. P. Nonlinear dynamics for broadband energy harvesting: Investigation of a bistable piezoelectric inertial generator. *Physica D* [online]. 2010, **239**(10), p. 640-653. ISSN 0167-2789. Available from: <https://doi.org/10.1016/j.physd.2010.01.019>
- [50] MASANA, R., DAQAQ, M. F. Relative performance of a vibratory energy harvester in mono- and bi-stable potentials. *Journal of Sound and Vibration* [online]. 2011, **330**, p. 6036-6052. ISSN 0022-460X. Available from: <https://doi.org/10.1016/j.jsv.2011.07.031>
- [51] COTTONE, F., GAMMAITONI, L., VOCCA, H., FERRARI, M., FERRARI V. Piezoelectric buckled beams for random vibration energy harvesting. *Smart Materials and Structures* [online]. 2012, **21**(3), 035021. ISSN 0964-1726, eISSN 1361-665X. Available from: <https://doi.org/10.1088/0964-1726/21/3/035021>
- [52] COTTONE, F., BASSET, P., VOCCA, H., GAMMAITONI, L., BOUROUINA T. Bistable electromagnetic generator based on buckled beams for vibration energy harvesting. *Journal of Intelligent Material Systems and Structures* [online]. 2013, **25**(3), p. 1-12. ISSN 1045-389X, eISSN 1530-8138. Available from: <https://doi.org/10.1177/1045389x13508330>
- [53] LITAK, G., FRISWELL, M. I., ADHIKARI S. Magnetopiezoelectric energy harvesting driven by random excitations. *Applied Physics Letters* [online]. 2010, **96**, 214103. ISSN 0003-6951, eISSN 1077-3118. Available from: <https://doi.org/10.1063/1.3436553>
- [54] FRISWELL, M. I., ALI, S. F., ADHIKARI, S., LEES, A. W., BILGEN, O., LITAK, G. Nonlinear piezoelectric vibration energy harvesting from a vertical cantilever beam with tip mass. *Journal of Intelligent Material Systems and Structures* [online]. 2012, **23**, p. 1505-1521. ISSN 1045-389X, eISSN 1530-8138. Available from: <https://doi.org/10.1177/1045389X12455722>
- [55] COCCOLO, M., LITAK, G., SEOANE J., SANJUAN, M. A. F. Optimizing the electrical power in an energy harvesting system. *International Journal of Bifurcation and Chaos* [online]. 2015, **25**, 1550171. ISSN 0218-1274, eISSN 1793-6551. Available from: <https://doi.org/10.1142/S0218127415501710>
- [56] HUANG, D., ZHOU, S., LITAK, G. Theoretical analysis of multi-stable energy harvesters with high order stiffness terms. *Communications in Nonlinear Science and Numerical Simulation* [online]. 2019, **69**, p. 270-286. ISSN 1007-5704. Available from: <https://doi.org/10.1016/j.cnsns.2018.09.025>
- [57] AMBROZKIEWICZ, B., LITAK, G., WOLSZCZAK, P. Modelling of electromagnetic energy harvester with rotational pendulum using mechanical vibrations to scavenge electrical energy. *Applied Sciences* [online]. 2020, **10**(2), 671. eISSN 2076-3417. Available from: <https://doi.org/10.3390/app10020671>

FUZZY LOGIC METHOD FOR THE SPEED ESTIMATION IN ALL-WHEEL DRIVE ELECTRIC RACING VEHICLES

Angelo Bonfitto, Stefano Feraco*, Marco Rossini, Francesco Carlomagno

Department of Mechanical and Aerospace Engineering - Mechatronics Laboratory, Politecnico di Torino, Torino, Italy

*E-mail of corresponding author: stefano.feraco@polito.it

Resume

This paper presents a method for the vehicle speed estimation with a Fuzzy Logic based algorithm. The algorithm acquires the measurements of the yaw rate, steering angle, wheel velocities and exploits a set of five Fuzzy Logics dedicated to different driving conditions. The technique estimates the speed exploiting a weighted average of the contributions provided by the longitudinal acceleration and the credibility assigned by the Fuzzy Logics to the measurements of the wheels' speed. The method is experimentally evaluated on an all-wheel drive electric racing vehicle and is valid for the front and rear wheel drive configurations. The experimental validation is performed by comparing the obtained estimation with the result of computing the speed as the average of the linear velocity of the four wheels. A comparison to the integral of the vehicle acceleration over time is reported.

Article info

Received 19 May 2020

Accepted 10 August 2020

Online 26 January 2021

Keywords:

automotive engineering,
vehicle dynamics,
fuzzy logic,
electric vehicles,
speed estimation

Available online: <https://doi.org/10.26552/com.C.2021.2.B117-B129>

ISSN 1335-4205 (print version)

ISSN 2585-7878 (online version)

1 Introduction

In the last years, the automotive industry is experiencing a wide technological innovation involving several aspects. Modern cars are equipped with active driver assistance systems and intelligent algorithms allowing the design of more efficient, less polluting and safer vehicles [1]. Many of the recent solutions rely on electro-mechanical subsystems exploiting sensors, actuators and feedback control. In this context, an important enabling role is played by the latest development in the computer technology, control systems, microelectronics and artificial intelligence, which are strongly promoting the current trend of innovation [2-3]. For most of these solutions, a complete and robust real-time assessment of the vehicle dynamics is required [4]. Specifically, the estimation of the vehicle speed is a task that is considered pivotal for the vehicle's active control systems, especially when dealing with racing vehicles, which are characterized by extreme performances in terms of longitudinal and lateral dynamics. However, the direct measurement of this parameter may require an expensive and cumbersome instrumentation that, in most of the cases, cannot be adopted for the large scale production. A solution is the adoption of optical sensors, that are not used in series production cars because of their prohibitive costs, low robustness, and high sensitivity to the environmental conditions [5]. A feasible alternative is represented by the GPS-based sensors that, however, may suffer signal latency and are not effective in tunnels or in urban environments

with tall buildings. Moreover, the latency of these devices can be in the order of magnitude of seconds and the sensing may be inaccurate due to the unavailability of the satellites signal [6]. These drawbacks discourage the employment of these solutions and induce to investigating alternative techniques based on the indirect measurement and estimation of the speed. A common method allows achieving this objective by computing the vehicle speed as the average of the linear velocity of the wheels. However, this simple approach may be strongly inaccurate when one or more wheels are locking or skidding during the extreme maneuvers, which is a common condition for racing vehicles and in the case of dirty asphalt, as well as icy or wet roads. On the other hand, model-based and filter/observer-based methods have been also investigated [7], such as nonlinear observers [8], Kalman Filter (KF) [9-10], Adaptive KF (AKF) [11-12], Extended KF (EKF) [13-14], and Unscented Kalman Filter (UKF) [15-16]. Although effective, these methods may suffer severe inaccuracies due to unmodeled dynamics or when the reference model is not tuned to represent all the driving conditions and possible vehicle setups and tuning, which can be a frequent situation when dealing with the high-performance or racing vehicles. To avoid the dependency of the vehicle model, adopting the artificial intelligence, such as Artificial Neural Networks (ANNs) [17-21], represents a possibility. Nevertheless, these solutions are strongly dependent on the network architecture and training datasets, which must include all the possible driving maneuvers and road



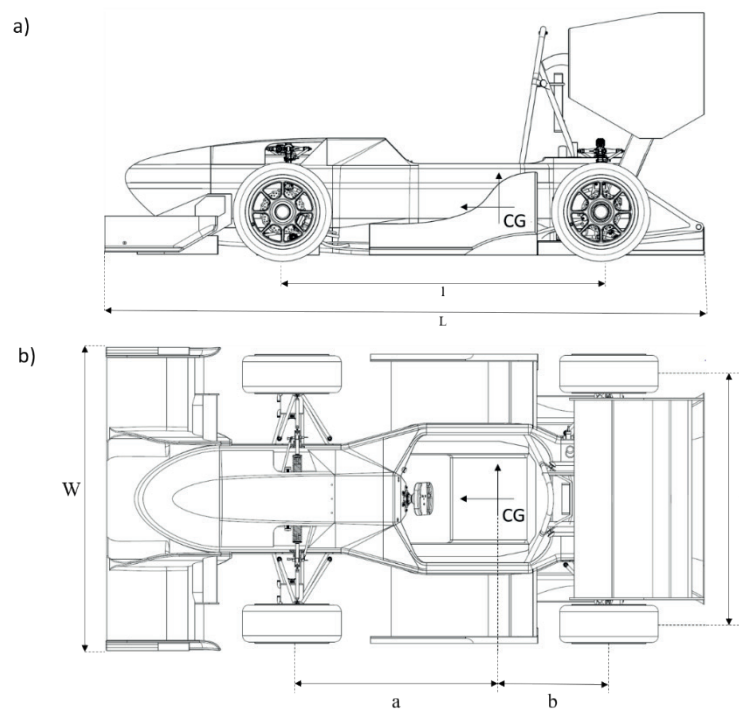


Figure 1 Considered racing vehicle: a) side view; b) upper view. The values associated with the parameters indicated in the figure are defined in Table 1

conditions to compute a sufficiently accurate estimation [22]. A promising approach is represented by the adoption of Fuzzy Logic (FL), that is well known in the literature to tackle control and estimation tasks in automotive engineering [23-24]. This approach is based on experience of a designer in representation of the system behavior by means of linguistic definitions. When designing an FL-based system, different layouts and processing task definitions are possible. A solution exploiting a FL to support the electronic stability control system of a light-duty pickup truck is presented in [25]. It is based on an analysis of velocity of the four wheels and exploits the FL to evaluate the reliability of these values in acceleration, braking and sliding conditions. This solution lacks accuracy since the contribution of acceleration is not included in the speed estimation and this is the cause of poor results in the case of full locking or spinning condition. A method for the speed estimation of a front wheel drive (FWD) vehicle is presented in [26]. The solution exploits two FLs to identify two classes of driving condition: a) loss of contact while cornering and b) a set composed of oversteering, front wheel sliding out and lateral sliding. This information is provided to a further FL, which estimates the vehicle speed. This method can only be applied in the case of FWD vehicles and is based on a two-stage estimation task. A combination of the FL with a state variable filter is presented in [27] for a four-wheel (4WD) drive vehicle. This technique is validated in the case of velocities that are lower than 5 km/h and in simulation only. Finally, a method based on a single stage FL is reported in [28], which does not consider different driving conditions and is not validated in the case of locking and spinning conditions.

In this paper, a method for the vehicle speed

estimation, based on the combination of five FLs, is proposed. The method is designed and experimentally validated for an instrumented All-Wheel Drive (AWD) electric racing vehicle, which has competed in the 2018 Formula Student events. The estimation is based on the computation of the weighted average of the wheel velocities and of the contribution given by the longitudinal acceleration. This average exploits the outputs of the FL block, which are four coefficients indicating the reliability of the measured speed of the four wheels and a coefficient related to the acceleration of a vehicle. The FL block is composed of five different logics dedicated to five driving conditions: acceleration, strong acceleration, braking, strong braking and coasting. An external routine allows identifying the driving condition and selecting the corresponding FL. The technique is validated experimentally by deploying the algorithm on the vehicle's ECU and comparing it to another solution computing the vehicle speed as the average of the linear velocity of the four wheels. The integral of the vehicle acceleration over time is also considered in the validation as an additional reference for evaluation of the estimation accuracy. The system was not compared to a direct measurement of velocity due to the excessive costs of the needed sensors.

The main contribution of the paper is the proposal of an FL-based technique considering different driving conditions and therefore, reliable also in the case of locking and spinning of the wheels. This is made possible by the contribution of the vehicle acceleration, which is included in the speed estimation algorithm. The technique is designed for an AWD vehicle and consequently, it is valid also for other traction architectures. The layout is based on an one-stage estimation task and does not require additional enabling

Table 1 Set of the vehicle parameters (*included driver)

parameter	symbol	value	unit
mass*	m	275	(kg)
moment of inertia about z -axis*	I_z	103.2	(kgm ²)
vehicle wheelbase	l	1.525	(m)
overall length	L	2.873	(m)
front axle distance to COG	a	0.854	(m)
rear axle distance to COG	b	0.671	(m)
vehicle track width	t	1.2	(m)
overall width	W	1.38	(m)
height of cog*	h_{CG}	0.245	(m)
wheel radius	R_w	0.241	(m)
maximum power (total vehicle)	P_{max}	80	(kW)
motors peak torque (total vehicle)	T_{max}	84	(Nm)
transmission ratio	τ	14.82	(-)
maximum energy stored (battery pack)	E_{bp}	7.78	(kWh)
battery pack voltage	V_{bp}	600	(V)

processing routines. The presented experimental validation allows demonstrating the effectiveness in different driving conditions and in the case of demanding maneuvers.

2 Description of the vehicle

Figure 1 shows the lateral (a) and upper view (b) of the racing vehicle that is used for the study. The vehicle is compliant with the Electric Formula Student Germany (FSG) regulation for the year 2018 [29]. It features an integral carbon fiber chassis built with honeycomb panels, double wishbone push-rod suspensions, an on-wheel planetary transmission system and an aerodynamic package, which can generate about 630 N of downforce at 60 km/h. The height of the vehicle Centre of Gravity (COG) is located at 0.245 m. Four synchronous electric servo-motors AMK DD5-14-10 are installed on the vehicle wheels. The electric motors are characterized by a peak torque of 21 Nm and a maximum speed of 20000 rpm and are customized for the racing purpose.

The vehicle features a 0 to 100 km/h acceleration in 2.76 s and a maximum velocity equal to 120 km/h. It is also able to reach accelerations close to 2g and 1.6g in the lateral and longitudinal direction, respectively. The vehicle battery pack has a nominal voltage equal to 600 V and it can store energy up to 7.78 kWh. Table 1 reports a list of the vehicle characteristics.

The input signals are obtained by direct measurements acquired at a frequency of 100 Hz. Specifically, digital encoders integrated in the motors provide the measurements of the wheels' velocity, a Hall effect sensor integrated in the steering rack measures the wheel steering position δ_w and an Inertial Measurement Unit (IMU) Bosch MM5.10, which is mounted close the vehicle COG, is used to obtain both the measurements of the accelerations in the three

principal directions (x , y , and z) and yaw rate r , featuring a sensitivity of 0.01 g and 0.1 deg/s, respectively. Moreover, the adopted IMU is equipped with a designed 15 Hz low-pass filter allowing to filter the measurement noise. The adopted control platform is a dSPACE MicroAutobox II, supplied with an IBM PPC 750GL-900 MHz processor and with a Real-Time Interface library block-set allowing to implement the vehicle controller developed in the MATLAB/Simulink environment.

3 Layout of the estimation method

The overall layout of the velocity estimator is shown in Figure 2. The estimator is divided in two parts: a) pre-processing block and b) FL-based system.

The inputs of the algorithm are: the rotational wheels speed (n_{fl} , n_{fr} , n_{rl} , n_{rr}), yaw rate of a vehicle γ , steering angle of the front wheels δ_w and longitudinal acceleration a_x . Additional inputs are the vehicle track width t and the geometric distance of the front and rear axles with respect to the COG (a and b in Figure 1 and Table 1, respectively). Further details of the inputs are presented in Table 2.

A driving condition selection block is fed with the measurement of the longitudinal acceleration and allows identifying five different conditions: strong braking, braking, coasting, acceleration, and strong acceleration. These are classified considering the longitudinal acceleration range definition given in Table 3.

The pre-processing phase consists of the two blocks: a) wheel speed processing and b) FL input computation. In the first task, the rotational velocities of the four wheels are transformed into linear velocity S_{fl} , S_{fr} , S_{rl} , S_{rr} , and then transposed into the vehicle COG CG reference frame, by means of the following set of kinematic expressions:

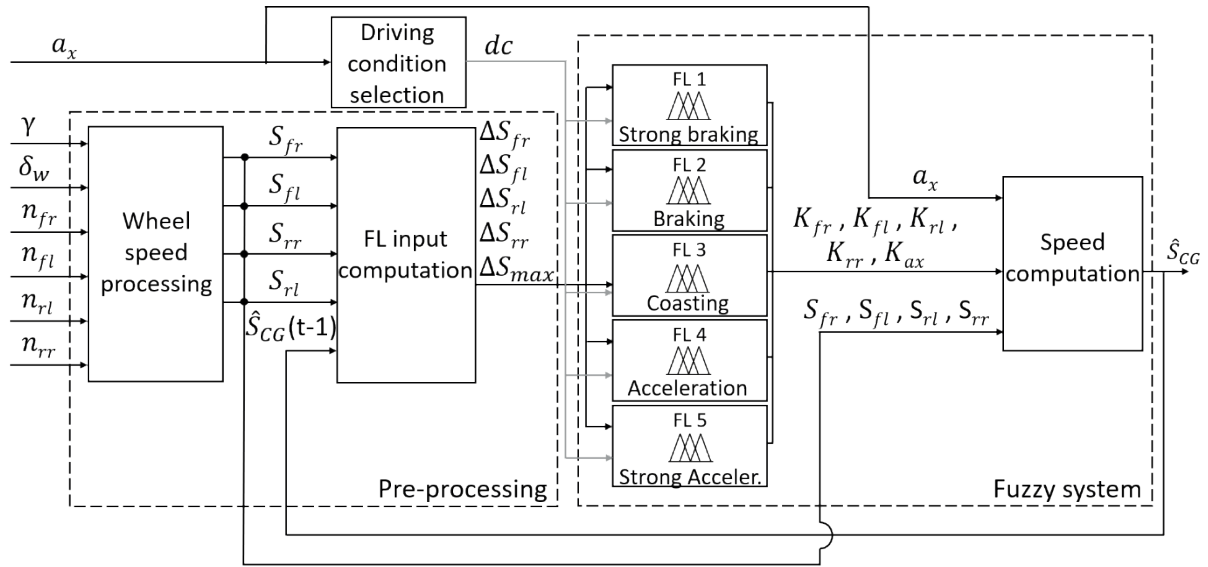


Figure 2 Layout of the estimation method

Table 2 Input signals of the estimation method. $i = \{\text{front, rear}\}; j = \{\text{left, right}\}$

variable	symbol	unit	range
rotational speed of the ij -wheel	n_{ij}	(rpm)	(0÷20000)
front wheels steering angle	δ_w	(deg)	(±105.4)
longitudinal acceleration	a_x	(g)	(±4.2)
yaw rate	γ	(deg/s)	(±163)
vehicle track width	t	(m)	(1.2)
front axle distance to COG	a	(m)	(0.854)
rear axle distance to COG	b	(m)	(0.671)

Table 3 Range definition of the five driving conditions

symbol	driving condition	longitudinal acceleration range	
		Min. (g)	Max. (g)
dc_1	strong braking	-	-0.8
dc_2	braking	-0.8	-0.3
dc_3	coasting	-0.3	0.3
dc_4	acceleration	0.3	0.8
dc_5	strong acceleration	0.8	-

$$\begin{aligned} S_{fr} &= \left[\left(n_{fr} \cdot \left(\frac{\pi}{30} \right) \cdot \left(\frac{R_w}{\tau} \right) \right) - \gamma \left(\frac{t}{2} \right) \right] \cdot \cos(\delta_w) \\ S_{fl} &= \left[\left(n_{fl} \cdot \left(\frac{\pi}{30} \right) \cdot \left(\frac{R_w}{\tau} \right) \right) + \gamma \left(\frac{t}{2} \right) \right] \cdot \cos(\delta_w) \\ S_{rl} &= \left[\left(n_{rl} \cdot \left(\frac{\pi}{30} \right) \cdot \left(\frac{R_w}{\tau} \right) \right) + \gamma \left(\frac{t}{2} \right) \right] \\ S_{rr} &= \left[\left(n_{rr} \cdot \left(\frac{\pi}{30} \right) \cdot \left(\frac{R_w}{\tau} \right) \right) - \gamma \left(\frac{t}{2} \right) \right] \end{aligned} \quad (1)$$

where $n_{fr}, n_{fl}, n_{rl}, n_{rr}$ are the angular speeds of each wheel, R_w is the wheel radius, τ is the transmission ratio. In this computation, since the sideslip angle ranges from -15° to 15° , it can be neglected with minor effects [30].

In the second task, the difference between the tire-ground contact patch and the vehicle velocity at the previous instant is computed for each wheel as:

$$\Delta S_{ij} = S_{ij}(t) - \hat{S}_{CG}(t-1). \quad (2)$$

Then, the maximum deviation between the faster and the slower tire-ground contact patch velocity is computed, using the following relation:

$$\Delta S_{\max} = |\max\{S_{ij}\}| - |\min\{S_{ij}\}|, \quad (3)$$

where $i = \{\text{front, rear}\}$ and $j = \{\text{left, right}\}$.

Here ΔS_{ij} and ΔS_{\max} are selected as inputs of the Fuzzy Logic because they contain information about the status of the wheels. i.e. normal grip, skidding, locking, spinning. In particular, ΔS_{\max} allows detecting the occurrence of limit conditions in at least one wheel and the ΔS_{ij} allows identifying the status of each wheel.

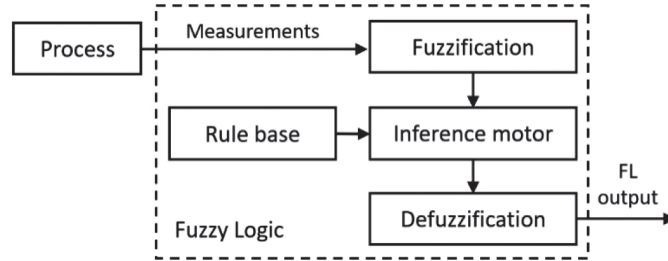


Figure 3 General architecture of a Fuzzy Logic

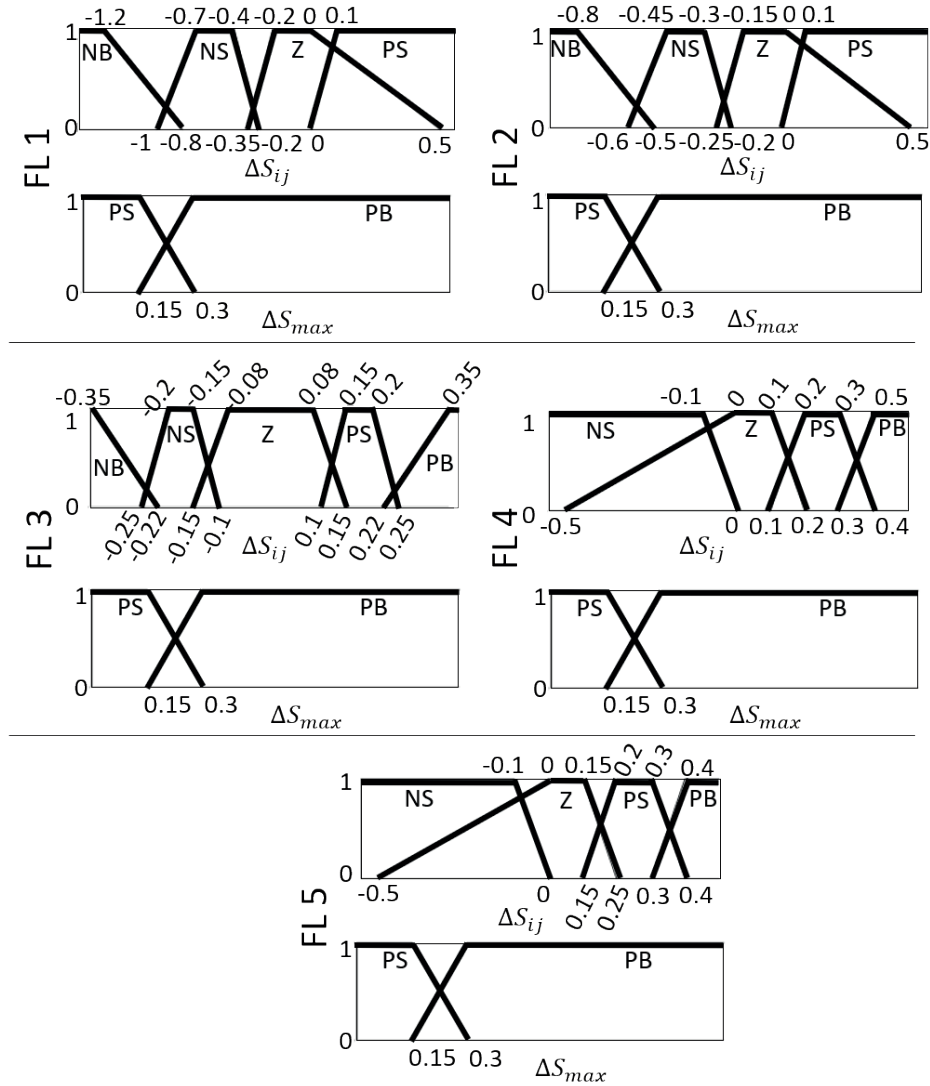


Figure 4 Input membership functions of the FLs. FL1: Strong braking. FL2: braking. FL3: coasting. FL4: acceleration. FL5: strong acceleration. Linguistic definitions: NB (Negative Big). NS (Negative Small). Z (Zero). PS (Positive Small). PB (Positive Big). S (Small) B: Big. $i = \{f, r\}$; $j = \{l, r\}$

The driving conditions' selection dc , ΔS_{ij} and ΔS_{max} are the inputs of the Fuzzy system, which include five FLs, one per each driving condition and a speed computation block implementing the following relation:

$$\dot{S}_{CG} = \frac{k_{fr} \cdot S_{fr} + k_{fl} \cdot S_{fl} + k_{rl} \cdot S_{rl} + k_{rr} \cdot S_{rr} + k_{ax} \cdot (T_s \cdot a_x)}{k_{fr} + k_{fl} + k_{rl} + k_{rr} + k_{ax}}, \quad (4)$$

where k_{fr} , k_{fl} , k_{rl} , k_{rr} , k_{ax} are the outputs of the five FLs. These coefficients express the level of credibility of the measured

velocity of each wheel. They will be equal to zero at the occurring of spinning and locking of the wheel and equal to 1 when the vehicle and tire-ground contact patch velocity are equal. In Equation (4), the contribution of the velocity, computed by integrating the longitudinal acceleration, is also considered ($k_{ax} \cdot (T_s \cdot a_x)$ at the numerator). This value is important in the case of limit adherence conditions, e.g. when the coefficients k_{fr} , k_{fl} , k_{rl} , k_{rr} are null, i.e. during the spinning and locking, even if the vehicle is still moving.

Table 4 Rules of the inference motor of FL1 (strong braking) and FL5 (strong acceleration)

	rules	input			output	
		$\Delta S_{\{fr,fl,rl,rr\}}$	ΔS_{max}	$k_{\{rl,fr\}}$	$k_{\{rl,rr\}}$	k_{ax}
FL1 (FL5)	1	Z (Z)	PS(PS)	M (M)	B (B)	-
	2	Z (Z)	PB(PB)	S (S)	M (B)	-
	3	NS (PS)	PS(PS)	S (Z)	M (M)	-
	4	NS (PS)	PB(PB)	Z (Z)	S (S)	-
	5	NB (PB)	PS(PS)	Z (Z)	Z (S)	-
	6	NB (PB)	PB(PB)	Z (Z)	Z (S)	-
	7	PS (NS)	PS(PS)	Z (Z)	Z (Z)	-
	8	PS (NS)	PB(PB)	Z (Z)	Z (Z)	-
	9	-	PS(PS)	-	-	M (M)
	10	-	PB(PB)	-	-	B (B)

Table 5 Rules of the inference motor of FL2 (braking) and FL4 (acceleration)

	rules	input			output	
		$\Delta S_{\{fr,fl,rl,rr\}}$	ΔS_{max}	$k_{\{rl,fr\}}$	$k_{\{rl,rr\}}$	k_{ax}
FL2 (FL4)	1	Z (Z)	PS(PS)	M (B)	B (B)	-
	2	Z (Z)	PB(PB)	S (N)	M (B)	-
	3	NS (PS)	PS(PS)	S (Z)	M (M)	-
	4	NS (PS)	PB(PB)	Z (Z)	S (M)	-
	5	NB (PB)	PS(PS)	Z (Z)	Z (S)	-
	6	NB (PB)	PB(PB)	Z (Z)	Z (S)	-
	7	PS (NS)	PS(PS)	Z (Z)	Z (Z)	-
	8	PS (NS)	PB(PB)	Z (Z)	Z (Z)	-
	9	-	PS(PS)	-	-	S (S)
	10	-	PB(PB)	-	-	M (M)

Table 6 Rules of the inference motor of FL3 (coasting)

	rules	input			output	
		$\Delta S_{\{fr,fl,rl,rr\}}$	ΔS_{max}	$k_{\{rl,fr\}}$	$k_{\{rl,rr\}}$	k_{ax}
FL3	1	Z	PS	M	B	-
	2	Z	PB	M	B	-
	3	PS	PS	M	M	-
	4	PS	PB	S	S	-
	5	NS	PS	M	M	-
	6	NS	PB	S	S	-
	7	PB	PS	S	S	-
	8	PB	PB	Z	Z	-
	9	NB	PS	S	S	-
	10	NB	PB	Z	Z	-
	11	-	PS	-	-	Z
	12	-	PB	-	-	S

The integration time T_s is equal to the sampling time of the estimation algorithm (0.01 s).

4 Fuzzy logic design

The overall layout of the designed FL-based system is based on the classical architecture of a Fuzzy Logic

represented in Figure 3. The first stage is the fuzzification, which converts the input measured variables, that are discretized through the adoption of membership functions, in linguistic variables. The output of this block is provided to the inference motor. This block also receives the rule base, which is defined on the basis of the designer experience. Finally, the output of the inference motor is processed by the defuzzification block by means of the

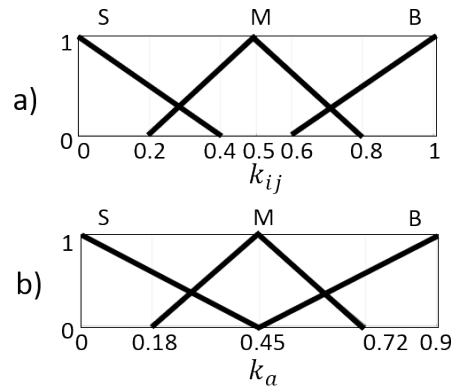


Figure 5 Output membership functions for all the FLs. a) Outputs related to the wheel velocities coefficients. b) Output related to the vehicle acceleration coefficient. Linguistic definitions: S (Small). M: Medium. B: Big. $i = \{f, r\}$; $j = \{l, r\}$

membership functions allowing to translate the output linguistic variables in numbers defined in physical units.

The inputs of the Fuzzy system adopted in this study are: the driving condition (dc), the difference between the tire-ground contact patch and the vehicle velocity (ΔS_{ij}), and the maximum deviation between the faster and the slower tire-ground contact patch velocity (ΔS_{\max}). The driving conditions allow selecting the correct FL. The inputs ΔS_{ij} and ΔS_{\max} are converted in linguistic variables and discretized by means of the membership functions. Afterwards, they are provided to the inference motor. The outputs of the Fuzzy system are the five weighting coefficients (k_{fl} , k_{fr} , k_{rl} , k_{rr} , k_{ax}) allowing to perform the final speed estimation task.

4.1 Input membership functions

The inputs ΔS_{ij} (Equation (2)) and ΔS_{\max} (Equation (3)) are provided to two sets of input membership functions. Each ΔS_{ij} input is associated to five levels (NB , NS , Z , PS , PB) through trapezoidal membership functions, which are depicted in Figure 4. The numerical definition of these levels is different for each driving condition. The selection of the membership functions is conducted with a trial and error procedure. On the other hand, the ΔS_{\max} input is associated with two levels (PS and PB) through trapezoidal membership functions, which are the same for each driving condition. The numerical levels of the functions have been defined considering that the limit condition occurs for values of ΔS_{\max} higher than 0.3.

4.2 Rule base and output membership functions

For each driving condition, the rules have been defined according to the vehicle state, in order to assign a high level of credibility to the velocity if the wheels are in the normal conditions and vice versa. During the strong braking for instance, the front axle has a higher torque applied to the wheels and this can bring to the locking of the wheels. Therefore, the rules of the rear wheels will assign a higher coefficient of reliability to the measurements of the real

wheels speed, although the reliability coefficient of all the four wheels is still the same.

Since the design of the rule base is conducted on a 4WD architecture, it is valid also for other types of vehicle's drivetrain. As a matter of fact, it is well known that the 4WD vehicle is the most critical configuration, since each wheel can spin or be locked, at any time. The rules for all the considered driving conditions (FL1, FL2, FL3, FL4 and FL5) are listed in Table 4, Table 5 and Table 6 for the strong braking and strong acceleration, braking and acceleration and coasting, respectively.

The output membership functions allow performing the defuzzification process and are defined with triangular functions on three levels (S , M , B), as represented in Figure 5. The selected defuzzification method is the centroid algorithm [31].

5 Results and discussion

The algorithm performance has been evaluated experimentally by comparing the speed estimated by the proposed technique to that obtained by a method based on the average of the speed of the four wheels. The latter is a common algorithm in many passenger vehicles and, in this study, it was already deployed on the electronic control unit of the car. The integral of the vehicle longitudinal acceleration is taken as the reference condition for both cases. In this case, possible error drifts, caused by the integral computation, are limited by resetting the integral accumulation when all the four wheels are rotating at the same speed and the steering angle is zero. In this condition, the tires are supposed to be within the adhesion limits and, consequently, the velocity of the wheels contact patch is equal to the velocity of the vehicle. This method allows obtaining a sufficiently reliable reference value. A comparison to a direct measurement of the speed is not provided in this work due to the high costs of the needed sensor.

Figure 6 shows results of the first test, which is aimed to evaluate the estimation accuracy in the case of high values of longitudinal accelerations and braking. Figure 6.a shows a severe acceleration occurring in the initial part

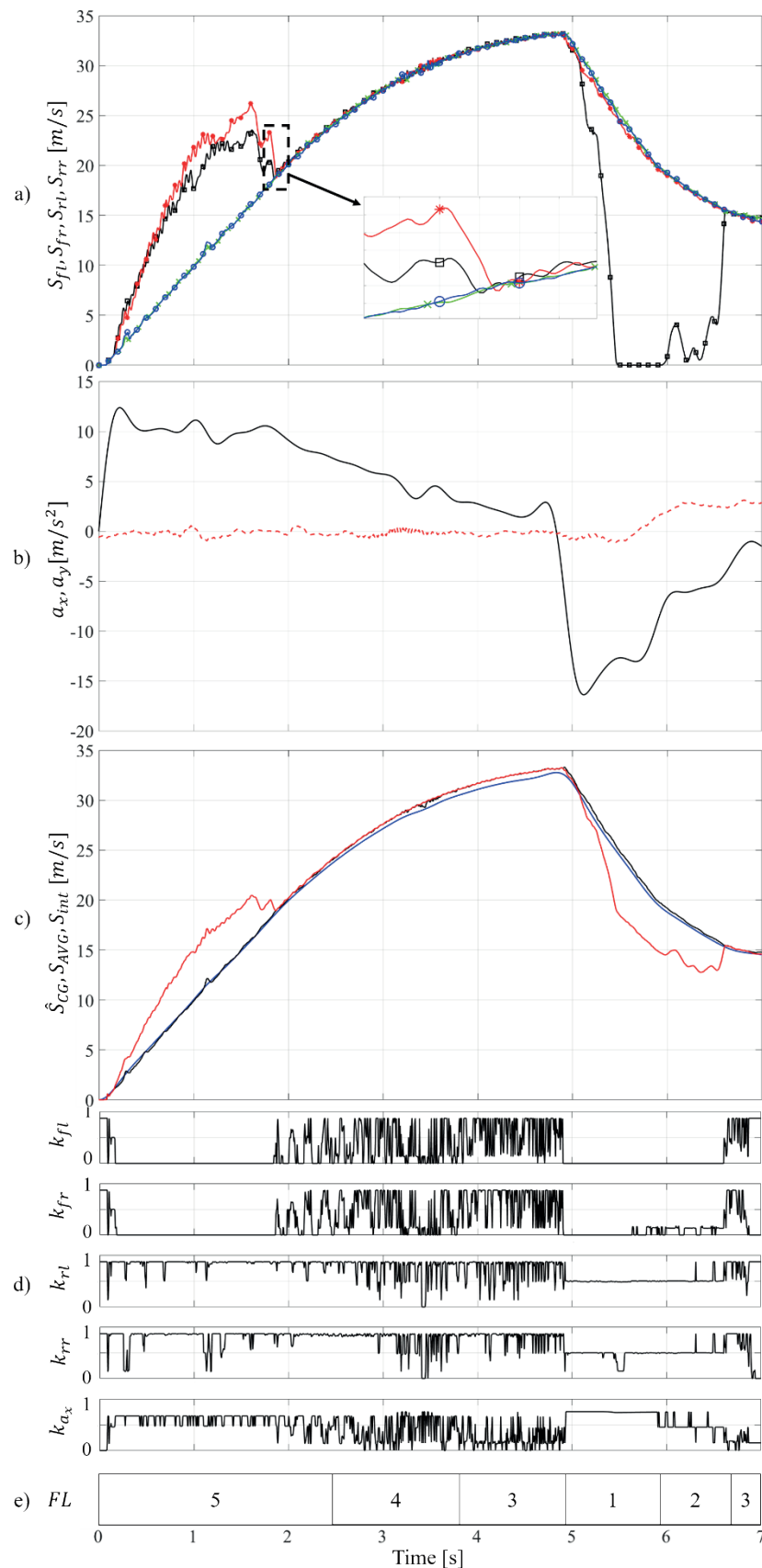


Figure 6 Strong acceleration and braking maneuver. a) Wheel speed S_{fl} (solid, black; marker: square), S_{fr} (solid, red; marker: star), S_{rl} (solid, blue; marker: circle), S_{rr} (solid, green; marker: cross). b) Longitudinal a_x (solid, black) and lateral a_y (dashed, red) acceleration. c) Estimated vehicle speed \hat{S}_{CG} (black), vehicle speed computed as the average of the four wheels speed S_{AVG} (red), reference vehicle speed obtained by integrating the acceleration \hat{S}_{int} (blue); d) Output coefficients $k_{fl}, k_{fr}, k_{rl}, k_{rr}, k_{ax}$. e) Selection of the FL obtained according to the driving condition

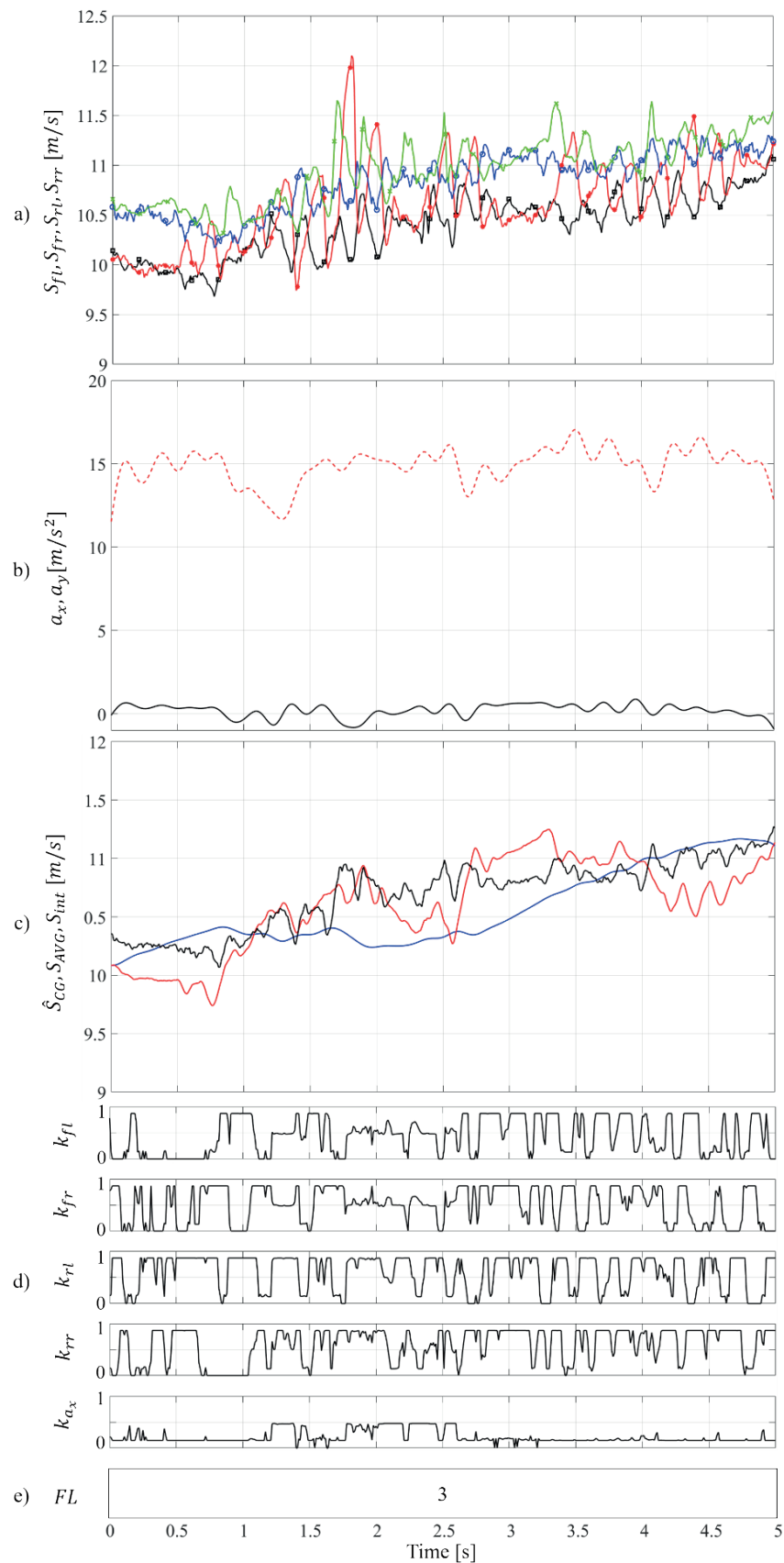


Figure 7 Skid pad maneuver. a) Wheel speed S_{fl} (solid, black; marker: square), S_{fr} (solid, red; marker: star), S_{rl} (solid, blue; marker: circle), S_{rr} (solid, green; marker: cross). b) Longitudinal a_x (solid, black) and lateral a_y (dashed, red) acceleration. c) Estimated vehicle speed \hat{S}_{CG} (black), vehicle speed computed as the average of the four wheels speed S_{AVG} (red), reference vehicle speed obtained by integrating the acceleration S_{int} (blue); d) Output coefficients $k_{fl}, k_{fr}, k_{rl}, k_{rr}, k_{ax}$. e) Selection of the FL obtained according to the driving condition

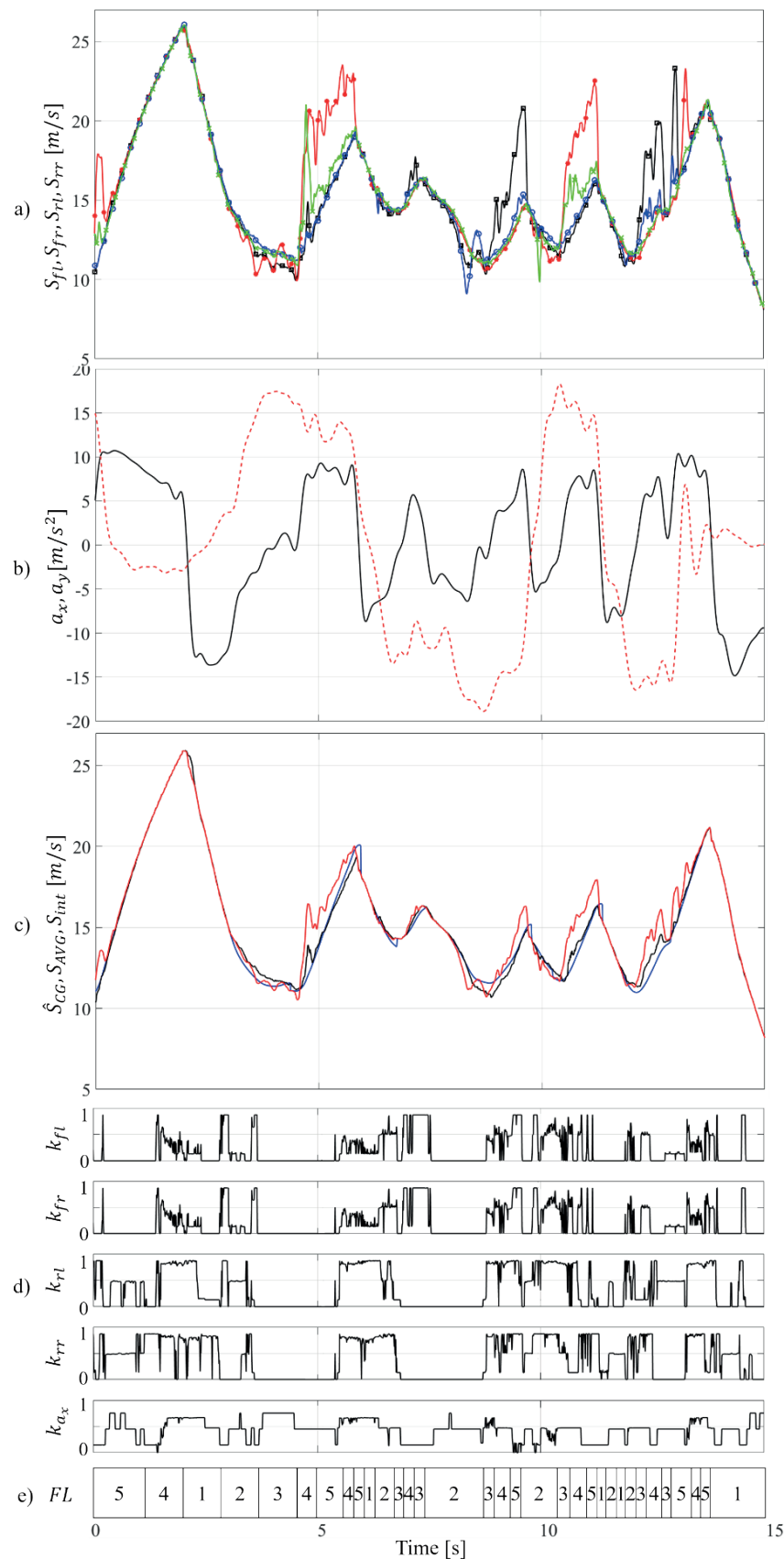


Figure 8 Portion of the complete lap track. a) Wheel speed S_{fl} (solid, black; marker: square), S_{fr} (solid, red; marker: star), S_{rl} (solid, blue; marker: circle), S_{rr} (solid, green; marker: cross). b) Longitudinal a_x (solid, black) and lateral a_y (dashed, red) acceleration. c) Estimated vehicle speed \hat{S}_{CG} (black), vehicle speed computed as the average of the four wheels speed S_{AVG} (red), reference vehicle speed obtained by integrating the acceleration S_{int} (blue); d) Output coefficients $k_{fl}, k_{fr}, k_{rl}, k_{rr}, k_{ax}$. e) Selection of the FL obtained according to the driving condition

of the acquisition. The vehicle starts from standstill with a longitudinal acceleration of about 1.3g (solid line in Figure 6.b), which leads the vehicle to hard spinning conditions caused by a huge reduction of the vertical forces on the front wheels, as visible from the solid line with the star marker (front right wheel velocity) and solid line with the square marker (front left wheel velocity). In the last part of the acquisition, a sudden deceleration takes place causing a complete lock of the front left wheel (solid line with the square marker). Figure 6.c shows comparison of estimation of the proposed method \hat{S}_{CG} (black line) to that obtained from the average of the four wheel velocities S_{AVG} (red line). Both results are compared to the reference output obtained from the integral of the acceleration S_{int} (blue line). The occurrence of the spinning and locking conditions on the front wheels causes a lack of accuracy in S_{AVG} , with an error of about 5 m/s. The estimation \hat{S}_{CG} , on the contrary, is closer to S_{int} . Figure 6.d illustrates behaviour of the output coefficients (k_{fp} , k_{fr} , k_{rp} , k_{rr}), which assume a low value in correspondence of the locking and spinning conditions and a value close to 1 in normal adherence condition.

The coefficient k_{ax} , adopted to include the contribution of the longitudinal acceleration, as described in Equation (4), varies according to the four wheels behaviour: its value is low in the case of the normal adherence conditions and is higher otherwise. The detail of the alternance of the FLs involved in the computation of the output coefficients is shown in Figure 6.e.

The second test is conducted to evaluate the method performance during the skid-pad manoeuvre, where the car is driven along a figure-of-eight circuit. The lateral acceleration is almost constant and equal to about 1.5g (dashed line in Figure 7.b) and the longitudinal acceleration has an almost null value (solid line in Figure 7.b). The plot of velocities of the four wheels is given in Figure 7.a and it shows that the wheels are very close to the adherence limit, due to the high lateral acceleration, which is the cause of slight spinning. The two rear wheels are generally faster than the front ones because of the vehicle torque distribution. Moreover, the internal wheels are slightly slower than the external ones. Figure 7.c shows that the estimation \hat{S}_{CG} is accurate with respect to the speed obtained by integrating the acceleration S_{int} . The speed computed as the average of the four wheels speed S_{AVG} is accurate as well, since the four speeds have always a similar velocity (Figure 7.a). The small difference between the four values is caused by the slip ratio of the tires and by the occurrence of the small local spinning. Figure 7.d presents behaviour of the FL

output coefficients. The occurrence of the wheels spinning is visible when one of the coefficients k_{fp} , k_{fr} , k_{rp} , k_{rr} goes to zero. In correspondence to these conditions, the coefficient related to the longitudinal acceleration (k_{ax}) increases. Figure 7.e shows that the involved FL in this case is always FL3, since the value of the longitudinal acceleration recorded during the test is always included within the range $(-0.3 \div 0.3) \text{ m/s}^2$ and, therefore, the driving condition is always *dc3*, as indicated in Table 3.

The results obtained during the portion of the track lap are illustrated in Figure 8. During the acquisition, a lateral acceleration of 2g and a longitudinal acceleration of 1.5g are recorded. In correspondence to demanding manoeuvres, front wheels spinning occurs. These conditions are visible in Figure 8.a and in Figure 8.d, where the coefficients related to the spinning wheel go to zero. The results represented in Figure 8.c demonstrate the accuracy of the proposed method both during the braking-cornering phase and the acceleration-cornering phase, even during the spinning conditions. As illustrated in Figure 8.c, the estimated vehicle speed \hat{S}_{CG} is similar to the reference S_{int} , whilst S_{AVG} is affected by a considerable estimation error. The output coefficients k_{fp} , k_{fr} , k_{rp} , k_{rr} and k_{ax} are represented in Figure 8.d. When a wheel loses the grip, k_{ax} increases its value, while the coefficients related to the wheel speed decrease. Figure 8.e shows the involved FLs according to the driving conditions.

6 Conclusions

In this paper, a vehicle speed estimation exploiting a Fuzzy Logic based algorithm has been presented. The method exploits a weighted average of the wheel velocities and longitudinal acceleration integral based on weighting coefficients produced by an FL. These coefficients allow evaluating the credibility of the measured values of the wheels speed. Five different FLs are adopted, corresponding to five driving conditions, detected by a dedicated routine based on the longitudinal acceleration. The method was validated experimentally on an AWD electric racing car in the case of different driving conditions and extreme maneuvers. The effectiveness of the solution was demonstrated by comparing the results to the output of an algorithm already deployed on the electronic control unit of the car, computing the speed as the average of velocities of the four wheels. A further comparison to the integral of the acceleration of the vehicle was presented.

References

- [1] KALA, R. *On-road intelligent vehicles: motion planning for intelligent transportation systems*. Butterworth-Heinemann, 2016. ISBN 978-0-12-803729-4.
- [2] LI, J., CHENG, H., GUO, H., QIU, S. Survey on artificial intelligence for vehicles. *Automotive Innovation* [online]. 2018, 1(1), p. 2-14. ISSN 2096-4250, eISSN 2522-8765. Available from: <https://doi.org/10.1007/s42154-018-0034-8>
- [3] ELLIOTT, D., KEEN, W., MIAO, L. Recent advances in connected and automated vehicles. *Journal of Traffic and*

- Transportation Engineering* [online]. 2018, **6**(2), p. 109-131. ISSN 2095-7564. Available from: <https://doi.org/10.1016/j.jtte.2018.09.005>
- [4] YU, F., LI, D. F., CROLLA, D. A. Integrated vehicle dynamics control - State-of-the art review. In: IEEE Vehicle Power and Propulsion Conference: proceedings [online]. IEEE, 2008. ISSN 1938-8756, p. 1-6. Available from: <https://doi.org/10.1109/VPPC.2008.4677809>
 - [5] RIND, S., REN, Y., JIANG, L. Traction motors and speed estimation techniques for sensorless control of electric vehicles: a review. In: 49th International Universities Power Engineering Conference UPEC: proceedings [online]. IEEE, 2014. p. 1-6. Available from: <https://doi.org/10.1109/10.1109/UPEC.2014.6934646>
 - [6] BEVLY D. M., GERDES J. C., WILSON C., ZHANG, G. The use of GPS based velocity measurements for improved vehicle state estimation. In: American Control Conference ACC: proceedings [online]. IEEE, 2000. ISSN 0743-1619, ISBN 0-7803-5519-9. Available from: <https://doi.org/10.1109/ACC.2000.878665>
 - [7] GUO, H., CHEN, H., LU, C., WANG, H., YANG, S. Vehicle dynamic state estimation: state of the art schemes and perspectives. *IEEE/CAA Journal of Automatica Sinica* [online]. 2018, **5**(2), p. 418-431. ISSN 2329-9266, eISSN 2329-9274. Available from: <https://doi.org/10.1109/JAS.2017.7510811>
 - [8] ZHAO, L., LIU, Z., CHEN H. Design of a nonlinear observer for vehicle velocity estimation and experiments. *IEEE Transactions on Control Systems Technology* [online]. 2011, **19**(3), p. 664-672. ISSN 1063-6536, eISSN 1558-0865. Available from: <https://doi.org/10.1109/TCST.2010.2043104>
 - [9] MOAVENI, B., ABAD, M. K. R., NASIRI, S. Vehicle longitudinal velocity estimation during the braking process using unknown input Kalman filter. *Vehicle System Dynamics* [online]. 2015, **53**(10), p. 1373-1392. ISSN 0042-3114, eISSN 1744-5159. Available from: <https://doi.org/10.1080/00423114.2015.1038279>
 - [10] KLOMP, M., GAO, Y., BRUZELIUS, F. Longitudinal velocity and road slope estimation in hybrid electric vehicles employing early detection of excessive wheel slip. *Vehicle System Dynamics* [online]. 2014, **52**, p. 172-188. ISSN 0042-3114, eISSN 1744-5159. Available from: <https://doi.org/10.1080/00423114.2014.887737>
 - [11] CHU, L., SHI, Y., ZHANG, Y., LIU, H., XU, M. Vehicle lateral and longitudinal velocity estimation based on adaptive Kalman filter. In: 3rd International Conference on Advanced Computer Theory and Engineering ICACTE: proceedings [online]. IEEE, 2010. Available from: <https://doi.org/10.1109/ICACTE.2010.5579565>
 - [12] GAO, Y., FENG, Y., XIONG, L. Vehicle longitudinal velocity estimation with adaptive Kalman filter. In: FISITA 2012 World Automotive Congress: proceedings. Berlin, Heidelberg: Springer, 2013. p. 415-423.
 - [13] CHU, L., XHANG, Y., SHI, Y., XU, M., OU, Y. Vehicle lateral and longitudinal velocity estimation using coupled EKF and RLS methods. *Applied Mechanic and Materials* [online]. 2010, **29-32**, p. 851-856. ISSN 1662-7482. Available from: <https://doi.org/10.4028/www.scientific.net/AMM.29-32.851>
 - [14] TONG, L. An approach for vehicle state estimation using extended Kalman filter. In: International Computer Science Conference ICSC 2012: proceedings [online]. Vol. 326. Communications in Computer and Information Science. Berlin, Heidelberg: Springer, 2012. ISBN 978-3-642-34380-3, eISBN 978-3-642-34381-0, p. 56-63. Available from: https://doi.org/10.1007/978-3-642-34381-0_7
 - [15] CHU, L., ZHANG, Y., SHI, Y., LIU, M., XU, M. Vehicle lateral and longitudinal velocity estimation based on unscented Kalman filter. In: 2nd International Conference on Education Technology and Computer: proceedings [online]. IEEE, 2010. ISSN 2155-1812. Available from: <https://doi.org/10.1109/ICETC.2010.5529507>
 - [16] ZHAO, Z., CHEN, H., YANG, J., WU, X., YU, Z. Estimation of the vehicle speed in the driving mode for a hybrid electric car based on an unscented Kalman filter. *Proceedings of the Institution of Mechanical Engineers, Part D: Journal of Automobile Engineering* [online]. 2015, **229**(4), p. 437-456. ISSN 0954-4070, eISSN 2041-2991. Available from: <https://doi.org/10.1177/0954407014546918>
 - [17] BANERJEE, K., VAN DINH, T., LEVKOVA, L. Velocity estimation from monocular video for automotive applications using convolutional neural networks. In: IEEE Intelligent Vehicles Symposium IV: proceedings [online]. IEEE, 2017. Available from: <https://doi.org/10.1109/IVS.2017.7995747>
 - [18] BONFITTO, A., FERACO, S., AMATI, N., TONOLI, A. Virtual sensing in high-performance vehicles with artificial intelligence. In: ASME 2019 International Design Engineering Technical Conferences and Computers and Information in Engineering Conference: proceedings [online]. Vol. 59216. American Society of Mechanical Engineers, 2019. ISBN 978-0-7918-5921-6, V003T01A005. Available from: <https://doi.org/10.1115/DETC2019-97906>
 - [19] BONFITTO, A., FERACO, S., TONOLI, A., AMATI, N. Combined regression and classification artificial neural networks for sideslip angle estimation and road condition identification. *Vehicle System Dynamics* [online]. 2019, p. 1-22. ISSN 0042-3114, eISSN 1744-5159. Available from: <https://doi.org/10.1080/00423114.2019.1645860>
 - [20] BONFITTO, A., FERACO, S., TONOLI, A., AMATI, N., MONTI, F. Estimation accuracy and computational cost analysis of artificial neural networks for state of charge estimation in lithium batteries. *Batteries* [online]. 2019, **5**(2), 47. eISSN 2313-0105. Available from: <https://doi.org/10.3390/batteries5020047>
 - [21] ABDELGAWAD, N. E. A., EL MAHDY, A., GOMAA, W., SHOUKRY, A. Estimating vehicle speed on highway roads from smartphone sensors using deep learning models. In: 2019 IEEE 31st International Conference on Tools with

- Artificial Intelligence ICTAI: proceedings [online]. Vol. 1. IEEE, 2019. p. 979-986. Available from: <https://doi.org/10.1109/ICTAI.2019.00138>
- [22] RUTHERFORD, S. J., COLE, D. J. Modelling nonlinear vehicle dynamics with neural networks. *International Journal of Vehicle Design* [online]. 2010, **53**(4), p. 260-287. ISSN 0143-3369, eISSN 1741-5314. Available from: <https://doi.org/10.1504/IJVD.2010.034101>
- [23] UZUNSOY, E. A brief review on fuzzy logic used in vehicle dynamics control. *Journal of Innovative Science and Engineering (JISE)*. 2018, **2**(1), p. 1-7. ISSN 2602-4217.
- [24] IVANOV, V. A review of fuzzy methods in automotive engineering applications. *European Transport Research Review* [online]. 2015, **7**(3), p. 1-10. ISSN 1867-0717, eISSN 1866-8887. Available from: <https://doi.org/10.1007/s12544-015-0179-z>
- [25] JIN, L., CHEN, P., ZHANG, R., LING, M. Longitudinal velocity estimation based on fuzzy logic for electronic stability control system. *Advances in Mechanical Engineering* [online]. 2017, **9**(5), p. 1-12. Available from: <https://doi.org/10.1177/1687814017698662>
- [26] BASSET, M., ZIMMER, C., GISSINGER, G. L. Fuzzy approach to the real time longitudinal velocity estimation of a FWD car in critical situations. *Vehicle System Dynamics* [online]. 1997, **27**(5-6), p. 477-489. ISSN 0042-3114, eISSN 1744-5159. Available from: <https://doi.org/10.1080/00423119708969343>
- [27] GAO, X., YU, Z. XU, T. Longitudinal velocity estimation of electric vehicle with 4 in-wheel motors. *Vehicle Dynamics and Simulation* [online]. 2008, **01**, 0605. ISSN 0148-7191, eISSN 2688-3627. Available from: <https://doi.org/10.4271/2008-01-0605>
- [28] DAISS, A., KIENCKE, U. Estimation of vehicle speed fuzzy-estimation in comparison with Kalman-filtering. In: IEEE Proceedings of International Conference on Control Applications: proceedings [online]. 1995. ISBN 0-7803-2550-8, p. 281-284. Available from: <https://doi.org/10.1109/CCA.1995.555716>
- [29] Electric Vehicles - Formula Student Rules 2018 [online]. Version: 1.1. 2018, p. 68-86. Available from: https://www.formulastudent.de/uploads/media/FS-Rules_2018_V1.1.pdf
- [30] TAHAMI, F., FARHANGI, S., KAZEMI, R. A fuzzy logic direct yaw-moment control system for all-wheel-drive electric vehicles. *Vehicle System Dynamics* [online]. 2004, **41**(3), p. 203-211. ISSN 0042-3114, eISSN 1744-5159. Available from: <https://doi.org/10.1076/vesd.41.3.203.26510>
- [31] SIVANANDAM, S. N., SUMATHI, S., DEEPA, S. N. *Introduction to fuzzy logic using MATLAB*. Vol. 1. Berlin: Springer, 2007. ISBN 978-3-540-35781-0.

ASSESSMENT OF TECHNICAL CONDITION OF AN ACCUMULATOR COMMON RAIL INJECTOR BY TEMPERATURE OF ITS UNITS

Ildar Gabitov^{1,*}, Andrei Negovora¹, Azamat Valiev¹, Vladimir Ilin², Danila Plotnikov¹, Mahmut Razyapov³

¹Department of Automobiles and Machine - Tractor Complexes, Federal State Budgetary Educational Establishment of Higher Education Bashkir State Agrarian University, Ufa, Russian Federation

²Department of Computer Science and Information Technology, Federal State Budgetary Educational Establishment of Higher Education Bashkir State Agrarian University, Ufa, Russian Federation

³Department of Infectious Diseases, Zoohygiene and Veterinary Sanitary Inspection, Federal State Budgetary Educational Establishment of Higher Education Bashkir State Agrarian University, Ufa, Russian Federation

*E-mail of corresponding author: gabitov.ildar@yahoo.com

Resume

This paper presents a method for the vehicle speed estimation with a Fuzzy Logic based algorithm. The algorithm acquires the measurements of the yaw rate, steering angle, wheel velocities and exploits a set of five Fuzzy Logics dedicated to different driving conditions. The technique estimates the speed exploiting a weighted average of the contributions provided by the longitudinal acceleration and the credibility assigned by the Fuzzy Logics to the measurements of the wheels' speed. The method is experimentally evaluated on an all-wheel drive electric racing vehicle and is valid for the front and rear wheel drive configurations. The experimental validation is performed by comparing the obtained estimation with the result of computing the speed as the average of the linear velocity of the four wheels. A comparison to the integral of the vehicle acceleration over time is reported.

Article info

Received 2 April 2020

Accepted 19 August 2020

Online 4 February 2021

Keywords:

automotive engineering,
vehicle dynamics,
fuzzy logic,
electric vehicles,
speed estimation

Available online: <https://doi.org/10.26552/com.C.2021.2.B130-B138>

ISSN 1335-4205 (print version)

ISSN 2585-7878 (online version)

1 Introduction

Almost all the modern diesel fuel equipment (FE) is provided with microprocessor controls and is characterized by high injection pressures (up to 220-250 MPa), due to high requirements for the level of energy, economic and primarily environmental indicators of internal combustion engines [1-6]. The most promising from fulfilling all the strict requirements for emission of harmful substances, noise level and fuel economy are accumulator fuel supply systems of the Common Rail (CR) type [7-10].

The design documentation establishes the criteria for the limit state of diesel fuel supply systems, by the design documentation of its manufacturers and their values are measured during diagnosis, which is aimed at identifying the correspondence of the actual parameters to the pre-launch ones. The comparative analysis of more than 500 major electronic injectors malfunctions of the CR type was carried out in the service companies for technical maintenance of diesel FE Bashdiesel LLC (Russia, Ufa) and Carwood Motor Units Ltd. (Great Britain, Birmingham). They showed that the main wear of units of this type in Russia is of the shut-off valve (control unit). In the UK they are of the atomizer (loss of hydro-density along the leading

surface of the atomizing unit) (Figure 1). It is explained, first of all, by the worse operating conditions and the quality of diesel fuel (the friction medium is low molecular weight liquid (fuel) [1, 9]. It is currently impossible to determine the malfunction of a particular unit by the *in situ* way even by measuring fuel consumption for control [1, 7, 11], because its increase may indicate a malfunction of the sprayer and / or control valve. It is necessary to disassemble the injector from the engine and conduct the non-motor tests to assess the compliance of operational parameters with the pre-launch ones for specific modes (VL - maximum load (maximum torque), EM - average load, LL - idle speed, VE - preliminary injection) specified in the test plan [9, 12-13]. The technical condition of a particular unit can be assessed, in the most cases, only after passing through the entire test cycle with the subsequent replacement/adjustment of "faulty" elements. The complexity of such a work is 15-30 min/person for each injector, since replacing one of its units does not guarantee the serviceability of another (re-conducting the entire test cycle is required) [1, 7].

The purpose of this research is to determine the operational parameters of the CR-injectors, allowing them to evaluate the technical state of the units in an *in situ* way. The research objective is to define a dependency between



This is an open access article distributed under the terms of the Creative Commons Attribution 4.0 International License (CC BY 4.0), which permits use, distribution, and reproduction in any medium, provided the original publication is properly cited. No use, distribution or reproduction is permitted which does not comply with these terms.

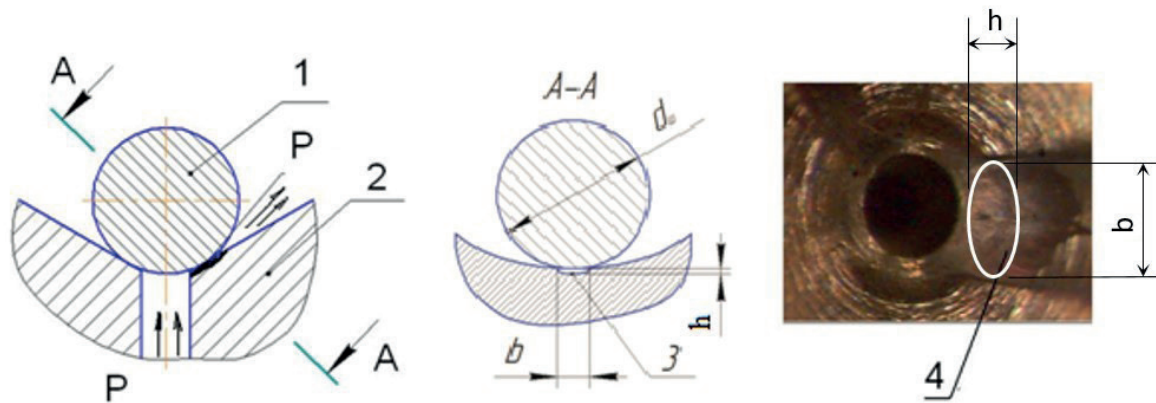


Figure 1 Design of the gap (darkened) in the pair “valve seat - ball” d_b - is the diameter of the ball; h - is the depth of the wear groove; b is the width of the wear groove; 1 - valve ball; 2 - valve seat; 3 - profile of the wear groove (clearance); 4 - a view of a valve seat wear groove (top view without a ball)

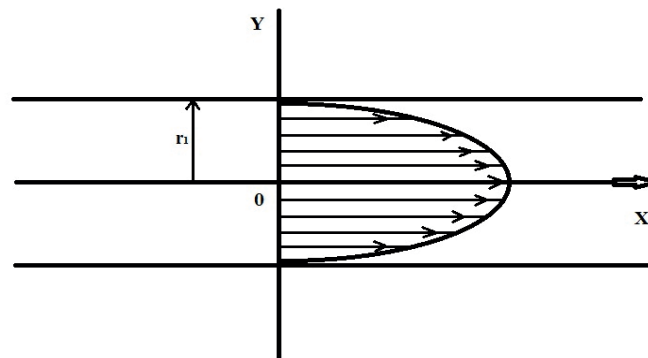


Figure 2 Distribution of flow rates of a viscous fluid in a circular pipeline with a steady flow

the technical state of CR units and the temperature. There are various methods (vibroacoustic, spectrographic, magnetoelectric, thermal, hydraulic, gas-analytical, kinematic) of *in situ* and disassembled diagnostics are used to assess the technical condition of CR type FE. In this case, the thermal method was preferable.

2 Materials and methods

2.1 Equipment

The non-motor tests were carried out in accordance with the State Standard 105178 and 10579, ISO 4008, ISO 8984 [14-16] using a specialized test bench for adjusting and testing diesel FE EPS 708 with Bosch electronic measuring system KMA 802 [12-13]. The diesel FE tests were carried out according to the test plans in its software control system, with a CRI retrofit kit for testing Common Rail injectors of the corresponding makes and models. As a test fluid, Shell Calibration Fluid S.9365 process fluid was used, which meets the requirements of ISO 4113 [7, 12].

The test bench has the water cooling and an electric heater built into the fuel tank, which allows to set and maintain the required temperature of the process fluid at the injector inlet. In the case of using the KMA 802

measuring system, the measurement of the cyclic fuel supply is much faster than in the “beaker” system, i.e. in the course of one measurement, the temperature of the fuel inside the tested FE can be considered constant. In addition, the use of electronic KMA 802 allows to exclude errors in the deposition of fuel / drain and the impact of the subjective human factor on the measuring process [9].

For the experiments, a Testo-875 thermal imager was used, the calibration of which (determination of the emissivity) for taking thermograms was carried out using an electronic thermometer W1209. The radiation coefficient for the CR-injector of the Altai Precision Devices Factory (APDF) A- 04-011-00-00-03 was 0.35.

2.2 Modeling

For more than 95% of time during the operation, the electronic injector shut-off valve is in the closed state and the size of the section of the valve clearances during wear is no more than 5% of its bore in the open state [1, 9]. Fuel leaks in the closed valve position occur only through the clearance in the valve seat mating (Figure 1).

According to studies [1], the surface wear section of a technically faulty valve is half the ellipse (item 4 in Figure 1) and the maximum wear occurs on the valve seat [2].

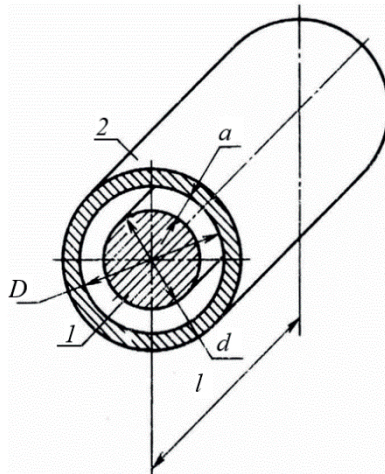


Figure 3 Design scheme of the annular gap

The main movement of the fluid flow in this case occurs along the wear groove (Figure 2), representing the outflow of fluid through the nozzle. For a steady flow (constant pressure at the inlet of the injector) it can be expressed by the transformation of the Navier-Stokes equation at $r = r_1$; $u_x = 0$ and $r = 0$ ($\frac{du_x}{dr} = 0$) (Equations (1)-(4)), where μ is the flow coefficient (dynamic viscosity); u is the fuel flow rate through the gap; V is the fluid flow rate; l is the hydraulic diameter of the gap (gap length); ΔP - differential pressure in the gap; Q is the fluid flow rate; F is the wear cross-sectional area. Thus, with a steady flow characteristics of the CR systems, the maximum fluid velocity will be two times higher than the average flow velocity [17-18].

$$\frac{dP}{dx} = \mu \left(\frac{d^2 u_x}{dr^2} + \frac{d^2 u_x}{r dr} \right) = \mu \frac{1}{r} \frac{d}{dr} \left(r \frac{\partial u_x}{\partial x} \right), \quad (1)$$

$$u_{\max} = \frac{\Delta P}{4\mu l} r_1^2, \quad (2)$$

$$V_{cr} = \frac{Q}{F} = \frac{1}{\pi r_1^2} \int_0^{r_1} \frac{\Delta P}{4\mu l} (r_1^2 - r^2) 2\pi r dr = \frac{\Delta P}{8\mu l} r_1^2, \quad (3)$$

$$V_{cp} = \frac{1}{2} u_{\max}. \quad (4)$$

The fluid flow through a precision pair of “atomizer guide - its body” (with their fluid density not meeting the technical requirements) can be represented by Equation (5). Thad defines fluid movement through an annular gap (where the height a is much smaller than the diameter d , and the gap can be considered flat, where height $a_0 = (D - d)/2$, width $b = \pi d$) (Figure 3).

$$Q_{a.g.} = \frac{\pi d a^3}{12\mu l} \Delta p. \quad (5)$$

If the annular gap is not concentric, which is typical when the nozzle is worn along the needle guide part, then the height of the gap is:

$$a = \frac{D}{2} - \frac{d}{2} + e \cos \varphi = a_0 (1 + \varepsilon \cdot \cos \varphi), \quad (6)$$

where:

e is the eccentricity;

φ is the angle determined by the eccentricity over a length l ,

$\varepsilon = e / a_0$ - relative eccentricity.

Upon the contact of the plunger 1 with the sleeve 2 (Figure 1) (relative eccentricity $e = 1$), a stream will flow through the resulting non-concentric annular gap, 2.5 times more than the flow in the concentric gap:

$$Q_{n.a.g.} = Q_{a.g.} \left(1 + \frac{3}{2} \varepsilon^2 \right) = 2.5 Q_{a.g.}. \quad (7)$$

Thus, an increase in the liquid flow rates of the worn-out precision pairs of control units and spraying of the CR injector (2 and 2.5 times, respectively) can affect the temperature regime of their operation due to the hydrodynamic friction of the fuel in its channels.

2.3 Data analysis

The experimental technique was as follows: several CR-injectors of the APDF A-04-011-00-00-03 of the YaMZ-6565 / -6585 EURO-4 diesel engine, with previously known malfunctions of the corresponding units, as well as injectors in the entirely correct technical condition, were selected. Then, they were installed alternately on the EPS 708 stand with KMA 802 and tests were carried out with an absolute ramp pressure (for 160 MPa) indicated in the test plan. During the tests, the temperatures of the control units and injector atomization, cyclic supply and fuel consumption for control, were measured (Figures 4-7). The temperature at the inlet of the injector inlet was maintained in the range of 40 ± 1 °C, the duration of the “warm-up” of the injector before testing was 1000 cycles (1 minute at an injection frequency of 1000 injections / min). As the most informative mode affecting the temperature of the CR-injector units, the maximum torque mode was selected at which the pressure at the injector inlet is maximum and, as a result, the hydrodynamic friction and heating of the units were the greatest.

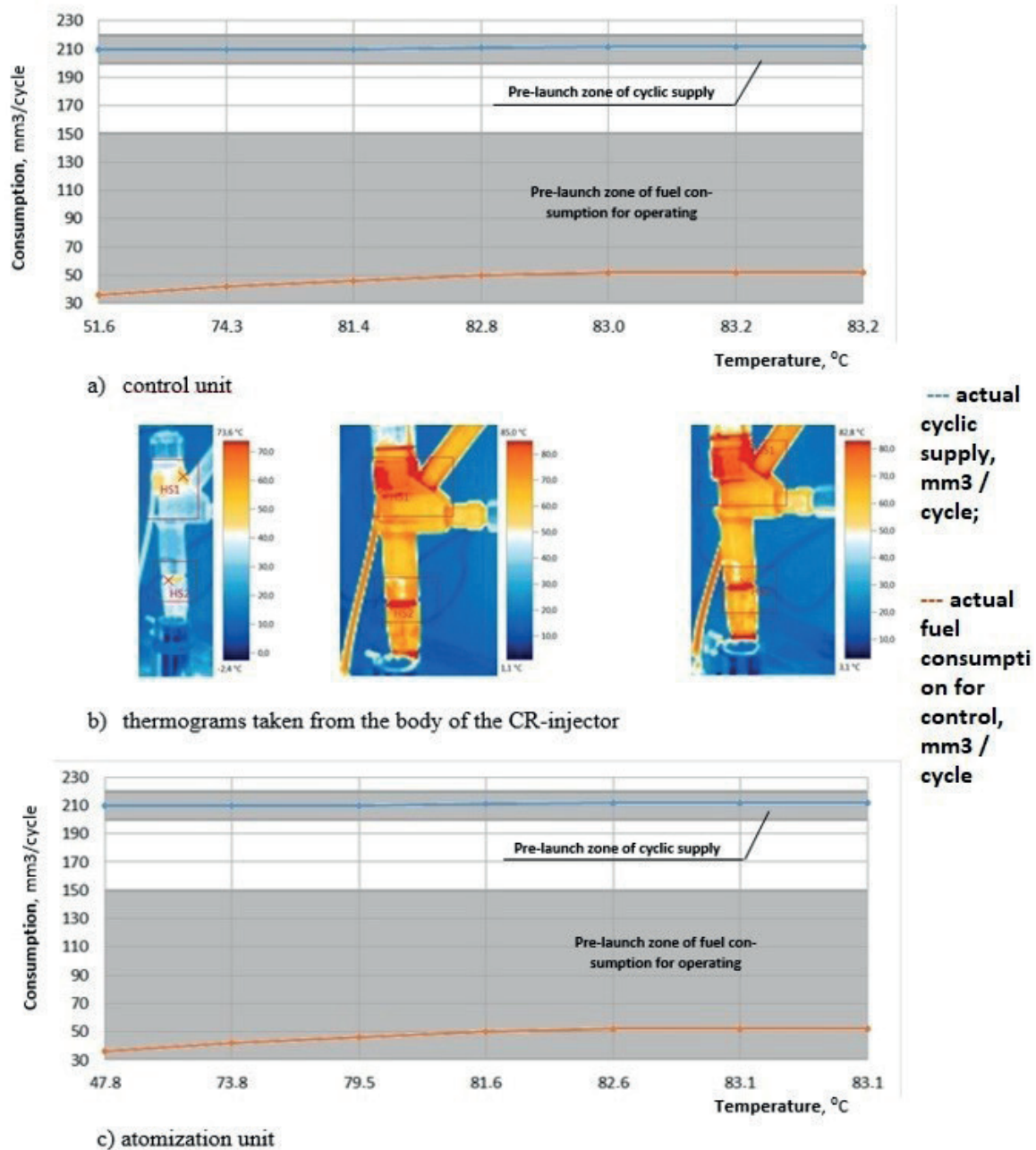


Figure 4 Dependences of the cyclic supply and fuel consumption for control on temperature of the housing of injection units (c) and control (a); thermograms taken from the body of the CR-injector of the APDF A - 04-011-00-00-03 with a serviceable control valve and atomizer (b)

3 Results and discussion

At the first stage, to verify the assumption about the dependence of operational parameters on temperature of the CR-injector units, the tests were carried out on a technically correct injector, the parameters of which are in the pre-launch zone according to the manufacturer's test plan (Figure 4). Changes in the cyclic flow at different temperatures of the body units are not significant and amounted to 204-206 mm³ / cycle, which corresponds to pre-launch values of 210 ± 10 mm³ / cycle. The temperature differences between the control and spraying units are practically negligible. Figure 6 shows that the temperature

increase of the CR-injector units is observed in the range of 1000-6000 injections (the first 6 minutes, not counting the warm-up mode) and then, due to heat and mass transfer, it stabilizes and evens out.

The second stage of the tests was to determine dependences of the operating parameters on the temperature of the CR-injector units under various technical conditions ("faulty control unit - correct atomization unit", "serviceable control unit - faulty atomization unit", "faulty control unit-defective atomization unit") (Figures 5-7). With a faulty control unit and a working atomizer, the temperature of the first unit is 10-20 °C higher during the first 4000 test cycles than the second (as in the case of a failure of both units)

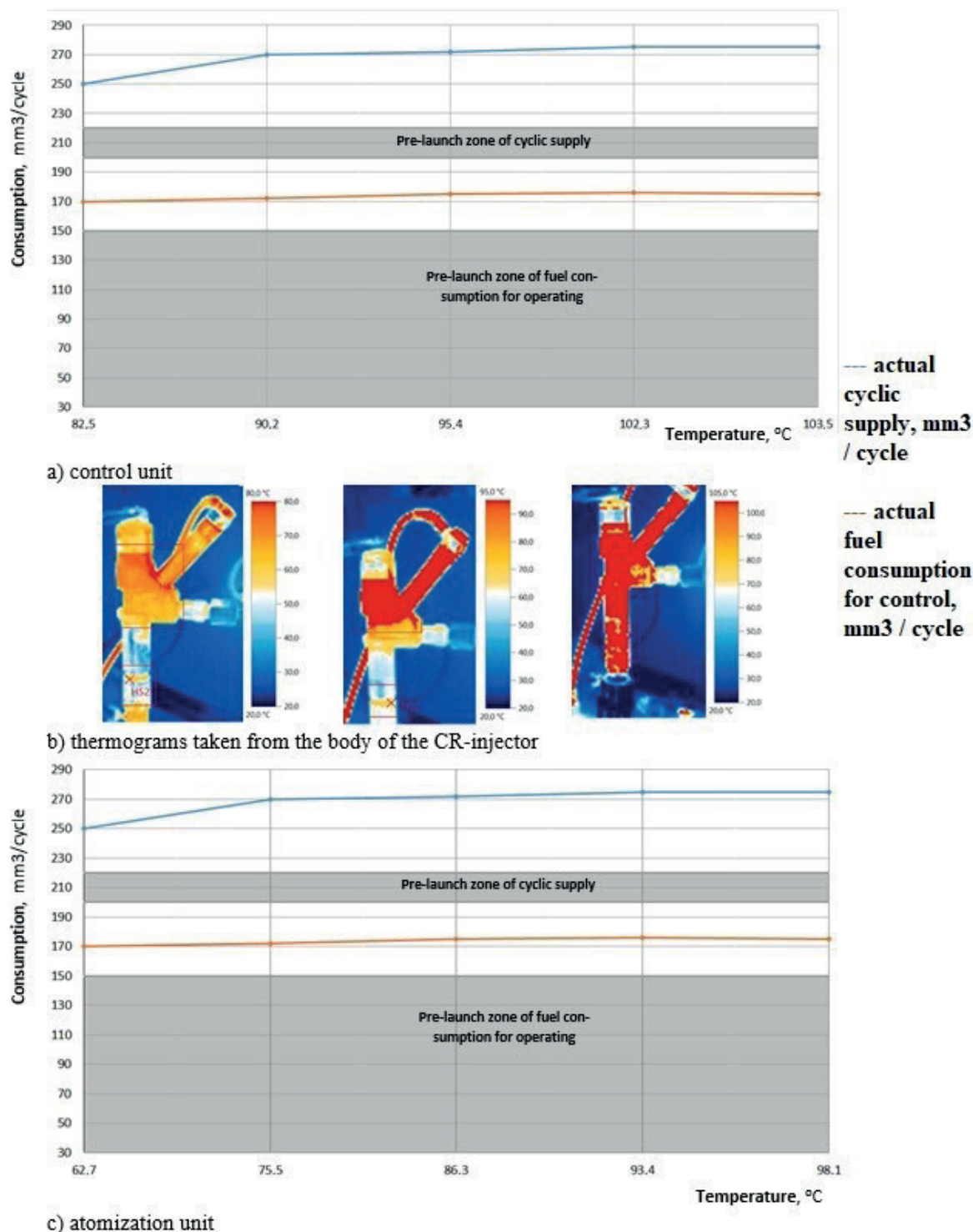


Figure 5 Dependences of the cyclic supply and fuel consumption for control on temperature of the housing of injection units (c) and control (a); thermograms taken from the body of the CR-injector of the APDF A - 04-011-00-00-03 (b) with a faulty control valve and serviceable sprayer

(Figures 5, 7) With the opposite faulty units - the situation changes to the opposite, but the temperature difference is already less significant $\approx 5^\circ\text{C}$ (Figure 8).

The test results showed that the temperature of the units of the electronic injector can unambiguously characterize the technical condition of its units (scale: “working-faulty”) and can be used to develop an *in situ* diagnostic method. Thus, a significant temperature difference between the

control and spraying units characterizes the malfunction of the first.

The injector with faulty units can heat up to temperatures above 100°C , which is not safe when working on a car.

In existing technologies for diagnosing the CR-injectors, the technical condition of the product is evaluated only by measuring the fuel consumption for control and fuel delivery [1-2, 5, 7-8, 11-13, 17, 19-20], which characterizes

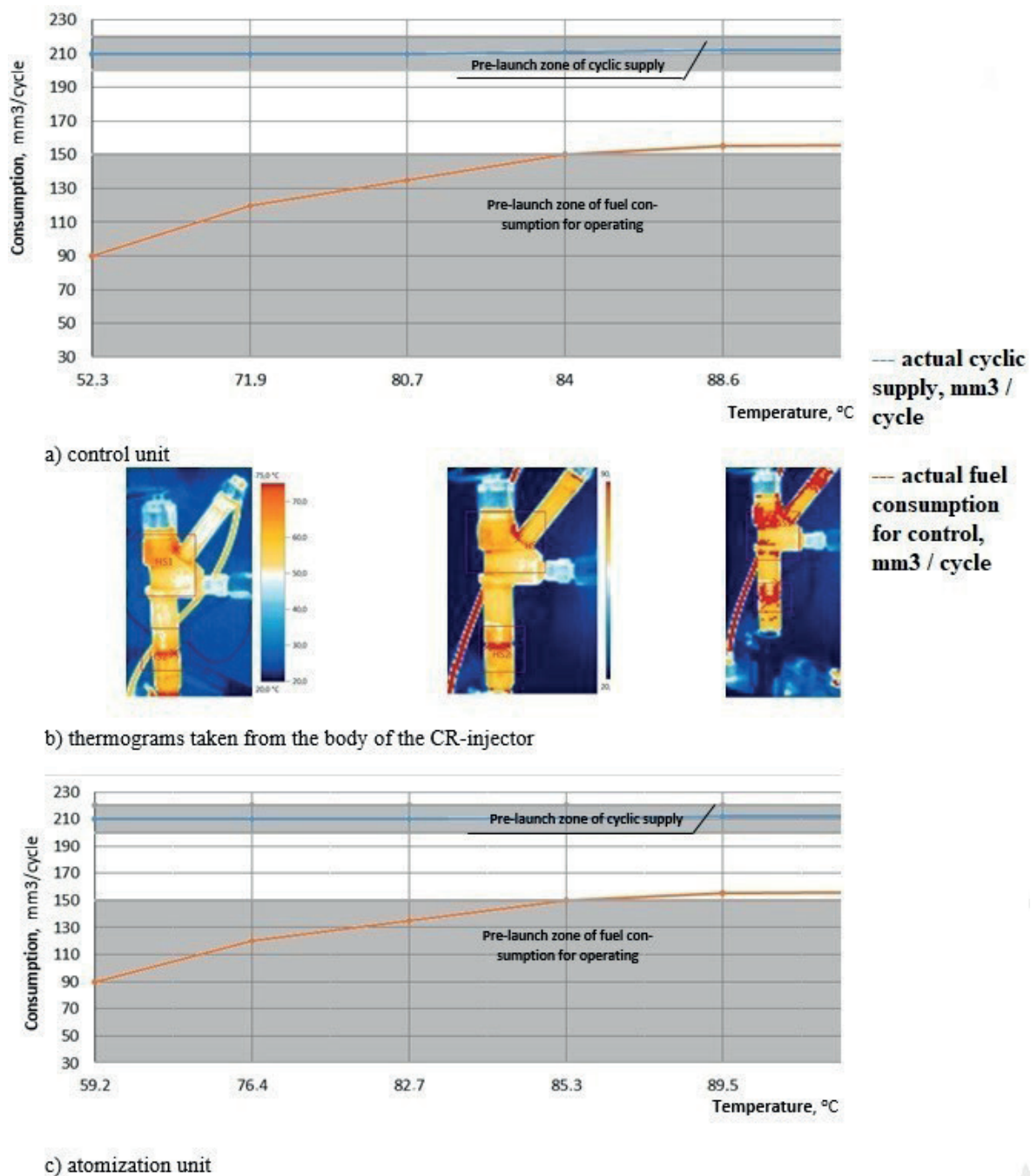


Figure 6 Dependences of the cyclic supply and fuel consumption for control on temperature of the housing of injection units (c) and control units (a); thermograms taken from the body of the CR-injector of the APDF A - 04-011-00-00-03 with a serviceable control valve and a faulty atomizer (b)

the technical condition of the whole product. For example, in research [1] the authors suggest a hardening injectors valve unit to increase the life cycle of injectors. In article [4] researchers give a result of influences of fuel temperature on electromagnetic actuator operation. But they use standard Bosch's technologies to test the technical state of the whole unit. In publications [8, 12] various technologies and test benches are reported, but none of them uses temperature as a diagnostic parameter.

The results of the obtained experimental studies coincide with the works of Kolev [6] and Versteeg and Malalasekera [18], who established the pressure dependence

on its temperature increase (at pressures of 200 MPa, the temperature increased to 120 °C), by methods of numerical simulation the solution of the Navier-Stokes equation on an unstructured grid for hydrodynamic processes of a single-phase fluid flow. It is due to fluid flows through small gaps at high speeds (the so-called viscous heating), which is typical for the fuel movement through "ball-to-seat", "seat-stem" pairs of the control valve and the "atomizer needle - its body" of the atomizer unit [18, 21-31]. Use of temperature of the housing units for atomizing and control as a diagnostic parameter makes it possible to determine the malfunction of a specific injector unit.

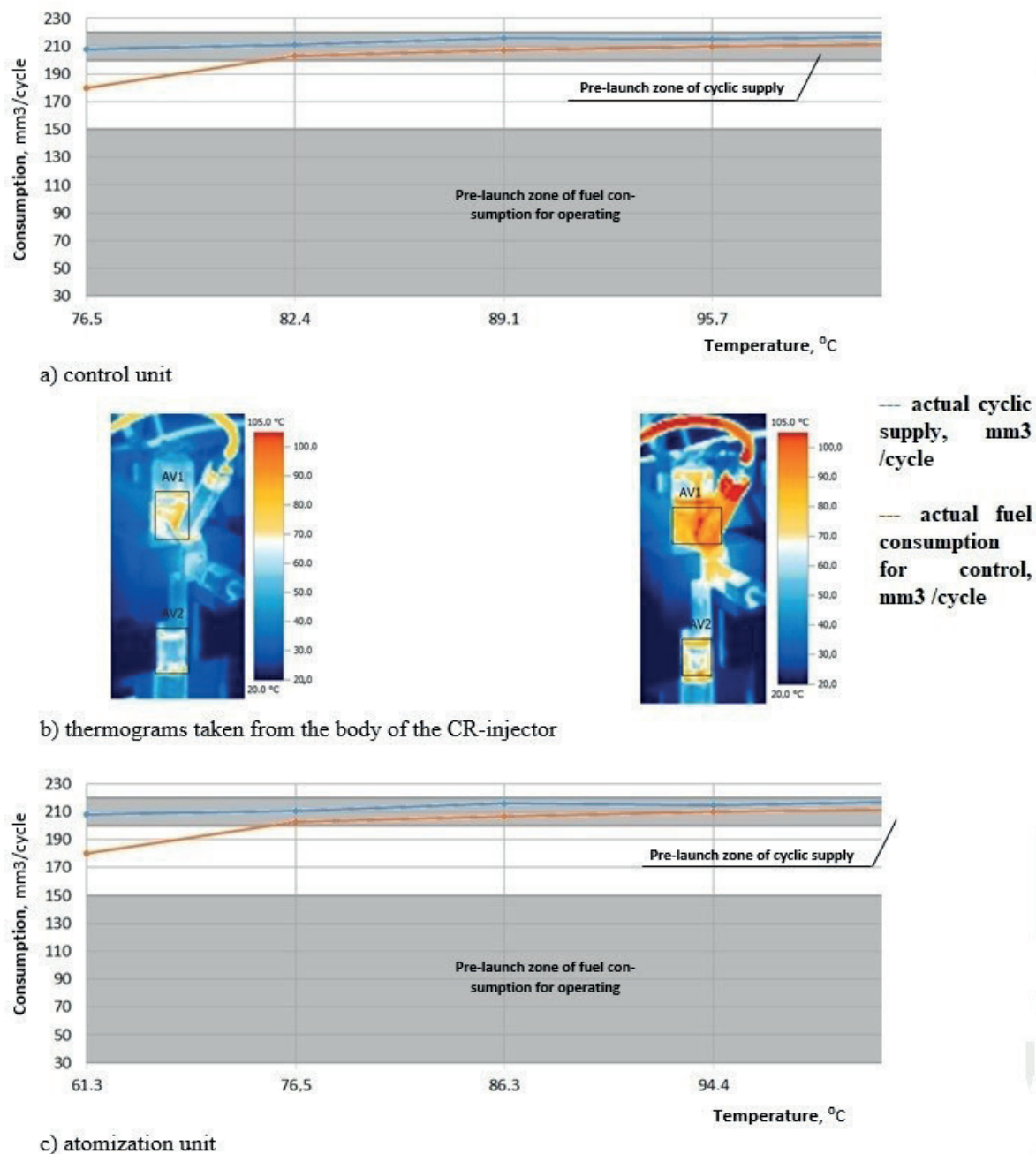


Figure 7 Dependences of the cyclic supply and fuel consumption for control on temperature of the housing of injection units (c) and control (a); thermograms taken from the body of the CR nozzle of the AZPI A - 04-011-00-00-03 with a faulty control valve and sprayer (b)

4 Conclusions

In existing technologies, replacement of one broken CR unit does not guarantee the serviceability of another (repeated testing of the entire test cycle is required). Suggested technology guarantees the more exact detection of the broken node(s) of CR injectors. So, the labor time is decreased from 30 to 15 min/person for each injector in the cases of the control and spraying units malfunction, either at the same time or one of them. The tests should be carried out at maximum torque mode, as the pressure at the inlet of the injector is maximum (according to the test plans of the FE manufacturing plants) and,

as a result the hydrodynamic friction and heating of the units are the greatest. The temperature of the electronic injector units characterizes the technical condition of its units: a significant temperature difference between the control and atomizing units "indicates" the malfunction. It is necessary to "warm-up" the electronic injector by leakage to the "return", it is necessary to "warm it up" to ≈ 70 °C ("run" the injector at the pressure of the VL point (1600 bar) for the first 3000 cycles (but not later than 5000 cycles) and only then to search for a "worn-out" unit by measuring the temperature of its units. "Run" (injector heating) is due to the time required to heat the elements of the "worn-out" units by the hydrodynamic friction of the fuel through

the element gaps. However, due to the heat-mass transfer effect after 5000 test cycles the temperature of the units is equalized.

The presented studies can serve as a basis for development of an *in situ* method for diagnosing the nodes of the CR-injectors by their temperature.

References

- [1] GABITOV, I. I., SAIFULLIN, R. N., FARHSHATOV, M. N., NEGOVORA, A. V., MUDARISOV, S. G., KHASANOV, E. R., VALIEV, A. R. Hardening of electrohydraulic injectors valve units of diesels at repair. *Journal of Engineering and Applied Sciences* [online]. 2018, **13**(S8), p. 6478-6486. ISSN 1816-949x, eISSN 1818-7803. Available from: <https://doi.org/10.36478/jeasci.2018.6478.6486>
- [2] ZHENG, L., XINGWANG, G. Factor analysis used in pulsed infrared thermographic NDT. *Journal of Beijing University of Aeronautics and Astronautics* [online]. 2010, **36**(5), p. 622-626. ISSN 1001-5965.
- [3] FERRARI, A., PIZZO, P. Fully predictive Common Rail fuel injection apparatus model and its application to global system dynamics analyses. *International Journal of Engine Research* [online]. 2017, **18**(3), p. 273-290. ISSN 1468-0874, eISSN 2041-3149. Available from: <https://doi.org/10.1177/1468087416653246>
- [4] SHAO, J., GREKHOV, L. Effect of fuel temperature on operation of high-speed electromagnetic actuator common rail injector. In: International conference on industrial engineering, applications and manufacturing ICIEAM 2019: proceedings. Institute of Electrical and Electronics Engineers Inc, 2019. eISBN 978-1-5386-8119-0, p. 1-6.
- [5] THEVENIN, D., JANIGA, G. *Optimization and computational fluid dynamics*. Springer Science & Business Media, 2008. ISBN 978-3-540-72152-9.
- [6] KOLEV, N. I. *Multiphase flow dynamics 1: fundamentals*. Vol. 1. Springer Science & Business Media, 2007. ISBN 978-3-540-69832-6.
- [7] GREKHOV, L. V., GABITOV, I. I., NEGOVORA, A. V. *Design, calculation and technical service of fuel-supplying diesel systems: training manual for students of universities enrolled in the specialties Internal Combustion Engines, Technology of service and repair of machinery in the agricultural sector, Agricultural mechanization: rivers*. Legion-Avtodata, 2013. ISBN 978-5-88850-582-3.
- [8] GABITOV, I. I., NEGOVORA, A. V., FEDORENKO, V. F. *Intellectualization of the technical service of fuel-supplying diesel systems*. Moscow: Rosinformagroteh, 2018. ISBN 978-5-7367-1398-1.
- [9] BASHIROV, R. M. *Automotive engines: design, the basics of theory and calculation*. 2. ed. Ufa: Bashkir State Agrarian University, 2017. ISBN 978-5-7456-0391-4
- [10] ZHAO, J., YUE, P., GREKHOV, L., WEI, K., MA, X. Temperature and frequency dependence of electrical iron effects on electromagnetic characteristics of high-speed solenoid valve for common rail injector. *International Journal of Applied Electromagnetics and Mechanics* [online]. 2019, **60**(2), p. 173-185. ISSN 1383-5416, eISSN 1875-8800. Available from: <https://doi.org/10.3233/JAE-180022>
- [11] GREKHOV, L., DENISOV, A., STARKOV, E. Diesel fuel injection by pressure up to 400 MPa. *International Journal of Pharmacy and Technology*. 2016, **8**(4), p. 27208-27215. eISSN 0975-766X.
- [12] MASING, M. V., TER-MKRTICHYAN, G. G., STARKOV, E. E. On certified tests of the new generation fuel equipment. *Journal of Automobile Engineers*. 2015, **3**(92), p. 50-53. ISSN 2073-9133, eISSN 2073-9141.
- [13] SALVADOR, F. J., PLAZAS, A. H., GIMENO, J., CARRERES, M. Complete modelling of a piezo actuator last-generation injector for diesel injection systems. *International Journal of Engine Research* [online]. 2014, **15**(1), p. 3-19. ISSN 1468-0874, eISSN 2041-3149. Available from: <https://doi.org/10.1177/1468087412455373>
- [14] State Standard 10578-95 Fuel diesel pumps. General specifications. Interstate standard diesel fuel pumps [online] [accessed 2020-03-05]. Available from: <http://docs.cntd.ru/document/120023277>.
- [15] State Standard 10579-2017. Diesel nozzles. Technical requirements and test methods ISO 4008-1:1980. Road vehicles - Fuel injection pump testing - Part 1: Dynamic conditions [online] [accessed 2020-03-05]. Available from: https://standartgost.ru/g/%D0%93%D0%9E%D0%A1%D0%A2_10579-2017.
- [16] ISO 8984-2:1993 Diesel engines - Testing of fuel injectors - Part 2: Test methods [online] [accessed 2020-03-05]. Available from: <https://www.iso.org/ru/standard/16513.html>.
- [17] KAMALTDINOV, V. G., ROZHDESTVENSKY, Y. V., LYSOV, I. O., POPOV, A. Y., NIKIFOROV, S. S. Experimental investigations of the effects of electric control impulse on injection characteristics of common rail type injector. *Indian Journal of Science and Technology* [online]. 2016, **9**(42), p. 104-225. ISSN 0974-6846, eISSN 0974-5645. Available from: <https://doi.org/10.17485/ijst/2016/v9i42/104225>
- [18] VERSTEEG, H. K., MALALASEKERA, W. *An introduction to computational fluid dynamics: the finite volume method*. Pearson Education, 2007. ISBN 978-0-13-127498.
- [19] Presentation of Common Rail piezo injectors from Bosch - Robert Bosch GmbH, Automotive Aftermarket [online] [accessed 2020-03-07]. Available from: <https://www.bosch-mobility-solutions.com/de/produkte-und-services/pkw-und-leichte-nutzfahrzeuge/antriebssysteme/common-rail-system-piezo/>.

- [20] YAN, F., WANG, J. Common rail injection system on-line parameter calibration for precise injection quantity control. In: 2010 American Control Conference: proceedings. IEEE, 2010. ISBN 978-1-4244-7427-1, p. 2248-2253.
- [21] ZHAO, H., QUAN, S., DAI, M., POMRANING, E., SENECAI, P. K., XUE, Q., BATTISTONI, M., SOM, S. Validation of a three-dimensional internal nozzle flow model including automatic mesh generation and cavitation effects. In: Internal Combustion Engine Division Fall Technical Conference ASME 2013: proceedings. American Society of Mechanical Engineers Digital Collection, 2013. ISBN 978-0-7918-5610-9.
- [22] ANDO, K., COLONIUS, T., BRENNEN, C. Numerical simulation of shock propagation in a polydisperse bubbly liquid. *International Journal of Multiphase Flow* [online]. 2011, **37**(6), p. 596-608. ISSN 0301-9322. Available from: <https://doi.org/10.1016/j.ijmultiphaseflow.2011.03.007>
- [23] FUSTER, D., COLONIUS, T. Modelling bubble clusters in compressible liquids. *Journal of Fluid Mechanics* [online]. 2011, **688**, p. 352-389. ISSN 0022-1120. Available from: <https://doi.org/10.1017/jfm.2011.380>
- [24] JAMALUDDIN, A., BALL, G., TURANGAN, C., LEIGHTON, T. The collapse of single bubbles and approximation of the far-field acoustic emissions for cavitation induced by shock wave lithotripsy. *Journal of Fluid Mechanics* [online]. 2011, **677**, p. 305-341. ISSN 0022-1120. Available from: <https://doi.org/10.1017/jfm.2011.85>
- [25] SALVADOR, F. J., MARTINEZ-LOPEZ, J., ROMERO, J. V., ROSELLO, M. D. Computational study of the cavitation phenomenon and its interaction with the turbulence developed in diesel injector nozzles by Large Eddy Simulation (LES). *Mathematical and Computer Modelling* [online]. 2013, **57**(7-8), p. 1656-1662. ISSN 0895-7177. Available from: <https://doi.org/10.1016/j.mcm.2011.10.050>
- [26] SOTERIOU, C., ANDREWS, R., SMITH, M., TORRES, N., SANKHALPARA, S. The flow patterns and sprays of variable orifice nozzle geometries for diesel injection. *SAE Transactions* [online]. 2000, **109**, p. 1007-1029. ISSN 0096-736X. Available from: <https://doi.org/10.4271/2000-01-0943>
- [27] STADTKE, H. Gasdynamic aspects of two-phase flow: hyperbolicity, wave propagation phenomena and related numerical methods. John Wiley & Sons, 2006. ISBN 978-3-527-405-78-7.
- [28] STROTOS, G., KOUKOUVINIS, P., THEODORAKAKOS, A., GAVAISES, M. Quantification of friction-induced heating in tapered diesel orifices. In: Rouen 2014 International Conference and Exhibition: proceedings. France: SIA Powertrain, 2014.
- [29] STROTOS, G., KOUKOUVINIS, P., THEODORAKAKOS, A., GAVAISES, M., WANG, L., LI, J., MCDAVID, R. M. Fuel heating in high pressure diesel nozzles. In: International Conference Thiesel 2014: proceedings. Valencia, Spain: Universitat Politècnica de València, 2014.
- [30] THEODORAKAKOS, A., MITROGLOU, N., STROTOS, G., ATKIN, C., GAVAISES, M. Friction induced heating in nozzle hole micro-channels under extreme fuel pressurisation. *Fuel* [online]. 2014, **123**, p. 143-150. ISSN 0016-2361. Available from: <https://doi.org/10.1016/j.fuel.2014.01.050>
- [31] STROTOS, G., KOUKOUVINIS, P., THEODORAKAKOS, A., GAVAISES, M., BERGELES, G. Transient heating effects in high pressure diesel injector nozzles. *International Journal of Heat and Fluid Flow* [online]. 2015, **51**, p. 257-267. ISSN 0142-727X. Available from: <https://doi.org/10.1016/j.ijheatfluidflow.2014.10.010>

INTERPRETING THE MAIN POWER CHARACTERISTICS CHOICE OF THE WHEEL VEHICLES GUIDED CUSHIONING SYSTEM

Bogdan Sokil¹, Oleg Lyashuk², Mariya Sokil³, Yuriy Vovk^{4*}, Volodymyr Dzyura⁴, Victor Aulin⁵, Roman Khoroshun²

¹Department of Engineering Mechanics, Hetman Petro Sahaidachnyi National Army Academy, Lviv, Ukraine

²Department of Automobiles, Ternopil Ivan Puluj National Technical University, Ternopil, Ukraine

³Department of Transport Technologies, Lviv Polytechnic National University, Lviv, Ukraine

⁴Department of Transport Technologies and Mechanics, Ternopil Ivan Puluj National Technical University, Ternopil, Ukraine

⁵Department of Maintenance and Repair of Machines, Central Ukrainian National Technical University, Kropyvnytskyi, Ukraine

*E-mail of corresponding author: vovkyuriy@ukr.net

Resume

The method of investigation of the non-linear vibrations of the wheel vehicles with the guided cushioning system has been developed. It is based on the idea of the perturbation methods combined with the theory of special periodic Ateb-functions. All these made possible to obtain analytical relations, which describe the characteristic features of the cushioning area vibrations. These relations can be the basis for creation of the software product of the guided cushioning system with the purpose to minimize the dynamic loadings on the transported people and cargo and to increase the stability characteristics of the vehicle movement along the curvilinear areas of the bump road.

Article info

Received 31 August 2020

Accepted 25 September 2020

Online 23 February 2021

Keywords:

non-linear vibration,
Ateb-function,
stability,
vehicle,
guided cushioning system

Available online: <https://doi.org/10.26552/com.C.2021.2.B139-B149>

ISSN 1335-4205 (print version)

ISSN 2585-7878 (online version)

1 Introduction

Guided or semi-guided suspension system [1-4] has been widely used for improving of the wheel vehicle (WV) smooth movement for the last decades. It makes possible to adjust the main characteristics of the suspension system so that the dynamic loading on people or cargo would be minimum. The basis of "adjustment" of these characteristics is the physical and corresponding to it mathematical model of the WV dynamics along the bump road, as well as the response of the latter to this or that type of motion perturbation. However, the mathematical instrument for the analytical investigation of the WV dynamics under their different physical models [5-6] is developed generally for the small vibrations under linear dependence or recovering forces on the deformation of the elastic elements (tires in particular) or the damper devices deformation rate. The adaptive control process is carried out in addition to the speed of the spring part, which is an important special case of the regulated suspension [6-9]. In addition, it is necessary to investigate the relationship between the parameters v_1 and v_2 for which the nonlinear suspension has similar characteristics to the linear one. In some papers, the method of the analytical investigations

of the non-linear elastic forces of absorbers on vertical rolling vibrations and stability of the vehicle's movement along the curvilinear parts of the road has been developed only for the simplest physical and corresponding non-linear mathematical models of the WV dynamics [7, 10-12]. The static deformation and nonlinearity of the system are the main parameters for progressive (regressive) suspensions. That suspension is more comfortable for transportation of dangerous goods and passengers.

The obtained results, which can be the basis for creation of the software of the guided suspension, show that the elastic absorbers, with non-linear law of the recovering force change, affect not only the numerical characteristics of the cushioning mass (CM) vibrations, but provide them with the qualitative new property - their own frequency depends on the amplitude, as well. Thus, the WV with such a cushioning system along the road with the ordered bumps obtains new characteristics. If one is to look at the process from a mathematical point of view, it is non-periodic, since the oscillations amplitude of the damping device due to the impact of the obstacle attenuates and the natural frequency of oscillations depends on its amplitude. These cyclic periodic signals have been outlined by [13]. Furthermore, the critical



$$\begin{aligned}\bar{\Delta}_1 &= \bar{j}l_1\varphi \cos\left(\frac{\varphi}{2} + \beta_1\right) + \bar{k}\left[z + l_1\varphi \sin\left(\frac{\varphi}{2} + \beta_1\right)\right], \\ \bar{\Delta}_2 &= \bar{j}l_2\varphi \cos\left(\beta_2 - \frac{\varphi}{2}\right) + \bar{k}\left[z - l_2\varphi \sin\left(\beta_2 - \frac{\varphi}{2}\right)\right];\end{aligned}\quad (2)$$

relative rates of points, which coincide with the ends of the mentioned vectors $(\bar{\Delta}_1, \bar{\Delta}_2)$ -

$$\begin{aligned}\dot{\bar{\Delta}}_1 &= \bar{j}l_1\dot{\varphi} \cos\left(\frac{\varphi}{2} + \beta_1\right) - \bar{j}l_1\varphi \frac{\dot{\varphi}}{2} \sin\left(\frac{\varphi}{2} + \beta_1\right) + \\ &+ \bar{k}\left[\dot{z} + l_1\dot{\varphi} \sin\left(\frac{\varphi}{2} + \beta_1\right) + l_1\varphi \frac{\dot{\varphi}}{2} \cos\left(\frac{\varphi}{2} + \beta_1\right)\right], \\ \dot{\bar{\Delta}}_2 &= \bar{j}l_2\dot{\varphi} \cos\left(\beta_2 - \frac{\varphi}{2}\right) - \bar{j}l_2\varphi \frac{\dot{\varphi}}{2} \sin\left(\beta_2 - \frac{\varphi}{2}\right) + \\ &+ \bar{k}\left[\dot{z} - l_2\dot{\varphi} \sin\left(\beta_2 - \frac{\varphi}{2}\right) + l_2\varphi \frac{\dot{\varphi}}{2} \cos\left(\beta_2 - \frac{\varphi}{2}\right)\right];\end{aligned}\quad (3)$$

elastic elements δ_1, δ_2 deformations:

$$\begin{aligned}\delta_1 &= \sqrt{(z^*)^2 + l_1^2\varphi^2 + 2z^*l_1\varphi \sin\left(\frac{\varphi}{2} + \beta_1\right)}, \\ \delta_2 &= \sqrt{(z^*)^2 + l_2^2\varphi^2 - 2z^*l_2\varphi \sin\left(\beta_2 - \frac{\varphi}{2}\right)},\end{aligned}\quad (4)$$

where $z^* = z - \Delta_{st}, \Delta_{st}$ - static deformation of the elastic elements, $l_1, l_2, \beta_1, \beta_2$ - geometric parameters, which specify the location of elastic elements relatively the masses center, \bar{k}, \bar{j} - unit vectors directed along the axis stable reading system OZ and OY correspondingly (Figure 1). In the case of symmetric location of the cushioned area weight centre relatively the elastic elements $l_1 = l_2$ and $\beta_1 = \beta_2$.

Equations (2)-(4), as well as the assumptions as to the power characteristics of the cushioning system (See 3), make possible to present the active force components acting on the CM (\bar{F}_1 and \bar{F}_2) as follows:

$$\begin{aligned}\bar{F}_1 &= \delta_1^{v2}(\alpha_1 + \chi_1\dot{\Delta}_1^{v1}) \cdot \\ &\cdot \left(\bar{j}l_1\varphi \sin\left(\frac{\varphi}{2} + \beta_1\right) + \bar{k}\left(z^* + l_1\varphi \sin\left(\frac{\varphi}{2} + \beta_1\right)\right)\right), \\ \bar{F}_2 &= \delta_2^{v2}(\alpha_2 + \chi_2\dot{\Delta}_2^{v1}) \cdot \\ &\cdot \left(\bar{j}l_2\varphi \sin\left(\beta_2 - \frac{\varphi}{2}\right) + \bar{k}\left(z^* - l_2\varphi \sin\left(\beta_2 - \frac{\varphi}{2}\right)\right)\right).\end{aligned}\quad (5)$$

The projection sum of the mentioned above forces and the cushioned area weight force on the vertical axis (CZ) will be nothing else but the active component of the generalized force, which corresponds to the generalized coordinate z that is,

$$\begin{aligned}Q_z^a &= \delta_1^{v2}(\alpha_1 + \chi_1\dot{\Delta}_1^{v1})\left(z^* + l_1\varphi \sin\left(\frac{\varphi}{2} + \beta_1\right)\right) + \\ &+ \delta_2^{v2}(\alpha_2 + \chi_2\dot{\Delta}_2^{v1})\left(z^* - l_2\varphi \sin\left(\beta_2 - \frac{\varphi}{2}\right)\right) - P.\end{aligned}\quad (6)$$

The active component of the generalized force, which corresponds to the generalized coordinates φ that is, Q_φ^a is found based on the following [14]: - from one side, the work of active forces acting on the CM, at the possible displacement of the mentioned generalized coordinate $\delta\varphi$, is found by the ratio $\delta A_\varphi^a = Q_\varphi^a\delta\varphi$, from the other - $\delta A_\varphi^a = M_C^a\delta\varphi$, where M_C^a - the sum of active forces moments acting on the cushioned area

relatively the mass centre. The last value, according to the Varignon theorem [14] is found due to the dependence $M_C^a = F_{1z}^ay_1 - F_{1y}^az_1 + F_{2z}^ay_2 - F_{2y}^az_2$, where F_{1y}^a, F_{1z}^a and F_{2y}^a, F_{2z}^a - the projections on the axis OY and OZ of the active forces acting on the right and left areas of the CA WV; y_1, z_1 and y_2, z_2 - coordinates of these forces application points, that is, $y_1 = l_1\sin\beta_1, z_1 = -l_1\cos\beta_1$, $y_2 = l_2\sin\beta_2, z_2 = -l_2\cos\beta_2$.

Thus, $Q_\varphi^a = F_{1z}^ay_1 - F_{1y}^az_1 + F_{2z}^ay_2 - F_{2y}^az_2$.

If corresponding values are substituted in the last dependence, one will obtain:

$$\begin{aligned}Q_\varphi^a &= (\alpha_1 + \chi_1\dot{\Delta}_1^{v1}) \cdot \\ &\cdot \left((z^*)^2 + l_1^2\varphi^2 + 2z^*l_1\varphi \sin\left(\frac{\varphi}{2} + \beta_1\right)\right)^{\frac{v2}{2}} \cdot \\ &\cdot \left\{l_1\sin\beta_1\left(z^* + l_1\varphi \sin\left(\frac{\varphi}{2} + \beta_1\right)\right) + \right. \\ &\left. + l_1\cos\beta_1\left(z^* + l_1\varphi \sin\left(\frac{\varphi}{2} + \beta_1\right)\right)\right\} + \\ &+ (\alpha_2 + \chi_2\dot{\Delta}_2^{v1}) \cdot \left\{(z^*)^2 l_2^2\varphi^2 - \right. \\ &\left. - 2z^*l_2\varphi \sin\left(\beta_2 - \frac{\varphi}{2}\right)\right\}^{\frac{v2}{2}} \cdot \\ &\cdot \left\{l_2\sin\beta_2\left(z^* + l_2\varphi \sin\left(\beta_2 - \frac{\varphi}{2}\right)\right) + \right. \\ &\left. + l_2\cos\beta_2\left(z^* + l_2\varphi \sin\left(\beta_2 - \frac{\varphi}{2}\right)\right)\right\}.\end{aligned}\quad (7)$$

Following the similar way as for the active components of the recovering force one will obtain the passive components of the generalized forces

$$\begin{aligned}Q_{iz}^p &= -\gamma_i|\bar{F}_i(\varphi, z, \dot{\varphi})| \times \\ &\times \left[2\dot{z} + \dot{\varphi}\left(l_1\sin\left(\frac{\varphi}{2} + \beta_1\right) - l_2\sin\left(\beta_2 - \frac{\varphi}{2}\right)\right) + \right. \\ &\left. + \varphi \frac{\dot{\varphi}}{2}\left(l_1\cos\left(\frac{\varphi}{2} + \beta_1\right) + l_2\cos\left(\beta_2 - \frac{\varphi}{2}\right)\right)\right], \\ Q_\varphi^p &= -\gamma_i|\bar{F}_i(\varphi, z, \dot{\varphi})| \times \\ &\times \left\{l_1\left[\dot{z} + \dot{\varphi}l_1\left(\sin\left(\frac{\varphi}{2} + \beta_1\right) + \frac{\varphi}{2}\cos\left(\frac{\varphi}{2} + \beta_1\right)\right)\right] \times \right. \\ &\times \left(\sin\beta_1 + \varphi \cos\left(\frac{\varphi}{2} + \beta_1\right)\right) - \\ &- l_1^2\left[\dot{\varphi}\left(\cos\left(\frac{\varphi}{2} + \beta_1\right) - \frac{\varphi}{2}\sin\left(\frac{\varphi}{2} + \beta_1\right)\right)\right] \times \\ &\times \left(\cos\beta_1 - \varphi \sin\left(\frac{\varphi}{2} + \beta_1\right)\right) + \\ &+ l_2\left[\dot{z} - \dot{\varphi}l_2\left(\sin\left(\beta_2 - \frac{\varphi}{2}\right) - \frac{\varphi}{2}\cos\left(\beta_2 - \frac{\varphi}{2}\right)\right)\right] \times \\ &\times \left(\sin\beta_2 - \varphi \cos\left(\beta_2 - \frac{\varphi}{2}\right)\right) - \\ &- l_2^2\left[\dot{\varphi}\left(\cos\left(\beta_2 - \frac{\varphi}{2}\right) + \frac{\varphi}{2}\sin\left(\beta_2 - \frac{\varphi}{2}\right)\right)\right] \times \\ &\times \left(\cos\beta_2 - \varphi \sin\left(\beta_2 - \frac{\varphi}{2}\right)\right)\}.\end{aligned}\quad (8)$$

In the presented above ratio $\bar{F}_i(\varphi, z, \dot{\varphi})$ - the known functions specified according to the assumptions dealing with the damping device resistance forces. Thus, the vibration process of the cushioned mass is described by the system of differential equations in which the right-hand parts are found according to the Equations (6)-(8).

$$\begin{aligned} M \frac{d^2 z}{dt^2} &= Q_z^a + Q_z^\Pi, \\ I_C \frac{d^2 \varphi}{dt^2} &= Q_\varphi^a + Q_\varphi^\Pi. \end{aligned} \quad (9)$$

To obtain the analytical solution of the obtained system of non-linear differential equations is not possible. That is why let us analyze only the CM vertical and rolling vibrations separately.

3 The cushioning mass (CM) vertical vibrations

These vibrations occur when their perturbation is caused by the bump road, similar under the right and the left wheels. In the mathematical model of the CM dynamics it equals $\varphi \equiv 0$. The mentioned factor, as well as the conditions combined with the power factors acting on the WV CM, make possible to present the first part of the differential system in Equation (9) as follows:

$$\begin{aligned} \ddot{z}^* + \frac{\chi_1 + \chi_2}{M} (z^*)^{v_2+1} (\dot{z}^*)^{v_1} = \\ = -g + \frac{\alpha_1 + \alpha_2}{M} (z^*)^{v_2+1} - \frac{\gamma_1 + \gamma_2}{M} |\dot{z}^*| \dot{z}^*. \end{aligned} \quad (10)$$

It should be noted that the maximum value of the right-hand part of the differential equation is a small value in comparison to the maximum value of the function $g(z, \dot{z}) = \frac{\chi_1 + \chi_2}{M} (z^*)^{v_2+1} (\dot{z}^*)^{v_1}$. All the mentioned above makes possible to apply the general rules of the non-linear differential equations perturbation theory with “small” right-hand part [15]. Effectiveness of application of the mentioned methods depends on the possibility to build a real solution of the non-perturbed option of the equation in question. For the non-linear differential CM vertical vibrations this equation looks like

$$\ddot{z}^* + \frac{\chi_1 + \chi_2}{M} (z^*)^{v_2+1} (\dot{z}^*)^{v_1} = 0. \quad (11)$$

Both the perturbed and non-perturbed differential equations have to describe the CM vibration processes and the necessary condition for this type of solution in Equation (11) is non-conjugated with respect to the generalized coordinate non-conservative recovering force that is, $(-z^*)^{v_2+1} (\dot{z}^*)^{v_1} = -(z^*)^{v_2+1} (\dot{z}^*)^{v_1}$. Thus, the differential Equations (11) and (10) will describe the vibration process, if $v_i + 1 = (2p_i + 1)/(2q_i + 1), p_i, q_i = 0, 1, 2, \dots$. Having provided the above mentioned condition, the periodic solution of Equation (11) is described by Equation (13) taking advantage of the periodic Ateb-function [16] as follows

$$z^*(t) = asa \left(v_2 + 1, \frac{1}{1 - v_1}, \omega(a)t + \theta \right), \quad (12)$$

where a - amplitude, $\omega(a)t + \theta$ - phase, θ - initial

phase, $\omega(a)$ - natural frequency of vibration. The latter, being dependent on amplitude for the most of non-linear vibration systems, is found by relation

$$\omega(a) = \frac{v_2 + 2}{2} \left(\frac{2 - v_1}{(1 - v_1)(v_2 + 2)} \frac{\chi_1 + \chi_2}{M} \right)^{\frac{1}{2 - v_1}} a^{\frac{v_1 + v_2}{2 - v_1}}.$$

If in the expression for the natural frequencies of the vertical vibrations more convenient notion “rigidity” is used, that is the static deformation, one will obtain

$$\omega(a) = \frac{v_2 + 2}{2} \left(\frac{2 - v_1}{(1 - v_1)(v_2 + 2)} \times \frac{(\chi_1 + \chi_2)g}{(\alpha_1 + \alpha_2)\Delta_{st}^{v_2+1}} \right)^{\frac{1}{2 - v_1}} a^{\frac{v_1 + v_2}{2 - v_1}}. \quad (13)$$

Reliability of the presented above results can be described as follows: at $v_1 = 0$ the known values can be found, which deal with the non-linear conservative [12], and at $v_1 = v_2 = 0$ - linear characteristics of the elastic absorbers. Besides that, at $v_1 = v_2$ the CM natural frequency does not depend on the amplitude. It means that in the case of the non-linear non-conservative cushioning system (CS) force, which is changed according to the law $F_i(\Delta_i, \frac{d\Delta_i}{dt}) = (\alpha_i + \chi_i (\frac{d\Delta_i}{dt})^v) \Delta_i^{1-v}$, the CS dynamic process is isosynchronous.

The dependencies obtained above are the basis for creation of the software product for control of the non-linear non-conservative recovering force of the absorbers to provide the most comfortable conditions of people transporting. It is known that the most comfortable conditions of transporting are those, when the vibration frequency of the WV CM varies within $0.8 < f < 1.5$ Hz, [17-18]. That is why, if the main factor of the frequency control is the static deformation of the cushioning system, it is found as the function of the vertical vibrations amplitude according to the relation

$$\Delta_{st} = \left[\frac{(2 - v_1)(\chi_1 + \chi_2)g}{(1 - v_1)(v_2 + 2)(\alpha_1 + \alpha_2)} \times \frac{1}{\left(\frac{(v_2 + 2)}{4\Pi f} \right)^{2 - v_1} a^{v_1 + v_2}} \right]^{\frac{1}{v_2 + 1}}, \quad (14)$$

where $\Pi = \frac{\Gamma(1/(v_2 + 2))\Gamma((1 - v_1)/(2 - v_1))}{\Gamma(1/(v_2 + 2) + (1 - v_1)/(2 - v_1))}$ - the semi-period according to the phase of the used special Ateb-functions.

In Figure 2 it is shown, according to Equation (14), the laws of the CM static deformation change (the main parameter of the guided CS, at which the frequency of the natural CM vibrations is of the most comfortable for transportation of dangerous goods and passengers.

Presented graphic dependencies show that in order to meet the ergonomic requirements as to the frequency of the vertical vibrations, in the case of the great CM vibration amplitudes ($a > 0.1$ m) it is recommended to choose the CS with the static deformation $0.2 < \Delta_{st} < 0.35$ in the cases of the progressive CS power characteristics

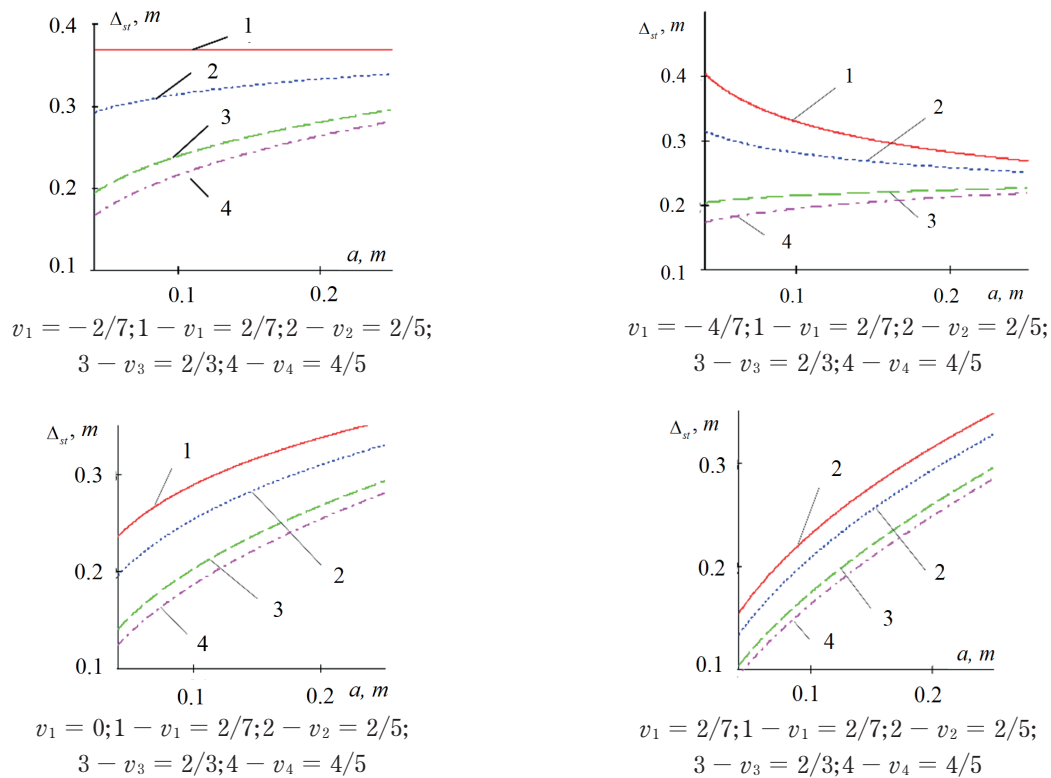


Figure 2 Dependence of the static deformation on amplitude of the vertical vibrations of the WV guided CS with the non-conservative power characteristics of the cushioning system

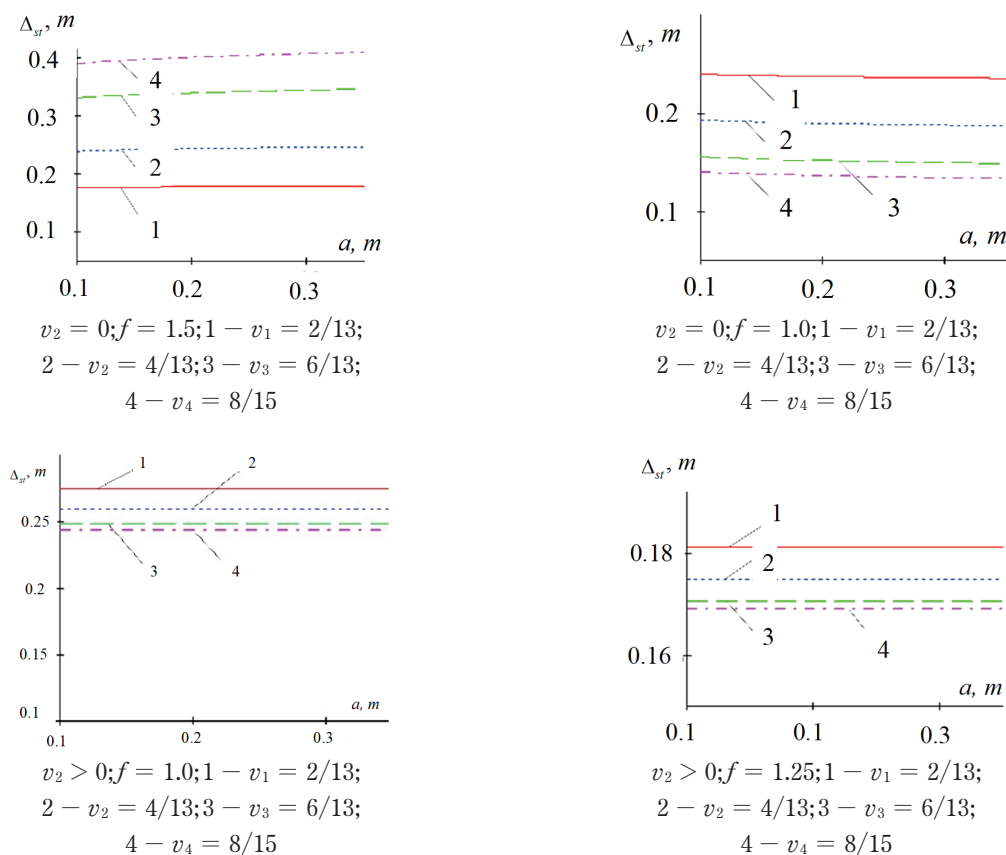


Figure 3 Dependence of the static deformation on the vertical vibration amplitude of the WV guided CS $v_1 = -v_2$ and $v_2 = 0, 0 < v_1 < 1$

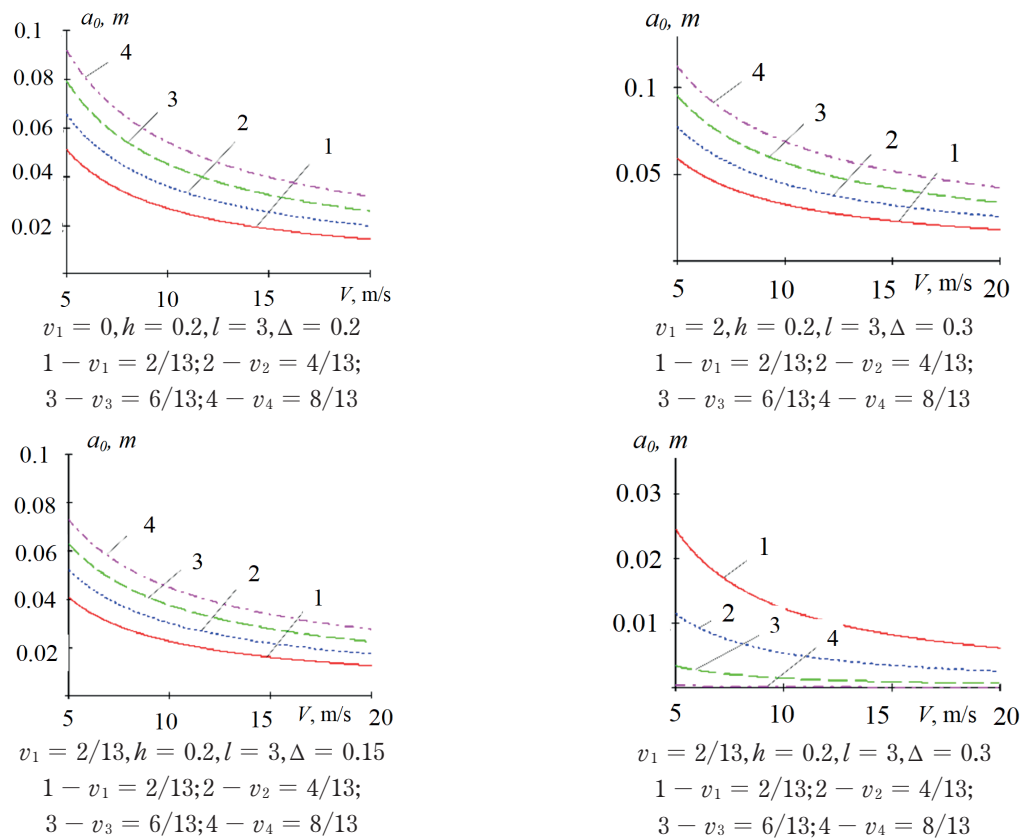


Figure 4 Dependences of the initial perturbation amplitude on the speed of getting into the bump

(at $v_1 = 0$; $-0 < v_2 < 1$) and non-conservative at $-0.4 < v_1 < 0$; $0 < v_2 < 1$. What concerns the small vibration amplitudes, it is necessary for the progressive cushioning system and non-conservative one (with the parameter values $-0.4 < v_1 < 1$, $0 < v_2 < 1$) that the cushioning system static deformation of elastic absorbers was varying within $0.1 < \Delta_{st} < 0.2$ and in the case $-0.7 < v_1 < -0.4$, $0 < v_2 < 1$ within $0.25 < \Delta_{st} < 0.4$ m. The CS with values of the power parameters of its non-conservative recovering force $v_1 = -v_2$ and $v_2 = 0$, $0 < v_1 < 1$ is of the great practical importance, which is seen in Figure 3. The ergonomic requirements for such a CS as to the vibration frequencies are provided, when the static deformation is stable and does not depend on the CM vibration amplitudes (Figure 3).

The dependencies obtained above can be the basis for finding the amplitude of the initial perturbation of the vertical vibrations under the condition when the bump road under the right and left wheels are of similar profiles. If one assumes that the latter are described by relation $z = h \sin \frac{\pi}{l} x$ and that the WV moves with the constant speed V , then the relative component of the initial CM speed from the one side is equal $V_0 = V \sin \alpha_0$, (α_0 - the tangent inclination angle to the bump at the moment, when the wheel gets into the bump) and from the other - $V_0 = \frac{dz}{dt} \Big|_{t=0} = \frac{2a_0}{v_2 + 2} \omega(a_0)$. All the presented makes possible the obtain Equation (15) for finding the amplitude of the initial perturbation a_0 in the case of the slope road bump:

$$a_0 = \left(V \frac{h\pi}{l} \right)^{\frac{2-v_1}{2+v_2}} \times \left(\frac{(1-v_1)(v_2+2)(\alpha_1 + \alpha_2)\Delta_{cm}^{v_2+1}}{v_2+2} \right)^{\frac{1}{v_2+2}}. \quad (15)$$

According to dependencies in Equation (15), dependence of the amplitude of the initial perturbation ($a_0 = a_1(x)$) on the motion speed V is presented in Figure 4 and on the static deformation in Figure 5, at different values of the WV CS power.

The presented dependencies show that the amplitude of the WV CM initial vibration perturbation during getting into the bump:

- is smaller for the greater motion speed;
- greater values of the parameter v_2 , correspond to the greater values of the initial perturbation amplitude in the case of the progressive or regressive power characteristics;
- for the case $v_1 > 0$ and $v_2 > 0$; $v_1 < 0$ and $v_2 > 0$, the amplitude of the initial perturbation is greater than the amplitude of the CS initial perturbation with the CS linear characteristics (at all other parameters being constant), and for the cases $v_1 < 0$ and $v_2 < 0$; $v_1 > 0$ and $v_2 < 0$ it is smaller;
- the greater values of the elastic absorbers static deformation of the cushioning system correspond to the greater values of the initial perturbation amplitudes. Moreover, for its progressive power characteristics and for the cases when $v_1 > 0$ and $v_2 > 0$; $v_1 < 0$ and $v_2 > 0$, it is greater than the amplitude of the CS initial

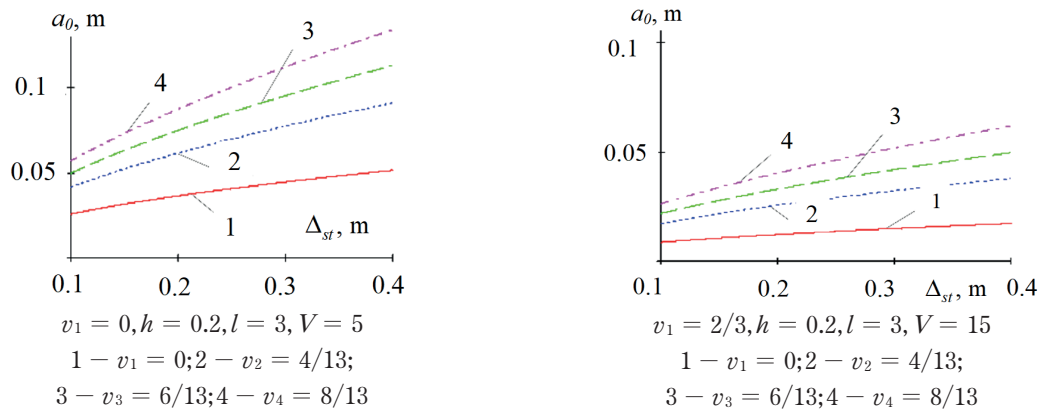


Figure 5 Dependences of the initial perturbation amplitude on the CS static deformation

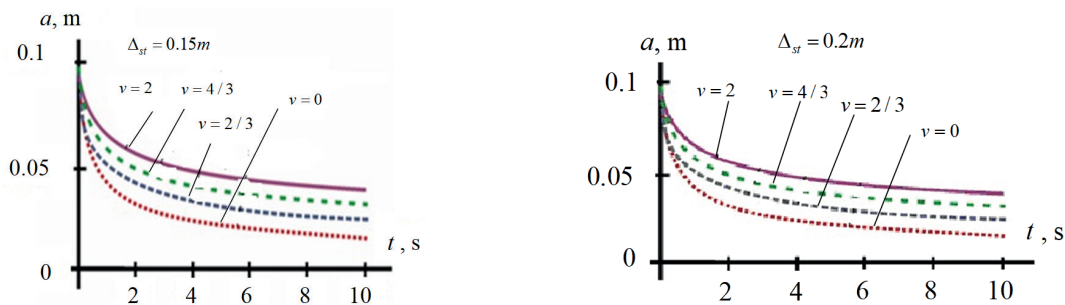


Figure 6 Time changes of the damped vertical vibrations amplitude at different values of the power characteristics of the guided CS

perturbation with the linear power characteristics and for the regressive one and the cases $v_1 < 0$ and $v_2 < 0$; $v_1 > 0$ and $v_2 < 0$ - it is smaller.

As to the effect of the “small” non-linear resistance forces of the WV CM dynamics, it is demonstrated in the change in time of both the amplitude and the vibration frequencies. To state the law of the mentioned parameters change, advantage of the Vander Paul method was employed to Equation (10) and the following was obtained [19-22]:

$$\frac{da}{dt} = \frac{2-v_1}{4\pi\omega(a)} \int_0^{2\pi} \left(ca \left(\frac{1}{1-v_1}, v_2+1, \psi \right) \right) \times \left[-g + \frac{\alpha_1 + \alpha_2}{M} a^{v_2+1} s a^{v_2+1} \times \right. \\ \left. \times \left(v_2+1, \frac{1}{1-v_1}, \psi \right) + \frac{\gamma_1 + \gamma_2}{M} \times \right. \\ \left. \times \left| \frac{2a(t)\omega(a)}{v_2+2} \left(ca \left(\frac{1}{1-v_1}, v_2+1, \psi \right) \right)^{\frac{1}{1-v_1}} \right|^s \right] d\psi, \quad (16)$$

$$\frac{d\psi}{dt} = \omega(a) - \frac{\alpha_1 + \alpha_2 (v_2+2)(2-v_1)a^{v_2}}{4\pi\omega(a)} \times \\ \times \frac{2\Gamma\left(\frac{2v_1-1}{v_1-2}\right)\Gamma\left(\frac{v_2+3}{v_2+2}\right)}{\Gamma\left(\frac{2v_1-1}{v_1-2} + \frac{v_2+3}{v_2+2}\right)}. \quad (17)$$

In Figure 6 the laws of the CM vertical vibrations amplitude change in time, for some values of the power

characteristics of the guided cushioning system, are presented.

The graph dependencies show that the qualitative nature of the CM vibration damping remains, but the amplitude damping rate greatly depends on the power characteristics of the absorbers.

4 The CM rolling vibrations

These vibrations occur under the condition when the CM motion perturbation was caused by getting on single bump by the right (left) WV tire. The mathematical model of the mentioned WV area vibration can be easily obtained from Equations (7) - (9), when $z^*(t) \equiv \Delta_{st}$. Only the non-perturbed equation, which corresponds to the WC CM rolling vibration, is presented below

$$I_0 \ddot{\phi} + \Xi^2 \dot{\phi}^{v_1} \phi^{v_2} = 0, \quad (18)$$

where $\Xi^2 = (\chi_1 l_1^{v_1+v_2+2} \sin \beta_1 (\sin \beta_1 + \cos \beta_1) + \chi_2 l_2^{v_1+v_2+2} \sin \beta_2 (\sin \beta_2 + \cos \beta_2))$.

The differential equation (18) is similar to Equation (10), according to its structure, that is why the method of its solution is not mentioned here, but the main relations, which describe the main characteristics of the rolling vibration, are presented. Thus, the natural frequency of these vibrations Ω , as a function of the rolling vibrations amplitude a_ϕ is found by relation

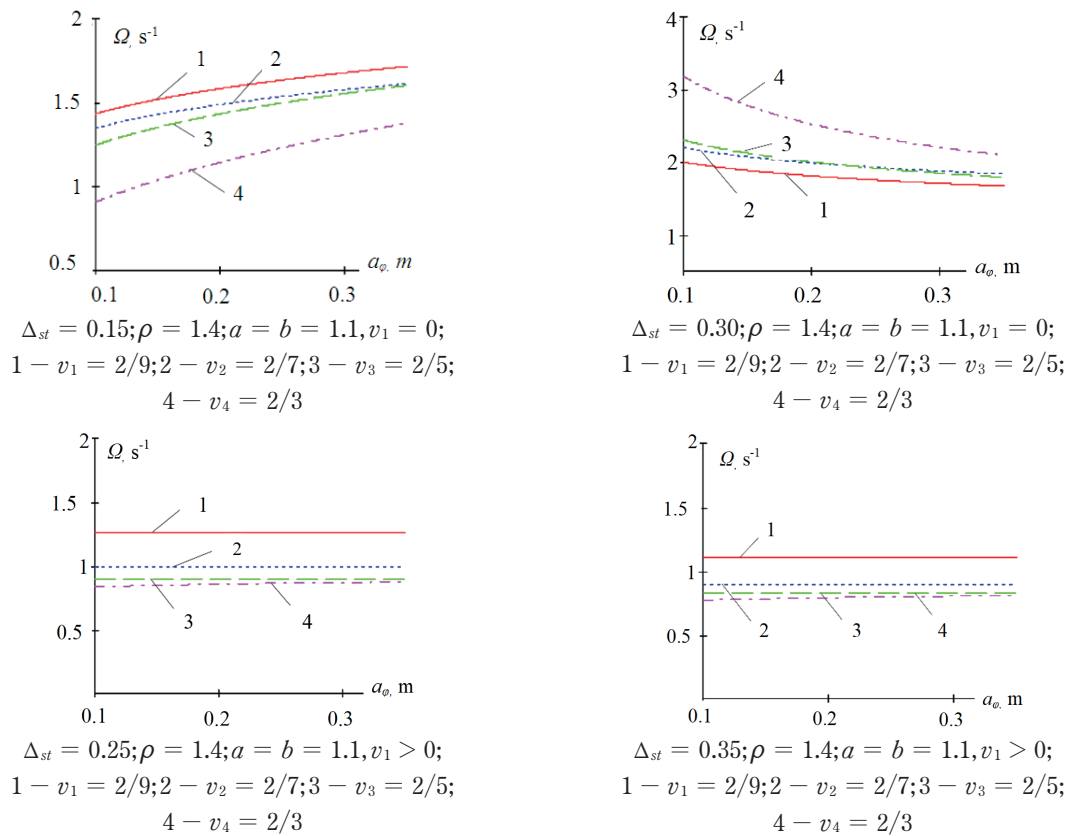


Figure 7 Dependence of the rolling vibration frequency on amplitude at different values of the power characteristics of the guided cushioning system

$$\Omega(a_\phi) = \frac{v_2 + 2}{2} \left(\frac{2 - v_1}{(1 - v_1)(v_2 + 2)} \times \right)^{\frac{1}{2 - v_1}} \times \frac{\Xi^2}{I_0} a_\phi^{\frac{v_1 + v_2}{2 - v_1}} =$$

$$= \frac{v_2 + 2}{2} \left(\frac{2 - v_1}{(1 - v_1)(v_2 + 2)} \times \right)^{\frac{1}{2 - v_1}} \times \frac{\Xi^2 g}{(\alpha_1 + \alpha_2) \Delta_{st.}^{v_2 + 1} \rho^2} a_\phi^{\frac{v_1 + v_2}{2 - v_1}}, \quad (19)$$

where ρ - CM inertia radius with respect to the longitudinal axis, which crosses the masses centre. In Figure 7 the dependence of the natural frequency of the rolling vibrations in H3 $\Omega(a_\phi)/2\pi$ on the amplitude of the mentioned vibrations, at different values of the CS power characteristics and its static deformation, are presented.

From the presented graphic dependencies can be seen that:

- for the progressive CS power characteristics, the greater vibration amplitude (vertical or rolling) is, the lesser is the natural vibration, moreover, when the values of the CS static deformation are greater (all other values being constant), it is smaller;
- for the regressive CS, the greater are the values of the vibration amplitude, the lesser are the values of the natural vibration frequencies;
- the ergonomic conditions of the WV operation with the progressive CS characteristics in the wide range of the vibration amplitudes are satisfied by the suspension with the static deformation $0.12 < \Delta_{st.} < 0.15$ m

at $2/9 < v_2 < 2/3$ and for the regressive at $0.2 < \Delta_{st} < 0.35$ m, $-2/3 < v_2 < -2/9$ and great values of the rolling vibration amplitudes;

- natural frequency of the CM vibrations with the non-conservative CS power characteristic at $v_1 > 0$, $v_2 > 0$ and greater vibration amplitudes becomes greater and satisfies the ergonomic conditions at $0.22 < \Delta_{st} < 0.35$ m;
- for the characteristics at $v_1 = -v_2, v_2 > 0$ in the case $|(V_1)| > V_2$ the greater values of the amplitude correspond to the smaller values of frequency;
- non-conservative CS power characteristics at $V_1 = -V_2, -V_2 > 0$ satisfies the ergonomic conditions at $0.15 < \Delta_{const} < 0.35$ m at the arbitrary amplitudes of the rolling vibrations.

As to the damping amplitude of the rolling vibrations, their qualitative characteristic is similar to those vertical. That is why they were not analysed.

5 The effect of the power characteristics of the guided suspension on stability of the WV motion along the curvilinear area of the road

The WV CM vibrations affect not only the comfortable transporting of people, but the stability of motion while going around the obstacles, manoeuvring motion along the curvilinear areas of the bump road. All mentioned above

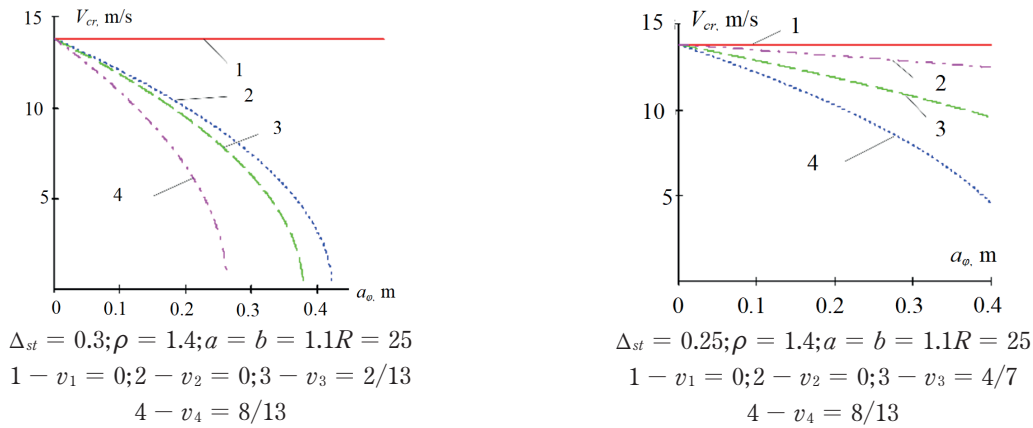


Figure 8 Laws of the critical change of the stable motion speed for capsizing at different values of the CS power characteristics.

is the curvilinear trajectory of motion of the cushionless area weight centre, as well as the point, which coincides with the weight centre of the cushioned area in its transient motion. From the mentioned above it is clear that all the cases of the WV motion are according to the kinetic-statistics equations, which besides the active and passive forces take into account the inertia forces of the mentioned areas [14-16, 19]. The main vector of the inertia forces of the cushionless area Φ_Q^e (in the case of the WV motion with the constant speed) equals $\Phi_Q^e = QV^2/gR$ and is directed to the opposite side to the trajectory inner normal of the mentioned point. As to the main vector of the CM inertia forces, it consists of two components: transferred $\Phi_{II}^e = QV^2/gR$ and relative $\Phi_{II}^r = -\frac{P}{g} \frac{d^2 \varphi}{dt^2}$.

If the first component of the CM inertia force was found similarly to that cushionless one, as to the direction, the second was by the vertical direction.

Furthermore, the main moment of the inertia force of the CM relative motion with respect to the arbitrary centre equals $M^r = -I_0 \frac{d^2 \varphi}{dt^2}$, where I_0 - inertia moment with respect to the mentioned centre.

From the other side, the most dangerous, because of the WV capsizing during the movement along the curvilinear areas of the road, are the rolling vibrations [23-29]. That is why to find the critical speed of the stable motion of the WV with non-conservative power CS characteristics, along the curvilinear area of the road, only the rolling CM vibrations will be taken into account. In this case, from the kinetic-static equations for the system cushionless-cushioned mass for finding the critical speed of the stable motion against capsizing V_{cr} , one obtains:

$$Pb + Q \frac{a+b}{2} - I_{A_2} \frac{d^2 \varphi}{dt^2} - \frac{P}{g} \frac{\tilde{V}_{cr}^2}{R} h_c - \frac{Q}{g} \frac{\tilde{V}_{cr}^2}{R} r = 0, \quad (20)$$

where I_{A_2} - inertia moment of the cushioned mass with respect to the contact point of the "outer" tire and the way, which, according to the Huygens-Steiner theorem, equals $I_{A_2} = \frac{P}{g} \left(\rho^2 + \left(\frac{a+b}{2} \right)^2 + h_c^2 \right)$, h_c - height of the

CM weight centre over the road in the static position.

It is considered that the road curvature radius is much greater than the WV base, that is why it is assumed that the curvature radius of the WV points in the transient motion is constant.

If in expression for the moment of the inertia forces relatively the CM motion one uses only the maximum values of the used Ateb-functions, Equation (20) would look like:

$$Pb + Q \frac{a+b}{2} - I_{A_2} \frac{4a_\varphi(1-v_1)}{(v_2+2)(2-v_1)} \Omega^2 \times \times (a_\varphi) - \frac{P}{g} \frac{\tilde{V}_{cr}^2}{R} h_c - \frac{Q}{g} \frac{\tilde{V}_{cr}^2}{R} r = 0. \quad (21)$$

The last dependence specifies the critical value of the stable motion speed taking into account the rolling vibrations as follows

$$\tilde{V}_{cr} = \sqrt{\frac{Pb + Q \frac{a+b}{2} - I_{A_2} \frac{4a_\varphi(1-v_1)}{(v_2+2)(2-v_1)} \Omega^2(a_\varphi)}{Ph_c + Qr}} Rg. \quad (22)$$

In Figure 8, for some WV geometric and power characteristics, the dependence of the critical speed of the stable motion against the capsizing on the amplitude of the rolling vibrations is presented.

As it was expected, the CM rolling vibrations cause the decrease of the stable motion critical speed. Besides that, at critical speed of the stable motion due to the capsizing:

- for the progressive or regressive CS power characteristics (at similar amplitudes of the rolling vibrations), the greater values v_2 correspond to the smaller values of the critical speed;
- for the non-concentrative characteristics at $v_1 > 0$, $v_2 > 0$, the greater values v_2 correspond to the smaller values of the critical speed;
- in the case of the greater values of the CS static deformation (all other kinematic and power characteristics being constant) the critical value of the stable motion speed is greater.

6 Conclusions

The presented method for investigation of the WV dynamics with the non-linear CS power characteristics made possible to obtain the analytical dependencies, which can be the basis for creation of the software product of the guided WV in order to: meet the ergonomic requirements related to the people transportation; minimize the dynamic loadings on the transported loads; improve the motion stability along the curvilinear areas of the bump road. As to the quantitative recommendations, resulted in the obtained data in order to meet the ergonomic requirements related to the frequency of the vertical vibrations, it is proposed, in the case of the WV movement along the sufficiently bump road, to choose the CS with the static deformation $0.2 < \Delta_{st} < 0.35$ m. In the case of

the progressive power characteristics of the cushioning system at $v_1 = 0; 0.1 < v_2 < 1$ and non-concentrative at $-0.4 < v_1 < 0; 0 < v_2 < 1$. As to the motion along the road with insufficient bumps - the progressive CS and non-concentrative with values $-0.4 < v_1 < 1$ are recommended to be chosen, $0 < v_2 < 1$ at the static deformation - $-0.1 < \Delta_{st} < 0.2$ m. The developed model allows to obtain the parameters of the resonant mode of oscillations, which have their own limiting velocity of the inequality path. The suspension has been designed to minimize the effects of overload caused by the movement of the vehicle on a pavement with irregularities with a frequency that meets the ergonomic conditions for the greatest comfort of transporting people. The following studies for this class of suspensions have been conducted by the authors in subsequent publications.

References

- [1] SOLTUS, A. P. *Theory of car performance characteristics*. Kyiv, Ukraine: Aristei, 2010. ISBN 966-8458-38-9
- [2] SOLIMAN, A., MOUSTAFA, S., SHOGAE, A. Parameters affecting vehicle ride comfort using half vehicle model. *SAE Technical Paper* [online]. 2008, 2008-01-1146. ISSN 0148-7191, eISSN 2688-3627. Available from: <https://doi.org/10.4271/2008-01-1146>
- [3] DEB, A., JOSHI, D. A study on ride comfort assessment of multiple occupants using lumped parameter analysis. *SAE Technical Paper* [online], 2012, 2012-01-0053. ISSN 0148-7191, eISSN 2688-3627. Available from: <https://doi.org/10.4271/2012-01-0053>
- [4] ZANDIEH, A. *Dynamics of a three - wheel vehicle with tadpole design* [online]. A thesis presented to the University of Waterloo in fulfilment of the thesis requirement for the degree of Master of Science in Mechanical Engineering. Ontario, Canada: 2014. Available from: <https://uwspace.uwaterloo.ca/bitstream/>
- [5] PREVIATI, G., GOBBI, M., MASTINU, G. Friction coefficient on snowy and icy surfaces of pneumatic tires fitted with or without anti-skid devices. *SAE Technical Paper* [online]. 2006, 2006-01-0560. ISSN 0148-7191, eISSN 2688-3627. Available from: <https://doi.org/10.4271/2006-01-0560>
- [6] GRUBEL, M. H., KRASYUK, O. P., NANIVSKYY, R. A., SOKIL, M. B. Vertical oscillations of wheeled vehicles cushion part under random disturbance conditions. *Scientific Notes of Lutsk National Technical University*. 2014, **46**, p. 112-116. ISSN 2415-3966.
- [7] KUZIO, I. V., SOKIL, B. I., PALYUKH, V. M. Suspension parameters effect on wheeled vehicles non-linear oscillations. *Bulletin of National University Lviv of Polytechnic, Dynamics, Durability and Design of Machines and Instruments*. 2007, **588**, p. 49-52. ISSN 0321-0499.
- [8] SOKIL, B., LYASHUK, O., PERENCHUK, O., SOKIL, M., POPOVICH, P., VOVK, Y. Dynamic effect of cushion part of wheeled vehicles on their steerability. *International Journal of Automotive and Mechanical Engineering* [online]. 2018, **15**(1), p. 4880-4892. ISSN 2229-8649, eISSN 2180-1606. Available from: <https://doi.org/10.15282/ijame.15.1.2018.1.0380>
- [9] LYASHUK, O., SOKIL, M., VOVK, Y., TSON, O., DZYURA, V. The impact of the kinematic parameters of bounce and pitch motions of sprung mass on wheeled vehicles handling. *Scientific Journal of Silesian University of Technology. Series Transport* [online]. 2017, **97**, p. 81-91. ISSN 0209-3324, eISSN 2450-1549. Available from: <https://doi.org/10.20858/sjsutst.2017.97.8>
- [10] TAMBOLI, J. A., JOSHI, S. G. Optimum design of a passive suspension system of a vehicle subjected to actual road random excitations. *Journal of Sound and Vibration* [online]. 1999, **219**(2), p. 193-205. ISSN 0022-460X. Available from: <https://doi.org/10.1006/jsvi.1998.1882>
- [11] BOGDEVICIUS, M., JUNEVICIUS, R.: Dynamic processes of the retrofitted rear suspension of the vehicle. *Transport* [online]. 2004, **19**(6), p. 262-268. ISSN 1648-4142. Available from: <https://doi.org/10.3846/16484142.2004.9637985>
- [12] PECELIUNAS, R., LUKOSEVICIENE, O., PRENTKOVSKIS, O. A mathematical model of the vibrating system equivalent to the vehicle in the mode of emergency braking. *Transport* [online]. 2003, **18**(3), p. 136-142. ISSN 1648-4142. Available from: <https://doi.org/10.3846/16483840.2003.10414082>
- [13] LITVINENKO, I. V., MARUSHCHAK, P. O., LUPENKO, S. A. Processing and modeling of ordered relief on the surface of heat-resistant steels after laser irradiation as a cyclic random process. *Automatic Control and Computer Sciences* [online]. 2014, **48**, p. 1-9. ISSN 0146-4116, eISSN 1558-108X. Available from: <https://doi.org/10.3103/S0146411614010040>

- [14] TAGHAVIFAR, H., MARDANI, A. *Off-road vehicle dynamics: analysis, modelling and optimization* [online]. Switzerland: Springer, 2017. ISBN 978-3-319-42519-1, eISBN 978-3-319-42520-7. Available from: <https://doi.org/10.1007/978-3-319-42520-7>
- [15] GILLESPIE, T. D. *Fundamentals of vehicle dynamics*. Warrendale, PA: Society of Automotive Engineers, 1992. ISBN 978-1-56091-199-9.
- [16] BALTHAZAR, M., MOOK, D. T., WEBER, H. I., BRASIL, R. M. L. R. F., FENILI, A., BELATO D., FELIX, J. L. P. An overview on non-ideal vibrations. *Meccanica* [online]. 2003, **38**(6), p. 613-621. ISSN 0025-6455, eISSN 1572-9648. Available from: <https://doi.org/10.1023/A:1025877308510>
- [17] BLEKHMANN, I. I. *Vibrational mechanics: nonlinear dynamic effects, general approach, applications*. Singapore: World Scientific, 2000. ISBN 978-9810238902.
- [18] SERTA, E., BOYRAZ, P. Optimization of suspension system and sensitivity analysis for improvement of stability in a midsize heavy vehicle. *Engineering Science and Technology, an International Journal* [online], 2017, **20**(3), p. 997-1012. ISSN 2215-0986. Available from: <https://doi.org/10.1016/j.jestch.2017.03.007>
- [19] RILL, G. *Road vehicle dynamics: fundamentals and modeling*. Boca Raton FL: CRC Press, 2012. ISBN 9781439838983.
- [20] ARTYUSHENKO, A., SUYARKOV, O. Study of influence of suspension characteristics of small size car on ride quality and its modernization. *Bulletin NTU KhPI. Series: Transport Mechanical Engineering*. 2013, **31**(1004), p. 21-27. ISSN 2078-6840.
- [21] PODRYHALO, M. A., KORBKO, M. I., KLETS, D. M. Evaluation of automobile dynamic ability. *Bulletin NTU KhPI, Automobile and Tractor Manufacture*. 2008, **58**, p. 134-137. ISSN 2078-6840.
- [22] PODRYHALO, M. A., VOLKOV, V. P., BOBOSHKO, A. A., PAVLENKO, V. A., BAITSUR, M. V., NAZAROV, A. I., ALEKSEV, V. O. *Wheeled vehicles resistance to skidding whilst breaking and ways of its rising*. Kharkiv: KNARU, 2006
- [23] GRUBEL, M. H., NANIVSKYY, R. A., SOKIL, M. B. Effect of elastic suspension restoring force on wheeled vehicles stable motion. In: International Scientific and Technical Conference: proceedings. Lviv: ACB, 2014.
- [24] COLE, J. *Disturbance methods in applied mathematics*. Moscow: Mir. 1972.
- [25] BOHOLYUBOV, N. N., MYTROPOLSKYY, Y. A. *Asymptomatic methods in non-linear oscillations theory*. Moscow: Science, 1974.
- [26] SENYK, P. M. Inversion of the incomplete beta function. *Ukrainian Mathematical Journal* [online]. 1969, **21**(3), p. 271-278. ISSN 0041-5995, eISSN 1573-9376. Available from: <https://doi.org/10.1007/BF01085368>
- [27] SENYK, P. M., SOKIL, B. I. About U-method use for one class of oscillation system. *Report Academy of Sciences USSR*. 1977, **1**, p. 12-16.
- [28] SOKIL, B. I., SENYK, P. M. Parameters determination of non-linear oscillation system on amplitude - frequency characteristic. *Mathematical Methods and Physical and Mechanical Fields*. 1977, **7**, p. 94-99.
- [29] PAVLENKO, V. M., KRYVORUCHKO, O. O. Modern state of development of active suspensions of motor cars. *Bulletin NTU KhPI, Automobile and Tractor Manufacture* [online]. 2014, **1052**, p. 54-60. ISSN 2078-6840.

FORMING COMFORTABLE MICROCLIMATE IN THE BUS COMPARTMENT VIA DETERMINING THE HEAT LOSS

Oleksandr Kravchenko¹, Ivan Hrabar², Juraj Gerlici³, Serhii Chuiko¹, Kateryna Kravchenko^{3,*}

¹Department of Automobiles and Transport Technologies, Zhytomyr Polytechnic State University, Zhytomyr, Ukraine

²Department of Processes, Machines and Equipment, Polissya National University, Zhytomyr, Ukraine

³Department of Transport and Handling Machines, University of Zilina, Slovakia

*E-mail of corresponding author: kkatherina@ukr.net

Resume

Methodology of the heat outcome from the bus compartment in terms of duration factor of cooling and heating capacity is introduced. Value of the air temperature change in the compartment was calculated. The balance method of the spent heat is used to assess the level of keeping a proper temperature environment in the bus saloon when a comfortable microclimate is created for passengers via the proper conditioning system functioning. Models of the heat transmission notions were used for calculation regarding different categories of the heat load creation. A developed numeric algorithm was introduced in the article as well as a program for modelling the transitory heat processes in the compartment of the city bus equipped with an air-conditioner enabling to take into account various constructive decisions in the system of comfortable provision of city buses and model unstable heat processes.

Article info

Received 17 July 2020

Accepted 23 August 2020

Online 4 March 2021

Keywords:

city bus,
compartment,
temperature environment,
heat capacity of air,
heat balance,
comfortable conditions

Available online: <https://doi.org/10.26552/com.C.2021.2.B150-B157>

ISSN 1335-4205 (print version)

ISSN 2585-7878 (online version)

1 Introduction

The system of air-conditioning is an important subsystem in transport means regarding comfort support, in particular, in a while, for city buses. The heat loads, affecting a microclimate in a bus compartment while performing transport work, are rather difficult to determine due to processes of the turbulent stream and heat exchange. They consist of many thermal forms and undergo influence of many factors, such as outer temperature, intensity of sun radiation, materials for body cladding, number of passengers, motion velocity of transport means, geographic location etc. [1-3].

The microclimate in the bus compartment depends on the properties of the heating systems, ventilation, conditioning and the range of constructive parameters of the bus itself (tightness of the saloon, location of engine, its thermal insulation, heat conductivity of cladding materials, number of passengers, type of windows), as well.

The air humidity, along with temperature, may affect the human body substantially. As the doctors-hygienists state, the most favourable combinations for a human body are the conditions, when relative humidity equals 50% and the temperature is equal to 16 to 18°C, [4].

The existing mathematical models of unstable heat processes in the city bus do not completely reflect the heat processes within the compartment with passengers

inside [5]. Besides that, the unstable heat processes are often studied in the stable mode, when the heat streams and parameters of the heat circuit are constant and do not depend on time [6]. An important influence on heat exchange between outer temperature is imposed by the massive construction of the bus and due to that, the temperature fluctuations on its inner surfaces are decreased.

Due to appearance of the more effective technical solutions of the life support system, a necessity appears for creating the new mathematic apparatus that would enable to take into account these properties and their influence on the course of unstable heat processes during the whole time of performing the process of passengers' transportation.

The aim of the article comprises developing the method of solving the tasks regarding the system of comfortable provision of the city bus compartment via a suggested heat mode through the heat costs analysis.

To assess the efficiency of the conditioner functioning and to determine the period of its switching, while performing the passengers transportation process in the city route (at the example of the bus (MAZ - 206), a methodology of the heat balance calculation in the cycle "heating - cooling" was introduced. The experimental results of testing [7] by the modelling methodology [8] were used for mathematic modelling. A comparison of experimental testing and mathematic modelling was conducted. The method of elementary counterweight was



used for solving the complex system of equations. The developed mathematic model of the heat processes in the city bus compartment, unlike the existing ones, enables to research unstable heating engineering indexes in the bus compartment, under different operation conditions (level of anisotropy) and compare the work of various systems of life support in terms of their constructive decisions.

2 The latest research analysis

Scientists, such as Zhukovskiy [5], Kulikov et al. [9], Matveev [10], Palutin [11] and others [3, 12-15] researched the requirements to climate systems and microclimate normalization of wheeled vehicles. However, the constructive decisions of modern buses equipment change with time. Conditions of their exploitation also differ between the types, especially in the cities due to insufficient speed modes of traffic and unstable driving.

Results of the design technology development and calculation of inner aerodynamics of the heating system and ventilation of a passenger car were introduced in [10]. The thermal resistance of each layer of surfaces of the roof, sidewalls and facings is proposed to be taken into account separately, via indexes of the heat dissipation, heat conductivity and heat perception. The calculation method of the air exchange in a car compartment was presented under the following conditions:

- equal temperature both inside and outside of the car;
- position of hatches and windows (open or closed) do not influence the character of the air penetration into the car;
- excessive pressure in the car compartment is equal in all its volumes;
- air pressure in the compartment is established.

Parameters of the air environment of their compartments were determined due to the research of ventilation systems in cars' bodyworks [11]. Measurement of summing the effective surfaces of looseness enabled to access tightness of separate parts and a bodywork as a whole of some domestic and foreign cars. The conducted calculation of the air-exchange value in a bus saloon that have two rows of passenger double-seats and roof height of 196-205 cm, resulted in the upper limit equal to 2000 m³/h.

Analytical dependencies of the heat mode of the bus saloon during its motion, under conditions of the summer operation, were obtained in [5]. Influence of the air exchange through doorway at the stops and infiltration due to looseness of a bodywork was determined.

In calculating the loading on the intercity bus, radiation from windows was considered in the work [12], whereas the heat dissipation from roof, floor, back and front sidebars were taken into account via conductivity only. The maximum increase of heat was calculated as 25.96 kW at 17:00 during July, and this case is a peak loading and a peak time as heat dissipation. The temperature of outer atmospheric air in Adana city, in July, was accepted as 36°C

and accordingly 25.7°C in the bus compartment.

In [13] was stated that the trip duration in a car and a factor of passenger loading have a sufficient impact on the perception of a comfort level by a driver and passengers.

The conducted research of scientists in [14] proved that the cars with venting of different colors have an excellent reflecting capacity of opaque elements of a bodywork. Regarding this, the indexes were developed in accordance with a certain color of opaque elements of a bodywork classified as solar reflection indexes (SRI) and were calculated considering the solar reflection and heat radiation. The measurements proved that the cold colors have the solar spectral reflecting ability much lower than the light tones. The solar reflection fluctuates within the range of 0.04 (usually black) up to 0.70 (usually white) with many cold sub tones from the solar reflection, approximately 0.20 - 0.50. All the patterns with coating demonstrated a high thermal release (0.82 - 0.95).

It was proved by the authors of [15] that the efficient microclimate control in transport means is at least traditionally considered to serve the comfort, but under the negative effects of a temperature mode; it has a negative influence on a driver's efficiency and is considered as a safety factor in traffic. A great influence on a driver's alertness at temperature of +27°C was established in comparison to temperature +21°C in transport means: the drivers missed 50% more signals given within the first hour and reaction time got for 22% longer at the increased temperature level.

The dominating parameter of a microclimate in a closed space is an air temperature that is stated by authors of [16].

The demands to the micro-climate of the bus saloons is changing due to the peculiarity of commissioning city buses, equipped by the conditioners, that used to be a comfort feature only for the intercity buses. Another approach to microclimate quality is required by the bus operation conditions during the city traffic jams and rationing fuel cost by that [7].

3 Determination of the micro-climate in the city bus compartment

3.1 General characteristics of micro-climate provision in the saloon of the city shuttle bus

One of the crucial factors of microclimate in the bus saloon at its ventilation is its air exchange providing a normalized temperature difference between the compartment and outer environment and mobility and humidity of indoor air. At the same time a necessary air exchange of the compartment is determined on conditions of assimilation of the heat input from the solar radiation and from the passengers [5]. The main requirement to the microclimate lies in supporting meteorological and sanitary parameters in the room. Meteorological parameters comprise temperature (t_a , °C), relative humidity (φ_a , %)

and mobility (v_a , m/s) of indoor air in the room; sanitary parameters include radiation temperature of surfaces (t_r , °C), intensity of thermal (infrared radiation), level of noise, brightness, maximum permissible concentration of dust and gases [17]. The given statement corresponds to microclimate requirements of the city bus compartment to the full extent.

There are no unified requirements for the microclimate in the compartments of the city shuttle buses in the requirements to the products that undergo a compulsory certification in Ukraine. It is, primarily based on the lack of standards containing regulations to the given requirements. At the same time, among current standards of Ukraine comprising assessment of moderate and extreme thermal environments, the feeling of discomfort level (thermal dissatisfaction) of people in buildings and systems is reflected in the international standard ISO 7730:2005 [18].

Review and analysis of calculation methods for ventilation systems and heating showed that their basis lies in the integrated approach enabling to determine only average parameters implying assessment of local and linear expenditures. For example, regulatory document [19] regulates the air temperature in railway passenger carriages of all the types, in winter at the level of $+20^{\circ}\text{C} \pm 2^{\circ}\text{C}$, and in summer $+24^{\circ}\text{C} \pm 2^{\circ}\text{C}$ (in the carriages with conditioners).

While operating the bus MAZ-206 on the city routes of the automobile enterprise one comes across the problem of rationing fuel costs while working with the conditioner. It relates to activating it under the conditions of providing the optimal microclimate able to change regardless of the temperature of the outer environment. It is caused by the seating capacity, motion conditions, management of setting the whole air conditioning system etc.

The thermal perception of a person in the bus saloon is affected mainly by four factors: air humidity and velocity, temperature and properties of the surfaces surrounding a person [10]. It is worthy to consider that though the heat perception is determined by the enumerated parameters, not any ratio of these parameters may provide comfortable conditions. Each of them may not be changed at random, but only within some appropriate limits that satisfy the conditions of a comfortable thermal perception while staying in the bus saloon. Knowledge of the permissible limits of temperature fluctuations, air humidity and mobility enables regulating application of some types of air conditioning systems.

3.2 Factors of proper heat productivity and its systems

The heat costs of the city bus compartment mainly depend on:

- the temperature difference between the bus saloon and outer environment (the bigger the difference, the higher the costs);
- the heat-protective properties of the bodywork

constructions (sidebars and floor, window glass constructions and doors).

Optimal management of the conditioning system lies in the general regulation of compressor velocity that enables to control cooling power that can regulate the temperature to maintain comfort in the bus saloon and reduce the fuel consumption.

Power of air-cooling is determined by the thermal loading of the saloon and it is a complex process. It consists of many thermal forms depending on various factors: temperature of environment, solar energy intensity, material of constructions, number of passengers, motion speed of a transport means etc. [20-21].

To create the thermal comfort inside the bus it is necessary to take into account all the factors considered as they may change within time and at the same time consider the fact that each person perceives the conditions of being in the closed space inside the bus in a different way. As all the people are different, the thermal comfort usually refers to the set of optimal parameters where the highest percentage of the present passengers feel comfortable in the external environment.

As the environment inside the city bus while performing the transport process depends on many conditions, a transport means may not maintain a stable temperature inside the compartment, as it may not affect the time of opening and closing of doors, time of the day, trip duration, number of passengers and internal temperature.

The heat transmission is a complex process comprising separate processes of the heat dissipation in a hot and a cold heat bearer and heat transfer via the heat conductivity via the wall parting heat bearers. The bus saloon as any chamber is an anisotropic environment in various directions and with nonhomogeneous properties. This notion is characteristic for the heat conductivity [22].

The body surface of an average person is about 1.8 m^2 . Air and barriers of the room percept this heat. Consequently, the temperature of the room is an important factor characterizing a microclimate of the room and defines the state of thermal comfort in it. The temperature values of inner air for rooms of different application in cold and warm seasons are recommended by the norms (DBN and rules, EN ISO, ASHRAE etc.). Usually, temperature modes $+20^{\circ}\text{C}$ to 22°C , in the cold season and $+22^{\circ}\text{C}$ to 25°C in the warm season are recommended as optimal [22].

3.3 Approach to choosing experimental research method

Calculation of the heat input via elements of the bus constructions cladding in the summer period is complicated by sufficient temperature fluctuations of outer air and even bigger fluctuations of the heat stream on outer surfaces from the solar radiation. At the same time, an especially important factor lies in the heat input from the present passengers that also depends on outdoor air parameters. Thermal insulation of air conduits, pipelines and bodywork

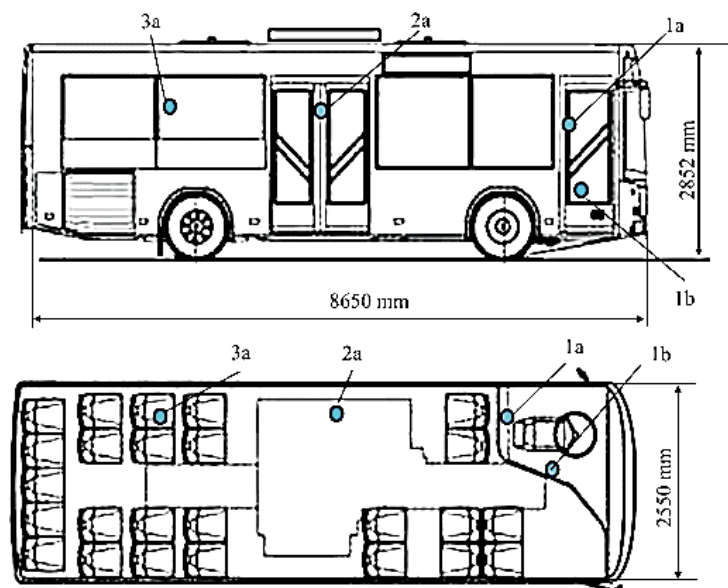


Figure 1 Points of measuring the temperature indexes in the bus compartment

construction generally caters to prevent heat and cold loss. Massiveness of the compartment's framing and noise and heat protective materials serve as a passive protection decreasing or increasing the peak loading that influences the heat exchange of the room [6, 23].

The heat loss due to fencing constructions in the cold season of the year is calculated in a stationary mode assumption, as in winter substantial temperature fluctuations of external air, especially temperature fluctuations of the external side of fencing, are not observed [6].

Considering the fact that temperature mode in the saloons of transport means is rather complex, it has complex mathematic approaches for defining optimal decisions, there is a necessity for conditional perception of a bus saloon as a chamber with a proper capacity to maintain a favorable microclimate and the heat consumption in time, through the constructive elements of a chamber.

A simplified method of calculating values of support (transmission) of the heat comfort in the saloon for a possibility of determining the moment of switching a conditioner at some heat loading, may be applied for city buses and, vice versa, its turning off, when there is no need. Such conditions occur in the warm season of the year due to the excessive input of solar radiation or when there is many passengers even at insufficient temperature indexes of external air.

Due to the complexity of applying automated devices of management of conditioner's work, nonuniform passenger layout in the saloon, large saloon capacity as a room, unstable passenger flow, duration of door opening at technological stops, complexity of the passengers' structure, complexity of determining coefficient of the heat transmission of cladding constructions of the bus saloon, complexity of the heat dissipation index from the passengers, there is a necessity of a simplified approach to determine thermal processes in the saloon via modelling heat loss.

3.4 Determining the heat loss of a city bus compartment

Accelerated experimental determining of the heat costs of a bus was carried out according to the methodology [8]. The research conducted directly in the bus saloon implying the autonomous heater of calibrated power.

The main heat factor, determining the microclimate in the city bus saloon, that is characteristic to a short-term passenger presence, is the air temperature [16]. As comfort is a subjective notion, then the efficiency evaluation of the bus saloon thermal loading, equipped by the conditioner, is reasonable to conduct according to temperature and time characteristics of the air in the checkpoints located in the zone of passengers' layout in the compartment and in a driver's cabin (Figure 1). The factor of checkpoints location in the zone of passengers' and driver's head is dominating as the surface of the saloon floor is located at different levels. The figure shows the layout of checkpoints in the process of conducting the experimental research: points 1a - zone of driver's head, 1b - zone of passenger's head (at a height of 1.3 and 1.2 m from the floor, respectively); point 2a - zone of a standing passenger's head (at a height of 1.75 m from the floor); points 3a, 3b - zone of sitting/seated passenger's head (at a height of 1.2 m from the floor).

Heating the bus saloon was conducted via the heater with calibrated heat capacity N_1 in the set range of temperatures (t_{min} °C and t_{max} °C). The characteristics of heating (t_1) and cooling (t_2) are introduced in Figures 2-4.

Characteristics of heating (t_1) and cooling (t_2). Had to be sampled. The process of heating and cooling the saloon of the bus MAZ $t_{max} = 22.5^\circ\text{C}$ is shown in Figure 3. At the same time, the temperature of the external environment comprises $t_{ext} = +7^\circ\text{C}$. The heating phase lasted 274, and the whole cycle - 683 s.

Having conducted a range of the cross-sections $C_1, C_2, C_3, L_1, L_2, L_3, K_1, K_2, K_3$ (Figure 2, b), the power of the heat

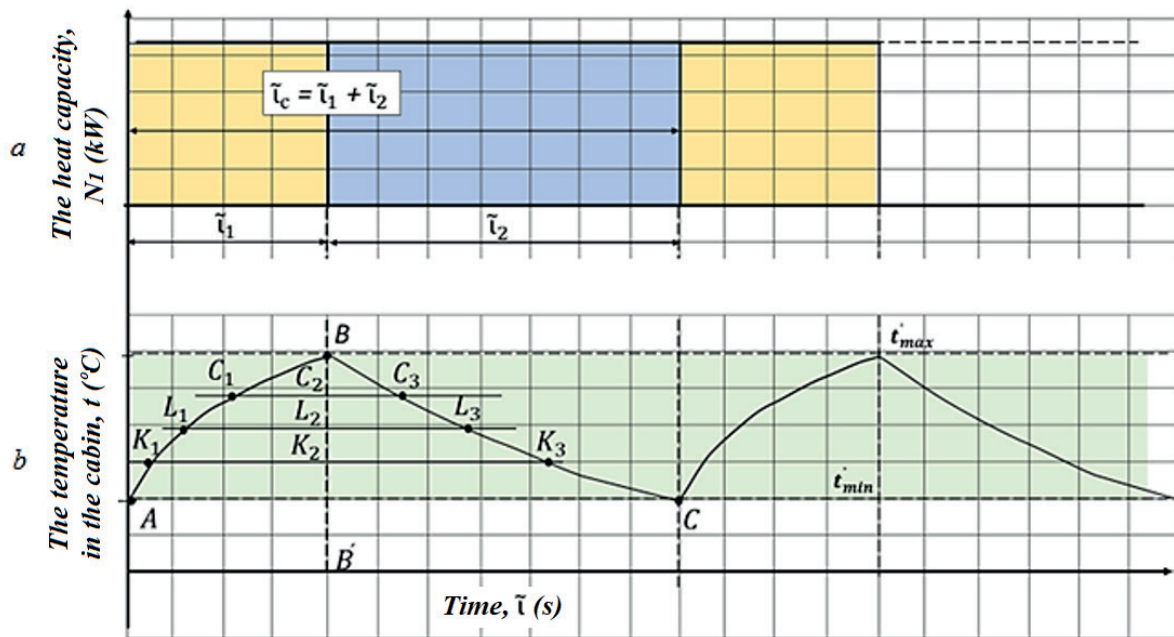


Figure 2 Processes of heating and cooling: a - temperature change, b - heat capacity change

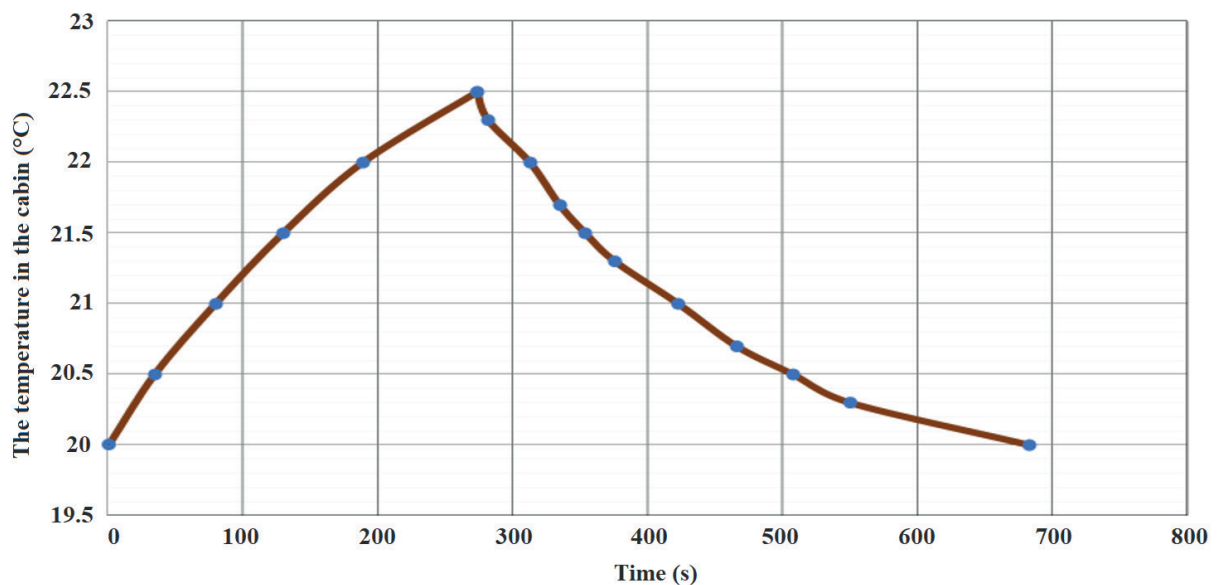


Figure 3 The full cycle of "heating-cooling" the compartment within the range of temperatures 20°C - 22.5°C

costs were calculated as

$$\dot{N}_{L1} = N_1 \cdot \frac{L_1 \cdot L_2}{L_1 t_2 + L_2 L_3} = N_1 \cdot \frac{L_1 L_2}{L_1 L_3}, \quad (1)$$

where L_2 is a point of switching a calibrated heater off.

Using the processes of heating and cooling (Figure 2), values of the heat loss power was obtained as 22°C; 21.5°C; 21°C; 20.5°C; 20°C, or, taking into account $t_{ext}^{\circ} = +7^{\circ}\text{C}$, it results in a sequence $\Delta t^{\circ} = 15^{\circ}\text{C}$; 14.5°C ; 14°C ; 13.5°C ; 13°C , respectively. The calculation results are shown in Table 1.

Accordingly,

$$N_{loss} = \frac{N_{heat} \cdot \tilde{t}}{\tilde{t}_1 + \tilde{t}_2} = \frac{2 \cdot 274}{683} = 0.802 \text{ kW}. \quad (2)$$

According to the results obtained (Table 1), the relationship between the heat loss of the compartment and temperature difference in and outside the saloon (external environment) - Figure 4. Resulting from Figure 4, one gets:

$$N_{loss} = 0.272 \cdot \Delta t^{\circ} - 2.72. \quad (3)$$

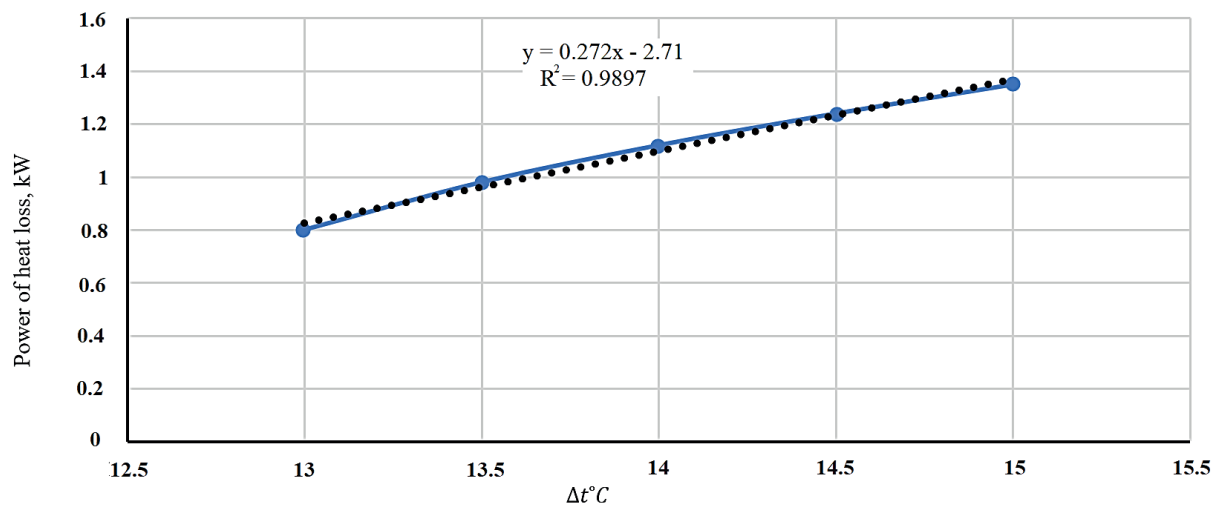
The derivative of Equation (3) reads:

$$\frac{\partial N_{loss}}{\partial (\Delta t^{\circ})} = 0.272 \frac{\text{kW}}{\text{degree}}, \quad (4)$$

where dependency $\frac{\partial N_{loss}}{\partial (\Delta t^{\circ})}$ is the power of loss in the researched bus compartment, $\frac{\text{kW}}{\text{degree}}$.

Table 1 Determining dependency of the heat costs on temperature in the compartment and the external environment

no.	temperature in the compartment, t_{LI}°	$\Delta t^{\circ} = t_{LI}^{\circ} - t_{ext}^{\circ}$	$L_1, L_2,$ mm	$L_1, L_3,$ mm	$N_{loss} = N_1 \cdot \frac{L_1 L_2}{L_1 L_2},$ kW
1	22°C	15°C	13.5	20	$2 \cdot \frac{13.5}{20} = 1.35$
2	21.5°C	14.5°C	23	37	$2 \cdot \frac{23}{37} = 1.24$
3	21°C	14°C	31	53	$2 \cdot \frac{31}{55} = 1.12$
4	21°C	13.5°C	38	77	$2 \cdot \frac{38}{77} = 0.98$
5	21°C	13°C	44	110	$2 \cdot \frac{44}{110} = 0.8$

**Figure 4** Power of the heat loss of the compartment in terms of Δt °C

Equations (3) and (4) are a linear approximation of the heat exchange dynamics between the bus compartment and the external environment. By the limitations:

- bus speed is neglected;
- the range of temperature fluctuations in the system “saloon - outside” amounts to:
 $10^{\circ}\text{C} \leq \Delta t^{\circ} \leq 20^{\circ}\text{C}$;

- heat flows are considered to be symmetrical $Q_1 (t_{saloon}^{\circ} > t_{ext.}^{\circ})$ and $Q_2 (t_{outside}^{\circ} > t_{saloon}^{\circ})$

$$\frac{\partial Q_1}{\partial t^{\circ}} = \frac{\partial Q_2}{\partial t^{\circ}}; \quad (5)$$

- at $\Delta t^{\circ} < 10^{\circ}\text{C}$, the heat exchange between the saloon and the external environment may be neglected.

Thus, the heat balance in the cycle “heating-cooling” amounts to: when the heater with calibrated power N_1 is on, during the time \tilde{t}_1 the amount of heat, supplied to the saloon (chamber), is:

$$Q_1 = N_1 \cdot \tilde{t}_1. \quad (6)$$

During that time the temperature in the saloon rises from t_{min}° to t_{max}° in the range set. When it reaches the

temperature t_{max}° , the heater is off and the saloon cools down from t_{max}° to t_{min}° for the time \tilde{t}_2 . Then, the amount of the heat emitted by the compartment into the external environment amounts to:

$$Q_2 = N_{2costs} \cdot (\tilde{t}_1 + \tilde{t}_2). \quad (7)$$

Having compared Q_1 to Q_2 , one gets:

$$Q_1 = Q_2; N_1 \tilde{t}_1 = N_{2exp} (\tilde{t}_1 + \tilde{t}_2). \quad (8)$$

The power of the heat costs of the researched object is calculated from Equation (8) as:

$$N_2 = N_1 \frac{\tilde{t}_1}{\tilde{t}_1 + \tilde{t}_2}. \quad (9)$$

The obtained results allow determining integrated index of the heat loss - power of heat loss of the researched object - compartment of MAZ -206 bus. It enables to get the power of the heat loss for a necessary range of temperatures Δt° , as well to establish dependency N_{2exp} on Δt° . The calculations were performed without taking into account the possible violation of the tightness of the bus saloon.

4 Conclusion.

An approach for determining the models of the heat costs of the bus saloon is proposed that regulates the way of defining the need for the air-conditioner activation of a city bus via the characteristics of the whole system "bus compartment - environment". To obtain the qualitative and quantitative indexes of the temperature change in the bus saloon at the set change of cold air cost, it is worthy to take into account that the heat capacity of the simultaneous air volume is much smaller compared to the sum of the heat capacities of the constructive bodywork elements, seats and partitions. The considered methodology may be

used for compartments of other bus models. Studies have confirmed that the cabin interior air inertia does not exceed 1-2 minutes.

This approach can be used for the saloon of other bus models with a larger volume of saloon space, or articulated, for example, Solaris New Urbino 18, using a larger number autonomous calibrated heaters. This is explained by the inertia of the space heating, increased due to the heat perception by the components of the saloon. The setting of the temperature indicators should be delayed for stability of temperature in the whole salon because of the small internal air inertia and the number of recorders to determine the average value in the cabin should be increased.

References

- [1] KURCIK, P., BLATNICKY, M., DIZO, J., PAVLIK, A., HARUSINEC, J. Design of a technical solution for a metro door system. *Transportation Research Procedia* [online]. 2019, **40**, p. 767-773. ISSN 2352-1465. Available from: <https://doi.org/10.1016/j.trpro.2019.07.108>
- [2] DIZO, J. Evaluation of ride comfort for passengers by means of computer simulation. *Manufacturing Technology* [online]. 2015, **15**(1), p. 8-14. ISSN 1213-2489. Available from: <https://doi.org/0.21062/ujep/x.2015/a/1213-2489/MT/15/1/8>
- [3] MEI, Y., HONGWEN, H., CHO, S., YUI, J. Stochastic dynamic programming of air conditioning system under time-varying passenger condition for electric bus. *Energy Procedia* [online]. 2016, **104**, p. 360-365. ISSN. 1876-6102. Available from: <https://doi.org/10.1016/j.egypro.2016.12.061>
- [4] BOGOLYUBOVA, V. M. *Medical rehabilitation* (in Russian). Book 1. Moscow: Binom, 2010. ISBN 978-5-9518-0408-2.
- [5] ZHUKOVSKIY, S. S. *Organized natural ventilation of bus interiors* (in Ukrainian). PhD thesis. Lvov: Lviv Polytechnic National University, 1984.
- [6] ANANEV, V. A., BALUEVA, L. N., GALPERIN, A. D., GORODOV, A. K., EREMIN, M. Y., ZVYAGINTSEVA, S. M., MURASHKO, V. P., SEDYKH, I. V. *Ventilation and air conditioning systems. Theory and practice* (in Russian). 4. ed. Moscow: Evroklimat, 2003. ISBN 5-89520-044-3.
- [7] KRAVCHENKO, O. P., CHUYKO, S. P. Research of bus interior heat balance in the year warm period (in Ukrainian). *Scientific Journal of Vladimir Dahl East Ukrainian National University*. 2019, **3**(251), p. 101-106. ISSN 1998-7927.
- [8] GRABAR, I. G., GRABAR, O. I. Method of accelerated energy audit of the investigated volume (drying and refrigeration chambers, industrial and residential premises, other volumes with a given temperature and thermal insulation coating) (in Ukrainian).. Application for a patent for an invention of Ukraine a 2019 10343 from 15.10.2019.
- [9] KULIKOV, Y. A., GRIBINICHENKO, M. V., GONCHAROV, A. V. *Car cooling, ventilation and heating systems* (in Ukrainian). Monograph. Lugansk: V. Dahl EUNU, 2006. ISBN 966-590-557-0.
- [10] MATVEEV, D. V. *Development of technology for calculating the heating and ventilation system of a car* (in Russian). PhD thesis. Izhevsk, 2006.
- [11] PALUTIN, Y. I. *Methodological basis for improving the parameters of the air environment of car interiors* (in Russian). PhD thesis. Novgorod, 1997.
- [12] TOSUN, E., BILGILI, M., TUCCAR, G., YASAR, A., AYDIN, K. Exergy analysis of an inter-city bus air-conditioning system. *International Journal of Exergy* [online]. 2016, **20**(4), p. 445-464. ISSN 1742-8297. Available from: <https://doi.org/10.1504/IJEX.2016.078094>
- [13] XIANGHAO, S., SHUMIN, F., ZHENNING, L. Analysis of bus passenger based on passenger load factor and in-vehicle time. *Springer Plus* [online]. 2016, **5**(1), 62. ISSN 2193-1801. Available from: <https://doi.org/10.1186/s40064-016-1694-7>
- [14] LEVINSON, R., AKBARI, H., BANWEISS, G., PAN, H., PAOLINI, R., ROSADO, P., SPEARS, M., TAM, J. *Cool-colored cars to reduce air-conditioning energy use and reduce CO₂ emission*. Berkeley: Lawrence Berkeley National Laboratory One Cyclotron Road. 2011.
- [15] NORIN, F., WYON, D. Driver vigilance - the effects of compartment temperature. *SAE Technical Papers* [online]. 1992, 90092. ISSN 0148-7191. Available from: <https://doi.org/10.4271/920168>
- [16] DRAGANOV, B. K., BESSARAB, O. S., DELIISKIY, A. A., LAZORENKO, V. O., MISHCHENKO, A. V., SHELIMANOVA, O. V. *Heat engineering: textbook* (in Ukrainian). 2. ed. Kiev: Firma Inkos, 2005. ISBN 966-8347-12-9.
- [17] VOZNYAK, O. T., SAVCHENKO, O. O., MIRONYUK, CH. V., SHAPOVAL, S. P., SPODINYUK, N. A., GULYAJ, B. I. *Heat and gas supply and ventilation* (in Ukrainian). Lviv: Lviv Polytechnic National University, 2013. ISBN 978-617-607-436-6

- [18] ISO 7730:2005 Ergonomics of the thermal environment - Analytical determination and interpretation of thermal comfort using calculation of the PMV and PPD indices and local thermal comfort criteria [online] [accessed 2020-05-20]. 2015. Available from: <https://www.iso.org/standard/39155.html>
- [19] DSP 7.7.2.015 - 99. State sanitary rules and norms, hygienic standards of railway rolling stock for passenger transportation (in Ukrainian) [online] [accessed 2020-05-20]. Available from: <https://zakon.rada.gov.ua/rada/show/v0015588-99>
- [20] WANG, R, DING, G. Advanced Refrigeration and Air Conditioning Technology. Beijing: Science Press, 2002. ISBN 7-03-010677-6.
- [21] FAYAZBAKHS, M. A., BAHRAMI, M. Comprehensive modeling of vehicle air conditioning loads using heat balance method. *SAE Technical Paper* [online]. 2013, 2, 97364. Available from: <https://doi.org/10.4271/2013-01-1507>
- [22] ZHUKOVSKIY, S. S., LABAY, V. Y. *Ventilation aerodynamics: a textbook* (in Ukrainian). Lviv: Lviv Polytechnic National University, 2003. ISBN 966-553-303-7.
- [23] GRABAR, I. G., GRABAR, O. I., GUTNICHENKO, O. A., KUBRAK, YU. O. *Percolation-fractal materials: properties, technologies, applications* (in Ukrainian). Zhytomir: Zhytomyr Polytechnic State University, 2007. ISBN 978-966-683-135-7.

DYNAMICS AND CONTROL OF THE GYROSCOPIC HEAD USED FOR THE LASER ILLUMINATION OF A GROUND TARGET FROM THE QUADCOPTER DECK

Zbigniew Koruba, Izabela Krzysztofik*

Faculty of Mechatronics and Mechanical Engineering, Kielce University of Technology, Kielce, Poland

*E-mail of corresponding author: pssik@tu.kielce.pl

Resume

In the paper authors investigate dynamics of a controlled quadcopter in terms of the possibility of its use for detection, observation, tracking and laser illuminating of both stationary and moving ground targets in the conditions of impact of random and kinematic excitations. The drone is equipped with a scanning and tracking Gyroscopic Head (GH) coupled with a laser target indicator. The drone is affected by random disturbances in the form of wind gusts or explosions of missiles. Kinematic excitations, such as drone maneuvers and vibrations from engines, act on the GH. This paper focuses mainly on control and stabilization of the gyroscopic head placed on the drone during the search, tracking and simultaneous laser illuminating of the target.

Article info

Received 17 September 2020

Accepted 29 October 2020

Online 11 March 2021

Keywords:

control and dynamics of quadcopter, scanning and tracking by gyroscopic head, modeling and guidance

Available online: <https://doi.org/10.26552/com.C.2021.2.B158-B164>

ISSN 1335-4205 (print version)

ISSN 2585-7878 (online version)

1 Introduction

In recent years, four-rotor unmanned aerial vehicles (quadcopters) have become a very popular unmanned platform that is still in the stage of intensive research and finds a variety of applications. Currently, they are used, among others, for shooting collective events, monitoring communication infrastructure, supporting rescue operations, monitoring the state of air pollution. The paper proposes the use of this type of QuadCopter Unmanned Aerial Vehicle (QCUAV) for the laser pointing of ground targets, both stationary and mobile, using the scanning and tracking gyroscopic head [1-2]. In addition, a mathematical model was developed for controlling the movement of the gyroscopic scanning and tracking head as well as the mathematical model of the drone's dynamics [3-5].

It should be emphasized that the advantage of the considered QCUAV is its ability to stay in hover for a certain period of time. The system of laser pointing of a target (SLPT) can thus act independent from drone's movement and therefore stably determines the target observation line (TLOS) regardless of disturbances acting on the drone itself. While searching for a target, the GH is put into a programmed motion that allows scanning the ground surface [6]. The infrared sensor and the laser target pointer are attached to the GH axis. At the moment of receiving a thermal signal from the target, the drone goes to hover and GH begins to illuminate it with laser pulses, so that target

can become the object of attack [7-8].

To ensure the high precision in maintaining the TLOS in a given position, an optimal controller was designed for the GH. For this reason, despite many control methods used for the unmanned aerial vehicle, known in the literature [9-11] a simple PID controller was used to control the flight of the QCUAV, since the drone movement in space does not have to be precisely determined [12-16]. Simplified operation diagram of the system of detection, tracking and laser pointing of a target from the QCUAV deck is shown in Figure 1.

2 Mathematical model of dynamics of the QCUAV and controlled gyroscopic head

The executive unit in the scanning and tracking head, mentioned above, is a controlled gyroscope system. The general view of the gyroscope system with forces and moments of forces is shown in Figure 2.

Mathematical model of the controlled gyroscope system dynamics is presented in the following form [17]:

$$\begin{aligned}
 & J_{y1} \frac{d\omega_{gy1}}{dt} + (J_{y2} + J_{y3}) \frac{d}{dt} (\omega_{gy2} \cos \theta_g) - J_{z2} \times \\
 & \times \frac{d}{dt} (\omega_{gz2} \sin \theta_g) - J_{z3} \frac{d}{dt} (\omega_{gz3} \sin \theta_g) + m_g l_g \times \\
 & \times \frac{d}{dt} [V_{gx2} (1 + \cos \theta_g)] + (J_{x1} + J_{z1}) \omega_{gx1} \omega_{gz1} + \\
 & + (J_{x2} + J_{x3}) \omega_{gx2} \omega_{gz1} - (J_{y2} + J_{y3}) \omega_{gy2} \omega_{gx1} \sin \theta_g -
 \end{aligned} \quad (1)$$



This is an open access article distributed under the terms of the Creative Commons Attribution 4.0 International License (CC BY 4.0), which permits use, distribution, and reproduction in any medium, provided the original publication is properly cited. No use, distribution or reproduction is permitted which does not comply with these terms.

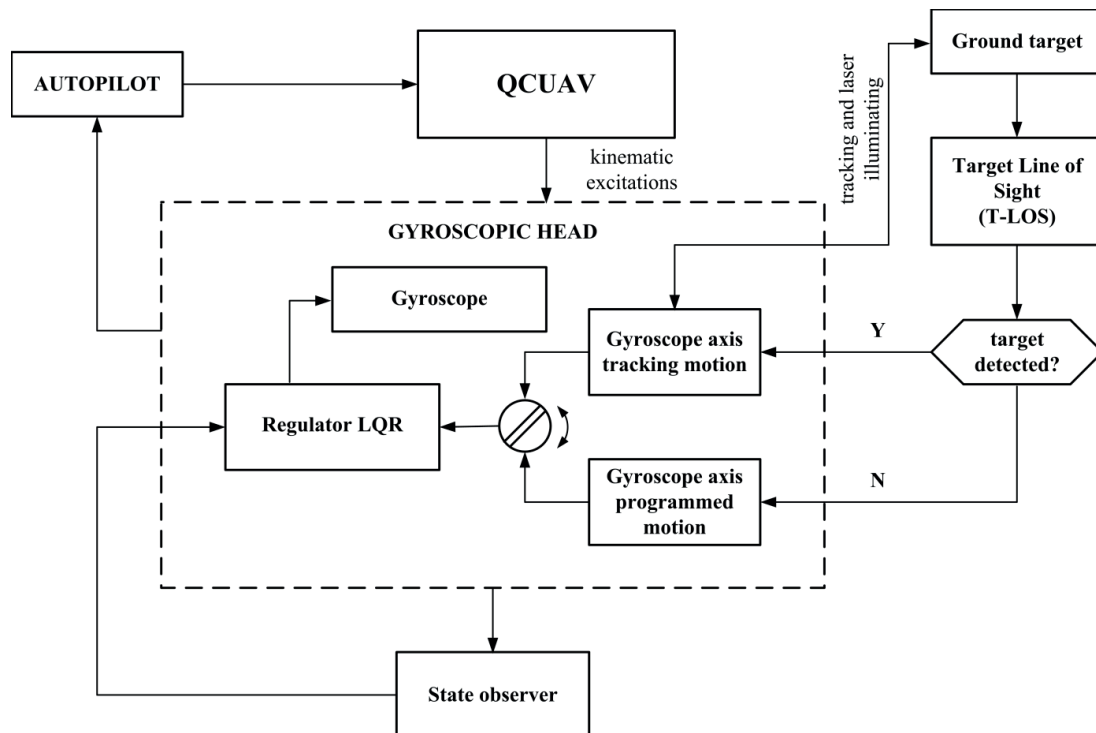


Figure 1 Simplified operation diagram of the system of detection, tracking and laser pointing of a target from the QCUAV deck

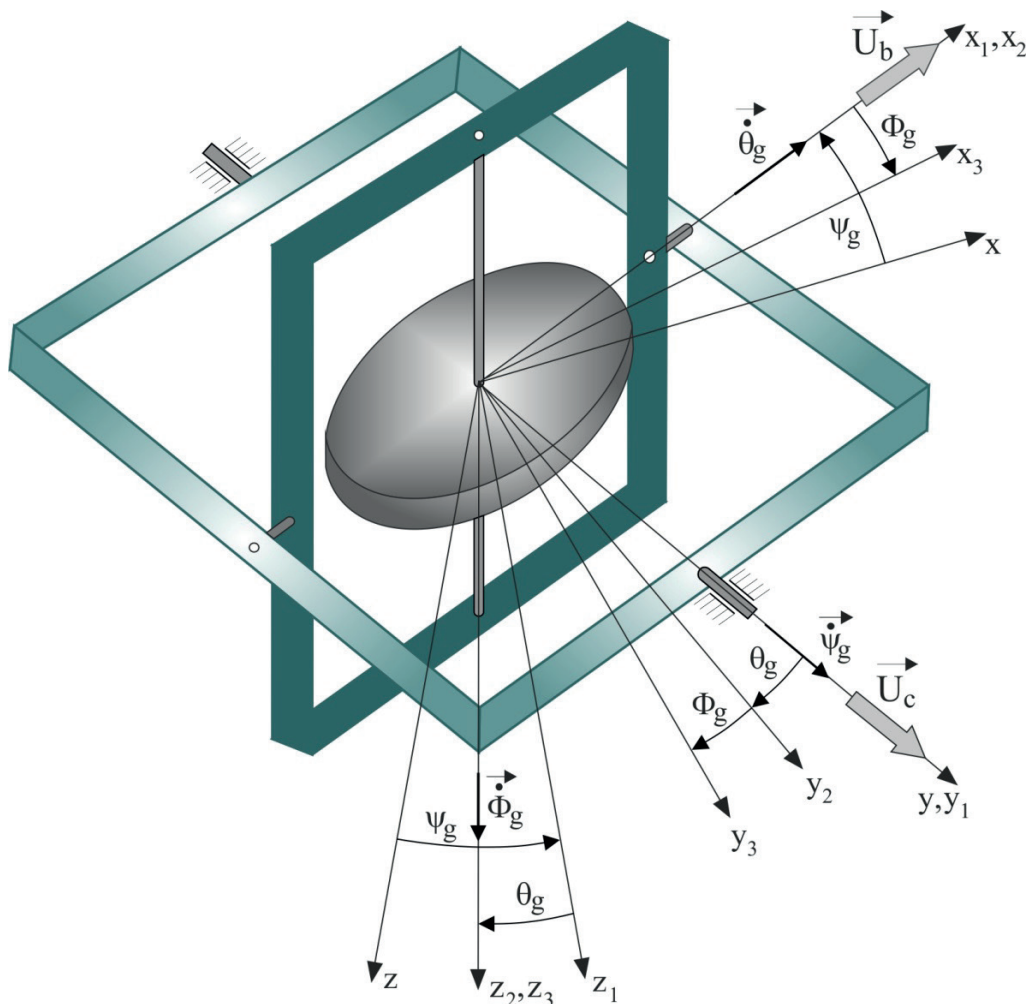


Figure 2 General view of the gyroscope system

$$-(J_{z2}\omega_{gz2} + J_{z3}\omega_{gz3})\omega_{gx1}\cos\theta_g - m_g V_{gz2}[-V_{gz1} + \omega_{gx1}l_g\sin\theta_g] - m_g V_{gz2}[V_{gx1}\sin\theta_g + \omega_{gz1}l_g \times (1 + \cos\theta_g)] - m_g V_{gz2}[V_{gx1}\cos\theta_g - \omega_{gz1}l_g\sin\theta_g] = U_c - U_{cf},$$

$$(J_{x2} + J_{x3})\frac{d\omega_{gx2}}{dt} - m_g l_g \frac{dV_{gy2}}{dt} - (J_{y2} + J_{y3} - J_{z2}) \times \omega_{gy2}\omega_{gz2} - J_{z3}\omega_{gz3}\omega_{gy2} - m_g l_g V_{gx2}\omega_{gz2} - m_g V_{gy2} \times V_{gz2} - m_g V_{gz2}[-V_{gz1}\sin\theta_g - V_{gy1}\cos\theta_g + \omega_{gx1} \times l_g \cos\theta_g] = U_b - U_{bf}, \quad (2)$$

where:

$$\begin{aligned} \omega_{gx1} &= p_v \cos\phi_g - r_v \sin\phi_g; \omega_{gy1} = \dot{\phi}_g + q_v; \\ \omega_{gz1} &= p_v \sin\phi_g + r_v \cos\phi_g; \\ \omega_{gx2} &= \omega_{gx1} + \dot{\theta}_g; \\ \omega_{gy2} &= \omega_{gz1}\sin\theta_g + \omega_{gy1}\cos\theta_g; \\ \omega_{gz2} &= \omega_{gz1}\cos\theta_g + \omega_{gy1}\sin\theta_g; \\ \omega_{gz3} &= \omega_{gz2} + n_g; \\ V_{gx1} &= u_v \cos\phi_g - w_v \sin\phi_g; V_{gz1} = v_v; \\ V_{gz1} &= u_v \sin\phi_g - w_v \cos\phi_g; \\ V_{gx2} &= V_{gx1} + l_g(\omega_{gy1} + \omega_{gy2}); \\ V_{gy2} &= V_{gz1}\sin\theta_g + V_{gy1}\cos\theta_g - l_g(\omega_{gx1}\cos\theta_g + \omega_{gx2}); \\ V_{gz2} &= V_{gz1}\cos\theta_g - V_{gy1}\sin\theta_g + l_g\omega_{gx1}\sin\theta_g; \end{aligned}$$

and

$$\begin{aligned} \phi_g, \theta_g, \dot{\phi}_g &- \text{angles determining the rotor position in space;} \\ p_v, q_v, r_v &- \text{components of the quadcopter angular speed;} \\ u_v, v_v, w_v &- \text{components of the quadcopter linear speed;} \\ J_{x1}, J_{y1}, J_{z1} &- \text{moments of inertia of the external frame;} \\ J_{x2}, J_{y2}, J_{z2} &- \text{moments of inertia of the internal frame;} \\ J_{x3}, J_{y3}, J_{z3} &- \text{moments of inertia of the rotor;} \\ n_g &- \text{rotation speed of the rotor;} \\ m_g &- \text{mass of the internal frame and rotor;} \\ l_g &- \text{distance from the gyroscope mass centre to the gyroscope centre of rotation;} \\ \eta_b, \eta_c &- \text{friction coefficients in the suspension bearings;} \\ U_b, U_c &- \text{gyroscope control moments;} \\ U_{bf}, U_{cf} &- \text{moments of friction forces in the bearings of the internal and external frame respectively, determined by relationships;} \end{aligned}$$

for viscous $U_{bf} = \eta_b \dot{\theta}_g; U_{cf} = \eta_c \dot{\phi}_g$ and
for dry friction $U_{bf} = \frac{1}{2} d_{bf} T_{bf}; U_{cf} = \frac{1}{2} d_c T_{cf}$

with: $T_{bf} = \mu_b N_b \text{sign}(\dot{\theta}_g); T_{cf} = \mu_c N_c \text{sign}(\dot{\phi}_g)$
 $\eta_b, \eta_c, \mu_b, \mu_c$ - friction coefficients in the suspension bearings;
 N_b, N_c - normal reactions in the frame bearings;
 d_b, d_c - diameters of bearing pivots.

Occurrence of friction in the suspension bearings causes formation of moments acting on gyroscope, depending on the angular velocity of the vehicle on which the gyroscope is located. Assuming that the moments of friction forces are of the viscous type, one has:

$$U_{bf} = \eta_b \dot{\phi}_g; U_{cf} = \eta_c \dot{\theta}_g. \quad (3)$$

Out of numerous gyro control methods [17], the

optimum LQR method has been adopted in this paper [18-20]. The control law \mathbf{u}_g for GH was determined using the linear-quadratic optimization method with the function in the form of:

$$I = \int_0^\infty (\mathbf{x}_g^T \mathbf{Q} \mathbf{x}_g + \mathbf{u}_g^T \mathbf{R} \mathbf{u}_g) dt. \quad (4)$$

This law is presented by equation:

$$\mathbf{u}_g = -\mathbf{K}_g (\mathbf{x}_g - \mathbf{x}_{gz}), \quad (5)$$

where \mathbf{x}_g is a vector of actual state variables determining the position of gyroscope system axis in space and \mathbf{x}_{gz} is a set (desired) state variables.

The \mathbf{K}_g matrix of gains is determined using the Matlab function [21-22]:

$$\mathbf{K}_g = \text{lqr}(\mathbf{J}, \mathbf{B}, \mathbf{Q}, \mathbf{R}), \quad (6)$$

where \mathbf{J} , matrix constituting the argument of lqr function, is a Jacobian of the gyroscope system.

To determine components of Jacobian \mathbf{J} , the motion Equations (1)-(2) were simplified to the following form, respectively:

$$J_{gk} \dot{\phi}_g + J_{gk} \dot{\phi}_g \sin 2\theta_g + J_{go} n_g \dot{\theta}_g \cos \theta_g = U_c - U_{cf}, \quad (7)$$

$$J_{gk} \dot{\theta}_g - 0.5 J_{gk} (\dot{\phi}_g)^2 \sin 2\theta_g - J_{go} n_g \dot{\phi}_g \cos \theta_g = U_b - U_{bf}, \quad (8)$$

where:

$$J_{gk} = J_{x3} = J_{y3} \text{ and } J_{go} = J_{z3}.$$

Then, components of the \mathbf{J} matrix are determined as follow:

$$\begin{aligned} J_{11} &= 0, J_{12} = 1, J_{13} = 0, J_{14} = 0; \\ J_{21} &= (-J_{gk} \dot{\phi}_g^2 \cos 2\theta_g + J_{go} n_g \dot{\phi}_g \sin \theta_g) / J_{gk}; \\ J_{22} &= -\frac{n_b}{J_{gk}}, J_{23} = 0, J_{24} = \left(-J_{gk} \dot{\phi}_g \sin 2\theta_g - \right) / J_{gk}; \\ J_{31} &= 0, J_{32} = 0, J_{33} = 0, J_{34} = 1; \\ J_{41} &= 2 \sin \theta_g \left(-\eta_c \dot{\phi}_g + J_{gk} \dot{\theta}_g \dot{\phi}_g \sin 2\vartheta_g + \right) / J_{gk} \cos^3 \theta_g \\ &+ (2 J_{gk} \dot{\theta}_g \dot{\phi}_g \cos 2\theta_g - J_{go} n_g \dot{\theta}_g \sin \vartheta_g) / J_{gk} \cos^2 \theta_g; \\ J_{41} &= (J_{gk} \dot{\phi}_g \sin 2\theta_g + J_{go} n_g \cos \vartheta_g) / J_{gk} \cos^2 \theta_g; \\ J_{43} &= 0, J_{44} = (-\eta_c + J_{gk} \dot{\theta}_g \sin 2\vartheta_g) / J_{gk} \cos^2 \theta_g. \end{aligned}$$

If the state observer is used, instead of the \mathbf{x}_g state, the regulator is entered by an estimate $\hat{\mathbf{x}}_g$ from the observer, i.e. the control will take the form of

$$\mathbf{u}_g(t) = -\mathbf{K}_g(t) \hat{\mathbf{x}}_g(t). \quad (9)$$

The QCUAV configuration with rotational speeds, forces and moments generated by the four motors is presented in Figure 3.

Using the Euler-Lagrange formalism, the following mathematical model of the quadcopter dynamics was derived:

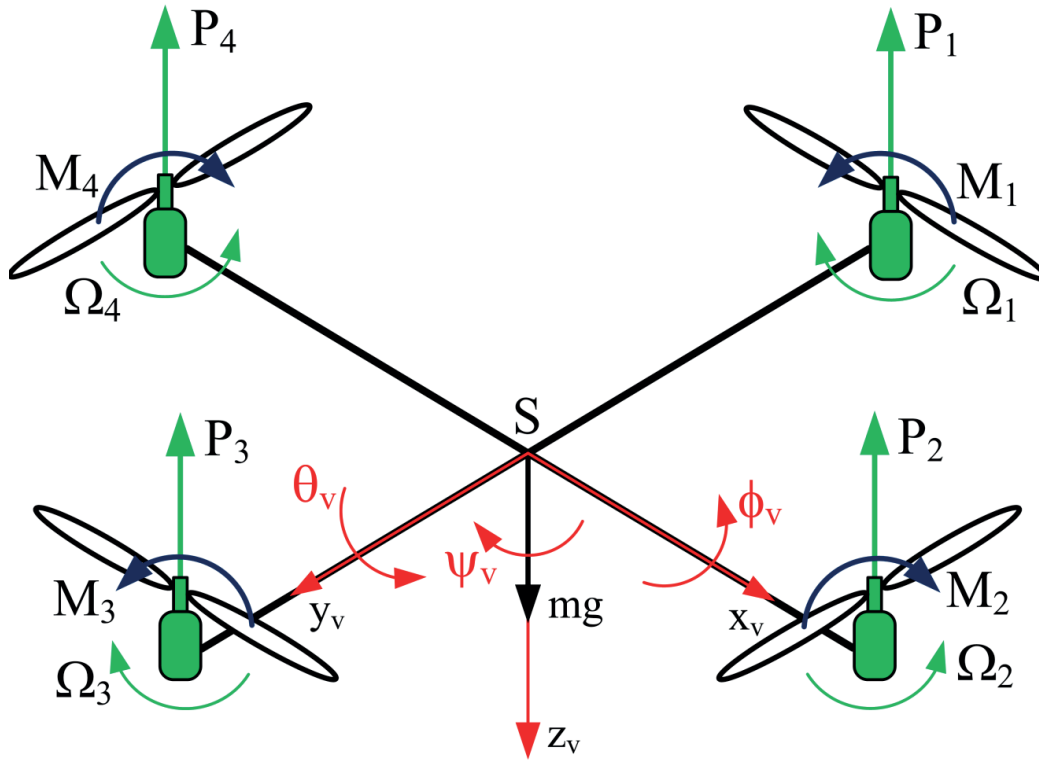


Figure 3 Angles of the quadcopter position

$$\begin{bmatrix} \ddot{x}_v \\ \ddot{y}_v \\ \ddot{z}_v \\ \dot{\phi}_v \\ \dot{\theta}_v \\ \dot{\psi}_v \end{bmatrix} = \begin{bmatrix} U_1(\cos \phi_v \sin \theta_v \cos \psi_v + \sin \phi_v \sin \psi_v)/m_v \\ U_1(\sin \phi_v \sin \theta_v \cos \psi_v - \cos \phi_v \sin \psi_v)/m_v \\ U_1 \cos \theta_v / m_v + g \\ [(I_y - I_z)\dot{\phi}_v \dot{\theta}_v - J_r \dot{\theta}_v \dot{\Omega}_r + l_v U_2]/I_x \\ [(I_z - I_x)\dot{\phi}_v \dot{\psi}_v + J_r \dot{\phi}_v \dot{\Omega}_r + l_v U_3]/I_y \\ [(I_x - I_y)\dot{\theta}_v \dot{\psi}_v + U_4]/I_z \end{bmatrix}, \quad (10)$$

with

$$\Omega_r = \Omega_1 + \Omega_3 - \Omega_2 - \Omega_4;$$

$\Omega_1, \Omega_2, \Omega_3, \Omega_4$ - rotational speeds of the individual motors,

l_v - arm's length,

m_v - drone's mass,

I_x, I_y, I_z - moments of inertia of the QCUAV,

J_r - moment of inertia of the rotor and

U_1, U_2, U_3, U_4 - controls.

The control vector \mathbf{U} is determined by the following formula:

$$\begin{bmatrix} U_1 \\ U_2 \\ U_3 \\ U_4 \end{bmatrix} = \begin{bmatrix} -b(\Omega_1^2 + \Omega_2^2 + \Omega_3^2 + \Omega_4^2) \\ b(\Omega_1^2 - \Omega_2^2) \\ b(\Omega_2^2 - \Omega_4^2) \\ d(\Omega_2^2 + \Omega_4^2 - \Omega_1^2 - \Omega_3^2) \end{bmatrix}, \quad (11)$$

where b is the thrust coefficient and d is the drag coefficient.

3 Results and conclusions

In order to verify the correct operation of the gyro head during the laser illuminating the ground target from the deck of drone, appropriate simulation tests were carried out. The drone movement from a given starting point in space to a point on a fixed height $H_{do} = 20$ m - exactly

above and at a fixed distance from the target, moving on the surface of the earth, was considered. The drone's GH tracks the moving target and at the same time illuminates it with a laser. This is shown in the Figures 4-12.

The tests were conducted in the Matlab/Simulink environment using the ode45 integration procedure for the following parameters:

- gyro system parameters

$$J_{x1} = 2.5 \cdot 10^{-5} \text{ kgm}^2; J_{y1} = J_{x1}; I_{z1} = J_{x1};$$

$$J_{x2} = 5 \cdot 10^{-5} \text{ kgm}^2; J_{y2} = J_{x2}; I_{z2} = J_{x2};$$

$$J_{x3} = 2.5 \cdot 10^{-4} \text{ kgm}^2; J_{y3} = J_{x3}; I_{z3} = 5 \cdot 10^{-4} \text{ kgm}^2;$$

$$n_g = 600 \text{ rad/s}; \eta_b = 0.01 \text{ Nms}; \eta_c = 0.01 \text{ Nms};$$

$$m_g = 0.24 \text{ kg}; l_g = 0.001 \text{ m};$$

optimal LQR gain matrix for the gyro system

$$K_g = \begin{bmatrix} 9.5114 & 0.3709 & 41.9258 & 0.1695 \\ -2.0134 & 0.0004 & 0.4585 & 0.0031 \end{bmatrix};$$

- quadcopter parameters

$$m_v = 0.65 \text{ kg}; l_v = 0.23 \text{ m}; b = 3.13 \cdot 10^{-5} \text{ Nms}^2;$$

$$d = 7.5 \cdot 10^{-7} \text{ Nms}^2; J_r = 6.0 \cdot 10^{-5} \text{ kgm}^2;$$

$$\Omega_{\max} = 500 \text{ rad/s}; I_x = 7.5 \cdot 10^{-3} \text{ kgm}^2;$$

$$I_y = 7.5 \cdot 10^{-3} \text{ kgm}^2; I_z = 1.3 \cdot 10^{-2} \text{ kgm}^2;$$

the values of the PID regulator coefficients for the drone

$$k_{p1} = 11.8; k_{d1} = 10.8; k_{i1} = 0.9;$$

$$k_{p2} = 0.65; k_{d2} = 0.46;$$

$$k_{p3} = 0.45; k_{d3} = 0.36;$$

$$k_{p4} = 0.12; k_{d4} = 0.12;$$

$$k_{px} = 8.8; k_{dx} = 8.9;$$

$$k_{py} = 8.8; k_{dy} = 8.9.$$

The graphs show the movement of the gyroscope axis, having the task at keeping the line of sight from

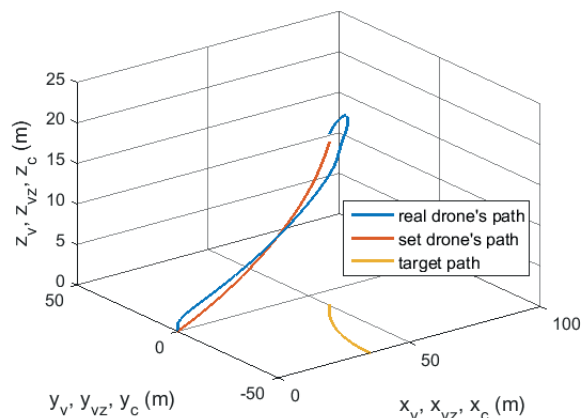


Figure 4 Drone's flight path and target trajectory

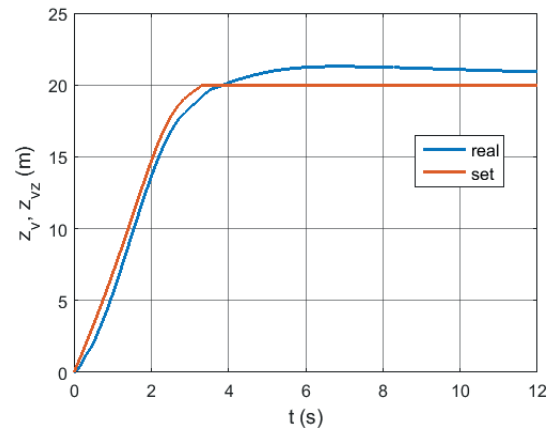


Figure 6 Changes of the state variables z_v and z_{vz} - real and set - as a function of time

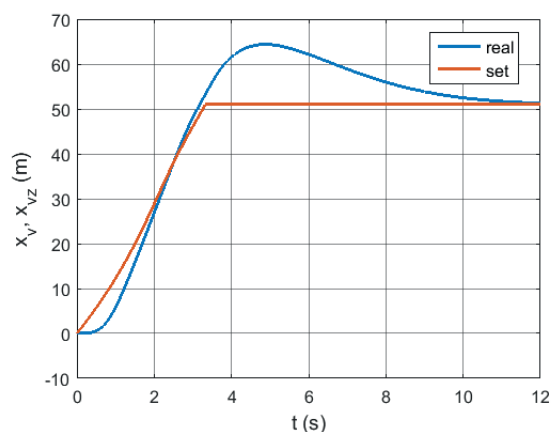


Figure 5 Changes of the state variables x_v and x_{vz} - real and set - as a function of time

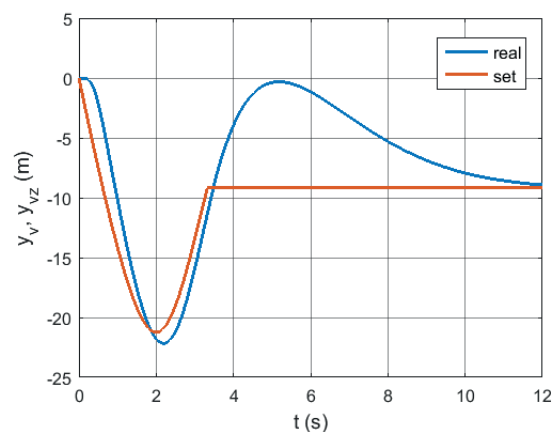


Figure 5 Changes of the state variables y_v and y_{vz} - real and set - as a function of time

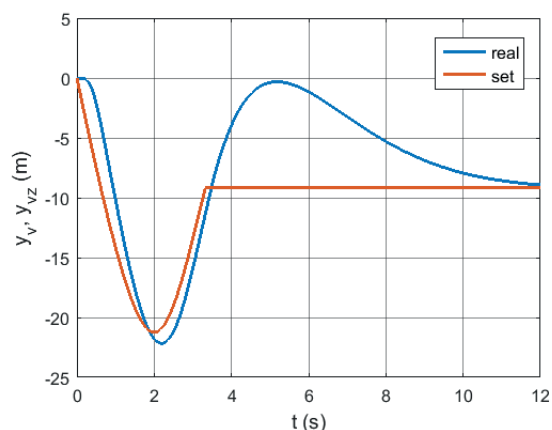


Figure 5 Changes of the state variables y_v and y_{vz} - real and set - as a function of time

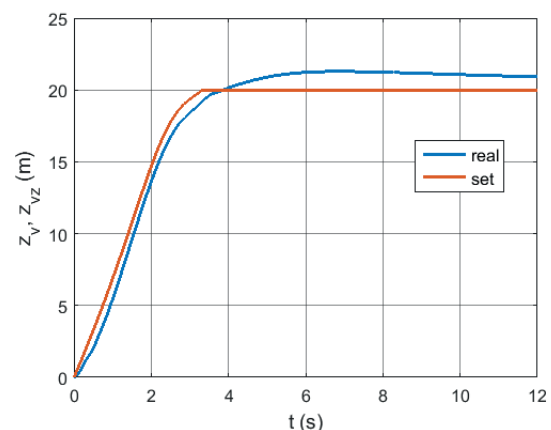


Figure 6 Changes of the state variables z_v and z_{vz} - real and set - as a function of time

the deck of the drone from the moment of gaining the height to the passage and maintaining the hover. At the starting moment of the drone, the initial conditions of the gyroscope axis motion are unknown. For this reason, a series compensator was used (the state observer with the LQR controller). In the initial phase of tracking, i.e. for a period of about 1 second, the large dynamic effects are

visible, after which the compensator follows the target with sufficient accuracy. However, it should be noted, that the transitional period also appears when the drone is moved to hover and lasts only about 0.5 s. It was also assumed that during the reaching heights and hover, the wind is blowing on the drone. These gusts significantly disturb the drone flight trajectory, however, they do not have much

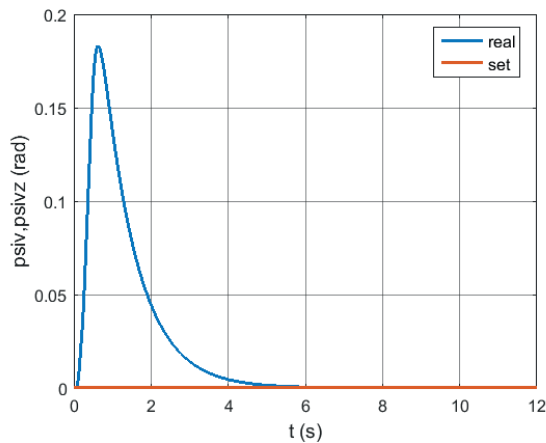


Figure 7 Changes of the state variables $psiv$ and $psivz$ - real and set - as a function of time

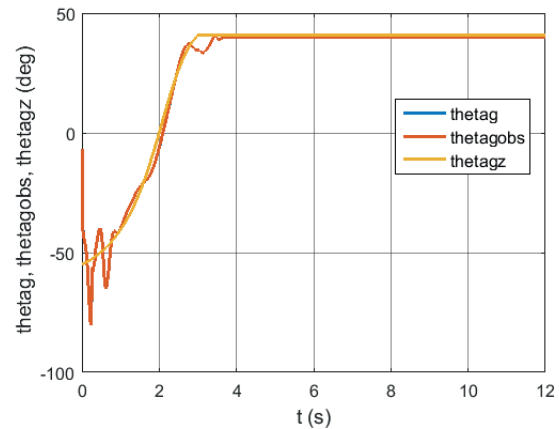


Figure 10 Changes of the state variables $tetag$, $tetagobs$ and $tetagz$ - real, observer and set - as a function of time

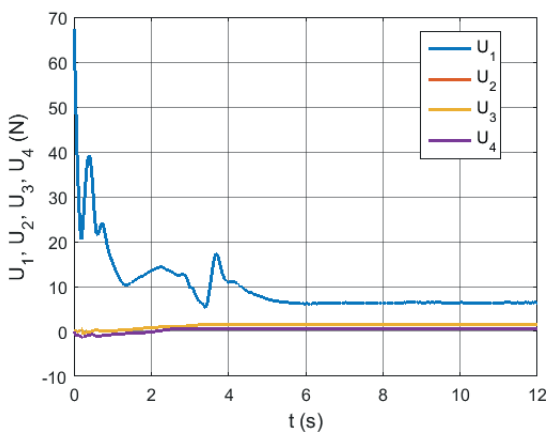


Figure 8 Changes of the drone's controls U_1 , U_2 , U_3 , U_4 as a function of time

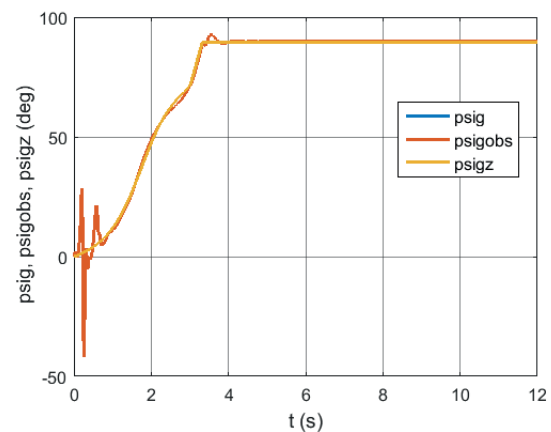


Figure 11 Changes of the state variables $psig$, $psigobs$ and $psigz$ - real, observer and set - as a function of time

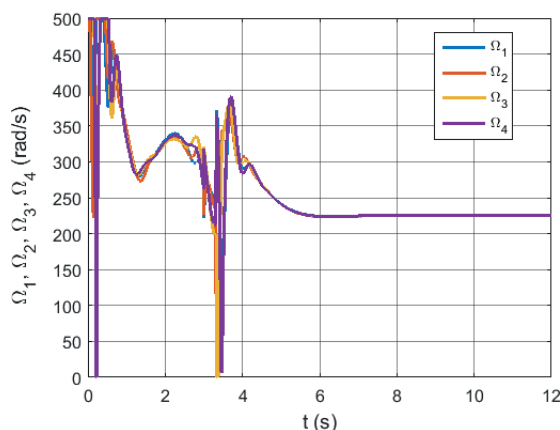


Figure 9 Changes of angular velocities of the drone's rotors as a function of time

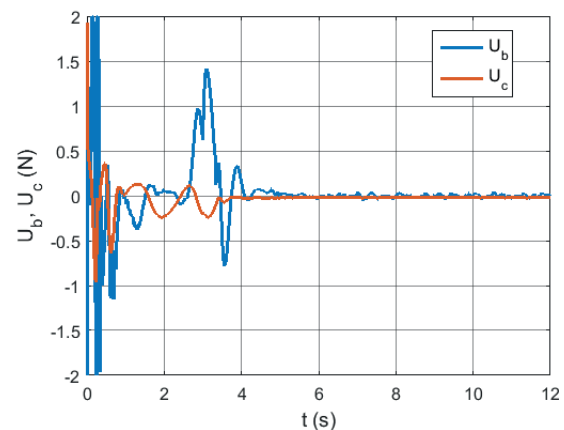


Figure 12 Changes of the gyro controls U_b and U_c as a function of time

impact on accuracy of the target illumination by the gyro axis. In figures, the position of the gyro axis determines the angles $tetag$ and $psig$ (blue), while the set position is $tetagz$ and $psigz$ angles (yellow) and angles determined by the observer are $tetagobs$ and $psigobs$.

Initial simulations demonstrated that the system laser illuminating ground target from the deck of a drone,

using the gyro scanning and tracking head, is robust to large external interference from QCUAV and even its complete descent from both the pre-set trajectory and the hovering.

In addition, the gyro head and drone control algorithm proposed in this paper works correctly and ensures the precise laser target illumination capability.

References

- [1] KORUBA, Z., KRZYSZTOFIK, I. Nonlinear model of quadrotor dynamics during observation and laser target illumination. In: LACARBONARA, W., BALACHANDRAN, B., MA, J., TENREIRO MACHADO, J., STEPAN, G. (eds) *Nonlinear dynamics and control*. Springer, 2020, p. 187-196. ISBN 978-3-030-34746-8.
- [2] KRZYSZTOFIK, I., KORUBA, Z. Analysis of quadcopter dynamics during programmed movement under external disturbance. In: LACARBONARA, W., BALACHANDRAN, B., MA, J., TENREIRO MACHADO, J., STEPAN, G. (eds) *Nonlinear dynamics and control*. Springer, 2020, p. 177-185. ISBN 978-3-030-34746-8.
- [3] BOUABDALLAH, S. Design and control of quadrotors with application to autonomous flying. PhD thesis. EPFL, 2007.
- [4] BRESCIANI, T. Modelling, identification and control of a quadrotor helicopter. Master Thesis. Lund University, 2008.
- [5] NAIDOO, Y., STOPFORTH, R., BRIGHT, G. Quad-rotor unmanned aerial vehicle helicopter modelling and control. *International Journal of Advanced Robotic Systems* [online]. 2011, **8**(4), p. 139-149. ISSN 1729-8814. Available from: <https://doi.org/10.5772/45710>
- [6] KRZYSZTOFIK, I., KORUBA, Z. Mathematical model of movement of the observation and tracking head of an unmanned aerial vehicle performing ground target search and tracking. *Journal of Applied Mathematics* [online]. 2014, **2014**, 934250. ISSN 1110-757X. Available from: <https://doi.org/10.1155/2014/934250>
- [7] ZUO, Z. Quadrotor trajectory tracking control: a PD control algorithm. In: 3rd International Conference on Computer and Electrical Engineering: proceeding. Vol. 53(2). IACSIT Press, 2012. ISSN 2010-460X.
- [8] MANJUNATH, A., MEHROK, P., SHARMA, R., RATNOO, A. Application of virtual target based guidance laws to path following of a quadrotor UAV. In: International Conference on Unmanned Aircraft Systems ICUAS 2016: proceedings. IEEE, 2016. ISBN 978-1-4673-9334-8, p. 252-260.
- [9] BOUABDALLAH, S., SIEGWART, R. Backstepping and sliding-mode techniques applied to an indoor micro quadrotor. In: IEEE International Conference on Robotics and Automation: proceedings. IEEE, 2005. ISBN 0-7803-8914-X, p. 2259-2264.
- [10] ZULU, A., JOHN, S. A review of control algorithms for autonomous quadrotors. *Open Journal of Applied Sciences* [online]. 2014, **4**(14), p. 547-556. ISSN 2165-3917. Available from: <https://doi.org/10.4236/ojapps.2014.414053>
- [11] THU, K.M., GAVRILOV, A.I. Designing and modeling of quadcopter control system using L1 adaptive control. *Procedia Computer Science* [online]. 2017, **103**, p. 528-535. ISSN 1877-0509. Available from: <https://doi.org/10.1016/j.procs.2017.01.046>
- [12] BOUABDALLAH, S., NOTH, A., SIEGWART, R. PID vs LQ control techniques applied to an indoor micro quadrotor. In: IEEE/RSJ International Conference on Intelligent Robots and Systems IROS 2004: proceedings. IEEE, 2004. ISBN 0-7803-8463-6, p. 2451-2456.
- [13] HE, Z., ZHAO, L. A Simple attitude control of quadrotor helicopter based on Ziegler-Nichols rules for tuning PD parameters. *The Scientific World Journal* [online]. 2014, **2014**, 280180. ISSN 2356-6140. Available from: <https://doi.org/10.1155/2014/280180>
- [14] KADA, B., GHAZZAWI, Y. Robust PID controller design for an UAV flight control system. In: World Congress on Engineering and Computer Science: proceedings. 2011. Vol. II. ISBN 978-988-19251-7-6.
- [15] PRAVEEN, V., PILLAI, A. S. Modeling and simulation of quadcopter using PID controller. *International Journal of Control Theory and Applications*. 2016, **9**(15), p. 7151-7158. ISSN 0974-5572.
- [16] HASSENI, S., ABDOU, L. Decentralized PID control by using GA optimization applied to a quadrotor. *Journal of Automation, Mobile Robotics and Intelligent Systems* [online]. 2018, **12**(2), p. 33-44. ISSN 1897-8649. Available from: https://doi.org/10.14313/JAMRIS_2-2018/9
- [17] AWREJCEWICZ, J., KORUBA, Z. *Classical mechanics: applied mechanics and mechatronics*. New York: Springer, 2012. ISBN 978-1-4614-3978-3.
- [18] KRZYSZTOFIK, I., KORUBA, Z. Application of the sliding controller for the gyroscope system of the anti-aircraft missile. In: 23rd International Conference Engineering Mechanics 2017: proceedings. Brno University of Technology, 2017. ISBN 978-80-214-5497-2, p. 530-533.
- [19] KORUBA, Z., KRZYSZTOFIK, I. A control with the use of LQR modified method in the gyroscope system of target tracking. In: 23rd International Conference Engineering Mechanics 2017: proceedings. Brno University of Technology, 2017. ISBN 978-80-214-5497-2, p. 486-489.
- [20] KORUBA, Z., KRZYSZTOFIK, I. Control of the non-stationary gyroscopic system in the target tracking process. In: 24th International Conference Engineering Mechanics 2018: proceedings. Institute of Theoretical and Applied Mechanics of the Czech Academy of Sciences, 2018. ISBN 978-80-86246-88-8, p. 397-400.
- [21] TEWARI, A. *Modern control design with Matlab and Simulink*. Chichester: John Wiley & Sons, 2002. ISBN 0-471-49679-0.
- [22] LEWIS, F. L., VRABIE, D. L., SYRMOS, V. L. *Optimal control*. Hoboken: John Wiley & Sons, 2012. ISBN 978-0-470-63349-6.

A FRAMEWORK COUPLING VISSIM AND OMNET++ TO SIMULATE FUTURE INTELLIGENT TRANSPORTATION SYSTEMS

Tibor Petrov^{1,*}, Ilya Finkelberg², Nina Zarkhin², Peter Počta³, Ľuboš Buzna^{1,4}, Ayelet Gal-Tzur², Tatiana Kováčiková¹, Tomer Toledo², Milan Dado³

¹Department of International Research Projects - ERAdiate+, University of Zilina, Zilina, Slovakia

²Transportation Research Institute, Technion - Israel Institute of Technology, Haifa, Israel

³Department of Multimedia and Information - Communication Technologies, Faculty of Electrical Engineering and Information Technology, University of Zilina, Zilina, Slovakia

⁴Department of Mathematical Methods and Operations Research, Faculty of Management Science and Informatics, University of Zilina, Zilina, Slovakia

*E-mail of corresponding author: tibor.petrov@uniza.sk

Resume

With the spread of connected vehicles (CVs), a growth of novel information services exploiting data transmitted by CVs is expected. Wireless communication systems, in particular in vehicular applications, operate with a varying level of transmission reliability, which may affect the quality of V2X-data-driven intelligent transport systems (ITS). Therefore, the performance of ITS should be evaluated in a variety of conditions and the configuration of parameters should be fine-tuned in a safe testbed, using computer simulations. A simple framework is presented, which couples VISSIM traffic simulation and OMNeT++ communication networks simulation in real time, enabling an assessment of the relationship between a communication reliability and transport service quality. A functionality of the framework is demonstrated by applying it to a scheme controlling signalized intersections while estimating traffic flows from the V2I data.

Article info

Received 30 June 2020

Accepted 10 August 2020

Online 15 January 2021

Keywords:

connected vehicles,
traffic control,
communications reliability,
simulation framework

Available online: <https://doi.org/10.26552/com.C.2021.2.C23-C29>

ISSN 1335-4205 (print version)

ISSN 2585-7878 (online version)

1 Introduction

As the population grows, so does the road congestion in urban areas and this trend is expected to continue in the near future. One of the means to counter the increased delays at the bottlenecks of urban network - signalized intersections, is to develop more advanced and efficient signal control algorithms utilizing emerging technologies. One of the promising near future solutions is the utilization of traffic data from connected vehicles (CVs) for a more advanced and efficient traffic control. Contrary to today's common practice, where approaching vehicles are detected by sensors at fixed locations, the Vehicle to Infrastructure (V2I) communications allow the intersection controller to receive richer and more precise traffic data (e.g. current location, speed and direction of travel) [1] for every connected vehicle, allowing a more advanced and efficient intersection signal control. A large variety of control algorithms and methods are being developed [2], where the connected vehicle data is used as an input for the decision making process and where the main distinction between the proposed algorithms is the specific green light allocation scheduling technique and the used objective function.

The proposed techniques rely heavily on an assumption of perfect communication (i.e. no latency and message loss), however, in the real world applications the reliability of communication networks might be affected by various factors [3-4]. Several studies investigate communication networks performance in connected vehicles environment [5-6] and while the effect of information transmission quality on vehicles' routing decisions in a signalized urban network has been investigated [7], the direct, real-time impact of imperfect communication on traffic control decisions at signalized intersections is less studied. As a field test validation of various traffic scenarios in connected vehicle environment might be too expensive and complex to set up, a common practice in traffic control research is to create simulation models. In this study, a simulation framework that integrates VISSIM traffic micro-simulation software and OMNeT++ communication networks simulator was built in order to provide a testbed for realistic interaction scenarios. In the future work, the developed test bed/framework may provide some valuable insights into an impact of imperfect communication on, for example, signal traffic control performance in connected vehicles environment and possible ways to decrease the



sensitivity of the control algorithm to communication faults, or warning applications such as notification of the CV drivers about an approaching emergency vehicle [8].

1.1 Traffic simulation platform

VISSIM [9], a state-of-the-art traffic microsimulation software and preferred platform for evaluation of connected vehicle environment scenarios, is used in this study. The software package comes with advanced traffic behavioral models, a large variety of customization options and a built-in API (Application Programming Interface) module, which makes VISSIM a good choice for advanced traffic control applications. The COM (Component Object Model) and API interface provide a powerful development tool to simulate a connected vehicle environment control with vehicle-infrastructure communication, where the simulation of communication network performance at each step is carried out by an external program.

1.2 Communication network simulation platform

Current communication technologies have gradually evolved into mathematically complex and highly dynamic systems [10]. Hence, the easiest and most precise way of evaluating their performance and behavior, besides conducting field measurements, is running computer simulations. Among many simulation engines available, the Objective Modular Network Testbed in C++ (OMNeT++) has gained extensive popularity due to its scalability, efficient memory usage and wide range of available simulation models [11]. Instead of being a simulator of a concrete aspect of communication networks, it rather provides infrastructure and tools for writing simulations [12]. The generic architecture of OMNeT++ therefore enables simulation of various problem domains, e.g. wired/wireless networks, communication protocols, queuing networks and many more [13]. This versatility and modularity of its architecture led the community to develop a wide range of open-source simulation modules and model libraries for OMNeT++, including the most extensive one - INET framework [14]. The INET supports a variety of communication networks, including wired, wireless, mobile, ad hoc and sensor networks. It contains models for the Internet stack, application modules, routing protocols, link layer protocols and physical layer models among many other components. The INET also provides a support for node mobility and serves as a base or as an extension to other simulation frameworks extending OMNeT++ towards a specific direction, such as Veins [15], designed particularly for simulating vehicular networks.

1.3 Federated telco-traffic simulators

The simulation of vehicular communications implies meeting of specific requirements on the side of the

communication network simulator. Besides the support of the vehicular communication protocols, which are different than in the case of conventional networks, it also has to be able to mimic vehicle mobility to model movements of the communication network nodes. To achieve realistic vehicular-like mobility in communication network simulation, an output from a traffic simulation is needed. This is a complex problem, since the position of a particular vehicle in the next simulation step can often depend on the result of previous data transmissions in the communication network. Hence, both simulators need to be coupled and perform a bi-directional synchronization.

Such a simulation framework – Veins - has been in development since 2006 [7]. The Veins bi-directionally couples the OMNeT++ with Simulation of Urban Mobility (SUMO) [16], an open-source microscopic traffic simulator. Moreover, Veins package provides simulation models of vehicular communication protocols, messages, nodes and sample applications, all compliant with IEEE WAVE family of standards [17].

However, many municipalities, transport planning experts and researchers around the world prefer using the VISSIM for traffic simulation, which, compared to the SUMO, has easier network coding, built-in ability to model public transport and pedestrians, GIS support and 3D visualization [18]. As a result, the variety of realistic and calibrated test cases available in VISSIM format is much higher. If these existing traffic simulation models are to be extended to employ the CVs, there is no straightforward way to convert them into a format compatible with the SUMO without the expense of extensive manual modifications. Hence, the Veins framework cannot be used for simulating these models without their complete and time-consuming rebuild in the SUMO.

To address the above-mentioned issue, a simulation framework is proposed, which integrates the VISSIM and OMNeT++ to allow simulations involving the CVs in both traffic and telecommunications domains.

2 Framework description

A simulation utilizing the proposed framework includes one or more pairs of the following elements:

- VISSIM entity – a model of an element occurring in the traffic simulation that is expected to have communication capabilities, i.e. a connected vehicle, a pedestrian exploiting V2P communication, etc. Each such component is defined, among other parameters, by a unique VISSIM ID and its instantaneous position;
- OMNeT++ node – a model of an element occurring in the communication network simulated by the OMNeT++ simulator. Each OMNeT++ node represents a single coupled VISSIM entity present in the traffic simulation.

Architecture of the framework containing developed simulator extension modules and flows of data is depicted in Figure 1.

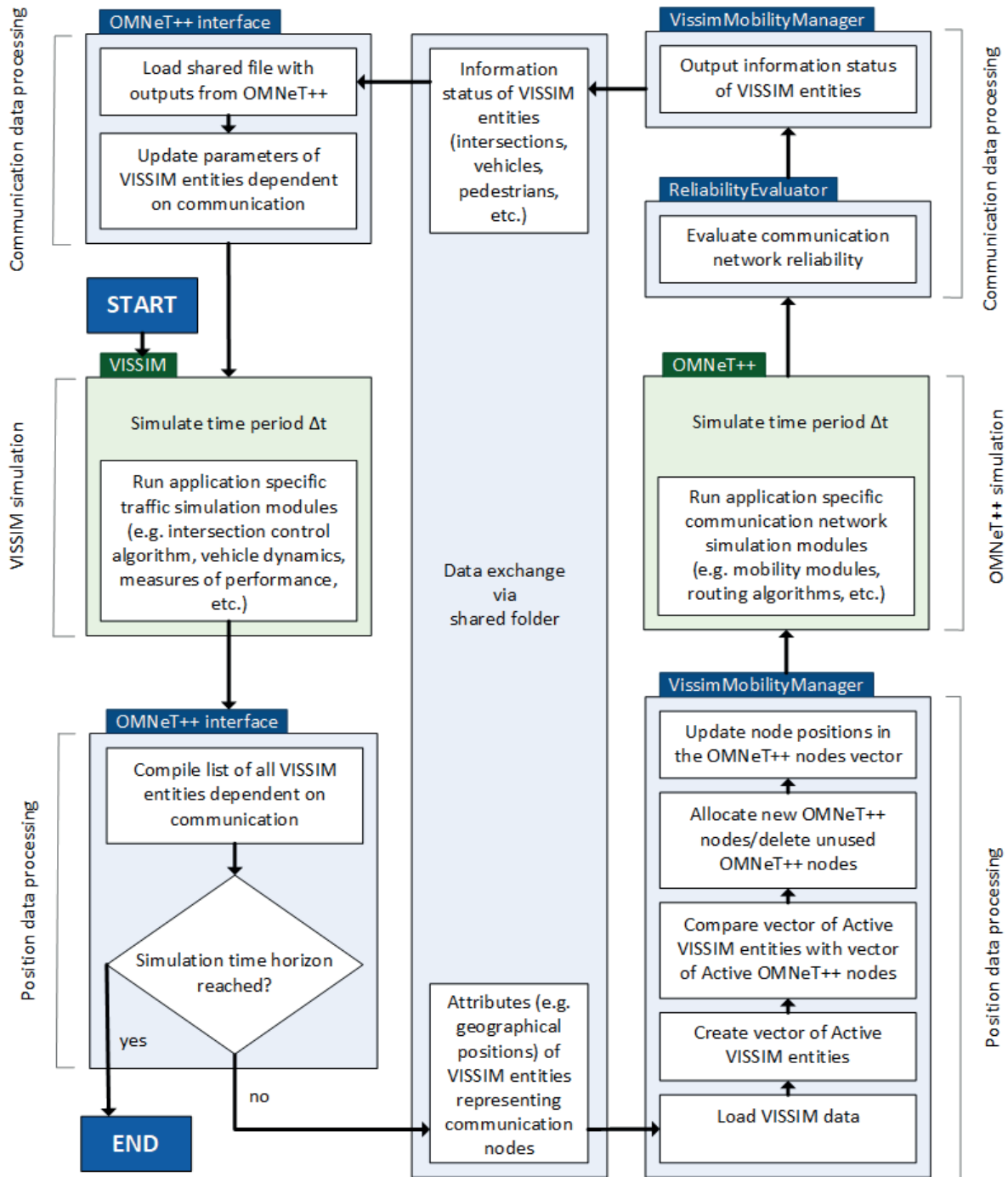


Figure 1 Architecture of the VISSIM-OMNeT++ simulation framework

The framework consists of two separate interfaces (implemented in VISSIM and OMNeT++), which exchange data via a shared folder. The VISSIM's interface (see Figure 1 - the left-hand side) controls updating of the VISSIM entities' parameters, based on their communication status received from the OMNeT++ in the previous simulation period Δt_{i-1} . The VISSIM subsequently runs the specific traffic simulation modules responsible for implementation of the traffic control algorithms used in the simulation, as well as for generation of the VISSIM entities' position updates. After simulating current period Δt_i with updated

parameters of the VISSIM entities, interface compiles a list of all the VISSIM entities and their attributes for simulation step Δt_v , and writes them to the shared file. Afterwards, the interface suspends the simulation in the VISSIM until a shared file containing communication network simulation output from the OMNeT++ is created.

The interface implemented in the OMNeT++ (see Figure 1 – the right-hand side) consists of three modules, which execute the framework’s communication network simulation management:

- **VissimMobilityManager** - a core module of the

OMNeT++ part of the framework. It is responsible for managing positions of all the OMNeT++ nodes, writing an output of communication network simulation and maintaining synchronization with the VISSIM;

- VissimMobility - a mobility module, where each OMNeT++ node has to take part in the federated simulation. It is responsible for updating node's position and visual representation in the OMNeT++ GUI;
- Communication network ReliabilityEvaluator - a module responsible for collecting and storing statistics about communication reliability parameters, e.g. number of sent and received messages, average message loss, end-to-end delay, etc.

A shared file containing the VISSIM IDs of all the communicating entities and their position in the current simulation step is generated as an output. This file is loaded by the VissimMobilityManager module. The OMNeT++ nodes are managed by the two main data structures in the VissimMobilityManager, i.e. Active VISSIM Entities (AVE) vector and Active OMNeT++ Nodes (AON) vector. The AVE vector contains the IDs of all the VISSIM entities present in the simulation within the current simulation period Δt_i . The AON vector contains IDs of all the active OMNeT++ nodes present in the simulation within Δt_i , as well as their positions and mapping to the IDs of VISSIM entities.

After loading the VISSIM entity data from the shared file, the AVE vector is initialized. The AVE vector is subsequently compared to the AON vector containing entries from the previous simulation period Δt_{i-1} . For each new VISSIM entity in the AVE vector, an object in the AON vector is created and OMNeT++ node is assigned. The AON entries not present in the AVE are then destroyed along with the OMNeT++ nodes they represent. In the next step, the position of all the objects present in the AON vector is updated. After that, the positions of the OMNeT++ nodes are updated from the AON vector by rewriting previous coordinates in each OMNeT++ node's VissimMobility module.

Once the positions of all the OMNeT++ nodes are updated, the OMNeT++ proceeds with a simulation of data transmissions in the communication network. During this period, the corresponding OMNeT++ modules log target output parameters to the ReliabilityEvaluator and VissimMobilityManager modules. At the end of the current simulation period Δt_i , the VissimMobilityManager creates a shared file with communication status of each VISSIM entity and halts the OMNeT++ simulation until a next shared file with the input from the VISSIM for a simulation period Δt_{i+1} is created and stored in the shared directory.

3 Demonstration of the framework functionality and applicability

To showcase the framework functionality and applicability, a demonstration scenario, involving a dense network of the CVs broadcasting messages to a Roadside Unit (RSU), was implemented. A four-leg intersection was

simulated, which is controlled by an adaptive traffic control algorithm utilizing data from connected vehicles received by the RSU.

3.1 Traffic Signal Control Algorithm

The traffic control algorithm relies on received input data from the CVs, thus the performance of the communication network is expected to have an impact on the traffic control efficiency. Each vehicle in the vicinity of the intersection serves as a traffic detector by transmitting its speed, location and planned route to the intersection controller via Vehicle-To-Infrastructure communication channel. The signal control algorithm, which represents an extension of the existing work [19], uses the received data to assign a weight coefficient to every CV. A coefficient value is calculated as a function of vehicles' distance from the stopline, where the closer vehicles receive higher values and higher priority in a green light allocation process. Given each vehicle's planned route, the approaching CVs are then grouped into Signal Groups (SGs) that will service them. At the next step, the SGs are combined into Signal Phases (SPs), i.e. the combinations of Signal Groups that can receive green light simultaneously. By this type of aggregation, using vehicles coefficients, each SP is assigned a score, which has a direct relationship with its priority level in the green light allocation process. As the minor extension of the original work [19], a waiting time constraint was implemented, i.e. all the SGs with non-zero demand need to be serviced before starting the next signal cycle. In addition, the SP scores from the current cycle influence the maximum green duration in the next cycle, providing more green duration if necessary for the SPs with a higher demand.

3.2 Communication network simulation

In the simulation, the RSU antenna was located on a traffic light pole, 5.897 meters above the ground (corresponding to the top of the traffic lights) to ensure a line-of-sight communication. Each vehicle was equipped with an IEEE 802.11p [20] compliant communication module and broadcasted messages with a 1 Hz frequency. To simulate a challenging communication environment, an electromagnetic interference was modelled by setting the communication channel's background noise power to -86 dBm. A path loss of the wireless signal was modeled by the Two-Ray Interference model [21].

For the visualization purpose, the framework alters vehicle colors according to their communication status (operational/non-operational) in the current simulation time period Δt . The RSU successfully received messages from vehicles visualized in black color, while the information from the yellow vehicles was not available to the RSU at the corresponding simulation time period (see Figure 2 for illustration).

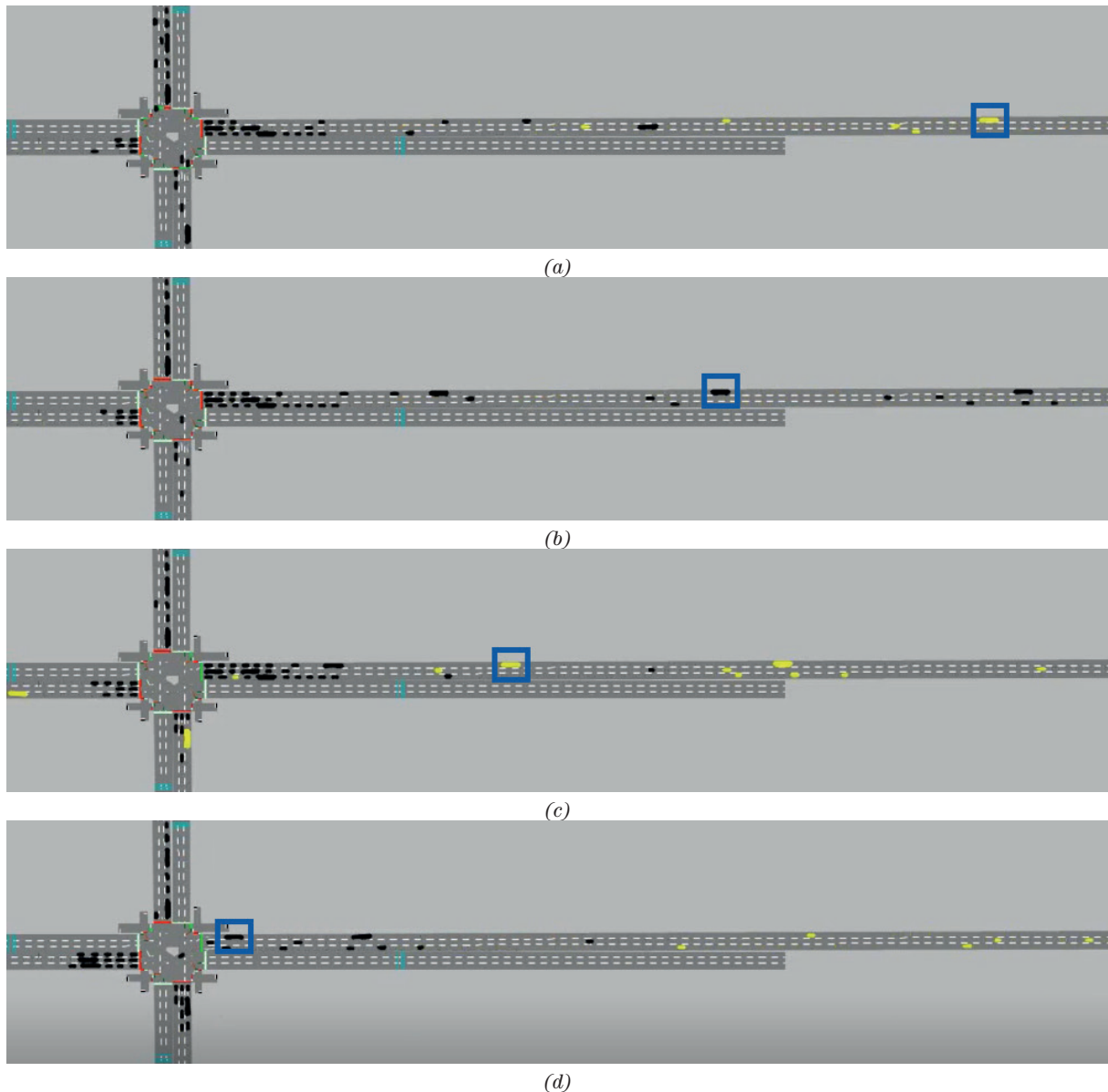


Figure 2 Communication status of a selected vehicle (a public transport bus in the blue square) during the simulation: (a) communication with the RSU is faulty due to an RF signal distortion caused by electromagnetic interference; (b) the bus has successfully sent a message to the RSU; (c) a message from the vehicle was lost due to the hidden node problem [22]; (d) the vehicle is close enough to the RSU to communicate successfully despite the relatively high level of interference

The communication errors are more likely to occur with the increasing distance between the CVs and the RSU due to the combined effects of electromagnetic interference and signal attenuation. As the same communication channel is shared by all the vehicles, errors can also occur at the closer ranges due to a co-channel interference between transmissions from other vehicles (Figure 2c). The communication error rate achieves its minimum in the close vicinity of the RSU. Here, even when the communication channel is noisy, the vehicles are still able to transmit the data/information successfully. It is worth noting here that the information transmitted by the CVs can be utilized to optimize the green allocation process in order to decrease queueing delays.

4 Conclusions and discussion

To facilitate the use of existing calibrated traffic models implemented in the VISSIM for CV simulations, a simulation framework was proposed and implemented, coupling the VISSIM traffic simulator and OMNeT++ communication networks simulator. The framework supports a real-time bidirectional communication between both simulators, as well as a visualization of the CVs instantaneous communication status. Operation of the framework was demonstrated on the cross-shaped intersection controlled by a CV-data-based adaptive control algorithm.

Implementation of the framework revealed several pitfalls that had to be addressed prior to achieving

satisfactory performance, namely: (i) The synchronization of shared files' read/write operations has to be of a very high precision. If the final output file is constructed in a series of discrete write operations, it is advised to construct such a file outside of the shared folder until it is complete. (ii) Due to the complexity of the used models, the OMNeT++ simulation of a dense communication network involving a realistic model of a vehicular communications environment is very slow. Even with position updates and message generation frequency set to low values (1s both) and using moderately powerful simulation computer, the run of 2400 simulation seconds can take up to one day of the CPU time, i.e. 24 hours, to finish. For this reason, the framework exploits an optimization method introduced to skip simulation seconds when the simulated traffic control algorithm cannot benefit from the CV data, e.g. during an interstage, i.e. a predefined safety period between signal phases, where no intervention is possible.

The simulation run time can be further decreased by an

implementation of dynamic OMNeT++ node initialization. It is worth noting here that certain protocol models, e.g. IP network layer protocol model, could not be used along with OMNeT++ automatic IP assignment in such a case.

In the near future, the developed framework will be utilized for an investigation of the impact of imperfect communication on the traffic control performance in connected vehicle environment and development of more resilient traffic control algorithms.

Acknowledgement

This work was supported by the Slovak Research and Development Agency under the contract no. SK-IL-RD-18-005 ICT and smart cars for efficient emergency response and traffic management (SENECA). The authors would like to thank the Israel Ministry of Science, Technology and Space for co-funding this research.

References

- [1] ETSI. EN 302 637-2. Intelligent Transport Systems (ITS); vehicular communications; basic set of applications; part 2: specification of cooperative awareness basic service, 2014.
- [2] JING, P., HUANG H., CHEN, L. An adaptive traffic signal control in a connected vehicle environment: a systematic review. *Information* [online]. 2017, **8**(3), 101, [accessed 2020-06-22]. ISSN 2078-2489. Available from: <https://doi.org/10.3390/info8030101>
- [3] MOLISCH, A. F. *Wireless communications*. 2. ed. Los Angeles, CA: Wiley, 2011. ISBN 978-0-470-74186-3.
- [4] GOZALVEZ, J., SEPULCRE M., BAUZA, R. IEEE 802.11p vehicle to infrastructure communications in urban environments. *IEEE Communications Magazine* [online]. 2012, **50**(5), p. 176-183 [accessed 2020-06-22]. ISSN 0163-6804. Available from: <https://doi.org/10.1109/MCOM.2012.6194400>
- [5] VAN PHU, C. N., FARHI, N., HAJ-SALEM, H., LEBACQUE, J. A vehicle-to-infrastructure communication based algorithm for urban traffic control. In: 5th IEEE International Conference on Models and Technologies for Intelligent Transportation Systems MT-ITS 2017: proceedings [online]. Piscataway, NJ: IEEE, 2017. ISBN 978-1-5090-6484-7. Available from: <https://doi.org/10.1109/MTITS.2017.8005594>
- [6] SAEED, I., ELHADEF, M. Performance evaluation of an IoV-based intersection traffic control approach. In: IEEE International Conference on Internet of Things iThings and IEEE Green Computing and Communications GreenCom and IEEE Cyber, Physical and Social Computing CPSCom and IEEE Smart Data SmartData: proceedings [online]. Piscataway, NJ: IEEE, 2018. ISBN 978-1-5386-7975-3. Available from: https://doi.org/10.1109/Cybermatics_2018.2018.00296
- [7] SOMMER, C., GERMAN, R., DRESSLER, F. Bidirectionally coupled network and road traffic simulation for improved IVC analysis. *IEEE Transactions on Mobile Computing* [online]. 2010, **10**(1), p. 3-15 [accessed 2020-06-22]. ISSN 1536-1233. Available from: <https://doi.org/10.1109/TMC.2010.133>
- [8] PETROV, T., POCTA, P., ROMAN, J., BUZNA, L., DADO, M. A feasibility study of privacy ensuring emergency vehicle approaching warning system. *Applied Sciences* [online]. 2020, **10**(1), 298 [accessed 2020-06-23]. ISSN 2076-3417. Available from: <https://doi.org/10.3390/app10010298>
- [9] PTV GROUP. VISSIM 7: User Manual, 2014.
- [10] WEHRLE, K., GUNES M., GROSS, J. *Modeling and tools for network simulation*. Berlin, Heidelberg: Springer-Verlag, 2010. ISBN 978-3-642-12331-3.
- [11] THANH BINH, H., DEY N. *Soft computing in wireless sensor networks*. Boca Raton: Taylor & Francis, 2018. ISBN 978-0815395300.
- [12] OMNeT++ Discrete Event Simulator [online] [accessed 2019-11-25]. Available from: <https://omnetpp.org>
- [13] SIVAKUMAR, K., DALIN, G. The analysis and implementation of OMNeT++ framework. *Global Journal of Computer Science and Technology*. 2011, **11**(6), p. 65-70. ISSN 0975-4350.
- [14] INET Framework [online] [accessed 2019-12-10]. Available from: <https://inet.omnetpp.org/>
- [15] Vehicles in network simulation: the open source vehicular network simulation framework [online] [accessed 2019-12-10]. Available from: <https://veins.car2x.org>
- [16] KRAJZEWCZ, D., ERDMANN, J., BEHRISCH, M., BIEKER, L. Recent development and applications of SUMO -

- Simulation of Urban Mobility. *International Journal on Advances in Systems and Measurements*. 2012, **5**(3&4), p. 128-138. ISSN 1942-261x.
- [17] IEEE 1609.0-2019. IEEE Guide for Wireless Access in Vehicular Environments (WAVE) Architecture, 2019.
- [18] SAIDALLAH, M., EL FERGOUGUI, A., ELBELRHITI ELALAOUI, A. A comparative study of urban road traffic simulators. *MATEC Web of Conferences* [online]. 2016, **81**, 05002 [accessed on 2020-06-23]. ISSN 2261-236x. Available from: <https://doi.org/10.1051/mateconf/20168105002>
- [19] KWATIRAYO, S., ALMHANA, J., LIU, Z. Optimizing intersection traffic flow using VANET. In: IEEE International Conference on Sensing, Communications and Networking SECON 2013: proceedings. Piscataway, NJ: IEEE, 2013. ISBN 978-1-4673-1905-8.
- [20] IEEE 802.11p-2010. IEEE Standard for information technology - Local and metropolitan area networks - Specific requirements - Part 11: Wireless LAN Medium Access Control (MAC) and Physical Layer (PHY) Specifications Amendment 6: Wireless access in vehicular environment, 2010.
- [21] SOMMER, C., JOERER, S., DRESSLER, F. On the applicability of Two-Ray path loss models for vehicular network simulation. In: IEEE Vehicular Networking Conference VNC 2012: proceedings [online]. Piscataway, NJ: IEEE, 2012. ISBN 978-1-4673-4995-6. Available from: <https://doi.org/10.1109/VNC.2012.6407446>
- [22] RAHMAN, A., GBURZYNSKI, B. Hidden problems with the hidden node problem. In: 23rd Biennial Symposium on Communications: proceedings. Piscataway, NJ: IEEE, 2006. ISBN 0-7803-9528-X.

MODELS OF THE COMPUTER INTELLECTUALIZATION OPTIMAL STRATEGY OF THE POWER SUPPLY FAST-FLOWING TECHNOLOGICAL PROCESSES OF THE RAILWAYS TRACTION SUBSTATIONS

Aleksander Stasiuk¹, Valeriy Kuznetsov^{2,*}, Lidia Goncharova¹, Petro Hubsykyi²

¹Automation and Computer - Integrated Technologies of Transport Department, State University of Infrastructure and Technologies, Kyiv, Ukraine

²Electric Power Department, Railway Research Institute, Warsaw, Poland

*E-mail of corresponding author: vkuznetsov@ikolej.pl

Resume

Based on analysis of the problem of the power supply networks of railways innovative transformation, the direction of research is substantiated related to organization of the optimal strategy of computerized intellectualization of the power supply processes to the railways traction substations. The logical structure of a distributed computer environment developed in the form of graph, which adequately reflects the topology of the organization of the power supply system. A differential mathematical model of the computer architecture of the power supply control is proposed. An intelligent method for finding the optimal strategy for the intellectualization of the power supply processes was proposed to guarantee the specified indicators of the optimal functioning of individual nodes and segments of the power supply management computer network.

Article info

Received 12 May 2020

Accepted 16 July 2020

Online 18 January 2021

Keywords:

differential mathematical models, optimal strategy, intellectualization, power supply, optimization, minimax principle

Available online: <https://doi.org/10.26552/com.C.2021.2.C30-C36>

ISSN 1335-4205 (print version)

ISSN 2585-7878 (online version)

1 Introduction

Computer systems and networks are the main component in functioning of business, government organizations, military institutions, health systems, education and science. In the process of managing the complex energy and social systems that operate in normal and abnormal modes, there is a need for registration, storage and processing of large amounts of information and formation of the control actions. National competitiveness depends, first of all, on the procedures for conducting, in real time, information analysis and decision-making of flexible management of production or social facilities.

The experience of using information technology in the management of complex systems has shown that many of the limitations in solving the real problems are significantly reduced by adding intelligence to computer systems, or modelling intelligent control procedures [1-2]. Moreover, in many cases, classical methods are ineffective for many practical problems of production and business since it is impossible to accurately describe reality when creating a management model.

A study of evolution of the computer networks and systems development for managing complex objects showed that the maximum efficiency of their functioning

can be achieved by mutual integration of the intellectual resources of managers and modern capabilities of almost unlimited performance of distributed computing [3].

This fact led to creation of a new class of mathematical models and methods of intelligent information processing, as a basis for creation of the intelligent computer systems [3-6]. For example, in [7] a method was proposed based on use of simplified calculations of state of a train as a controlled system without the use of differential equations of motion, which can significantly increase the speed of calculations. This, in turn, will solve the problem of finding the optimal control in real time, taking into account the changing conditions during the movement of the train. To implement this method of calculation, a simplified model of the train was used as a controlled system.

2 Separation of previously unresolved parts of a common problem

Many authors' works are dedicated to the complex problem of the innovative transformation of traction electric lines by organizing energy-saving technologies and optimizing the processes of power supply in railway



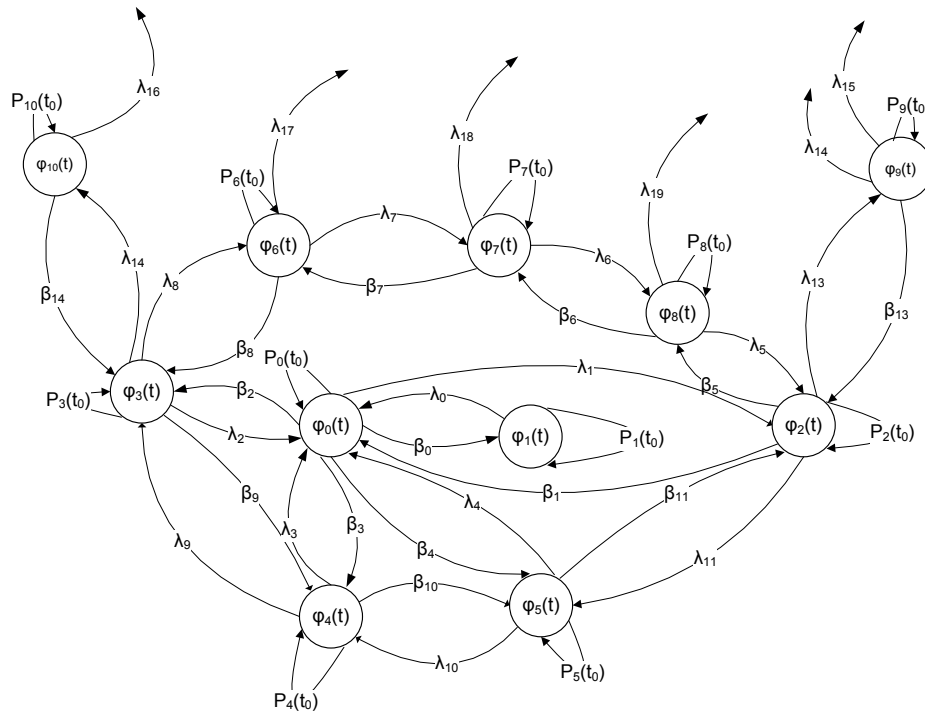


Figure 1 Graph of the architecture of the local computer network of the traction substation

transport [1, 6]. In [8], to improve energy efficiency, the possibility of using Smart Grid in urban transport conditions was considered. Thanks to the Smart Grid solutions, traction power systems are no longer passive energy consumers. They become a dynamic link in the power system. In electric transport systems, energy islands can be created that serve as elements of modern smart power systems [9]. In work [10], the solution to the scientific problem of increasing the energy efficiency of DC traction systems by the development of distributed power systems that fit into the existing infrastructure to ensure high-speed traffic, which is necessary for electric transport, is considered. Thus, in the scientific works there is a promising direction of research aimed at developing mathematical models for the traction power supply systems and methods that combine human intelligence and the computer environment. A new class of computer intelligent systems has appeared that is focused on the integrated intellectualization of a set of procedures for the operational and strategic management of the fast-flowing technological processes of energy supply and power consumption. This fact stimulated the emergence of new analytical and intelligent technologies, which, based on certain models, algorithms, and mathematical theorems, allow, according to known data, to estimate the values of unknown characteristics and parameters of a complex object of study [6, 11-13]. It became apparent that a qualitatively new set of intelligent traction power supply systems could be obtained by forming a deep mutual integration of topology of the power grid infrastructure of the power supply system and architecture of a distributed computer network. At the same time, truly little attention is paid to the previously unresolved parts of the problem of innovative transformation of traction electric lines - creation

of mathematical models and methods for analyzing and evaluating the optimal functioning of individual nodes and segments of intelligent computer networks for controlling the fast-flowing power supply technological processes.

3 Aim formulation

The aim of the work is the organization of an optimal computerization strategy for the fast-flowing technological processes of power supply lines by developing mathematical models and methods of increased intellectual complexity and dimensionality of analysis and assessment of the conditions for optimal functioning of individual nodes and segments of a distributed computer-based power management network.

4 The main research material

Distributed railway power supply systems represent a hierarchical system, the basic level of which is the level of traction substations as the basis for minimizing the system-wide costs, optimizing power consumption and transportation reliability. The emergence of promising areas of innovation and investment transformation of railway power supply systems has contributed to development of a new class of intelligent computer networks for optimal control of power supply systems. The organization of intelligent systems requires comprehensive research in the subject area, to create a new model of the optimal strategy for intellectualization of a wide range of technological processes of the power supply systems. The implementation of an adequate reflection of the distributed architecture of

the computer environment and the topology of the power supply system of the traction substation opens up the possibility of maximizing the managing efficiency of the fast-flowing technological processes of power consumption. The important issue in this case is the ability of computer architecture to control the electrical systems of traction substations in real time. To form models and criteria for computer intellectualization of technological processes for managing energy systems, the architecture of a local area network of power supply management at the level of traction substations is presented in the form of a graph, which reflects adequately the topology of the electric system.

Graph of the logical architecture of the local computer network (Figure 1) includes two types of topologies - a star and a circle. A fragment of a star topology includes a node $\varphi_0(t)$ - which is the central server of a computer network of a traction substation, a node $\varphi_1(t)$ - to organize a unified information environment for primary information and maintaining a database, a node $\varphi_2(t)$ - to exchange information within a corporate computer network railway power supply control, node $\varphi_3(t)$ - to exchange the information on Internet, node $\varphi_4(t)$ - is a server operational management and maintenance of a set of automated workstations for power supply management, monitoring of traction transformers, high-voltage circuit breakers and power equipment, as well as a $\varphi_5(t)$ node for organizing microprocessor and relay protection of the traction power line.

A segment of the circle graph topology includes a series of joint nodes $\varphi_0(t)$ $\varphi_1(t)$ $\varphi_2(t)$ $\varphi_3(t)$ $\varphi_4(t)$ $\varphi_5(t)$ considered above, as well as node $\varphi_6(t)$ - organization of commercial electricity metering at commercial tariffs differentiated by zones of the day, $\varphi_7(t)$ is the node for monitoring the parameters of the traction power supply system, node $\varphi_8(t)$ is for the intellectual processing of commercial and technological information. In addition, the topology under consideration includes nodes $\varphi_9(t)$, $\varphi_{10}(t)$ - a distributed local power management network at the highest level, that is the department of the railway power supply.

Assume that in the process of exchanging information between components of a computer network, the flow rate of applications is represented by the value $\lambda_i(t)$ and the intensity of the service flow of applications is determined by the following value $\beta_i(t)$. To analyse the computer architecture of the local network and determine the values of the probabilities $P_0(t)$, $P_1(t)$, $P_2(t)$, $P_3(t)$, $P_4(t)$, $P_5(t)$, $P_6(t)$, $P_7(t)$, $P_8(t)$, $P_9(t)$, $P_{10}(t)$ the graph is presented in the form of a Kolmogorov differential equation system with the corresponding initial conditions, which can be written in the following form [1-2]:

$$\begin{aligned} \frac{dP_0(t)}{dt} &= \lambda_0 P_1(t) + \beta_1 P_2(t) + \lambda_2 P_3(t) + \\ &+ \lambda_3 P_4(t) + \lambda_4 P_5(t) - (\beta_0 + \beta_2 + \beta_3 + \beta_4 + \lambda_1) \cdot P_0(t), \\ \frac{dP_1(t)}{dt} &= \beta_0 P_0(t) + \lambda_0 P_1(t), \end{aligned} \quad (1)$$

$$\begin{aligned} \frac{dP_2(t)}{dt} &= \lambda_1 P_1(t) + \lambda_5 P_8(t) + \lambda_2 P_3(t) - \\ &- (\beta_1 + \beta_5 + \lambda_{11} + \lambda_{13}) P_2(t) + \beta_{11} P_5(t) + \beta_{13} P_9(t), \\ \frac{dP_3(t)}{dt} &= \lambda_9 P_4(t) - (\lambda_2 + \lambda_8 + \lambda_{14} + \beta_9) P_3(t) + \\ &+ \beta_2 P_0(t) + \beta_8 P_6(t) + \beta_{14} P_{10}(t), \\ \frac{dP_{10}(t)}{dt} &= \lambda_{14} P_3(t) - \beta_{14} P_{10}(t), \end{aligned}$$

with the corresponding initial conditions written as follows:

$$P_0(t) + P_1(t) + P_2(t) + \dots + P_3(t) + P_{10}(t) = 1, \text{ with } t = 0, P_0(t) = t, P_0(t) + P_1(t) + P_2(t) + \dots + P_9(t) + P_{10}(t) = 1.$$

5 Differential mathematical models

Based on the system of Equations (1), a differential mathematical model is synthesized for calculating, first of all, probability values $P_0(t)$, $P_1(t)$, $P_2(t)$, $P_3(t)$, $P_4(t)$, $P_5(t)$, $P_6(t)$, $P_7(t)$, $P_8(t)$, $P_9(t)$, $P_{10}(t)$. In this regard, the principles of the theory of differential transformations of Pukhov are applied, the fundamental concepts of which are represented by the following mathematical equations [14]

$$\begin{aligned} P_i(k) &= \frac{H^k}{k!} \left[\frac{d^k P_i(t)}{dt^k} \right]_{t=0} \equiv P_i(t) = \\ &= \sum_{k=0}^{\infty} \left(\frac{t}{H} \right)^k P_i(k), \end{aligned} \quad (2)$$

where:

$P_i(t)$ is the initial function that can be differentiated n-times and which has a number of corresponding restrictions, including its derivatives;

$P_i(k)$ - differential T-images of the original function $P_i(t)$;

H - a scale factor, the dimension of which coincides with the dimension of the argument t , as a rule, is selected on conditions on $0 \leq t \leq H$ the entire range of the function - the original $P_i(t)$;

\equiv - a symbol of correspondence between the function - the original $P_i(t)$ and its differential T - image $P_i(k)$.

Based on the direct differential transformation, which is to the left of \equiv , a differentiated T-image of the function-original is formed - $P_i(t)$ as a discrete function $P_i(k)$, with integer argument $k = 0, 1, 2, \dots$. Based on the set of the T-discrete values of the integer argument function $P_i(k)$ $k = 0, 1, 2, \dots$, using the inverse differential transformation, which is located to the right of the symbol \equiv , one obtains the original functions $P_i(t)$. Note that for $k = 0$, according to Equation (2), for any instantaneous value t of each i -th parameter $P_i(t)$, the corresponding equality $P_i(t) = P_i(k)$ holds. $P_i(t) - P_i(k)$. Using the direct differential transformation $P_i(k) = \frac{H^k}{K!} \left[\frac{d^k P_i(t)}{dt^k} \right]_{t=0}$, one synthesizes a differential mathematical model focused on the study of network computing architecture [14]:

$$\begin{aligned} P_0(k+1) &= \frac{H}{k+1} \left[\lambda_0 P_1(k) + \beta_1 P_2(k) + \lambda_2 P_3(k) \right. \\ &\quad \left. + \lambda_3 P_4(k) + \lambda_4 P_5(k) - \gamma_1 P_0(k) \right], \\ P_1(k+1) &= \frac{H}{k+1} [\beta_0 P_0(k) + \lambda_0 P_1(k)], \\ P_2(k+1) &= \frac{H}{k+1} \left[\lambda_1 P_0(k) + \lambda_5 P_8(k) - \right. \\ &\quad \left. \gamma_2 P_2(k) + \beta_{11} P_5(k) + \beta_{13} P_9(k) \right], \\ P_3(k+1) &= \frac{H}{k+1} \left[\lambda_9 P_4(k) + \gamma_3 P_3(k) + \right. \\ &\quad \left. \beta_2 P_0(k) + \beta_8 P_6(k) + \beta_{14} P_{10}(k) \right], \\ P_{10}(k+1) &= \frac{H}{k+1} [\lambda_{14} P_3(k) + \beta_{14} P_{10}(k)], \end{aligned} \quad (3)$$

where:

$$\begin{aligned} \gamma_1 &= (\beta_0 + \beta_2 + \beta_3 + \beta_4 + \lambda_1); \\ \gamma_1 &= (\beta_1 + \beta_5 + \lambda_{11} + \lambda_{13}); \gamma_3 = (\lambda_2 + \lambda_8 + \lambda_{14} + \beta_9); \\ \gamma_4 &= (\lambda_3 + \lambda_9 + \beta_{10}); \gamma_5 = (\lambda_4 + \lambda_{10} + \beta_{11}); \\ \gamma_6 &= (\lambda_7 + \beta_8); \gamma_7 = (\lambda_6 + \beta_7); \gamma_8 = (\lambda_5 + \beta_6). \end{aligned}$$

The initial conditions, under $t = 0, k = 0$ are represented $P_0(t=0) = P_0(0) = 1$, respectively $P_i(t=0) = P_i(0) = 0$.

The differential mathematical model in Equation (3) is the basis for the formation, in an analytical form, of probabilities $P_0(t), P_1(t), P_2(t), P_3(t), P_4(t), P_5(t), P_6(t), P_7(t), P_8(t), P_9(t), P_{10}(t)$ state of nodes of a traction substation computer network.

Making the substitution of the initial conditions: $P_0(t=0) = P_0(0) = 1, P_i(t=0) = P_i(0) = 0, t = 0, k = 0, i = 1, 2, \dots, 10$ in the differential mathematical model in Equation (3) and for $k = 0$, one obtains the discrete spectrum in the form:

$$\begin{aligned} P_0(1) &= -\gamma_1 H; P_1(1) = \beta_0 H; P_2(1) = \lambda_1 H; \\ P_3(1) &= \beta_2 H; P_4(1) = \beta_3 H; P_5(1) = \beta_4 H; \\ P_6(1) &= 0; P_7(1) = 0; P_8(1) = 0; P_9(1) = 0; \\ P_{10}(1) &= 0. \end{aligned} \quad (4)$$

Values of $P_0(1) = -\gamma_1 H$ the T-discrete $P_1(1) = \beta_0 H, \dots, P_{10}(1) = 0$ are substituted in the differential model in Equation (3) and for $k = 1$ one obtains the following set of discrete in the form:

$$\begin{aligned} P_0(2) &= \frac{H^2}{2} \left(\lambda_0 \beta_0 + \lambda_1 \beta_1 + \lambda_2 \beta_2 + \right. \\ &\quad \left. + \lambda_3 \beta_3 + \lambda_4 \beta_4 + \gamma_1^2 \right), \\ P_0(2) &= -\frac{H^2 \beta_0}{2} (\gamma_1 + \lambda_0); \\ P_2(2) &= \frac{H^2}{2} [\beta_4 \beta_{11} - \lambda_1 (\gamma_1 + \gamma_2)]; \\ P_3(2) &= \frac{H^2}{2} [\lambda_9 \beta_3 - \beta_2 (\gamma_1 + \gamma_3)]; \\ P_4(2) &= \frac{H^2}{2} [\lambda_{10} \beta_4 - \beta_3 (\gamma_1 + \gamma_4) + \beta_2 \beta_9]; \\ P_5(2) &= \frac{H^2}{2} [\lambda_1 \lambda_{11} - \beta_4 (\gamma_1 + \gamma_5) + \beta_3 \beta_{10}]; \\ P_6(2) &= \frac{H^2}{2} \lambda_8 \beta_2; P_7(2) = 0; P_8(2) = \frac{H^2}{2} \lambda_1 \beta_5 \\ P_9(2) &= \frac{H^2}{2} \lambda_1 \lambda_{13}; P_{10}(2) = \frac{H^2}{2} \lambda_{14} \beta_2. \end{aligned} \quad (5)$$

Acting by analogy with $k = 2, k = 3 \dots k = n$ one obtains, respectively, the set of discrete $P_i(0); P_i(1); P_i(2), \dots, P_i(k)$ ($i = 1, 2, \dots, 10$) the number of n , which is determined from the conditions of necessary accuracy.

Obtained in this way, at $n = 2$, the set of discrete $P_i(0); P_i(1), P_i(2) i = 1, 2, \dots, 10$ is substituted into the inverse differential transformation $P_i(t) = \sum_{k=0}^{\infty} \left(\frac{t}{H} \right)^k P_i(k)$, mathematical dependence in Equation (2) is obtained in an analytical form, the probability values $P_0(t), P_1(t), P_2(t), P_3(t), P_4(t), P_5(t), P_6(t), P_7(t), P_8(t), P_9(t), P_{10}(t)$, the state of the nodes of the local computer network of power supply control at the level of traction substations, i.e.

$$\begin{aligned} P_0(t) &= 1 - \gamma_1 t + \left(\lambda_0 \beta_0 + \lambda_1 \beta_1 + \lambda_2 \beta_2 + \right. \\ &\quad \left. + \lambda_3 \beta_3 + \lambda_4 \beta_4 + \gamma_1^2 \right) \frac{t^2}{2}, \\ P_1(t) &= \beta_0 t - \beta_0 (\gamma_1 + \lambda_0) \frac{t^2}{2}; \\ P_2(t) &= \lambda_1 t + [\beta_4 \beta_{11} - \lambda_1 (\gamma_1 + \gamma_2)] \frac{t^2}{2}; \\ P_3(t) &= \beta_2 t + [\lambda_9 \beta_3 - \beta_2 (\gamma_1 + \gamma_3)] \frac{t^2}{2}; \\ P_4(t) &= \beta_3 t + [\lambda_{10} \beta_4 - \beta_3 (\gamma_1 + \gamma_4) + \beta_2 \beta_9] \frac{t^2}{2}; \\ P_5(t) &= \beta_4 t + [\lambda_1 \lambda_{11} - \beta_4 (\gamma_1 + \gamma_5) + \beta_3 \beta_{10}] \frac{t^2}{2}; \\ P_6(t) &= \lambda_8 \beta_2 \frac{t}{2}; P_7(t) = (\lambda_7 \lambda_8 \beta_2 + \beta_6 \lambda_1 \beta_5) \frac{t^3}{3!}; \\ P_8(t) &= \lambda_1 \beta_5 \frac{t^2}{2}; P_9(t) = \lambda_1 \lambda_{13} \frac{t^2}{2}; \\ P_{10}(t) &= \lambda_{14} \beta_2 \frac{t^2}{2}. \end{aligned} \quad (6)$$

6 Models of optimal computer intellectualization strategy

Represented by Equations (6), the probability values $P_0(t), P_1(t), P_2(t), P_3(t), P_4(t), P_5(t), P_6(t), P_7(t), P_8(t), P_9(t), P_{10}(t)$ conditions of each node of the graph can be used to formulate a criterion for the optimal strategy of power supply control procedures, which can be written as [14]

$$\Theta_i(t) = \frac{1}{T} \int_{t=t_0}^T P_i(t) dt, \quad i = 0, 1, 2, \dots \quad (7)$$

Since each node of the local computer network operates in a conflict between the intensity of the application flow $\lambda_i(t)$ and the intensity of the application flow $\beta_i(t)$, the dominance in such conditions is the observance by the conflict subjects of the minimax principle [2, 4]. Achievement of optimal functioning in each node of the computer network is possible by rational adherence to the strategy of formation of such values of service flow intensity $\beta_i(t)$ that minimize the fee $\Theta_i(\lambda_i, \beta_i)$ at the maximum flow rate of service flow $\lambda_i(t)$, i.e.

$$\Theta_i^*(\lambda_i, \beta_i) = \min_{\beta_i \in E_\beta} \max_{\lambda_i \in E_\lambda} \Theta_i(\lambda_i, \beta_i), \quad i = 0, 1, 2, \dots \quad (8)$$

In the process of modelling the optimal strategy, it is likely to proceed from the condition for formation of such $\lambda_i(t)$ that maximize the fee $\Theta_i(\lambda_i, \beta_i)$, provided it is minimized by the application service system $\beta_i(t)$, i.e.

$$\Theta_i^*(\lambda_i, \beta_i) = \min_{\lambda_i \in E_\lambda} \max_{\beta_i \in E_\beta} \Theta_i(\lambda_i, \beta_i), \quad i = 0, 1, 2, \dots \quad (9)$$

Obviously, subject to the fulfilment of mathematical dependencies in Equations (8), (9)

$$\min_{\beta_j \in E_\beta} \max_{\lambda_i \in E_\lambda} \theta_i(\lambda_i, \beta_i) = \min_{\lambda_i \in E_\lambda} \max_{\beta_j \in E_\beta} \theta_i(\lambda_i, \beta_i) = \theta_i^{opt}(\lambda_i^{opt}, \beta_i^{opt}), \quad (10)$$

search strategies $\lambda_i(t)$ $\lambda_i(t)^{opt}$; $\beta_i(t)^{opt}$ are called optimal [3, 11-12].

The strategy is to select the law of change in the flow of customer service intensity $\beta_i(t)$, which implements minimization of functional in Equation (10) with the stochastic intensity of the customer service flow $\lambda_i(t)$, within the appropriate limits. Therefore, in connection with the antagonism of the goals of the subjects of the information conflict, the dominant strategy for the optimal intellectualization of the fast technological processes will be a strategy based on the minimax principle, i.e. [3]

$$\min_{\beta_j \in E_\beta} \max_{\lambda_i \in E_\lambda} \theta_i(t, P_i, \lambda_i, \beta_i). \quad (11)$$

The minimax strategy in Equation (11) allows to minimize functional in Equation (7) even in the cases of the worst combination of flow intensities $\lambda_i(t)$ and $\beta_i(t)$. Using the direct differential transformation in Equation (2), the

criterion $\theta_0(t) = \frac{1}{T} \int_{t_0}^T P_0(t) dt$ takes the form [14]

$$\theta_i^* \sum_{k=0}^{\infty} \frac{p_i(k)}{k+1}. \quad (12)$$

Based on calculations of the corresponding set of T-discrete, $P_i(0); P_i(1); P_i(2); \dots, P_i(k)$, according to Equation (3), the optimization procedure based on the differential spectrum can be implemented as follows. After substituting the aggregate discrete $P_i(0); P_i(1); P_i(2); \dots, P_i(k)$ in Equation (12), the state model for the $\varphi_i(t)$ -th node of the local network, for $i = 0$, that is $P_0(k)$ $k = 0, 1, 2, \dots$, takes the form:

$$\theta_{i=0}^*(\lambda_i, \beta_i) = 1 - (\beta_0 + \beta_2 + \beta_3 + \beta_4 + \lambda) t + (\lambda_0 \beta_0 + \lambda_1 \beta_1 + \lambda_2 \beta_2 + \lambda_3 \beta_3 + \lambda_4 \beta_4 + \gamma_1^2) \frac{t^2}{2}. \quad (13)$$

The procedure for selecting the optimal strategies for the intensity of application flows λ_i^{opt} and the flow of service intensity of applications β_i^{opt} of a functional θ_i^* is linked with studying it to an extremum by substituting values of the corresponding discrete into Equation (12) $P_i(0); P_i(1); P_i(2); \dots (i = 1, 2, \dots, 10)$. It is known that the necessary conditions for existence of an extremum of a functional, according to the Kuhn-Tucker theorem, are conditions that allow us to determine the optimal strategy in the form [3, 8]

$$\begin{cases} \frac{d}{d\lambda_0}(\theta_0^*(\lambda_i, \beta_i)) = 0, & \frac{d}{d\beta_0}(\theta_0^*(\lambda_i, \beta_i)) = 0, \\ \dots & \dots \\ \frac{d}{d\lambda_{10}}(\theta_0^*(\lambda_i, \beta_i)) = 0, & \frac{d}{d\beta_{10}}(\theta_0^*(\lambda_i, \beta_i)) = 0, \end{cases} \quad (14)$$

Implementing the substitution $\theta_i^{opt}(\lambda_i, \beta_i)$, according to Equation (13), into the system of Equations (14) and taking partial derivatives, one obtains a system of linear algebraic equations, solving of which gives the optimal strategies λ_i^{opt} and β_i^{opt} . The signs of extremes in strategies λ_i^{opt} are β_i^{opt} , determined based on checking the sufficient conditions by:

$$\begin{cases} \frac{d^2}{d\lambda_0^2}(\theta_0^*(\lambda_i, \beta_i)) > 0, & \frac{d^2}{d\beta_0^2}(\theta_0^*(\lambda_i, \beta_i)) > 0, \\ \dots & \dots \\ \frac{d^2}{d\lambda_{10}^2}(\theta_0^*(\lambda_i, \beta_i)) > 0, & \frac{d^2}{d\beta_{10}^2}(\theta_0^*(\lambda_i, \beta_i)) > 0, \end{cases} \quad (15)$$

Carrying out studies analogically or substituting values of $\theta_{i=0}^{opt}(\lambda_i, \beta_i)$ from Equation (13) into the system of Equations (15) and taking the second derivatives, one obtains a system of algebraic equations, the solution of which indicates the fulfilment or non-fulfilment of sufficient conditions. Calculating the value of optimal strategies λ_i^{opt} and β_i^{opt} according to Equation (14), corresponding to conditions in Equation (15) and substituting them into Equation (13) the optimum functioning of the $\varphi_0(t)$ -th node of the graph is determined, which represents the local area network of controlling the power supply of traction substation.

7 Conclusions

1. Research was conducted on the problem of innovative transformation of railway power supply systems to create promising energy-saving technologies for the power consumption and the formation of the new knowledge. This direction of research is justified, related to formation of a qualitatively new set of intelligent power supply systems, which is achieved through deep mutual integration of the topology of the power grid infrastructure and the architecture of the distributed computer network for power supply management.
2. Based on the modern concept of the intelligent traction power supply systems' synthesis, a research direction has been formulated related to organization of an optimal strategy for computer intellectualization of the fast-flowing technological processes of power supply in traction substations of railways, by creating mathematical models and methods for determining the optimal functioning of individual nodes and segments of an intelligent computer network power management.
3. The logical structure of a distributed computer environment that adequately reflects the topology of the organization of the electric power supply system at the level of traction substations is proposed in the form of a graph, based on which a differential mathematical model of the computer architecture of the power supply control is formed and methods for determining, in an analytical form, the set of values of

- the probabilities of node states graph.
4. Due to the antagonism in each node or segment of the intelligent computer network for the power supply management, between the intensities of the application flow $\lambda_i(t)$ and the application service flow $\beta_i(t)$, an optimal computerization strategy for the fast power supply technological processes based on the minimax principle is proposed, which allows to minimize function even in the cases of poor combination of intensity of application flows and every law of service flow intensity.
 5. An intelligent method has been developed for finding

the optimal strategy for computer intellectualization of the power supply process to provide specified indicators for the optimal functioning of individual nodes and segments of an intelligent computer control network.

Acknowledgments

This paper is elaborated in the framework of the project co-financed by the Polish National Agency for Academic Exchange (project PPN/BUA/2019/1/00016/U/00001).

References

- [1] STASIUK, A. I., GONCHAROVA, L. L. Mathematical Models and Methods for Analyzing Computer Control Networks of Railway Power Supply. *Cybernetics and Systems Analysis* [online]. 2018, 54(1), p. 165-172. ISSN 1060-0396, eISSN 1573-8337. Available from: <https://doi.org/10.1007/s10559-018-0017-0>
- [2] STASIUK, A. I., GONCHAROVA, L. L. Differential mathematical models of computer research of the abnormal and transient modes of power supply systems of railways. *Journal of Automation and Information Sciences* [online]. 2018, 50(1), p. 76-84. ISSN 1064-2315, eISSN 2163-9337. Available from: <https://doi.org/10.1615/JAutomatInfScien.v50.i1.50>
- [3] STASIUK, A. I., HRYSHCHUK, R. V., GONCHAROVA, L. L. Mathematical differential models and methods for assessing the cybersecurity of computer networks intelligent control of technological processes of railway power supply. *Cybernetics and Systems Analysis* [online]. 2018, 54(4), p. 671-682. ISSN 1060-0396, eISSN 1573-8337. Available from: <https://doi.org/10.1007/s10559-018-0068-2>
- [4] STASIUK, A. I., GONCHAROVA, L. L. Differential mathematical models to investigate the computer network architecture of an all-mode system of control over a distance of railways. *Cybernetics and Systems Analysis* [online]. 2017, 53(1), p. 157-164. ISSN 1060-0396, eISSN 1573-8337. Available from: <https://doi.org/10.1007/s10559-017-9915-9>
- [5] STASIUK, A. I., GONCHAROVA, L. L. Mathematical models of computer intellectualization of technologies for synchronous phasor measurements of parameters of electric networks. *Cybernetics and Systems Analysis* [online]. 2016, 52(5), p. 825-830. ISSN 1060-0396, eISSN 1573-8337. Available from: <https://doi.org/10.1007/s10559-016-9883-5>
- [6] STASIUK, A. I., GONCHAROVA, L. L. Mathematical models and methods of the analysis of computer networks of control of power supply of railways traction substations. *Journal of Automation and Information Sciences* [online]. 2017, 49(2), p. 50-60. ISSN 1064-2315, eISSN 2163-9337. Available from: <https://doi.org/10.1615/JAutomatInfScien.v49.i2.50>
- [7] ZHELIEZNOV, K. I., AKULOV, A. S., ZABOLOTNYI, O. M., URSYLYAK, L. V., CHABANUK, E. V., SHVETS, A. O., KUZNETSOV, V. G., RADKEYCH, A. V. The revised method for calculating of the optimal train control mode. *Archives of Transport*. 2019, 51(3), p. 21-34. ISSN 0866-9546, eISSN 2300-8830. Available from: <https://doi.org/10.5604/01.3001.0013.6160>
- [8] BARTOLOMIEJCZYK, M. Smart grid in practice - implementation of the bilateral supply in Gdynia trolleybus network. In: 9th International Scientific Symposium on Electrical Power Engineering Elektroenergetika: proceedings. Kosice: TUKE, 2017. P. 133-37.
- [9] PEAREE, N. S.; SWAN, L. G. Electric vehicle charging to support renewable energy integration in a capacity constrained electricity grid. *Energy Conversion and Management* [online]. 2016, 109, p.130-139. ISSN 0196-8904. Available from: <https://doi.org/10.1016/j.enconman.2015.11.066>
- [10] BIALON, A., KUZNETSOV, V., SYCHENKO, V., HUBSKYI, P. Energy efficient distributed DC traction power supply system. In: 23rd International Conference Transport Means: proceedings. 2019. p.847-851.
- [11] STASIUK, A. I., GONCHAROVA, L. L., GOLUB, G. M. method for assessing cybersecurity of distributed computer networks for control of electricity consumption of power supply distances. *Journal of Automation and Information Sciences* [online]. 2017, 49(7), p. 48-57. ISSN 1064-2315, eISSN 2163-9337. Available from: <https://doi.org/10.1615/JAutomatInfScien.v49.i7.40>
- [12] STASIUK, A. I., HRYSHCHUK, R. V., GONCHAROVA, L. L. A mathematical cybersecurity model of a computer network for the control of power supply of traction substations. *Cybernetics and Systems Analysis* [online]. 2017, 53(3), p. 476-484. ISSN 1060-0396, eISSN 1573-8337. Available from: <https://doi.org/10.1007/s10559-017-9949-z>
- [13] STASIUK, A. I., GONCHAROVA, L. L. Mathematical models and methods of formation of intelligent computer networks for control of power supply and optimization of power consumption of railways. *Journal of Automation*

- and Information Sciences [online]. 2018, 50(8), p. 50-65. ISSN 1064-2315, eISSN 2163-9337. Available from: <https://doi.org/10.1615/JAutomatInfScien.v50.i8.50>
- [14] PUKHOV, G. E. Taylor transformations and their application in electrical engineering and electronics (in Russian). Kiev: Naukova dumka, 1978.

ENERGY CHARACTERISTICS OF THE DC DISTRIBUTED POWER SUPPLY SYSTEMS

Viktor Sychenko¹, Valeriy Kuznetsov^{2,*}, Artur Rojek², Petro Hubskyi², Yevhen Kosariev¹

¹Dnipro National University of Railway Transport named after Academician V. Lazaryan, Dnipro, Ukraine

²Electric Power Division, Railway Research Institute, Warsaw, Poland

*E-mail of corresponding author: vkuznetsov@ikolej.pl

Resume

Currently the circuit technology of the DC traction power supply system cannot provide the necessary requirements for introduction of high-speed traffic. Numbers of measures and tools have been developed to improve the traction lines that no longer meet current requirements. One of the most promising means for strengthening the traction DC lines is transition to the distributed power supply of the rolling stock. In this article, a comparative analysis was carried out of energy indicators of the classic centralized power system and distributed power systems with use of one aggregate traction substation and with use of the solar generators. That comparative analysis of these systems was performed on a simulation model with the same parameters of the traction line and rolling stock.

Article info

Received 16 June 2020

Accepted 10 August 2020

Online 27 January 2021

Keywords:

traction power system,
centralized power supply,
distributed power,
efficiency,
voltage and power mode,
power characteristics

Available online: <https://doi.org/10.26552/com.C.2021.2.C37-C43>

ISSN 1335-4205 (print version)

ISSN 2585-7878 (online version)

1 Introduction

The present-day of the traction power supply on the DC railways can be characterized by rapid aging of fixed assets of infrastructure. At the same time, the European efforts of Ukraine require the implementation of measures for introduction of the high-speed traffic, which requires modernization of existing power supply lines. Both the DC and AC power supply systems can provide the high-speed transportation, but to ensure a sustainable high speed one must increase the energy intensity for the electric DC lines in the first place. In Poland railway lines E65, E20, E30 are modernized. Implementation of such investment project requires to fulfil all the requirements indicated in TSI (Technical Specifications for Interoperability).

There is a political will to make a modal shift from the road and air modes of transport to railways. This cannot be achieved without taking into account technical and operational interoperability. There is a set of technical barriers between individual interoperable railway systems in civil engineering structures, traction power supply systems, interlocking devices etc. [1]. First of all, it is necessary to ensure the power supply for trains with a current up to 3.2 kA mean useful voltage at least 2.8 kV [2]. With introduction of the high-speed traffic, as shown by analysis of scientific publications, the main efforts of both Ukrainian and foreign scientists are aimed at providing the necessary mode of voltage in the traction line. However, the means and measures applied today in Ukraine do not allow to solve

the problem [3-4].

According to the norms of UIC for the double-track high-speed line with a maximum speed 300-350 km/h, it is estimated that the maximum specific power consumption for traction need is at a level of 3 MW·A/km [5]. The power of traction power devices is recommended to calculate based on the specific power consumption. Thus, there is a gradual evolution of requirements for the traction power supply systems (TPSS): not only the provision of rated voltage, but also providing the necessary energy intensity of the traction line. To ensure these requirements, the scientific idea evolved to the introduction of distributed power supply systems for traction line (DTPSS), which have the best technical and economic characteristics. The use of distributed power supply allows:

- to reduce power losses in the traction line;
- to reduce the cross-section of contact lines;
- to reduce expenses for the construction of external power supply;
- to increase the level of controllability of power processes in the traction line;
- to increase the level of unification of the used equipment.

The distributed power supply scheme of the contact line means the scheme in which consumers on the most loaded zones receive power not only from the nearest but also from a range of remote power points [6]. The work [7] outlines that the key aspects in implementation of the distributed system is assurance of reliable supply



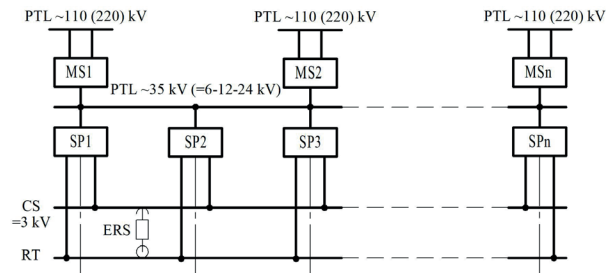


Figure 1 Block diagram of distributed power system:
MS - main substation, SP - supply point

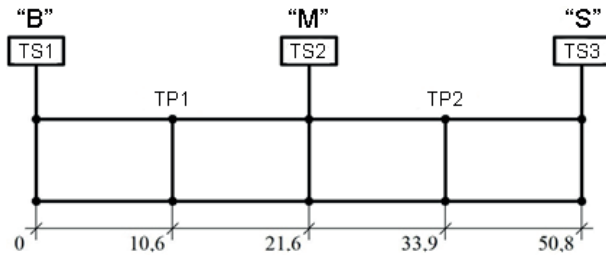


Figure 2 Scheme of the section of CTPSS

to prioritized loads. The less the power of traction units installed at one substation is, the greater becomes the participation of such points in supply of adjacent section between the substations (Figure 1).

Now in the Department of intellectual power supply systems in Dnipro National University of Railway Transport were formed two main approaches to circuit of DTPSS: System of distributed power with use of alternative sources of electric energy (DTPSSA) and a system of distributed power using single aggregate traction substations (DTPSSS) [8]. Assessment of feasibility of upgrading of centralized traction power supply (CTPSS) with application of one or another DTPSS should be done based on the energy indicators analysis. The indicators of the direct assessment of quality of energy-exchange processes in the TPSS are following: efficiency, specific electricity consumption, coefficient of equipment usage (load power factor), energy losses, nominal rating, rated voltage and current [9].

It should be noted that for railways with a speed up to 160 km/h the nature of the electric traction load is subject of the normal distribution. Devices of the traction line are chosen based on the maximum values of current loads during the train movement according to the schedule. However, for the high-speed railways and railways with high intensive traffic and increased carrying capacity, the nature of the electric traction load has a different character. Those lines have impulse load that increases peak loads on traction substations, increases losses of voltage and power in TPSS, complicates a current collection and increases the temperature of the contact wires [10]. It has been established that the specific power consumption increases with increasing of the speed as a result of increased aerodynamic resistance to the movement on horizontal section at an peak acceleration of the rolling stock $\alpha = 5$ km/h/s and speed 250 km/h, the specific electric energy consumption is bigger for more than 3 times than the value at speeds of 120 km/h, which is 50.8 W·h/t·km and 16.01 W·h/

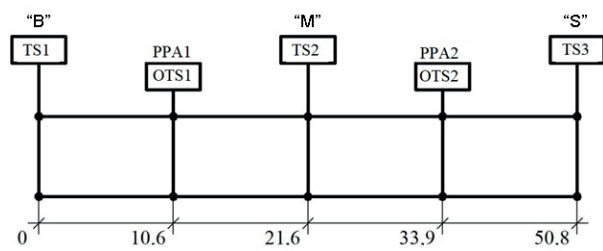


Figure 3 Scheme of the DTPSSS section with single-aggregate substations

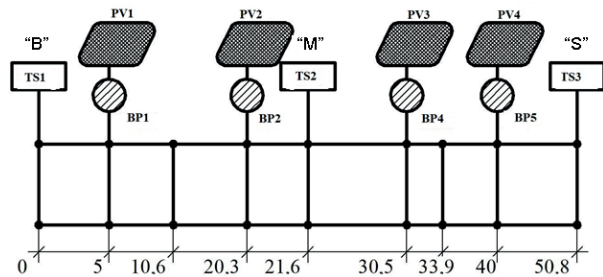


Figure 4 Scheme of tested section of DTPSSA

t·km, respectively.

Therefore, for comparative analysis of different systems of traction power supply, or their circuit design decisions, it is useful to use specific indicators, for example - specific power consumption, specific power, etc. It is also necessary to evaluate the load capacity of the wires of the contact lines and the equipment of the traction substations, sectioning point and the reinforcement points of traction line.

The purpose of the work is conducting a comparative analysis of the power characteristics of centralized power supply and distributed power supply systems.

2 Evaluation of voltage and power modes in the power supply systems

Calculations were made to evaluate the mode of voltage and power in the case of eventual introduction of the high-speed transportation for DC electrified 50.8km long section B - C of Pridneprovskaya railway. The system receives power from the three traction substations in a nodal scheme. The data for calculation are shown in Figure 2 and Table 1. For comparative analysis, the existing CTPSS was transformed into a DTPSSS (Figure 3) and DTPSSA (Figure 4).

The calculations assumed that the train is moving at an average speed of 160 km/h, with an average power consumption of 4.2 MW and a peak capacity of 8.8 MW. The calculations of the voltage level were carried out on a mathematical model [11], with the possibility of taking into account the mutual influence of each load on the associated and, depending on the power scheme, on adjacent tracks:

$$U_j(x) = U_b - I_j(x) \cdot f_R(x) - \sum_{k=1}^{n_1} \Delta U_k'(x, x_k) - \sum_{k=n_1}^{n_1+n_2} \Delta U_k''(x, x_k), \quad (1)$$

Table 1 Parameters of the power supply systems

power, MW	TS1	OTS1 (PPA1)		TS2	(OTS2) PPA2		TS3
CPSS	12.6	-		25.2	-		18.9
DTPSS	10.4	5.2		10.4	5.2		10.4
PSSA	12.6	6	2.5	12.6	2.5	6	12.6
no-load voltage, V	3500						
traction line	M120+2MΦ100+A185+P65						

where:

k - load number on the corresponding track;

n_1, n_2 - number of loads on the 1st and 2nd tracks;

U_b - voltage on the buses of the traction substation, V;

$\Delta U'_k(x, x_k)$ - voltage drop distribution function from k -th load on the passing track, V;

$\Delta U''_k(x, x_k)$ - the same on the adjacent track, V;

I_j - load of the j -th train with x coordinate;

$f_R(x)$ - resistance function.

As a result of calculation in the CTPSS, the minimum value of the voltage on the current collector was 2652 V, which is caused by a complex profile of the section and a sharp rise of the traction power to maintain a constant speed of the train. Thus, the mode of voltage on the electrified section does not meet the requirements for introduction of the high-speed traffic. Even in the cases where a mathematical expectations lay above the nominal value, the level of the voltage does not correspond to rated values, the confidence range of its changes is 875 V, but its lower limit beyond the maximum allowable voltage level for movement is 2900 V [12].

During the calculations, the change in the voltage level on the traction substation buses during the train moving was also determined. The obtained results indicate that the voltage level on the traction substation buses does not exceed the rated values, and its range is 92 V on average for three traction substations.

For estimation of the voltage mode for distributed supply, calculations were carried out under similar conditions of the train movement and track parameters. The difference concerned the power supply scheme of the traction line. For the DTPSSS the controlled transformer units PA-5200 were selected [13], with the number of two units per traction substation and one unit on the sectioning point. Application of the DTPSSS voltage on the current collector of rolling stock was within the permissible values, confidence interval of its changes was 705 V with an average value 3291 V. When applying the controlled rectifier units, the voltage range on the traction substations buses decreased and the average value was 80 V with mathematical expectation of 3490 V.

Evaluation of voltage on the current collector showed that when using the DTPSSA, the mathematical expectation of the voltage was 3397 V, confidence interval was 321 V. The mathematical expectation of voltage on buses of traction substations was 3492 V.

Estimation of the power mode in the case of implementation of the high-speed traffic was carried out based on the above calculations. In accordance with parameters of the comparable systems (Table 1), the total installed capacity of traction substations under centralized power supply is 56.7 MW, distributed power supply with one unit substations - 41.6 MW, distributed power supply with solar generators - 54.8 MW.

The specific power consumed by the rolling stock from 1 km of electrified line is determined by Equation (2):

$$p = \frac{W_e / T}{L}, \quad (2)$$

where:

W_e - consumed electricity by rolling stock during the movement on given section, kW·h;

T - time of movement of rolling stock on section, h;

L - length of the electrified section, km.

The specific power that can be provided by an existing system can be determined by the formula [13]:

$$p_{TS} = \frac{\int_0^T (P_{TS1}(t) + P_{TS2}(t) + P_{TS3}(t)) dt}{L \cdot T}, \quad (3)$$

where:

$P_{TS1}(t), P_{TS2}(t), P_{TS3}(t)$ - power generated by the corresponding traction substation during the rolling stock movement.

The power given by the traction substation to the load is determined by the formula:

$$P_{TS}(x(t)) = U_{BTS}(t) \cdot \varphi(x(t)) \cdot I_e(x(t)), \quad (4)$$

where:

$U_{BTS}(t)$ - voltage on the traction substation buses, V;

$\varphi(x(t))$ - current distribution function;

$I_e(x(t))$ - current of the rolling stock, A;

$x(t)$ - coordinate of the rolling stock location depending on time, km.

Functions of current distribution of traction substations are determined using the method of nodal potentials in the matrix form:

$$\overline{F}(x, S) = |G| \cdot |A(S)|^{-1} \cdot \overline{B}, \quad (5)$$

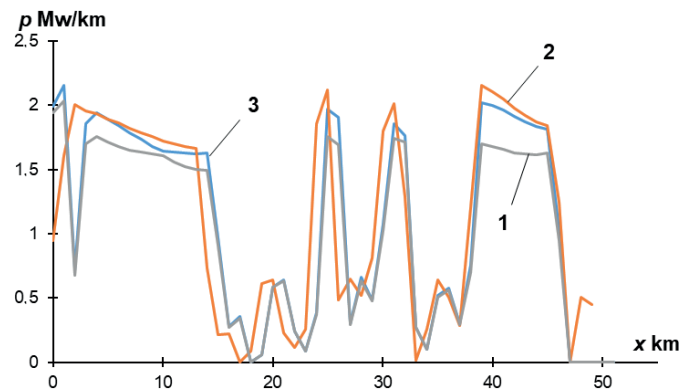


Figure 5 Specific power on the given section:
1 - with centralized supply; 2 - with distributed supply;
3 - rolling stock consumption

Table 2 Traction substation load factor, %

the value of the load factor	TS1	OTS1 (PPA1)	TS2	(OTS2) PPA2	TS3
CPSS	48.2	-	25.3	-	27.2
DTPSS	77.2	91.9	50.4	98.8	51.4
PSSA	72.4	89.7	84.5	78.6	97.4

where:

$|G|$ - diagonal matrix of conductivity of traction substations;
 $|A(S)|$ - basic matrix of the scheme, constructed using the method of nodal potentials;

\bar{B} - vector of predetermined currents (loads) in nodes.

Matrices $|A(S)|$, $|G|$ and are dynamic and change their size depending on the train situation on the given section and location of the individual load.

In turn, the voltage on the traction substation buses can be defined as:

$$U_{BTS}(t) = U_{iv} - \rho \cdot \varphi(x(t)) \cdot I_e(x(t)), \quad (6)$$

where:

U_{iv} - the idle voltage of the traction substation, which is determined by the position of the regulation device of the transformer and can be calculated according to [14], V;

ρ - internal resistance of the traction substation, Ω .

Hence, taking into account the foregoing formulas, one can compose an expression for determining the power generated by the traction substation as a part of a distributed power supply system, taking into account the current distribution in the given section:

$$P_{TS}(x(t)) = P_{zg}(x(t)) - AP_{zg}(x(t)) \cdot \left(\frac{P_{zg}(x(t))}{S_{K3}} - \frac{u_{kz}}{100} \cdot k_z(x(t)) \right), \quad (7)$$

where:

$P_{zg}(x(t))$ - power generated by traction substation for feeding the rolling stock, $P_{TS}(x(t)) = U_{iv} \cdot \varphi(x(t)) \cdot I_e(x(t))$;

$k_{zg}(x(t))$ - load factor of the traction substation,

$$k_z(x(t)) = \frac{P_{zg}(x(t))}{S_{nom} \cdot n}.$$

Based on the above expressions the curves of changes of power generation by traction substations of a centralized and distributed system for feeding the rolling stock moving along the section were obtained (Figure 5).

As it follows from analysis of Figure 5, the centralized power system is not able to meet the needs of the high-speed train for the consumption of power per kilometer of track, which, in turn, leads to impossibility of providing a standardized voltage level in the traction line.

3 Analysis of energy indicators

3.1 Traction substation load factor

The above calculations indicate that installed power in traction substations (for centralized power supply system) allows the high-speed transportation on the given section, but at the same time, the average value of the traction substation load factor is less than 50% (Table 2).

With distributed power, by reducing the installed power of the traction substations, and almost equal power, generated by traction substations, the load factor increased for 1.5 times, on average.

3.2 Loading capacity of the wires of the contact line

In many sections of electrified DC rail, the cross section of the wires of the contact line approaches the value of 600 mm² in copper equivalent. With growth of the peak electrical loads, it is impossible to provide the thermal stability of the contact line and reduce the voltage losses by suspending additional wires. So, on to the DC 1 - in

Table 3 Load capacity of contact lines

power system	centralized					distributed		
contact line type	M-120+2M- Φ100+A185	M-120+2M- Φ100+A185	M-120+2M- Φ100+A185	M-120+2M- Φ100+A185	M-120+2M- Φ100+A185	M-120+2M- Φ100+A185	M-120+2M- Φ100+A185	M-120+2M- Φ100+A185
acceptable current of contact line at 15% wear, a	1630	2120	2710	3290	1630	2120	2710	3290
maximum rated current in the contact line, a		2341.6				1880		
load capacity at current, %	- 43.7	- 10.6	13.6	28.8	- 15.3	11.3	30.6	42.8

*The minus sign indicates an excess of the load capacity of the contact line by current.

Table 4 Power indicators of traction power supply systems

Parameter	CPSS	DTPSS	PSSA
Voltage mode for current on pantograph of rolling stock, V	M(U)	3130	3291
	max(U)	3418	3500
	min(U)	2643	2901
	The value of the confidence interval of the change	875	705
Electricity consumption for traction, kWh	1495	1437	944.8 (from TS)+ 486.3 (from SP)
Average power losses, kW	Excluding higher harmonics	524	372
	Taking into account the higher harmonics	631	428
Electricity losses, kWh	Excluding higher harmonics	174.9	123.9
	Taking into account the higher harmonics	210.6	142.7
cosφ	0.77	0.79	0.81
Efficiency	0.92	0.95	0.97

Lviv railways to provide the standard voltage level on the pantograph of rolling stock and to assure the compliance with the conditions of the thermal resistance of contact, with the passage of two electric locomotives 2ES10 and 2ES6, five additional reinforcement wires were installed. According to the experimental data, the currents of heavy-weight trains can significantly exceed the load capacity of the contact line.

According to the calculation results for the centralized and distributed power system, the reserve load capacity of the wires for typical contact lines used on electrified Ukrainian railways are: (Table 3).

3.3 Investigation of the electric power losses in the distributed power system

The power losses or energy efficiency of traction power systems are one of the main criteria for assessing the energy efficiency of a powertrain network. They determine the operating costs of the electrified section.

Increasing the intensity of the movement, as is known, leads to an increase in current loads on all the elements of

the traction power system and, consequently, to increase of energy losses and reduction of energy efficiency. However, in some interurban interval, efficiency reaches a maximum and then it is reduced due to the prevalence of losses independent of current. In any case, with other equal conditions, the energy efficiency of a distributed system of the traction power supply is higher, the distance between the supply points is smaller, despite the fact that with decrease of the distance between them their power is decreasing, as well [15]. The loss of electricity is obtained by integrating the distribution power losses in the traction line, which, in turn, is defined as the product of the current flowing through the area of contact and losses of voltage on this area.

In accordance with [11], the current distribution in the traction line is determined by the received potentials in the nodes of the scheme in Equation (5), the resistance of the branches between them and the schedule of trains:

$$i_{K1} = \frac{\varphi_1 - \varphi_2}{r_1} \quad (8)$$

where:

φ_1, φ_2 - potentials of the first and second nodes, V;

r_1 - the value of the resistance of the branch between the first and second nodes, Ω .

Further, in the presence of another load on the calculated section, using the principle of superposition, the distribution of currents in the contact line from all the trains is determined:

$$I_{K1}(x) = \sum_{i=1}^{n_1} I_{K1}(2i-1, x) + \sum_{i=1}^{n_2} I_{K1}(2i, x) + I_{lev}, \quad (9)$$

where:

$2i-1, 2i$ - determine the numbers of the odd and even train;
 n_1, n_2 - number of trains correspondingly on the first and second track;

I_{lev} - leveling current on the section, A.

Determination of the voltage loss distribution function involves use of the currents distribution function in the contact line with the accumulated gain for the corresponding distance and the resistivity of the line.

$$\Delta U_{K1}(x) = \sum_{i=1}^{n_1} \Delta U_{K1}(2i-1, x) + \sum_{i=1}^{n_2} \Delta U_{K2}(2i, x) + I_{lev} \cdot r_0 \cdot x, \quad (10)$$

where:

$\Delta U_{K1}(2i-1, x)$ - voltage losses in the traction line from trains moving in the even direction, V;

$\Delta U_{K2}(2i, x)$ - voltage losses in the traction line from trains moving in the odd direction, V;

$I_{lev} \cdot r_0 \cdot x$ - voltage losses in the traction line from the compensating currents, V.

The statistical data in Table 4 were obtained from the results of processing 5200 values during the simulation. Losses of power from the higher harmonics for comparative

analysis of STE were calculated according to [16].

A comparative analysis of the energy performance of the proposed distributed systems and the existing centralized supply system is summarized in Table 4.

4 Conclusions

The conducted research has established that in the case of passing one high-speed train on calculated section with the given parameters, introduction of the distributed power system allows:

- to ensure the necessary level of specific power in traction line within 2 - 2.15 MW/km, allowing to provide the rated minimum voltage on current collector at the level of 2900 V;
- to reduce the load on the wire of the contact line thanks to the decentralization of power sources;
- to reduce inactive power and power losses in traction line thanks to improvement of voltage mode in the system of traction power supply;
- to achieve electricity savings of 57.2 kWh, representing 4.3% of the electricity consumed by the train.

Thus, application of the distributed power systems for the traction loads can provide the necessary requirements for introduction of the high-speed traffic and should be a priority direction for reinforcement of the DC traction power supply.

Acknowledgments

This paper is elaborated in the framework of the project co-financed by the Polish National Agency for Academic Exchange (project PPN/BUA/2019/1/00016/U/00001).

References

- [1] PAWLIK, M. Analyse of the challenges for safe transition from individual intraoperable railway systems to the single European interoperable railway system. *Archives of Civil Engineering* [online]. 2016, **62**(4), p. 169-180. ISSN 1230-2945, eISSN 2300-3103. Available from: <https://doi.org/10.1515/ace-2015-0114>
- [2] SZELAG, A. Electrical power infrastructure for modern rolling stock with regard to the railway in Poland. *Archives of Transport* [online]. 2017, **42**(2), p. 75-83. ISSN 0866-9546, eISSN 2300-8830. Available from: <https://doi.org/10.5604/01.3001.0010.0529>
- [3] SYCHENKO, V., SAENKO, Y., BOSIY, D. *Quality of electricity in traction lines of electrified railways* (in Ukrainian). Dnipro: PF Standard-Service, 2015. ISBN 978-966-97463-8-2
- [4] HUBSKYI, P., KUZNETSOV, V., DRUBETSKYI, A., AFANASOV, A., PULIN, M. Studying of the power modes in the traction line for ensuring the high-speed traffic (in Ukrainian). *Technology Audit and Production Reserves* [online]. 2018, **5**(1(43)), p. 42-51. ISSN 2664-9969, eISSN 2706-5448. Available from: <https://doi.org/10.15587/2312-8372.2018.146665>
- [5] BURKOV, A., BURKOV, S., SHARPILOVA, M. *Modes of movement and the characteristics of traction calculations in determining the load on the power supplies high-speed lines* (in Russian). St. Petersburg: State University of Railway Transport, 2013.
- [6] MARIKIN, A., MYZINTSEV, A. *E* (in Russian). Moscow: Marshrut, 2008. ISBN 978-5-89035-504-1
- [7] KUMAR, H., MAYADEVI, R., MINI, V., USHAKUMARI, S. Transforming distribution system into a sustainable isolated microgrid considering contingency. *Bulletin of the Polish Academy of Sciences Technical Sciences* [online]. 2019, **67**(5), p. 871-881. ISSN 0239-7528. Available from: <https://doi.org/10.24425/bpasts.2019.130875>
- [8] HUBSKYI, P. Energy channels of power of distributed systems of type electrical supply. *Electrification of Transport*

- [online]. 2018, **15**, p. 23-30. ISSN 2307-4221, eISSN 2312-6574. Available from: <https://doi.org/10.15802/etr.v0i15.155584>
- [9] SYCHENKO, V. G., KUZNETSOV, V. G., BOSIY, D. O., SABLIN, O. I. *Power engineering of traction lines* (in Ukrainian). Dnipro: PF Standard-Service, 2017. ISBN 978-617-73-82-04-0
- [10] BURKOV, A. T., MIRSAITOV, M. M. Features of the method of determining the power consumption when choosing the maximum speed of passenger trains (in Russian). *Izvestiya PGUPS*. 2015, **1**(42), p. 5-11. ISSN 1815-588X.
- [11] KOSAREV, E. M. Mathematical model of the controlled distributed DC power supply system (in Ukrainian). *Electrification of Transport* [online]. 2017, **14**, p. 15-27. ISSN 2307-4221, eISSN 2312-6574. Available from: <https://doi.org/10.15802/etr.v0i14.155013>
- [12] Temporary instruction on the Organization of High-Speed Passenger Traffic Trains. The requirements to the infrastructure and rolling stock (in Ukrainian). 2002.
- [13] KOSAREV, E., SYCHENKO, V., HUBSKYI, P. Research the voltage mode of system DC traction power supply (in Ukrainian). *Electrification of Transport* [online]. 2016, **11**, p. 61-70. ISSN 2307-4221, eISSN 2312-6574. Available from: <https://doi.org/10.15802/etr.v0i11.83718>
- [14] ROJEK, A. *Traction power supply in 3 kV DC system*. Warszawa: KOW media&marketing Sp. Z o.o., 2012. ISBN 8393373735
- [15] SMIRNOV, D. B. *Improvement of the method for calculation of distributed traction power supply system* (in Russian). The dissertation abstract on competition of a scientific degree of candidate of technical sciences. St. Petersburg, 2010.
- [16] SYCHENKO, V. G., HUBSKYI, P. V., KOSAREV, Y. M., ROGOZA, A. V. Evaluation of additional power losses in the power supply system of high-speed traffic (in Ukrainian). *Electrification of Transport* [online]. 2016, **12**, p. 59-63. ISSN 2307-4221, eISSN 2312-6574. Available from: <https://doi.org/10.15802/etr.v0i12.101593>

CLASSIFICATION ACCURACY ENHANCEMENT BASED MACHINE LEARNING MODELS AND TRANSFORM ANALYSIS

Hanan A. R. Akkar¹, Wael A. H. Hadi², Ibraheem H. Al-Dosari^{3,*}, Saadi M. Saadi⁴, Aseel Ismael Ali⁴

¹Department of Electrical Engineering, University of Technology, Baghdad, Iraq

²Department of Communications Engineering, University of Technology, Baghdad, Iraq

³Department of Computer Communications Engineering, Al-Rafidain University College, Baghdad, Iraq

⁴Ministry of Education, Minister's Office, Institute of Gifted Students, Baghdad, Iraq

*E-mail of corresponding author: ibraheemdoser77@gmail.com

Resume

The problem of leak detection in water pipeline network can be solved by utilizing a wireless sensor network based an intelligent algorithm. A new novel denoising process is proposed in this work. A comparison study is established to evaluate the novel denoising method using many performance indices. Hardy-rectified thresholding with universal threshold selection rule shows the best obtained results among the utilized thresholding methods in the work with Enhanced signal to noise ratio (SNR) = 10.38 and normalized mean squared error (NMSE) = 0.1344.

Machine learning methods are used to create models that simulate a pipeline leak detection system. A combined feature vector is utilized using wavelet and statistical factors to improve the proposed system performance.

Article info

Received 29 February 2020

Accepted 26 August 2020

Online 8 February 2021

Keywords:

zigbee,
wavelet transform,
statistical features,
wireless sensor network (wsn),
classification

Available online: <https://doi.org/10.26552/com.C.2021.2.C44-C53>

ISSN 1335-4205 (print version)

ISSN 2585-7878 (online version)

1 Introduction

Many signals in the real-time processing need filtering prior to feature extraction or further processing. The wavelet analysis tools play an important role in signal processing theory, also wavelet transformed coefficients are considered as features of signals, these features can be used for classification and recognition for some classes or objects respectively [1]. In this work a dataset for water pipelines network are used to train some machine learning based models. A comparison study for different classifier is established. Some performance measures are used to validate the comparison test. Although there exist some popular wavelet thresholding methods, such as soft and hard, however researcher still seek for the new thresholding method to improve the wavelet based denoising or compression algorithms. As a contribution to the knowledge of art, a novel thresholding method is proposed which try to improve the denoised signal in terms of increasing improved signal to noise ratio (ISNR) factor or minimize the mean squared error (MSE). The principal core for the proposed wavelet rectified thresholding method is demonstrated in the principle of cutting the details wavelet coefficients in the ripple manner rather than popular flat method. Basically, based on the frequency domain analysis this new thresholding technique will reserve some of the energy in the details wavelet coefficient and hence

improve the denoised signal after re-transforming back the threshold wavelet coefficients into time domain [2]. In the last decade many proposals are suggested by researchers for monitoring the water pipelines network, some of these methods are based on distributed sensor nodes and Wireless sensor network to read the status for the fluid inside the pipeline and monitor the network accordingly. Other methods used the statistical features for the gathered data and use them for diagnosing the system status at different scenarios [3]. In this work, different features are used to construct the feature vector, some of them based on statistical values and others used wavelet decomposition coefficients, the work also utilized some classifiers, which used the correlation between two features to enhance the classification accuracy. The real time signals are gathered from wireless pressure sensors, which are installed along a water pipeline at different locations. Artificial leak valves are inserted within the pipeline to make manual leak with different size ranging from small leak (less than 12.7mm) and through medium leak (between 0.5" and 1") continuing up to the large leak (more than 25.4mm) [4]. These measured pressure signals are processed and their extracted features are fed to different classifier models to diagnose the existence of a system leak. Three main classes are considered for this problem (large, medium, and small); classification confusion matrix is used for classification comparison test.



2 Theoretical background

2.1 Support vector machine

The support vector machine (SVM) is a machine learning tool that can be used for solving problems of seeking for the minimizing certain parameters such as MSE. The principle idea in the SVM theory is to transform the given data to other space using some transformation kernel. New representation for the data has been gotten, such that a hyper plane was used to classify the data into classes with different proposed intervals. Classification algorithms represent one of supervised learning which has ability to create a new model based on a given dataset. This predictive model can be used for further response estimation when the new test data is applied to the predictive model.

2.2 Nearest neighbor

This technique uses the principle of distance calculation between certain data point from the dataset and the closet predication. There are many distances' measure suggestion using different aspects such as Euclidian, Spearman, Jaccard, correlation, cosine, and Chebyshev distance. The KNN can be used for solving different kind of problems in machine learning such as classification, clustering, and regression. It has wide application in new area such as signal processing, data mining and database analysis.

2.3 Zigbee protocol

The IEEE STD 802.15.4 standard describes the physical layer (PHY) and medium access control (MAC) sub layer particulars for low-information rate remote availability with fixed, compact and moving gadgets with no battery or constrained battery utilization prerequisites, normally working in the individual working space of 10m. It is predicted that, contingent upon the application, a more drawn-out range at a lower information rate might be an adequate tradeoff. The IEEE 802.15.4 standard (2003) characterizes the gadget types that can be utilized in a low rate wireless personal area network (LR-WPAN), which are Full Functional Device (FFD) and Reduced Functional Device (RFD). The RFD can be utilized in basic applications in which they do not have to transmit a lot of information and they need to discuss just with a particular FFD. The FFD can fill in as a personal area network (PAN) organizer, as a facilitator, or as a straightforward gadget. It can speak with either another FFD or a RFD [5].

3 Proposed system

In this work, a new technique for the leak detection and classification is suggested, this technique combines

two methods from machine learning science. Dataset for the problem to be solved is provided from the real-time measurements for a water pipeline network. Artificial leaks are created with different sizes at various locations along the pipeline. After data gathering process from wireless pressure sensor nodes, the data is conditioning using denoising process based wavelet transform method. A new proposed Hardy-Rectified thresholding is suggested by authors of this work, a universal threshold and five decomposing levels are used to improve the SNR at the input to the proposed classifier. Both domains (statistical and wavelet) features are extracted and correlated, and then the new correlated features are used to construct a feature matrix that is used for training different classifier models. Comparison test is held between different classifiers types, in order to summarize the obtained results for about 23 classifiers with different criteria and kernels [6]. The Zigbee protocol and its transceiver modules are adopted for data transmission between wireless sensor nodes in the network. A comparison study between different modulation types is established, the results show a sample for the signal between transmitter and receiver of the two nodes with a proper choice of modulation scheme and signal to noise ratio.

4 Proposed wavelet thresholding mathematical models

Denoising for signals and images can be achieved using different methods, wavelet based method can be considered as a one of the well-known methods for denoising, which can be summarized by three main steps: firstly the wavelet decomposition for the signal or image into two coefficients known as approximations and details, then thresholding the details coefficients by proper threshold and finally reconstruct the approximations and threshold details coefficients to reconstruct the de-noised signal or image. There are many thresholding functions used in the literature, such as soft and hard thresholding, however in this work a new proposed thresholding function, known as rectified sine thresholding function, is proposed with two models (Softy and Hardy) in order to enhance the denoising process. The models of the thresholding techniques are given below:

Softy-rectified thresholding

$$Q_j = \begin{cases} [\text{sign}(W_j)(|W_j - \lambda|)] & |W_j| \geq \lambda \\ + a \text{ rectfied sin}(b\pi W_j) & |W_j| < \lambda \\ 0 & |W_j| < \lambda \end{cases}, \quad (1)$$

Hardy- rectified thresholding

$$Q_j = \begin{cases} [W_j] + a \text{ rectfied sin}(b\pi W_j) & |W_j| \geq \lambda \\ 0 & |W_j| < \lambda \end{cases}, \quad (2)$$

Hard thresholding

$$Q_j = \begin{cases} W_j & |W_j| \geq \lambda \\ 0 & |W_j| < \lambda \end{cases}, \quad (3)$$

Soft thresholding

$$Q_j = \begin{cases} [\text{sign}(W_j)(|W_j - \lambda|)] & |W_j| \geq \lambda \\ 0 & |W_j| < \lambda \end{cases}, \quad (4)$$

Softy-sawtooth thresholding

$$Q_j = \begin{cases} [\text{sign}(W_j)(|W_j - \lambda|) \\ + a \text{ sawtooth}(b\pi W_j) & |W_j| \geq \lambda \\ 0 & |W_j| < \lambda \end{cases}, \quad (5)$$

Hardy-sawtooth thresholding

$$Q_j = \begin{cases} [W_j] + a \text{ sawtooth}(b\pi W_j) & |W_j| \geq \lambda \\ 0 & |W_j| < \lambda \end{cases}, \quad (6)$$

where:

W_j - the input signal to wavelet thresholding at level j ,

λ - threshold,

Q_j - the output signal from wavelet thresholding at level j .

5 Results and discussion

Referring to the obtained results, Tables 1 through 3 explain the procedure followed by the wavelet denoising process. In Table 1 a comparison has been done for different wavelet mother functions from the coiflet family, which yields the success for coif2 wavelet mother function with hardy-rectified thresholding, while other parameters are set to: the thresholding rule as universal and 5 decomposing levels are used with two thresholding methods (hard and hardy-rectified). After success for coif 2 in the first stage, it is then used (as shown in Table 2) with different decomposing levels to search for the optimal level. However, level 5 is the best level, due to its highest ISNR and lowest MSE. In Table 3 different kinds for thresholding methods (soft, hard, softy-rectified, and hardy-rectified) have been used with various threshold selection rules (huresure, sqtwolog, rigrsure and minimaxi). The hardy-rectified thresholding with sqtwolog as threshold (universal) selection rule is the best obtained results from Table 3. Different classifiers are used with the same dataset,

which is divided to three parts - 60% for training the model, 30% for validating it and 10% for testing. The confusion matrix is used for comparison between different classifiers [7]. Referring to Table 4, the best classification accuracy is obtained with linear discriminant model, however, fine tree classifier model appeared to be a model with the highest prediction speed and minimum training time. Figure 1 shows the novel wavelet thresholding method (hardy-rectified and softy-rectified) as compared to the conventional methods (hard and soft); 22 machine learning models are trained with the same dataset (see Table 4), Figures 2 through 6 explain the performance for the best classifier model (linear discriminant). Figure 2 explains the confusion matrix between the true and predicted classes for 100 samples of different leak sizes. Figure 3 shows the percentage confusion matrix with positive predictive value and false discovery rate for each class. Figure 4 show the scatter plot for the prediction model with three leak size (large, medium, and small); where the cross mark indicates the misclassification point. From Receiver operating characteristic (ROC) curve in Figure 5 the classifier shows 98% true positive rate with 2% false positive rate [8]. Table 5 explains a comparison between the proposed method and different wavelet thresholding methods in recent researches, like the mixed method [9], improved method [10] hierarchical method [11] and adaptive method [12]. Finally, Figure 6 shows the classifier model with parallel coordinates for the four predictors and different standard deviation ranges.

6 Conclusions

In this work different classifiers from the machine learning toolbox in MATLAB program are used to solve the problem of the leak detection and size prediction in the water pipeline network. Pressure sensors are utilized and installed properly along the water pipelines for data gathering prior to feature extraction. Different features had been used for classification problem, statistical features and the wavelet-based features are the most popular

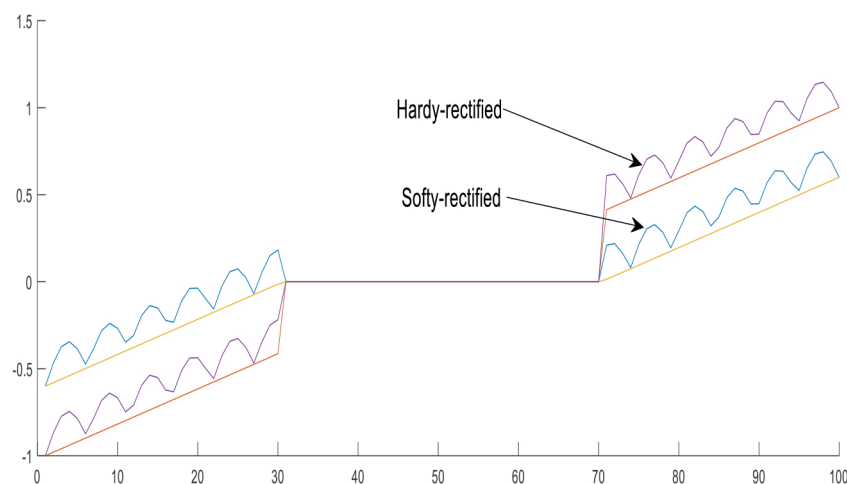


Figure 1 Proposed hardy and softy rectified thresholding methods

used features, but in this work the correlated features, which represent the combination between both features are utilized, as well. Simulation results for the novel wavelet-based rectified thresholding method open the way for further studies and research in deployment of this new technique in wavelet denoising or compression in signals and images. Although the classifiers have different classification accuracies; most of them show

excellent accuracy with acceptable predication speed and satisfactory training time. The Zigbee protocol has good bit error rate (BER) results for different values of the SNR as explained by Figure 7. So, it can be used for wireless sensor network (WSN) deployment and especially with QPSK 2450MHz, which shows excellent transceiver communications and minimum absolute error at the receiver side, see Figure 8.

True Class	Large	49	1	
	Medium	2	48	
	Small			50
		Large	Medium	Small
		Predicted Class		

Figure 2 Confusion matrix for the best model

True Class	Large	96%	2%	
	Medium	4%	98%	
	Small			100%
		Large	Medium	Small
		Predicted Class		
Positive Predictive Value		96%	98%	100%
False Discovery Rate		4%	2%	
		Large	Medium	Small
		Predicted Class		

Figure 3 PPV and FDR for the best model

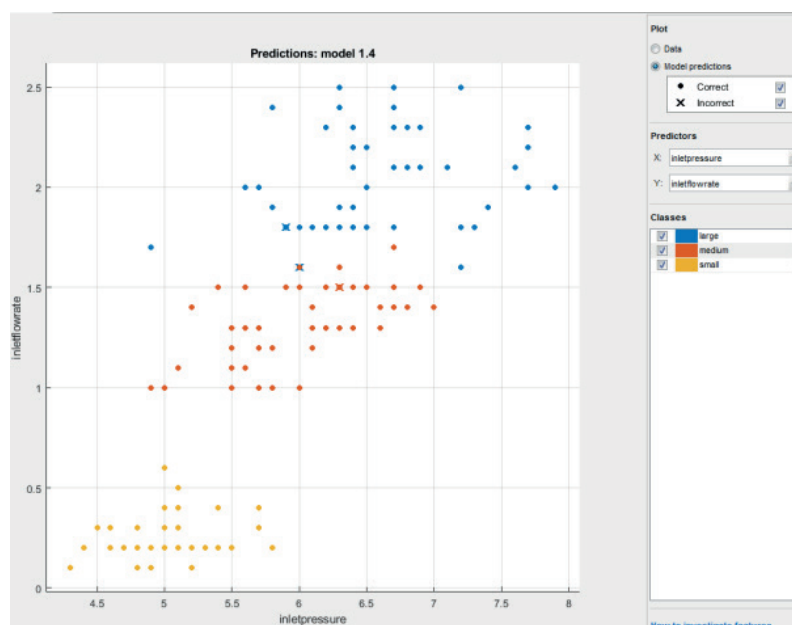


Figure 4 Scatter plot for the best model

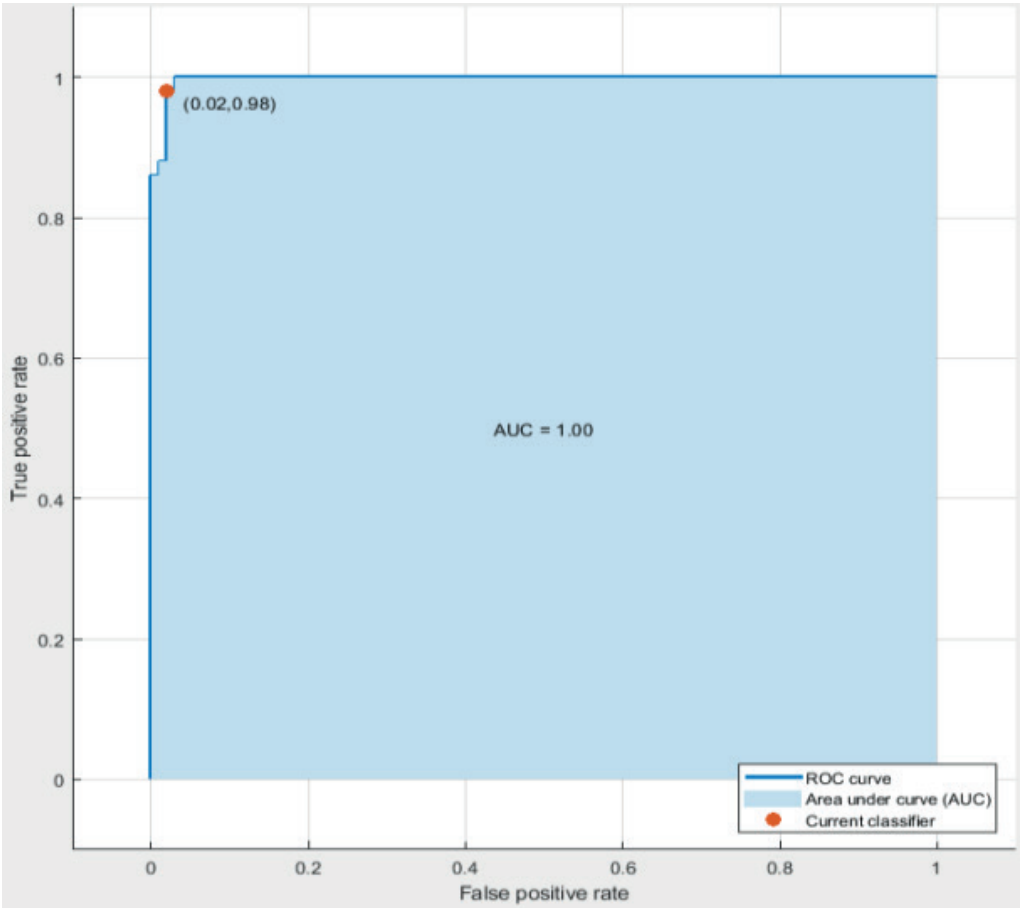


Figure 5 ROC for the best model

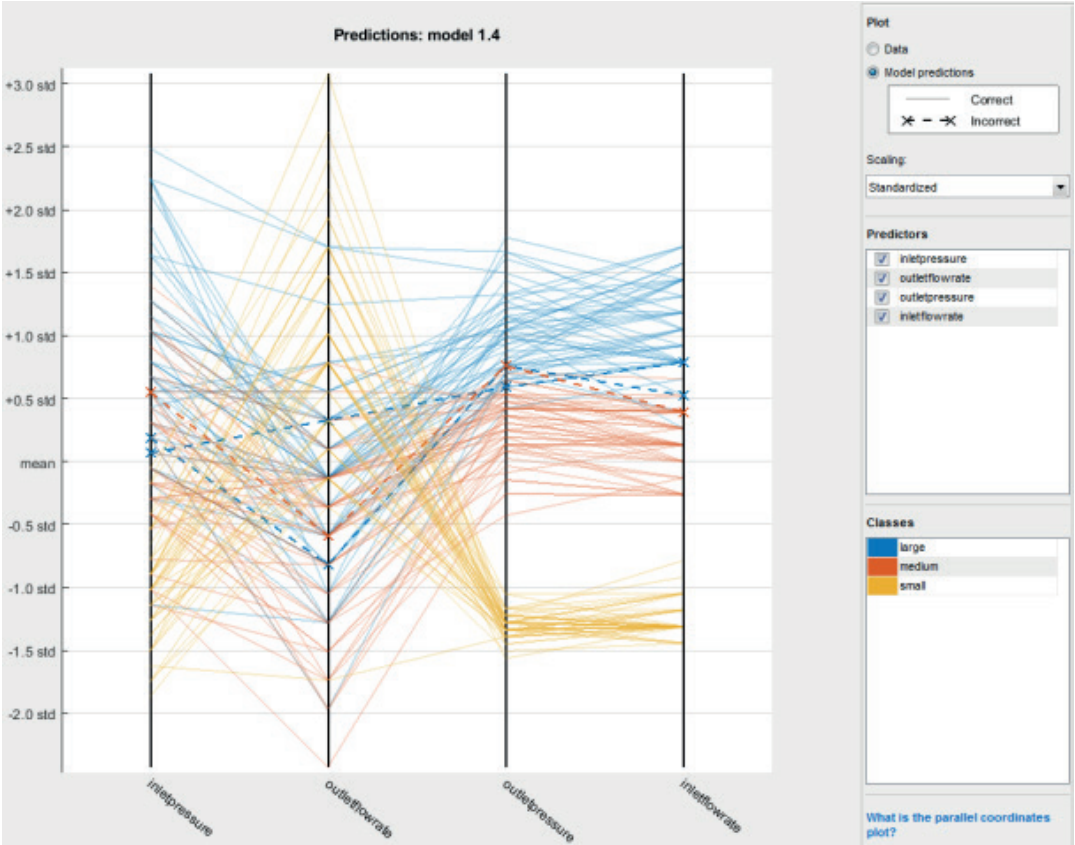


Figure 6 Parallel coordinates plot for the best model

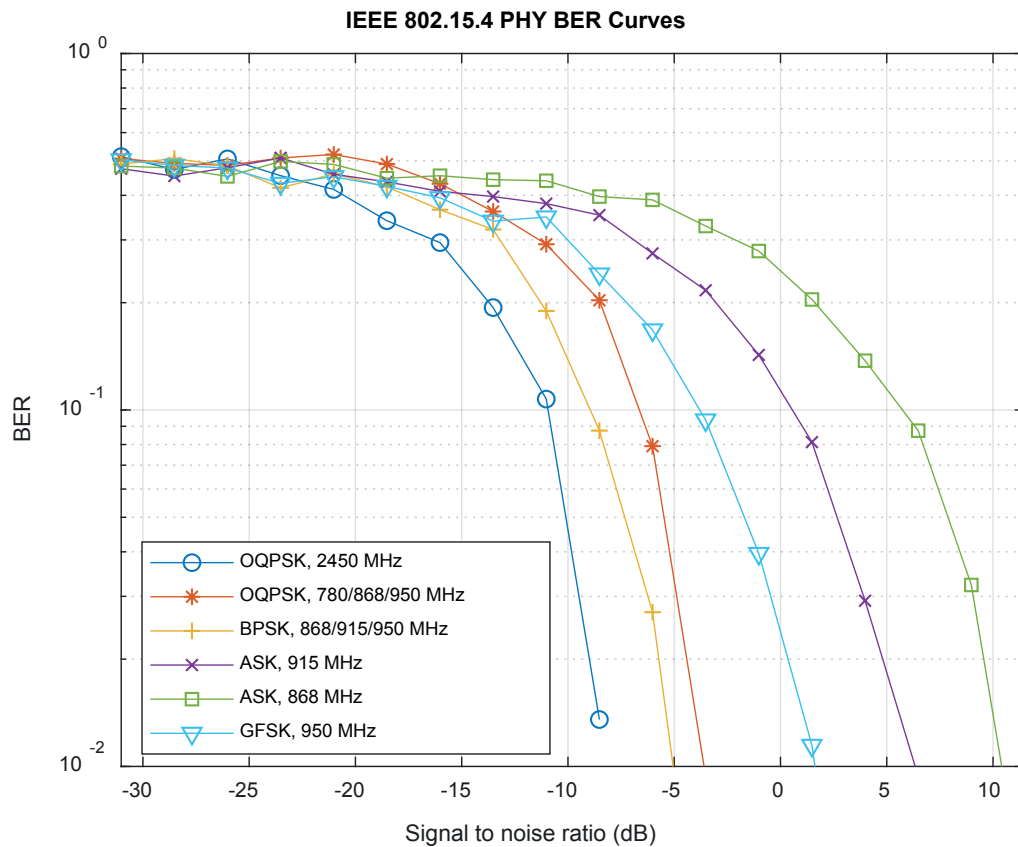


Figure 7 BER versus SNR for different modulation types in the Zigbee transceiver

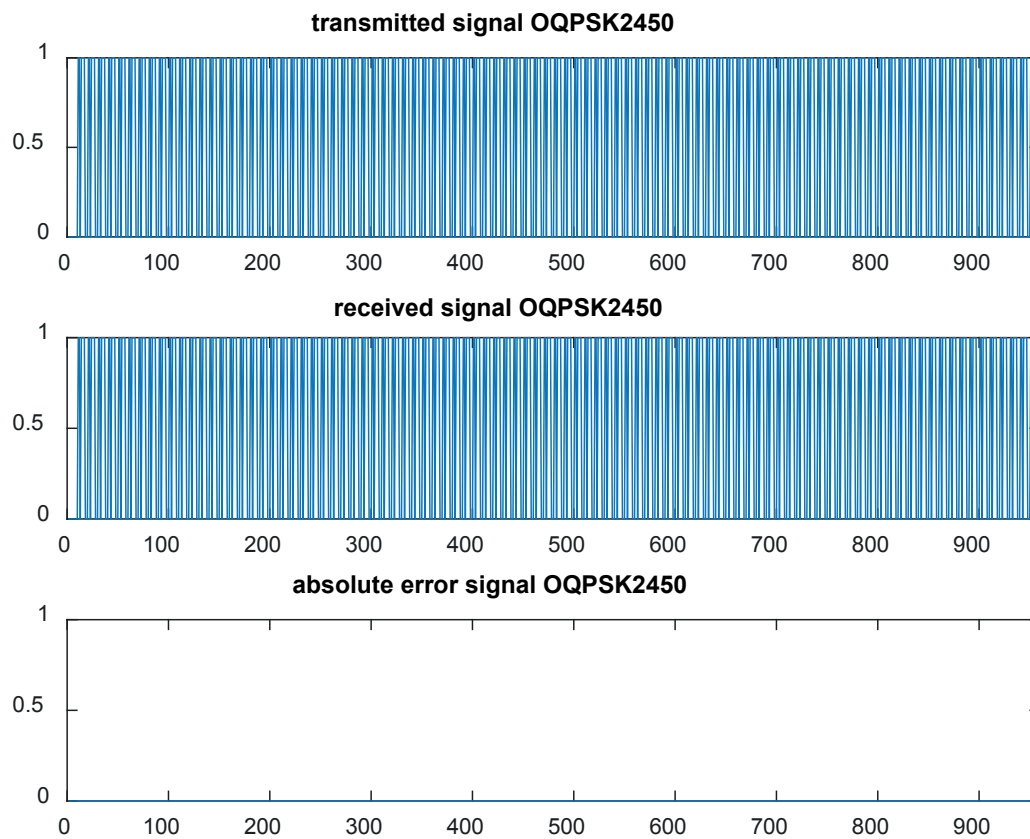


Figure 8 Zigbee transceiver with OQPSK 2450

Table 1 Signal denoising results with various Coiflet wavelets

type of signal		lev	rule of threshold			
noisy signal		5	square-root-log / hardy-rectified			
family of wavelet		coif 5	coif 4	coif 3	coif 2	coif 1
measure index	Norm MSE	0.1408	0.1473	0.1364	0.1345	0.15
	Root MSE	0.2329	0.2456	0.2236	0.2193	0.2506
	Enhanced SNR	9.3589	8.4989	10.0509	10.3875	8.1815
	PDR	0.1669	0.1727	0.1627	0.1607	0.175

type of signal		lev	rule of threshold			
noisy signal		5	square-root-log / hard			
family of wavelet		coif 5	coif 4	coif 3	coif 2	coif 1
measure index	Norm MSE	0.141	0.1473	0.1364	0.1348	0.1503
	Root MSE	0.2333	0.2456	0.2235	0.2201	0.2511
	Enhanced SNR	9.3274	8.4972	10.0549	10.3265	8.1474
	PDR	0.1671	0.1728	0.1626	0.161	0.1753

Table 2 Denoising results using the Coiflet 2 wavelet with various levels of decomposition

type of signal			method of thresholding		type of wavelet	rule of threshold	rescaling for threshold	
noisy signal			hard		coif 2	square root log	estimated noise for each level	
level of decomposition		1	2	3	4	5	6	7
Measured index	NMSE	0.2452	0.183	0.1497	0.1375	0.1348	0.1349	0.3284
	RMSE	0.37	0.3007	0.2501	0.226	0.2201	0.2202	0.4407
	ESNR	2.8075	5.5157	8.2126	9.8666	10.3265	10.3173	0.7111
	PDR	0.2298	0.198	0.1748	0.1638	0.161	0.1611	0.2622

type of signal			method of thresholding		type of wavelet	rule of threshold	rescaling for threshold	
noisy signal			hardy-rectified		coif 2	square root log	estimated noise for each level	
decomposition level		1	2	3	4	5	6	7
Measured index	NMSE	0.2452	0.183	0.1497	0.1375	0.1345	0.1348	0.328
	RMSE	0.37	0.3007	0.2501	0.226	0.2193	0.22	0.4404
	ESNR	2.8075	5.5157	8.2126	9.8666	10.3875	10.3306	0.7184
	PDR	0.2298	0.198	0.1748	0.1638	0.1607	0.161	0.2621

Table 3 Denoising results using the Coiflet 2 with various rules of threshold

rule of threshold		square-root-log		regular-sure		mini-maxi	
thresholding method		hard	soft	hard	soft	hard	soft
performance	norm MSE	0.1347	0.1441	0.2109	0.1432	0.1834	0.1385
	root MSE	0.22	0.2396	0.3345	0.2379	0.3013	0.2282
	enhanced SNR	10.3264	8.887	4.0853	9.0005	5.4826	9.6955
	PDR	0.1609	0.1699	0.2135	0.1692	0.1982	0.1647

rule of threshold		square-root-log		regular-sure		mini-maxi	
thresholding method		hardy-rectified	softy-rectified	hardy-rectified	softy-rectified	hardy-rectified	softy-rectified
performance	norm MSE	0.1344	0.1422	0.2022	0.1406	0.177	0.1393
	root MSE	0.2192	0.2359	0.3246	0.2327	0.2926	0.23
	enhanced SNR	10.3874	9.1432	4.4796	9.3634	5.8877	9.5587
	PDR	0.1606	0.1682	0.2089	0.1668	0.1943	0.1656

Table 4 Classification learning models comparison

model type	accuracy (%)	prediction speed (obs/ms)	training time (s)
fine tree	96	6.4	0.99
medium tree	96	5	1.25
coarse tree	96	4.7	1.17
linear discriminant	98	2.2	3.21
quadratic discriminant	97.3	1.5	2.85
linear SVM	97.3	1.4	6.11
quadratic SVM	97.3	1.5	5.85
cubic SVM	95.3	3	6.55
fine Gaussian SVM	92.7	2	6.43
medium Gaussian SVM	95.3	2.7	6.21
coarse Gaussian SVM	96	2.6	5.24
fine KNN	94.7	1.8	6.04
medium KNN	95.3	3.6	5.9
coarse KNN	66	3.2	5.74
cosine KNN	86	2.7	6.48
cubic KNN	95.3	3.4	6.33
weighted KNN	96.7	3.4	6.23
boosted trees	33.3	2.9	7.67
bagged trees	95.3	0.48	10.01
subspace discriminant	96	0.35	12.44
subspace KNN	96.7	0.24	14.33
RUSboosted trees	33.3	6.1	12.78

Table 5 Comparison between different thresholding methods in recent researches

reference	variance of the simulated signal	signal type	thresholding method	enhancement SNR
[9]	30	ECG	hard	7.2
[9]	30	ECG	soft	11.2
[9]	30	ECG	garrote	10.5
[9]	30	ECG	scad	9.5
[9]	30	ECG	mixed	8.9
[10]	15	battery	improved	14.99
[10]	15	battery	donoho	14.17
[10]	15	battery	standard	15.77
[10]	15	blocks	improved	15.18
[10]	15	blocks	donoho	14.53
[10]	15	blocks	standard	15.38
[10]	15	bumps	improved	14.5
[10]	15	bumps	donoho	15.67
[10]	15	bumps	standard	15.67
[11]	15	Lena	global	10.2
[11]	15	Lena	hierarchical	10.7
[11]	20	Lena	global	7.2
[11]	20	Lena	hierarchical	7.8
[12]	10	echo	soft	19.6
[12]	10	echo	hard	12.6
[12]	10	echo	proposed	22.6
[12]	10	echo	adaptive	21.8
this work	30	pressure	hardy-rectified	10.38
this work	30	pressure	softy- rectified	9.55
this work	30	pressure	hard	10.32
this work	30	pressure	Soft	9.69

References

- [1] RASHID, S., QAISAR S., SAEED H., FELEMBAN, E. Performance analysis of leak detection algorithm in long range pipeline networks using transform analysis. In: IEEE Conference on Systems, Process and Control ICSPC '13: proceedings. IEEE. 2013. p. 10-15.
- [2] SHAMSI, M. RAZZAGHI, M., NAZARZADEH, J., SHAFIEE, M. Haar wavelets method for solving pocklington's integral equation. *Kybernetika* [online]. 2004, **4**, p. 491-500. ISSN 0023-5954, eISSN 1805-949X. Available from: <http://www.kybernetika.cz/content/2004/4/491/paper.pdf>
- [3] SAEED, H., AIL, S., RASHID, S., QAISAR, S., FELEMBAN, E. Reliable monitoring of oil and gas pipelines using wireless sensor network (WSN). In: IEEE 9th International System of Systems Engineering Conference SOSE: proceedings. IEEE. 2014. eISBN 978-1-4799-5227-4. Available from: <https://doi.org/10.1109/SYSOSE.2014.6892493>
- [4] HAIDINE, A., EL HASSANI, S., AQQAL, A. Evaluation of deployment and technology scenarios for metropolitan wireless networks in smart distribution grid. *Journal of Engineering Science and Technology*. 2019, **14**(2), p. 998-1018. ISSN 1823-4690.
- [5] AKKAR, H., AL-SAMARRIE, A., SAEED, A. Simulation design of back propagation neural system of sensor network trained by particle swarm optimization. *International Journal of Scientific and Engineering Research*. 2016, **7**(4), p. 576-582. ISSN 2229-5518.
- [6] WIBOWO, A., SETIANTO D., WISNU, W. P., JATMIKO, W. Optimization of backpropagation using Nguyen-Widrow and stimulus-sampling for breast cancer classification and feature selection. *Journal of Engineering Science and Technology*. 2019, **14**(6), p. 3437-3456. ISSN 1823-4690.

- [7] AKKAR, H., JASIM, F. Intelligent Training Algorithm for Artificial Neural Network EEG Classifications. *International Journal of Intelligent Systems and Applications* [online]. 2018, **10**(5), p. 33-40. ISSN 2074-904X, eISSN 2074-9058. Available from: <https://doi.org/10.5815/ijisa.2018.05.04>
- [8] HUSSAIN, R. H., JABR, Z. F., SALEH, S. R. Improved localisation algorithm for wireless sensor networks by using XBEE. *Journal of Engineering Science and Technology*. 2019, **14**(6), p. 3470-3480. ISSN 1823-4690.
- [9] KOTESWARARAO, M. *Analysis of de-noising on different signals using new thresholding function' spaces-2018*. Department of ECE, 2018.
- [10] HUI, L., WEIDA, W., CHANGLE, X., LLJIN, H., HAIZHAO, N. A de-noising method using the improved wavelet threshold function based on noise variance estimation. *Mechanical Systems and Signal Processing* [online]. 2018, 99, p. 30-46. ISSN 0888-3270. Available from: <https://doi.org/10.1016/j.ymssp.2017.05.034>
- [11] ZHANG, J., ZHU, Q., ZHANG, J., SONG, L., WANG, J. A novel algorithm for threshold image de-noising based on wavelet construction. *Cluster Computing* [online]. 2019, **22**, p. 12443-12450. ISSN 1386-7857, eISSN 1573-7543. Available from: <https://doi.org/10.1007/s10586-017-1655-0>
- [12] XIAOBIN, X. Single pulse threshold detection method with lifting wavelet denoising based on modified particle swarm optimization. *Infrared Physics and Technology*. 2018, **88**, p. 174-83. ISSN 1350-4495. Available from: <https://doi.org/10.1016/j.infrared.2017.11.023>

MATHEMATICAL MODELLING OF OSCILLATORY PROCESSES IN TRANSMISSION OF MOVEMENT OF AN ELECTRIC DRIVE WITH NON-LINEAR LONG ELASTIC ELEMENTS

Andriy Chaban, Tomasz Perzyński*

Faculty of Transport, Electrical Engineering and Computer Science, Kazimierz Pulaski University of Technology and Humanities in Radom, Radom, Poland

*E-mail of corresponding author: t.perzynski@uthrad.pl

Resume

Mathematical model of transmission of movement of an electric drive system that includes long elastic elements, including the non-linear relation between tensors of strength and deformation is presented in this article. Mentioned type of transmission is applied in the tasks related to special-purpose transport. A method that is based on integral modification of variational Hamilton-Ostrogradsky principle was applied for the presented model. Results of the computer simulation of oscillatory processes in transmission of movement of an electromechanical system are presented in the article.

Article info

Received 19 March 2020

Accepted 10 August 2020

Online 25 February 2021

Keywords:

modelling of transport systems, Hamilton-Ostrogradsky principle, mathematical modelling, systems of distributed parameters, computer simulation

Available online: <https://doi.org/10.26552/com.C.2021.2.C54-C64>

ISSN 1335-4205 (print version)

ISSN 2585-7878 (online version)

1 Introduction

Mathematical modelling of unspecified processes in the dynamical systems is one of the most topical tasks of an analysis of complicated technical objects. The electric drive systems that are used in special-purpose transport systems have become a part of such process of modelling. These systems may have long shafts, analysed as long elastic elements of distributed mechanical parameters [1-2]. Modelling and analysis of such elements makes it necessary to map a model in a prototypical system. It is particularly important in the event that concealed movements are included what extends a model and complicates output equations of the state of a system [3-4]. Using the modelling of complex system states allows to analyse it more precisely and to resign from developing a prototype of a system [5]. Regardless of the type of the analyzed system, computer simulation carried out based on the mathematical apparatus allows to determine the parameters affecting the operation of the system [6-7]. It also allows for analysis of different event scenarios [8-9]. An example of use of simulation to analyze a complex special-purpose transport system is presented in the work [10].

An analysis of transmission of the electric drives' movement, including long shafts of linear relation between tensors of strength and deformation was presented in the articles [5, 11-12]. In the real tasks of applied mechanics,

the assumption, for example, in [4], is not always correct. Such analysis is applied to high-power drive systems that often work in hard, diverse conditions (special-purpose transport tasks - cranes, locomotives) [3, 13-14]. In such systems, the situations may emerge in which the linear relation between mentioned tensors is disrupted [15]. Then, the problem emerges how to include mentioned non-linear physical processes in an equation of the shaft. An attempt to solve this problem was made, for example, in the work [15]. Therefore, there is a need to include the non-linear mechanical processes using the non-linear elements in an equation of the shaft [15-16]. Another serious problem must be taken into account. If normal wave equation of torsional oscillations of a long shaft of linear distributed parameters has stable analytical solutions (e.g. Fourier method [17]), then in the case of the non-linear relations, analytical approach can be used only in some cases. To find a function of continuum of the shaft, numerical methods must be applied to solve boundary-value and mixed problems [5, 11-13].

Based on interdisciplinary modified Hamilton-Ostrogradsky method by extending Lagrangian function [5, 18-20], mathematical model of transmission of movement of a drive system is presented in the article. The goal of the article was mathematical modelling of unspecified processes in a system of transmission of movement of electric drives that includes non-linear elastic elements of



a long shaft, analysed as a system of distributed mechanical parameters. To solve equations in the article, the elements of applied mathematics were also presented.

2 Mathematical model of elastic long shaft of distributed parameters

To develop a mathematical model of transmission of movement, modified variation method was applied, which is based on modification of the Hamilton-Ostrogradsky principle [5], by extending Lagrangian function with two elements [16, 21]. The first element includes energy of dissipation forces and the second one - energy of external forces of non-potential character. Similar approach was suggested in an article [18], in which two mentioned additional elements were added formally to a conservative Lagrangian, whereas, in another article [5], adding these elements was justified mathematically. In addition, a method presented in [5] allows to analyse dynamical systems of not only lumped parameters, but also to analyse unspecified processes in the complicated dynamical systems of both lumped [22] and distributed parameters [1, 2].

Extended action functional according to Hamilton-Ostrogradsky is the following [5, 23]:

$$S = \int_{t_1}^{t_2} \left(L^* + \int_l L_l dl \right) dt, I = \int_l L_l dl, \quad (1)$$

where:

S - extended action functional according to Hamilton-Ostrogradsky,

I - internal energy functional [5, 16, 21],

L^* - modified Lagrangian function [5, 19],

L_l - linear density of modified Lagrangian function [5].

Extended Lagrangian function and its linear density are the following:

$$\begin{aligned} L^* &= T^* - P^* + \Phi^* - D^*, \\ L_l &= T_l - P_l + \Phi_l - D_l, \end{aligned} \quad (2)$$

respectively, where:

$T^*(\dot{T}^*)$ - kinetic energy (coenergy),

P^* - conservative energy,

Φ^* - dissipation energy,

D^* - energy of external forces of non-potential character.

Linear densities of mentioned functions are marked by subscript l [5].

Since the model of a shaft is analysed as a system of only distributed parameters, then the modified action functional (S), based on Equation (1) can be written in the following form:

$$S = \int_{t_1}^{t_2} \int_l (\tilde{T}_l - P_l + \Phi_l - D_l) dl dt, \quad (3)$$

where:

T_p, P_p, Φ_p, D_l - appropriate linear densities of energy functions.

To obtain an equation of movement of the shaft, an equation of the extremals of a functional - Equation (3) [18,

21] should be calculated; therefore, variation of internal functional, see Equation (1), with subsequent comparison to zero is searched for. Then, it looks in the following way [16, 21]:

$$\delta I = \delta \int_l (\tilde{T}_l - P_l + \Phi_l - D_l) dl = 0. \quad (4)$$

In order to find variation, the following procedures are applied: Gauss-Ostrogradsky theorem, rule of integration by parts, as well as assumption that the order of differentiation can be changed, because these procedures are independent [18-19]. Therefore, mechanical system may be analysed as a system of infinite degrees of freedom, which is a counterbalance to the systems of lumped parameters, in which the number of degrees of freedom is always determined [1, 2, 5, 15, 19].

An equation of extremals of this functional is the so-called Euler-Poisson equation [16]:

$$\begin{aligned} \frac{\partial L}{\partial q} - \frac{\partial}{\partial t} \left(\frac{\partial L}{\partial \dot{q}} \right) - \frac{\partial}{\partial x} \left(\frac{\partial L}{\partial q_x} \right) + \frac{\partial^2}{\partial x^2} \left(\frac{\partial L}{\partial q_{xx}} \right) + \\ + \frac{\partial^2}{\partial t^2} \left(\frac{\partial L}{\partial q_{tt}} \right) + \frac{\partial^2}{\partial x \partial t} \left(\frac{\partial L}{\partial q_{xt}} \right) = 0, \end{aligned} \quad (5)$$

where:

$$\begin{aligned} \frac{\partial q}{\partial t} &\equiv q_t, \quad \frac{\partial q}{\partial x} \equiv q_x, \quad \frac{\partial^2 q}{\partial x^2} \equiv q_{xx}, \\ \frac{\partial^2 q}{\partial t^2} &\equiv q_{tt}, \quad \frac{\partial^2 q}{\partial x \partial t} \equiv q_{xt}. \end{aligned} \quad (6)$$

In such a case, for the systems of distributed parameters, adding specific coordinates is not possible. Therefore, the so-called function of generalized coordinates is added $q(x, t)$ and its generalized velocity $\dot{q}(x, t)$. In the case of a long shaft $q(x, t) \equiv \varphi(x, t)$ - function of the shaft rotation angle and $\dot{q}(x, t) \equiv \omega(x, t)$ - function of rotational speed [5].

Therefore, system of elastic shaft can be presented using a function of two variables (x, t) , x - spatial coordinate along continuum of the shaft and t - time coordinate.

Elements of the linear densities of extended Lagrangian function are presented [5, 15]:

$$\begin{aligned} \frac{\partial T^*}{\partial x} &\equiv T_l = \frac{\rho J_p}{2} \left(\frac{\partial \varphi}{\partial t} \right)^2, \\ \frac{\partial P^*}{\partial x} &\equiv P_l = \frac{G(\Delta \varphi) J_p}{2} \left(\frac{\partial \varphi}{\partial x} \right)^2, \end{aligned} \quad (7)$$

$$\begin{aligned} \frac{\partial \Phi^*}{\partial x} &\equiv \Phi_l = \int_0^t \frac{\xi(\Delta \varphi)}{2} \left(\frac{\partial^2 \varphi}{\partial x \partial t} \right)_{t=\tau}^2 d\tau, \\ \frac{\partial D^*}{\partial x} &\equiv D_l = 0, \end{aligned} \quad (8)$$

where:

ρ - density of the shaft's material,

J_p - polar moment of inertia of a connecting element,

$G(\Delta \varphi)$ - shear modulus that depends on value of torsion between the shaft's elements,

$\xi(\Delta \varphi)$ - coefficients of internal dispersion in the shaft that also depend on value of torsion between elements of the shaft.

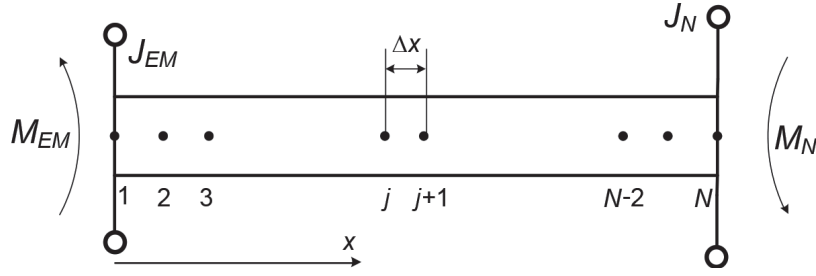


Figure 1 Diagram of a long shaft of transmission of movement of an electric drive

Assuming that $q \equiv \varphi, q_t \equiv \omega$, modified Lagrangian function will be the following:

$$L = \frac{\rho J_P}{2} q_t^2 - \frac{J_P G(\Delta\varphi)}{2} q_x^2 + \frac{1}{2} \int_0^t \xi(\Delta\varphi) q_{xt}^2 d\tau. \quad (9)$$

Since:

$$\frac{\partial L}{\partial q} \equiv 0, \frac{\partial^2}{\partial x^2} \left(\frac{\partial L}{\partial q_{xx}} \right) \equiv 0, \frac{\partial^2}{\partial t^2} \left(\frac{\partial L}{\partial q_{tt}} \right) \equiv 0, \quad (10)$$

Equation (5) is simplified to the following form:

$$-\frac{\partial}{\partial t} \left(\frac{\partial L}{\partial q_t} \right) - \frac{\partial}{\partial x} \left(\frac{\partial L}{\partial q_x} \right) + \frac{\partial^2}{\partial x \partial t} \left(\frac{\partial L}{\partial q_{xt}} \right) = 0. \quad (11)$$

Giving an Equation (9) to Equation (11), changing the order of differentiation (derivatives from the functions of generalized coordinates are determined and uninterrupted), as well as applying derivative theorem from an integral beyond its upper boundary, one can write:

$$-\frac{\partial}{\partial t} \frac{\partial L}{\partial q_t} = -\frac{\rho J_P}{2} \frac{\partial}{\partial t} \frac{\partial}{\partial q_t} q_t^2 = -\rho J_P q_{tt}, \quad (12)$$

$$\begin{aligned} -\frac{\partial}{\partial x} \frac{\partial L}{\partial q_x} &= -\frac{J_P}{2} \frac{\partial}{\partial x} \frac{\partial}{\partial q_x} [-G(\Delta\varphi) q_x^2] = \\ &= J_P \frac{\partial}{\partial x} [G(\Delta\varphi) q_x], \end{aligned} \quad (13)$$

$$\begin{aligned} \frac{\partial^2}{\partial x \partial t} \frac{\partial L}{\partial q_{xt}} &= \frac{1}{2} \frac{\partial}{\partial x} \frac{\partial^2}{\partial q_{xt}} \frac{\partial}{\partial t} \left[\int_0^t (\xi(\Delta\varphi) q_{xt})^2 d\tau \right] = \\ &= \frac{1}{2} \frac{\partial}{\partial x} \frac{\partial^2}{\partial q_{xt}} [\xi(\Delta\varphi) q_{xt}]^2 = \frac{\partial}{\partial x} [\xi(\Delta\varphi) q_{xt}]. \end{aligned} \quad (14)$$

Summing up Equations (12 - 14), including relations: $q \equiv \varphi, q_t \equiv \omega$, finally equation of the shaft of non-linear elastic and dissipative elements are obtained:

$$\begin{aligned} -\rho J_P \frac{\partial^2 \varphi}{\partial t^2} + J_P \frac{\partial}{\partial x} \left[G(\Delta\varphi) \left(\frac{\partial \varphi}{\partial x} \right) \right] + \\ + \frac{\partial}{\partial x} \left[\xi(\Delta\varphi) \left(\frac{\partial^2 \varphi}{\partial x \partial t} \right) \right] = 0 \end{aligned} \quad (15)$$

In a theory of non-linear applied mechanics, following assumptions are widely applied [15, 17, 24]:

$$\begin{aligned} G(\Delta\varphi) \left(\frac{\partial \varphi}{\partial x} \right) &\rightarrow G \left(\frac{\partial \varphi}{\partial x} \right)^{v+1}, \\ \xi(\Delta\varphi) \left(\frac{\partial^2 \varphi}{\partial x \partial t} \right) &\rightarrow \xi \left(\frac{\partial^2 \varphi}{\partial x \partial t} \right)^{\mu+1}, \end{aligned} \quad (16)$$

where coefficients are written in the following way [15]:

$$v = \frac{2n_1 - 1}{2m_1 - 1}, \mu = \frac{2n_2 - 1}{2m_2 - 1}, \quad (17)$$

$n_1, n_2, m_1, m_2 \in N,$

here: N - natural number.

Mentioned coefficients are calculated based on experimental data, including Equation (17), [15]. Assuming additionally that coefficients $G(\Delta\varphi)$ and $\xi(\Delta\varphi)$ do not depend on a coordinate x , an equation of a long shaft can be written in the following way:

$$\frac{\partial^2 \varphi}{\partial t^2} \frac{\partial}{\partial x} \left[\frac{G}{\rho} \left(\frac{\partial \varphi}{\partial x} \right)^{v+1} \right] + \frac{\partial}{\partial x} \left[\frac{\xi}{\rho J_P} \left(\frac{\partial^2 \varphi}{\partial x \partial t} \right)^{\mu+1} \right], \quad (18)$$

or presented in the form:

$$\begin{aligned} \frac{\partial^2 \varphi}{\partial t^2} &= \frac{G}{\rho} (v+1) \left(\frac{\partial \varphi}{\partial x} \right)^v \frac{\partial^2 \varphi}{\partial t^2} + \\ &+ \frac{\xi}{\rho J_P} (\mu+1) \left(\frac{\partial^2 \varphi}{\partial x \partial t} \right)^\mu \frac{\partial^3 \varphi}{\partial x^2 \partial t}. \end{aligned} \quad (19)$$

Therefore, consider the general case of a long shaft, as an element of transmission of movement of electric drives. The shaft is connected with a driving motor and load mechanism, Figure 1.

The following marks were used in Figure 1: M_{EM} - electromagnetic moment of a driving motor, M_N - load moment of a drive, J_{EM}, J_N - moments of inertia of an engine rotor and load system, respectively, x - spatial coordinate, N - the number of the nodes of discretization of Equation (19), Δx - step of discretization of spatial derivatives.

The boundary conditions for Equation (19) are based on equality of electromagnetic moments (or load) and elasticity and dissipation in the ends of the shaft in accordance with d'Alembert principle), [5, 17]

$$\begin{aligned} J_{EM} \frac{\partial^2 \varphi}{\partial t^2} \Big|_{x=0} - G J_P \left(\frac{\partial \varphi}{\partial x} \right)^{v+1} \Big|_{x=0} - \\ - \xi \left(\frac{\partial^2 \varphi}{\partial x \partial t} \right)^{\mu+1} \Big|_{x=0} = M_{EM}, \end{aligned} \quad (20)$$

$$\begin{aligned} J_N \frac{\partial^2 \varphi}{\partial t^2} \Big|_{x=L} + G J_P \left(\frac{\partial \varphi}{\partial x} \right)^{v+1} \Big|_{x=L} + \\ + \xi \left(\frac{\partial^2 \varphi}{\partial x \partial t} \right)^{\mu+1} \Big|_{x=L} = M_N. \end{aligned} \quad (21)$$

In order to simplify it, it was assumed that in the ends of the shaft, external moments are equal to specific moments of elasticity. Therefore, the following equations can be written:

$$GJ_P \frac{\Delta\varphi_1}{\Delta x} = M_{EM}, GJ_P \frac{\Delta\varphi_N}{\Delta x} = -M_N, \quad (22)$$

where, see Figure 1:

$$\Delta\varphi_1 = \varphi_2 - \varphi_1, \Delta\varphi_N = \varphi_N - \varphi_{N-1}. \quad (23)$$

Assuming that $\Delta x = L/2$, boundary conditions can be written in the following way (angle of torsions of transmission):

$$\varphi(x, t)|_{x=0} = \frac{LM_{EM}}{2GJ_P} = a = \text{const}, \quad (24)$$

$$\varphi(x, t)|_{x=L} = \frac{LM_N}{2GJ_P} = -a = \text{const}. \quad (25)$$

Due to the fact that the shaft is inhibited, use of boundary conditions in Equations (24) and (25) to examine non-linear shaft is not sufficient. Therefore, two types of boundary conditions should be used. In the first case, the conditions are analysed using the Heaviside function [17]:

$$a_1(t) = a \cdot 1(t) \quad (26)$$

From the point of view of applied physics, the use of such conditions means that the shaft was twisted and stabilized in such a state. Only mechanical wave moves towards the shaft, whereas, the ends of the shaft are immovable, which, with reference to applied mechanics, does not provide sufficient information about dynamics of the shaft.

In the second case, boundary conditions are analysed as a Dirac function:

$$a_2(t) = \frac{da_1(t)}{dt} = a \frac{d1(t)}{dt} = a\delta(t). \quad (27)$$

Equation (27) should be understood as an impulse of finite value of amplitude a . From the point of view of applied physics, use of the boundary conditions in Equation (27) means that the shaft was twisted in $t = t - 0$, and in a time moment $t = t + 0$ - the ends of the shaft were quickly relieved. Therefore, not only that the mechanical wave is moving in the shaft, just like in the previous cause, but the elements of the shaft also rotate. It is interesting from the point of view of applied mechanics, providing information about dynamics of movement.

To solve Equation (19), simple method was applied [5].

For the conditions of the first type, see Equation (26), discrete system of normal non-linear differential equations is the following:

$$\varphi_1 = a, \omega_1 = 0, \varphi_N = -a, \omega_N = 0, \quad (28)$$

$$\begin{aligned} \frac{d\omega_j}{dt} = (v+1) \frac{G}{\rho} \frac{\varphi_{j-1} - 2\varphi_j + \varphi_{j+1}}{(\Delta x)^2} \times \\ \times \left[\frac{\varphi_{j+1} - \varphi_{j-1}}{2\Delta x} \right]^v + (\mu+1) \frac{\xi}{\rho J_P} \times \\ \times \frac{\omega_{j-1} - 2\omega_j + \omega_{j+1}}{(\Delta x)^2} \left[\frac{\omega_{j+1} - \omega_{j-1}}{2\Delta x} \right]^\mu, \end{aligned} \quad (29)$$

$$\frac{d\varphi_j}{dt} = \omega_j, j = 2, 3, \dots, N-1. \quad (30)$$

For the boundary conditions of the second type, see Equation (27), system of equations is the following:

$$\frac{d\omega_1}{dt} = \frac{M_{EM} - c(\varphi_1 - \varphi_2) - \nu(\omega_1 - \omega_2)}{J_{EM} + J_1}, \quad (31)$$

$$\begin{aligned} \frac{d\omega_j}{dt} = (v+1) \frac{G}{\rho} \frac{\varphi_{j-1} - 2\varphi_j + \varphi_{j+1}}{(\Delta x)^2} \times \\ \times \left[\frac{\varphi_{j+1} - \varphi_{j-1}}{2\Delta x} \right]^v + (\mu+1) \frac{\xi}{\rho J_P} \times \\ \times \frac{\omega_{j-1} - 2\omega_j + \omega_{j+1}}{(\Delta x)^2} \left[\frac{\omega_{j+1} - \omega_{j-1}}{2\Delta x} \right]^\mu, \\ j = 2, 3, \dots, N-1, \end{aligned} \quad (32)$$

$$\frac{d\omega_N}{dt} = \frac{-M_N - c(\varphi_N - \varphi_{N-1}) - \nu(\omega_N - \omega_{N-1})}{J_N + J_{N-1}}, \quad (33)$$

$$\frac{d\varphi_j}{dt} = \omega_j, j = 1, 2, \dots, N-1, N, \quad (34)$$

where:

$$J_1 = J_N = \rho J_P \Delta x, c = GJ_P \Delta x, \nu = \xi J_P \Delta x. \quad (35)$$

Common integration is subject to the following non-linear system of differential equations:

- for the first experiment: Equations (28) - (30),
- for the second experiment: Equations (31) - (35).

3 The computer simulation results

Computer simulation was conducted for a long transmission shaft with the following parameters: length of the shaft $L = 6$ m, diameter $D = 0.15$ m, number of the nodes of discretization $N = 90$, $G = 8.1 \cdot 10^{10}$ N·m, $\rho = 7850$ kg/m³, $\xi = 0.5$ N·m²·s, $\Delta x = 0.0667$ m, $J_{EM} = J_N = 20$ N·m².

Two identical flywheels, of a moment of inertia $J = 20$ N·m², were mounted at the ends of the shaft. To activate dynamical system, the ends of the shaft twisted to initial values $\varphi(x, t)|_{x=0} = 0.2$ rad, $\varphi(x, t)|_{x=L} = -0.2$ rad, $\nu = 0.2$, $\mu = 0.1$, were calculated based on the comparative experiments [15].

Two experiments were conducted, in which the type of boundary conditions was changing. In the first experiment, mentioned conditions were considered as a Heaviside

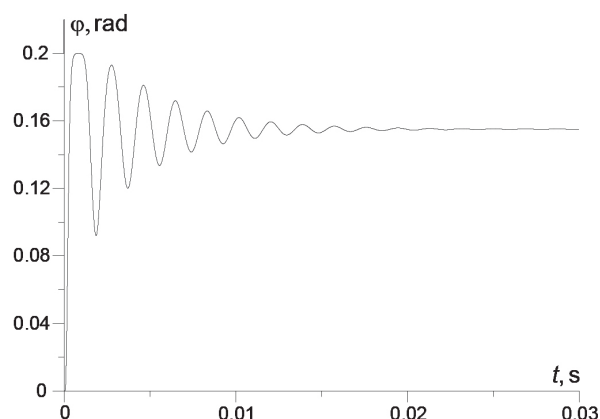


Figure 2 Angle of torsion of the shaft in the point of discretization No = 9 (0.6 m from the left end of the shaft) in terms of time (linear variant)

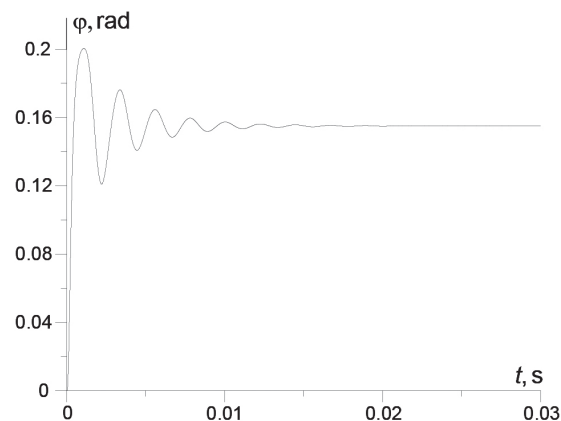


Figure 3 Angle of torsion of the shaft in the point of discretization No = 9 (0.6 m from the left end of the shaft) in terms of time (non-linear variant)

function, whereas, in the second experiment, the conditions were considered as a Dirac function. From the point of view of applied electromechanics, description of the experiment is the following: in the first experiment, the ends of the shaft were twisted, fixed and left in such a state, in the second experiment, the ends of the shaft were released after torsion, which caused angular motion of the shaft. The shaft both in linear and non-linear cases was analysed in the research.

Figures 2 and 3 show angle of torsion of the shaft in the point of discretization No=9 (see Figure 1), in linear (Figure 2) and non-linear (Figure 3) cases, in a function of time.

Therefore, the comparative analysis of descriptions from Figures 2 and 3 can be conducted:

- frequency of oscillation of the torsion angle function in the linear case is by about 20% higher in comparison to non-linear case: $f_{lin} \approx 500$ Hz, a $f_{nonlin} \approx 400$ Hz.
- time of vanishing of oscillation in the first case is about 0.02 s, and in the second case - about 0.015 s,
- maximal difference of amplitudes for the linear case is about $\Delta\varphi_{max}^{lin} \approx 0.11$ rad, and - $\Delta\varphi_{max}^{nonlin} \approx 0.08$ rad for the non-linear case.

Since the shaft practically does not rotate, one must ask what physical rules are the background of the mentioned phenomena? The answer to this questions should be searched based only on the theory of mechanical field of analytical mechanics of a system continuum [15]. Mechanical wave moves along transmission of movement and dispersion forces makes it vanishing. In the linear case, one does not include non-linear relation between tensors of deformation and elongation and tensors of internal dispersion and elongation, which causes a bit incorrect physical form of the wave motion along the shaft. Conducting an experiment when the ends of the shaft are fixed, allows to conclude that the simulation results reflect the impact of the real non-linear properties of elastic and dissipative material on the work of the transmission elements of the complicated drives movement.

Figure 4 shows a transition function of the shaft's torsion velocity in the point of discretization No = 9 (0.6 m from the left end of movement transmission). Figures 4 and

3 are interrelated, because the time derivative as a function of angle presents a function of angular velocity. The impact of the non-linear wave processes in the shaft can also be observed in this case, which results in various frequencies between the linear and non-linear variants. Within about 15 ms, the dissipation forces make mechanical wave practically vanishing. The shaft was twisted, which means that there is still potential energy in it.

Figure 5 shows the graphs of a function of moment of elasticity in the shaft in its beginning from the left side between the points of discretization No 3 - 4 - line 1 and in its central part: No 45 - 46 - line 2. From the point of view of applied physics, Figure 5 is of informative character because it demonstrates the wave processes in a continuum of the shaft. If in the beginning of the shaft, moment of elasticity reaches maximal value of amplitude of about 0.9 MN m, then, in the central part, moment of elasticity in the shaft is equal to zero. The shock step moments of torsion cause formation of mechanical wave that moves from both ends of the shaft towards the centre. The velocity of this wave is limited. Therefore, in the center of the shaft, moment of elasticity decreased to zero within 0.5 ms. It is obvious that oscillations of both functions are in a counterphase. Within 15 ms, in steady state, moment of elasticity assumes constant value of about 0.3 MN m. It should be added that time of stopping the mechanical wave is connected with time of counterphase of both functions.

Figures 6 - 9 show functional relations of an angle of torsions and velocity of torsion of the continuum elements of a shaft as a function of its length (spatial coordinate) for two time points: 0.2 ms and 2 ms. An analysis of these functions should be considered comparing Figures 6 and 8 and 7 and 9. Within $t = 0.2$ ms, one can clearly see how mechanical wave starts moving along the shaft. The end parts of the shaft were twisted, whereas, the central part of the shaft remained immovable. Therefore, there was no phenomenon of change of discrete angles in a central part of the shaft (see Figure 1). This means that within $t = 0.2$ ms, elastic wave would not reach the center of the shaft, therefore, in the center of the shaft, moment of elasticity should be practically equal to zero. This conclusion was

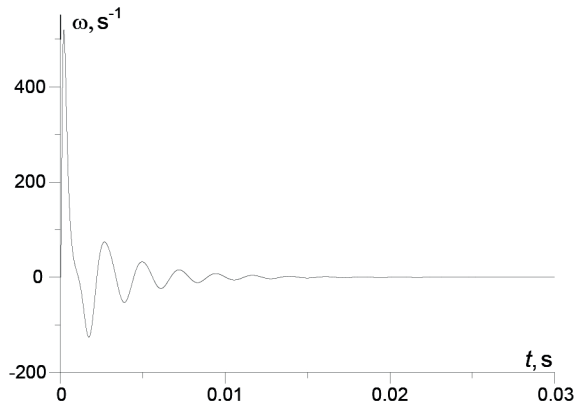


Figure 4 Angular velocity the shaft's torsion in the point of discretization No=9 (0.6 m from the left end of the shaft) in terms of time (non-linear variant)

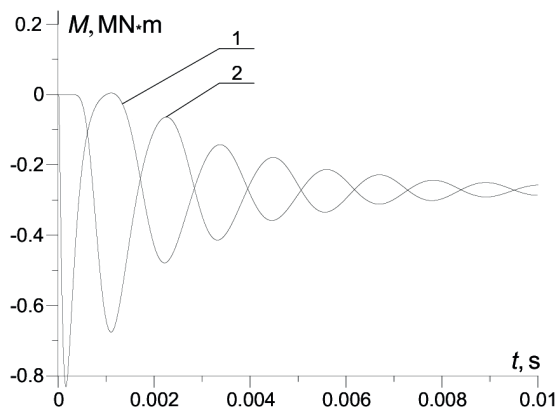


Figure 5 Moment of elasticity in a shaft in terms of time: 1 - left end of the shaft (No 3-4), 2 - center of the shaft (No 45-46)

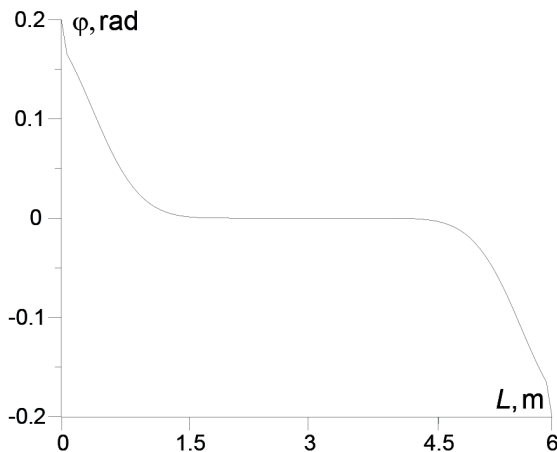


Figure 6 Angle of torsion of the shaft in terms of its length $t = 0.2 \text{ ms}$

confirmed in Figure 5. It must also be added that torsion of the ends of the shaft resulted in high values of amplitude of rotational speed, and there are no such values in the central part. The situation in the next pair of analysed figures (Figure 7 and 9) is different. Time increased 10 times here. The wave reached the center of the shaft and function of the torsions angle of the shaft's discrete parts in an argument of spatial coordinate approaches to linear value; whereas

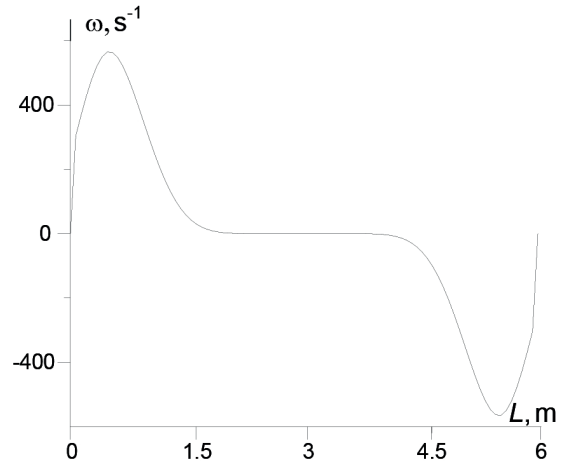


Figure 7 Angular velocity of the shaft in terms of its length $t = 0.2 \text{ ms}$

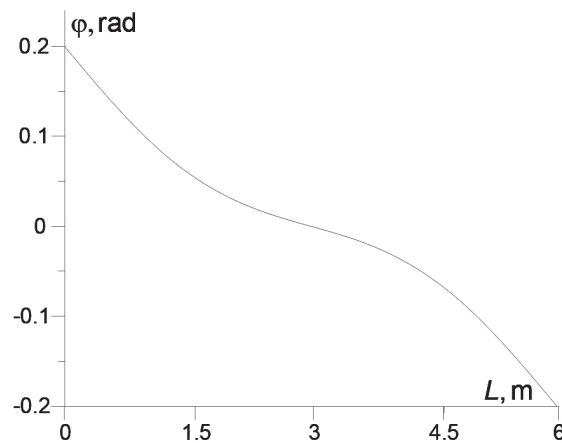


Figure 8 Angle of torsion of the shaft in terms of its length $t = 2 \text{ ms}$

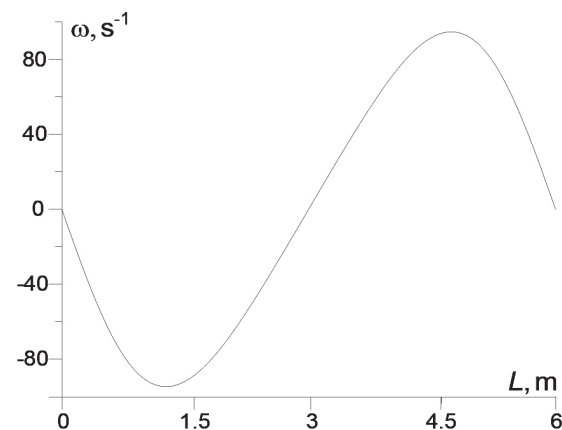


Figure 9 Angular velocity of the shaft in terms of its length $t = 2 \text{ ms}$

function of velocity of torsion of the shaft approaches to zero (it should be emphasized that time derivative from an angle of torsion is rotational speed). Therefore, it is obvious that in steady state, (about $t = 0.02 \text{ s}$) the shaft will be linearly twisted, (see Figures 2 and 3).

Figures 10 to 12 show spatiotemporal behaviour of the functions in a three-dimensional system. Figure 10 shows spatiotemporal distribution of function of an angle

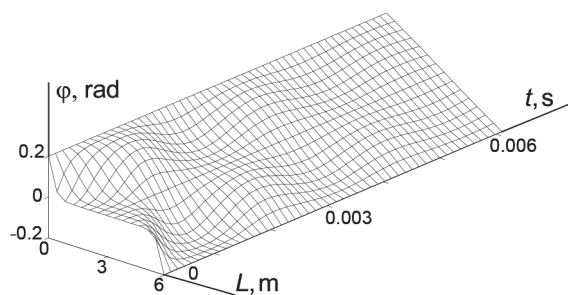


Figure 10 Spatiotemporal distribution of function of the shaft's torsion angle in a time range $t \in [0; 0.006]$ s

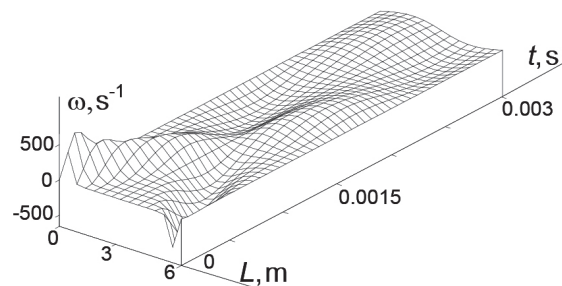


Figure 11 Spatiotemporal distribution of function of shaft's angular velocity in a time range $t \in [0; 0.003]$ s

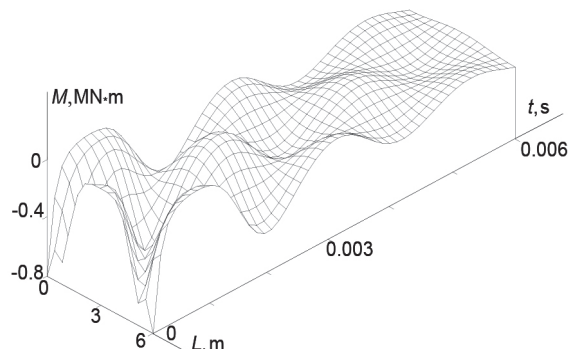


Figure 12 Spatiotemporal distribution of function of the shaft's moment of elasticity in a time range $t \in [0; 0.006]$ s

of torsion of the shaft in a time range $t \in [0; 0.006]$ s; and Figure 11 shows spatiotemporal distribution of function of angular velocity of the shaft in a time range $t \in [0; 0.003]$ s, and Figure 12 shows spatiotemporal distribution of function of moment of elasticity in the shaft in a time range $t \in [0; 0.006]$ s. Figure 10 should be analysed together with the Figures 2, 3 and 6, 8. Figure 11 should be analysed together with Figures 4 and 7, 9. Figure 12 should be analysed together with Figure 5. What is important is clear visualization of spatiotemporal movement of mechanical wave in an isotropic non-linear environment of continuum of the shaft.

An analysis of subsequent figures (Figures 13 to 20) refers to the second experiment. Figure 13 shows an angle of torsion of the shaft's discretization units in the point No = 9 (0.6 m from the left end) in terms of time (linear variant) and Figure 14 shows an angle of torsion of the shaft in the point No=9 (0.6 m from the left end) in a function of time (1st variant - linear and 2nd variant- non-linear) in a time range $t \in [2.4; 2.5]$ s.

With reference to the first experiment, the shaft was twisted and its ends were immobilized (boundary conditions - Heaviside function), in the second experiment, the shaft was quickly twisted and relieved, which resulted in the lack of torsion of the shaft; in steady state. That is, no force affects the shaft within more than 2.5 s, which can be seen in Figure 13. Amplitude of shaft's oscillation slowly vanishes to zero, in contrast with the first experiment (Figure 3). Figure 14 shows a comparative analysis for both cases: 1 - linear and 2 - non-linear. During the analysis of Figures 2 and 3, the causes of propagation of both lines were explained. In the analysed Figure 14, a very important

moment of the phase shifts of both graphs should be emphasized. This fact is very important. Analysing the transmissions of movement in a linear variant, data concerning amplitude and phase shift are obtained. Amplitude is not a priority information here, whereas, a phase shift is a significant information, particularly with reference to the precision systems (transmissions of movement with the engines of PMSM and BLDC type [5], in the special-purpose transport systems), in which accurate information about location of a rotor and output shaft of a load mechanism is required.

Figure 15 shows the instantaneous moment of elasticity in two parts of the shaft: between the points of discretization No 2 and No 3 (left end of the shaft), as well as No 45 and No 46 (center of the shaft) in a time range $t \in [0; 0.05]$ s. Figure 15 shows that within up to 10 ms, mechanical wave forms very complicated movements that were analysed above (see Figure 5); whereas within more than 10 ms, the situation radically changes, different from the first experiment. Oscillatory fluctuations of both functions are practically identical with a zero phase of oscillation. It means that after 10 ms, function of moment of elasticity along the shaft is practically identical. Figure 16 shows a current moment of elasticity in the shaft between the points of discretization No 45 - 46. The moments of elasticity in all parts of a long shaft have practically the same value.

Figures 17 and 18 show the shaft's torsion angle as a function of length for $t = 2$ ms and angular velocity of the shaft as a function of length for $t = 0.2$ ms. Figure 17 should be analysed together with Figure 6 and Figure 18 with Figure 10. One may conclude from the comparative

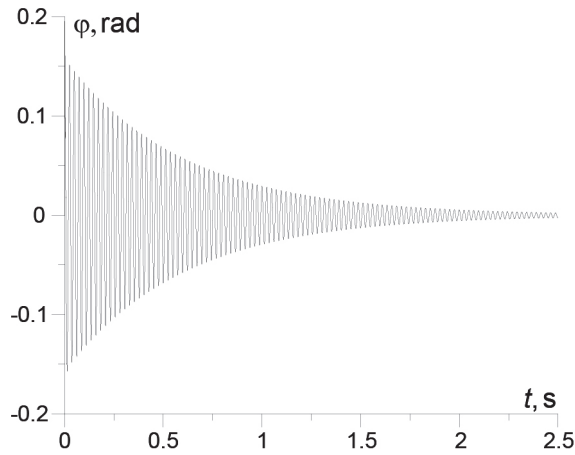


Figure 13 Angle of torsion of the shaft in the point No = 9 (0.6 m from the left end) in a function of time (linear variant)

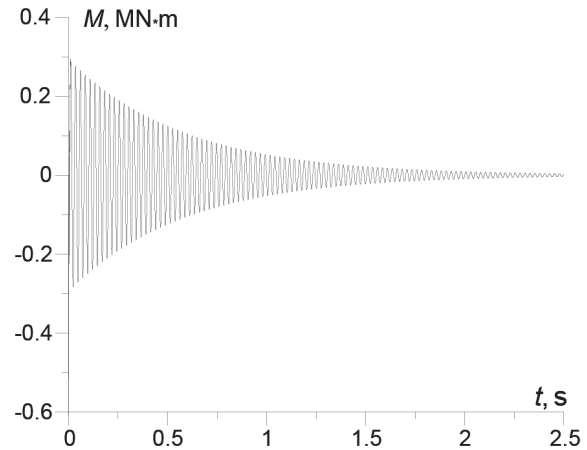


Figure 16 Moment of elasticity in the center of the shaft as a function of time (No 45 - 46)

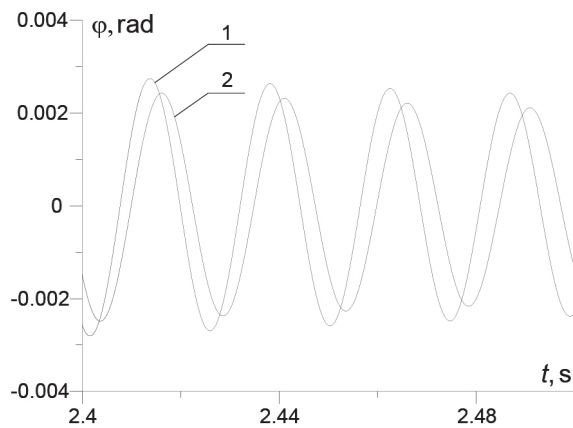


Figure 14 Angle of torsion of the shaft in the point No = 9 (0.6 m from the left end) in a function of time (1 variant - linear, 2 - non-linear variant)

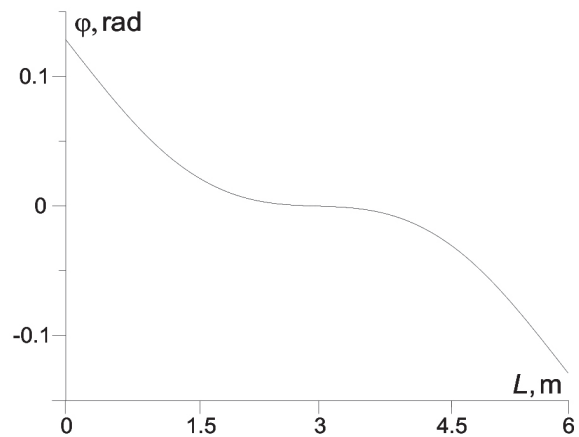


Figure 17 Angle of torsion of the shaft as a function of length $t = 2$ ms

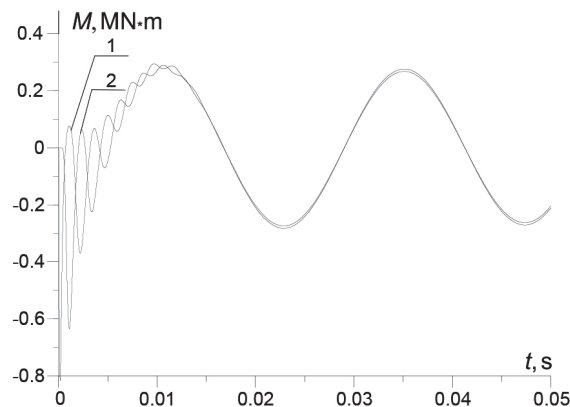


Figure 15 Moment of elasticity in the shaft as a function of time 1 - left end of the shaft (No 2-3), 2 - center of the shaft (No 45-46)

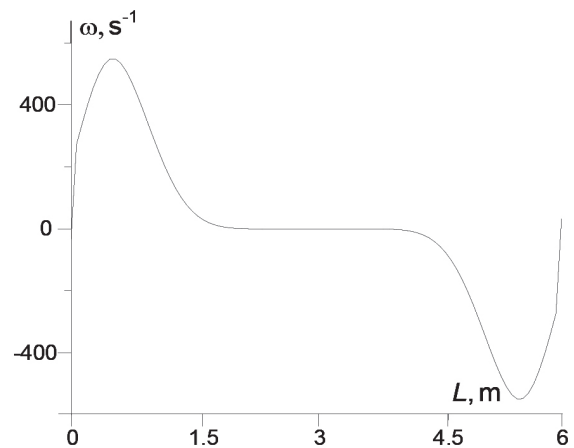


Figure 18 Angular velocity of the shaft as a function of length $t = 0.2$ ms

analysis that the wave processes for both experiments are visually similar. However, one important moment must be emphasized. In the first experiment, function of the torsions angle approaches to linear relation significantly faster in comparison to the second experiment. This means that oscillation of the shaft's ends (second experiment) triggers

an effect of the elastic wave braking. It shows that it is necessary to analyse the long transmissions of movement at the level of analytical mechanics of the continuous systems, that is, at the level of the field systems of distributed parameters [1, 2, 17].

Figures 19 and 20 show spatiotemporal distributions

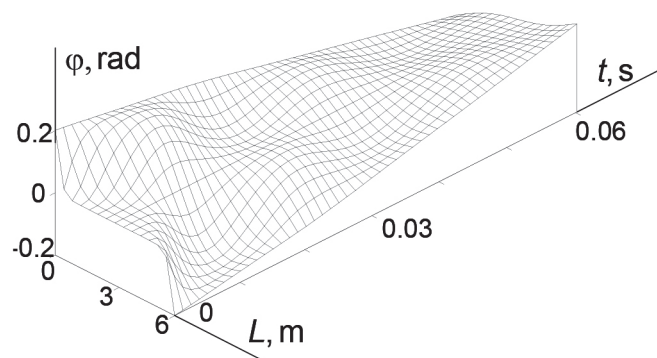


Figure 19 Spatiotemporal distribution of function of the shaft's torsion angle in a time range $t \in [0; 0.006]$ s

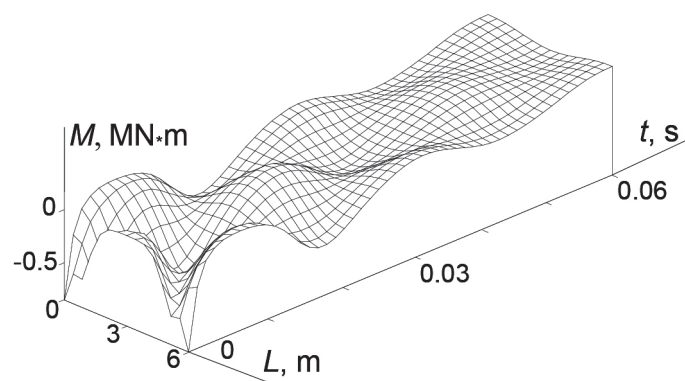


Figure 20 Spatiotemporal distribution of function the

of function of the torsion angle and function of velocity of this angle in a time range $t \in [0; 0.006]$ s. An analysis of Figures 19 and 20, including Figures 10 and 12, confirms again an effect of braking of mechanical wave in the second experiment with reference to the first one. Comparative analysis shows fivefold change of value of an effect of braking, whereas, the amplitudes of oscillation of analysed functional relations do not differ significantly.

Mentioned fact gives a basis for conclusion of usefulness of using the Dirichlet problem, including boundary conditions using the Heaviside and Dirac function (here of finite value of impulse) in a non-linear relation between tensors of deformation and elongation.

4 Conclusions

Use of the modified Hamilton-Ostrogradsky principle, using extended Lagrangian function to develop mathematical models of long transmission shafts, including non-linear relation between tensors of deformation and elongation, extends the possibilities of analysing oscillatory unspecified processes in a transmission of movement of electric drives in the transport tasks.

Conducted experiments showed that in the tasks connected with an analysis of a complex transmission of movement that includes long drive shafts as the systems of distributed parameters, practically all the mechanical states can be analysed: both transitional and fixed. It gives higher accuracy of mathematical calculations of dynamic

states of an object in comparison to considering such object in a multi-body system of lumped parameters, analysed as a system of lumped parameters.

While solving wave equation of oscillation torsions of a long shaft, as an element of complex transmission of movement of electric drives, boundary conditions in the form of the Heaviside function (constant value of step function) and Dirac function (finite value of impulse function) can be applied. On the one hand, such an approach simplifies using a numerical method of the spatial discretization of the shaft's state equations (simple method), on the other hand, it allows to obtain sufficient information about physical processes in the complex transmission of movement.

Based on the computer simulation results, it may also be concluded that:

- comparative analysis of both experiments, connected with examining a long shaft that includes linear and non-linear relation between tensors of deformation and elongation, shows significant difference for both experiments - concerning various frequencies and amplitude of oscillation of the torsion angle, as well as velocity of the shaft's torsion;
- in the first millisecond of a transitional process of the shaft's oscillations, it can be seen that mechanical wave does not move very quickly along continuum of the shaft. The movement starts from the ends of the shaft and moves towards its center. It causes an effect of counterphase that decreases with elapse of time;
- angular motion of the shaft's transmission causes an effect of braking of moving mechanical wave along

- continuum of the shaft in comparison to the case when the ends of the shaft are inhibited;
- phase shift of the shaft's rotation angle that emerges in both experiments connected with examination of shaft's movement transmission in a linear and non-linear system is a very important information. Slight deviations the shaft's rotation angle from the real value results in giving a control signal at the wrong moment in the automated control drives [4, 14];
- results of simulation in the 3D format are of informative value and can be applied to spatiotemporal distributions of analysed functions.

References

- [1] WANG, J., LIU, Y., SUN, C. Adaptive neural boundary control design for nonlinear flexible distributed parameter systems. *IEEE Transactions on Control Systems Technology* [online]. 2018, p. 1-15. ISSN 1063-6536, eISSN 1558-0865. Available from: <https://doi.org/10.1109/TCST.2018.2849072>
- [2] WANG, Z., WU, H., HAN, K. Sampled-data control for linear time-delay distributed parameter systems. *ISA Transactions* [online]. 2018, **92**, p. 75-83. ISSN 0019-0578. Available from: <https://doi.org/10.1016/j.isatra.2019.02.002>
- [3] POPENDA, A. Mathematical modelling of transmission shafts based on electrical and mechanical similarities. *Przegląd Elektrotechniczny*. 2019, **12**, p. 196-199. ISSN 0033-2097, eISSN 2449-9544.
- [4] ORLOWSKA-KOWALSKA, T., SZABAT, K. Control of the driver system with stiff and elastic couplings using adaptive neuro-fuzzy approach. *IEEE Transactions on Industrial Electronics* [online]. 2007, **54**(1), p. 228-240. ISSN 0278-0046. Available from: <https://doi.org/10.1109/TIE.2006.888787>
- [5] CHABAN, A. *Principle Hamilton-Ostrogradski in electromechanical systems*. Lviv, 2015. ISBN 978-966-2598-46-9.
- [6] KUCERA, L., GAJDAC, I., MRUZEK, M. Simulation of parameters influencing the electric vehicle range. *Communications - Scientific Letters of the University of Zilina* [online]. 2016, **18**(1A), p. 59-63. ISSN 1335-4205, eISSN 2585-7878. Available from: <http://komunikacie.uniza.sk/index.php/communications/article/view/360>
- [7] KORENCIAK, D., GUTTEN, M., ADAMEC, J., GLOWACZ, A., CICHY, A. Analysis of engine knock sensor. *Communications - Scientific Letters of the University of Zilina* [online]. 2018, **20**(1), p. 37-41. ISSN 1335-4205, eISSN 2585-7878. Available from: <http://komunikacie.uniza.sk/index.php/communications/article/view/43>
- [8] LEWINSKI, A., TORUN, A., PERZYNSKI, T. Risk analysis as a basic method of safety transmission system certification. In: *Modern Transport Telematics TST 2011: proceedings* [online]. Vol 239. Communications in Computer and Information Science. Berlin, Heidelberg: Springer, 2011. ISBN 978-3-642-24659-3, eISBN 978-3-642-24660-9, p. 47-53. Available from: https://doi.org/10.1007/978-3-642-24660-9_6
- [9] LEWINSKI, A., PERZYNSKI, T. Telematics as a new method of transport system safety verification. In: *Research Methods and Solutions to Current Transport Problems ISCT21 2019: proceedings* [online]. Vol 1032. Advances in Intelligent Systems and Computing. Cham: Springer, 2020. ISBN 978-3-030-27686-7, eISBN 978-3-030-27687-4. Available from: https://doi.org/10.1007/978-3-030-27687-4_27
- [10] BOJIC, N., NIKOLIC, R., BANIC, M., HADZIMA, B. Evaluation of mechanical properties of the two PVC conveyor belts. *Communications - Scientific Letters of the University of Zilina* [online]. 2018, **20**(4), p. 47-51. ISSN 1335-4205, eISSN 2585-7878. Available from: <https://doi.org/10.26552/com.C.2018.4.47-51>
- [11] LUKASIK Z., CZABAN A., SZAFRANIEC, A. Mathematical model of asynchronous pump drive with distributed mechanical parameters. *Przegląd Elektrotechniczny*. 2018, **6**, p.155-159. ISSN 0033-2097, eISSN 2449-9544.
- [12] LIS, M., SZAFRANIEC, A. Analysis of transient processes in a drive system with vertical pumps of susceptible motion transmission (in Polish). *Przegląd Elektrotechniczny*. 2019, **8**, p. 21-24. ISSN 0033-2097, eISSN 2449-9544.
- [13] CZABAN A., LIS, M. The use of the Hamilton formalism for modelling of power systems with a synchronous motors and susceptible transmission of mechanical power (in Polish). *Przegląd Elektrotechniczny*. 2018, **1**, p. 21-24. ISSN 0033-2097, eISSN 2449-9544.
- [14] CZABAN, A., LIS, M. Application of an artificial neural network for determination of rotor current in a driver system: a PMSM motor – a DC generator (in Polish). *Przegląd Elektrotechniczny*. 2014, **6**, p. 272 - 274. ISSN 0033-2097, eISSN 2449-9544.
- [15] RABOTNOW, J. *Mechanics of deformed bodies* (in Russian). Vol. 3. URSS, 2019, ISBN 978-5-9710-5637-9.
- [16] WASHIZU, K. *Variational methods in elasticity and plasticity*. Kittery, ME, U.S.A.: Pergamon Press, 1982. ISBN 978-0080267234.
- [17] PUKACH, P. Y. Qualitative methods for the investigation of a mathematical model of nonlinear vibrations of a conveyer belt. *Journal of Mathematical Sciences* [online]. 2014, **198**(1), p. 31-38. ISSN 1072-3374, eISSN 1573-8795. Available from: <https://doi.org/10.1007/s10958-014-1770-x>
- [18] WHITE, D. C., WOODSON, H. H. *Electromagnetic energy conversion*. New-York: John Wiley & Sons Inc, 1958. ISBN 978-1124129310.

- [19] ORTEGA, R., LORIA PEREZ, A., NICKLASSON, P. J., SIRA-RAMIREZ, H. *Passivity-based control of Euler-Lagrange systems: mechanical, electrical and electromechanical applications*. London: Springer Verlag, 1998. ISBN 978-1-4471-3603-3.
- [20] SPORYKHIN, A. N. Hamilton-Ostrogradski principle in the theory of nonlinear elasticity with the combined approach. *International Applied Mechanics* [online]. 1995, **31**, p. 294-297. ISSN 1063-7095, eISSN 1573-8582. Available from: <https://doi.org/10.1007/BF00846778>
- [21] ELSGOLTS, L. *Differential equations and the calculus of variations*. Moscow: Mir publishers, 1977.
- [22] YABUKI, A., OHISHI, K., MIYAZAKI, T., YOKOKURA, Y. Force control including contact process using acceleration-sensor-based instantaneous state observer for high-stiffness gear drive. In: IEEE 25th International Symposium on Industrial Electronics: proceedings [online]. 2016. eISSN 2163-5145, p. 651-656. Available from: <https://doi.org/10.1109/ISIE.2016.7744966>
- [23] SZAFRANIEC, A., Mathematical model of asynchronous pump drive and power transformer drive system with complex motion transmission. In: 13th International Scientific Conference Control of Power Systems: proceedings. 2018. p. 104-109.
- [24] XU, S., SUN, G., CHENG, Z. Fractional order modeling and residual vibration suppression for flexible two-mass system. In: *29th Chinese Control and Decision Conference CCDC 2017: proceedings* [online]. 2017. eISSN 1948-9447, p. 3658-3664. Available from: <https://doi.org/10.1109/CCDC.2017.7979140>

IMITATION MODELING OF AN INTER-TURN SHORT CIRCUIT OF AN ASYNCHRONOUS MOTOR STATOR WINDING FOR DIAGNOSTICS OF AUXILIARY ELECTRIC DRIVES OF TRANSPORT INFRASTRUCTURE

Sergey Goolak¹, Juraj Gerlici², Oleg Gubarevych^{3,*}, Tomáš Lack², Mikhail Pustovetov⁴

¹Department of Traction Rolling Stock, State University of Infrastructure and Technologies, Kyiv, Ukraine

²Department of Transport and Handling Machines, Faculty of Mechanical Engineering, University of Zilina, Zilina, Slovakia

³Department of Navigation and Operation of Technical Systems on Water Transport, Danube Institute of Water Transport, State University of Infrastructure and Technologies, Kyiv, Ukraine

⁴Department of Engineering Technology, Technological Institute (Branch) of Don State Technical University in the City of Azov, Azov, Russia

*E-mail of corresponding author: oleg.gbr@ukr.net

Resume

A scientific approach to calculating the parameters and characteristics of an asynchronous motor in the inter-turn short circuit mode in one phase of the stator is proposed to create the foundations of a diagnostic complex for assessing the condition of asynchronous motors of the transport infrastructure. This approach consists of the fact that in the model with which the research is carried out, it is proposed to take into account changes in the mutual inductance of the motor when the AC impedance of one of the stator phases changes. Using a new approach to modeling processes occurring in an asynchronous motor during the inter-turn short circuit in one phase of the stator, pulsations of the torque on the motor shaft were studied for different values of the AC impedance and resistance of one of the stator winding phases, which corresponds to varying degrees of the inter-turn short circuits.

Article info

Received 12 May 2020

Accepted 6 November 2020

Online 3 March 2021

Keywords:

transport infrastructure,
asynchronous motor,
inter-turn short circuit,
phase currents,
torque ripple

Available online: <https://doi.org/10.26552/com.C.2021.2.C65-C74>

ISSN 1335-4205 (print version)

ISSN 2585-7878 (online version)

1 Introduction

For each state, development and creation of advanced transport infrastructure is a priority task that characterizes the level of economic development of the country.

The operational efficiency and development of other industries depends on efficiency of transport, especially its main types of rail and water transportation.

Ensuring efficient and highly profitable operation of transport is possible by increasing the reliability of its operation, which is ensured by the continuous development and improvement of diagnostic methods of operational control to establish the current status and predict the period of trouble-free operation.

Railway, as well as water transport, as auxiliary equipment incorporates a large number of asynchronous motors with squirrel-cage rotor of various powers. The simplicity of design and the reliability of asynchronous motors implied a high level of reliability of auxiliary electric drives in transport. This principle was laid down in design of a number of electric locomotives, as evidenced by lack

of monitoring the asynchronous auxiliary machines status.

However, during the operation of these motors, a number of malfunctions can occur. These malfunctions can affect drive performance and make it partially or completely incapable to complete the process tasks.

Ensuring high-quality performance by the drive of the technological process is impossible without creation of modern diagnostic systems, both built-in (as part of the drive) and bench.

To build diagnostic systems, the choice of a diagnostic method is relevant. That choice requires an integrated approach to study of processes occurring in an asynchronous motor in the event of a malfunction. The purpose of this approach to the choice of diagnostic method is to study influence of the studied defect on the motor characteristics and determine the parameters by which the diagnosis will be performed.

An analysis of malfunctions of asynchronous motors, performed in [1-3], showed that about 15% of the total numbers of malfunctions of an asynchronous motor are associated with inter-turn short circuit of the

stator windings. Thus, an integrated approach to study of processes occurring in an asynchronous motor when an inter-turn short circuit occurs is an urgent task.

2 Methods for studying processes in an asynchronous motor in the event of an inter-turn short circuit

To effectively select the parameters by which the asynchronous motor diagnostics will be performed in order to determine the inter-turn short circuit in the stator windings, it is necessary to determine the design changes in the asynchronous motor caused by this defect. Studies conducted in [4-5] show that the inter-turn short circuit leads to asymmetrical modes in the stator winding. This is due to the fact that as a result of the inter-turn short circuit, both the resistant and inductive AC impedance's components of the phase, at which the circuit occurs, are reduced.

Study [6] showed that operation of an asynchronous motor with electric or magnetic asymmetry of the stator windings leads to an uneven distribution of losses in copper over the phases of the stator and appearance of variable components of the electromagnetic torque and power consumption. In [6], influence of the unbalance level of the phase currents on magnitude of the electromagnetic torque pulsations was not disclosed. The solution to this problem was investigated in [7-8]. In these works, it was shown that the unbalance of the stator phase currents leads to pulsations of the electromagnetic torque and the torque pulsations have a double frequency in comparison to frequency of the supply voltage.

Despite the fact that influence of the unbalance of the stator phase currents on the ripple of the electromagnetic torque was studied in [7-8], such questions as the effect of inter-turn short circuit on the active power consumed from the network and the power factor remain unresolved. These issues are considered in [9-10]. They noted that the inter-turn short circuit leads to an increase in the phase shift of the current relative to the voltage in all the three phases of asynchronous motors, which, in turn, leads to a decrease in the power factor. In addition, these works was shown that the inter-turn short circuit in the stator winding leads to an increase in the active power consumed by the motor from the network.

In the study, the effect of inter-turn short circuit on characteristics of an asynchronous motor should take into account a number of limitations associated with the quality of the motor supply voltage. Thus, in [11-12] it was noted that with a non-symmetrical power supply system, the voltage of the negative sequence causes pulsations of the electromagnetic torque in the motor with a stator, in which there is no inter-turn short circuit. The same effect is observed with a symmetrical system of voltages in the motor with inter-turn short circuit in the stator windings. In other words, in the presence of an asymmetrical power system, it will be difficult to identify the presence of inter-

turn short circuit or its absence.

With a non-sinusoidal form of the supply voltage, higher harmonic components of the stator phase currents arise, which increase the loss of active power in the stator windings, it was noted in the studies [13-14]. These losses lead to a decrease in the power factor, which also makes it difficult to identify the presence or absence of inter-turn fault in the stator windings.

The proposed approach to study of effect of the inter-turn fault on the parameters and characteristics of an asynchronous motor consists in a comprehensive approach to the analysis of the influence of this defect on the parameters and characteristics of the motor, comparing the degree of change of different characteristics and parameters from the degree of inter-turn fault. The limitations adopted in the work relate to the power system of an asynchronous motor. They consist in the fact that the motor power system is symmetrical and the shape of the voltage is sinusoidal.

The results of this work can be used to select an effective method for constructing diagnostic circuits for asynchronous motors with short circuit rotor as part of the drive.

3 The purpose and objectives of the study.

The purpose of the study: the development of a simulation model and the study of diagnostic parameters during the inter-turn short circuit of the stator winding of an asynchronous motor, designed for operation as a part of auxiliary electric drives of the transport infrastructure.

To achieve this goal it is necessary to solve the following tasks:

- choose a mathematical model of an asynchronous motor that can work under the condition of asymmetry of the stator windings. On the selected model to realize the asymmetry of the stator windings caused by the circuit of the windings;
- to study effect of the inter-turn short circuit degree on one of the stator windings of the motor on the ripple factor of the electromagnetic torque and the unbalance of the stator phase currents;
- to study effect of the inter-turn short circuit degree on one of the stator windings of the motor on the mechanical and operational characteristics of the motor;
- perform a comparison for each parameter studied and each characteristics about the inter-turn short circuit degree on dynamics of changes in the main parameters and motor characteristics.

4 The choice of a model for the study of processes in an asynchronous motor in the event of an inter-turn short circuit

The object of research was a series squirrel-cage asynchronous motor model *AIR132M4 11.0 kW*, nameplate

Table 1 Nameplate parameters of an asynchronous motor with a squirrel-cage rotor AIR132M4

parameter	designation	unit	value
shaft power rating	P_n	kW	11.0
rated phase voltage	U_s	V	220
rated frequency of supply voltage	f_s	Hz	50
rated rotation speed of a motor shaft in idle mode	$n_{n, idle}$	rpm	1500
no loadno-load torque	T_{idle}	$N \cdot m$	0.38
stator winding resistance	r_1	Ω	0.5
resistance of the rotor winding reduced to the stator winding	r'_2	Ω	0.36
stator winding reactance	x_1	Ω	0.56
rotor winding reactance reduced to stator winding	x'_2	Ω	0.938
nominal motor shaft speed	n_n	rpm	1450
rated torque on the motor shaft	T_n	$N \cdot m$	72.671

parameters of which are given in the Table 1.

Research was carried out using the model of an induction motor given in [15-16]. In [16], a mathematical model of an induction motor, its implementation in the OrCAD software environment taking into account the magnetization curve from the main magnetic flux, are presented. Implementation of the mathematical model, taking into account the change in mutual inductance, when changing the AC impedance of one or more phase windings of the motor, is given in [15].

In [15] and [16], a mathematical model of an induction motor, recorded in the three-phase stator reference frame, is presented. Systems of equations, describing operation of the motor in these coordinates, have the form [15-16]:

$$\left\{ \begin{array}{l} u_{s\alpha} = r_{s\alpha} \cdot i_{s\alpha} + \frac{d\psi_{s\alpha}}{dt}; \\ u_{s\beta} = r_{s\beta} \cdot i_{s\beta} + \frac{d\psi_{s\beta}}{dt}; \\ u_{s\gamma} = r_{s\gamma} \cdot i_{s\gamma} + \frac{d\psi_{s\gamma}}{dt}; \\ -u_{r\alpha} = r_{r\alpha} \cdot i_{r\alpha} + \frac{d\psi_{r\alpha}}{dt} + \frac{(\psi_{r\beta} - \psi_{r\gamma}) \cdot p \cdot \omega_r}{\sqrt{3}}; \\ -u_{r\beta} = r_{r\beta} \cdot i_{r\beta} + \frac{d\psi_{r\beta}}{dt} + \frac{(\psi_{r\gamma} - \psi_{r\alpha}) \cdot p \cdot \omega_r}{\sqrt{3}}; \\ -u_{r\gamma} = r_{r\gamma} \cdot i_{r\gamma} + \frac{d\psi_{r\gamma}}{dt} + \frac{(\psi_{r\alpha} - \psi_{r\beta}) \cdot p \cdot \omega_r}{\sqrt{3}}; \end{array} \right. \quad (1)$$

where:

u - voltage, V ;

i - current, A ;

t - time, S ;

r - resistance, Ω ;

ψ - flux linkage, Wb ;

p - number of pole pairs;

subscripts α, β, γ mean belonging to the corresponding phase;

subscript s - stator affiliation;

subscript r - rotor affiliation;

ω_r - mechanical rotor speed, rpm ;

Flux linkages are described by the following system of differential equations [15-16]:

$$\left\{ \begin{array}{l} \psi_{s\alpha} = L_{s\alpha} \cdot i_{s\alpha} - 0.5 \cdot M \cdot i_{s\beta} - \\ - 0.5 \cdot M \cdot i_{s\gamma} + M \cdot (i_{r\alpha} - 0.5 \cdot i_{r\beta} - 0.5 \cdot i_{r\gamma}); \\ \psi_{s\beta} = L_{s\beta} \cdot i_{s\beta} - 0.5 \cdot M \cdot i_{s\alpha} - \\ - 0.5 \cdot M \cdot i_{s\gamma} + M \cdot (i_{r\beta} - 0.5 \cdot i_{r\alpha} - 0.5 \cdot i_{r\gamma}); \\ \psi_{s\gamma} = L_{s\gamma} \cdot i_{s\gamma} - 0.5 \cdot M \cdot i_{s\alpha} - \\ - 0.5 \cdot M \cdot i_{s\beta} + M \cdot (i_{r\gamma} - 0.5 \cdot i_{r\alpha} - 0.5 \cdot i_{r\beta}); \\ \psi_{r\alpha} = L_{r\alpha} \cdot i_{r\alpha} - 0.5 \cdot M \cdot i_{r\beta} - \\ - 0.5 \cdot M \cdot i_{r\gamma} + M \cdot (i_{s\alpha} - 0.5 \cdot i_{s\beta} - 0.5 \cdot i_{s\gamma}); \\ \psi_{r\beta} = L_{r\beta} \cdot i_{r\beta} - 0.5 \cdot M \cdot i_{r\alpha} - \\ - 0.5 \cdot M \cdot i_{r\gamma} + M \cdot (i_{s\beta} - 0.5 \cdot i_{s\alpha} - 0.5 \cdot i_{s\gamma}); \\ \psi_{r\gamma} = L_{r\gamma} \cdot i_{r\gamma} - 0.5 \cdot M \cdot i_{r\alpha} - \\ - 0.5 \cdot M \cdot i_{r\beta} + M \cdot (i_{s\gamma} - 0.5 \cdot i_{s\alpha} - 0.5 \cdot i_{s\beta}); \end{array} \right. \quad (2)$$

where:

L - total phase inductance, H ;

M - mutual inductance of the stator and rotor phases, H ;

Equation of the electromagnetic torque of an induction motor [15-16] is:

$$T_{EM} = \frac{\sqrt{3}}{2} \cdot M \cdot p \cdot [(i_{s\alpha} \cdot i_{r\gamma} + i_{s\beta} \cdot i_{r\alpha} + i_{s\gamma} \cdot i_{r\beta}) - (i_{s\alpha} \cdot i_{r\beta} + i_{s\beta} \cdot i_{r\gamma} + i_{s\gamma} \cdot i_{r\alpha})]. \quad (3)$$

Equation of motion for a motor shaft with a single-mass mechanical system reads:

$$\frac{d\omega_r}{dt} = \frac{T_{EM} - T_C}{J}, \quad (4)$$

where:

J - moment of inertia of rotating masses on the rotor shaft, $kg \cdot m^2$;

T_C - static torque on the rotor shaft, $N \cdot m$.

When modeling the operation of the induction motor, using Equations (1) - (4), certain difficulties may arise associated with stability of the model implementation algorithm. This is due to presence of a large number of integration operations in the algorithm. To reduce the number of integration operations, the number of differential equations should be reduced. For this purpose, it is necessary to express derivatives of the phase flux

linkages in terms of the flux linkages themselves. To do this, one substitutes equations from system of Equations (2) into the system of equations (1). After the transformations, one gets [15]:

$$\begin{cases} \frac{d\psi_{s\alpha}}{dt} = z_{11} \cdot \psi_{s\alpha} + z_{12} \cdot \psi_{s\beta} + z_{13} \cdot \psi_{s\gamma} + \\ + z_{14} \cdot \psi_{r\alpha} + z_{15} \cdot \psi_{r\beta} + z_{16} \cdot \psi_{r\gamma}; \\ \frac{d\psi_{s\beta}}{dt} = z_{21} \cdot \psi_{s\alpha} + z_{22} \cdot \psi_{s\beta} + z_{23} \cdot \psi_{s\gamma} + \\ + z_{24} \cdot \psi_{r\alpha} + z_{25} \cdot \psi_{r\beta} + z_{26} \cdot \psi_{r\gamma}; \\ \frac{d\psi_{s\gamma}}{dt} = z_{31} \cdot \psi_{s\alpha} + z_{32} \cdot \psi_{s\beta} + z_{33} \cdot \psi_{s\gamma} + \\ + z_{34} \cdot \psi_{r\alpha} + z_{35} \cdot \psi_{r\beta} + z_{36} \cdot \psi_{r\gamma}; \\ \frac{d\psi_{r\alpha}}{dt} = z_{41} \cdot \psi_{s\alpha} + z_{42} \cdot \psi_{s\beta} + z_{43} \cdot \psi_{s\gamma} + \\ + z_{44} \cdot \psi_{r\alpha} + z_{45} \cdot \psi_{r\beta} + z_{46} \cdot \psi_{r\gamma}; \\ \frac{d\psi_{r\beta}}{dt} = z_{51} \cdot \psi_{s\alpha} + z_{52} \cdot \psi_{s\beta} + z_{53} \cdot \psi_{s\gamma} + \\ + z_{54} \cdot \psi_{r\alpha} + z_{55} \cdot \psi_{r\beta} + z_{56} \cdot \psi_{r\gamma}; \\ \frac{d\psi_{r\gamma}}{dt} = z_{61} \cdot \psi_{s\alpha} + z_{62} \cdot \psi_{s\beta} + z_{63} \cdot \psi_{s\gamma} + \\ + z_{64} \cdot \psi_{r\alpha} + z_{65} \cdot \psi_{r\beta} + z_{66} \cdot \psi_{r\gamma}; \end{cases} \quad (5)$$

where:

z_{ij} - coefficients obtained as a result of conversion and which are functions of the total inductances and the mutual inductance of the stator and rotor phases, i.e. [15]:

$$z = f(L, M), \quad (6)$$

where:

L - the total inductance of the corresponding stator or rotor phase, which is determined by formula [16]:

$$L = L_{\sigma} + M, \quad (7)$$

where:

L_{σ} - leakage inductance of the corresponding stator or rotor phase, H .

The mutual inductance is determined by formula [16]:

$$M = \frac{2}{3} \cdot L_{\mu}, \quad (8)$$

where:

L_{μ} - magnetization inductance.

Then the equations for determining phase currents have the form [15]:

$$\begin{cases} i_{s\alpha} = u_{s\alpha} - r_{s\alpha} \cdot (a_{11} \cdot \psi_{s\alpha} + a_{12} \cdot \psi_{s\beta} + a_{13} \cdot \psi_{s\gamma} + a_{14} \cdot \psi_{r\alpha} + a_{15} \cdot \psi_{r\beta} + a_{16} \cdot \psi_{r\gamma}); \\ i_{s\beta} = u_{s\beta} - r_{s\beta} \cdot (a_{21} \cdot \psi_{s\alpha} + a_{22} \cdot \psi_{s\beta} + a_{23} \cdot \psi_{s\gamma} + a_{24} \cdot \psi_{r\alpha} + a_{25} \cdot \psi_{r\beta} + a_{26} \cdot \psi_{r\gamma}); \\ i_{s\gamma} = u_{s\gamma} - r_{s\gamma} \cdot (a_{31} \cdot \psi_{s\alpha} + a_{32} \cdot \psi_{s\beta} + a_{33} \cdot \psi_{s\gamma} + a_{34} \cdot \psi_{r\alpha} + a_{35} \cdot \psi_{r\beta} + a_{36} \cdot \psi_{r\gamma}); \\ i_{r\alpha} = -r_{r\alpha} \cdot \left(a_{41} \cdot \psi_{s\alpha} + a_{42} \cdot \psi_{s\beta} + a_{43} \cdot \psi_{s\gamma} + a_{44} \cdot \psi_{r\alpha} + a_{45} \cdot \psi_{r\beta} + a_{46} \cdot \psi_{r\gamma} \right) + \frac{(\psi_{r\beta} - \psi_{r\gamma}) \cdot p \cdot \omega_r}{\sqrt{3}}; \\ i_{r\beta} = -r_{r\beta} \cdot \left(a_{51} \cdot \psi_{s\alpha} + a_{52} \cdot \psi_{s\beta} + a_{53} \cdot \psi_{s\gamma} + a_{54} \cdot \psi_{r\alpha} + a_{55} \cdot \psi_{r\beta} + a_{56} \cdot \psi_{r\gamma} \right) + \frac{(\psi_{r\gamma} - \psi_{r\alpha}) \cdot p \cdot \omega_r}{\sqrt{3}}; \\ i_{r\gamma} = -r_{r\gamma} \cdot \left(a_{61} \cdot \psi_{s\alpha} + a_{62} \cdot \psi_{s\beta} + a_{63} \cdot \psi_{s\gamma} + a_{64} \cdot \psi_{r\alpha} + a_{65} \cdot \psi_{r\beta} + a_{66} \cdot \psi_{r\gamma} \right) + \frac{(\psi_{r\alpha} - \psi_{r\beta}) \cdot p \cdot \omega_r}{\sqrt{3}}; \end{cases} \quad (9)$$

From the systems of Equations (3), (4), (5) and (8) a single system of differential equations of the first order is composed. Having solved this system in the MATHCad software environment, one obtains the value of the motor shaft rotation speed, electromagnetic torque, phase currents, which are needed for further calculations. In [15], realization of the mathematical model of the induction motor is given, made in the MATLAB.

For an intact stator, first in the no-load mode, then in the nominal mode, values of the motor shaft speed, average, maximum and minimum electromagnetic torque and ripple frequency are determined by the model. Values of the current currents of the stator phases, angles of the lag of the phase currents of the stator from the voltages, currents of the rotor phases, angles of the rotor phase currents and voltages of the stator are determined, as well.

When organizing an asymmetrical mode, changes in the mutual inductance should be taken into account. To determine the change in the mutual inductances of the windings, it is necessary to determine what effect the change in the AC impedance of one winding (several windings) has on the magnetic circuit inductance. In [17], a relationship was established between the windings inductances and their geometric dimensions and the air gap was assumed to be uniform. Then, analyzing values of expressions for the phase inductances of the leakage and phase mutual inductances, one can conclude that the leakage inductance of each phase and the mutual phase inductances can be written in the general form:

$$L_{ij}^{XY} = (L')_{ij}^{XY} \cdot F(\alpha_{ij}, \varphi_{ij}), \quad (10)$$

where:

$(L')_{ij}^{XY}$ - component that depends on the winding geometric dimensions;

(superscripts X, Y may take values s or r and show which windings are considered - stator s or rotor r . Subscripts i, j may take values A, B, C and show which phase windings are considered);

$F(\alpha_{ij}, \varphi_{ij})$ - component taking into account angular shifts between the phase voltages α_{ij} and the difference between the phase currents angular shifts of the stator and the rotor φ_{ij} of the respective windings in a symmetrical mode.

Since the component $F(\alpha_{ij}, \varphi_{ij})$ refers to the symmetric mode, one can restrict the considerations only

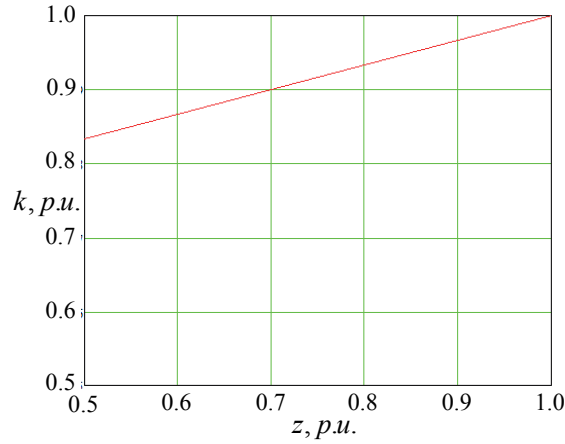


Figure 1 Dependence of the coefficient of change of the magnetic circuit inductance in terms of the AC impedance change of the stator winding

to the component $(L')_{ij}^{XY}$, which is equal to [17]:

$$(L')_{ij}^{XY} = l_\beta \cdot Z_i^X \cdot Z_j^Y \cdot \frac{\pi}{n^2} \cdot \frac{r_s^3}{g} \cdot \mu, \quad (11)$$

where:

μ - magnetic permeability;

n - the number of periods of the spatial distribution of the current sheet, which, for an explicitly polar machine, corresponds to number of pairs of poles p ;

$g = r_s - r_r$ - radial value of the air gap (subscripts show which windings are considered - stator s , rotor r);

r_s - stator radius;

r_r - rotor radius;

$Z_j^X = \frac{W}{l}$ - linear density of the conductor of the corresponding winding current sheet;

W_j^X - number of turns of the corresponding winding;

l_j^X - length of the corresponding winding;

l_β - axial air gap length.

The motor magnetic circuit inductance is determined by the expression [17]:

$$L_\mu = \sum_i \sum_j L_{ij}^{XX}, X \neq Y. \quad (12)$$

In Equation (12), one substitutes the value of inductances calculated using Equation (11) in a general form. The resulting equation is written in the form that corresponds to the form of a function of the winding number of turns, on which the change in the AC impedance is predicted during the inter-turn faults of various degrees. In Equation (12) one substitutes values of inductances calculated using Equation (11), taking into account the number of turns, which corresponds to a change in the AC impedance of the stator winding [15]:

$$L'_\mu = \sum_i \sum_j (L')_{ij}^{XX}, X \neq Y. \quad (13)$$

The resulting equation is presented in the form that corresponds to a function of the winding number of turns, on which a change in AC impedance is predicted.

Then, a coefficient, showing how the inductance of the

magnetic circuit changes with a corresponding change in the AC impedance of the stator winding, is calculated as [15]:

$$k = \frac{L'_\mu}{L_\mu}. \quad (14)$$

Using Equations (10) - (14), one calculates the coefficient of change in the magnetic circuit inductance from the change in the AC impedance of the stator winding, expressed in relative units and builds the dependence of this coefficient on the magnitude of the AC impedance change of the stator phase (Figure 1).

Using the value of the magnetic circuit inductance for the symmetric mode from Table 1, taking into account the coefficient, obtained using Equation (14) (Figure 1), one obtains value of the magnetic circuit inductance for the given conditions for the asymmetrical mode occurrence [15]:

$$L'_\mu = k \cdot L_\mu. \quad (15)$$

Value of the magnetic circuit inductance, obtained using Equation (15) for the asymmetrical mode, is then substituted into Equation (8), thus, one obtains the mutual inductance value for the given mode.

After that, using Equation (7), the total phase inductances are determined. The results obtained are substituted into expressions for coefficients z , Equation (6). The resulting changes in parameters are adjusted on the simulation model. After that, the simulation model is ready for study of electromagnetic processes in an asynchronous motor with asymmetrical windings.

When organizing an asymmetrical mode, the following factors must be considered:

1. The most convenient parameter by which one can determine the inter-turn short circuit on one of the motor phases is the phase resistance.
2. As seen from Equation (11), both the phase leakage inductance and the mutual inductance are a function of the number of turns squared.
3. The active resistance of the winding is determined by expression:

Table 2 Values of the of resistance, reactance, AC impedance of the stator phase and reactance of the mutual induction of the stator and rotor at different values of the AC impedance

$\frac{Z_1}{Z_{1nom}}$	Z_1, Ω	$w_1, p, u.$	$w_1^2, p, u.$	r_s, Ω	x_1, Ω	x_μ, Ω
1	0.751	1	1	0.5	0.56	0.559
0.9	0.676	0.934	0.872	0.467	0.489	0.547
0.85	0.639	0.9	0.81	0.45	0.454	0.54
0.8	0.601	0.864	0.746	0.432	0.418	0.534
0.72	0.537	0.8	0.64	0.4	0.358	0.522

$$r_s = k_r \cdot \rho_\theta \cdot \frac{l_{mean} \cdot w}{q_{e.c.} \cdot n_{e.c.} \cdot a}, \quad (16) \quad \text{formula [16]:}$$

where:

k_r - coefficient of increase in active resistance of the winding phase due to action of the current displacement effect;

ρ_θ - material resistivity at design temperature, $\Omega \cdot m$;

l_{mean} - average length of a winding turn, m ;

w - number of winding turns;

$q_{e.c.}$ - elementary conductor cross-sectional area, m^2 ;

$n_{e.c.}$ - number of elementary conductors;

a - number of parallel winding branches.

In other words, the active resistance of the stator phase is a function of the winding turns number.

For convenience of transition from the impedance of the complex resistance $\frac{Z_1}{Z_{1nom}}$ to resistance r_s , the inductive reactance's of the leakage inductance x_1 and the mutual inductance x_μ , as functions of the number of turns w , Table 2 shows values of these quantities, which will be used in the future when studying the operation of an induction motor with asymmetrical stator windings.

5 Investigation of the effect of the inter-turn short circuit on one of the stator phases of an asynchronous motor on the ripple of the torque on the motor shaft and the unbalance of phase currents

Here are now determined the values of similar parameters calculated for the symmetric mode, with a decrease in the phase resistance by 10% and 20%, caused by the inter-turn faults (degree of fault). One determines those values with a decrease in the AC impedance of phase by 10% and 20%. The simulation results are listed in Table 3.

A motor shaft speed of 1500 rpm cannot be obtained in practice for a four-pole asynchronous motor in the real no-load mode. During the computer simulation, using a rigid link that ensures the numerical equality of T_c and T_{EM} in each moment of time, realization of such a rotational speed is possible, if it is specified as the initial condition when integrating Equation (4). In the same way, one can simulate a mode of operation with any desired fixed speed value. In order to distinguish between the ideal no-load mode and the operating modes of the asynchronous motor with a load, the no-load speed, equal to 1500 rpm, was used when simulating.

In Table 3, the torque pulsations are calculated by

$$k_{pT} = \frac{T_{max} - T_{min}}{2 \cdot T_{mean}} \cdot 100\%, \quad (17)$$

where:

T_{max} - maximum torque, $N \cdot m$;

T_{min} - minimum torque, $N \cdot m$;

T_{mean} - average torque, $N \cdot m$.

The stator current unbalance coefficient is determined by formula [16]:

$$k_{imbl} = \frac{I_{Smax} - I_{Smin}}{I_{Ssym,mode}} \cdot 100\%, \quad (18)$$

where:

I_{Smax} - maximum stator phase current, A ;

I_{Smin} - minimum stator phase current, A ;

$I_{Ssym,mode}$ - phase current value in symmetrical mode, A .

Analysis of results of Table 3 shows that the moment ripple in the nominal mode is much less than the ripple of the no-load mode. Therefore, one builds dependences of the ripple coefficient of the electromagnetic moment on changes in the resistance and AC impedance of the stator phase A, only for the no-load operation (Figure 2, a).

According to results of Table 3 one constructs graphs of the unbalance coefficient of the stator phase currents depending on changes in the resistance and AC impedance of the stator phase A for the no-load mode (Figure 2, b) and nominal mode (Figure 2, c).

As can be seen from Figure 2, the most significant changes occur with pulsation of the electromagnetic torque when the resistance and AC impedance of one of the phases change at the no-load. The unbalance coefficient of the stator phase currents changes insignificantly when both the resistance and AC impedance of one of the motor phases change. In addition, from Figure 2 it follows that both the torque ripple coefficient and the unbalance coefficient of the stator phase currents are more dependent on changes in the phase A AC impedance than on changes in the resistance.

6 Investigation of the influence of inter-turn short circuit on mechanical and performance

We will study the changes in the mechanical and operating characteristics of the motor in the event of an inter-turn short circuit at the stator phase, taking into

Table 3 The simulation results for operation of an asynchronous motor in cases of absence and presence of the inter-turn short circuit

parameter	no-load mode					rated mode				
	intact stator	resistance		AC impedance		intact stator	resistance		AC impedance	
		90%	80%	90%	80%		90%	80%	90%	80%
rotation frequency, n, rpm	1500	1500	1500	1500	1500	1450	1450	1450	1450	1450
average electromagnetic torque $T_{mean}, N \cdot m$	0.38	0.381	0.382	0.381	0.382	72.443	72.8	74.4	72.6	72.88
max. electromagnetic torque $T_{max}, N \cdot m$	0.38	0.799	1.236	1.513	1.9	72.443	73.709	76.261	74.149	74.938
min. electromagnetic torque, $T_{min}, N \cdot m$	0.38	-0.04	-0.47	0.376	-1.13	72.443	71.9	72.6	71.1	68.89
ripple frequency, f_{puls}, Hz	0	100	100	100	100	0	100	100	100	100
RMS stator phase A current, I_{IA}, A	9.4	9.583	9.762	10.36	11.56	21.879	21.8	22.6	23.4	25.57
RMS stator phase B current, I_{IB}, A	9.4	9.379	9.371	9.486	9.814	21.879	21.3	21.7	20.7	20.29
RMS stator phase C current, I_{IC}, A	9.4	9.253	9.099	9.959	9.981	21.879	21.1	21.1	21.8	20.32
pulsation coefficient of electromagnetic torque, $k_{pulsT}, \%$	0	109.6	219.2	198.5	396.9	0	1.22	2.43	2.03	4.152
stator phase current unbalance coefficient, $k_{pulsI}, \%$	0	3.51	7.02	9.295	18.59	0	3.51	7.02	12.1	24.11

Table 4 The dependence of the torque on the motor shaft (T_C), net power (P_2), The dependence of the reactive power, (Q_1) the total power consumption of the network (S_1) from motor shaft speed (n), which must be provided

n, rpm	$T_C, N \cdot m$			P_2, W			$Q_1, V \cdot Ar$			$S_1, V \cdot Ar$		
	100%	90%	80%	100%	90%	80%	100%	90%	80%	100%	90%	80%
1425.7	100.865	101.344	101.823	15.059	15.131	15.202	10.545	11.499	11.643	20.268	20.955	21.218
1440.8	83.132	83.623	84.133	12.54	12.617	12.694	8.585	9.347	9.49	16.554	17.129	17.391
1450.0	72.443	72.641	72.878	11.0	11.03	11.066	7.513	7.019	8.301	14.44	14.319	15.128
1470.8	42.923	43.03	43.137	6.611	6.628	6.644	6.528	7.226	7.32	9.803	10.351	10.485
1485.8	20.573	20.573	20.573	3.201	3.201	3.201	6.137	6.643	6.782	7.091	7.568	7.726
1488.3	16.727	16.727	16.727	2.607	2.607	2.607	6.123	6.505	6.678	6.782	7.162	7.355
1490.8	12.824	12.824	12.824	2.002	2.002	2.002	6.121	6.515	6.822	6.527	6.931	7.257
1493.3	8.793	8.793	8.793	1.375	1.375	1.375	6.237	6.521	6.929	6.447	6.747	7.171
1494.8	6.458	6.458	6.458	1.012	1.012	1.012	6.204	6.555	6.988	6.333	6.694	7.138
1496.4	3.8596	3.8596	3.8596	0.605	0.605	0.605	6.223	6.564	6.846	6.282	6.629	6.919
1497.9	1.473	1.473	1.473	0.231	0.231	0.231	6.199	6.549	6.883	6.223	6.575	6.912
1500	0	0	0	0	0	0	6.204	6.553	6.799	6.206	6.557	6.905

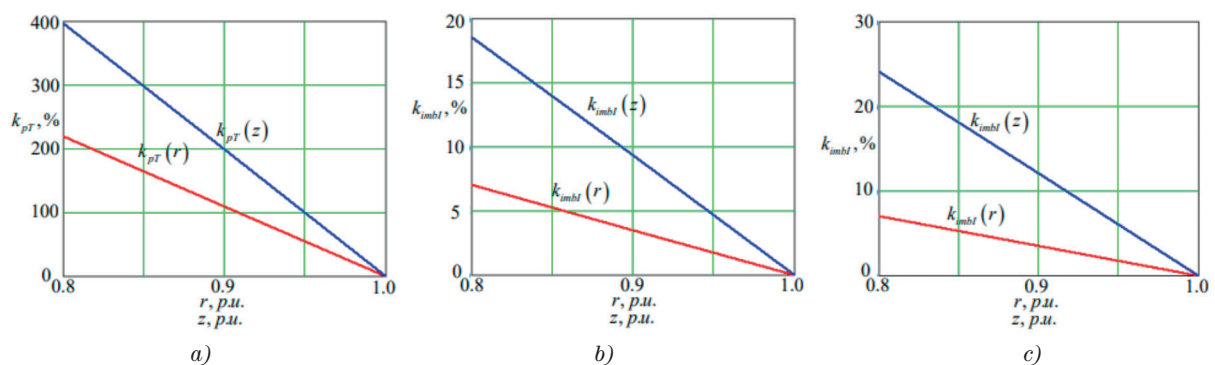


Figure 2 Dependence of the ripple coefficient of the electromagnetic torque on change in the resistance of the stator phase in the no-load mode (a); the dependence of the unbalance coefficient of the stator phase currents on change in the stator phase resistance in the no-load mode (b) and rated mode (c). ($k_{pT}, \%$ - coefficient electromagnetic torque ripple; $k_{ImbI}, \%$ - stator phase current unbalance; $r, p.u.$ - stator resistance; $z, p.u.$ - stator AC impedance)

Table 5 Dependence of the average stator current (I_{lmid}), active power consumed from the network (P_1), efficiency (η), power factor (γ) on the motor shaft speed (n), which must be provided

n, rpm	I_{lmid}, A			P_1, W			$\eta, p.u.$			$\gamma, p.u.$		
	100%	90%	80%	100%	90%	80%	100%	90%	80%	100%	90%	80%
1425.7	30.71	31.75	32.149	17.309	17.519	17.739	0.87	0.864	0.857	0.854	0.845	0.836
1440.8	25.082	25.953	26.351	14.153	14.543	14.574	0.886	0.879	0.836	0.855	0.847	0.838
1450.0	21.879	21.969	22.058	12.332	12.481	12.647	0.892	0.884	0.875	0.854	0.845	0.836
1470.8	14.853	15.683	15.887	7.313	7.411	7.507	0.904	0.895	0.885	0.746	0.731	0.716
1485.8	10.744	11.467	11.706	3.553	3.625	3.701	0.901	0.883	0.865	0.501	0.49	0.479
1488.3	10.275	10.852	11.143	2.916	2.997	3.082	0.894	0.87	0.846	0.43	0.418	0.419
1490.8	9.989	10.502	10.996	2.265	2.364	2.475	0.884	0.847	0.809	0.347	0.344	0.341
1493.3	9.768	10.223	10.865	1.631	1.73	1.846	0.843	0.795	0.745	0.253	0.242	0.227
1494.8	9.596	10.142	10.845	1.273	1.358	1.456	0.795	0.745	0.695	0.201	0.203	0.204
1496.4	9.518	10.044	10.484	0.861	0.926	1.003	0.703	0.653	0.603	0.137	0.14	0.145
1497.9	9.429	9.962	10.473	0.547	0.586	0.628	0.419	0.394	0.368	0.078	0.089	0.081
1500	9.403	9.935	10.467	0.156	0.221	0.285	0	0	0	0.025	0.034	0.041

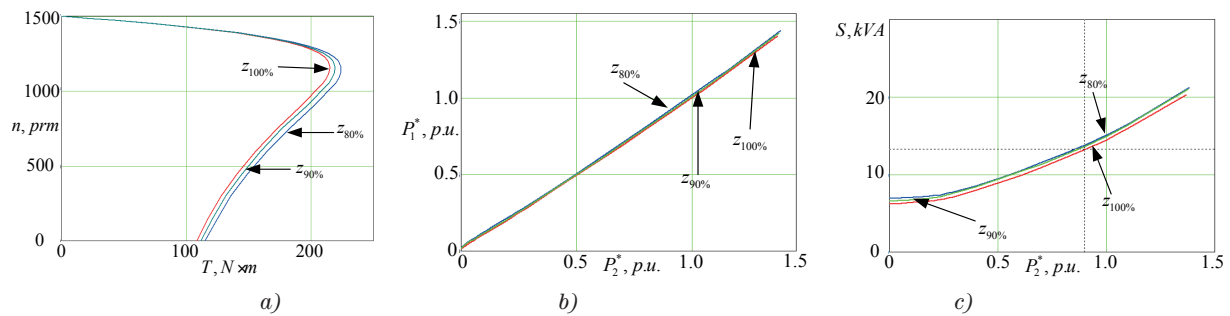


Figure 3 Dependence of the rotational speed of the motor shaft (n) on the motor shaft torque (T) (a); dependence of the relative value of the active power consumed from the network ($P_1^* = P_1/P_r$) (b); the dependence of the total power consumed on the network (S); (c) on the relative value of the net power ($P_2^* = P_2/P_{2r}$)

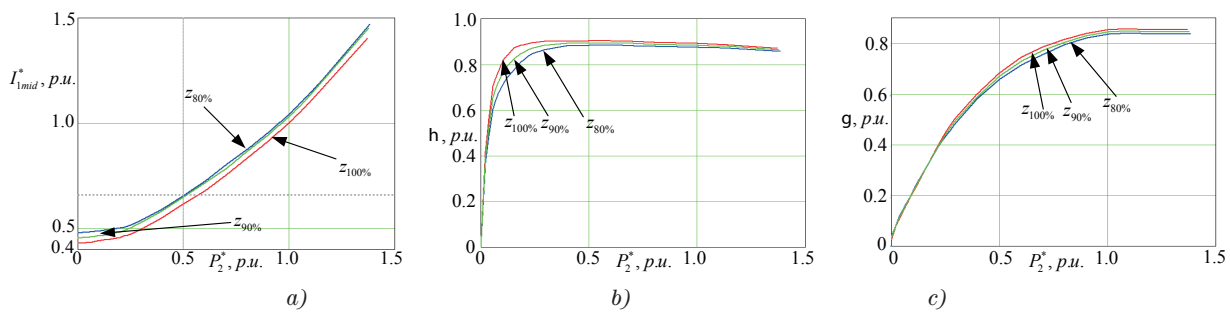


Figure 4 The relative value of the average stator current ($I_{lmid}^* = I_1/I_{1r}$) (a); the dependence of efficiency (η) (b) and power factor (γ) (c) on the relative value of the net power ($P_2^* = P_2/P_{2r}$)

account that 10%, then 20% of the turns of this winding were closed first. We assume that as a result of the inter-turn circuit, first 10%, then 20% of the turns, the AC impedance of the stator winding in this model has changed.

We model these processes on a simulation model. Modeling will be performed by fixing the rotation speed of the motor shaft, using $T_c = T_{EM}$ equation. The simulation results are entered in Tables 4, 5. Modeling will be carried out for 100%, 90% and 80% of the relative AC impedance of stator.

The net power is determined by [16]:

$$P_2 = T_c \cdot \omega_r. \quad (19)$$

Motor shaft mechanical speed is:

$$\omega_r = \frac{\pi \cdot n}{30}, \quad (20)$$

where:

n - motor shaft mechanical speed, rpm .

Instantaneous reactive power is determined by [16]:

$$Q_1 = -\frac{1}{\sqrt{3}} \cdot \left(u_{s\alpha} \cdot (i_{s\beta} - i_{s\gamma}) + u_{s\beta} \cdot (i_{s\gamma} - i_{s\alpha}) + u_{s\gamma} \cdot (i_{s\alpha} - i_{s\beta}) \right) \quad (21)$$

Instantaneous active power is determined by [16]:

$$P_1 = u_{s\alpha} \cdot i_{s\alpha} + u_{s\beta} \cdot i_{s\beta} + u_{s\gamma} \cdot i_{s\gamma}. \quad (22)$$

Then, the value of the instantaneous total power, consumed from the network, can be determined as:

$$S_1 = \sqrt{(P_1)^2 + (Q_1)^2}. \quad (23)$$

The average current in the stator phase, in the case of asymmetrical stator windings is determined by [16]:

$$I_{1mid} = \frac{I_{1A} + I_{1B} + I_{1C}}{3}. \quad (24)$$

The efficiency is given by [16]:

$$\eta = \frac{P_2}{P_1}. \quad (25)$$

The power factor can be determined using expression [16]:

$$\gamma = \frac{P_1}{S_1}. \quad (26)$$

According to results of Table 3, one constructs the mechanical characteristic (Figure 3, a). According to results of Tables 3 and 4, one constructs dependence of the relative value of the active power consumed from the network on the relative value of the useful power (Figure 3, b), the dependences of the total power consumed from the network (Figure 3, c).

According to results of Tables 4 and 5, one builds dependences of the relative value of the average stator current (Figure 4, a), the efficiency coefficients (Figure 4, b) and power (Figure 4, c) on the relative value of the useful power.

Figures 3-4 show that with an increase in the degree of inter-turn short circuit:

- value of the critical torque increases (Figure 3, a);
- increases the active (Figure 3, b) and the total power consumed from the network (Figure 3, c);

- the average value of the stator current increases (Figure 4, a);
- the efficiency value decreases (Figure 4, b) and the motor power factor (Figure 4, c).

7 Conclusions

The article proposes an integrated approach to study of the inter-turn short circuit effect on parameters and characteristics of asynchronous motors. To solve this problem, the following was accomplished:

- A mathematical model of an asynchronous motor was selected, which allows you to simulate operation of an asynchronous motor with asymmetrical windings. A method is proposed for organizing the asymmetry of stator windings, taking into account the change in mutual inductance.
- The effect of inter-turn fault in the winding of one of the stator phases on the ripple factor of the electromagnetic torque and the unbalance coefficient of the stator phase currents has been investigated. The research results showed that the greatest value of the ripple factor of the torque is in the no-load mode when the AC impedance changes (at 20% inter-turn short circuit, the ripple factor of the torque was 264%). The stator phase current unbalance coefficient is also greater when the AC impedance changes, but it has close values for the no-load mode and for nominal mode (16.5% for the no-load mode and 16.2% for the nominal mode).
- Studies of effect of inter-turn short circuit on mechanical characteristics showed that when the inter-turn short circuit is increased to 20%, the critical torque of the motor increases by 2%, which is also accompanied by an increase in the starting torque of the motor.
- Studies have shown that with a nominal motor operating mode the same increase in inter-turn short circuit leads to an increase in the total power consumed from the network by 7.1%, active - by 4.2%, average stator phase current - by 7.2%. This, in turn, leads to a decrease in the efficiency factor of 4.78%, power factor - by 3.2%.

This work can be used to select an effective method for diagnosing the inter-turn faults in the stator winding when constructing a diagnostic system for asynchronous motors as a part of drives of the transport equipment.

References

- [1] MERIZALDE, Y., HERNANDEZ-CALLEJO, L., DUQUE-PEREZ, O. State of the art and trends in the monitoring, detection and diagnosis of failures in electric induction motors. *Energies* [online]. 2017, **10**(7), 1056. eISSN 1996-1073. Available from: <https://doi.org/10.3390/en10071056>
- [2] MAIRTE, J., GABOURY, S., BOUCHARD, B., BOUZOUANE, A. A new computational method for stator faults recognition in induction machines based on hyper-volumes. In: *IEEE International Conference on Electro/Information Technology EIT 2015: proceedings* [online]. IEEE. 2015. ISSN 2154-0357, p. 216-220. Available from: <https://doi.org/10.1109/EIT.2015.7293343>

- [3] BELYAYEV, P. V., GOLOVSKIY, A. P. Damage to the stator winding of asynchronous motor and their diagnostics (in Russian). *Young Russia: Advanced Technologies -in Industry!* [online]. 2019, **1**, p. 33-37. ISSN 2310-9793. Available from: <https://doi.org/10.25206/2310-4597-2019-1-33-37>
- [4] PIETROWSKI, W., GORNY, K. Detection of inter-turn short-circuit at start-up of induction machine based on torque analysis. *Open Physics* [online]. 2017, **15**(1), p. 851-856. eISSN 2391-5471. Available from: <https://doi.org/10.1515/phys-2017-0101>
- [5] CIRA, F., ARKAN, M., GUMUS, B. Detection of stator winding inter-turn short circuit faults in permanent magnet synchronous motors and automatic classification of fault severity via a pattern recognition system. *Journal of Electrical Engineering and Technology*. [online]. 2016, **11**(2), p. 416-424. ISSN 2093-7423. Available from: <http://dx.doi.org/10.5370/JEET.2016.11.1.1921>
- [6] ZAGIRNYAK, M., KALINOV, A., MELNYKOV, V., STACHIN, P. Fault-tolerant control of an induction motor with broken stator electric circuit. In: *Electric Power Networks EPNet: proceedings* [online]. IEEE. 2016. ISBN 978-1-5090-5518-0, p. 1-6. Available from: <https://doi.org/10.1109/EPNET.2016.7999372>
- [7] GOAZZELLI, P. R. U., DE ANDRADE PEREIRA, W. C., DE OLIVEIRA, C. M. R., DE CASTRO, A. G., DE AGUIAR, M. L. Weighting factors optimization of predictive torque control of induction motor by multiobjective genetic algorithm. *IEEE Transactions on Power Electronics* [online]. 2018, **34**(7), p. 6628-6638. ISSN 1941-0107. Available from: <https://doi.org/10.1109/TPEL.2018.2834304>
- [8] MAHMOUD, H., ABDALLH, A. A. E., BIANCHI, N., EL-HAKIM, S. M., SHALTOUT, A., DUPRE, L. An inverse approach for interturn fault detection in asynchronous machines using magnetic pendulous oscillation technique. *IEEE Transactions on Industry Applications* [online]. 2015, **52**(1), p. 226-233. ISSN 1939-9367. Available from: <https://doi.org/10.1109/TIA.2015.2478882>
- [9] WELLINTON, P., DE MENDONCA ROBERLAM, G., LUCIANO, M. N. Comparative performance analysis of a standard three-phase induction motor and an asymmetric three-phase induction motor fed from a single-phase network. *Electric Power Systems Research* [online]. 2015, **125**, p. 211-219. ISSN 0378-7796. Available from: <https://doi.org/10.1016/j.epsr.2015.02.016>
- [10] GUESMI, H., SALEM, S. B., BACHA, K. Smart wireless sensor networks for online faults diagnosis in induction machine. *Computers and Electrical Engineering* [online]. 2015, **41**, p. 226-239. ISSN 0045-7906. Available from: <https://doi.org/10.1016/j.compeleceng.2014.10.015>
- [11] DONOLO, P., BOSSIO, G., De ANGELO, C., GARCIA, G., DONOLO, M. Voltage unbalance and harmonic distortion effects on induction motor power, torque and vibrations. *Electric Power Systems Research* [online]. 2016, **140**, p. 866-873. ISSN 0378-7796. Available from: <https://doi.org/10.1016/j.epsr.2016.04.018>
- [12] ALSAEDI, M. A. Fault diagnosis of three-phase induction motor: a review. *Optics* [online]. 2015, **4**(1-1), p. 1-8. ISSN 2328-7810. Available from: <https://doi.org/10.11648/j.optics.s.2015040101.11>
- [13] KUMAR, N., CHELLIAH, T. R., SRIVASTAVA, S. P. Analysis of doubly-fed induction machine operating at motoring mode subjected to voltage sag. *Engineering Science and Technology, an International Journal* [online]. 2016, **19**(3), p. 1117-1131. ISSN 2215-0986. Available from: <https://doi.org/10.1016/j.jestch.2016.01.015>
- [14] JANDA, M., JANDOVA, K. Vibration Simulation of Electric Machines. In: *Finite Element Method-Simulation, Numerical Analysis and Solution Techniques* [online]. IntechOpen, 2017. ISBN 978-953-51-3849-5, eISBN 978-953-51-3850-1, p. 193-204. Available from: <https://doi.org/10.5772/intechopen.72266>
- [15] GOOLAK, S., GUBAREVYCH, O., YERMOLENKO, E., SLOBODYANYUK, M., GOROBCHENKO, O. Development of mathematical model of induction motor for vehicles. *Eastern-European Journal of Enterprise Technologies* [online]. 2020, **2/2**(104), p. 24-35. ISSN 1729-3774, eISSN 1729-4061. Available from: <https://doi.org/10.15587/1729-4061.2020.199559>
- [16] PUSTOVETOV, M. Y. Approach to computer implementation of mathematical model of 3-phase induction motor. *IOP Conference Series: Materials Science and Engineering* [online]. 2018, **327**(2), 022085. ISSN 1757-8981, eISSN 1757-899X. Available from: <https://doi.org/10.1088/1757-899X/327/2/022085>
- [17] GOOLAK, S., GERLICI, J., SAPRONOVA, S., TKACHENKO, V., LACK, T., KRAVCHENKO, K. Determination of parameters of asynchronous electric machines with asymmetrical windings of electric locomotives. *Communications - Scientific Letters of the University of Zilina* [online]. 2019, **21**(2), p. 24-31. ISSN 1335-4205, eISSN 2585-7878. Available from: <https://doi.org/10.26552/com.C.2019.2.24-31>

Project

Systemic Public Research Infrastructure - Biobank for Cancer and Rare Diseases

is co-financed by the European Union

Project objective:

Expansion and completion of research and innovation infrastructure and capacities for the development of excellence in research and innovation through the establishment of a biobanking system for cancer and rare diseases and its integration into the international network of research infrastructures.

Project description:

The project is in a full scope focused on building a modern, efficient and systematic system of biobanking (long-term storage of human biospecimen), which is one of the fundamental pillars of excellent biomedical research.

In all its specific objectives, the project supports the integration, optimization and further development of research infrastructure, including international scientific and technical cooperation, which is a key element in the implementation of particular project activities.

The construction of a research infrastructure of national importance - the Biobank in Martin - and the introduction of a functional biobanking system in Slovakia will improve the provision of health care for the inhabitants of the Slovak Republic.

Beneficiary: Comenius University in Bratislava

In cooperation with:

Biomedical Centre of the SAS, Bratislava

Centre of Social and Psychological Sciences of the SAS, Bratislava

Ministry of Health of the Slovak Republic

National Cancer Institute in Bratislava

National Institute of Rheumatic Diseases, Piešťany

University of Žilina

Contracted amount of the Non-Repayable Financial Contribution:

17 894 129,32 EUR

Project duration: 06/2020 - 06/2023

ITMS2014+ code: 313011AFG5

This publication has been produced with the support of the Integrated Infrastructure Operational Program for the project: Systemic Public Research Infrastructure - Biobank for Cancer and Rare diseases, ITMS: 313011AFG5, co-financed by the European Regional Development Fund.



EUROPEAN UNION
European Regional Development Fund
OP Integrated Infrastructure 2014 – 2020



MINISTRY
OF TRANSPORT
AND CONSTRUCTION
OF THE SLOVAK REPUBLIC

MEASUREMENT AND ANALYSIS OF THE NOISE LEVEL IN SELECTED ZONES OF BUS STOPS IN THE CITY OF RADOM

Tomasz Perzyński

Faculty of Transport, Electrical Engineering and Computer Science, Kazimierz Pulaski University of Technology and Humanities in Radom, Poland

*E-mail of corresponding author: t.perzynski@uthrad.pl

Resume

The noise from means of transport is one of the main factors of environmental noise pollution and is one of the factors having an effect on human health. The article presents the problem of noise emitted by urban means of transport. The work focuses on analysis of the acoustic climate in the bus stop zone. In order to estimate the noise level, research was conducted in selected points in one of the Polish cities - Radom. The obtained results allowed assessment of the impact of transport on the noise level in the area of selected bus stops.

Article info

Received 22 June 2020

Accepted 25 September 2020

Online 26 January 2021

Keywords:

urban transport,
noise at the bus stops,
noise measurements

Available online: <https://doi.org/10.26552/com.C.2021.2.D26-D33>

ISSN 1335-4205 (print version)

ISSN 2585-7878 (online version)

1 Introduction

Noise is a complex issue, emitted by various sources, which is a serious problem for the human environment [1]. It is defined as unwanted sound [2]. It negatively affects human health and is an important public health problem [3]. Noise is the second most harmful factor after the polluted air, which affects the environment. One of the sources of noise that people fight with every day is the noise generated by means of transport. According to European Commission data, the road transport has the greatest impact on noise levels [4]. Other places include: rail transport, air transport and industry [5]. In the European Union, more than 210 million people are affected by the street noise [6]. As estimated over 10 years ago, social costs of noise reached 2% of GDP [7]. Regarding the Directive [8], the noise protection is an element that achieves a high level of health and environmental protection. This directive obliges Member States and their local government units to create the noise maps and to make acoustic planning. In addition to the abovementioned directive, individual EU member states have their own appropriate legal acts defining its acceptable level [9]. Scientists and engineers are trying to identify technologies and methods that can help reduce noise. However, the problem is the lack of uniform regulations for all the member states. Noise from the means of the city transport is such an important social

problem that many researchers deal with its analysis. The problem of the street noise affects adults, children and animals. Even moderate road traffic disturbs cognitive function, especially in children [10]. The authors of [11] presented correlation between the blood pressure in children and the noise from public transport. They showed that the street noise was associated with an increase in systolic pressure. On the other hand, the authors in [12] showed a relationship between noise from means of transport and blood pressure of adults.

A helpful tool in reducing the noise is modeling and forecasting, which was presented in [13-14]. The authors of [15] conducted an analysis of effects of the road traffic on people's state of mind. The authors [16] proposed a multi-criteria tool to support decision making regarding the road noise activities. As indicated in the study [17], the problem of road noise also applies to the nighttime. In addition, in [18], the authors investigated the impact of the urban noise on sleep. Test results indicated that noise has an impact on quality of sleep and level of rest. The authors of [19] indicate, however, that increased noise at night increases the risk of cardiovascular diseases. In the paper [20], the authors present the results of research on representative sample of the US urban adolescents. The results showed a correlation between noise and bedtime.

As the number of motor vehicles increases, so does the number of people exposed to noise hazards. It should be noted that in most cases noise measurements only



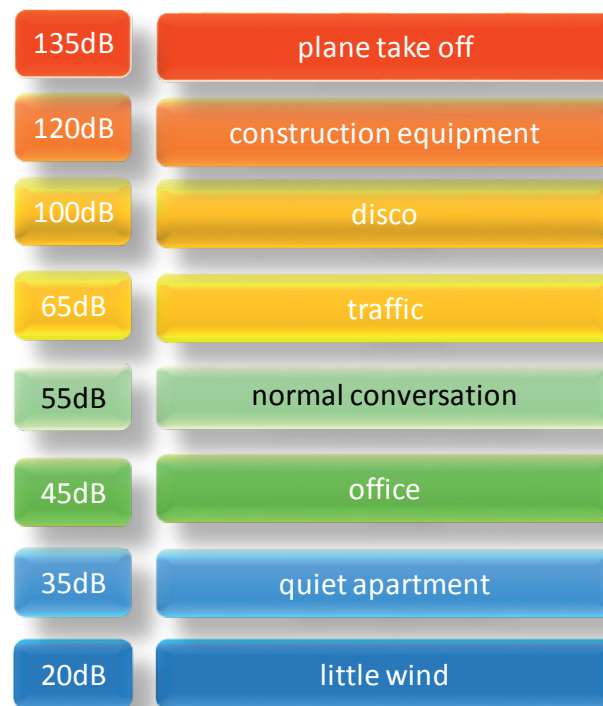


Figure 1 Approximate sound level values

Table 1 Rolling noise requirements [25]

tyre class	nominal section width (mm)	limit values in dB(A)
C1A	≤ 185	70
C1B	$> 185 \leq 215$	71
C1C	$> 215 \leq 245$	71
C1D	$> 245 \leq 275$	72
C1E	> 275	74

apply to the human audible band. This band is in the range of 20Hz-20kHz. Noise testing is also an important issue for frequencies below 20 Hz (infrasound) and above 20 kHz (ultrasound). Infrasound waves can be a source of anxiety, fear and even depression. Ultrasounds are used in medicine or technological processes, but in this case they are controlled processes. Other uncontrolled sources of ultrasound emissions may be harmful to human health, as indicated in [21].

The article presents the measurements results of noise emitted by means of transport in the area of selected public transport stops, city of Radom (Poland). The city of Radom is a medium-sized city (about 200.000 inhabitants) located in the central-eastern part of Poland. The measurements were carried out while passengers were waiting for the bus to arrive. The authors of [22] presented similar concept of research related to noise, among others at bus stops, however, the research was focused on analysis of noise during the bus approaching the bus stop and departure from the stop.

The measurements were carried out at four selected points of the city. The data obtained allowed estimation of

an equivalent sound level for each bus stop zone. Due to exceeding the maximum values of the noise level in one zone (access road to the center - city beltway), detailed measurements of the traffic intensity were carried out.

2 Transport noise and its sources

Noise is an unwanted sound. The measure of sound intensity is the sound pressure level. This level is measured in decibels (dB), which is usually given in relation to the level of the corrected sound measurement value according to audio filter A - dB(A). Filter A allows to optimize the measurement due to the characteristics of human hearing. It is worth to note that decibel is a logarithmic unit. One dB more causes a 26% increase in energy compared to the previous state (2 dB is a 59% increase). Figure 1 shows approximate values of sound intensity in different surroundings.

Factors affecting the level of noise from the road transport can include:

- the number of vehicles traveling in a unit of time,

Table 2 Permissible levels of the traffic noise for roads and railways [33]

no.	type of area	permissible noise levels in (dB)	
		roads or railways	
		the reference time interval is 16 hours (daytime) <i>LAeqD</i>	the reference time interval is 8 hours (night time) <i>LAeqN</i>
1	Protective zone "A" of the spa. Hospital area outside the city.	50	45
2	Single-family housing development areas. Development areas related to the permanent or temporary stay of children and young people. Areas of social care homes. Hospital areas in cities.	61	56
3	Areas of multi-family housing and collective housing. Farm buildings. Recreation areas. Residential and service areas.	65	56
4	Areas in the downtown area of cities over 100.000 residents.	68	60

- type of tyres,
- driving type,
- speed of motor vehicles,
- technical condition of motor vehicles,
- pavement type,
- technical condition of the pavement,
- meteorological conditions,
- aerodynamics of a motor vehicle.

Regarding the factors mentioned above, one of the main factors is noise from vehicle tyres. It becomes the dominant source of noise at speeds above 35 km/h (for passenger vehicles) and above 60 km/h for heavy vehicles [23]. As indicated by authors of study [24], the noise of the tyre interaction with the road pavement becomes dominant for the speed of passenger vehicles above 40 km/h and for heavy goods vehicles above 70 km/h. Table 1 presents data on noise limit values for the summer tyres according to passenger cars (class C1). For the snow tyres the limits shall be increased by 1 dB(A) [25].

Currently, tyres are available for passenger cars with the noise levels starting from 66 dB, although the typical values are around 70-71dB. As authors of [26] indicate, connecting a quiet tyre with an appropriate pavement can reduce noise by 6dB. The noise from the road pavement and that related to the speed of vehicles is also significant. Reducing the speed from 70 km/h to 50 km/h can reduce noise by more than 5dB. The study of the pavement type impact on the noise generated by the tyre is presented in publications [24] and [27]. Authors of [28] have presented the methodology for assessing noise at the interface between the road pavement and the tyre. They also showed a relationship between the type of pavement, its age and impact on noise levels. Authors of [29] and [30] presented the dependence of noise from the motor vehicles on dry and wet surfaces. The problem of noise coming from the motor vehicles concern not only vehicles in motion but also standing e.g. in traffic jams. Authors of [31] drew attention to the problem of noise generated by standing vehicles at various levels of

engine speed. In the case of the urban zone, buildings and landforms are also a problem with reference to noise. The noise in this case is affected by reflection and diffraction of the waves. Therefore, appropriate urban planning measures can contribute to reducing the noise levels.

3 Parameters and indicators

Measurements of environmental noise coupled with traffic can be made using [1]:

- indirect method (single acoustic events),
- direct method of measuring noise using sampling,
- direct continuous measurement method for a limited time.

One of the criteria for choosing the method of measuring noise is the volume of vehicle traffic. For roads over 300 vehicles / hour it is recommended to use the direct method with the use of sampling [32].

In accordance with announcement of the Polish Minister of the Environment of October 15, 2013 regarding the publication of a uniform text of the Regulation of the Minister of the Environment on permissible noise levels in the environment, Table 2 presents the permissible noise levels in the environment, excluding:

- take-offs, landings and flights of aircraft,
- power lines.

Acceptable noise levels were expressed by the indicators *LAeqD* and *LAeqN*, which mean:

- *LAeqD* - indicator for the equivalent sound level for the daytime (from 6.00 to 22.00), expressed in [dB],
- *LAeqN* - indicator for the equivalent sound level for the night (from 10:00 p.m. to 6:00 a.m.), expressed in [dB].
- *LAeq* (D and N) can be calculated based on the formula:

$$LA_{eq} = 10 \log \left(\frac{1}{T} \sum_{i=1}^n \tau_i 10^{0.1L_i} \right), \quad (1)$$

where:



Figure 2 Location of the measuring zones: a) center zone "30", b) downtown
c) access road to the center - city beltway, d) downtown - shopping mall

L_i - sound level over a period of time,

τ_i - duration of noise level L_i ,

T - observation time.

Based on the data obtained, the mean logarithmic exposure value for each series can be estimated according to:

$$L_{Amin} = 10 \log \left(\frac{1}{n} \sum_{i=1}^n 10^{0.1 L_{Ae}} \right), \quad (2)$$

where:

L_{Ae} is the exposure level for a single acoustic event and n is the number of events in the series.

Standard deviation can be estimated based on expression:

$$\sigma = \sqrt{\frac{1}{n-1} \sum_{i=1}^n (L_{Ae} - L_{Amin})^2} \quad (3)$$

4 Research and measurement results

To measure the sound level of transport means in the city of Radom, the sound meter Steinberg SBS-SM-130C was used. Measuring device data: meter operating band 31.5 Hz - 8 kHz, accuracy ± 1.4 dB. The measuring device has been set up to perform measurements according to A - weighted sound level for the FAST time constant. With reference to recommendations contained in [32], a direct measurement method using sampling was proposed for measurements. The measuring device was set on a tripod, height from the ground 1.5m in the stop zone. Despite the good conditions (weak wind), the microphone had

a windscreen. In all the measuring sessions measurements were made in meteorological conditions ensuring stable conditions: temperature above 2 °C, light wind, moderate cloud cover, no rainfall. Measurements were carried out on sections where the road pavement was made of asphalt, good condition, no defects in the road.

Four places were selected for the measurements:

- city center - zone 30,
- downtown,
- access road to the city center, beltway,
- city center - shopping mall.

The measurement sites were located in the bus stops area. The measurement hours were set for morning and afternoon hours on different days of the week (excluding weekends). All the measurements points were in the urban zone - the city of Radom, Poland. Two measuring sessions were carried out in each zone on different days. It was assumed that the average waiting time of passengers at the bus stop is about 5 minutes. Every 5 s instantaneous sound pressure values were read. Figure 2 shows locations of zones where the measurements were carried out.

Based on Equations (1), to (3), calculations were carried out, results of which are shown in Table 3.

Taking into account the higher of the average values for each zone (L_{mid} - Table 3), Figure 3 shows the graphical form of the collected data for measurement session 2, 4, 6 and 7.

Since in the zone of the access street to the center - the city beltway, the permissible noise level values were exceeded, it was decided to carry out an additional test to obtain data on the number of vehicles, vehicle speed, type of vehicles. The tests were carried out for one direction of

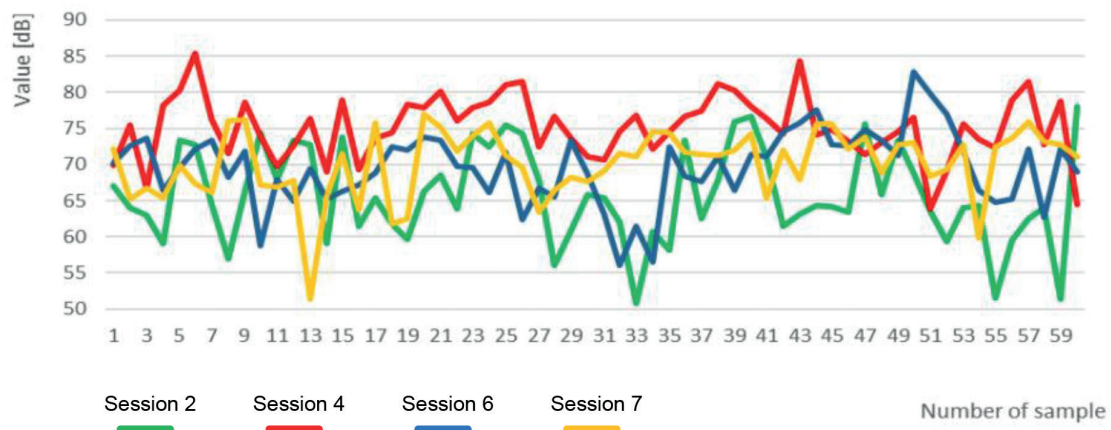


Figure 3 Graphical form of the collected data - measurement session 2, 4, 6 and 7

Table 3 Calculation results for collected measurement data

zone	session number	L_{mid} (dB)	L_{eqD} (dB)	σ (dB)
city center "30"	1	68.25	61.26	8.04
	2	69.91	62.91	6.55
beltway	3	77.03	70.03	6.06
	4	77.25	70.26	4.4
downtown (25 Czerwca st.)	5	71.58	64.85	4.58
	6	72.35	65.35	5.09
downtown - shopping mall	7	71.99	64.99	4.73
	10	69.99	62.99	7.08

Table 4 Results of the vehicle traffic measurements - the city beltway - Kielecka Street

speed range	car	vans	heavy	together
21-30 km/h	0	0	1	1
31-40 km/h	0	0	0	0
41-50 km/h	16	1	9	26
51-60 km/h	46	4	13	63
61-70 km/h	34	5	4	43
71-80 km/h	9	0	1	10
81-90 km/h	1	0	1	2
> 90 km/h	0	0	0	0
together	106	10	29	145

travel. The ViaCount II traffic meter, which works based on the Doppler radar, was used to conduct the tests. Speed limit on the test section of the road: 50 km/h. Measurements were made: 03-02-2020 from 16:43:39 to 16:54:50. Results are shown in Table 4.

On the examined section 145 vehicles were registered, including 106 passenger vehicles, 10 delivery vehicles, 29 heavy vehicles.

5 Discussion of the results

The main purpose of the measurements was to determine the current state of the acoustic climate in areas

subjected to acoustic protection, which are in the zone of selected bus stops. The research has been in a pilot-phase to indicate potential bus stop zones that should be analyzed in terms of improving the acoustic climate. To carry out the measurements it was decided to use the direct measurement method in the form of sampling. Measurements have shown that the noise from means of transport is not in all the bus stop zones below the permissible values specified in the Regulation [33]. Calculations made for "zone 30" showed that the noise was there at the lowest level and was below the permissible values. In the downtown area noise levels were also below the permissible values, however, higher than for "zone 30". The highest levels were recorded at the bus stop on the city beltway, Kielecka Street. The

estimated equivalent sound level of $LeqD$ was: 70.03 dB and 70.26 dB. In the other examined zones, the noise from means of transport was not exceeded, however, due to the relatively high results, further tests should be carried out. It is worth adding that the World Health Organization (WHO) in its report [34] recommends limiting the $LeqD$ value below 53 dB (recommendation for the road traffic), considering it as a value above which it causes adverse effects on human health. It should also be noted that in Poland the limit values indicated in [33] for the city center zone were raised about 3 dB in relation to the Act [35] of 2007 (before amendment). With some anxiety one can also note the fact that in the case of pollution caused by motor vehicles (exhaust), we are dealing with the introduction of new restrictions, in the case of transport noise such restrictions cannot be seen.

It should be noted that the highest traffic intensity was noted on Kielecka Street - the city beltway. Therefore, for this bus stop zone additional research was carried out to measure vehicle traffic. For this purpose, measurements were taken on February 3, 2020, measurement time ~ 12 minutes. The research was made in the afternoon due to the dusk and to skipping the drivers' reaction to see the radar. There is a speed limit of 50 km/h on the analyzed road section. During the analysis 145 vehicles were registered (in one direction). The analysis shows that as much as 81.38% of the vehicles were traveling at speeds above the maximum permissible (118 vehicles). As many as 55 vehicles traveled at speeds above 61 km/h. For heavy goods vehicles: 19 vehicles were traveling at speeds over 51 km/h. One of the causes of increased noise values on the examined road section can be excessive speed of the vehicles.

The obtained results allow the commencement of research related to use of the noise reduction solutions at selected stops. The next stage may be the analysis of

the construction of the bus shelters, their reconstruction toward use as acoustic screens.

6 Conclusion

Undoubtedly, the urban transport noise, its reduction, must be a part of further research and analysis. The need to develop acoustic maps of cities, indicated by the European Commission, will allow, at the stage of urban spatial planning, to introduce solutions that can reduce the traffic noise. Building parks is a natural method of reducing urban noise. The so-called green screens can effectively protect against the street noise. Use of active transport telematics systems can also be an effective solution. Such a system could continuously analyze the noise level in a given urban area and, if necessary, limit the speed of vehicles, which in combination with the appropriate road pavement can bring measurable effects in the form of a lower noise level. As indicated in the paper, first of all, drivers must comply with speed limits. Reducing the speed of a truck from 60 km/h to 50 km/h reduces the noise for almost 2 dB [36]. Effective measures to prevent excessive levels of the traffic noise is to reduce the number of vehicles and to use the better technologies (tyres, surfaces) [37]. Reducing the number of vehicles in cities is possible by promoting the public transport [38]. As the tests of one of the electric bus manufacturers show, use of the electric propulsion in buses, instead of an internal combustion engine, in the urban speed range (up to 50 km/h) can be seen to reduce the external noise by up to 8 dB [39]. Noise or pollution reduction can also be limited by the proper urban traffic management, e.g. by optimizing traffic light control systems [40]. There is no doubt that only coherent actions towards the use of new technologies, full vehicle traffic control, regulations and urban planning can reduce the noise which surrounds us every day.

References

- [1] GORZELANCZYK, P. The road transport noise emission in Pila (in Polish). *Autobusy*. 2016, **6**, p. 876-880. ISSN 1509-5878.
- [2] Commonwealth of Australia as represented by the Department of Health. *The health effects of environmental noise*. Publications Number: 12214. 2018.
- [3] World Health Organization. *Environmental noise. Guidelines for the European Region*. 2018.
- [4] Road traffic remains biggest source of noise pollution in Europe - European Environment Agency [online] [accessed 2020-01-30]. Available from: <https://www.eea.europa.eu/highlights/road-traffic-remains-biggest-source>
- [5] European Commission. *Science for environment policy. Noise abatement approaches*. Issue 17. 2017. ISBN 978-92-79-67011-4.
- [6] JACYNA, M., WASIAK, M., LEWCZUK, K., KARON, G. Noise and environmental pollution from transport: Decisive problems in developing ecologically efficient transport systems. *Journal of Vibroengineering* [online]. 2017, **19**, p. 5639-5655. ISSN 1392-8716, eISSN 2538-8460. Available from: <https://doi.org/10.21595/jve.2017.19371>
- [7] FIGLUS, T., GNAP, J., SKRUCANY, T., SZAFRANIEC, P. Analysis of the influence of different means of transport on the level of traffic noise. *Scientific Journal of Silesian University of Technology. Series Transport* [online]. 2017, **97**, p. 27-38. ISSN 0209-3324, eISSN 2450-1549. Available from: <https://doi.org/10.20858/sjsutst.2017.97.3>
- [8] Directive 2002/49/EE of The European Parliament and of The Council of 25 June 2002 relating to the assessment and management of environmental noise.
- [9] Handbook on the implementation of EC environmental legislation. Section 9 - Noise legislation [online]. 2020. Available from: <https://ec.europa.eu/environment/archives/enlarg/handbook/noise.pdf> (12-01-2020)

- [10] BHATIA, R. Noise pollution: managing the challenge of urban sounds [online] [accessed 2020-02-13]. Available from: <https://earthjournalism.net/resources/noise-pollution-managing-the-challenge-of-urban-sounds>
- [11] PAUNOVIC, K., BELOJEVIC, G., JAKOVljeVIC, B. Blood pressure of urban school children in relation to road-traffic noise, traffic density and presence of public transport. *Noise and Health* [online]. 2013, **15**, p. 253-260. ISSN 1463-1741, eISSN 1998-4030. Available from: <http://www.noiseandhealth.org/text.asp?2013/15/65/253/113521>
- [12] DRATVA, J., PHULERIA, H., FORASTER, M., GASPOZ, J.-M., KEIDEL, D., KUNZLI, N., LIU, L.-J., PONS, M., ZEMP, E., SCHINDLER, CH. Transportation noise and blood pressure in a population-based sample of adults. *Environmental Health Perspectives* [online]. 2011, **120**(1), p. 50-55. ISSN 1552-9924. Available from: <https://doi.org/10.1289/ehp.1103448>
- [13] MELO, R. A., PIMENTEL, R. L., LACERDA, D. M., SILVA, W. M. Applicability of models to estimate traffic noise for urban roads. *Journal of Environmental Health Science and Engineering* [online]. 2015, **13**, 83. eISSN 2052-336X. Available from: <https://doi.org/10.1186/s40201-015-0240-9>
- [14] ECE, M., TOSUN, I., EKINCI, K., YALCINDAG, N. S. Modeling of road traffic noise and traffic flow measures to reduce noise exposure in Antalya metropolitan municipality. *Journal of Environmental Health Science and Engineering* [online]. 2018, **16**, 1. eISSN 2052-336X. Available from: <https://doi.org/10.1007/s40201-018-0288-4>
- [15] GOKDAG, M. Study of the road traffic noise in Erzurum-Turkey. *Iranian Journal of Environmental Health Science and Engineering* [online]. 2012, **9**, 22. eISSN 2052-336X. Available from: <https://doi.org/10.1186/1735-2746-9-22>
- [16] RUIZ-PADILLO, A., RUIZ, D., TORIJA, A., RAMOS-RIDAO, A. Selection of suitable alternatives to reduce the environmental impact of road traffic noise using a fuzzy multi-criteria decision model. *Environmental Impact Assessment Review* [online]. 2016, **61**, p. 8-18. ISSN 0195-9255. Available from: <https://doi.org/10.1016/j.eiar.2016.06.003>
- [17] MURPHY, E., KING, E., RICE, H. Estimating human exposure to transport noise in central Dublin, Ireland. *Environment International* [online]. 2008, **35**(2), p. 298-302. ISSN 0160-4120. Available from: <https://doi.org/10.1016/j.envint.2008.07.026>
- [18] STOSIC, L., BELOJEVIC, G., MILUTINOVIC, S. (2009). Effects of Traffic Noise on sleep in an urban population. *Arhiv za Higijenu Rada i Toksikologiju* [online]. 2009, **60**, p. 335-342. ISSN 0004-1254, eISSN 1848-6312. Available from: <https://doi.org/10.2478/10004-1254-60-2009-1962>
- [19] BABISCH, W. *Transportation noise and cardiovascular risk. Review and synthesis of epidemiological studies. Dose-effect curve and risk estimation* [online]. 2006. ISSN 0175-4211. Available from: <http://www.umweltbundesamt.de>
- [20] RUDOLPH, K., SHEV, A., PAKSARIAN, D., MERIKANGAS, K., MENNITT, D., JAMES, P., CASEY, J. Environmental noise and sleep and mental health outcomes in a nationally representative sample of urban US adolescents. *Environmental Epidemiology* [online]. 2019, **13**(3(4)), e056. eISSN 2474-7882. Available from: <https://doi.org/10.1097/EE9.0000000000000056>
- [21] SMAGOWSKA, B. & PAWLACZYK-LUSZCZYŃSKA, M. (2013). Effects of Ultrasonic Noise on the Human Body—A Bibliographic Review. *International Journal of Occupational Safety and Ergonomics*: JOSE. 19. 195-202. 10.1080/10803548.2013.11076978.
- [22] GERSHON, R., NEITZEL, R., BARRERA, M., AKRAM, M. Pilot survey of subway and bus stop noise levels. *Journal of Urban Health* [online]. 2006, **83**, 802. ISSN 1099-3460, eISSN 1468-2869. Available from: <https://doi.org/10.1007/s11524-006-9080-3>
- [23] CEDR report 2017/03. State of the art in managing road traffic noise: summary report. [online]. 2020. Available from: <https://www.cedr.eu/download/Publications/2017/CEDR2017-03-State-of-the-art-in-managing-road-traffic-noise.pdf>
- [24] LINK, R. E., BENNETT, T., HANSON, D., MAHER, A., VITILLO, N. Influence of pavement surface type on tire/pavement generated noise. *Journal of Testing and Evaluation* [online]. 2005, **33**(2), p. 94-100. ISSN 0090-3973. Available from: <https://doi.org/10.1520/JTE12641>
- [25] Regulation (EC) No 1222/2009 of the European Parliament and of the Council of 25 November 2009 on the labelling of tyres with respect to fuel efficiency and other essential parameters
- [26] BERGE, T., MIODUSZEWSKI, P., EJSZONT, J., SWIECZKO-ZUREK, B. Reduction of road traffic noise by source measures - present and future strategies. *Noise Control Engineering Journal* [online]. 2017, **65**(6), p. 549-559. ISSN 0736-2501. Available from: <https://doi.org/10.3397/1/376568>
- [27] LI, T. (2018). Literature review of tire-pavement interaction noise and reduction approaches. *Journal of Vibroengineering* [online]. 2018, **20**, p. 2424-2452. ISSN 1392-8716, eISSN 2538-8460. Available from: <https://doi.org/10.21595/jve.2018.19935>
- [28] BOODIHAL, M., CHETHAN, A., RUDRARADHYA, S., SAHU, R., BILIGIRI, K. P. Development of tyre/road noise assessment methodology in India. *Case Studies in Construction Materials* [online]. 2014, **1**, p. 115-124. ISSN 2214-5095. Available from: <https://doi.org/10.1016/j.cscm.2014.06.001>
- [29] GARDZIEJCZYK, W. Comparison of vehicle noise on dry and wet road surfaces. *Foundations of Civil and Environmental Engineering*. 2007, **9**, p. 5-15. ISSN 1642-9303.
- [30] FREITAS, E., PEREIRA, P., DE PICADO-SANTOS, L., SANTOS, A. Traffic noise changes due to water on porous and dense asphalt surfaces. *Road Materials and Pavement Design* [online]. 2009, **10**(3), p. 587-607. ISSN 1468-0629, eISSN 2164-7402. Available from: <https://doi.org/10.1080/14680629.2009.9690215>

- [31] SARKAN, B., STOPKA, O., LI, CH. The issues of measuring the exterior and interior noise of road vehicles. *Communications - Scientific Letters of the University of Zilina* [online]. 2017, **19**(2), p. 50-55. ISSN 1335-4205, eISSN 2585-7878. Available from: <http://komunikacie.uniza.sk/index.php/communications/article/view/182>
- [32] Republic of Poland. Journal of laws (in Polish). No. 140. Item 824. 2011.
- [33] Republic of Poland. Journal of laws (in Polish). Item 112. 2014.
- [34] World Health Organization. *Noise guidelines. Environmental noise guidelines for European Region*. Executive summary. 2018. ISBN 978 92 890 5356 3.
- [35] Republic of Poland. Journal of laws (in Polish). No. 120. Item 826. 2007.
- [36] Noise increases with vehicle speed [online] [accessed 2020-02-04]. Available from: <https://www.nonoise.org/resource/trans/highway/spnoise.htm>
- [37] Environmental noise - European Environment Agency [online] [accessed 2020-01-30]. Available from: <https://www.eea.europa.eu/airs/2018/environment-and-health/environmental-noise>
- [38] PERZYNSKI, T., LEWINSKI, A. (2019) Selected telematics solutions in city transport. In: Development of Transport by Telematics TST 2019: proceedings [online]. Vol 1049. Communications in Computer and Information Science. MIKULSKI, J. (ed.). Cham, Springer, 2019. ISBN 978-3-030-27546-4, eISBN 978-3-030-27547-1, p. 202-215. Available from: https://doi.org/10.1007/978-3-030-27547-1_16
- [39] TURCSANY, J. Electric buses and noise [online] [accessed 2020-01-28]. Available from: http://www.bullernatverket.se/wp-content/uploads/2014/05/Electric-buses-and-noise_Volvo-Bus.pdf
- [40] GREGOR, M., JANOTA, A., SLOVACEK, L. (2019). Optimization of fixed time control of road intersection by evolution strategies. In: Development of Transport by Telematics TST 2019: proceedings [online]. Vol 1049. Communications in Computer and Information Science. MIKULSKI, J. (ed.). Cham, Springer, 2019. ISBN 978-3-030-27546-4, eISBN 978-3-030-27547-1, p. 151-164. Available from: https://doi.org/10.1007/978-3-030-27547-1_12



Dear colleague,

Journal Communications - Scientific Letters of the University of Zilina are a well-established open-access scientific journal aimed primarily at the topics connected with the field of transport. The main transport-related areas covered include Civil engineering, Electrical engineering, Management and informatics, Mechanical engineering, Operation and economics, Safety and security, Travel and tourism studies. The full list of main topics and subtopics is available at: <http://komunikacie.uniza.sk/index.php/communications/topics>

Journal Communications - Scientific Letters of the University of Zilina are currently indexed by EBSCO and SCOPUS.

We would like to invite authors to submit their papers for consideration. We have an open-access policy and there are no publication, processing or other fees charged for published papers. Our journal operates a standard double-blind review procedure, the successful completion of which is a prerequisite for paper publication.

The journal is issued four times a year (in January, in April, in July and in October).

I would also like to offer you the opportunity of using already published articles from past issues as source of information for your research and publication activities. All papers are available at our webpage: <http://komunikacie.uniza.sk>, where you can browse through the individual volumes.

For any questions regarding the journal Communications - Scientific Letters of the University of Zilina please contact us at: komunikacie@uniza.sk

We look forward to future cooperation.

Sincerely

Branislav Hadzima
editor-in-chief

THE GPS / EGNOS POSITIONING QUALITY IN APV-1 AND LPV-200 FLIGHT PROCEDURES

Grzegorz Grunwald^{1,*}, Adam Ciećko¹, Kamil Krasuski², Rafał Kaźmierczak¹

¹Faculty of Geoengineering, University of Warmia and Mazury in Olsztyn, Olsztyn, Poland

²Institute of Navigation, Military University of Aviation, Deblin, Poland

*E-mail of corresponding author: grzegorz.grunwald@uwm.edu.pl

Resume

Accuracy, integrity, continuity and availability are the basic quality parameters extremely important in satellite navigation. The article presents results of research using the European Geostationary Navigation Overlay Service (EGNOS) that belongs to the group of Satellite Based Augmentation Systems (SBAS). The measurement data adopted for analysis were recorded in years: 2012, 2014, 2015, 2017 and 2018 in the north-eastern Poland. Results of the analysis showed a significant reduction in the maximum GPS / EGNOS positioning error values from 2014 onwards (compared to results from 2012). In general, values of parameters characterizing accuracy, integrity and availability meet the requirements for EGNOS applications in APV-1 and LPV-200 aviation procedures. In the case of continuity the requirements are not met.

Article info

Received 19 March 2020

Accepted 10 August 2020

Online 18 January 2021

Keywords:

satellite navigation,
SBAS,
EGNOS,
GNSS positioning

Available online: <https://doi.org/10.26552/com.C.2021.2.E23-E34>

ISSN 1335-4205 (print version)

ISSN 2585-7878 (online version)

1 Introduction

The European Geostationary Navigation Overlay Service (EGNOS) is designed to support the operation of Global Navigation Satellite Systems (GNSS), belonging to the SBAS (Satellite Based Augmentation System) group. Currently, it supports the GPS (Global Positioning System) system only, and theoretically GNSS / SBAS positioning should improve the quality of position determination [1-4]. This is associated with use of EGNOS mainly in aviation. Its proper functioning and development have been overseen by the European Union represented by the European Commission, the European Space Agency (ESA) and Eurocontrol (European Organization for the Safety of Air Navigation) since 1994 [5-6].

EGNOS provides its products through three services: OS (Open Service), SoL (Safety of Life), EDAS (EGNOS Data Access Service) and is being gradually modernized [7]. Since the launch of the Safety of Life Service in 2011 [8], there have been 6 new EGNOS versions introduced. The ESR (EGNOS System Release) V2.2 (Initial Entry into Service) was launched in 2011 and the ESR V2.3.1 (software corrections) was commenced in 2012. The ESR V2.3.2 was launched in 2013 in order to improve the EGNOS resistance to influence of the ionosphere effect; however, during the very high ionosphere activity some complications were observed. These deficiencies were corrected in 2015 by the ESR V2.4.1M, which also introduced the LPV-200 operability [9]. The ESR V2.4.1N launched in 2017 was associated with

the new geostationary satellite and new uplink stations. In 2018, further modernizations related to the new RIMS (Ranging Integrity Monitoring Station) activation in Haifa (72° North Lat) and GPS week number rollover, were introduced.

Previous studies on positioning quality using the EGNOS system indicate the possibility of positioning with an accuracy of less than 2m [9-13]. However, in air navigation, values of parameters related to integrity, continuity and availability of positioning are also very important.

Motivation of this article is to examine quality of the GPS / EGNOS positioning in the north-eastern Poland, taking into account modifications of the EGNOS system since 2011. This type of analysis gives an overview of the possibilities of application and expectations of the system in applications related, among others, to air transport.

2 Quality parameters of the GPS / EGNOS positioning

Quality of the real-time positioning is very important in application of satellite systems in aviation. Four main parameters are the most significant in air applications, i.e. accuracy, integrity, availability and continuity [14-16].

Accuracy of the estimated or measured position, at a given time, is defined as its level of certainty relative to the real position of a receiver at that time [14]. Values of the HPE (Horizontal Position Error) and VPE (Vertical Position



Error) can be determined based on the following formulas:

$$HPE_i = \sqrt{(B_i - B_{REF})^2 + (L_i - L_{REF})^2}, \quad (1)$$

$$VPE_i = |H_i - H_{REF}|, \quad (2)$$

where:

HPE_i - horizontal position error for a given epoch,

B_i, L_i - horizontal coordinates determined by the receiver in a topocentric system,

B_{REF}, L_{REF} - horizontal reference coordinates in a topocentric system,

VPE_i - vertical position error for a given epoch,

H_i - ellipsoidal height determined by the receiver for a given epoch,

H_{REF} - ellipsoidal reference height.

Integrity should be understood as the probability and correctness of information provided by the navigation system [14]. The Horizontal Protection Level (HPL) and Vertical Protection Level (VPL) are closely related to integrity of the real-time positioning [4, 17]. The Protection Level (PL) in the horizontal plane (HPL) according to RTCA [17] is the radius of the centre circle in the real position, which corresponds to the area containing the position calculated by the system. In contrast, the vertical Protection Level (VPL) is the length of half the cylinder axis with the centre in the true position, which corresponds to the area containing the vertical position calculated by the system.

The HPL and VPL values are influenced by ionosphere and troposphere activity, satellite geometry, ephemeris errors, satellite clock errors and those related to receiver operation.

During the research, a model for determining the HPL and VPL values in accordance with RTCA guidelines was used. The PL values are determined by the formulas [17-19]:

$$HPL = K_H d_{major}, \quad (3)$$

$$VPL = K_V \sigma_U, \quad (4)$$

where:

K_H - coefficient limiting the horizontal position with probability 10^{-9} (for "en-route" and NPA (Non-Precision Approach) $K_H = 6.18$; for APV-1 approach (Approach with Vertical Guidance) and LPV-200 (Localizer Performance with Vertical Guidance) $K_H = 6.0$),

K_V - coefficient limiting the vertical position with a probability 0.5×10^{-7} ($K_V = 5.33$).

$$d_{major} = \sqrt{\frac{d_E^2 + d_N^2}{2}} + \sqrt{\left(\frac{d_E^2 - d_N^2}{2}\right)^2 + d_{EN}^2}, \quad (5)$$

$$\begin{aligned} d_E^2 &= \sum_{i=1}^n S_{E,i}^2 \sigma_i^2, \quad d_N^2 = \sum_{i=1}^n S_{N,i}^2 \sigma_i^2, \\ d_{EN} &= \sum_{i=1}^n S_{E,i} S_{N,i} \sigma_i^2, \quad d_v^2 = \sum_{i=1}^n S_{U,i}^2 \sigma_i^2, \end{aligned} \quad (6)$$

$$S = \begin{bmatrix} S_{E,1} & S_{E,2} & \cdots & S_{E,n} \\ S_{N,1} & S_{N,2} & \cdots & S_{N,n} \\ S_{U,1} & S_{U,2} & \cdots & S_{U,n} \\ S_{t,1} & S_{t,2} & \cdots & S_{t,n} \end{bmatrix}, \quad (7)$$

where:

S - projection matrix,

d_E^2, d_N^2, d_U^2 - variances of East, North and Up components, expressed in a topocentric system,

d_{EN} - covariance between the East and North axes.

Variance of the pseudo-distance measurement for positioning using the SBAS systems can be determined according to RTCA requirements:

$$\sigma_i^2 = \sigma_{i,flt}^2 + \sigma_{i,UIRE}^2 + \sigma_{i,air}^2 + \sigma_{i,tropo}^2, \quad (8)$$

where:

σ_i^2 - pseudorange measurement variance,

$\sigma_{i,flt}^2$ - variance of fast and long-term corrections,

$\sigma_{i,UIRE}^2$ - variance of ionospheric delay,

$\sigma_{i,air}^2$ - variance related to the operation of the GNSS receiver,

$\sigma_{i,tropo}^2$ - tropospheric delay variance.

For the integrity condition to be met, the PL (HPL and VPL) values must not exceed the Alarm Limits (AL) defined for a given flight stage [20]. The AL should be understood as the maximum allowable HPL and VPL value defined separately for operations NPA, APV-1 and LPV-200 [17]. Loss of integrity occurs when $xPE > xPL$. Ratio of the positioning error to the corresponding PL value is expressed by SI (Safety Index) according to the formula [21]:

$$xSI = \frac{xPE}{xPL}, \quad (9)$$

where:

xSI - safety index, horizontal or vertical,

xPE - horizontal or vertical positioning error,

xPL - horizontal or vertical protection level.

There is a risk of MI (Misleading Information) when the SI value is greater than 0.75. If, however, the ratio is greater than 1, then real MI or HMI (Hazardous Misleading Information) occurs.

Continuity is defined as the ability of the system (containing all the elements necessary to maintain the object's positioning in a given space) to provide a given function for the duration of the intended operation [17]. It is expressed by the probability of maintaining the certain system functions for the duration of the operation phase (assuming that the system was available at the beginning) and is predicted for the duration of the operation. The lack of continuity may occur when the receiver is unable to determine the position or when the PL values exceed the defined AL.

There are two types of loss of continuity [17]:

- long-term loss of continuity (lasting more than 3 seconds)
- independent loss of continuity (it constitutes loss of continuity lasting not less than 3 seconds, determined

Table 1 Required values of quality parameters of the SoL service of the EGNOS system used in aviation [7, 20]

aircraft phase of flight	horizontal accuracy 95%	vertical accuracy 95%	integrity	time to alert (tta)	horizontal alarm limit (hal)	vertical alarm limit (val)	continuity	availability
en-route (oceanic/ continental low density)	3.7 km	n/a	1-1x10 ⁻⁷ /h	5 min	7.4 km	n/a	1-1x10 ⁻⁴ /h to 1-1x10 ⁻⁸ /h	0.99 to 0.99999
en-route (continental)					3.7 km	n/a		
en-route, terminal	0.74 km	n/a	1-1x10 ⁻⁷ /h	15 s	1.85 km	n/a	1-1x10 ⁻⁴ /h to 1-1x10 ⁻⁸ /h	0.99 to 0.99999
initial approach, intermediate approach, non-precision approach (npa), departure	220 m	n/a	1-1x10 ⁻⁷ /h	10 s	556 m	n/a	1-1x10 ⁻⁴ /h to 1-1x10 ⁻⁸ /h	0.99 to 0.99999
approach operations with vertical guidance (apv-1)	16 m	20 m	1-2x10 ⁻⁷ in any approach	10 s	40 m	50 m	1-8x10 ⁻⁶ per 15 s	0.99 to 0.99999
category I precision approach	16 m	6.0 m to 4.0 m	1-2x10 ⁻⁷ in any approach	6 s	40 m	35 m to 10 m	1-8x10 ⁻⁶ per 15 s	0.99 to 0.99999

after the system has been available (PL <AL) for at least 15 seconds).

Continuity risk is the probability of a detected but unscheduled navigation interruption after initiation of an operation. During the analysis performed, the long-term loss of continuity and independent loss of continuity were examined. Risk of the loss of continuity P_{disc} , which is related to independent loss of continuity and P_{slide} , which is related to the long-term loss of continuity, are given below.

Risk of loss of continuity P_{disc} is expressed by Equation (10):

$$P_{disc} = \frac{N_{indep}}{N_{total}} 15, \quad (10)$$

where:

N_{indep} - number of independent single continuity breaks,

N_{total} - number of all the valid measurement epochs.

Risk of loss of continuity P_{slide} can be determined according to:

$$P_{slide} = \sum_{i=1}^{N_d} \frac{\max(15, disc(i))}{N_{total}}, \quad (11)$$

where:

$disc(i)$ - duration of loss of continuity,

N_d - number of single continuity breaks,

N_{total} - number of all valid measurement epochs.

Availability of the navigation system is its ability to provide the required services and appropriate operation at the beginning of the planned operation [17]. It is also the ability of the system to provide the full-fledged services in a specific area. The service is available when the requirements for accuracy, integrity and continuity are met [21].

Availability of the GNSS system is a complex parameter to determine due to the movement of the satellites in relation to the area of operation and the long recovery time in case of a failure detection [22]. It is often determined based on modelling and analysing, rather than by measuring it. However, the real availability of the system can only be

determined by calculations after its operation. The signal availability is the percentage of time in which the signal is transmitted from an external source in a form that is usable. It is a function of physical phenomena surrounding the system and the technical capabilities of transmitting devices. Studies on availability of the EGNOS system in its area of operation have been successively published by the ESSP (monthly and annual reports). However, it should be indicated that availability is a parameter, which should also be studied locally [23-24]. In the study performed as a part of this work, analysis of the EGNOS signal availability, local availability and operational availability were performed. Availability of the EGNOS signal (AV_{SIS}) should be understood as the time ratio, in which at least one geostationary satellite transmits EGNOS messages (Σt_{VS}) to the time of complete test (Σt_{TS}), according to the formula [17]:

$$AV_{SIS} = \frac{\Sigma t_{VS}}{\Sigma t_{TS}}. \quad (12)$$

Availability of the Open Service (AV_{OS}) is a ratio of the number of epochs, in which HPE < 3 m and VPE < 4 m (t_{OS}), to the number of all the measurement epochs (t_{TS}) [21]:

$$AV_{OS} = \frac{\Sigma t_{OS}}{\Sigma t_{TS}}. \quad (13)$$

The operational availability of the EGNOS system (S_{AV}) can be defined as a ratio of the number of samples that are available for a given operation to the total number of the valid epochs. This relationship can be described by [17, 21]:

$$S_{AV} = \frac{\Sigma S_{OS}}{\Sigma S_{TS}}, \quad (14)$$

where:

S_{AV} - operational availability,

ΣS_{TS} - the number of samples that are available for the operation (number of epochs for which in the case of NPA, HPL < 556 m, while in the case of APV-1 and LPV-200, HPL < 40 m and VPL < 50 m),

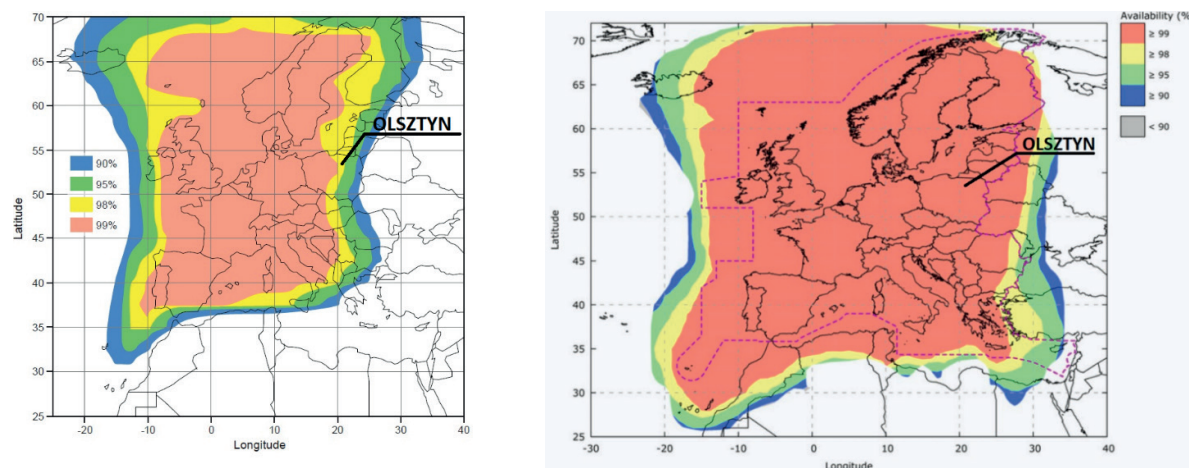


Figure 1 Location of the examined station in Olsztyn against the availability of the EGNOS approach with APV-1 before 2012 (left) and current availability of the EGNOS approach with LPV-200 service (right) [7-8]

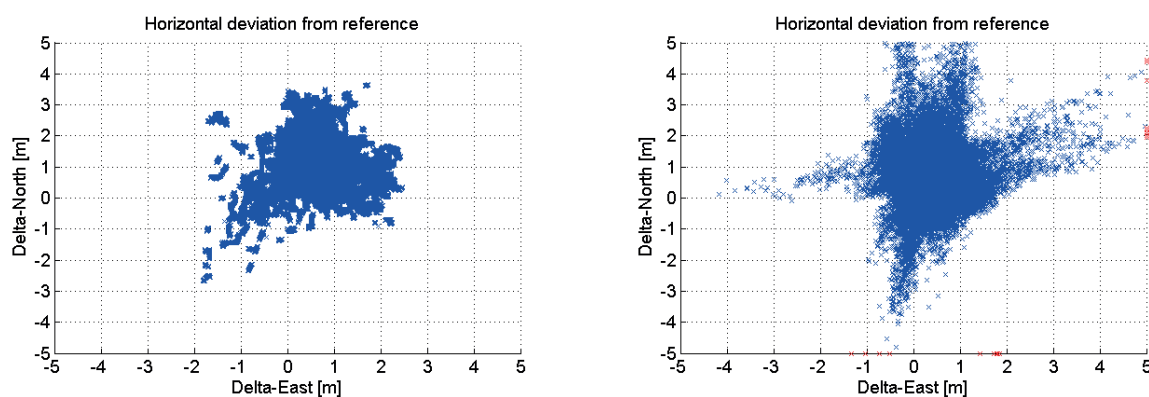


Figure 2 Results of the analyses of the horizontal accuracy of autonomous GPS (left) and GPS / EGNOS (right) positioning during the period 10-14 Dec 2012

ΣS_{OS} - sum of all the available measurement epochs.

The quality of the positioning service must comply with existing requirements for the use of the SBAS systems in aviation [20]. Table 1 contains defined values of parameters characterizing accuracy, integrity, continuity and availability of positioning using the SoL service.

3 Research and results

In order to analyse quality of the GPS / EGNOS positioning, measurement data, collected with the Septentrio AsteRx2 receiver installed at the Warmia-Mazury Aeroclub in Olsztyn (north-eastern Poland), were used. Figure 1 presents location of the examined station against the availability of the EGNOS approach with APV-1 before 2012 and current availability of EGNOS approach with LPV-200 service.

Five days long data sets, from periods that were characterized by operation of different versions of the EGNOS system, were selected for testing. These data sets come from: 10-14 Dec 2012 (ESR V2.3.1), 10-14 Dec 2014 (ESR V2.3.2), 10-14 Dec 2015 (ESR V2.4.1 M), 10-14 Dec 2017 (ESR V2.4.1 N) and 10-14 Dec 2018 (ESR V2.4.1 N). Due to aviation applications, the registration interval was set to 1 second and the elevation mask was set to 5 degrees. When

selecting the location of the receiver, the impact of a possible multipath effect and other satellite signal interference on the measurement results was taken into account.

The data was examined using the latest version of the software for analysing the quality of the SBAS positioning in aviation - PEGASUS v.19.07.03, Septentrio Post Processing SDK package and the self-developed tool - PP_SBAS_Analyzer.

The analyses were carried out in two calculation variants:

- GPS / EGNOS positioning in the APV-1 and LPV-200 mode, using data from the EGNOS geostationary satellites in the positioning process,
- autonomous GPS in the NPA positioning mode, using only data from the GPS satellites.

In the case of the NPA configuration, only measurement periods for which HPL < 556m were taken into account. The APV-1 variant is characterized by periods for which HPL < 40m and VPL < 50m. For the LPV-200 operations, HPL < 40m and VPL < 35m.

3.1 GPS autonomous vs GPS / EGNOS positioning

In the first stage of research the preliminary comparison of the GPS / EGNOS and autonomous GPS positioning is

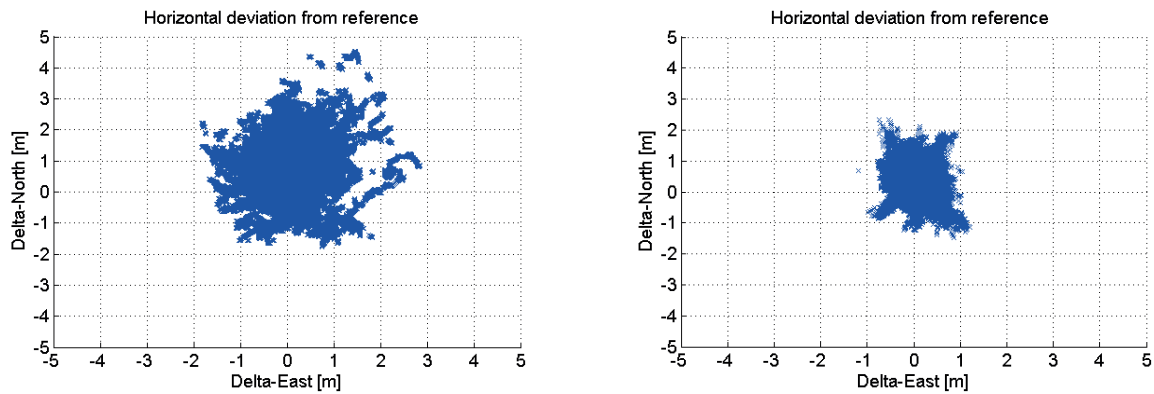


Figure 3 Results of the analyses of the horizontal accuracy of autonomous GPS (left) and GPS / EGNOS (right) positioning during the period 10-14 Dec 2014

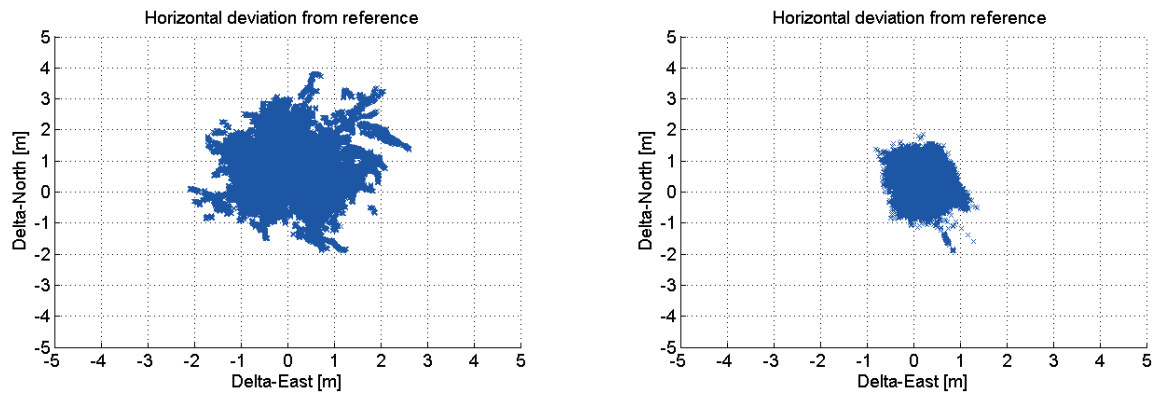


Figure 4 Results of the analyses of the horizontal accuracy of autonomous GPS (left) and GPS / EGNOS (right) positioning during the period 10-14 Dec 2015

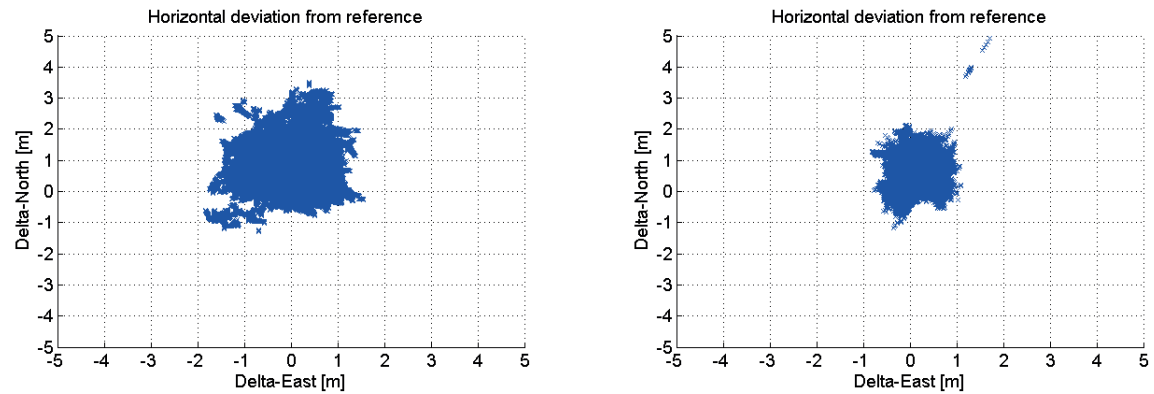


Figure 5 Results of the analyses of the horizontal accuracy of autonomous GPS (left) and GPS / EGNOS (right) positioning during the period 10-14 Dec 2017

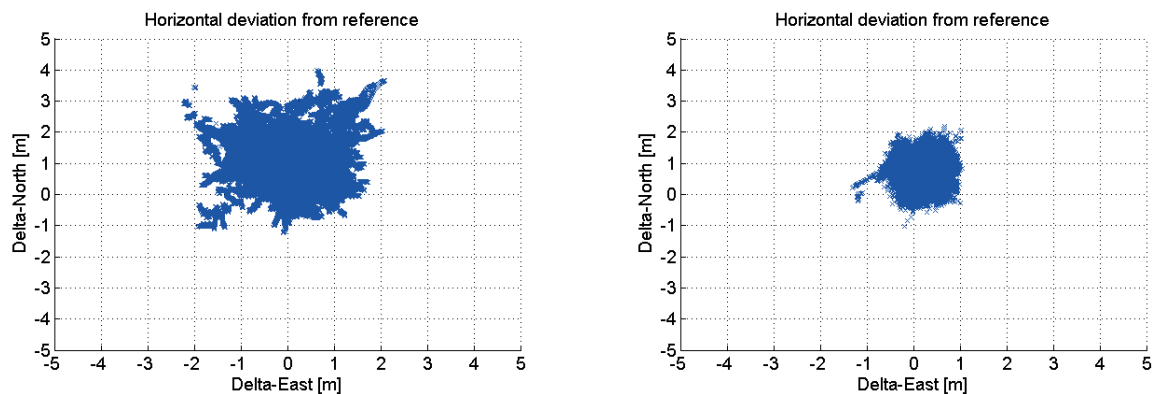


Figure 6 Results of the analyses of the horizontal accuracy of autonomous GPS (left) and GPS / EGNOS (right) positioning during the period 10-14 Dec 2018

Table 2 Results of 95% accuracy values (comparison of autonomous GPS and GPS / EGNOS positioning)

parameter		10-14 December 2012	10-14 December 2014	10-14 December 2015	10-14 December 2017	10-14 December 2018
accuracy	HPE 95% GPS (m)	2.82	2.33	2.07	2.01	2.18
	HPE 95% GPS/ EGNOS (m)	1.41	0.97	0.98	1.12	1.21
	VPE 95% GPS (m)	5.28	6.52	6.17	4.51	4.37
	VPE 95% GPS/ EGNOS (m)	1.53	1.37	1.39	1.21	1.23

Table 3 GPS / EGNOS positioning accuracy results

parameter	10-14 December 2012	10-14 December 2014	10-14 December 2015	10-14 December 2017	10-14 December 2018
HPE 95% APV-1 (m)	1.40	0.97	0.98	1.12	1.21
HPE 95% LPV-200 (m)	1.40	0.97	0.98	1.12	1.21
VPE 95% APV-1 (m)	1.59	1.37	1.39	1.21	1.23
VPE 95% LPV-200 (m)	1.59	1.37	1.39	1.21	1.23
HPE _{max} (m)	19.10	3.55	2.08	5.20	2.30
VPE _{max} (m)	51.48	3.37	3.42	6.26	1.15
HPE _{mean} (m)	0.87	0.54	0.57	0.67	0.74
VPE _{mean} (m)	0.64	0.57	0.54	0.48	0.50
HPE _{stand. dev.} (m)	0.32	0.25	0.24	0.25	0.26
VPE _{stand. dev.} (m)	0.50	0.42	0.43	0.38	0.39

presented. Such an analysis allowed for the evaluation of the EGNOS system itself and elimination of the possibility of the local measurement conditions impact (e.g. multipath effect) on the measurement results. For this purpose, horizontal positioning accuracy analyses were done and compiled in Figures 2-6.

Based on the horizontal analyses, it is possible to observe a similar value of the HPE (up to about 4m) for the autonomous GPS variant in all of the examined measurement sessions. At the same time, the GPS / EGNOS HPE seems to be more differentiated for the test sessions. Noteworthy is the high value of GPS / EGNOS positioning errors in 2012 (even above 5 m). During the measurement sessions in subsequent years, values of these errors were more concentrated and were within 2m (except for several epochs in 2017). The results obtained may indicate a significant impact of the change in the EGNOS software on accuracy since 2014. Table 2 presents results of the horizontal and vertical analyses of the GPS autonomous and GPS / EGNOS positioning accuracy.

Analysis of the HPE 95% and VPE 95% values showed similar improvement in GPS / EGNOS positioning compared to autonomous GPS in each measurement session. In the case of horizontal positioning, the ratio of the HPE 95% for GPS / EGNOS to HPE 95% for autonomous GPS is similar in each session (about 0.50). The situation is similar in the case of the vertical analysis: the ratio of VPE 95% for GPS / EGNOS to VPE 95% for autonomous GPS is about 0.30 in each of the examined sessions. Therefore, these analyses did not show a significant improvement in the quality of positioning in measurement sessions related to different

versions of the EGNOS system. Considering the significant differences in horizontal positioning errors presented in horizontal plots (Table 2), it can be stated that the modernization of the EGNOS system after 2012 significantly reduced the maximum values of positioning errors.

In the next stage of research, changes in the GPS / EGNOS positioning quality related to the implementation of subsequent versions of the EGNOS system were analysed in detail.

3.2 GPS/EGNOS accuracy analysis

The first quality parameter analysed is positioning accuracy. Results of the GPS / EGNOS positioning accuracy analysis are presented in Table 3:

Results of the APV-1 and LPV-200 horizontal and vertical accuracy analyses are the same. The maximum xPE 95% values were obtained for the 2012 session (HPE 95% = 1.40m, VPE 95% = 1.59 m). In the same measurement session, maximum positioning errors were also obtained (HPE_{max} = 19.10m, VPE_{max} = 51.48 m). The results from the other measurement sessions are at a similar level, significantly better than that from 2012.

3.3 GPS/EGNOS integrity analysis

The next stage of research is analysis of parameters characterizing the integrity of GPS / EGNOS positioning. This was carried out using Stanford diagrams presenting

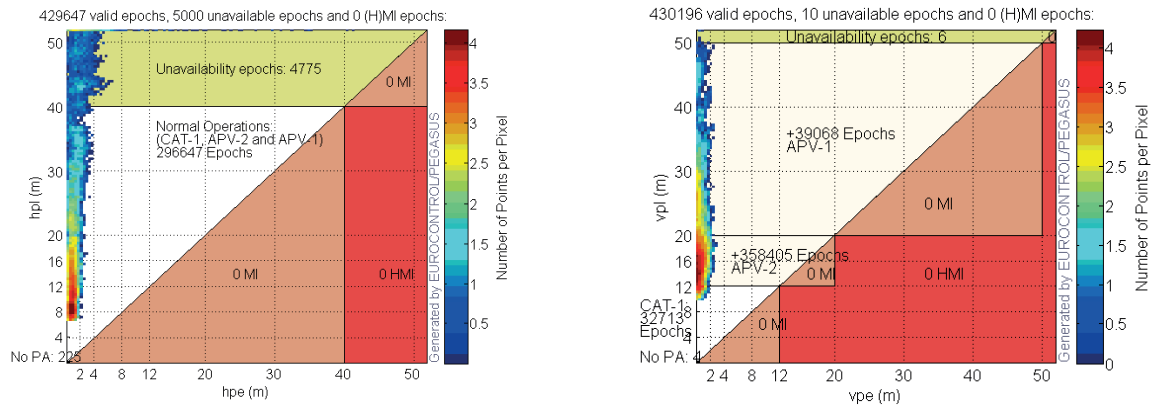


Figure 7 Horizontal (left) and Vertical (right) Stanford diagrams related to integrity analysis for the period 10-14 Dec 2012

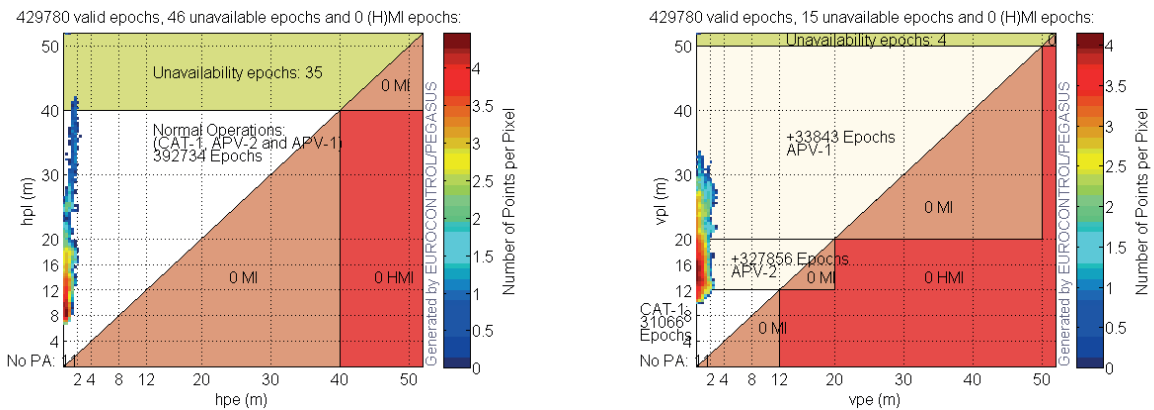


Figure 8 Horizontal (left) and Vertical (right) Stanford diagrams related to integrity analysis for the period 10-14 Dec 2014

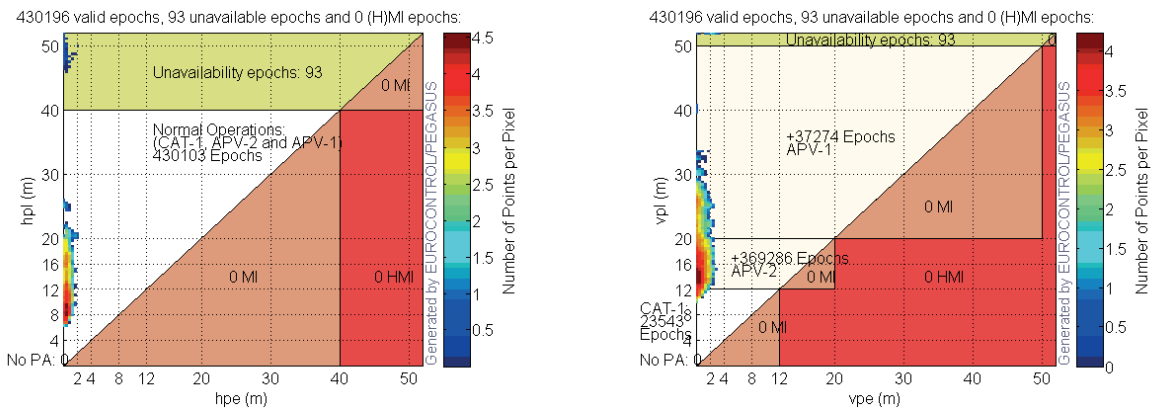


Figure 9 Horizontal (left) and Vertical (right) Stanford diagrams related to integrity analysis for the period 10-14 Dec 2015

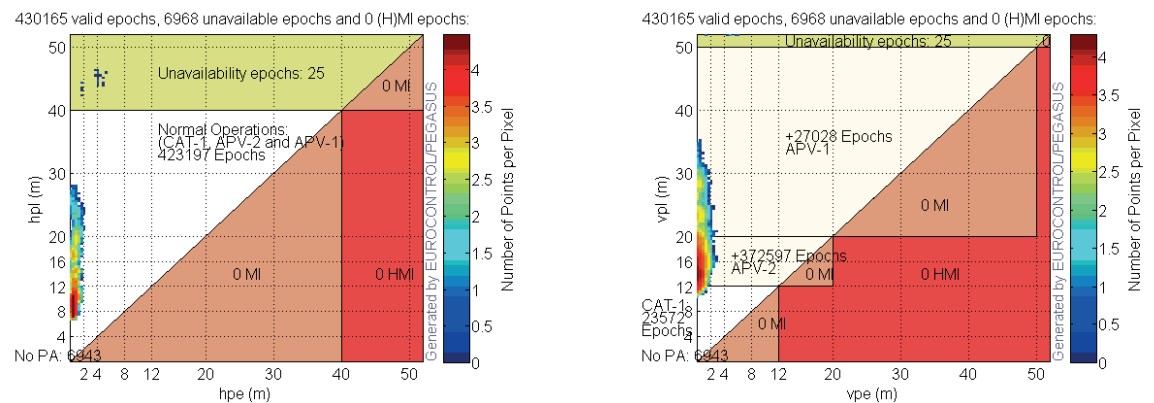


Figure 10 Horizontal (left) and Vertical (right) Stanford diagrams related to integrity analysis for the period 10-14 Dec 2017

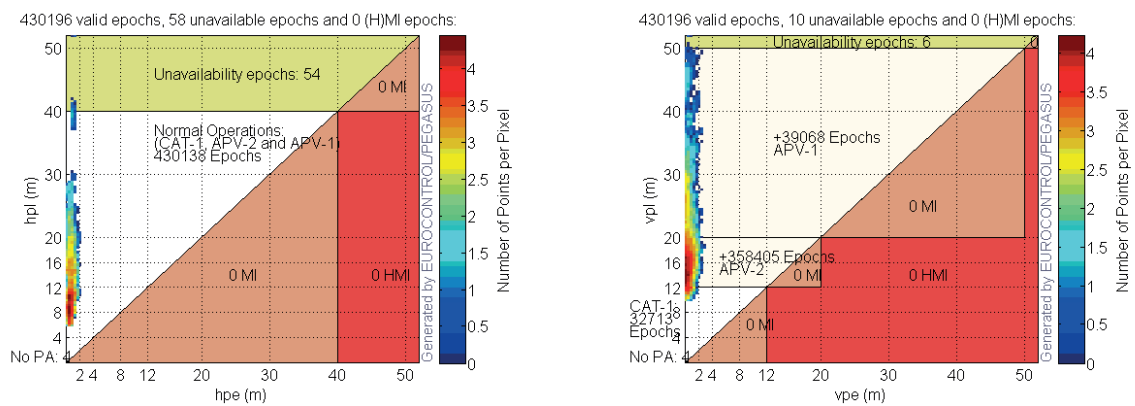


Figure 11 Horizontal (left) and Vertical (right) Stanford diagrams related to integrity analysis for the period 10-14 Dec 2018

Table 4 Results of the integrity analysis

parameter	10-14 December 2012	10-14 December 2014	10-14 December 2015	10-14 December 2017	10-14 December 2018
HPL 99% (m)	19.56	19.39	18.66	19.86	21.40
VPL 99% (m)	28.44	26.15	26.45	28.02	30.41
HPL _{min} (m)	6.11	6.77	6.34	6.43	5.63
VPL _{min} (m)	10.21	10.01	9.92	10.27	9.71
HPL _{mean} (m)	10.53	10.21	10.00	9.68	10.13
VPL _{mean} (m)	15.87	15.51	15.57	15.36	15.87
HPL _{stand. dev.} (m)	3.06	2.69	2.70	2.56	3.09
VPL _{stand. dev.} (m)	3.71	3.21	3.25	3.08	3.92
HSI LPV-200 100%	0.20	0.16	0.17	0.18	0.21
VSI LPV-200 100%	0.19	0.22	0.20	0.18	0.17

the values of HPL, VPL, HPE and VPE on the background of requirements at individual stages of aviation operations. Figures 7-11 present results of the integrity analysis.

The worst results were obtained for data from 2012. In this period 4775 measurement epochs did not meet the requirements of horizontal accuracy for procedures in accordance with APV-1, which coincides with the worst results obtained for this period from the accuracy analysis. The analyses carried out for the rest of periods are characterized by much better results, all at a similar level. The number of epochs not available for APV-1 procedures ranges from a few to about 100. Table 4 presents results of a detailed analysis related to the HPL and VPL values.

The HPL 99% and VPL 99% values are at a comparable level during all of the measurement sessions. Analysis of the HSI and VSI values showed very good and similar results in all the measurement sessions (about 0.20 for both horizontal and vertical analysis). These results met the integrity requirements for the safe air navigation. There was no risk of MI (SI values greater than 0.75) in any of the measurement sessions.

The research was additionally extended by analysis of a parameter characterizing differences between the protection levels and positioning errors. The SI coefficient values should be as low as possible for air navigation applications. However, protection levels that are too high, in

relation to actual positioning accuracy, can have a negative impact on the optimal application possibilities of the SBAS. Therefore, it was proposed to introduce parameters presenting differences between the protection levels and the real positioning errors:

$$\Delta HP = HPL - HPE, \quad (15)$$

$$\Delta VP = VPL - VPE. \quad (16)$$

Such analysis allows to assess the quality of the integrity model used in the examined cases. Values of ΔHP and ΔVP were determined for each of the tested measurement sessions. Then, the mean values (ΔHP_{mean} and ΔVP_{mean}) and their median ($\Delta HP_{\text{median}}$ and $\Delta VP_{\text{median}}$) of obtained values were determined. Table 5 shows the values obtained from the analysis for ΔHP and ΔVP .

The mean values of ΔHP and ΔVP are the largest for the 2012 session (10.94 m and 17.33 m respectively), which is due to quite large maximum positioning errors (HPE and VPE) for these measurement data. For the remaining sessions in the years 2014, 2015, 2017 and 2018 the average values of horizontal and vertical differences are smaller and are at a similar level (from 8.80 m to 9.71 m for the horizontal parameter and from 14.55 m to 15.30 m for the vertical parameter).

Table 5 Results of the analysis of differences between the *xPL* and *xPE*.

parameter	10-14 December 2012	10-14 December 2014	10-14 December 2015	10-14 December 2017	10-14 December 2018
$\Delta\text{HP}_{\text{mean}}$ (m)	10.94	9.71	9.40	8.80	9.35
$\Delta\text{VP}_{\text{mean}}$ (m)	17.33	14.93	14.96	14.55	15.30
$\Delta\text{HP}_{\text{median}}$ (m)	8.79	9.09	8.54	8.50	8.78
$\Delta\text{VP}_{\text{median}}$ (m)	14.33	14.48	14.20	14.17	14.60

Table 6 The results of the availability analysis

parameter	10-14 December 2012	10-14 December 2014	10-14 December 2015	10-14 December 2017	10-14 December 2018
signal in space availability	0.997916	0.996143	1.00000	0.996860	0.999991
local availability	0.996421	0.991146	0.995824	0.992712	0.995815
operational availability APV-1	0.992581	0.991053	0.995609	0.992623	0.995685
operational availability LPV-200	0.990833	0.990910	0.995569	0.990623	0.991692

Table 7 Results of the continuity analysis

parameter	10-14 December 2012	10-14 December 2014	10-14 December 2015	10-14 December 2017	10-14 December 2018
all discontinuity events APV-1	8	17	1	-	7
all discontinuity events LPV-200	23	13	2	-	9
long discontinuity events APV-1	5	4	1	-	1
long discontinuity events LPV-200	6	4	2	-	6
independent discontinuity events APV-1	3	3	1	-	1
independent discontinuity events LPV-200	3	3	2	-	1
P_{disc} APV-1	0.000188652	0.000105107	0.000034875	-	0.000034873
P_{disc} LPV-200	0.000188984	0.000105122	0.000069754	-	0.000210079
P_{slide} APV-1	0.000357782	0.000226564	0.000034875	-	0.000255733
P_{slide} LPV-200	0.000198545	0.000175204	0.000069754	-	0.000837980

On the other hand, the median values of the ΔHP and ΔVP are at a similar level for each measurement session (from 8.50m to 9.09m for horizontal parameter and from 14.17m to 14.60m for vertical parameter). These results are due to the fact that the median values are resistant to the extreme values of ΔHP and ΔVP .

The results of the ΔHP and ΔVP analyses showed a significant improvement in the performance of the integrity model after 2012, which resulted in better alignment of the protection levels with positioning errors.

3.4. GPS/EGNOS availability analysis

According to [21], the time at which the EGNOS data

is transmitted via at least one geostationary satellite was analysed. The PRN 120 satellite was selected as the basic satellite for the periods 10-14 Dec 2012, 10-14 Dec 2014 and 10-14 Dec 2015, while the satellite PRN136 was selected for the periods 10-14 Dec 2017 and 10-14 Dec 2018.

Table 6 presents the results of the availability analysis prepared based on observations carried out on 10-14 Dec in 2012, 2014, 2015, 2017 and 2018. Signal availability, local availability, APV-1 operational availability and operational availability of LPV-200 were examined.

Availability of the EGNOS Signal in Space in each of the examined periods obtains a result close to 100%. Local availability, operational availability of the EGNOS APV-1 and LPV-200 reaches the better result than 99% in each measurement session tested, which meets the requirements

of the guidelines for the EGNOS applications in aviation [17].

3.5 GPS/EGNOS continuity analysis

In the studies, occurrence of all the cases of the continuity loss for the APV-1 and LPV-200, i.e. long-term phenomena of loss of continuity (APV-1 and LPV-200), independent phenomena of loss of continuity (APV-1 and LPV-200), risk of loss of continuity P_{disc} , P_{slide} (APV-1 and LPV-200) were analysed. In the case of the APV-1 variant, only the measurement periods for which the APV-1 solution was available ($HPL < 40\text{m}$ and $VPL < 50\text{m}$) were included in the calculation. The LPV-200 variant covers all the measurement epochs for which $HPL < 40\text{m}$ and $VPL < 35\text{m}$. Table 7 presents results of the EGNOS system continuity analysis over the periods considered.

Only in the 2017 session there were no instances of loss of continuity. Most of them occurred in the session of 2014 (17 cases). Due to the diversity of results in individual sessions, it was not possible to combine results of the continuity test with the modernization of the EGNOS system. The EGNOS system, according to requirements, can be used if $P_{disc}^{APV-1} < 8 \times 10^{-6}$. The same requirements must be met for the LPV-200 operations. Thus, the positioning results of each measurement session do not meet the requirements for GPS / EGNOS APV-1 and LPV-200 positioning continuity. It should be noted, however, that measurement sessions lasting 5 days are not long enough to

test the continuity of the GPS / EGNOS positioning. Thus, the results obtained can only be an indication of a problem that should be further investigated.

4 Conclusions

The analysis results presented in the article may suggest the readiness of the EGNOS system for applications using APV-1 and LPV-200 aviation procedures. The presented results of the analysis carried out in 2012, 2014, 2015, 2017 and 2018 indicate an improvement of the GPS / EGNOS positioning since 2014, which has significantly reduced value of the maximum positioning errors. For the safe air navigation, horizontal and vertical positioning accuracy of a few meters is sufficient. Much more important is the integrity of navigation data received by pilots through navigation devices. Results of analyses confirm that the integrity requirements for the safe air navigation are met. Additionally, the authors proposed an introduction of new parameters ΔHP and ΔVP , which show the differences between the protection levels and real positioning errors. This comparison allows to assess the quality of the integrity model used in the analysed cases. Values of the ΔHP and ΔVP parameters show a great improvement in functioning of the GPS/EGNOS integrity model after 2012. Results of the continuity analysis indicate disturbances in the operation of the system that are not associated with software upgrades occurring with different versions of the EGNOS system. The availability analysis presents satisfactory results for applications in the APV-1 and LPV-200 procedures.

References

- [1] JAIN, C., BAGCHI, S. GNSS based ionosphere characterization for SBAS. *International Journal of Engineering Technology Science and Research* [online]. 2018, **5**(3), p. 788-796 [accessed 2020-01-12]. ISSN 2394 - 3386. Available from: http://www.ijetsr.com/images/short_pdf/1521730491_788-796-dyp177_ijetsr.pdf
- [2] EL-MOWAFY, A., WANG, K. Second generation SBAS-performance analysis and bridging positioning and integrity monitoring during SBAS outages in the urban environment. In: 32nd International Technical Meeting of the Satellite Division of the Institute of Navigation ION GNSS+ 2019: proceedings. 2019. ISBN: 0-936406-23-2, p. 2842-2854.
- [3] IMPARATO, D., EL-MOWAFY, A., RIZOS, C., WANG, J. Vulnerabilities in SBAS and RTK positioning in intelligent transport systems: an overview. In: International Global Navigation Satellite Systems Association IGNSS Symposium 2018: proceedings [online] [accessed 2020-01-11]. 2018. Available from: http://www.ignss2018.unsw.edu.au/sites/ignss2018/files/u80/Papers/IGNSS2018_paper_10.pdf
- [4] LI, L., JIA, C., ZHAO, L., CHENG, J., LIU, J., DING, J. Real-time single frequency precise point positioning using SBAS corrections. *Sensors* [online]. 2016, **16**(8), 1261 [accessed 2020-01-11]. ISSN 1424-8220. Available from: <https://doi.org/10.3390/s16081261>
- [5] ALLIEN, A., TAILLANDER, C., CAPO, C. User guide for EGNOS application development - ESA [online] [accessed 2020-01-03]. 2009. Available from: <https://op.europa.eu/en/publication-detail/-/publication/9028327b-8122-4cfc-97a8-4243c7d78039>
- [6] About EGNOS [online] [accessed 2020-01-05]. Available from: http://egnos-user-support.essp-sas.eu/new_egnos_ops/?q=content/about-egnos
- [7] GSA - European global navigation satellite systems agency. Safety of life service definition document [online] [accessed 2019-12-20]. V 3.3. 2019. Available from: https://egnos-user-support.essp-sas.eu/new_egnos_ops/sites/default/files/library/official_docs/egnos_sol_sdd_in_force.pdf
- [8] GSA - EUROPEAN COMMISSION. Safety of life service definition document. V 1.0. 2011.

- [9] ESSP ready to provide LPV-200 [online] [accessed 2012-01-08]. Available from: https://ec.europa.eu/transport/modes/air/ses/ses-award-2016/projects/essp_en 2019
- [10] CIECKO, A., GRUNWALD, G., Klobuchar, NeQuick G, and EGNOS ionospheric models for GPS/EGNOS single-frequency positioning under 6-12 September 2017 space weather events. *Applied Sciences* [online]. 2020, **10**, 1553 [accessed 2020-03-10]. ISSN 2076-3417. Available from: <https://doi.org/10.3390/app10051553>
- [11] GRUNWALD, G., BAKULA, M., CIECKO, A., KAZMIERCZAK, R. Examination of GPS/EGNOS integrity in north-eastern Poland. *IET Radar Sonar and Navigation* [online]. 2016, **10**(1), 114 [accessed 2020-01-06]. ISSN 1751-8784. Available from: <http://dx.doi.org/10.1049/iet-rsn.2015.0053>
- [12] GRUNWALD, G., BAKULA, M., CIECKO, A. Study of EGNOS accuracy and integrity in eastern Poland. *The Aeronautical Journal* [online]. 2016, **120**(1230), p. 1275-1290 [accessed 2020-01-06]. ISSN: 2059-6464. Available from: <https://doi.org/10.1017/aer.2016.66>
- [13] SPECHT, M. Method of evaluating the positioning system capability for complying with the minimum accuracy requirements for the international hydrographic organization orders. *Sensors* [online]. 2019, **19**, 3860 [accessed 2020-01-22]. eISSN 1424-8220. Available from: <https://doi.org/10.3390/s19183860>
- [14] Federal radionavigation plan - Department of Defense. Department of Homeland Security, and Department of Transportation. [online] [accessed 2019-12-22]. 2017. Available from: <https://www.navcen.uscg.gov/pdf/FederalRadioNavigationPlan2017.pdf>
- [15] KRZYKOWSKA, K., KRZYKOWSKI, M. Forecasting parameters of satellite navigation signal through artificial neural networks for the purpose of civil aviation. *International Journal of Aerospace Engineering* [online]. 2019, **2019**, 7632958 [accessed 2020-12-10]. ISSN 1687-5974. Available from: <https://doi.org/10.1155/2019/7632958>
- [16] NIE, Z., ZHOU, P., LIU, F., WANG, Z., GAO, Y. Evaluation of orbit, clock and ionospheric corrections from five currently available SBAS L1 services: methodology and analysis. *Remote Sensing* [online]. 2019, **11**(4), 411 [accessed 2020-01-05]. eISSN 2072-4292. Available from: <https://doi.org/10.3390/rs11040411>
- [17] RTCA - RADIO TECHNICAL COMMITTEE FOR AERONAUTICS. Minimum operational performance standards for airborne equipment using global positioning system/wide area augmentation system. Doc. DO-229D. RTCA, Inc. (RTCA). 2013.
- [18] WALTER, T., BLANCH, J., ENGE, P. L5 Satellite based augmentation systems protection level equations. In: International Symposium on GPS/GNSS: proceedings. 2007.
- [19] TIBERIUS, C., ODIJK, D. Does the HPL bound the HPE? In: NaviTec'08 workshop: proceedings. ESA-Estec. 2008.
- [20] ICAO - INTERNATIONAL CIVIL AVIATION ORGANIZATION. Radio navigation aids. Standards and recommended practices (SARPS). 2014, Annex 10 Volume I.
- [21] EGNOS SERVICE PROVIDER. Monthly performance report [online] [accessed 2020-03-10]. 2020. Available from: https://egnos-user-support.essp-sas.eu/new_egnos_ops/sites/default/files/documents/105%20-%20Monthly%20Performance%20Report%20-%20January%202020.pdf
- [22] OCHIENG, W. Y., SAUER, K., WALSH, D., BRODIN, G., GRIFFIN, S., DENNEY, M. GPS integrity and potential impact on aviation safety. *The Journal of Navigation*. 2003 **56**(1), p. 51-65. ISSN 0373-4633.
- [23] FELSKI, A., NOWAK, A., WOZNIAK, T. Accuracy and availability of EGNOS - results of observations. *Artificial Satellites* [online]. 2011, **46**, p. 111-118 [accessed 2020-01-10]. ISSN 2083-6104, Available from: <https://doi.org/10.2478/v10018-012-0003-0>
- [24] FELSKI, A., NOWAK, A. On EGNOS monitoring in local conditions. artificial satellites [online]. 2013, **48**(2), p. 85-92 [accessed 2020-01-10]. ISSN 2083-6104, Available from: <https://doi.org/10.2478/arsa-2013-0007>

Annex

Abbreviation	Full name
EGNOS	European Geostationary Navigation Overlay Service
SBAS	Satellite Based Augmentation Systems
GPS	Global Positioning System
RTCA	Radio Technical Commission for Aeronautics
GNSS	Global Navigation Satellite Systems
ESA	European Space Agency
OS	Open Service
SoL	Safety of Life
EDAS	EGNOS Data Access Service
ESR	EGNOS System Release
HPE	Horizontal Position Error
VPE	Vertical Position Error
HPL	Horizontal Protection Level
VPL	Vertical Protection Level
PL	Protection Level
NPA	Non-Precision Approach
APV-1	Approach with Vertical Guidance
LPV-200	Localizer Performance with Vertical Guidance
AL	Alarm Limits
SI	Safety Index
MI	Misleading Information
HMI	Hazardous Misleading Information

SELECTED ASPECTS OF THE ROAD TRAFFIC SAFETY MANAGEMENT SYSTEM

Monika Stoma¹, Jacek Caban², Agnieszka Dudziak^{1,*}, Andrzej Kuranc¹

¹Department of Power Engineering and Transportation, Faculty of Production Engineering, University of Life Sciences in Lublin, Lublin, Poland

²Department of Automation, Faculty of Mechanical Engineering, Lublin University of Technology, Lublin, Poland

*E-mail of corresponding author: agnieszka.dudziak@up.lublin.pl

Resume

The article is an attempt to present the two modern concepts of safety management systems. The first is the sunflower pyramid used especially in Europe, the second is the ISO 39001 standard (Road Safety Management System) of international scope. The idea and possibilities offered by use of both concepts of safety management, as well as an attempt to assess the impact of their actions on decrease in fatalities in selected EU countries, were presented. As a result of the conducted analyses, a downward trend was noted as to the number of certificates issued for compliance with the ISO 39001 standard in the world, which may indicate an appearance of the more adequate management systems, or other tools or concepts to improve the road safety, or inadequate education society and low level of awareness in this area of stakeholders, including politicians, scientists, producers, drivers (professional and reliable), as well as other road users, including unprotected ones.

Article info

Received 17 September 2020

Accepted 21 October 2020

Online 12 March 2021

Keywords:

city logistics,
traffic safety,
standardisation,
road situation

Available online: <https://doi.org/10.26552/com.C.2021.2.F33-F42>

ISSN 1335-4205 (print version)

ISSN 2585-7878 (online version)

1 Introduction

Transportation of goods and people is a fundamental concern of modern societies [1]. The transport sector is influenced by a wide range of external social and economic factors, such as demographics, living standards of the population, urban planning, organization of production, structural changes in society and accessibility to transport infrastructure [2]. One of the trends of the last decade is a significant increase in road traffic [3]. As a result, the problem of the road traffic safety is now an important and often even a key issue in many countries. This is due to a large number of traffic incidents, especially those resulting in serious injuries or deaths of their participants. Since the road traffic safety is a growing concern for societies and governments around the world, more emphasis should be placed on improving infrastructure, vehicle condition and professionalism through training of drivers in the road transport sector. A necessary condition for reducing the number of road traffic accidents is also increasing knowledge of their main causes, as well as awareness of the road traffic safety of all interested parties, including politicians, scientists, manufacturers, machines operators, professional drivers, individual drivers and other road users.

2 Literature review

Road traffic accidents are a serious social problem in modern societies. Every year, about 1.35 million people die on the roads and about 50 million are injured [4-6]. It should be added that the so-called Unprotected Road Users (URU), i.e. pedestrians, cyclists and users of the two-wheel motor vehicles, by the European Union statistics, have a share in the road fatal accidents, which in 2014 was: 22% for pedestrians, 8% for cyclists and 18% for users of two-wheeled motor vehicles. Thus, unprotected road users make up 48% of all the fatalities and about two-thirds of all road traffic accidents victims [7]. The situation is similar in relation to other countries in the world - according to the WHO report for 2017, more than half of fatalities are pedestrians, cyclists and motorcyclists [6]. Most pedestrians are killed in Africa (40%) and in the Middle East (34 %). In Poland, this ratio is 29% (it was also at a similar level in Egypt, Estonia, Israel, Slovakia, Cyprus and Sudan). In contrast, for motorcyclists, the worst situation is in Southeast Asia (43% killed) and in the western Pacific (36 %). The average for all of Europe is 11%, this indicator is also at the same level in Poland.

Injuries in the road traffic accidents are the eighth leading cause of death in the world [8], more people die



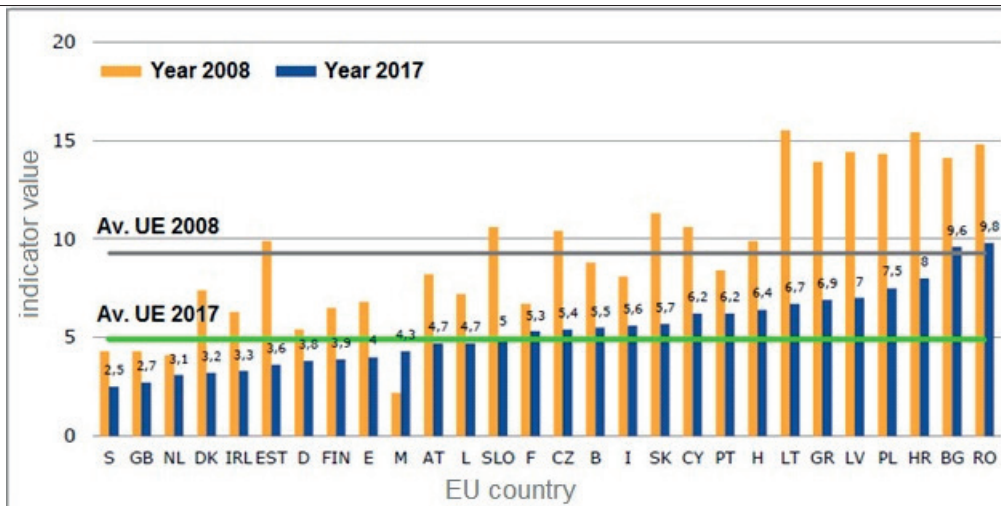


Figure 1 Demographic indicator: number of people killed/100,000 residents in EU countries in 2008 and 2017, prepared based on data provided by the European Commission [10]

on the road than die of AIDS or tuberculosis. It should be added that, according to WHO data, more than half of the people killed in the road traffic accidents are young people, aged from 15 to 44 years. Even worse, these statistics fall for people in the 10-24 age bracket, where the road traffic accidents kill more people than any other cause and - according to WHO forecasts - it is expected that by 2030 this value will increase by 65%. Especially in the low- and middle-income countries, the percentage of road traffic accidents is twice as high as in the high-income countries and is still rising. This is mainly due to the rapid increase in the automotive index in developing countries, without investments related to the road traffic safety at the same time. Current trends suggest that, unless an action is taken, the road traffic accidents will become the fifth most common cause of death by 2030, compared to e.g. tuberculosis (26th place) or malaria (15th place). It should be added that differences between the high- and low-income countries will constantly increase [6]. It is also estimated that death as a result of road traffic accidents will become the second cause of health losses for men in 2030 and the main cause for children (age 5-14) from 2015 [9]. Such a scenario can be realistic if no new initiatives are taken to improve the state of the road traffic safety. Figure 1 presents a comparison of the demographic indicator: number of killed/100,000 residents in EU countries in 2008 and 2017.

The smallest value of this indicator in 2017 was in Sweden - 2.5 (in addition, the member countries with the best results in terms of the road safety were also the United Kingdom and the Netherlands), the highest in Romania - 9.8 (a high rate can also be seen in Bulgaria and Croatia). In Poland the value of this indicator was 7.5. It should be added that European roads are among the safest in the world [11].

Other data and statistics contained in the WHO Report on fatalities in the road traffic accidents in the European Union in 2017 are also worrying. It follows from them that:

- 8% of traffic fatalities occurred on motorways, 55% on rural roads and 37% in urban areas.

- 76% of traffic fatalities on EU roads are men and 24% are women.
- almost 14% of road traffic fatalities are young people, aged from 18 to 24 years, while only 8% of the European population belongs to this age group.
- the proportion of elderly fatalities increased from 22% in 2010 to 27% in 2017, because of demographic trends manifested around the world today (aging population).

It is worth noting that, as can be seen from the data presented in Figure 1, Poland has a permanently high rate of people killed in road traffic accidents. It should be added that in 2018 there were 31,674 road traffic accidents, as a result of which 2,862 people were killed and 37,359 people were injured [12]. In the same year, 436,414 road traffic collisions were reported to Police units. It is worth adding that in 2008 it was 5,437 traffic fatalities.

The consequences of collisions and road traffic accidents can be considered in both health and financial aspects. They represent a burden on individuals and society; they are important for various social groups and institutions: for people who participate in road traffic, for units directly involved in the road traffic safety (e.g. road rescue units) and for the whole society. For example, Kucmin et al. in [13], presented a study on the symptoms of post-traumatic stress disorder of paramedics caused by work in road traffic accidents. Social and psychological effects related to the road traffic safety are widely presented in monograph [14]. In [15], Hanzl also presents research on traffic management and control and possible costs related to its organization, caused by a road traffic accident and temporary traffic closure on the highway. The change in the organization of road traffic also affects the level of traffic safety in this area, because it increases the movement of trucks and passenger cars, causes communication difficulties in the local community. In turn, Drozdziel and Wrona [16] studied the issues of vehicles traveling on expressways and motorways in Poland. They indicated the legal conditions that regulate the rules for vehicles traveling on this type of

roads and presented selected road incidents with serious consequences.

It should be added that it is expected that the share of the road traffic accidents, including fatal accidents, especially in relation to URUs may increase, despite development of information technologies, mainly due to the aging of the population, as well as the intensification of urbanization. Some of them can be prevented with relatively simple measures, while others require much more investment, especially in the areas of infrastructure, legislation and law enforcement [8].

Therefore, the new procedural solutions should be sought that would allow reducing the negative impact of the road traffic on society, the environment and economy. Improving global road safety is due to the broader vision of sustainable development and poverty reduction. Therefore, there was a need to create optimized road traffic safety management systems, under the basic assumption that effective organization of the road traffic safety management is one of the conditions for better results in this area [17-18]. Johnston [19] argues that key success factors in countries with the lowest mortality rates or greatest progress are due to the proper identification of problems and development, evidence-based strategies, combined with ambitious quantitative goals and transparent institutional accountability. The road traffic safety management contains all these elements.

Therefore, there is a need to create optimized concepts and the road traffic safety management systems. This is a challenge from the point of view of social benefits, but also political and economic [20]. It should be remembered, however, that to achieve a significant improvement in the road traffic safety at the national level, a systematic approach to the traffic safety management with precisely defined obligations and responsibilities is necessary. As shown by experience of some countries, this is not so obvious, because in many cases the undertaken actions are unsystematic, fragmented and not based on knowledge, which causes their ineffectiveness [21]. Bliss and Breen [22] suggest that effective of the road traffic safety management can be achieved through a variety of structural and procedural forms, making it difficult to identify one: "good practice" model. Papadimitriou and Yannis [23] conducted comprehensive research on the road traffic safety management systems in 14 European countries, which showed that not all the elements of a "good practice" of the road traffic safety management are always met in all the countries, especially in those in worse condition economic.

3 Objective of the work

Therefore, the aim of this work is to present opportunities to improve the road traffic safety by implementing the concept of the road traffic safety management systems. As already mentioned, one of the solutions is the sunflower pyramid used in European Union

countries. The second option is management according to the international ISO 39001 standard. The article is therefore an attempt to present the possibilities of both systems (concepts) in reducing the number of traffic fatalities in selected countries of the European Union and their relation to the demographic indicator (number of people killed/100,000 residents).

4 Methodology

In this study the possibilities offered by use of two concepts of the safety management are presented, as well as an attempt to assess the impact of their actions on the decrease in fatalities in selected EU countries.

Among the many standards and procedures functioning in relation to the RTSMS and allowing for benchmarking of the road traffic safety and safety trends and for a quantitative representation of national security, there is the so-called "SUNflower pyramid". It is intended to be used for security comparisons between all the countries in the European Union, as well as other countries around the world. This approach creates a conceptual framework to identify factors that improve the road traffic safety.

The second option is management according to the international ISO 39001 standard Road Traffic Safety Management System (RTSMS). This standard has been designed in such a way as to help organizations in implementing best practices, achieving compliance and meeting the requirements of partners and participants, while minimizing impact on the community and environment.

5 Road traffic safety management

The road traffic safety management is defined in accordance with the OECD road safety report as "a systematic process to reduce the number and severity of road traffic accidents" [24]. Studies and experience of many countries have shown that a significant reduction in the serious consequences of long-term road traffic accidents can be achieved by adopting a holistic road traffic safety system. This approach combines analysis of all the aspects of the road transport system that contribute to traffic accidents. Decisive here is the recognition that there are limits to human action that affect how people behave in traffic [25].

Improving the functioning of the road safety should therefore be considered in the context of the overall road traffic safety management system. This system can be described as "complex institutional structures involving cooperation and interaction involving the authorities that support the tasks and processes necessary to prevent and reduce the road traffic accidents" [26]. The road traffic safety management should be seen as a "production process" consisting of three interrelated components: institutional management functions create interventions that give concrete results [9].

For years, scientists have been trying to analyze the road traffic safety management systems in various countries and to assess the impact of the road traffic safety management elements on the effects in this area. Wong and Sze [27] conducted research to determine the impact of setting quantitative goals on reducing mortality for 7 European countries and found a significant positive impact. In turn, Broughton and Knowles [28] tried to estimate the expected reduction in deaths as a result of the implementation of the national the road traffic safety program in Great Britain. Chapelon and Lassarre [29] analyzed the structures, processes, data and methods used in the road traffic safety management system in France, with particular emphasis on showing how specific performance indicators are monitored to assess the progress of specific road traffic safety problems. Schulze and Kossman [30] described the road traffic safety management tools implemented in Germany in order to explain the reasons for the safety deficit, define and recommend measures based on test results, assess the safety impact of one measure and constantly monitor to what extent the objectives of the national action plan for the road traffic safety are met.

Literature analysis allows one to state that the road traffic safety management systems are composed of many different components (structures, plans, processes, products, results, tools etc.), which makes it extremely difficult to describe them in a standard way. Moreover, despite the common belief that the better management structures and processes of the road traffic safety are associated with better effects of the road traffic safety, it turns out that this relationship is more complex and needs to be considered for specific cases. In fact, the relationship between the road traffic safety management system in the country as a whole and results of the road traffic safety in terms of road traffic fatalities has not been properly investigated [23].

6. SUNflower approach

6.1 The genesis of the SUNflower approach

Road traffic safety is often defined in terms of mortality: the number of fatalities in a given population. Mortality rates are primarily used to illustrate the rank of the road traffic safety or other traffic hazards in relation to mortality due to illness, work accidents or accidents at home. Such indicators and comparisons have the disadvantage that the degree of motorization is not taken into account here. Hence, another indicator is commonly used as a road traffic safety criterion, namely the mortality rate, defined as the number of fatalities per kilometre in the automotive sector. For those countries where such data are not available, the mortality rate is in turn defined as the number of fatalities per motor vehicle [31].

In order to solve problems in comparisons between countries in the field of the road traffic safety, the SUNflower model was developed, under which a target road traffic

safety hierarchy was created. The name “SUNflower” comes from the abbreviation of a series of preliminary projects that concerned research on the state of the road traffic safety in Sweden, Great Britain and the Netherlands (the first letters of the names of countries: Sweden, United Kingdom, Netherlands), considered the three safest countries in the world [32]. The main research questions posed were: how have these countries become relatively safe countries over the years, what exactly has improved their road traffic safety, how can these countries learn from each other and what are the options for moving these aspects to other countries [33].

Later it was extended to six other European countries, in which three groups of three countries (SUN, Southern, Central) compared using the same methodology and the approach was given the name “Sunflower + 6”, [34]. It also allowed an additional translation of the methodology name, because the six countries that the study was extended to include traditional sun countries: three countries in the south of Europe: Greece, Portugal, Spain (with a particular focus on Catalonia) and three in Central Europe: the Czech Republic, Hungary and Poland. Third and latest research, conducted by Wegman and the team [35], they were referred to as SUNflowerNext. They created the framework for a comparative analysis of the state of security of countries and made the first attempt to capture this process in the index of security performance.

6.2 The essence and elements of the SUNflower pyramid

The SUNflower approach requires an understanding of the road traffic safety processes at various levels in the hierarchy of causes and effects, which in turn leads to road traffic accidents and costs for society. The main reference point is the model that describes the hierarchy of the road traffic safety objectives from “structure and culture” to “social costs” [32], as shown in Figure 2.

As it results from Figure 2, the “SUNflower” pyramid describes the road traffic safety management system in the context of a five-level hierarchy: (1) structure and culture, (2) safety measures and programs, (3) indirect effects - safety performance indicators, (4) final results - number of fatalities and injuries and (5) social costs. Therefore, its basis is the structure and culture of a given country, but no less important are social trends such as aging of the society or urbanization.

The first, lowest layer consists of two main elements. The “structure” component refers to two dimensions: physical and operational (functional) structure, while the “culture” component focuses on how society and its citizens perceive the problem of the road traffic safety compared to e.g. the role of road traffic in society and its impact on the one hand on economic growth and prosperity and on the other - environmental effects. The term “security culture” is also used here. This layer describes the policy context, such as the public’s attitude to risk and security, the organization

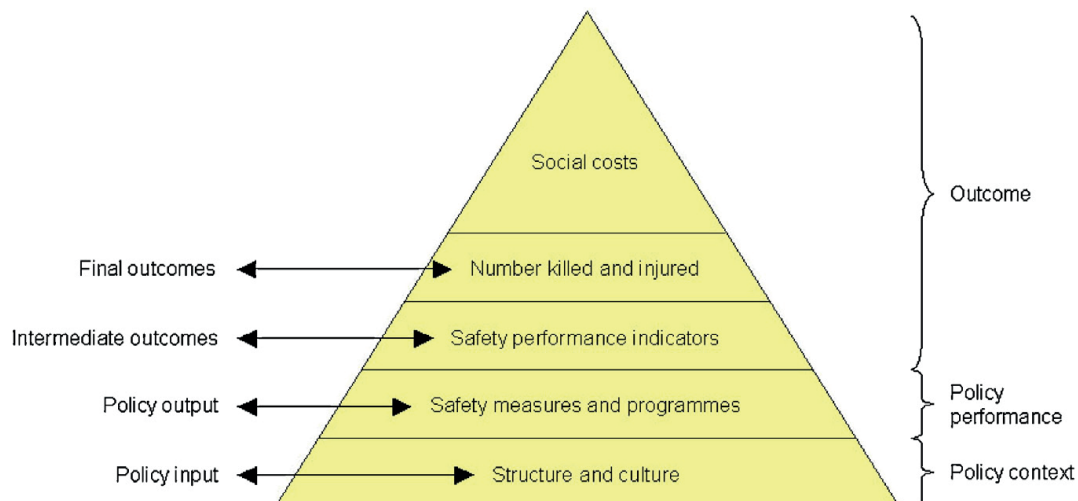


Figure 2 The hierarchy of the objectives of the road traffic safety, [32]

of the country, its history and culture. It follows that the level of the road traffic safety refers to the country's structural features and cultural (i.e. Policy "at the input"). The first level is closely related to the second, i.e. security measures and programs - "exit policy" - resulting from structural and cultural characteristics. This level reflects the effectiveness of the policy. Implementation of the policy concerns the quality of the road traffic safety strategy and the quality of its implementation. So it is a combination of how well the strategy was designed and how well the strategy-based action plans were implemented [36].

The next level is an intermediate layer that allows one to combine the first two layers with the real effects of road traffic accidents. It defines the operational level of the road traffic safety in the country and includes indicators for the road traffic safety regarding excessive speed, drunk driving, or the road network and the main features of vehicles. Level 4 provides information on the final results expressed in the number of road traffic accident victims; consists of different types of road risk indicators. They are necessary to understand the scale of the problem. The top of the pyramid (level 5) provides an estimate of the total economic and social costs of road traffic accidents [23].

To understand the state of the road traffic safety in a given country, one can move in the pyramid in both directions: from the bottom to top or from the top to bottom. For example, from a sociological point of view, one can first describe social attitudes towards drinking or excessive speed (the lowest layer "structure and culture"), then move up the pyramid to identify measures (such as legal restrictions and their enforcement) and thereby understand the extent of the offense and the associated losses and costs. On the other hand, from the point of view of the cost-effectiveness, the opposite direction can be taken by identifying which problems are associated with the highest costs and then tracking these problems to their origins and solving them in a cost-effective way. It should also be added that it is not necessary to start the analysis only from the lower or upper level, for example when monitoring the effects of established security measures.

Furthermore, some mechanisms are not related to the pyramid level sequence, e.g. a change in the number of unfortunate accidents as a result of government actions (the so-called publicity) can directly affect social attitudes [31].

6.3 Road traffic safety indicators and the SUNflower pyramid

The road traffic safety indicators relate to the operational level of the road traffic safety, which is affected by both the structural and cultural characteristics of a given country and the road traffic safety policy and thus are often referred to as "indirect effects" [23]. The purpose of their use is to try to fill the gap in the lack of knowledge about the causal relationship between the actions taken and the final results [37].

The road traffic safety indicators have three main functions: simplification, quantification and communication [38]. Basically, they are used to capture complex phenomena in a relatively simple way and therefore there is a risk of losing important information or observations. Nevertheless, according to Adriaanse, indicators usually use simplifications so that the complex phenomena can be quantified in such a way that communication is either enabled or stimulated. In addition, these indicators can be used for comparison between countries, their ranking and benchmarking.

Safety indicators are a kind of intermediate step in determining the impact of road traffic safety [31, 34]. They reflect those operating conditions of the road traffic system that affect the level of system security. The objectives of the indicators are [36]:

1. taking into account the current conditions of the road traffic safety system;
2. measuring the impact of various security activities;
3. comparison of different road traffic systems (e.g. countries, regions, etc.).

Therefore, Wegman and his team [35] proposed to

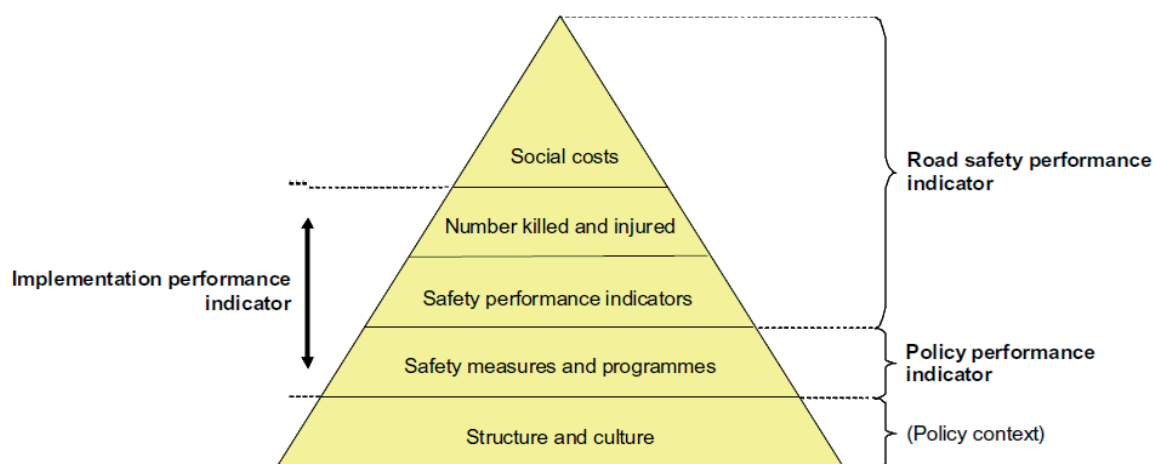


Figure 3 Three types of performance indicators and the SUNflower pyramid, [31]

distinguish three types of indicators in the sunflower pyramid and thus try to condense a huge amount of information - so he developed a comprehensive set of indicators - Composite Performance Safety Index - to measure road safety results in a given country. The first indicator - indicator of efficiency (effectiveness) of the road traffic safety - also called the result indicator - is based on the number of fatalities and injured road users; also takes into account indirect results (SPI) and social costs. It reflects the quality of the road traffic safety in the country. The second type of indicators indicates the quality of the road traffic safety policy implementation - it is an indicator of policy implementation efficiency. It combines its individual layers in the pyramid: “security measures and programs”, performance indicators and the number of fatalities and injured. This indicator also includes elements of the lowest layer of “structure and culture”. However, the third type of indicators indicates the quality of political documents for improving the road traffic safety (the so-called policy effectiveness indicator). It has two elements: the quality of conditions (strategies, programs, resources, coordination, institutional arrangements, etc.) and the quality of action plans and individual remedies for the road traffic safety. Thus, three types of indicators: efficiency indicator of the road traffic safety, policy implementation efficiency indicator and policy efficiency indicator can be integrated into the SUNflower pyramid (Figure 3). These three types of indicators are embedded in the political, economic, historical and geographical context, which are treated as a variable background [31].

Papadimitriou and Yannis [23] analysed the relationship between RTSMS and the road traffic safety at national level for 30 European countries based on the theoretical framework of the “SUNflower” pyramid. A composite index has been implemented for each of the five levels of the hierarchy. The results suggest that the RTSMS had no direct effect on the lethal outcome. However, it also turned out that such activities and tools as: a special budget for the road traffic safety, systematic assessment of the results of the road traffic safety programs and regular measurements of attitudes and behaviour of road users were positively

linked to the operational level of the road traffic safety of the country based on performance indicators Safety Performance Indicators (SPIs), which are the third level in the SUNflower pyramid [21].

The theory of the road traffic safety indicators (SPI) was also dealt with by Hakkert and his team [39], who proposed SPI in seven main areas, such as alcohol and drug use; speed; protection systems; day lights; vehicles; roads and injury management. These areas were identified as key ones to achieve a significant improvement in the road traffic safety in EU countries. In turn, Hollo et al. [37], came to the conclusion that the SPIs do not allow full understanding of the road traffic safety trends, because - in addition to established and frequently used SPIs - there are many other explanatory variables for the national safety outcome, such as demography or technological development, etc. Therefore, they proposed that the analysis of the road traffic safety situation take into account various aspects of the complex socio-technical road traffic safety system, as well as organizational and structural factors.

In summary, it can be said that the SUNflower model describes the hierarchy of the road traffic safety goals from “structure and culture” to “social costs”. This approach enables benchmarking of the road traffic safety and safety trends, as well as a quantitative representation of national security. It applies to security comparisons between all the countries in the European Union, as well as other countries around the world. It also creates a conceptual framework to identify factors that improve the road traffic safety.

7. Results the ISO 39001 standard

7.1 The nature and scope of ISO 39001

The ISO 39001 standard - Road Traffic Safety Management System is a standard introduced in 2012 [40]. It was developed with the support of experts from 40 countries and 16 liaison organizations, including the World Health Organization, the World Bank and the International Road Federation [41]. Its purpose is to encourage organizations

Table 1 Number of certificates issued worldwide in the last three years - as of December 31, 2016, December 31, 2017 and December 31, 2018

management system (MS)	number of certificates issued until 31.12.2016	number of certificates issued until 31.12.2017	number of certificates issued until 31.12.2018
ISO 39001:2012	478	620	547
all MS	1,644,357	1,556,758	1,307,622

Based on data obtained from The ISO Survey of Certifications-2018 [43].

to actively promote the road traffic safety, including by reducing the risk of injury resulting from the road traffic accidents. This standard is based on a process approach in quality management, including the Plan-Do-Check-Act cycle and the requirement for continuous improvement.

The ISO 39001 standard specifies the minimum requirements for the Road Traffic Safety Management System and establishes a set of best practices for the road traffic safety management, mainly by improving consistency within the organization. This is due to the very definition of the road traffic safety management system that should meet several “good practices” criteria, covering the entire policy development cycle, from program development to policy formulation, implementation and evaluation [23]. This system therefore provides instructions that serve as a basis for designing one’s own tailored backbone of the road traffic safety activities by enabling one to transfer all the relevant processes and their control to one management system.

The ISO 39001 standard sets out harmonized requirements, based on international knowledge, to support public or private sector organizations that are involved in the regulation, design and operation of the road transport and interact with the road traffic safety system through: transport of goods and people; operation of devices generating transport demand; employees participating in the road transport system; road design, construction, operation and maintenance; design and production of passenger cars, trucks and other road vehicles and provision of medical assistance to emergency victims [25]. Therefore, the standard is a practical tool, among others for governments, vehicle fleet operators and all the organizations around the world who want to reduce the risk of death or serious injury from the road traffic accidents. In addition, for organizations involved in activities related to the road traffic safety, including by testing the effectiveness of the road traffic safety programs, analysing “black spots”, or providing funding or awarding road traffic safety. It includes organizations of various sizes, locations and operating ranges. In addition to establishing a set of best practices for managing road traffic safety in organizations, it also sets out stakeholder requirements, such as legal requirements related to the role of organizations in the road system. Those requirements enable systematic identification and assessment of the degree of compliance with applicable legal requirements in the field of road traffic safety enforcement.

The ISO 39001 standard is a standard that aims to encourage organizations to actively contribute to the road

traffic safety. By adopting the best practice management framework set out in ISO 39001, companies and enterprises can actively contribute to reducing the risk of death and serious injury due to the road traffic in their area of influence [42]. Hence, the implementation of the RTSMS in accordance with the ISO 39001 standard in the organization allows, above all, to reduce and sometimes eliminate the risk of death and serious injury resulting from the road traffic accidents. The standard also defines hazards and possibilities in the field of the road traffic safety, so that actions to improve processes and assess their effectiveness can be determined. In addition, it identifies and manages organizational processes that interact with the road traffic system and affect the road traffic safety. By adopting the structured holistic approach set out in PN-ISO 39001, organizations should be able to improve the road traffic safety performance in accordance with the law, while contributing to a broader goal for society through fewer road traffic accidents and fatalities.

For several years, the International Organization for Standardization (ISO) annually conducts a review of certificates for management system standards, which enables the certification market to be globally analysed. This is an excellent indicator, which, apart from the development of certification of individual management systems, also illustrates the indicator of development of the world economy. According to data presented in the last edition of the ISO survey (The ISO Survey of Certifications), which appeared in 2018 [43], by the end of December 2018 1,307,622 certificates were issued worldwide in relation to all the applicable management systems and 547 certificates for compliance with ISO 39001. Table 1 presents the number of certificates issued worldwide in the last three years as of December 31, 2016, December 31, 2017 and December 31, 2018. Although the ISO 39001 standard has been in force since 2012, the ISO Survey data on the number of certificates issued for compliance with this standard began to appear only from 2016.

As it results from the data summarized in Table 1, for all the management systems whose analysis was included in the ISO Survey, a downward trend can be observed - if at the end of 2016 there were more than 1.64 million certificates in the world, then a year later there were just over 1.55 million (decrease by 5.33%) and at the end of 2017 - only 1.3 million (decrease by as much as 16 %). It is therefore not surprising that the number of certificates issued in 2018 for compliance with the ISO 39001 standard (RTSMS) is reduced - a decrease of 11.8%, although in 2017 the number of these certificates increased by almost

Table 2 Countries with the largest number of certificates issued regarding compliance with the requirements of ISO 39001 - as of 31.12.2018

no.	country	number of certificates issued (ISO 39001)
1.	Italy	218
2.	Spain	79
3.	Greece	43
4.	Japan	39
5.	Argentina	28
6.	Norway	14
7.	Thailand	14
8.	United Kingdom of Great Britain and Northern Ireland	12
9.	Peru	11
10.	Malaysia	10

Based on data obtained from The ISO Survey of Certifications-2018 [43].

30%. Since - as already mentioned - data on the number of certificates issued for compliance with the ISO 39001 standard began to appear in the ISO Survey only since 2016, so for now reliable conclusions cannot be drawn regarding the trend in the number of certificates issued in the world for compliance with this standard. Table 2 presents the ranking of ten countries that in 2018 recorded the largest number of certificates issued for compliance with the ISO 39001: 2012 standard.

Based on the data contained in Table 2, it can be concluded that the majority of certificates for compliance with ISO 39001: 2012 were issued in Italy, Spain, Greece and Japan. Noteworthy are also countries such as Thailand, Peru and Malaysia, which, although they do not belong to highly developed countries, with appropriate infrastructure, sufficient legal assumptions and systems and tools in the field of the road traffic safety, they have a relatively large - in relation to other countries, especially highly developed European economies - the number of certificates issued for compliance with the ISO 39001 standard.

8 Discussions

The current development of the geopolitical situation also has a significant impact on international transport and important transport connections; therefore the diversification of these threats is a logical factor ensuring efficient delivery of goods and thus the development of international trade [44]. The task of the transport sector is to meet the market requirements in terms of quality, flexibility, speed and safety of people and goods transport [45]. For the safety of transport systems, diagnostics of these systems and transport infrastructure facilities is important, as well. To compare the level of the road traffic safety in many countries, many indicators are used, including the most popular demographic indicators. Due to certain differences in transport systems, the automotive index and the industrialization of countries, the presented data cannot always be reflected equally. This causes

some restrictions in assessing the state of safety, for these reasons systems were sought that would facilitate interpretation of data for individual countries. The road traffic safety management systems are more comprehensive solutions.

In general, the SUNflower model seeks to establish a causal relationship between the road traffic safety plans and programs with their results in terms of changes in the number of fatalities and injured and related costs [33]. The introduction of an intermediate level SPI and consequently, monitoring of progress through the SPI provides a much better understanding than monitoring only result indicators [36]. The popularity of this method in Europe is demonstrated by numerous studies presented in the literature [21, 23, 32, 35-37, 39].

In turn, the Road Traffic Safety Management System ISO 39001 is an important standard for identifying and managing risks related to the road traffic safety and road traffic for enterprises. It contains requirements and guidelines that allow companies implementing it to increase consistency, both within the company itself and between companies, as well as to create their own road traffic safety framework, which on the one hand reduces the complexity of this problem and on the other - allows including all the processes and control tools in one management system. In addition, the Road Traffic Safety Management System helps companies meet legal, industry and stakeholder requirements and - above all - reduce their negative impact on the environment and local communities.

9 Conclusions

The purpose of this article was to present the possibility of safety assessment in the field of the road traffic safety management systems based on two concepts: the SUNflower model and the ISO 39001 standard. The SUNflower pyramid with its various levels / layers turns out to be an excellent platform for managing the road traffic safety and the associated data collection system. As

a result of the conducted analyses, however, a downward trend was noted as to the number of certificates issued for compliance with the ISO 39001 standard in the world. This may result from the fact that, first of all, it may indicate the emergence of more adequate management systems, or other tools or concepts to improve the road traffic safety; secondly, indicate inadequate public education and low levels of awareness in this area of stakeholders, including politicians, scientists, manufacturers, drivers (professional and non-professional), as well as other road users, including the vulnerable ones.

A positive sign of commitment to improving the road traffic safety is that, over the last decade, the demographic indicator: number of killed/100,000 residents in EU countries has decreased in almost all the member countries and has even decreased by half in some.

Therefore, given the growing number of vehicles on the road and the amount of transported goods and thus the occurring risks in the form of the road traffic accidents and congestion, issues of the road traffic safety management not only in the European Union are still a challenge and will have to be discussed in more detail.

References

- [1] TURSKA, S., CHINORACKY, R., MADLENKOVA, L., COREJOVA, T. Optimization of the delivery process in the urban area. In: 23rd International Conference. Transport Means 2019: proceedings. Part 2. 2018. p. 809-813.
- [2] VETERNIK, M., GOGOLA, M. Examining of correlation between demographic development of population and their travel behaviour. *Procedia Engineering* [online]. 2017, **192**, p. 929-934. ISSN 1877-7058. Available from: <https://doi.org/10.1016/j.proeng.2017.06.160>
- [3] MAKKA, K., STACHOVA, D., KAMPOVA, K. Assessment of the mobile risk source in road transport. *Communications - Scientific Letters of the University of Zilina* [online]. 2019, **21**(1), p. 68-73. ISSN 1335-4205, eISSN 2585-7878. Available from: <https://doi.org/10.26552/com.C.2019.1.68-73>
- [4] GASIOROWSKA-DENIS, E. The journey to safer roads [online]. 2013. Available from: www.iso.org
- [5] World Health Organization. Global status report on road safety - time for action. Geneva: WHO, 2009.
- [6] World Health Organization. Global status report on road safety. Geneva: WHO, 2018.
- [7] METHORST, R., EENINK, R., CARDOSO, J., MACHATA, K., MALASEK, J. Single unprotected road user crashes: Europe we have a problem! *Transportation Research Procedia* [online]. 2016, **14**, p. 2297-2305. ISSN 2352-1465. Available from: <https://doi.org/10.1016/j.trpro.2016.05.246>
- [8] YANNIS G., PAPADIMITRIOU E., FOLLA K., NIKOLIC N., MOLNAR E. Developing a global road safety model. In: 97th Annual Meeting of the Transportation Research Board TRB: proceedings. 2018. 18-05057.
- [9] BLISS, T., BREEN, J. Meeting the management challenges of the decade of action for road safety. *IATSS Research* [online]. 2012, **35**(2), p. 48-55. ISSN 0386-1112. Available from: <https://doi.org/10.1016/j.iatssr.2011.12.001>
- [10] The state of road safety and the activities carried out in this field in 2017 /Stan bezpieczeństwa ruchu drogowego oraz działania realizowane w tym zakresie w 2017 r (in Polish). Report of the National Road Safety Council / Raport Krajowej Rady Bezpieczeństwa Ruchu Drogowego, 2017.
- [11] SHAN, Y., HERMANS, E., BAO, Q., BRIJS, T. WETS, G.: Road safety development in Europe: a decade of change (2001-2010). *Accident Analysis and Prevention* [online]. 2013, **60**, p. 85-94. ISSN 0001-4575. Available from: <https://doi.org/10.1016/j.aap.2013.08.013>
- [12] Road accidents in Poland in 2018. Warsaw: Polish Police Headquarters, 2019.
- [13] KUCMIN, T., KUCMIN, A., TURSKA, D., TURSKI, A., NOGALSKI, A. Coping styles and dispositional optimism as predictors of post-traumatic stress disorder (PTSD) symptoms intensity in paramedics. *Psychiatria Polska* [online]. 2018, **52**(3), p. 557-571. ISSN 0033-2674, eISSN 2391-5854. Available from: <https://doi.org/10.12740/PP/68514>
- [14] BAK-GAJDA, D., BAK, J. *Psychology of transport and road safety / Psychologia transportu i bezpieczeństwa ruchu drogowego* (in Polish). Diffin, 2010. ISBN 9788376412139.
- [15] HANZL, J. Analytical model assessing the effect of increased traffic flow intensities on the road administration, maintenance and lifetime. *Open Engineering* [online]. 2019, **9**(1), p. 359-366. eISSN 2391-5439. Available from: <https://doi.org/10.1515/eng-2019-0045>
- [16] DROZDZIEL, P., WRONA, R. Legal and utility problems of accidents on express roads and motorways. In: 11th International Science and Technical Conference Automotive Safety 2018: proceedings. 2018. ISBN 9781538645796.
- [17] OECD. Towards zero: ambitious road safety targets and the safe system approach. Paris: Organisation for Economic Co-operation and Development, 2008.
- [18] World Health Organization. Global status report on road safety - time for action. Geneva: WHO, 2009.
- [19] JOHNSTON, I. Beyond "best practice" road safety thinking and systems management - a case for cultural change. *Safety Science* [online]. 2010, **48**(9), p. 1175-1181. ISSN 0925-7535. Available from: <https://doi.org/10.1016/j.ssci.2009.12.003>
- [20] POLIAK, M., MRNIKOVA, M., SIMURKOVA, P., MEDVID, P., POLIAKOVA, A., HERNANDEZ, S. Social law in road transport like tool safety road transport. In: 11th International Science and Technical Conference Automotive Safety 2018: proceedings. 2018. ISBN 9781538645796.

- [21] VARHELYI, A. Road safety management - the need for a systematic approach. *The Open Transportation Journal* [online]. 2016, **10**, p. 137-155. ISSN 1874-4478, eISSN 2667-1212. Available from: <https://doi.org/10.2174/1874447801610010137>
- [22] BLISS, T., BREEN, J. Implementing the recommendations of the world report on road traffic injury prevention. Country guidelines for the conduct of road safety. Capacity reviews and the related specification of lead agency reforms, investment strategies and safety projects. Washington, DC: World Bank Global Road Safety Facility, 2009.
- [23] PAPADIMITRIOU, E., YANNIS, G. Is road safety management linked to road safety performance? *Accident Analysis and Prevention* [online]. 2013, **59**, p. 593-603. ISSN 0001-4575. Available from: <https://doi.org/10.1016/j.aap.2013.07.015>
- [24] OECD. Road safety: What's the vision? Paris: Organisation for Economic Co-operation and Development, 2002.
- [25] CRACKEL, L. R., SMALL, M. ISO 39001: A new tool for safe systems. In: Australasian Road Safety Research Policing and Education Conference: proceedings. 2010.
- [26] MUHLRAD, N., GITELMAN, V., BUTTLER, I. Road safety management investigation model and questionnaire. Deliverable 1.2 of the EC FP7 Project DaCoTA. 2011.
- [27] WONG, S. C., SZE, N. N. Is the effect of quantified road safety targets sustainable? *Safety Science* [online]. 2010, **48**(9), p. 1182-1188. ISSN 0925-7535. Available from: <https://doi.org/10.1016/j.ssci.2009.12.020>
- [28] BROUGHTON, J., KNOWLES, J. Providing the numerical context for British casualty reduction targets. *Safety Science* [online]. 2010, **48**(9), p. 1134-1141. ISSN 0925-7535. Available from: <https://doi.org/10.1016/j.ssci.2010.01.008>
- [29] CHAPELON, J., LASSARRE, S.: Road safety in France: the hard path toward science based policy. *Safety Science* [online]. 2010, **48**(9), p. 1151-1159. ISSN 0925-7535. Available from: <https://doi.org/10.1016/j.ssci.2010.04.015>
- [30] SCHULZE, H., KOSSMANN, I. The role of safety research in road safety management. *Safety Science* [online]. 2010, **48**(9), p. 1160-1166. ISSN 0925-7535. Available from: <https://doi.org/10.1016/j.ssci.2009.12.009>
- [31] WEGMAN, F., OPPE, S.: Benchmarking road safety performances of countries. *Safety Science* [online]. 2010, **48**(9), p. 1203-1211. ISSN 0925-7535. Available from: <https://doi.org/10.1016/j.ssci.2010.02.003>
- [32] KOORNSTRA, M., LYNAM, D., NILSSON, G., NOORDZIJ, P., PETTERSSON, H. E., WEGMAN, F., WOUTERS, P. SUNflower. A comparative study of the development of road safety in Sweden, the United Kingdom and the Netherlands. Leidschendam, The Netherlands: SWOV Institute for Road Safety Research, 2002.
- [33] WEGMAN, F., SCHERMERS, G., VAN SCHAGEN, I. Towards a national road safety strategy for South Africa. The inception report. Leidschendam, The Netherlands: SWOV Institute for Road Safety Research, 2013.
- [34] WEGMAN, F., EKSLER, V., HAYES, S., LYNAM, D., MORSINK, P., OPPE, S. SUNflower+6. A comparative study of the development of road safety in the SUNflower+6 countries. Final report. Leidschendam, The Netherlands: SWOV Institute for Road Safety Research, 2005.
- [35] WEGMAN, F., COMMANDEUR, J., DOVEH, E., EKSLER, V., GITELMAN, V., HAKKERT, S., LYNAM, D., OPPE, S. SUNflower next: towards a composite performance index. Leidschendam, The Netherlands: SWOV Institute for Road Safety Research, 2008.
- [36] WEGMAN, F., BERG, H-Y., CAMERON, I., THOMPSON, C., SIEGRIST, S., WELJERMARS, W. Evidence-based and data-driven road safety management. *IATSS Research* [online]. 2015, **39**, p. 19-25. ISSN 0386-1112. Available from: <https://doi.org/10.1016/j.iatssr.2015.04.001>
- [37] HOLLO, P., EKSLER, V., ZUKOWSKA, J. Road safety performance indicators and their explanatory value: a critical view based on the experience of Central European countries. *Safety Science* [online]. 2010, **48**(9), p. 1142-1150. ISSN 0925-7535. Available from: <https://doi.org/10.1016/j.ssci.2010.03.002>
- [38] ADRIAANSE, A. Environmental policy performance indicators. A study on the development of indicators for environmental policy in the Netherlands. Hague: Ministry of Housing, Physical Planning and the Environment, Sdu Publishers, 1993.
- [39] HAKKERT, A. S., GITELMAN, V., VIS, M. A. Road safety performance indicators: theory. Deliverable D3.6 of the EU FP6 project SafetyNet. Loughborough University Institutional Repository, 2007.
- [40] EN ISO 39001:2012. Road traffic safety (RTS) management systems - requirements with guidance for use. Geneva, International Organization for Standardization, 2012.
- [41] FROST, R. ISO road safety standard could help save thousands of lives [online] 2012. Available from: www.iso.org
- [42] BREEN, J., WALTON, S. ISO 39001: tackling occupational road risk. Safety Management [online]. 2013. Available from: <https://www.bsigroup.com/Documents/iso-39001/resources/ISO-39001-Tackling-Occupational-Road-Risk-UK-EN.pdf>
- [43] ISO Survey of certifications to management system standards. 2018.
- [44] DROZDZIEL, P., BUKOVA, B., BRUMERCIKOVA, E.: Prospects of international freight transport in the East-West direction. *Transport Problems* [online]. 2015, **10**(4), p. 5-13. eISSN 2300-861X. Available from: <https://doi.org/10.21307/tp-2015-043>
- [45] PECYNA, A., KRZYSIAK, Z., CABAN, J., SAMOCIUK W., BRUMERCIKOVA, E., BUKOVA, B., BUCZAJ, A. Analysis of transport of chemical products in the European Union (in Polish). *Przemysł Chemiczny* [online]. 2019, **98**(8), p. 1330-1334. ISSN 0033-2496, eISSN 2449-9951. Available from: <https://doi.org/10.15199/62.2019.8.25>

A CASE STUDY INTO THE SAFETY COMPLIANCE WITHIN THE ROAD FREIGHT TRANSPORT SECTOR WITH REGARDS TO SECURING CARGO

Ján Ližbetin*, Mária Stopková

The Institute of Technology and Business in Ceske Budejovice, Faculty of Technology, Department of Transport and Logistics, Czech Republic

*E-mail of corresponding author: lizbetin@mail.vstecb.cz

Resume

This article deals with the issue of safety within the road freight transport sector with regards to the securing of cargo on a vehicle. The first part of the article focuses on the legal framework that regulates this issue in the Czech Republic. The second part is based on a case study and survey conducted among drivers of the road freight transport vehicles into their awareness of what they understand is meant by securing and secure cargo. The case study was carried out in a specific transport company and includes an analysis of the current situation and concrete measures for improving safety while securing timber for transport.

Article info

Received 17 September 2020

Accepted 30 October 2020

Online 12 March 2021

Keywords:

road freight transport,
lashing and securing cargo,
safety,
case study

Available online: <https://doi.org/10.26552/com.C.2021.2.F43-F48>

ISSN 1335-4205 (print version)

ISSN 2585-7878 (online version)

1 Introduction

Road freight transport affects all of us, either directly, when we sit behind the wheel, or indirectly, when we pass such vehicles. For some, this means moving products and goods efficiently and conveniently from location to location, for others, it means daily congestion problems. Despite this, there is one thing that binds these groups together, their dependence on cars and trucks.

Road accidents occur on a daily basis, either smaller ones involving only material damage, or serious ones involving the loss of human life. Within this context, it is important to realize that, despite the best efforts of the authorities, the traffic accidents cannot be avoided and we, as traffic participants, must try to prevent them accordingly [1].

The number of accidents as a result of the improper loading or securing of cargo is increasing year by year. For example, in 2009, according to available statistics, an incredible 447 accidents were caused by a technical defect. This represents 5.1% of the total number of recorded road traffic accidents. The improper loading and securing of cargo represents 39.5% of this total, with the remainder of the other accidents caused by, among other things, punctured tires, brake failure and apostasy the wheel [2].

2 Theoretical bases

Act No. 361/2000 Coll., on Road Traffic and on Amendments to Some Acts, Decree No. 341/2014 Coll., on Approval of Technical Capability and on Technical Conditions of Vehicle Operation on Roads, which repeals Decree No. 283/2009 Coll. are the generally valid regulations relating to the carriage of cargo in the Czech Republic. Act No. 361/2000 Coll. on Road Traffic Section 4 regulates rights and obligations regarding the transport of persons and cargo. The focus of this article is § 52 Carriage of Cargo [3-7].

In the Act on the Conditions of Vehicle Operation on Roads, the amendment of Act No. 168/1999 Coll., on Liability Insurance for Damage Caused by Vehicle Operation and amendments to some related acts (Act on Vehicle Third Party Liability Insurance), as amended by Act No. 307/1999 Coll., the third part (Title II) is the most important. Title II refer to the vehicles type approval in §16 and §17 about application of vehicles type approval. Of particular importance is the following: "The load on the vehicle, even a combination of vehicles, must be evenly distributed and properly secured by suitable technical equipment against movement. If a lashing and clamping set is used to secure the load, it must be in good technical condition and comply with: DIN EN 12195-2 Load restraint assemblies on road



vehicles - Safety - Part 2: Web lashing made from man-made fibers; DIN EN 12195-3 Load restraint assemblies on road vehicles - Safety - Part 3: Lashing chains; DIN EN 12195-4 Load restraint assemblies on road vehicles - Safety - Part 4: Lashing steel wire ropes; and DIN EN 12195-1 Load restraining on road vehicles - Safety - Part 1: Calculation of securing forces in number and position" [8-13].

DIN EN 12195 applies to design of methods for securing and lashing cargo for transport by road vehicles or parts thereof (trailers, semi-trailers, containers and swap bodies), including their transport on board a ship or by rail and/or combinations thereof. DIN EN 12640 Securing of cargo on road vehicles - Lashing points on commercial vehicles for goods transportation - Minimum requirements and testing specifies the minimum requirements and test methods for lashing points on vehicles and semi-trailers, whereby the maximum permissible weight of the loading structure for general use is 3.5 tons, [14-15]. DIN EN 12642 Securing of cargo on road vehicles - Body structure of commercial vehicles - Minimum requirements specifies the minimum requirements for bodywork (for example sidewalls, end walls, etc.) and provides appropriate test methods to ensure that a vehicle's body structure is able to secure loads, if it is not secured by lashing equipment. This standard applies to vehicle body and semi-trailer structures with a maximum permissible laden weight of more than 3.5 tons [16-19].

Directive 2014/47/EU of the European Parliament and of the Council of 3 April 2014 on the technical roadside inspection of the roadworthiness of commercial vehicles circulating in the Union and repealing Directive 2000/30/EC imposes an obligation on member states to define an undertaking's responsibilities for maintaining a vehicle in a safe and serviceable condition without prejudice to responsibility of a driver of such a vehicle [20-21].

3 Materials and methods

The two main aims of this article are to establish how aware the freight drivers are about lashing and securing cargo and, based on a practical example, to determine what conditions must be met with respect to a specified transport to fulfil all the safety requirements.

3.1 Driver survey

During the driver training courses in several companies, a short questionnaire survey was conducted among drivers. The survey focused on establishing their awareness of the issue of securing a cargo. In total, 100 drivers completed the questionnaire. Results of the survey are presented in the following graphs (Figures 1 - 5).

The pie charts above are striking in what they reveal. Firstly, only 6% of respondents were aware of Directive 2014/47 EU. Similarly, in response to question 5, 6% of drivers do not consider how much lashing equipment they actually need to sufficiently secure cargoes.

The company owner responded to this issue by stating that most drivers and companies secure cargoes according to the country through which the cargo is to be transported. The reason for this being that the severity of any penalty depends on the place where the controlling authority detects a deficiency. It can therefore be assumed that in the Czech Republic, where it is considered difficult to punish perpetrators based on a vehicle's technical state, not all the companies will comply exactly with the letter of the law.

3.2 Analysis of securing cargo in a specific company

The transport company under scrutiny has been operating on the Czech market for four years and can be said to be growing and prospering. The company currently has eight vehicle combinations - six semi-trailers and two trailers - at its disposal. Timber, in the form of logs or full lengths, is the most commonly transported good. The drivers working for this company also completed the aforementioned questionnaire survey. The following pie charts (Figures 6 and 7) show the outcomes for the two most important questions.

Friction lashing is usually used to secure logs or full lengths of wood. The analysis showed that drivers do not pay sufficient attention to the proper loading and securing of their cargoes. Evidence of this can be seen in Figure 8 below. The photograph shows that the cargo is not sufficiently secured and does not comply with the rules that apply to cargoes that exceed a permitted length. If the vehicle were to move or brake suddenly, there is a major risk that the cargo will dislodge itself.

In general, lashing points should be designed and implemented in such a way as to transmit the forces applied to the vehicle's component parts. However, as is evident in Figure 9, there are no lashing points on the vehicle. This is a serious mistake and extremely dangerous, both for the driver and for other road participants.

The lashing equipment used by the company is completely unsuitable. In Figure 10, it is evident that the lashing straps are twisted, which is not permitted under DIN EN 12195-2. This is a major mistake on the part of the driver, who failed to fulfil his obligation to secure the cargo properly. The company responded to this with the following statement: "We will talk about the identified misconduct with the driver and will try to ensure that it does not happen again. We will also remind other drivers of their obligations and will conduct more rigorous checks before the departure of individual vehicles."

Figure 11 shows another mistake made on the part of the driver. The driver has ignored regulation DIN EN 12195-2, which deals with the component parts of the lashing equipment. Should the driver have been subjected to an inspection by the authorities, the driver would have been obliged to pay a (hefty) fine.

Figures 10 and 11 show the poor quality of the lashing equipment used by the company. Unfortunately, no information could be obtained from the lashing straps

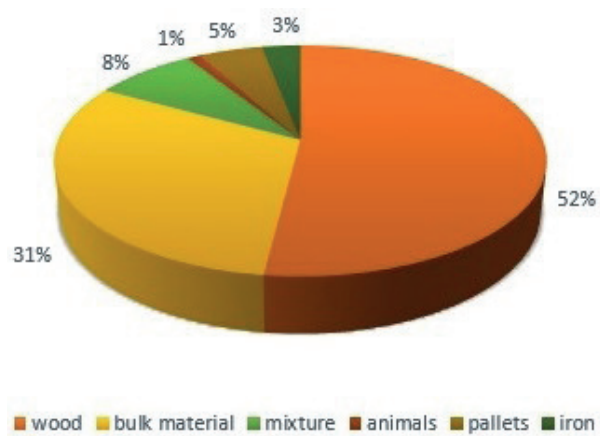


Figure 1 Question 1 results - type of cargo

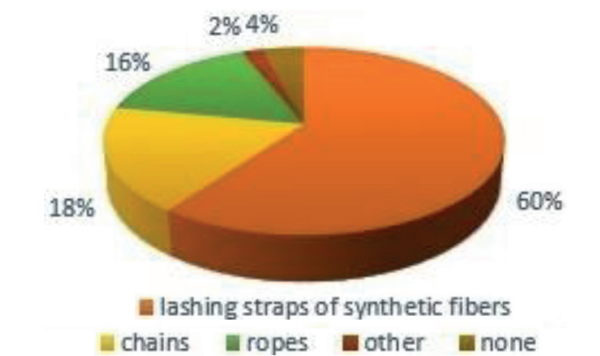


Figure 2 Question 2 results - types of lashing equipment

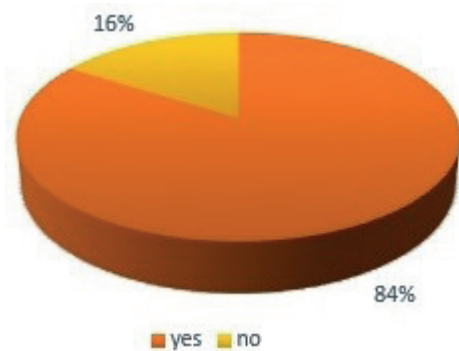


Figure 3 Question 3 results - lashing equipment checks



Figure 4 Question 4 results - method for determining the number of lashing straps



Figure 5 Question 5 results - knowledge about Directive 2014/47 EU



Figure 6 Method for determining the number of lashing straps

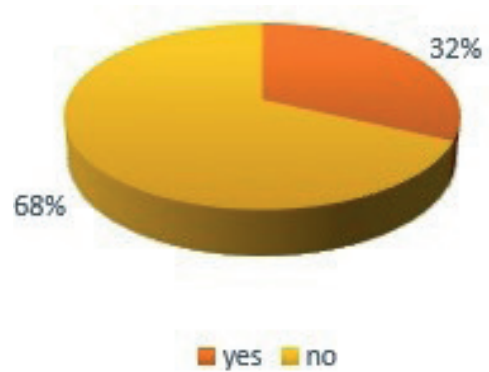


Figure 7 Lashing equipment check



Figure 8 Secured cargo

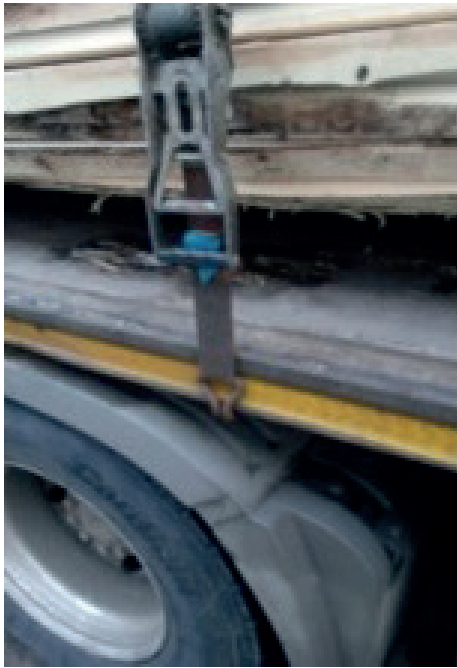


Figure 9 *Lashing points*



Figure 10 *Synthetic lashing straps*



Figure 11 *Lashing equipment*

to correctly calculate the number of straps required. This raises the question: How do the drivers determine the number of lashing straps required?

4 Discussion

The current situation within the company is striking, almost negligent. The company clearly does not care about properly securing loads. This is evidenced by the

fact that it has been fined thousands of Czech crowns on many occasions. Unfortunately, this does not appear to be a strong enough deterrent for the company to change its ways.

The company did not want to comment on the missing lashing points on some vehicles. The lashing equipment, which also does not meet the company's standard requirements, will also not be replaced for the time being.

According to the authorities, the general condition of the vehicles means that they should not be used on the

roads at all. It is their opinion that this, in combination with the unsatisfactory securing of cargo, is endangering the safety of all the road transport participants. Following the adoption of Directive 2014/47 EU, an inspection by the authorities would result in the vehicle being declared roadworthy and the imposition of a fine [22-24].

References [25] include detailed methods for calculating the required number of lashing straps and points, as well as for calculating the total investment for installing the lashing points and purchasing the necessary number of lashing straps.

Calculations by authors suggest that 14 lashing straps are required for the semi-trailers, 5 lashing straps for the trucks and 7 lashing points on the trailers, representing a total investment of CZK 185,264 (cca 6 806 €).

5 Conclusion

Several measures were put forward to improve the safety of the company's vehicles. Since it owns two types of vehicles, measures were proposed for both.

Firstly, the number of lashing points was calculated. In certain cases, the company was advised to add lashing points to their vehicles. Secondly, the number of lashing straps was calculated according to the DIN EN 12195-1 standard. A fully calculated proposal was subsequently submitted. All this was realized in accordance with applicable standards and in accordance with Directive 2014/47 EU.

As the share of the road freight transport in total traffic increases year by year, it is an imperative to respond appropriately. With the increasing number of vehicles on the roads, the road transport safety is therefore also becoming increasingly important. Due to the increasing range of legislation within this area, authorities may therefore increase their oversight of compliance.

The authors would like to conclude this paper by citing a Supreme Court judgment with regards to a company's appeal against an overloaded vehicle, as determined by the Road Services Center. The judgment was:

"The company's interest in safe roads and traffic is always higher than the fact that the consequences of the uncontrolled shifting of cargo will be to the detriment of the vehicle operator or driver. The load on the vehicle shall be adequately secured, in particular so that both the maximum authorized mass of the vehicle and the maximum permissible mass per axle of the vehicle are not exceeded. If such a condition cannot be achieved and guaranteed for the entire transport, then there is no other option than to not realize the transportation of the cargo at all or to realize the transportation in the form of the authorized special use of a road in compliance with legal conditions."

It is clear from this judgment that any carrier, whether road, rail or otherwise, should take into consideration the safety of traffic first and only then to take economic factors into account. In the case of an accident or prevention, the administrative authority will therefore always take into account the safety aspect.

References

- [1] MCDONALD, N., YUAN, Q., NAUMANN, R. Urban freight and road safety in the era of e-commerce. *Traffic Injury Prevention* [online]. 2019, **20**(7), p. 764-770. ISSN 1538-9588, eISSN 1538-957X. Available from: <https://doi.org/10.1080/15389588.2019.1651930>
- [2] THAMZIL, M., KUSTUNO, D., PURNOMO, SUDJIMAT, D. A., MARDJI. Design engineering freight vehicle load detection perspective competence as an operator, inspectors and auditors for road transport safety. *Advanced Science Letters* [online]. 2017, **23**(2), p. 722-725. ISSN 1936-6612. Available from: <https://doi.org/10.1166/asl.2017.7525>
- [3] Act no. 361/2000 coll. on road traffic. Parliament of the Czech Republic, Czech Republic, 2000.
- [4] Decree no. 341/2014 coll. on approval of technical capability and on technical conditions of vehicle operation on roads. Ministry of Transport, Czech Republic, 2014.
- [5] HITKA, M., LORINCOVA, S., LIZBETINOVA, L., BARTAKOVA, G.P., MERKOVA, M. Cluster analysis used as the strategic advantage of human resource management in small and medium-sized enterprises in the wood-processing industry. *BioResources* [online]. 2017, **12**(4), p. 7884-7897. ISSN 1930-2126. Available from: <https://doi.org/10.15376/biores.12.4.7884-7897>
- [6] SABADKA, D., MOLNAR, V., FEDORKO, G. Shortening of life cycle and complexity impact on the automotive industry. *TEM Journal-Technology Education Management Informatics* [online]. 2019, **8**(4), p. 1295-1301. ISSN 2217-8309, eISSN 2217-8333. Available from: <https://doi.org/10.18421/TEM84-27>
- [7] CEMPIREK, V., GASPARIK, J., ZITRICKY, V., BLAHO, P. Control of modular conveyor and automated handling devices interconnection. *Advances in Science and Technology-Research Journal* [online]. 2018, **12**(3), p. 210-215. ISSN 2299-8624. Available from: <https://doi.org/10.12913/22998624/94963>
- [8] Act no. 168/1999 coll. on liability insurance for damage caused by vehicle operation. Parliament of the Czech Republic, Czech Republic, 1999.
- [9] DIN EN 12195-2 Load restraint assemblies on road vehicles - safety - part 2: web lashing made from man-made fibres. Czech Office for Standards, Metrology and Testing, Czech Republic.
- [10] DIN EN 12195-3 Load restraint assemblies on road vehicles - safety - part 3: lashing chains. Czech Office for Standards, Metrology and Testing, Czech Republic.

- [11] DIN EN 12195-4 Load restraint assemblies on road vehicles - Safety - part 4: lashing steel wire ropes. Czech Office for Standards, Metrology and Testing, Czech Republic.
- [12] LI, S., LANG, M., YU, X., ZHANG, M., JIANG, M., TSAI, S., WANG, CH.-K., BIAN, F. A Sustainable transport competitiveness analysis of the China railway express in the context of the belt and road initiative. *Sustainability* [online]. 2019, **11**(10), 2896. eISSN 2071-1050. Available from: <https://doi.org/10.3390/su11102896>
- [13] CERNA, L., ZITRICKY, V., DANIS, J. The methodology of selecting the transport mode for companies on the Slovak transport market. *Open Engineering* [online]. 2017, **7**(1), p. 6-13. eISSN 2391-5439. Available from: <https://doi.org/10.1515/eng-2017-0002>
- [14] DIN EN 12195-1 Load restraining on road vehicles - safety - part 1: calculation of securing forces in number and position. Czech Office for Standards, Metrology and Testing, Czech Republic.
- [15] DIN EN 12640 Securing of cargo on road vehicles - lashing points on commercial vehicles for goods transportation - minimum requirements and testing. Czech Office for Standards, Metrology and Testing, Czech Republic.
- [16] DIN EN 12642 Securing of cargo on road vehicles - body structure of commercial vehicles - minimum requirements. Czech Office for Standards, Metrology and Testing, Czech Republic.
- [17] JASKIEWICZ, M., LISIECKI, J., LISIECKI, S., POKROPINSKI, E., WIECKOWSKI, D. Facility for performance testing of power transmission units. *Scientific Journals of the Maritime University of Szczecin / Zeszyty Naukowe Akademii Morskiej w Szczecinie*. 2015, **42**(114), p. 14-25. ISSN 1733-8670.
- [18] KAMPF, R., STOPKA, O., BARTUSKA, L., ZEMAN, L. Circulation of vehicles as an important parameter of public transport efficiency. In: International Conference Transport Means 2015: proceedings. 2015. ISSN 1822-296X, p. 143-146.
- [19] KOLAROV, I. Training needs on health and safety of drivers at work in road freight transport sector. In: 7th International Conference Efficiency and Responsibility in Education 2010: proceedings. 2010. ISBN:978-80-213-2084-0, p. 174-184.
- [20] Directive 2014/47/EU of the European Parliament and of the council of 3 April 2014 on the technical roadside inspection of the roadworthiness of commercial vehicles circulating in the Union and repealing directive 2000/30/EC. European Committee for Standardisation (CEN), European Parliament and of the Council, 2014.
- [21] SARKAN, B., STOPKA, O., GNAP, J., CABAN, J. Investigation of exhaust emissions of vehicles with the spark ignition engine within emission control. *Procedia Engineering* [online]. 2017, **187**, p. 775-782. ISSN 1877-7058. Available from: <https://doi.org/10.1016/j.proeng.2017.04.437>
- [22] CABAN, J., VRABEL, J., SARKAN, B., ZARAJCZYK, J., MARCZUK, A. Analysis of the market of electric tractors in agricultural production. *MATEC Web of Conferences* [online]. 2018, **244**, 03005. eISSN 2261-236X. Available from: <https://doi.org/10.1051/mateconf/201824403005>
- [23] SIPUS, D., ABRAMOVIC, B. The possibility of using public transport in rural area. *Procedia Engineering* [online]. 2017, **192**, p. 788-793. ISSN 1877-7058. Available from: <https://doi.org/10.1016/j.proeng.2017.06.136>
- [24] BABIN, M., BUDA, M., MAJERCAK, J. Terminals for transportation of dangerous goods. In: International Conference Transport Means 2012: proceedings. 2012. ISSN 1822-296X, p. 166-170.
- [25] CHALUPNA, L. Lashing of cargo in road transport in a selected company / Upevnění nakladu v silnicní dopravě ve vybrané firmě (in Czech). Diploma thesis. Ceske Budejovice: The Institute of Technology and Business, 2018

USING DATA ON BIKE-SHARING SYSTEM USER STOPOVERS IN SMART TOURISM: A CASE STUDY

Krystian Banet

Department of Transportation Systems, Cracow University of Technology, Cracow, Poland

*E-mail of corresponding author: kbanet@pk.edu.pl

Resume

Bike-sharing systems are an important element in development of the smart cities and datasets from these systems are one of the ways to obtain large amount of information on bicycle traffic. These usually contain data on the origin and destination of each trip, as well as its time and duration. Alongside the basic data, some operators also provide information on the exact route picked by each user. This allows researchers to study stopovers, which may serve as a source of interesting information on human behaviour in public spaces and, as a consequence, help improve its analysis and design. However, using the raw data may lead to important errors because most stops occur in the vicinity of bike stations or are related to traffic problems, as evidenced by the case study of Cracow. The data filtering method proposed below opens up the possibility for using such datasets for further research on bike user behaviour and public spaces.

Available online: <https://doi.org/10.26552/com.C.2021.2.G1-G12>

Article info

Received 2 September 2020

Accepted 11 October 2020

Online 9 March 2021

Keywords:

bicycle traffic,
bike-sharing,
transport geography,
stopover behaviours

ISSN 1335-4205 (print version)

ISSN 2585-7878 (online version)

1 Introduction

The advent of the bicycle forever changed the way we travel and increased our freedom. The growth of bike traffic was only halted by the rise of the automotive industry; however, because of their many advantages, bicycles are once again becoming popular as means for the daily commute. The vision of “smart cities” rests on the central idea that investment in social capital, technology and infrastructure should fuel the growth of the city and continually improve the quality of life for its residents. One of the pillars of the “smart” philosophy is to provide modern and integrated transportation, the pivotal element of which is development of the bike-sharing systems, which have been growing in importance in recent years, not only in the largest metropole, but in the medium-sized towns and even the smallest municipalities, as well [1]. Better understanding of users of the bike-sharing systems can help in smart tourist management in urban areas. Cities around the world are increasingly recognizing the smart tourism city concept and related strategies as means of optimizing sustainable environments. Particularly for cities facing emerging issues of residents’ negative perceptions towards tourism, smart tourism city empowers a city to rise to this challenge by creating urban spaces that residents and visitors can enjoy together [2].

Apart from becoming a convenient means of the last-mile transportation, city bikes have become a valuable source of information on trips taken by hundreds of thousands of cyclists, a data pool impossible to collect with

use of classical traffic measurement methods. Thanks to bike-sharing datasets, it is now possible to perform a more accurate modelling of the bicycle traffic and examine the individual elements that shape the demand for such services. Over the last few years, a number of studies have already focused on analysing the factors that affect the traffic within the framework of city bike systems. These surveys usually aim to identify potential locations for new stations, estimate traffic flows and bike use, and include social and demographic variables, as well as data on spatial organization.

In contrast, this article focuses on analysing datasets from a single city bike system to look at the issue of stopovers; no previous study of this kind was identified in the literature review process. The bike-sharing systems are an interesting source of data on human behaviour in public spaces, which can be useful for spatial analysis and design, including in terms of developing bike infrastructure. Analysis in question is focused on a case study of Cracow. Once the dataset obtained from the city bike system was cleansed, user stopovers were visualized to create a map of local-related stop concentrations, which largely overlapped with rental stations. Analysing data in this form would be ineffective; a method of filtering data on city bike user stopovers had to be developed, which is the main objective of this article, to help understand the bike-sharing system stopovers behaviour and obtain more precious data to delimit attractive public spaces in the city. The visualization of the final data sample demonstrated the effectiveness of the method and enabled further analysis, which may prove



useful for urban planners and sociologists, allowing them to better understand cyclists' behaviour and user preferences regarding areas in which their stopovers occur.

The paper is organised as follows. In the next section, the background to city bike systems, the data collected and their usage are introduced. In section 3, a generic method is introduced to identify and filter the stopovers in mobility traces and apply it to the city bike data. In section 4, the method is illustrated using the example of Cracow. Finally, in section 5, the results are synthesized and the potential applications and limitations of the proposed method are discussed.

2 Literature review

With acceleration of urbanization, a number of cities face challenges to design and develop a better city for living [2]. The concept of the smart city is to optimize infrastructures in order to ideally ensure quality of citizens' life: transportation, water and power supply, waste management, IT connectivity, efficient urban mobility, e-governance and citizen participation, [3]. Cycling has strategic importance for the sustainable development of cities and has become one of the fundamental parts of the urban mobility strategies. Use of bikes as a transportation solution in urban and/or tourist contexts is universally recognized as positive due to the lack of polluting emissions, the reduction of traffic congestion and improvement of users' health [4]. Transportation with accommodation, gastronomy, attraction and ancillary service is one of the essential components of the smart tourism [2]. There are six main tourist-related elements of the smart cities: smart mobility, smart government, smart economy, smart people, smart living and smart environment [5]. Presence of an effective bike sharing service, being part of a smart mobility, can indeed make a city more attractive and easier to visit, strongly motivating tourists to choose it as a holiday destination. Bike trips can also become an integral part of the tourist experience, even when implemented to connect specific points of interest to the city center [4].

The growth in bike traffic has attracted the attention of researchers and spawned multiple studies of its various aspects. The bicycle traffic has long been appreciated for its health benefits. However, it has important advantages not only for health and physical fitness, but also for the natural environment. Choosing the bike as a means of transportation may be dictated by various individual and environmental factors, including age and gender [6]. Because of its seasonal nature, randomness of choice and dependence on weather conditions, however, bike traffic is far from easy to forecast and model. Reliable studies on the subject are also difficult to carry out. The most extensive data on pedestrian and bicycle traffic usually come from Complex Traffic Studies, conducted on a local and regional level in individual households. However, the most popular way to collect bike traffic data continues to consist of counting cyclists in the field, despite its rather limited

value for understanding the human transport behaviour [7]. Until not so long ago, exact figures on bike demand were extremely difficult to come by because of insufficient data; today, however, we observe a rapid rise in availability of relevant statistics. The new, exhaustive datasets that have come to complement classical methods rely on automated meters or publicly available GPS traces [8]. One way to obtain large quantities of data on bike traffic today is to analyse records from the short-term bike-sharing systems [9]. This data source meets the definition criteria for big datasets and has enormous potential for study of urban dynamics and aggregate human behaviour [10]. Recently, bicycle sharing has been becoming increasingly popular around the world. As a potential travel mode for both the "first mile" and "last mile" transportation solutions, bicycle sharing is usually used at the beginning or end of the trip chain and play an important role in bridging the gap among existing transportation networks and is useful for recreation and tourism-related activities [11].

The Global Positioning System (GPS) has been gaining importance for travel surveys since the 1990s. While it is successfully used to collect accurate information about travelled routes and travel times, only little is known on extracting added information like transport modes and trip purposes [12]. City bike systems store multiple records of trips by thousands of cyclists, who, by using the service, consent to the collection of their GPS traces, along with data on each individual trip. This allows improvements to accuracy of the bike traffic modelling, as well as in studying the factors that shape the demand for the city bike system services.

Compared to other public travel modes, the bicycle sharing travel data usually include the starting or ending point of the original trip chains, which is more useful for the land-use analysis [11]. Over the last few years, a number of studies have been devoted to analysing the factors that affect traffic within the framework of city bike systems. These surveys are usually aimed at identifying potential locations for new stations and estimating traffic flows and bike use and include social and demographic variables, data on spatial organization (such as population and job density), as well as topological and meteorological parameters for all the proposed spots [13-15]. Data from the city bike systems have also been used to study the systems already in place [16], e.g. in Turin, Italy to estimation of passenger transport flows for development of the transport models in urban contexts [17]. Such studies look at how, for instance, bike trips are affected by factors such as: the number of retail stores and business offices near bike stations, various demographic features, job density, type of buildings and spatial organization, purpose of buildings in the area, impact of meteorological factors, the closest bike infrastructure, or the type of available transport solutions [13, 18-26]. The spatio-temporal usage patterns of dockless bike-sharing service, linking to metro stations, have been analysed e.g. in Shanghai, China [27]. Using the data from the bike-sharing in Beijing, China, Wang et al. applied the geographic weighted regression model to

carry out a spatiotemporal characteristic analysis of the relationship between the bike-sharing usage in railway-station service areas and its determinants, including the passenger flow in stations, land use, bus lines and road-network characteristics [28]. However, the literature review has not identified any in-depth analyses of city bike user stopovers to identify and delimit attractive public spaces. Identified attractive spaces were usually based on arbitrary expert knowledge. Other traditional methods include data from accommodation providers and guest surveys, which are time consuming and expensive. Data can also be taken from official guides, but these fail to adapt to the rapidly-changing tastes of tourists and their actual preferences [29]. Today, everyone leaves digital footprints on the internet, which can be used as data what is essential of smart tourism. The literature contains works that aimed to identify tourist hotspots based on user activity on recommendation websites and social media such as Flickr or Twitter [29-31]. The similar idea is followed in this paper and explore how the bike-sharing system data may help in revealing spatial patterns of touristic cities. Mobility traces from public bikes, were broadly employed in transport and spatial analyses, yet, so far, have not been used to identify tourist hotspots [32].

3 Methodology

This article presents a data filtering method, which allows the dataset to be trimmed down to guarantee that it only includes user stopovers that were not related to traffic problems or technical activities involved in locking and unlocking the bike at the rental station or checking its technical condition before the trip. Dataset obtained after filtering process can be used for further analysis of attractive public spaces.

The dataset first needs to be cleansed in order to discard data, like for instance records where location tracking failed or the bike was rented only to be returned moments later due to, e.g. a technical glitch. The datasets from the GPS transmitters are stored in GPX-files (GPX is an XML schema designed as a common GPS data format). To read the data in these GPX files, a Python code was developed that presents it as a set of trip parameters: the trip identification number, the number of segments, trip duration, idle times, total distance and mean velocity. Accordingly, the dataset obtained from the city bike system was first cleansed of corrupt records related to signal failures in the GPS transmitters. The trip data were eliminated if the GPS outage lasted at least five minutes. After the first filtering stage, the sample continued to contain many trips with an average speed of 0 km/h. Therefore, it is also decided to eliminate all the trips with a duration or distance of 0, most likely related to situations where a bike was unlocked, but not taken out of the stand, and then locked again, e.g. because of a technical problem. At the last stage, the records that contained information on very short trips, which could correspond to situations

where a technical problem was discovered soon after the bike was rented or the user decided not to continue with the trip, were removed, [33]. The final sample was subsequently studied to analyse the remaining stopovers. The stopover is a set of consequent travel segments characterized by zero value of covered distance:

$$Stopover = TS_{idle} \{TS_k, TS_l : l = k + 1\}, k, l = 1 \dots N_{TS}, \quad (1)$$

where TS_{idle} is a set of all the segments within the trip that have zero travel distance; TS_k is the k -th trip segment of the journey track; N_{TS} is the total number of trip segments.

The first step was to identify locations where users started their trips, which did not always overlap with the bike rental stations, since, in Cracow, the operator allowed users to leave the bike anywhere within the city for an extra charge. The corresponding heatmap, however, shows that almost all the trips began at bike stations. First, the number of stops within a radius of 1 to 20m from the trip origin was studied and it was looked at percentage drops in the number of stopovers in the vicinity of the origin site to identify the point of stability, beyond which the number could be described by a linear function with the coefficient of determination R^2 equal to 99%. The data thus filtered then underwent another round of filtering.

The second stage served to eliminate stops related to traffic problems. In order to include stopovers by cyclists who used bicycle lanes and sidewalks, as well as those cycling on public roads, it was decided to focus on areas around pedestrian crossings and traffic lights. This stage relied on vector data from the Open Street Map, which included information on their geographical coordinates. The analysis focused on stopovers that occurred within a radius of 5 to 50 meters from a pedestrian crossing. Once again, percentage drops were studied to identify the point of stability, but manual corrections had to be introduced at this stage. A number of control points were examined at which long waiting lines of bicycles were identified at pedestrian crossings and adjusted the radius accordingly so as to discard data from such spots. The same approach was adopted at the third stage regarding the railway crossings.

The last step focused on stopover duration. It was decided to discard very short stops, which could be related e.g. to temporary stopovers at the intersections of uncontrolled neighbourhood roads that did not have a pedestrian crossing (and which, for this reason, had not been eliminated at the second filtering stage). A fixed time threshold was calibrated at several known locations where cyclists typically stopped and then adjusted to effectively filter out the traffic-related stopovers. The data sample obtained after the last filtering stage were also visualized as a heatmap.

In addition, after every stage of filtering factor of filtering effectiveness was checked. It is described by formula:

$$F_i = \frac{x_F}{x_i}, i = 0 \dots 4, \quad (2)$$

Table 1 Weather conditions measured at the Cracow-Balice station (developed based on [34])

day	mean temperature [°C]	max temperature [°C]	total rainfall [mm]	mean pressure [hPa]
31 May 2017	19.5	24.5	0.1	1016.0
1 June 2017	17.1	22.2	0.0	1019.0
2 June 2017	16.7	24.4	0.0	1018.1
3 June 2017	17.3	24.4	0.0	1016.6
4 June 2017	19.6	28.9	3.6	1010.8
5 June 2017	18.0	22.7	0.0	1015.3
6 June 2017	21.3	28.4	0.0	1008.1
7 June 2017	16.9	26.0	0.0	1014.2

Table 2 The number of stopovers near the trip origin

radius r [m]	stopovers within a radius r from the trip origin	other stopovers	difference [%]
1	38375	15768	-
2	42541	11602	-0.26421
3	43487	10656	-0.08154
4	43865	10278	-0.03547
5	44110	10033	-0.02384
6	44321	9822	-0.02103
7	44504	9639	-0.01863
8	44684	9459	-0.01867
9	44834	9309	-0.01586
10	44972	9171	-0.01482
11	45109	9034	-0.01494
12	45233	8910	-0.01373
13	45358	8785	-0.01403
14	45455	8688	-0.01104
15	45550	8593	-0.01093
16	45652	8491	-0.01187
17	45748	8395	-0.01131
18	45828	8315	-0.00953
19	45922	8221	-0.0113
20	46007	8136	-0.01034

where x_i is a number of all the stopovers after the i -th stage of the filtering procedure; x_i is the total number of stopovers obtained after the final stage of filtering. Factor F allows the numerical assessment of results obtained at the corresponding stage of filtering. To sum up, the adopted methodology of data filtering allows for obtaining information about stops of the city bike users from the raw data set, which:

- were not related to renting a bike at a station and checking its technical condition,
- were not stops related to the road traffic obstructions, e.g. in vicinity of pedestrian crossings, railway crossings and traffic lights,
- were not short stops related to the difficulties in general traffic.

4 Case study: stopovers in the bike-sharing system of Cracow

The filtering method was tested using the example of Cracow, in a case study based on datasets obtained from the local bike-sharing system, the first of this kind in Poland. Known as “Wawelo”, the system was established in 2008 and, in different guises, continued in place until 2019. The records in question covered one week of the high tourist season in 2017, i.e. the period between 31 May and 7 June. According to data provided by the Institute of Meteorology and Water Management, weather conditions at the time were auspicious for bike traffic and recreation (Table 1). The sample represented the total population of city bike users in Cracow over the analysed period and

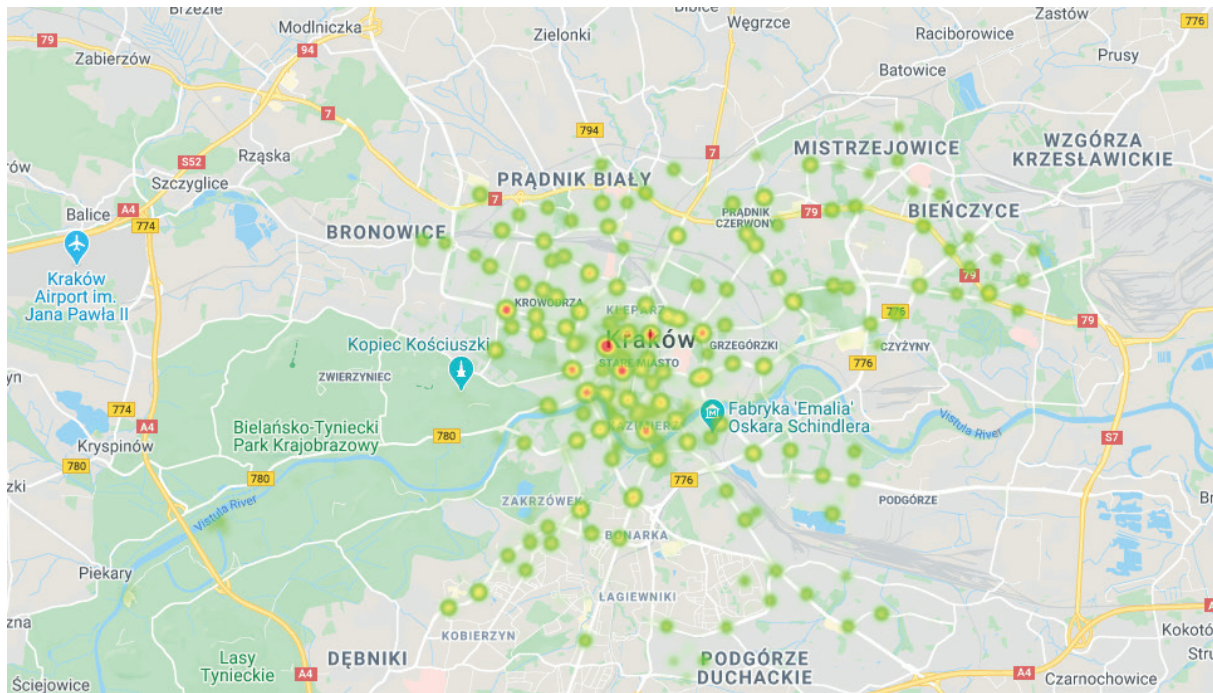


Figure 1 A heatmap showing the stopover locations of the city bike users in Cracow - cleansed sample before filtering (background: Google Maps)

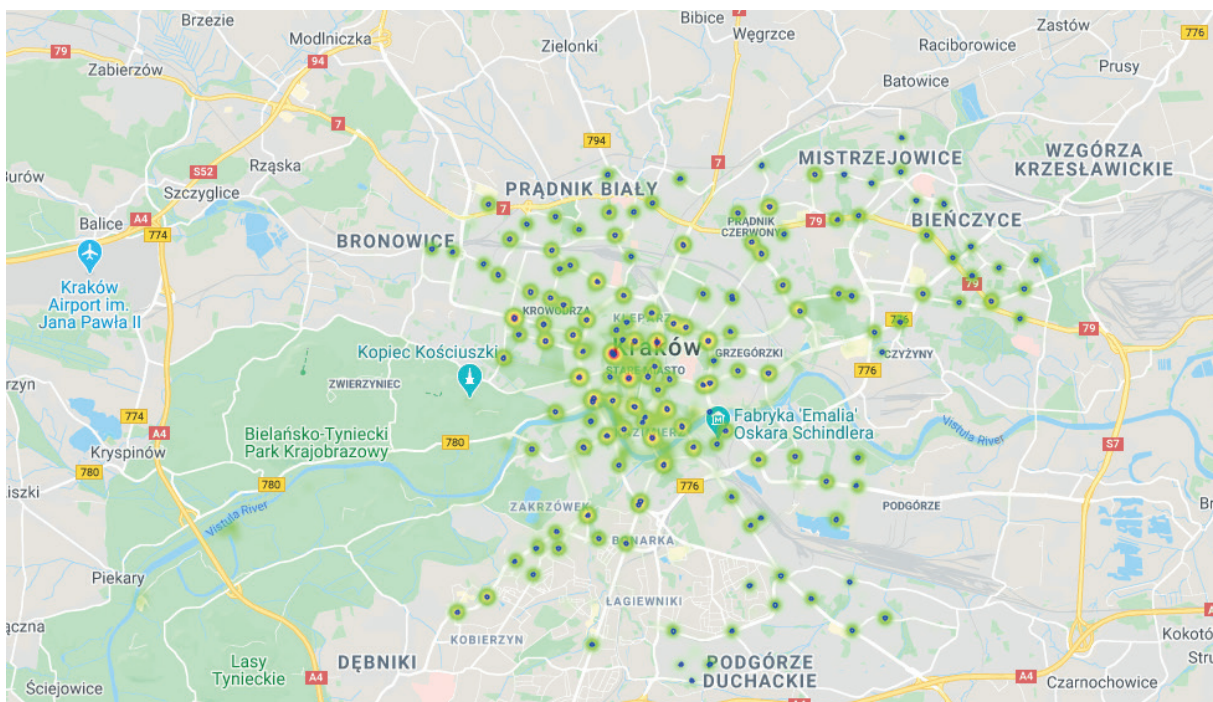


Figure 2 A heatmap showing the origin and destination of trips by the city bike users in Cracow with information about locations of the public bike rental stations (background: Google Maps)

was judged sufficient for analysis, containing a total of 34,969 tracks. The data on routes was obtained from the GPS transmitters attached to every Wavelo bike; apart from the origin and destination of each trip, the devices also recorded its itinerary. The data on each trip were presented as a list of points, with specific locations (geographical latitude and longitude) and readout times.

The first step was to cleanse the dataset provided by the city bike system. First, all the data corrupted by the

GPS transmission failures (a total of 5,946 trips) were eliminated. At the second stage, 40 trips with a duration of zero and 635 trips with a distance of zero were discarded. The third stage, which involved filtering out short trips, identified 421 trips with a distance shorter than 50 m. Once these were eliminated, the final sample consisted of 27,927 routes.

The number of stopovers in the cleansed sample was 54,143, with a mean duration of 79.17 seconds. A heatmap

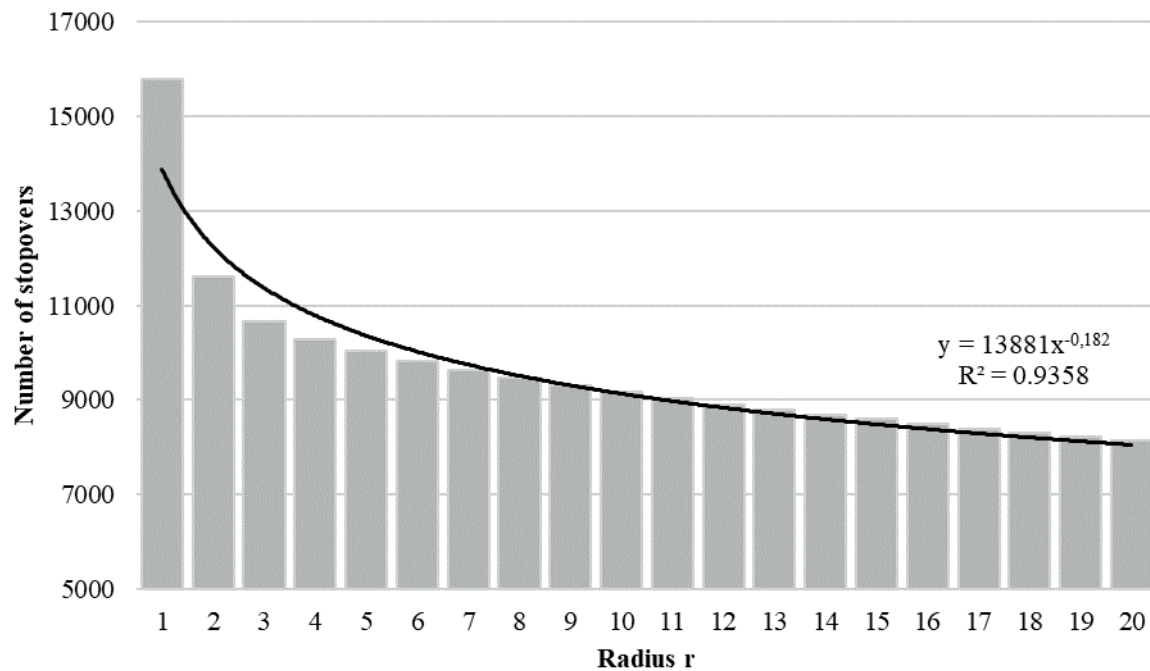


Figure 3 The number of stops at a radius greater than r from the trip origin

Table 3 The number of stopovers near the pedestrian crossings

radius r [m]	stopovers within radius r from the crossing	other stopovers	difference [%]
5	312	9327	-
10	1301	8338	-0.10604
15	2055	7584	-0.09043
20	2551	7088	-0.0654
25	2976	6663	-0.05996
30	3362	6277	-0.05793
35	3717	5922	-0.05656
40	4072	5567	-0.05995
45	4389	5250	-0.05694
50	4695	4944	-0.05829

in Figure 1 shows the stopovers included in the cleansed dataset before filtering.

The map indicates that most stopovers concentrated around the city bike stations, i.e. the origin and destination of each trip, which are shown in Figure 2.

In accordance with the adopted methodology, the first filtering stage discarded all stopovers in the vicinity of the trip origin. The stopovers within a radius of 20m, spaced at intervals of 1m were considered (Table 2).

As evidenced by the table, the drop in the number of stopovers beyond radius r stabilizes at a distance of 7 meters. The number of stops beyond the radius of 1 to 20m can be described by a linear function with $R^2 \approx 0.94$; beyond the radius of 7 to 20m, the coefficient is even higher and equals: $R^2 \approx 0.99$. A histogram showing the number of stops beyond radius r (from 1 to 20m) is presented in Figure 3.

After the first filtering stage, the sample included all the stopovers that occurred at a distance of more than 7m from the trip origin. The second step studied stops in the vicinity of pedestrian crossings, analysing those within a radius of 50m, spaced at 5m intervals (Table 3).

The table indicates that the drop in number of stopovers beyond radius r stabilized at 15m. The number of stops beyond the radius of 5 to 50m could be described by a linear function with $R^2 \approx 0.96$; beyond the radius of 15 to 50m, however, the coefficient was even higher and equalled $R^2 \approx 0.99$. A histogram showing the number of stops beyond radius r (from 5 to 50m) is presented in Figure 4.

However, an analysis performed at selected control points, i.e. pedestrian crossings situated along main bike traffic corridors, showed that the 15m radius was not sufficient to eliminate all the stops related to the presence

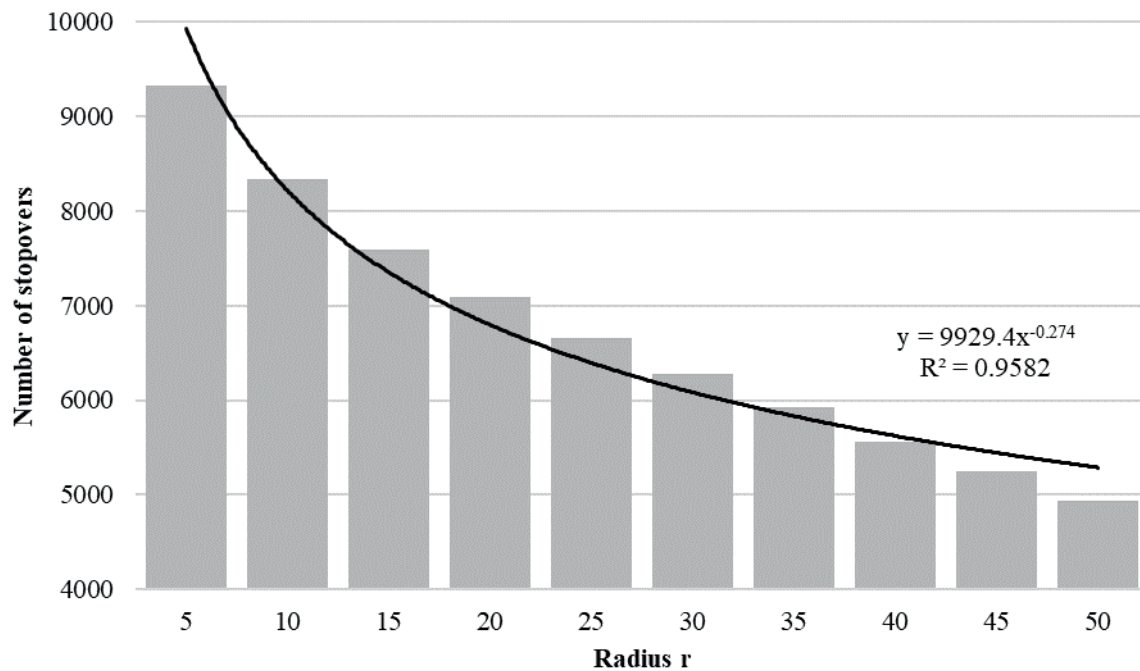


Figure 4 The number of stops within a radius greater than r from the pedestrian crossing

Table 4 Stopovers in the vicinity of the railway crossings

radius r [m]	stopovers within radius r from the crossing	other stopovers	difference [%]
5	0	6277	-
10	8	6269	-0.00127
15	20	6257	-0.00191
20	41	6236	-0.00336
25	52	6225	-0.00176
30	58	6219	-0.00096
35	61	6216	-0.00048
40	61	6216	0
45	61	6216	0
50	63	6214	-0.00032

of pedestrian crossings, since cyclists tended to cluster in long lines at such spots. To discard all such data, a 30-m cut-off radius had to be adopted for the purposes of the study. After the second filtering stage, the sample thus included all the stopovers that occurred at a distance of more than 7 m from the trip origin and 30 m from pedestrian crossings. The third step was to discard all the data from the vicinity of railway crossings. To do so, the stopovers that occurred within a radius of 50 m, spaced at 5 m intervals, were studied (Table 4).

In this case, the number of stopovers beyond radius r remained nearly constant at distances of 30, 35, 40, 45 and 50 m, which means it was easy to determine the upper distance limit. This cut-off radius was also confirmed at control points, i.e. cyclists tended to cluster in lines of max. 30 m. A histogram showing the number of stopovers beyond

radius r is presented in Figure 5.

After the third filtering stage, the sample thus contained stopovers that occurred at a distance of more than 7 m from the trip origin, 30 m from a pedestrian crossing and 30 m from a railway crossing. An analysis performed at control points, however, revealed that the data still included some traffic-related stops, e.g. those on uncontrolled neighbourhood roads without a pedestrian crossing (which had not been eliminated at the previous filtering stages). The fourth stage thus focused on stopover duration. The span of 30 seconds was confirmed at selected control points as a reliable cut-off point for stopovers unrelated to traffic. A table was then drawn up to illustrate the number of stopovers and their duration (Table 5).

A histogram showing stopovers longer than the minimum duration T is presented in Figure 6.

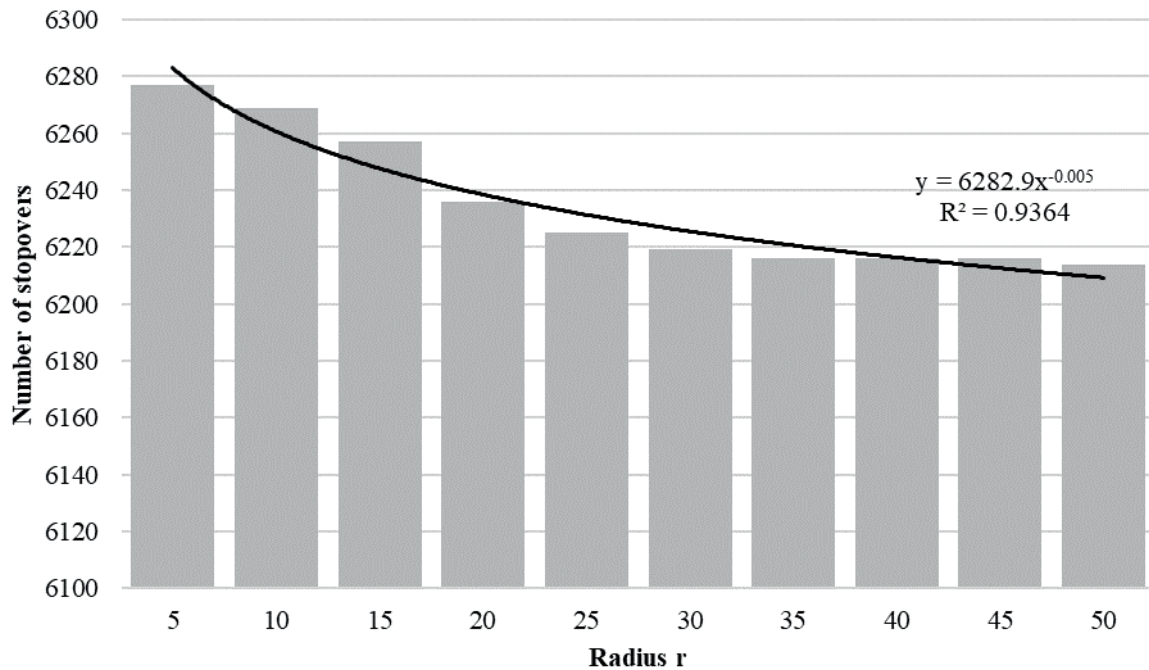


Figure 5 The number of stops within a radius greater than r from the railway crossing

Table 5 Stopovers and their minimum duration

minimum stopover duration T [s]	stopovers shorter than T	other stopovers	difference [%]
5	116	6103	-
10	257	5962	-0.0231
15	320	5899	-0.01057
20	368	5851	-0.00814
25	411	5808	-0.00735
30	428	5791	-0.00293
35	443	5776	-0.00259
40	452	5767	-0.00156
45	461	5758	-0.00156
50	469	5750	-0.00139
55	471	5748	-0.00035
60	471	5748	0

Table 6 Stopover statistics at each filtering stage

stage	number of stops	time [s]							
		mean	std	min	25%	50%	75%	max	sum [h]
before filtering	54143	79.17	291.63	1	15	25	65	27350	1190.77
1 st	9639	280.93	559.30	1	85	90	255	8290	752.2
2 nd	6277	335.83	647.13	1	85	155	275	8290	585.56
3 rd	6219	337.74	649.78	1	85	160	275	8290	583.45
4 th	5791	361.80	667.09	31	85	170	335	8290	582.00

The fourth stage was the last in the filtering process. The final sample contained all the stopovers that occurred at a distance of more than 7 m from the trip origin, 30 m

from a pedestrian crossing, 30 m from a railway crossing and lasted more than 30 seconds. The number of stopovers in the filtered sample was 5,791, with a mean duration of

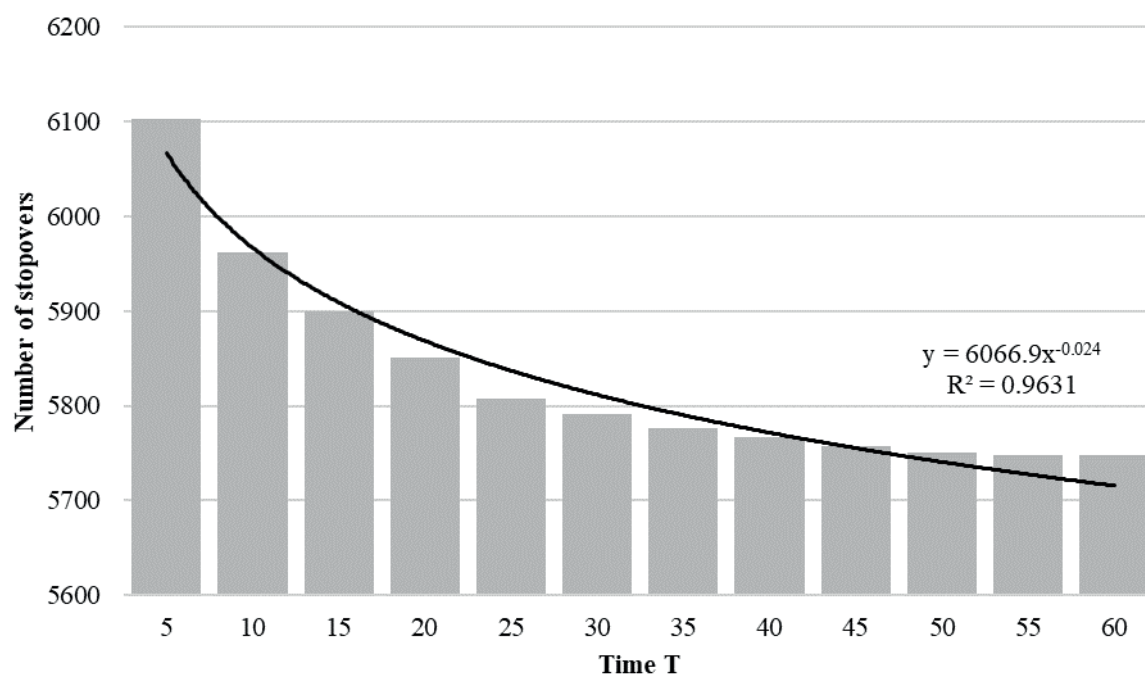


Figure 6 The number of stopovers longer than the minimum duration T

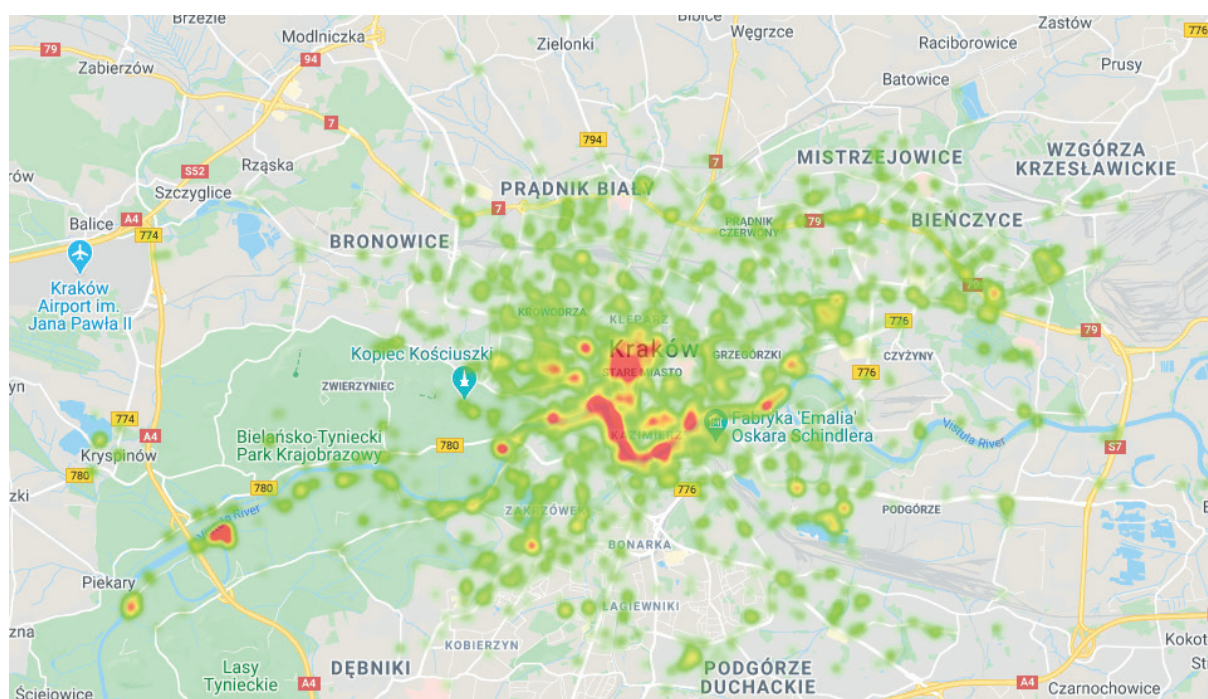


Figure 7 A heatmap showing the stopover locations of the city bike users in Cracow - a cleansed and filtered sample (background: Google Maps)

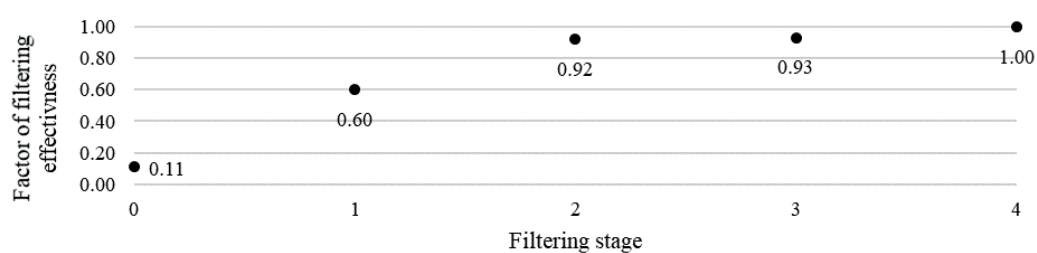


Figure 8 Factor of filtering effectiveness after each stage of filtering

a little over 6 minutes; only 25% of all the stops, however, were longer than 5 minutes 35 seconds. Table 6 shows the basic sample statistics obtained after each filtering stage. The largest drop in the number of stopovers was recorded after the first step, which involved eliminating all those within a radius of 7m from the trip origin. Further decreases were less steep, but a clear relationship could still be observed between an increase in the mean duration and the lower number of stopovers in the sample.

The stopovers that remained after the filtering process were visualized in the form of a heatmap shown in Figure 7.

Analysis of the obtained data shows that the concentration of the city bike users stopovers takes place in areas indicated by guidebooks as the most attractive in Cracow, i.e. in the Old Town area - around the Main Market Square, Old Jewish District Kazimierz and the Vistula Boulevards. A visual analysis of the heatmap shows that the areas of Blonia Common Green, the canoeing track and the monastery in Tyniec are also attractive for bike-sharing system users.

At the end of each filtering stage the filtering effectiveness factor F was checked (Figure 8). It shows that only 11% of stopovers in raw sample were not connected with the rental stations or traffic. The most visible difference is observed after the first stage - 60% of stopovers were connected with recreation or services (not with rental or traffic). After the second stage it was 92% and finally, after the whole procedure all the stopovers were not related to rental or traffic.

5 Conclusion

The article contributes to a better understanding and use of data on the city bike travel. Research thus far has

focused mainly on number and the spatial structure of such trips, looking into the various factors that affect the use of city bikes. In contrast, this study draws attention to possibility of employing data on the user stopovers for purposes of designing the bike infrastructure; it could also help to improve understanding of urban sociology, determine the patterns of urban mobility and identify the sites that are attractive for the city residents and tourists. This, in turn, may help municipal decision-makers to assess the potential of various public spaces and plan the urban development accordingly.

The proposed method has helped to use the new kind of data source to delimit attractive public spaces. The analysed example of Cracow showed that a large proportion of stopovers occurred in places widely recognized as tourist attractions, including the Vistula Boulevards and the Main Market Square. The data, however, would not have been useful without the proposed data filtering method, which discarded all the traffic-related stopovers from the sample. Using the raw data sample could have led to wrong conclusions, since for instance 82% of stopovers were connected with the bike-sharing stations. The proposed method allows to use the bike-sharing big datasets in the process of identifying the attractive public spaces. The proposed method is generally applicable to any city where the city bike data are available.

As the bike-sharing system in Cracow, Poland, case study shows, big data analytics is a technology with the potential to develop smart city services. These new data largely contribute to understanding the consumption of space within the urban tourist destinations and therefore enable to differentiate the overcrowded places from those with the potential to grow. This allows the decision-makers to imagine new ways of planning and managing towards a sustainable “smart” future.

References

- [1] FALL, M., DABROWSKI, M. Jak rowery miejskie tworzą „smart cities”. In: *Biała Księga Mobilności 2015* [online]. Warsaw: Wydawnictwo Tor, 2015, p. 118-121. Available from: <https://transport-publiczny.pl/BKM/BialaKsiegaMobilnosc2015.pdf>
- [2] LEE, P., HUNTER, W. C., CHUNG, N. Smart tourism city: developments and transformations. *Sustainability* [online]. 2020, **12**(10), 3958. ISSN 2071-1050. Available from: <https://doi.org/10.3390/su12103958>
- [3] BAKICI, T., ALMIRALL, E., WAREHAM, J. A smart city initiative: the case of Barcelona. *Journal of the Knowledge Economy* [online]. 2013, **4**(2), p. 135-148. ISSN 1868-7865, eISSN 1868-7873. Available from: <https://doi.org/10.1007/s13132-012-0084-9>
- [4] BARDI, A., MANTECCHINI, L., GRASSO, D., PAGANELLI, F., MALANDRI, C. Flexible mobile hub for e-bike sharing and cruise tourism: a case study. *Sustainability* [online]. 2019, **11**(19), 5462. ISSN 2071-1050. Available from: <https://doi.org/10.3390/su11195462>
- [5] BUHALIS, D., BOES, K., INVERSINI, A. Smart tourism destinations: ecosystems for tourism destination. *International Journal of Tourism Cities* [online]. 2016, **2**(2), p. 108-124 [accessed 2020-06-26]. ISSN 2056-5607. Available from: <https://doi.org/10.1108/IJTC-12-2015-0032>
- [6] PUCHER, J., BUEHLER, R. Cycling for everyone: lessons from Europe. *Transportation Research Record: Journal of the Transportation Research Board* [online]. 2008, **2074**(1), p. 58-65. ISSN 0361-1981, eISSN 2169-4052. Available from: <https://doi.org/10.3141/2074-08>
- [7] KUZMYAK, J. R., DILL, J. Walking and bicycling in the United States: the who, what, where, and why. *TR News* [online]. 2012, **280**, p. 4-15. ISSN 0738-6826. Available from: <http://onlinepubs.trb.org/onlinepubs/trnews/trnews280www.pdf>

- [8] PROULX, F. R., POZDNUKHOV, A. Bicycle traffic volume estimation using geographically weighted data fusion. *Journal of Transport Geography*. 2017, p. 1-14. ISSN 0966-6923.
- [9] NAIR, R., MILLER-HOOKS, E., HAMPSHIRE, R. C., BUSIC, A. Large-scale vehicle sharing systems: analysis of Velib. *International Journal of Sustainable Transportation* [online]. 2013, **7**(1), p. 85-106. Available from: <https://doi.org/10.1080/15568318.2012.660115>
- [10] FROEHLICH, J., NEUMANN J., OLIVER, N. Sensing and predicting the pulse of the city through shared bicycling. In: 21st International Joint Conference on Artificial Intelligence IJCAI-09: proceedings. Vol. 3. 2009. p. 1420-1426. Available from: <https://doi.org/10.1.1.150.4370>
- [11] ZHAO, J., FAN, W., ZHAI, X. Identification of land-use characteristics using bicycle sharing data: A deep learning approach. *Journal of Transport Geography* [online]. 2020, **82**, 102562. ISSN 0966-6923. Available from: [10.1016/j.jtrangeo.2019.102562](https://doi.org/10.1016/j.jtrangeo.2019.102562).
- [12] SHEN, L., STOPHER, P. R. Review of GPS travel survey and GPS data-processing methods. *Transport Reviews* [online]. 2014, **34**(3), p. 316-334. ISSN 0144-1647, eISSN 1464-5327. Available from: <https://doi.org/10.1080/01441647.2014.903530>
- [13] IMANI, A. F., ELURU, N., EL-GENEIDY, A., RABBAT, M., HAQ, U. How does land-use and urban form impact bicycle flows: evidence from the bicycle-1 sharing system (BIXI) in Montreal. *Journal of Transport Geography* [online]. 2014, **41**, p. 306-314. ISSN 0966-6923. Available from: <https://doi.org/10.1016/j.jtrangeo.2014.01.013>
- [14] FRADE, I., RIBEIRO, A. Bicycle sharing systems demand. *Procedia - Social and Behavioral Sciences* [online]. 2014, **111**, p. 518-527. ISSN 1877-0428. Available from: <https://doi.org/10.1016/j.sbspro.2014.01.085>
- [15] CANTELMO, G., KUCHARSKI, R., ANTONIOU, C. A low dimensional model for bike sharing demand forecasting. In: 6th International Conference on Models and Technologies for Intelligent Transportation Systems MT-ITS 2019: proceedings [online]. 2019. Available from: <https://doi.org/10.1109/MTITS.2019.8883283>
- [16] ETIENNE, C., LATIFA, O. Model-based count series clustering for bike sharing system usage mining: a case study with the Velib' system of Paris. *ACM Transactions on Intelligent Systems and Technology* [online]. 2014, **5**(3), p. 1-21. ISSN 2157-6904, eISSN 2157-6912. Available from: <https://doi.org/10.1145/2560188>
- [17] NOUSSAN, M., CARIONI, G., SANVITO, F. D., Colombo, E. Urban mobility demand profiles: time series for cars and bike-sharing use as a resource for transport and energy modelling. *Data* [online]. 2019, **4**(3), 108. eISSN 2306-5729. Available from: <https://doi.org/10.3390/data4030108>
- [18] BUCK, D., BUEHLER, R. Bike lanes and other determinants of capital bikeshare trips. Transp. In: Transportation Research Board 91st Annual Meeting: proceedings. 2012. p. 703-706.
- [19] RIXEY, R. Station-level forecasting of bikesharing ridership. *Transportation Research Record: Journal of the Transportation Research Board* [online]. 2013, **2387**(1), p. 46-55. ISSN 0361-1981, eISSN 2169-4052. Available from: <https://doi.org/10.3141/2387-06>
- [20] WANG, X., LINDSEY, G., SCHONER, J. E., HARRISON, A. Modelling bike share station activity: the effects of nearby businesses and jobs on trips to and from stations. In: TRB's 92nd Annual Meeting and Publication in the Transportation Research Record: proceedings. 2012.
- [21] TRAN, T. D., OVTRACHT, N., D'ARCIER, B. F. Modeling bike sharing system using built environment factors. *Procedia CIRP* [online]. 2015, **30**, p. 293-298. ISSN 2212-8271. Available from: <https://doi.org/10.1016/j.procir.2015.02.156>
- [22] SALON, D., CONWAY, M. W., WANG, K., ROTH, N. Heterogeneity in the relationship between biking and the built environment. *Journal of Transport and Land Use* [online]. 2019, **12**(1), p. 99-126. ISSN 1938-7849. Available from: <https://doi.org/10.5198/jtlu.2019.1350>
- [23] EREN, E., UZ, V. E. A review on bike-sharing: the factors affecting bike-sharing demand. *Sustainable Cities and Society* [online]. 2020, **54**, 101882. ISSN 2210-6707. Available from: <https://doi.org/10.1016/j.scs.2019.101882>
- [24] ZHANG, Y., THOMAS, T., BRUSSEL, M., VAN MAARSEVEEN, M. Exploring the impact of built environment factors on the use of public bikes at bike stations: case study in Zhongshan, China. *Journal of Transport Geography* [online]. 2017, **58**, p. 59-70. ISSN 0966-6923. Available from: <https://doi.org/10.1016/j.jtrangeo.2016.11.014>
- [25] CAULFIELD, B., O'MAHONY, M., BRAZIL, W., WELDON, P. Examining usage patterns of a bike-sharing scheme in a medium sized city. *Transportation Research Part A: Policy and Practice* [online]. 2017, **100**, p. 152-161. ISSN 0965-8564. Available from: <https://doi.org/10.1016/j.tra.2017.04.023>
- [26] WANG, J., LINDSEY, G. Neighborhood socio-demographic characteristics and bike share member patterns of use. *Journal of Transport Geography* [online]. 2019, **79**, 102475. ISSN 0966-6923. Available from: <https://doi.org/10.1016/j.jtrangeo.2019.102475>
- [27] YAN, Q., GAO, K., SUN, L., SHAO, M. Spatio-temporal usage patterns of dockless bike-sharing service linking to a metro station: a case study in Shanghai, China. *Sustainability* [online]. 2020, **12**(3), 851. eISSN 2071-1050. Available from: <https://doi.org/10.3390/su12030851>
- [28] WANG, Z., CHENG, L., LI, Y., LI, Z. Spatiotemporal characteristics of bike-sharing usage around rail transit stations: evidence from Beijing, China. *Sustainability* [online]. 2020, **12**(4), 1299. eISSN 2071-1050. Available from: <https://doi.org/10.3390/su12041299>

- [29] KOERBITZ, W., ONDER, I., HUBMANN-HAIDVOGEL, A. C. Identifying tourist dispersion in Austria by digital footprints. In: *Information and Communication Technologies in Tourism 2013: proceedings* [online]. Berlin Heidelberg: Springer, 2013. ISBN 978-3-642-36308-5, eISBN 978-3-642-36309-2, p. 495-506. Available from: https://doi.org/10.1007/978-3-642-36309-2_42
- [30] MIAH, S. J., VU, H. Q., GAMMACK, J., McGRATH, M. A big data analytics method for tourist behaviour analysis. *Information and Management* [online]. 2017, **54**(6), p. 771-785. ISSN 0378-7206. Available from: <https://doi.org/10.1016/j.im.2016.11.011>
- [31] HASNAT, M. M., HASAN, S. Identifying tourists and analyzing spatial patterns of their destinations from location-based social media data. *Transportation Research Part C: Emerging Technologies* [online]. 2018, **96**, p. 38-54. ISSN 0968-090X. Available from: <https://doi.org/10.1016/j.trc.2018.09.006>
- [32] BRINKMANN, J. *Active balancing of bike sharing systems* [online]. Berlin Heidelberg: Springer, 2020. ISBN 978-3-030-35011-6, eISBN 978-3-030-35012-3. Available from: <https://doi.org/10.1007/978-3-030-35012-3>
- [33] NAUMOV, V., BANET, K. Estimating parameters of demand for trips by public bicycle system using GPS data. In: *Smart and Green Solutions for Transport Systems TSTP 2019: proceedings* [online]. Advances in Intelligent Systems and Computing. Vol. 1091. Cham: Springer, 2020. ISBN 978-3-030-35542-5, eISBN 978-3-030-35543-2. Available from: https://doi.org/10.1007/978-3-030-35543-2_17
- [34] Cracow-Balice. Historical measurement data of the Polish Institute of Meteorology and Water Management / Cracow-Balice. Historyczne dane pomiarowe IMGW (in Polish) [online] [accessed 2020-04-19]. Available from: <https://meteomodel.pl/dane/historyczne-dane-pomiarowe/?data=2017-06-07&rodzaj=st&imgwid=350190566&dni=60&ord=desc>

Author guidelines

- All papers have to deal with the topic of transport and be submitted strictly within one of the listed subtopics. Please, refer to list of topics and subtopics here and indicate it clearly when submitting your paper.
- Submitted papers must be unpublished and must not be currently under review for any other publication.
- Manuscripts written in good English must include abstract and keywords also written in English. The abstract should not exceed 10 lines. Please provide minimum three up to maximum seven keywords which express the principal topics of the paper.
- Submitted manuscripts should not exceed 20 pages including figures and graphs.
- Submission should be sent by e-mail – as an attachment – to the following address: komunikacie@uniza.sk.
- The author's exact mailing address, full names, E-mail address, telephone or fax number, the name and address of the organization and workplace (also written in English) must be enclosed.
- For all manuscripts a double-blind peer review by at least two independent reviewers and language correction is mandatory.
- After reviewing and incorporating the editor's comments, the final draft (before printing) will be sent to authors for final review and minor adjustments.

The full author guidelines are available at:
<http://komunikacie.uniza.sk/index.php/communications/guidelines>

Editor-in-chief:
Branislav HADZIMA - SK

Associate editor:
Jakub SOVIAR - SK

Executive editor:
Sylvia DUNDEKOVA - SK

Honorary members:
Otakar BOKUVKA - SK
Jan COREJ - SK (in memoriam)
Milan DADO - SK
Pavel POLEDNAK - CZ

Editorial board:
Greg BAKER - NZ
Abdelhamid BOUCHAIR - FR
Pavel BRANDSTETTER - CZ
Mario CACCIATO - IT
Jan CELKO - SK
Andrew COLLINS - GB
Samo DROBNE - SI
Erdogan H. EKIZ - MA
Michal FRIVALDSKY - SK
Juraj GERLICI - SK
Vladimir N. GLAZKOV - RU
Ivan GLESK - GB
Mario GUAGLIANO - IT
Andrzej CHUDZIKIEWICZ - PL
Jaroslav JANACEK - SK
Zdenek KALA - CZ
Antonin KAZDA - SK
Michal KOHANI - SK
Jozef KOMACKA - SK
Matyas KONIORCZYK - HU
Tomas LOVECEK - SK
Frank MARKERT - DK
Jaroslav MAZUREK - SK
Marica MAZUREKOVA - SK
Vladimir MOZER - CZ
Jorge Carvalho PAIS - PT
Peter POCTA - SK
Maria Angeles Martin PRATS - ES
Pavol RAFAJDUS - SK
Che-Jen SU - TW
Giacomo SCELBA - IT
Janka SESTAKOVA - SK
Eva SVENTEKOVA - SK
Eva TILLOVA - SK
Anna TOMOVA - SK
Franco Bernelli ZAZZERA - IT

Address of the editorial office:
University of Zilina
EDIS – Publishing House
Univerzitná 8215/1
010 26 Zilina, Slovakia

E-mail: komunikacie@uniza.sk

Individual issues of the journal can be found on:
<http://komunikacie.uniza.sk>

Each paper was reviewed by two reviewers.

Journal is excerpted in **SCOPUS** and **EBSCO host**.

Published quarterly by University of Zilina
in EDIS – Publishing House of University of Zilina

Registered No: EV 3672/09

ISSN (print version) 1335-4205
ISSN (online version) 2585-7878

ICO 00397 563

April 2021